

# Pulsar Discoveries by Volunteer Distributed Computing

and the Strongest Continuous Gravitational Wave Signal

Von der Fakultät für Mathematik und Physik  
der Gottfried Wilhelm Leibniz Universität Hannover  
zur Erlangung des Grades

**Doktor der Naturwissenschaften**  
**Dr. rer. nat.**

genehmigte Dissertation  
von

**Dipl.-Phys. Benjamin Knispel**  
geboren am 23. Februar 1983 in Großburgwedel

2011

Referent: Herr Prof. Dr. Bruce Allen  
Korreferent: Herr Prof. Dr. Michael Kramer  
Tag der Promotion: 04. Juli 2011

*"Those waves will open up to us many vistas unknown to man, and several unknown to anything we consider organic life. (...) We shall see these things, and other things which no breathing creature has yet seen. We shall overleap time, space, and dimensions, and without bodily motion peer to the bottom of creation."*

H. P. Lovecraft, From Beyond



# Abstract

Neutron stars are the endpoints of stellar evolution and one of the most compact forms of matter in the universe. They can be observed as radio pulsars and are promising sources for the emission of continuous gravitational waves. Discovering new radio pulsars in tight binary orbits offers the opportunity to conduct very high precision tests of General Relativity and to further our understanding of neutron star structure and matter at super-nuclear densities. The direct detection of gravitational waves would validate Einstein's theory of Relativity and open a new window to the universe by offering a novel astronomical tool.

This thesis addresses both of these scientific fields: the first fully coherent search for radio pulsars in tight, circular orbits has been planned, set up and conducted in the course of this thesis. Two unusual radio pulsars, one of them in a binary system, have been discovered. The other half of this thesis is concerned with the simulation of the Galactic neutron star population to predict their emission of continuous gravitational waves. First realistic statistical upper limits on the strongest continuous gravitational-wave signal and detection predictions for realistic all-sky blind searches have been obtained.

The data from a large-scale pulsar survey with the 305-m Arecibo radio telescope were searched for signals from radio pulsars in binary orbits. The massive amount of computational work was done on hundreds of thousands of computers volunteered by members of the general public through the distributed computing project Einstein@Home. The newly developed analysis pipeline searched for pulsar spin frequency below 250 Hz and for orbital periods as short as 11 min. The structure of the search pipeline consisting of data preparation, data analysis, result post-processing, and set-up of the pipeline components is presented in detail.

The first radio pulsar, discovered with this search, PSR J2007+2722, is an isolated radio pulsar, likely from a double neutron star system disrupted by the second supernova. We present discovery and initial characterisation using observations from five of the largest radio telescopes worldwide. Only a dozen similar systems were previously known.

The second discovered radio pulsar, PSR J1952+2630, is in a 9.4-hr orbit with most likely a massive white dwarf of at least  $0.95 M_{\odot}$ . We characterise its orbit by analysis of the apparent spin period changes. This pulsar most likely belongs to the very rare class of intermediate-mass binary pulsars, from which only five systems were previously known. It is a promising target for the future measurement of relativistic effects.

In the second half of this thesis, the emission of continuous gravitational waves from a Galactic population of neutron stars is studied. For the first time, realistic estimates of the statistical upper limit of the expected gravitational wave signal are obtained, improving previous estimates by about a factor of six. The simulation is used to obtain for the first time detectability predictions for these objects with ground based gravitational wave detectors and realistic blind searches. It is also shown how to improve possible searches by maximising the number of detections for a fixed amount of computation cycles.

**keywords:** radio pulsars, data analysis, gravitational waves



# Kurzfassung

Neutronensterne sind die Endzustände stellarer Evolution und stellen eine der kompaktesten Materieformen im Universum dar. Sie sind als Radiopulsare beobachtbar und gelten als vielversprechende Quellen für die Abstrahlung kontinuierlicher Gravitationswellen. Die Entdeckung neuer Radiopulsare in engen Doppelsternsystemen bietet die Möglichkeit, hochgenaue Tests der Allgemeinen Relativitätstheorie durchzuführen und unser Verständnis des Neutronenaufbaus und der Materie bei supernuklearen Dichten zu erweitern. Die direkte Messung von Gravitationswellen würde Einsteins Relativitätstheorie bestätigen und ein neues Beobachtungsfenster zum Universum aufstoßen.

Diese Arbeit beschäftigt sich mit beiden erwähnten Wissenschaftsbereichen: die erste, vollkommen kohärente Suche nach Pulsaren in engen Kreisbahnen wurde im Rahmen dieser Arbeit geplant, aufgebaut und durchgeführt. Zwei ungewöhnliche Radiopulsare wurden entdeckt, von denen sich einer in einem Binärsystem befindet. Die zweite Hälfte der Arbeit beschäftigt sich mit der Simulation der galaktischen Neutronensternpopulation, um deren Abstrahlung kontinuierlicher Gravitationswellen zu untersuchen. Erste realistische obere Grenzen für das statistisch stärkste kontinuierliche Gravitationswellensignal und Detektionsvorhersagen für realistische Gesamthimmelsuchen wurden berechnet.

Daten einer Pulsardurchmusterung mit dem 305-m Arecibo-Radioteleskop wurden nach Binärpulsaren durchsucht. Der gewaltige Rechenaufwand wird von hunderttausenden Computern erbracht, die Freiwillige über das verteilte Rechenprojekt Einstein@Home zur Verfügung stellen. Die Analysemethode suchte nach Pulsaren mit Frequenzen unter 250 Hz und Bahnperioden länger als 11 min. Der Aufbau der Suche aus Datenvorbereitung, -analyse, Analyse der Ergebnisse, und die einzelnen Komponenten werden dargestellt.

Der zuerst entdeckte Radiopulsar, PSR J2007+2722, ist ein isolierter Radiopulsar, vermutlich hervorgegangen aus einem Doppelneutronensternsystem, das von der zweiten Supernova zerrissen wurde. Wir präsentieren die Entdeckung und eine erste Charakterisierung mit fünf der weltweit größten Radioteleskope. Nur zwölf ähnliche Radiopulsare waren zuvor bekannt.

Der als zweites entdeckte Pulsar, PSR J1952+2630, befindet sich auf einer 9.4-Stunden-Bahn mit höchstwahrscheinlich einem massereichen Weißen Zwerg von mindestens  $0.95 M_{\odot}$ . Die Bahn wird durch Analyse der scheinbaren Drehfrequenz charakterisiert. Dieser Pulsar gehört zu einer seltenen Klasse von Binärpulsaren, von denen zuvor nur fünf andere Objekte bekannt waren. Er ist ein vielversprechendes Ziel für die Messung relativistischer Effekte.

In der zweiten Hälfte der Arbeit wird die Abstrahlung kontinuierlicher Gravitationswellen von einer galaktischen Neutronensternpopulation betrachtet. Zum ersten Mal werden realistische Abschätzungen des statistisch stärksten kontinuierlichen Gravitationswellensignals errechnet, die um einen Faktor sechs unter vorherigen Werten liegen. Mit der Simulation erhalten wir zum ersten Mal realistische Detektionsvorhersagen für realistische Gesamthimmelsuchen mit irdischen Gravitationswellendetektoren. Außerdem zeigen wir auf, wie mögliche Suchen durch die Maximierung der Detektionsanzahl für gegebenen Rechenaufwand verbessert werden können.

---

**Schlagworte:** Radiopulsare, Datenanalyse, Gravitationswellen

# Contents

|   |            |
|---|------------|
| <b>Abstract</b>   | <b>i</b>   |
| <b>Kurzfassung</b>  | <b>iii</b> |
| <b>Contents</b>   | <b>v</b>   |
| <b>List of Figures</b>                                      | <b>xi</b>  |
| <b>List of Tables</b>                                       | <b>1</b>   |
| <b>1 Synopsis</b>   | <b>3</b>   |
| 1.1 Main results and structure of the thesis . . . . .      | 3          |
| 1.1.1 Main results . . . . .                                | 3          |
| 1.1.2 Structure of the thesis . . . . .                     | 4          |
| 1.2 List of publications . . . . .                          | 5          |
| <b>2 Introduction</b>                                       | <b>7</b>   |
| 2.1 Pulsars . . . . .                                       | 7          |
| 2.1.1 Neutron stars . . . . .                               | 8          |
| 2.1.2 The lighthouse model . . . . .                        | 10         |
| 2.1.3 Searching for pulsars . . . . .                       | 12         |
| 2.1.4 A short history of pulsars . . . . .                  | 15         |
| 2.2 Pulsar spin period evolution . . . . .                  | 20         |
| 2.2.1 Spin-down luminosity . . . . .                        | 21         |
| 2.2.2 The characteristic age . . . . .                      | 22         |
| 2.2.3 Magnetic field strength . . . . .                     | 22         |
| 2.3 Magnetosphere, beam geometry and polarisation . . . . . | 23         |
| 2.3.1 Goldreich-Julian model . . . . .                      | 23         |
| 2.3.2 Radio emission from acceleration gaps . . . . .       | 26         |
| 2.3.3 Beam geometry . . . . .                               | 27         |
| 2.3.4 Rotating vector model . . . . .                       | 30         |
| 2.4 Pulse broadening in the interstellar medium . . . . .   | 31         |
| 2.4.1 Dispersion . . . . .                                  | 32         |
| 2.4.2 Multi-path propagation . . . . .                      | 34         |
| 2.5 The Galactic population of pulsars . . . . .            | 34         |
| 2.5.1 Spatial distribution of Galactic pulsars . . . . .    | 34         |
| 2.5.2 The $P-\dot{P}$ diagram . . . . .                     | 35         |
| 2.5.3 Isolated young pulsars . . . . .                      | 37         |
| 2.5.4 Recycled pulsars . . . . .                            | 37         |
| 2.5.5 X-ray pulsars . . . . .                               | 38         |

|          |  |           |
|----------|--|-----------|
| 2.5.6    | Isolated and binary pulsars . . . . .                                      | 38        |
| 2.6      | Neutron stars as gravitational-wave sources . . . . .                      | 38        |
| 2.6.1    | Gravitational-wave emission mechanisms . . . . .                           | 40        |
| 2.6.2    | Gravitars . . . . .  | 43        |
| 2.6.3    | Simulating the galactic gravitar population . . . . .                      | 43        |
| <b>3</b> | <b>Einstein@Home Radio Pulsar Search</b>                                   | <b>45</b> |
| 3.1      | Overview and context . . . . .   | 45        |
| 3.2      | PALFA survey . . . . .   | 45        |
| 3.2.1    | Data acquisition . . . . .   | 47        |
| 3.2.2    | Sky coverage . . . . .   | 47        |
| 3.2.3    | Observation setup and data volume . . . . .                                | 48        |
| 3.2.4    | Data storage and movement . . . . .  | 51        |
| 3.2.5    | Data analysis . . . . .  | 51        |
| 3.3      | Volunteer distributed computing . . . . .                                  | 53        |
| 3.3.1    | Constraints on suitable problems . . . . .                                 | 54        |
| 3.3.2    | GPUs and future volunteer computing . . . . .                              | 56        |
| 3.3.3    | Einstein@Home . . . . .  | 56        |
| 3.3.4    | Einstein@Home’s search for radio pulsars in tight binaries . . . . .       | 58        |
| 3.3.5    | The Berkeley Open Infrastructure for Network Computing . . . . .           | 59        |
| 3.3.6    | BOINC server side and client side . . . . .                                | 60        |
| 3.3.7    | Validation workflow . . . . .  | 64        |
| 3.4      | Phase model and parameter space . . . . .                                  | 64        |
| 3.4.1    | The fully coherent search . . . . .  | 64        |
| 3.4.2    | Phase model for circular orbits . . . . .                                  | 65        |
| 3.4.3    | Parameter space description . . . . .                                      | 66        |
| 3.4.4    | Constraining the parameter space for Einstein@Home . . . . .               | 67        |
| 3.4.5    | Justification of the circular approximation . . . . .                      | 71        |
| 3.4.6    | Parameter space metric . . . . .   | 72        |
| 3.4.7    | Isomismatch surfaces . . . . .   | 75        |
| 3.5      | Orbital parameter template bank construction . . . . .                     | 77        |
| 3.5.1    | Random template banks . . . . .  | 78        |
| 3.5.2    | Determinant of the projected metric for the Einstein@Home search . . . . . | 82        |
| 3.5.3    | Stochastic template banks . . . . .  | 82        |
| 3.5.4    | Efficient parallel construction of stochastic template banks . . . . .     | 84        |
| 3.5.5    | The Einstein@Home template banks . . . . .                                 | 88        |
| 3.6      | Einstein@Home radio pulsar search overview . . . . .                       | 92        |
| 3.7      | Data preparation on the server side . . . . .                              | 97        |
| 3.7.1    | Data preprocessing and data format conversion . . . . .                    | 97        |
| 3.7.2    | De-dispersion . . . . .  | 99        |
| 3.7.3    | Down-sampling . . . . .  | 101       |
| 3.7.4    | Data type conversion . . . . .   | 104       |
| 3.8      | Client search code . . . . .   | 105       |
| 3.8.1    | Data type conversion . . . . .   | 105       |
| 3.8.2    | Spectral normalisation and RFI mitigation . . . . .                        | 107       |
| 3.8.3    | Time domain demodulation . . . . .   | 110       |
| 3.8.4    | Fourier analysis . . . . .   | 112       |
| 3.8.5    | Harmonic summing . . . . .   | 118       |

|          |  |            |
|----------|--|------------|
| 3.8.6    | Einstein@Home search Fourier techniques . . . . .          | 121        |
| 3.8.7    | Detection statistic . . . . .                              | 122        |
| 3.8.8    | GPU search code . . . . .                                  | 127        |
| 3.8.9    | Result file format . . . . .                               | 129        |
| 3.9      | Validation . . . . .                                       | 130        |
| 3.10     | Post-processing . . . . .                                  | 131        |
| 3.10.1   | Result collection . . . . .                                | 132        |
| 3.10.2   | Overview plots . . . . .                                   | 132        |
| 3.10.3   | Candidate number reduction . . . . .                       | 136        |
| 3.10.4   | Candidate refinement . . . . .                             | 141        |
| 3.10.5   | Total amount of data analysed . . . . .                    | 142        |
| 3.11     | Mini mock data challenge . . . . .                         | 142        |
| <b>4</b> | <b>Discovery of PSR J2007+2722</b>                         | <b>147</b> |
| 4.1      | Overview and context . . . . .                             | 147        |
| 4.2      | Discovery of PSR J2007+2722 . . . . .                      | 148        |
| 4.3      | Improving sky position accuracy . . . . .                  | 150        |
| 4.3.1    | Gridding observations with the Arecibo telescope . . . . . | 152        |
| 4.3.2    | Gridding observations with the WSRT . . . . .              | 152        |
| 4.3.3    | Imaging and NVSS Catalog Identification . . . . .          | 152        |
| 4.3.4    | VLA archival data . . . . .                                | 153        |
| 4.3.5    | High-Energy and optical counterparts . . . . .             | 154        |
| 4.3.6    | Spectrum from multifrequency GBT observations . . . . .    | 155        |
| 4.4      | Obtaining the spin parameters . . . . .                    | 156        |
| 4.5      | Emission geometry . . . . .                                | 157        |
| 4.5.1    | Rotating vector model . . . . .                            | 157        |
| 4.5.2    | Polarisation data reduction . . . . .                      | 158        |
| 4.5.3    | Three possible polarisation models . . . . .               | 160        |
| 4.5.4    | Results for the three models . . . . .                     | 160        |
| 4.6      | Future Work . . . . .                                      | 161        |
| <b>5</b> | <b>Discovery of PSR J1952+2630</b>                         | <b>165</b> |
| 5.1      | Overview and Context . . . . .                             | 165        |
| 5.2      | Discovery of PSR J1952+2630 . . . . .                      | 165        |
| 5.3      | Follow-up observations . . . . .                           | 167        |
| 5.4      | Spin period-based orbital solution . . . . .               | 170        |
| 5.4.1    | First estimates of the orbital parameters . . . . .        | 171        |
| 5.4.2    | Refining the orbital parameters . . . . .                  | 172        |
| 5.4.3    | Markov Chain Monte Carlo sampling . . . . .                | 173        |
| 5.4.4    | Upper limit on orbital eccentricity . . . . .              | 173        |
| 5.5      | Discussion . . . . .                                       | 174        |
| 5.6      | Conclusions and future work . . . . .                      | 178        |
| <b>6</b> | <b>The Strongest Continuous Gravitational Wave Signal</b>  | <b>181</b> |
| 6.1      | Overview and context . . . . .                             | 181        |
| 6.2      | Blandford’s argument: an analytic description . . . . .    | 182        |
| 6.2.1    | Frequency evolution and a first analysis . . . . .         | 182        |
| 6.2.2    | Restating Blandford’s argument . . . . .                   | 184        |

# CONTENTS

---

|          |  |            |
|----------|--|------------|
| 6.2.3    | A natural limit to the result . . . . .                            | 187        |
| 6.3      | Numerical model . . . . .  | 188        |
| 6.3.1    | Galactic potential and equations of motion . . . . .               | 188        |
| 6.3.2    | Initial spatial distribution . . . . .                             | 189        |
| 6.3.3    | Initial velocity . . . . .   | 190        |
| 6.3.4    | Initial period distribution . . . . .                              | 192        |
| 6.3.5    | Coding and implementation . . . . .                                | 192        |
| 6.4      | Results . . . . .  | 192        |
| 6.4.1    | Frequency distributions . . . . .                                  | 192        |
| 6.4.2    | Spatial steady-state distribution and timescales . . . . .         | 194        |
| 6.4.3    | Scaling dimension of the spatial distribution . . . . .            | 195        |
| 6.5      | The strongest continuous gravitational-wave signal . . . . .       | 196        |
| 6.5.1    | Numerical method . . . . .   | 197        |
| 6.5.2    | Maximum expected amplitude . . . . .                               | 197        |
| 6.5.3    | Remarks on an upper limit . . . . .                                | 199        |
| 6.6      | Conclusions . . . . .  | 202        |
| <b>7</b> | <b>Gravitar Population Modelling</b>                               | <b>203</b> |
| 7.1      | Overview and context . . . . .                                     | 203        |
| 7.2      | Methods . . . . .  | 204        |
| 7.2.1    | Galactic potentials and equations of motion . . . . .              | 204        |
| 7.2.2    | Initial velocity . . . . .   | 206        |
| 7.2.3    | Initial spatial and age distribution . . . . .                     | 206        |
| 7.2.4    | Coding and implementation . . . . .                                | 207        |
| 7.2.5    | Frequency evolution . . . . .                                      | 208        |
| 7.2.6    | Initial frequency distribution . . . . .                           | 209        |
| 7.2.7    | Ellipticity distribution . . . . .                                 | 209        |
| 7.2.8    | Analytical frequency distribution evolution . . . . .              | 210        |
| 7.2.9    | Search sensitivity modelling . . . . .                             | 212        |
| 7.2.10   | Simulated search sensitivity . . . . .                             | 215        |
| 7.3      | Results . . . . .  | 216        |
| 7.3.1    | Expected number of detections . . . . .                            | 216        |
| 7.3.2    | Sky maps . . . . .   | 217        |
| 7.3.3    | Age distributions . . . . .  | 219        |
| 7.3.4    | Distance distributions . . . . .                                   | 224        |
| 7.3.5    | Frequency distributions . . . . .                                  | 225        |
| 7.4      | Optimisation of the search strategy . . . . .                      | 227        |
| 7.4.1    | General description . . . . .                                      | 228        |
| 7.4.2    | Optimising cost-efficiency . . . . .                               | 228        |
| 7.4.3    | Analytical toy model . . . . .                                     | 230        |
| 7.4.4    | Example application to the simulated gravitar population . . . . . | 231        |
| 7.5      | Conclusions . . . . .  | 235        |
| <b>8</b> | <b>Technical details</b>   | <b>239</b> |
| 8.1      | Zap list for the Einstein@Home radio pulsar search . . . . .       | 239        |
| 8.2      | Commonly used probability distributions . . . . .                  | 243        |
| 8.2.1    | Gaussian distribution . . . . .                                    | 243        |
| 8.2.2    | Normalised power . . . . .   | 243        |

---

|                             |  |            |
|-----------------------------|--|------------|
| 8.2.3                       | Chi-square distribution . . . . .                        | 244        |
| 8.2.4                       | Chi-square distribution fact sheet . . . . .             | 249        |
| 8.3                         | Beam geometry and Goldreich-Julian model . . . . .       | 250        |
| 8.3.1                       | Beam geometry . . . . .                                  | 250        |
| 8.3.2                       | Goldreich-Julian model . . . . .                         | 251        |
| 8.4                         | Doppler modulation in elliptical orbits . . . . .        | 254        |
| 8.5                         | Derivation of the metric from the phase model . . . . .  | 256        |
| 8.6                         | The full parameter space metric . . . . .                | 258        |
| 8.7                         | The frequency-projected parameter space metric . . . . . | 259        |
| 8.8                         | Polynomial phase models . . . . .                        | 262        |
| 8.8.1                       | Expansion up to cubic order in $t$ . . . . .             | 262        |
| 8.8.2                       | Alternative phase model . . . . .                        | 263        |
| 8.8.3                       | Acceleration phase model . . . . .                       | 264        |
| 8.8.4                       | Acceleration + jerk phase model . . . . .                | 265        |
| 8.8.5                       | Parameter space of $a$ and $j$ . . . . .                 | 265        |
| 8.8.6                       | Signal recovery with polynomial phase models . . . . .   | 266        |
| <b>Bibliography</b>         |  | <b>269</b> |
| <b>Acknowledgements</b>     |  | <b>285</b> |
| <b>Curriculum Vitae</b>     |  | <b>287</b> |
| <b>List of publications</b> |  | <b>289</b> |



# List of Figures

|      |   |     |
|------|---|-----|
| 2.1  | The pulsar “toy model” . . . . .  | 11  |
| 2.2  | Variety of pulse profiles . . . . .   | 12  |
| 2.3  | Schematic of the signal pathway for radio pulsar observation . . . . .              | 13  |
| 2.4  | Geometry of beamed pulsar emission . . . . .  | 28  |
| 2.5  | Schematics of beam structure models . . . . .                                       | 29  |
| 2.6  | Schematic of the rotating vector model . . . . .                                    | 31  |
| 2.7  | Dispersion in the interstellar medium . . . . .                                     | 33  |
| 2.8  | Positions of the known Galactic pulsars projected onto the Galactic plane . . . . . | 35  |
| 2.9  | The $P$ - $\dot{P}$ diagram . . . . .   | 36  |
| 2.10 | The schematic evolution of pulsars . . . . .  | 39  |
|      |   |     |
| 3.1  | View of the Arecibo telescope . . . . .   | 46  |
| 3.2  | The “Arecibo sky” . . . . .   | 49  |
| 3.3  | Tiling strategy for the PALFA survey . . . . .                                      | 50  |
| 3.4  | The structure of the BOINC server side . . . . .                                    | 61  |
| 3.5  | Pulsar in a circular orbit . . . . .  | 67  |
| 3.6  | Constraining the Einstein@Home orbital parameter space . . . . .                    | 69  |
| 3.7  | Probability of detection as a function of the masses . . . . .                      | 71  |
| 3.8  | Slices through isomismatch surfaces at $\psi = 0$ . . . . .                         | 76  |
| 3.9  | Square root of the projected metric determinant . . . . .                           | 83  |
| 3.10 | Efficient parallelisation of stochastic template bank generation . . . . .          | 85  |
| 3.11 | Illustration of the initial pruning and the merging process . . . . .               | 86  |
| 3.12 | The Einstein@Home orbital template bank . . . . .                                   | 90  |
| 3.13 | Template bank test results for circular orbits . . . . .                            | 91  |
| 3.14 | Template bank test results for $e = 10^{-4}$ and $e = 10^{-3}$ . . . . .            | 93  |
| 3.15 | Template bank test results for $e = 10^{-2}$ and $e = 2.5 \times 10^{-2}$ . . . . . | 94  |
| 3.16 | Template bank test results for $e = 5 \times 10^{-2}$ and $e = 10^{-1}$ . . . . .   | 95  |
| 3.17 | Overview of the processing steps in the Einstein@Home search . . . . .              | 97  |
| 3.18 | Schematic of the de-dispersion . . . . .  | 99  |
| 3.19 | Einstein@Home trial DMs . . . . .   | 101 |
| 3.20 | Multi-path scattering time scale . . . . .  | 102 |
| 3.21 | Illustration of the down-sampling . . . . .   | 103 |
| 3.22 | Main steps of the search code . . . . .   | 106 |
| 3.23 | Schematic of time-domain resampling . . . . .                                       | 112 |
| 3.24 | Illustration of scalloping . . . . .  | 115 |
| 3.25 | Illustration of mean-padding . . . . .  | 117 |
| 3.26 | Illustration of DFT sensitivity and mean padding . . . . .                          | 119 |
| 3.27 | Illustration of comb of harmonics . . . . .   | 120 |
| 3.28 | Chi-square probability distribution functions of $2\mathcal{P}$ . . . . .           | 124 |

## LIST OF FIGURES

---

|      |   |     |
|------|---|-----|
| 3.29 | Significance as a function of summed harmonic power . . . . .   | 125 |
| 3.30 | Relative error of the asymptotic significance . . . . .   | 126 |
| 3.31 | Illustration of thresholds on $2\mathcal{P}_\Sigma$ . . . . .   | 128 |
| 3.32 | Overview plot fro quick result inspection . . . . .   | 134 |
| 3.33 | Use of hyper-surface coordinates for plotting . . . . .   | 136 |
| 3.34 | Candidate consolidation with the top-down algorithm . . . . .   | 139 |
| 3.35 | Candidate consolidation with the clustering algorithm . . . . .                                       | 140 |
| 3.36 | Example result plots from the MDC . . . . .   | 145 |
|      |   |     |
| 4.1  | Einstein@Home discovery plot for J2007+2722 and its pulse profile . . . . .                           | 148 |
| 4.2  | Einstein@Home result overview plots from the J2007+2722 discovery beam . . . . .                      | 149 |
| 4.3  | PSR J2007+2722 diagnostic PRESTO plots from the discovery observation . . . . .                       | 151 |
| 4.4  | Gridding observations with the WSRT . . . . .   | 153 |
| 4.5  | WSRT Imaging and VLA archival data . . . . .  | 154 |
| 4.6  | VLA archival data at 4.86 GHz . . . . .   | 155 |
| 4.7  | Spectrum of PSR J2007+2722 . . . . .  | 157 |
| 4.8  | Polarisation measurement of PSR J2007+2722 . . . . .  | 159 |
| 4.9  | RVM fit to the model without further assumptions . . . . .  | 162 |
| 4.10 | RVM fit to the model with OPM in the second pulse peak . . . . .                                      | 163 |
| 4.11 | RVM fit to the model with full phase wrap between the pulse peaks . . . . .                           | 164 |
|      |   |     |
| 5.1  | Einstein@Home result overview plots from the J1952+2630 discovery beam . . . . .                      | 168 |
| 5.2  | PSR J1952+2630 diagnostic PRESTO plots from the discovery observation . . . . .                       | 169 |
| 5.3  | Folded pulse profile of PSR J1952+2630 . . . . .  | 170 |
| 5.4  | Measured barycentric spin periods and derived barycentric accelerations . . . . .                     | 172 |
| 5.5  | Histograms of pulsar parameter posterior distributions . . . . .                                      | 174 |
| 5.6  | Scatter plots of pulsar parameter posterior distributions . . . . .                                   | 175 |
| 5.7  | Spin period residuals for the orbital model. . . . .  | 177 |
| 5.8  | Histograms of the eccentricity posterior distribution . . . . .                                       | 178 |
| 5.9  | Scatter plots of the two-dimensional eccentricity posterior distributions . . . . .                   | 179 |
| 5.10 | Measurable Shapiro delay amplitude for J1952+2630 . . . . .   | 180 |
|      |   |     |
| 6.1  | Initial spatial gravitar distributions . . . . .  | 191 |
| 6.2  | The distribution in frequency after $\bar{t} = 13.6$ Gyrs for varying ellipticity . . . . .           | 193 |
| 6.3  | The distribution in frequency space after $\bar{t} = 13.6$ Gyrs for $\varepsilon = 10^{-7}$ . . . . . | 194 |
| 6.4  | Distribution of gravitars as a function of radial distance from the Sun . . . . .                     | 195 |
| 6.5  | Local scaling dimension $D(r)$ of the spatial gravitar distribution . . . . .                         | 196 |
| 6.6  | Maximum strain amplitude of gravitational waves from Galactic gravitars . . . . .                     | 198 |
| 6.7  | Expected distance to the strongest gravitar . . . . .   | 199 |
|      |   |     |
| 7.1  | Schematic of the Gould belt model . . . . .   | 208 |
| 7.2  | The evolved frequency distribution for fixed ages $t$ . . . . .                                       | 212 |
| 7.3  | Sensitivity curves $h_{\min}(f)$ . . . . .  | 215 |
| 7.4  | Part I of the most optimistic sky density maps . . . . .  | 220 |
| 7.5  | Part II of the most optimistic sky density maps . . . . .   | 221 |
| 7.6  | Part III of the most optimistic sky density maps . . . . .  | 222 |
| 7.7  | Detectability distribution as a function of the source age . . . . .                                  | 223 |
| 7.8  | Detectability distribution as a function of the source distance . . . . .                             | 224 |
| 7.9  | Distribution of detectable sources in frequency ( $\bar{\varepsilon} = 10^{-6}$ ) . . . . .           | 226 |

---

|      |  |     |
|------|--|-----|
| 7.10 | Distribution of detectable sources in frequency ( $\bar{\epsilon} = 10^{-7}$ ) . . . . . | 227 |
| 7.11 | Toymodel distribution function and cost function . . . . .                               | 231 |
| 7.12 | Toy model fractional number of detections vs. fractional search costs . . . . .          | 232 |
| 7.13 | Example inexpensive semi-targeted gravitar search . . . . .                              | 234 |
| 7.14 | Frequency bands for an inexpensive semi-targeted gravitar search . . . . .               | 236 |
| 8.1  | Chi-square propability distribution functions . . . . .                                  | 249 |
| 8.2  | Parametrisation of elliptic motion . . . . .   | 254 |
| 8.3  | Mapping templates from the full orbital search $a$ - $j$ space . . . . .                 | 266 |
| 8.4  | Signal recovery from pulsars in circular orbits with polynomial searches. . . . .        | 267 |



# List of Tables

|     |   |     |
|-----|---|-----|
| 3.1 | Injected and recovered signals in the MDC . . . . .                           | 143 |
| 4.1 | Measured flux densities for PSR J2007+2722 . . . . .                          | 156 |
| 4.2 | The best-fitting rotating vector model parameters . . . . .                   | 161 |
| 5.1 | PSR J1952+2630 Parameters from a Spin-period based Analysis . . . . .         | 176 |
| 6.1 | Mass and scale parameters for the Galactic potential . . . . .                | 189 |
| 6.2 | Maximum values for the gravitational-wave amplitude . . . . .                 | 200 |
| 7.1 | Parameters of the Galactic gravitational potential $\Phi_1 (R, z)$ . . . . .  | 205 |
| 7.2 | Parameters for the Galactic gravitational potential $\Phi_2 (R, z)$ . . . . . | 205 |
| 7.3 | The value of $\tau$ . . . . .   | 210 |
| 7.4 | Expected detection number (lognormal spin frequency distribution) . . . . .   | 218 |
| 7.5 | Expected detection number (power-law spin frequency distribution) . . . . .   | 218 |
| 8.1 | Zap list for the Einstein@Home radio pulsar search . . . . .                  | 239 |
| 8.2 | Chi-square distribution fact sheet . . . . .                                  | 250 |



# 1

## Synopsis

### 1.1 Main results and structure of the thesis

---

This thesis reports new work and discoveries in two main scientific fields: a) two radio pulsar discoveries by novel search techniques using distributed volunteer computing and b) novel methods for population synthesis studies of Galactic neutron stars as sources of continuous gravitational waves.

#### 1.1.1 Main results

In the field of radio pulsars, the most sensitive search for radio pulsars in tight circular orbits has been planned, set up, and conducted. Two new unusual radio pulsars were discovered. First characterisations of these systems have been conducted.

The first discovered pulsar is isolated and has a surprisingly slow spin-down for its spin frequency similar to newborn pulsars. This indicates that it might belong to the rare class of disrupted recycled pulsars. Only a dozen similar sources were previously known; they are believed to originate from binary systems that failed to form the (similarly rare) double neutron stars, because the second supernova explosion disrupted the binary.

The second pulsar discovered in the course of this thesis has a spin frequency of 48.2 Hz and is in a binary system, orbiting the centre of mass in 9.4 h with a (most likely white dwarf) companion of at least  $0.95 M_{\odot}$ . This system very likely belongs to the very rare class of intermediate-mass binary pulsars, of which only five other systems were previously known. This system could further allow to measure relativistic effects like the Shapiro delay or, in the long term, the orbital decay due to gravitational wave emission.

In the second scientific area covered in this thesis, the emission of continuous gravitational waves from a Galactic population of neutron stars has been studied. For the first time, realistic estimates of the statistical upper limit of the expected gravitational wave signal have been obtained, improving previous estimates by about a factor of six. Further, the emission from this population is studied in detail and compared to realistic search pipeline sensitivities for the first time to obtain predictions of the detection rates of these objects with ground based gravitational wave detectors. The results will also allow to improve searches

for these objects by maximising the number of detections for a fixed amount of computation cycles. With these novel simulations it is possible to conduct deep searches on the most “cost-effective” parts of the parameter space.

### 1.1.2 Structure of the thesis

In Chapter 2 we present an overview of the scientific areas of relevance to the work presented in the later chapters. After a short history of pulsar discoveries, survey, and observations, we provide an introduction into the nature of neutron stars as radio pulsars at the current level of knowledge. We review the canonical picture of a neutron star as radio pulsar, the emission mechanism, effects of the interstellar medium on the radio wave propagation, and the known population of radio pulsars. We further review the instruments and search methods used to detect known and find unknown radio pulsars. We then conclude by an overview of neutron stars as continuous gravitational wave sources.

Chapter 3 provides a detailed account of the search for radio pulsars in tight binary systems conducted using the distributed computing project Einstein@Home. We review the PALFA survey for radio pulsars with the Arecibo telescope, Puerto Rico; data collected from this ongoing survey are the basis of the Einstein@Home search described in more detail afterwards. We present a quick overview, followed by more thorough descriptions. Firstly, the mathematical and statistical basics of the parameter space description and signal detection, as well as the efficient construction of parameter space templates are elucidated; secondly, the data flow from the raw survey data, through the pre-processing stage on the server side, processing on public volunteer computer attached to Einstein@Home, validation of result integrity, and different algorithms developed for the result post-processing are detailed.

In Chapter 4 we describe the first discovery of a radio pulsar by global distributed volunteer computing. In July 2010, the Einstein@Home radio pulsar search on PALFA survey data from the Arecibo radio telescope discovered the isolated pulsar J2007+2722. We describe the discovery observation, follow-up observations with five of the largest radio telescopes worldwide and analysis of archival Very Large Array data that allowed to identify the pulsar with a source in the latter data set and gave an exact sky position within very short time. This is unlike usual radio pulsar observations where exact sky position can only be obtained by coherent pulsar timing. This usually requires multiple observations over the course of a year. The exact position allows to combine the discovery data from early 2007 with the follow-up data from mid 2010 to obtain an upper limit on the spin-down; the low upper limit of  $2 \times 10^{-17} \text{ s s}^{-1}$  indicates that PSR J2007+2722 likely is a disrupted recycled pulsar, a failed double neutron star system disrupted by the second supernova explosion. We further use polarisation measurements to determine the beam geometry of PSR J2007+2722, which indicate that this pulsar has a close alignment of the magnetic and the spin axis and a wide opening angle in a conal beam model.

Within less than three weeks after the first discovery, Einstein@Home discovered a second radio pulsar, PSR J1952+2630. Chapter 5 describes this pulsar in more detail. The discovery observation already hinted at a companion accelerating the pulsar. Follow-up observations with the Arecibo telescope soon revealed that PSR J1952+2630 was orbiting the common centre of mass in an almost perfectly circular orbit with a companion of at least  $0.95 M_{\odot}$ , assuming a canonical pulsar mass. We describe the follow-up observations, an analysis based on the Doppler-modulated spin period observations over several months, which allows us to obtain the parameters of the binary system. The companion most likely

is a massive white dwarf, although a neutron star currently cannot be ruled out. We obtain an upper limit on the eccentricity, and show that future observations could measure the relativistic Shapiro delay, which could allow to determine the individual masses of both compact objects and constrain the orbital geometry further. Our observations indicate that PSR J1952+2630 most likely belongs to the very rare class of intermediate-mass binary pulsars, of which only five other systems were previously known.

The next Chapter 6 switches gears from radio pulsar discoveries to population studies of Galactic neutron stars spinning down dominantly through gravitational wave emission as opposed to electromagnetic spin-down; a population of these objects, called *gravitars* could exist (yet undetected) in our Galaxy. For the first time, we have tested an argument by Blandford (documented in Thorne, 1987, that relates the maximum expected gravitational wave strain from a population of non-axisymmetrically deformed Galactic neutron stars to simple factors like the birth rate and size of the Galaxy, but is independent of the (assumed equal) deformation of the neutron stars and of their spin frequency. This is due to two specific assumptions used in Blandford's argument. We use a realistic model of the Galaxy and its neutron star population to test the validity of these assumptions in a more general and realistic framework. We find that these assumptions are not fulfilled in the more general case; this leads to a weak dependence of the maximum expected gravitational wave strain on the frequency and a stronger dependence on the ellipticity. We find that for realistic ellipticities our values are lower by a factor of six compared to the previously best estimates. We further show that gravitars can be used as an upper limit case for the expected emission of gravitational waves, if other channels for energy loss (e.g. electromagnetic spin-down) are allowed as well.

Chapter 7 then uses the Galactic neutron star population model to obtain novel estimates of the detectable population of gravitars using *realistic* sensitivity curves for existing pipelines and anticipated sensitivity curves for future searches. Earlier population studies had used very high sensitivities assuming a coherent integration over months; this is computationally prohibitive and therefore unrealistic. For the first time we obtain expected detection numbers for different searches and population realisations. We also show in a general framework how the results from these simulations can be used to maximise the number of detections for a given amount of computational power.

Finally, Chapter 8 describes some technical details of computations used in other places of the thesis. This includes among other things the derivation of some formulae for the beam geometry, the Doppler modulation in elliptical orbits, and the derivation of the parameter space metric.

## 1.2 List of publications

---

The work in this thesis is based on and has been published in the publications listed here.

### Refereed publications

1. **B. Knispel** and B. Allen, *Blandford's argument: The strongest continuous gravitational wave signal*, **Phys. Rev. D** 78, 044031 (2008)
2. **B. Knispel**, B. Allen, J. M. Cordes, J. S. Deneva, D. Anderson, C. Aulbert, N. D. R. Bhat, O. Bock, S. Bogdanov, A. Brazier, F. Camilo, D. J. Champion, S. Chatterjee,

F. Crawford, P. B. Demorest, H. Fehrmann, P. C. C. Freire, M. E. Gonzalez, D. Hammer, J. W. T. Hessels, F. A. Jenet, L. Kasian, V. M. Kaspi, M. Kramer, P. Lazarus, J. van Leeuwen, D. R. Lorimer, A. G. Lyne, B. Machenschalk, M. A. McLaughlin, C. Messenger, D. J. Nice, M. A. Papa, H. J. Pletsch, R. Prix, S. M. Ransom, X. Siemens, I. H. Stairs, B. W. Stappers, K. Stovall, and A. Venkataraman, *Pulsar Discovery by Global Volunteer Computing*, **Science**, 329, 5997 (2010)

3. **B. Knispel**, P. Lazarus, B. Allen, C. Aulbert, N. D. R. Bhat, O. Bock, S. Bogdanov, A. Brazier, F. Camilo, S. Chatterjee, J. M. Cordes, F. Crawford, J. S. Deneva, G. Desvignes, H. Fehrmann, P. C. C. Freire, D. Hammer, J. W. T. Hessels, F. A. Jenet, V. M. Kaspi, M. Kramer, J. van Leeuwen, D. R. Lorimer, A. G. Lyne, B. Machenschalk, M. A. McLaughlin, C. Messenger, D. J. Nice, H. J. Pletsch, R. Prix, S. M. Ransom, X. Siemens, I. H. Stairs, B. W. Stappers, K. Stovall, and A. Venkataraman, *Arecibo PALFA Survey and Einstein@Home: Binary Pulsar Discovery by Volunteer Computing*, **The Astrophysical Journal Letters**, 732, 1, L1 (2011)

### **Publications in preparation and popular science publications**

1. **B. Knispel**, *Gravitational Population Modelling and Detection Predictions for LIGO Searches*, to be submitted to **Phys. Rev. D**
2. **B. Knispel**, *Pulsare mit dem Heimcomputer entdeckt!*, **Sterne und Weltraum**, 12/2010 (2010)

# 2

## Introduction

### 2.1 Pulsars

---

This section provides an overview of the most important physical properties of pulsars. Pulsars are thought to be highly magnetised spinning neutron stars emitting radio waves; we give an overview of neutron star physics including mass, radius, and interior structure in Section 2.1.1. We then present a toy model of radio pulsars in Section 2.1.2, known as the “lighthouse model” because of the similarity of radio pulsar emission to its terrestrial analogue. A walk-through of the most important steps in a search for new pulsars is presented in Section 2.1.3, where we follow the signal path from the observation to the data analysis. We conclude with a history of important milestones in pulsar astronomy in Section 2.1.4.

Section 2.2 shows how the simple lighthouse model can be used to describe the observed evolution of pulsar spin period, and provide age and magnetic field strength estimates. We then review a more complex model of the pulsar emission and the surrounding magnetosphere in Section 2.3 to conclude the discussion of the pulsar emission. We then follow the radio waves on their way to the terrestrial radio telescope and describe their interaction with the interstellar medium in Section 2.4; the interaction manifests itself in a broadening of the radio pulse.

We then consider the Galactic population of known pulsars and review the different pulsar classes and evolution paths thereof in Section 2.5.

Finally, we review how neutron stars can manifest themselves as gravitational wave sources in Section 2.6. Neutron stars, and also pulsars, are possible sources of continuous gravitational waves by different mechanisms, each of which we describe. Another possibility is the existence of a class of neutron stars with weak magnetic fields and not emitting a significant amount of electromagnetic radiation. If non-axisymmetrically deformed, they could emit continuous gravitational waves over very long timescales. We show how a Galactic population of such objects can be studied and how to predicts the strain of gravitational wave signals emitted by such a population.

### 2.1.1 Neutron stars

Neutron stars are the remainders of massive stars where a supernova explosion ends their stellar lives, as correctly speculated about by Baade and Zwicky (1934). Their internal structure and composition is likely complex and not definitely known to date. The main physical tool describing neutron stars is the *equation of state* which links thermodynamical variables like pressure and temperature. There is a wide range of possible equations of state for neutron stars (Lattimer and Prakash, 2004), however it is unknown which one of these (if any) is the correct one. If we knew the equation of state we could obtain the physical properties of neutron stars, like a mass-radius relationship (i.e. how large is a neutron star of a given mass).

#### Physical properties

The physical properties of neutron stars are determined by their equation of state. First attempts to formulate an equation of state were made by Oppenheimer and Volkoff (1939), an overview of the current state of knowledge can be found in Lattimer and Prakash (2004). All of these descriptions are of theoretical nature, since the neutron star matter is very different from what can be obtained in terrestrial laboratories.

The canonical mass of a neutron star usually is assumed to be around the Chandrasekhar mass (Chandrasekhar, 1931, 1935) of  $1.4 M_{\odot}$  (solar masses), at which a white dwarf collapses into a neutron star under its own gravity. The maximum mass of a neutron star marking the transition to a black hole is unknown and depends on the equation of state, but values around  $2.5 M_{\odot}$  are considered likely (Lattimer and Prakash, 2004). Mass measurements of pulsars in binary systems yield masses consistent with this picture, with the most light-weight neutron star at  $1.25 M_{\odot}$  (Kramer et al., 2006b) and the most massive neutron star at  $2.0 M_{\odot}$  (Demorest et al., 2010). The latter mass, only recently measured, in fact rules out many of the proposed equations of state that do not predict neutron stars of masses that high. These equations of state all include exotic particles in addition to neutrons within neutron stars.

The radii of neutron stars are much more difficult to obtain than their masses. One possibility is the observation of thermal radiation from the neutron star surface in X-rays. The size of the emitting region can then be inferred from the observed luminosity (Lorimer and Kramer, 2005). This method has some drawbacks related to the compactness and strong gravity of neutron stars: the strong gravity near the emitting surface redshifts the electromagnetic waves before they reach the observer. Thus, the observed temperature is smaller than the intrinsic value and the inferred size of the emission region changes accordingly. A second problem arises from the fact that neutron stars are expected to possess thin atmospheres of plasma (Miller, 1992; Romani, 1987; Zavlin and Pavlov, 2002) and strong magnetic fields, which can also modify the observed spectrum of X-rays compared to a simple black body spectrum (Lloyd, 2003).

Lower and upper limits on neutron star radii can be obtained from indirect arguments. Lattimer et al. (1990) and Glendenning (1992) derive a lower limit on the neutron star radius based on the fact that the speed of sound in the neutron star interior has to be less than the speed of light and on properties of the equation of state in the transition from low to high densities (Lorimer and Kramer, 2005). These arguments lead to a relation between the Schwarzschild radius  $R_S$  and the minimum neutron star radius  $R_{\min}$  with the neutron star

mass  $M$  as follows:

$$R_{\min} \approx 1.5R_S = \frac{3GM}{c^2} = 6.2 \text{ km} \left( \frac{M}{1.4M_\odot} \right). \quad (2.1)$$

An upper limit can be obtained from the mass-shedding limit, i.e. that the neutron star has to withstand the centrifugal forces without breaking up. Assuming a spin period  $P$ , Lattimer and Prakash (2004) find the relation between break-up spin period  $P$  and mass  $M$  and radius  $R$  as

$$R = \left( \frac{GMP^2}{4\pi^2} \right)^{\frac{1}{3}} \quad (2.2)$$

$$= 16.8 \text{ km} \left( \frac{P}{1 \text{ ms}} \right)^{\frac{2}{3}} \left( \frac{M}{1.4M_\odot} \right)^{\frac{1}{3}}. \quad (2.3)$$

In fact, the currently fastest known pulsar, J1748-2446ad, see second pulsar history landmark in 2006 in Section 2.1.4, with a spin period of 1.396 ms provides an upper limit on the neutron star radius of 20.9 km, assuming it has a mass of  $1.4M_\odot$ . Most numerical models predict radii in the range of 10 to 14 km, see Figure 2 in Lattimer and Prakash (2004), which agree well with theoretically derived limits.

The moment of inertia  $I$  will be important later when we consider the simple lighthouse model, the derived spin-down of radio pulsars, and neutron stars as gravitational wave sources. In general, for any sphere with some internal mass distribution we can write

$$I = \kappa MR^2. \quad (2.4)$$

The constant  $\kappa$ , which depends on the internal mass distribution and thus, composition, of the sphere. For a uniform mass distribution it is straightforward to show that  $\kappa = \frac{2}{5}$ . Most numerical neutron star models predict  $0.30 \lesssim \kappa \lesssim 0.45$  for the usual mass-radius range (Lorimer and Kramer, 2005). The canonical value of  $I = 10^{38} \text{ kg m}^2$  is obtained from the above formula inserting the canonical mass  $1.4M_\odot$ , and radius 10 km. Direct measurements of a neutron star's moment of inertia have not been achieved yet; Lyne et al. (2004) show that it might be possible to use measurements of the perihelion shift in the double pulsar J0737-3039 to observe relativistic spin-orbit coupling for the first time ever. This also would allow to obtain the first measurement ever of a neutron star's moment of inertia.

### Neutron star structure

The internal structure of neutron stars is unknown. Theoretical models allow predictions of the constituents and the physical properties of the neutron star interior. From the canonical mass and radius it is clear that the average density of the canonical neutron star is  $\bar{\rho} = 6.6 \times 10^{17} \text{ kg m}^{-3}$ . For comparison, the density of an atomic nucleus is of order  $2.7 \times 10^{17} \text{ kg m}^{-3}$ . On average, a neutron star's density thus exceeds that of an atomic nucleus.

Numerical neutron star models do not predict a uniform density in the stellar interior (Shapiro and Teukolsky, 1983). Most of the neutron star models predict a different structure (Pines and Alpar, 1985). The outermost layer is possibly a crystalline outer crust of nuclei and highly relativistic electrons, which is of order a few hundred meters thick. Below that, an inner crust follows. It consists of a neutron superfluid, neutron-rich nuclei and electrons and is a few kilometres thick. The density increases from a value

of  $\sim 10^9 \text{ kg m}^{-3}$  to  $\sim 10^{14} \text{ kg m}^{-3}$  in the outer crust. When the density exceeds the critical value of  $4 \times 10^{14} \text{ kg m}^{-3}$  (the so-called *neutron drip point* or *neutron drip line*<sup>1</sup>), more and more neutrons are released from the nuclei. In the inner crust the density increases up to  $\sim 10^{17} \text{ kg m}^{-3}$ . The remaining, major part of the neutron star's nucleus consists of free, superfluid nucleons and a few percent of superconducting protons and electrons. The composition of the innermost part of the neutron star differs between the different models. Some predict a composition purely of neutrons, while other models for example predict pion condensates or quark matter, for an overview see e.g. Baym and Pethick (1979).

### 2.1.2 The lighthouse model

The simplest model of a radio pulsar, often referred to as a toy model of a pulsar, is called the “lighthouse model”, because of its analogy to a lighthouse emitting two rotating beams of light along a common axis.

The lighthouse model consists of a rapidly rotating, highly magnetised neutron star with a dipolar magnetic field. The magnetic field axis is inclined with respect to the rotation axis. Broadband radio emission is generated above the magnetic polar caps by the acceleration of charged particles (electrons) in the surrounding plasma-filled magnetosphere (Goldreich and Julian, 1969). Because the charged particles are accelerated along the curved field lines, electromagnetic radiation is emitted in a beam along the magnetic field axis above both magnetic poles. Figure 2.1 shows a schematic of this model.

As one beam (or sometimes both beams) of radiation sweep by Earth, a narrow radio pulse can be registered by a radio telescope (see Figure 2.2 for examples of observed pulse profiles). The width of this pulse as fraction of the pulse period is roughly given by the ratio of the opening angle of the beam and a full rotation of  $360^\circ$ . This generally accepted model of the simple cone-shaped beam along the magnetic axis was formulated early by Radhakrishnan and Cooke (1969) and Komesaroff (1970). A more detailed description is given in Section 2.3 of this thesis; we already point out here that while the toy model can describe some observed aspects of radio pulsars fairly well, it fails for example to explain the wide variety of observed pulse profiles. The profiles in Figure 2.2 were randomly chosen from the data archive of the European Pulsar Network (EPN)<sup>2</sup>.

It has to be noted that the lighthouse model simplifies the complex processes leading to the emission of radio waves from pulsars. On the other hand, at the time of writing there is no model that fully and satisfactorily explains all observed properties of pulsar emission, while the lighthouse model can account reasonably well for the main observed properties of pulsars: the periodicity of the pulsed emission, the (in most cases) narrow shape of the pulse as well as the increase in pulse period over time.

In the following sections we will look into some of the aspects of pulsar physics in some more detail. For a more complete description the reader is referred to e.g. Lorimer and Kramer (2005) and Lyne and Graham-Smith (2005).

---

<sup>1</sup>This is the point at which adding a neutron to an atomic nucleus will create an unstable isotope that immediately decays by emission of a neutron. Colloquially this is expressed as the neutron “dripping” or “leaking” out of the nucleus. A similar concept exists for protons.

<sup>2</sup><http://www.mpifr-bonn.mpg.de/div/pulsar/epn/>

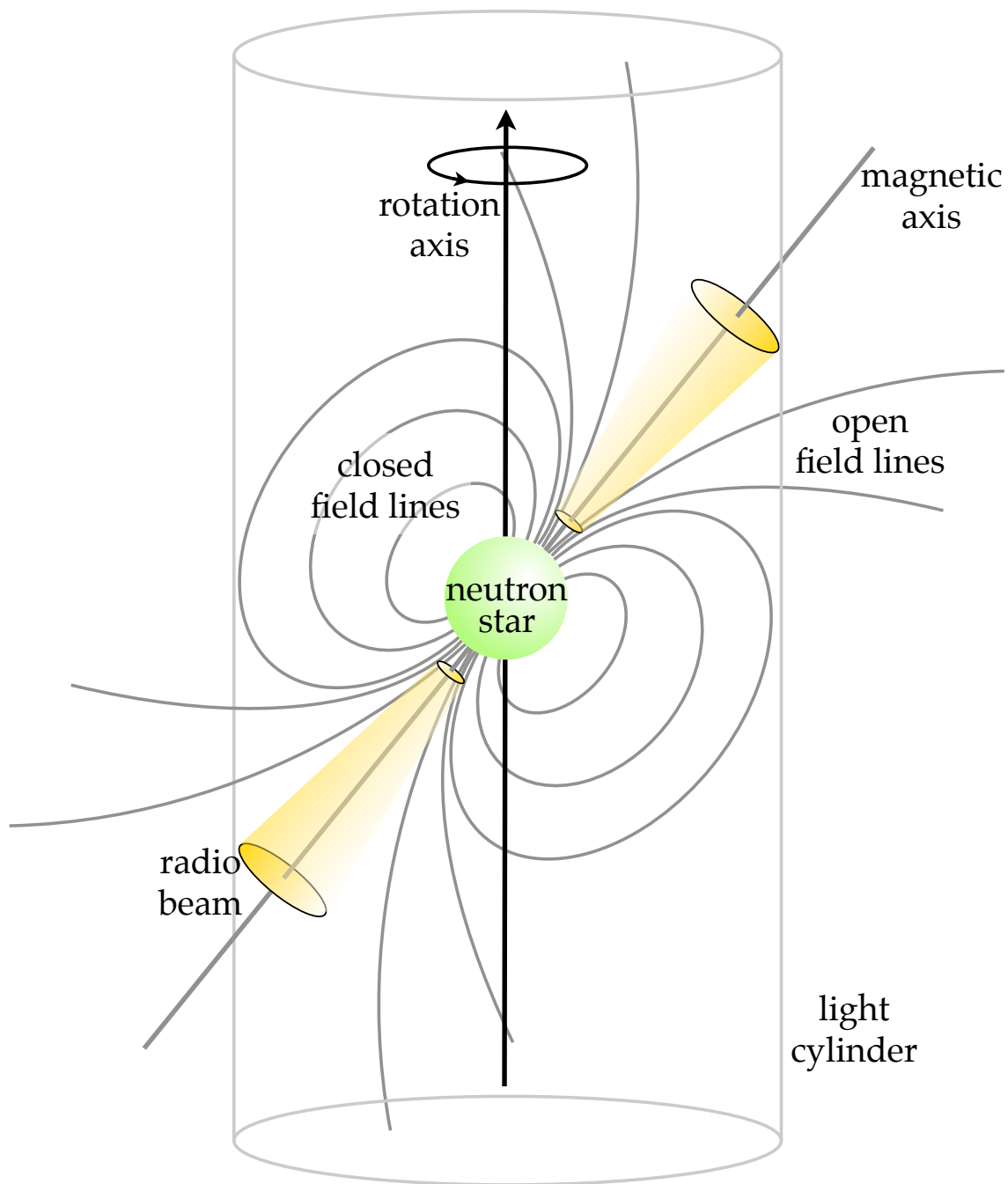


**Figure 2.1:** The pulsar “toy model”, adapted from Lorimer and Kramer (2005). A highly magnetised neutron star surrounded by a plasma-filled magnetosphere emits beams of radio waves along the magnetic axis inclined with respect to the rotation axis. The emission regions are limited to the region of open field lines indicated here by the yellow cones. The light cylinder is the surface at which the angular velocity of the co-rotating magnetosphere equals the speed of light.

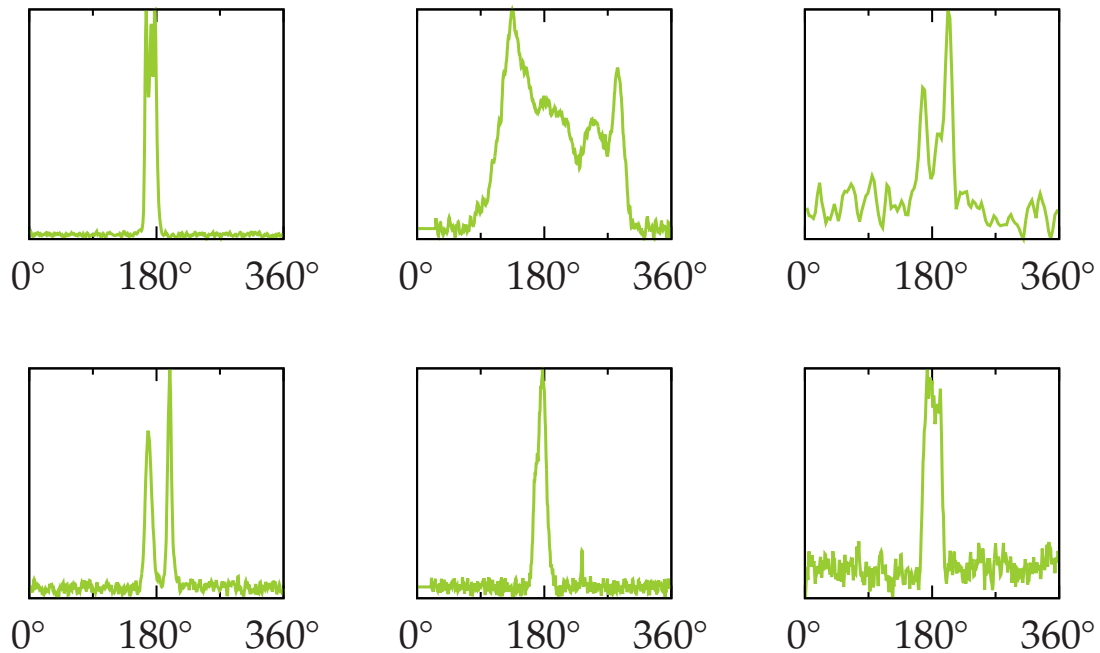


**Figure 2.2:** The variety of observed radio pulsar pulse profiles. Each panel shows the radio emission over one rotation of the pulsar, averaged over many rotations. Top row, left to right: profiles of pulsars B1826-17, B1831-04, and B1913+16. Bottom row, left to right: profiles of pulsars B2224+65, B2315+21, and B2323+63.

### 2.1.3 Searching for pulsars

The discovery of the first pulsar was a serendipitous one. The combination of the observation parameters at Mullard Radio Astronomy Observatory, Cambridge University, allowed for the lucky detection. The large collecting area radio telescope, observing at low radio frequencies and over a small bandwidth, in combination with a low time-resolution pen-chart recorder worked well for the first pulsar, CP 1919 (PSR B1919+21); as we now know, only few of the  $\sim 2000$  pulsars known today would be detectable with such instrumentation. Most pulsars are faint radio sources and exhibit a strong signal dispersion from the interstellar medium. Thus, observations over a wide bandwidth (to increase the signal-to-noise ratio) and data analysis to remove the dispersive delay are necessary to detect new pulsars. Both special instrumentation as well as computationally expensive data analysis are therefore required nowadays.

The schematic of a modern radio telescope with pulsar observing and searching instrumentation is shown in Figure 2.3.

The radio signal is collected by a large-area main (or primary) reflector, with a metallic surface. Depending on the telescope, the primary reflector has a parabolic shape (e.g., Effelsberg telescope), or a spherical shape (e.g., Arecibo telescope). If the primary reflector has spherical shape, the locus of the focused radio waves is a line. There are two ways of collecting signals from this focus line: a) using a line feed that delays the signals in such a way that they all arrive in phase at the receiver, or b) using additional (secondary and tertiary) reflectors to focus the telescope beam onto a single focus point. Both methods

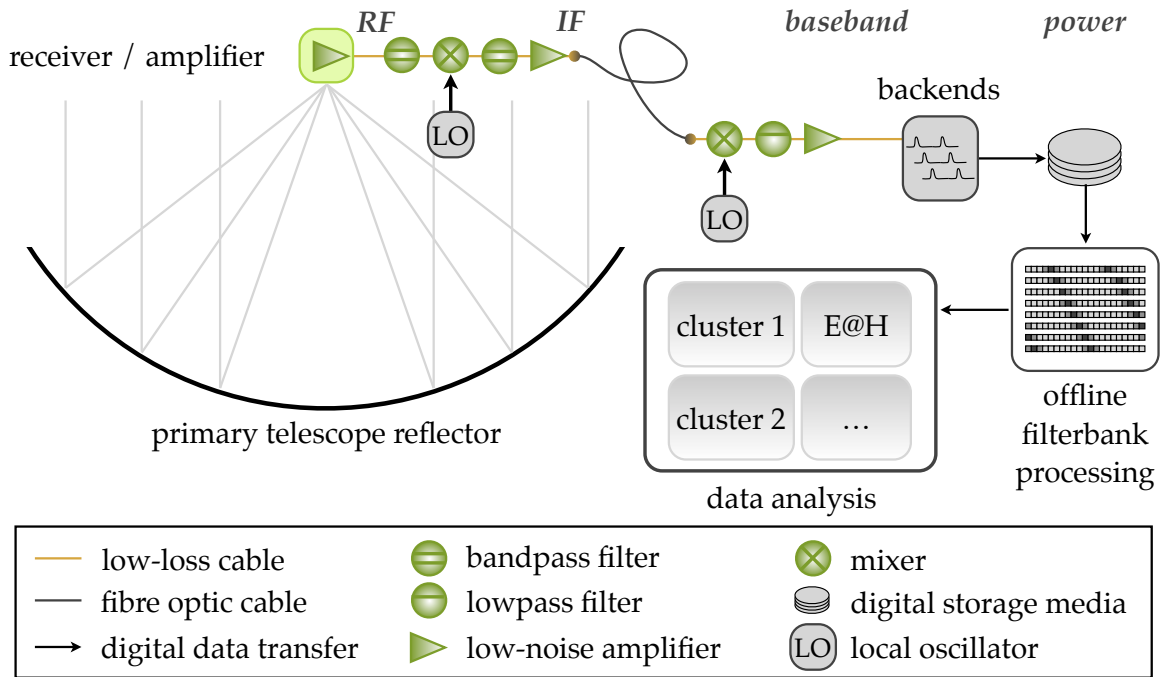


**Figure 2.3:** Schematic of the signal pathway for radio pulsar observation. This figure was adapted from Lorimer and Kramer (2005) and Eatough (2009). *RF* = “radio frequency”, *IF* = “intermediate frequency”, and *LO* = “local oscillator”. For explanations on the different components, see Section 2.1.3.

are used at the Arecibo telescope, the line feed can be seen on the left of the platform in Figure 3.1, while the additional reflectors are inside the dome on the right.

At the focus point (or the end of the line feed) the receiver is positioned. It usually consists of cryogenically cooled orthomode transducers translating the radio signals into two electric signals, one for each of the orthogonal polarisation modes, also called polarisation channels. These signals are amplified by low-noise amplifiers with specifically optimised design for the radio frequency band of interest, i.e. 1.4 GHz for most pulsar survey observations. Then, the signal is band-pass filtered to reject any harmonics from radio signals outside the radio frequency band of interest. Sources of this radio frequency interference (RFI) are TV stations, mobile phones, other communication devices, or WLAN computer devices. At this point the signal’s frequency content is at radio frequencies  $f_{\text{RF}}$  (labeled *RF* in Figure 2.3), with a bandwidth given by the bandwidth of the band-pass filter used.

Now, the RF signal is usually down-converted to lower frequencies by mixing it with the signal from a local oscillator (labeled *LO* in Figure 2.3). This down-conversion is applied for two reasons: a) the signal transmission at lower frequency is more efficient, because losses, e.g. from skin effect, increase with signal frequency; and b) the digital data acquisition hardware usually used at the end of the observation process can only operate on data in a smaller frequency range. The local oscillator provides a monochromatic signal at a specific frequency  $f_{\text{LO}}$ . In practice this signal can be provided by a hydrogen maser, operating at a frequency of 1420 MHz, or a wavelength of 21 cm. Its monochromatic signal is mixed with the observed signal. A radio frequency component at a frequency  $f$  is mapped to two frequency components<sup>3</sup> in the mixed signal: one is at the sum  $f + f_{\text{LO}}$ , the other at

<sup>3</sup>This follows from the trigonometric identity  $\mathcal{A} \cos(\omega t + \varphi) \times 2\mathcal{A}_{\text{LO}} \cos(\omega_{\text{LO}} t + \varphi_{\text{LO}}) =$

the difference  $f - f_{\text{LO}}$ . Usually, the latter case is used; this yields a so-called intermediate frequency  $f_{\text{IF}} = f_{\text{RF}} - f_{\text{LO}}$  (labeled *IF* in Figure 2.3), around which signals in the filtered bandwidth are transmitted. Depending on whether  $f_{\text{RF}} < f_{\text{LO}}$ , or  $f_{\text{RF}} > f_{\text{LO}}$ , the IF signal frequencies are reversed, or not reversed, respectively, in their frequency sense (Lorimer and Kramer, 2005).

For the Arecibo telescope, all the above steps take place near the focus of the telescope, i.e. in the dome housing on the observation platform above the main reflector. For Arecibo, the IF signals are again amplified before they are converted into optical signals and transmitted to the control room via fibre optical cables, where they are again turned into electrical signals. These IF signals can be used directly for certain types of observations with backends operating at intermediate frequencies. For pulsar observations, they are mixed with the signal from a second local oscillator to bring the intermediate frequency band to *baseband* frequencies (same label in Figure 2.3), i.e. a frequency band starting at zero frequency. Finally, the baseband signals are also low-pass filtered (to reject any frequency component outside the frequency band of interest) and amplified. Note, that although we only show a single signal path in Figure 2.3, actually both orthogonal polarisation modes are transmitted through to the baseband stage.

The baseband signals can be sent to different devices, the simplest of which is a combination of squaring and summing the two polarisation channels and integrating the value of this power over short intervals of time and plotting the result with a pen chart recorder. Such a device was used by Bell to discover the pulsations from the first radio pulsar found.

In modern radio telescopes, the baseband information is sent to backends, tailor-made observation hardware for the needs of pulsar observations: covering a large radio bandwidth to observe as much of the broadband emission as possible, providing a fine spectral resolution to mitigate the deleterious effects of dispersion in the interstellar medium, high temporal resolution<sup>4</sup> to increase sensitivity to pulsars with short spin periods. These devices can, for example, be analog filterbank spectrometers, or autocorrelation spectrometers. The latter are used at the Arecibo observatory for pulsar surveys. They compute the autocorrelation function of the baseband data, which is then recorded to digital storage media (disk or tape). The autocorrelation is computed by convolving the data with a time-shifted version of the data. In a digital autocorrelator, the immediate data are multiplied with data from a delayed line, and processed in a digital accumulator (this is the analogue of the integration process in the pen chart recorder). After a pre-defined time interval (the sampling time), the accumulator is read out and written to disk. From the autocorrelation function the power spectral density can be computed by the Wiener-Khinchin theorem, which then allows the decomposition of the radio frequency bandwidth into discrete channels in the offline processing.

The offline processing is the final step in the search for pulsars. Depending on the format of the raw observational data, they have to be converted into other formats at this stage. A commonly used format are filterbank data: these are radio spectra in discrete frequency channels, one of these radio spectra generated at each time sample. From this format, they can be sent to a de-dispersion code that digitally removes the dispersive delay, schematically shown in the box above the label “offline filterbank processing” in Figure 2.3. The de-dispersion is conducted for a certain set of trial values and de-dispersed time series are

---

$\mathcal{A}_{\text{LO}} [\cos((\omega - \omega_{\text{LO}})t + \varphi - \varphi_{\text{LO}}) + \cos(\omega + \omega_{\text{LO}})t + \varphi + \varphi_{\text{LO}}]$ , which shows that the mixed signal is composed of the above mentioned two frequency components.

<sup>4</sup>short integration time in the example of the pen chart recorder

generated. These time series are then searched for pulsar signals by different methods and pipelines, each optimised for a specific type of signal, running on single computers, cluster of computers, or on volunteer computing projects like Einstein@Home.

These offline searches are usually computationally very expensive. Depending on the kind of signal searched for, the search may require computation times exceeding the observation time by many orders of magnitude. The main reason is the need to typically search multiple hundreds of trial DM values and for each of these to conduct an equally costly search. The computational costs of the latter increase rapidly if, for example, signals from pulsars in tight binary orbits are searched for. In this case, the unknown orbital parameters make it necessary to search the de-dispersed time series with many possible orbital parameter combinations.

#### 2.1.4 A short history of pulsars

Note: this section is adapted from Lorimer and Kramer (2005) and Lyne and Graham-Smith (2005). It is updated it to include the latest discoveries and important events.

It was a long way from the theoretical proposition that exotic, compact objects like neutron stars might exist and the realisation that pulsars were indeed rapidly-rotating, highly-magnetised neutron stars. This history has two parts: the possible existence of neutron stars and their birth in supernovae was speculated about already in 1934. The following three decades brought theoretical considerations about these objects and their physical properties. Shortly before the serendipitous discovery of the first radio pulsar, theoretical calculations lead to assume a well-known supernova remnant, the Crab Nebula, might be powered by a rapidly rotating, highly-magnetised neutron star at its centre.

The existence of neutron stars was speculated about by Walter Baade and Fritz Zwicky in 1934. They proposed that a new form of star could result from the supernova explosion ending the life of massive stars. Baade and Zwicky (1934) write<sup>5</sup>

With all reserve we advance the view that a super-nova represents the transition of an ordinary star into a *neutron star*, consisting mainly of neutrons. Such a star may possess a very small radius and an extremely high density. As neutrons can be packed much more closely than ordinary nuclei and electrons, the “gravitational packing” energy in a *cold* neutron star may become very large, and, under certain circumstances, may far exceed the ordinary nuclear packing fractions. A neutron star would therefore represent the most stable configuration of matter as such.

These remarks seemed untestable by any observational means in 1934; the neutron stars proposed by Baade and Zwicky would be small and cold, and thus would emit only minor amounts of electromagnetic radiation. Back then, no one would have assumed the possibility of strong electromagnetic fields in these objects and their now known important observational consequences.

In 1939, Tolman formulated a simple equation of state describing static solutions for the field equations of fluid spheres in General relativity (Tolman, 1939). Oppenheimer and Volkoff applied this solution to described spheres composed purely of neutrons and to describe their density, mass, and diameter (Oppenheimer and Volkoff, 1939). These calculations did not yield the neutron star masses known to date but estimates at the correct order

<sup>5</sup>On a science-historical note: the same paper Baade and Zwicky (1934) also features the sentence beginning: “Although we ourselves are by no means convinced that the universe is expanding...”.

of magnitude were obtained: Oppenheimer and Volkoff (1939) calculated a maximum mass of  $0.7 M_{\odot}$  for neutron stars, treating them as a simple Fermi gas. A more precise treatment yields to the nowadays accepted (nonetheless still debated) value of  $\sim 2.5 M_{\odot}$ .

Hoyle et al. (1964) derive estimates for the magnetic fields of neutron stars, assuming that the fields form from catastrophic contraction, as large as  $10^6$  T ( $1 \text{ T} = 10^4 \text{ G}$  to convert to the also used cgs unit system). They go on to show that such an object would emit energy by the emission of electromagnetic waves with a total power of  $10^{34}$  W ( $1 \text{ W} = 10^7 \text{ erg s}^{-1}$  in cgs units), which as they further show agrees very well with the observed energetics of the Crab Nebula, formed from a supernova explosion.

Finally, less than three weeks before the discovery of the first pulsar, Pacini (1967) put forward the idea that a rapidly-rotating, highly-magnetised neutron star might be the source of energy at the centre of the Crab Nebula.

The discovery of the first radio pulsar was a serendipitous event, radio astronomers did not set out to try to observe neutron stars as sources of radio waves. The advance of radio astronomical observation techniques in the three decades after World War II enabled other lucky discoveries like that of the first discrete radio source (Cyg A) in an investigation of the radio background, or the unexpected discovery of quasars (Lyne and Graham-Smith, 2005). The difficulties in pulsar observation are technical and at the time of the discovery also sociological, both of which might have delayed the discovery of the first radio pulsar. For the identification of the pulsations, a high time resolution is necessary, which at that time was difficult to achieve with observational hardware available. Moreover, most radio astronomers did not even expect there would be rapidly oscillating radio sources in the sky; rapid fluctuations were usually thought to be a feature of terrestrial interference from man-made sources. Thus, observing hardware was usually set up to average the signal over intervals of seconds to smooth out these interferences. There are even reports of observers having made pulsar observations that pre-date the first discoveries; in these a regularly pulsating signal was seen on the then used pen-chart recorders, which was thought to be a technical malfunction of the observation hardware.

The discovery of the first radio pulsar in 1968 is the begin of our timeline of important milestones in the history of pulsar astronomy.

**1968** Jocelyn B. Burnell and Anthony Hewish at the Mullard Radio Astronomy Observatory, Cambridge University, discovered a radio source pulsating with an extremely accurately maintained period of 1.337 s. They could soon establish its celestial origin<sup>6</sup> and the absence of any measurable parallax indicated a source outside the solar system at distances in excess of  $10^3$  AU. Initially, the source was half-humorously named LGM-1 for “little green men 1”, as Burnell and Hewish considered the origin of these regular pulses from an extra-terrestrial civilisation. This observation was the first discovery of a radio pulsar (Hewish et al., 1968); its initial designation was CP 1919 but it is now known as PSR B1919+21 or PSR J1921+2153<sup>7</sup>. Gold (1968) and Pacini (1968) identified pulsars with rapidly rotating, highly-magnetised neutron stars<sup>8</sup>. The dis-

---

<sup>6</sup>in the celestial constellation of Vulpecula, or “little fox”

<sup>7</sup>Pulsars are named by a prefix “B” or “J” followed by the sky position. The prefix denotes the reference system: “B” stands for the Besselian system with reference epoch 1950.0; “J” denotes the J2000.0 system. The B1950.0 system was used for pulsar discoveries until  $\sim 1990$  (Lorimer and Kramer, 2005).

<sup>8</sup>Interestingly, also the existence of a satellite orbiting around a neutron star as source of the regular pulsation was discussed by Pacini and Salpeter (1968) but found “to be a very unlikely explanation for the pulsating radio sources.”.

covery of the first radio pulsar and Hewish's contributions to radio astronomy were honoured with the receipt of the 1974 Nobel prize in Physics together with M. Ryle.

- 1971** The first X-ray pulsar, Cen X-3 was discovered in 1971 by measurements from the Uhuru satellite (Giacconi et al., 1971). Cen X-3 was previously identified as a strong X-ray source with an experiment on board a sounding rocket in 1968 (Chodil et al., 1967). The Uhuru measurements found pulsations with a period of 4.84 s in the observed X-rays on top of a background of non-pulsating, continuous X-ray emission. A period variation, decreasing by about 0.02%, then increasing by about 0.04% within two hours was also observed. Also, phases where the emission dropped by a factor of ten were observed. Schreier et al. (1972) could show that variation in periodicity and emission can be explained by an eclipsing binary system. The orbital period is 2.09 d and the binary system consists of a massive star and a highly-magnetized neutron star, spinning with a period of 4.84 s (Ash et al., 1999). The X-ray emission is fuelled by accretion of matter from the massive companion, overflowing its Roche lobe, onto the neutron star, whose high magnetic fields funnel the matter onto hot spots near the magnetic poles. The rotation of the neutron star carries the spots in and out of the field of view, causing the X-ray pulsations. Cen X-3 is a typical accretion powered high-mass X-ray binary.
- 1974** The first pulsar in orbit with a companion star, PSR B1913+16 was discovered by Hulse and Taylor (1975a). This binary pulsar consists of a pair of neutron stars with an orbital period of 7.75 hr and an orbital eccentricity of 0.617. This system is an excellent test-bed for General Relativity; the orbital evolution is in perfect agreement as predicted by General Relativity and the existence of gravitational waves (Weisberg and Taylor, 2005). This measurement is interpreted as the first indirect measurement of gravitational waves. The system will coalesce in 200 Myrs as the orbits shrink further and further by the emission of gravitational waves (Peters, 1964). Hulse and Taylor received the 1993 Nobel prize in Physics for their achievements.
- 1982** The progress in observational instrumentation allowed for the detection of pulsars with increasingly shorter spin periods. In 1982 this led to the detection of the first millisecond pulsar<sup>9</sup>, PSR B1937+21, today also known as PSR J1939+2134, also in the constellation of Vulpecula. This pulsar spins at a frequency of 641.93 Hz, close to the theoretical upper mass-shedding limit (formula (3) and thereafter in Lattimer and Prakash (2004)). The mass-shedding limit is the point where the velocity of an orbiting particle equals that of the rotating stellar surface. Furthermore, like most nowadays known millisecond pulsars, PSR B1937+21 turns out to be a highly stable clock. High-precision *timing*<sup>10</sup> of millisecond pulsars has yielded some of the most accurate astrometric measurements (Verbiest et al., 2008) and most stringent test of General Relativity (Kramer and Wex, 2009) ever made.
- 1987** The first millisecond pulsar in a globular cluster (M28) was found by Lyne et al. (1987) at Jodrell Bank in 1987. Globular clusters are very special stellar environments,

<sup>9</sup>The definition of a millisecond pulsar is somewhat fuzzy. Spin periods  $P_0 < 30$  ms (or spin frequency  $f_0 > 33$  Hz) are usually required, although sometimes a more stringent limit of  $P_0 < 10$  ms, or  $f_0 > 100$  Hz is used. In any case, accretion of matter and angular momentum from a companion star is necessary to spin up the pulsar to the observed high frequencies.

<sup>10</sup>obtaining a model that perfectly describes the arrival time of each single radio pulse at the terrestrial detector over decades.

where, because of the high stellar density, frequent interactions between the cluster stars are much more likely than in the regular Galactic field. These interactions also enable the increased formation of millisecond pulsars by accretion processes in binary systems. To date, 143 pulsars in 27 distinct globular cluster have been found<sup>11</sup>. In the globular cluster Terzan 5 alone, 35 pulsars are known, about half of them in binary systems. Millisecond pulsars in the globular cluster Tuc 47 were also used to detect intra-cluster gas for the first time in a globular cluster (Freire et al., 2001b). The globular cluster NGC 1851 also contains the millisecond pulsar with the highest orbital eccentricity ( $e = 0.888$ ) (Freire et al., 2007).

- 1990** The first exoplanet system to be found was not the one around Pegasi 51. Often it is forgotten that the discovery by Mayor and Queloz (1995) was in fact five years after the discovery of a planetary system around the millisecond pulsar B1257+12 by Wolszczan and Frail (1992); they report that at least two planets orbit the millisecond pulsar. Further papers Wolszczan (1994) and Wolszczan et al. (2000) revealed more details about the planetary system, and Konacki and Wolszczan (2003) provide orbital inclinations and masses of the earth-mass planets B ( $4.3 M_{\oplus}$ ) and C ( $3.9 M_{\oplus}$ ) by analysis of gravitational perturbations between the two objects. The system also contains a much smaller planet of  $0.020 M_{\oplus}$ .
- 1993** The brightest and closest known millisecond pulsar, PSR J0437-4715 was found by Johnston et al. (1993) and is today one of the “best-timing” pulsars known, yielding one of the most precise astrometric measurements ever achieved, see Table 2 in Verbiest et al. (2008). This system also allows to set upper limits on the time variation of Newton’s gravitational constant  $G$ . This is based on the anomalous orbital period derivative a non-vanishing time variation of  $G$  would cause.
- 1993** The first triple system composed of a pulsar, a white-dwarf and a Jupiter-mass planet was discovered by Backer (1993) and Thorsett et al. (1993). This system also resides in a globular cluster (M4) and underlines the variety of possible interaction processes in such dense stellar environments.
- 1998** The first accreting millisecond X-ray pulsar, SAX J1808.4-3658 was discovered. Wijnands and van der Klis (1998) report on the discovery of transient pulsating X-ray emission from this source with a frequency of 401 Hz. This system is an accretion-powered low-mass X-ray binary in a 2-h orbit with a lightweight companion of likely less than  $0.1 M_{\odot}$  (Chakrabarty and Morgan, 1998). Systems like this are thought to be predecessors of spun-up recycled binary millisecond pulsars. As soon as the accretion in this system stops, it could be visible as millisecond radio pulsar in a tight orbit with a very lightweight companion; alternatively, the companion could also be completely ablated leading to the formation of an isolated MSP<sup>12</sup>.
- 1999** The pulsar with the longest spin period known to data, PSR J2144-3933, was found by Young et al. (1999). They showed that this pulsar, previously thought to spin with a period of 2.84 s, in fact spins with a period of 8.51 s, much longer than most other known pulsars. According to known equations of state and emission models this pulsar should not emit any radio beam; its existence challenges these models and means that they must be revised.

---

<sup>11</sup>An excellent overview is provided by P. Freire at <http://www.naic.edu/~pfreire/GCpsr.html>.

<sup>12</sup>See also the discovery by Archibald et al. (2009).

- 2003** The fascinating double pulsar PSR J0737-3039 was discovered in 2003 (Burgay et al., 2003; Lyne et al., 2004). This unique system consists of two eclipsing neutron stars, both of which are visible as a pulsar. One of them has a spin period of 22.7 ms, the other one of 2.77 s. Since both neutron stars are visible as pulsars this enables the most stringent tests of General Relativity so far and an extremely rich variety of observational phenomena like eclipses, geodetic precession, and tests of alternative gravitational theories (Kramer and Wex, 2009).
- 2006** PSR B1931+24 was initially found in 1985 and was thought to be a regular, slow pulsar (Stokes et al., 1985). Timing observations with the Lovell Telescope at Jodrell Bank revealed an unexpected, unique activity pattern in the emission of this pulsar (Kramer et al., 2006a). The pulsar was not visible in many of the regular timing observations, just as if it was switching on and off. Detailed analysis revealed that this was indeed the case and that this behaviour, known from no other pulsar, followed a period of roughly 30 to 40 days. It was further shown that the pulsar spin-down rate increases by  $\sim 50\%$  when the pulsar is on. It is thought that this increased spin-down is due to the presence of plasma in the magnetosphere; the outflow of the plasma accelerated by the magnetic field increases the energy loss from the pulsar and thus, the spin-down. The cause of the observed sudden shut-down of emission is not completely understood.
- 2006** Hessels et al. (2006) reported on the discovery of the fastest known millisecond pulsar, PSR J1748-2446ad, spinning at a frequency of 716 Hz. This pulsar is located in the globular cluster Terzan 5, and is part of a binary system with an orbital period of about 26 hr. Eclipses from the extended companion object of only  $0.14 M_{\odot}$  are visible for about 40% of its orbit. It is conjectured that the companion could be a bloated main sequence star, filling its Roche lobe. The pulsar's high spin period challenges equations of state since the pulsar spins close to the mass-shedding limit.
- 2006** McLaughlin et al. (2006) found the first rotating radio transient (RRAT). These are sources of bright, short radio pulses. The radio pulses are similar to those known from pulsars with the exception of the periodic regularity known from pulsars. RRATs typically emit single pulses with time intervals of minutes or hours between them, making them visible for less than second on any given day (McLaughlin et al., 2006). Measured periods are longer than about half second. Gaensler et al. (2007) revealed the neutron star nature of RRATs by identifying an X-ray counterpart to RRAT J1819-1458, which has an X-ray spectrum consistent with that of a young neutron star. There is currently no widely accepted model for the emission from RRATs, also it is unclear how they fit into the "zoo" of known neutron star "species" (Keane and Kramer, 2008).
- 2008** The first millisecond pulsar in an eccentric orbit ( $e = 0.44$ ), which is not located in a globular cluster, was found in 2008 with the Arecibo observatory (Champion et al., 2008) in the PALFA survey (Cordes et al., 2006). The pulsar spins at 465 Hz and orbits in 95 d around the common centre of mass with one-solar mass companion. The formation of this very unusual system has been looked at very recently (Freire et al., 2011). It is assumed that this system started out as a binary with the current companion as a tertiary component around the neutron star and another star. The

latter spun up the neutron star by accretion and later disappeared either by chaotic three-body interactions or ablation by the millisecond pulsar.

**2008** The Fermi Gamma-ray Space Telescope discovers the first  $\gamma$ -ray pulsar identified only by its  $\gamma$ -ray pulsations at the centre of the supernova remnant CTA 1 (Abdo et al., 2008). The Large Area Telescope (LAT) onboard the Fermi Satellite was used for the observations, collecting about 900 photons from a point source. The source position is consistent with the sky position of a previously known X-ray source from Chandra observations, for which no pulsations had been detected<sup>13</sup>. Photons with energy  $> 100$  MeV from within  $1^\circ$  around the source position were bary-centred to the solar system barycentre and analysed for periodicity. Pulsations with a period of  $P_0 = 315.9$  ms and a spin period derivative of  $3.615 \text{ s s}^{-1}$ , typical of a young, energetic pulsar were found. As of today, more than 46  $\gamma$ -ray pulsars are known (Abdo et al., 2010).

**2009** Archibald et al. (2009) found the missing link that was speculated about since the discovery of X-ray binaries. Some of these systems should become visible as millisecond radio pulsars after the phase of accretion has ceased. In 2009, the first of these system was discovered. PSR J1023+0038 with a spin period of 1.69 ms was discovered as part of a binary system with a companion mass in the range of  $0.14 M_\odot$  to  $0.42 M_\odot$  and an orbital period of 0.198 d. Prominent eclipses were detectable over wide ranges of the orbit, depending on the observation wavelength; this suggests gas flowing out from the companion, creating a cloud of plasma, impenetrable to the radio waves. However, no accretion could be detected in 2009. In 2000/2001 however, the object was visible in V-band as a rapidly flickering source with emission lines typical of accretion. Also, a mild variation of optical brightness with a period of 0.198 d was known before 2009, which, as we now know, is caused by the orbital motion of the binary system. Understanding this system will provide valuable information about the formation and evolution of millisecond pulsars.

**2010** The relativistic delay of light in a gravitational field, also known as the Shapiro delay was used to measure the mass of the PSR J1614-2230, which is in a binary system with a  $0.500 M_\odot$  white dwarf (Demorest et al., 2010). The neutron star mass is found to be  $1.97 \pm 0.04 M_\odot$ , the heaviest neutron star known to date. The very high orbital inclination of the binary system ( $89.17^\circ$ ) allowed the measurement of the Shapiro delay with very high signal-to-noise ratio at superior conjunction when the radio pulses pass through the gravitational field of the white dwarf. This high mass excludes all current equations of state predicting the existence of strange matter in neutron stars (Lattimer and Prakash, 2001).

## 2.2 Pulsar spin period evolution

---

A property of all observed pulsars is a steady increase of their spin period  $P$ . The observed rates  $\dot{P} = dP/dt$  of change are in a 10-order-of-magnitude range  $10^{-21} \text{ s s}^{-1} \leq \dot{P} \leq 10^{-11} \text{ s s}^{-1}$ . Here, we review how the observed periods and period derivatives can be used to estimate the energy loss, age, and magnetic field strength of pulsars.

---

<sup>13</sup>Other radio-quiet pulsars seen in  $\gamma$ -rays before had also been detected in X-rays, like Geminga (Bertsch et al., 1992; Halpern and Holt, 1992).

### 2.2.1 Spin-down luminosity

The period increase implies a steady loss of rotational energy from the pulsar. To relate the energy loss to a change in pulsar period consider the time derivate of the rotational energy defined with the help of the moment of inertia  $I$

$$\dot{E}_{\text{rot}} = -\frac{d}{dt} \left( \frac{1}{2} I \Omega^2 \right) = -I \Omega \dot{\Omega} = 4\pi^2 I \frac{\dot{P}}{P^3}, \quad (2.5)$$

where  $\Omega = 2\pi P^{-1}$  is the angular spin velocity of the pulsar. The canonical moment of inertia for neutron stars is assumed to be  $10^{38} \text{ kg m}^2$ , see Equation (2.4). With this value we find for the energy loss, which usually is called, the *spin-down luminosity*:

$$\dot{E}_{\text{rot}} = 3.94 \times 10^{24} \text{ W} \times \left( \frac{\dot{P}}{10^{-15} \text{ s s}^{-1}} \right) \left( \frac{1 \text{ s}}{P} \right)^3, \quad (2.6)$$

where  $3.94 \times 10^{24} \text{ W} = 1.03 \times 10^{-2} L_{\odot}$  with the solar luminosity  $L_{\odot} = 3.839 \times 10^{26} \text{ W}$  for comparison. Traditionally, astronomers measure the spin-down energy in erg rather than in W. The conversion equation simply is  $1 \text{ W} = 10^7 \text{ erg}$ .

In our “toy model”, we expect the pulsar to be a rotating dipole magnet; simplifying a little further by neglecting the plasma-filled magnetosphere for now, one can compute the spin-down luminosity of a rotating magnetic dipole in vacuo. A rotating magnetic dipole moment  $\vec{m}$  has a power output of  $\dot{E} = \frac{2\mu_0}{12c^3} \ddot{m}^2$  with the vacuum permeability  $\mu_0$ . If it rotates at an angle  $\alpha$  between rotation and magnetic axis we find (Landau and Lifshitz, 1997):

$$\dot{E}_{\text{dipole}} = \frac{\mu_0}{6c^3} m^2 \sin^2(\alpha) \Omega^4. \quad (2.7)$$

Assuming a surface magnetic field strength  $B$  at radius  $R$  the magnetic moment<sup>14</sup> is  $m = 2\pi BR^3 / \mu_0$ . The power output is given by

$$\dot{E}_{\text{dipole}} = \frac{2\pi}{3c^3 \mu_0} B^2 R^6 \sin^2(\alpha) \Omega^4. \quad (2.8)$$

Equating  $\dot{E}_{\text{dipole}}$  and  $\dot{E}_{\text{rot}}$  one can formulate the differential equation governing pulsar electromagnetic dipole spin-down

$$\dot{\Omega} = -\frac{2\pi}{3c^3 \mu_0} \frac{B^2 R^6}{I} \sin^2(\alpha) \Omega^3 \quad \text{or} \quad (2.9)$$

$$\dot{P} = \frac{8\pi^3}{3c^3 \mu_0} \frac{B^2 R^6}{I} \sin^2(\alpha) P^{-1}. \quad (2.10)$$

In a more general form, Equations (2.9) and (2.10) can be re-written as

$$\dot{\Omega} = \gamma_{\text{dip}} \Omega^n \quad \text{and} \quad \dot{P} = (2\pi)^{n-1} \gamma_{\text{dip}} P^{2-n}, \quad \text{with} \quad \gamma_{\text{dip}} = \frac{2\pi}{3c^3 \mu_0} \frac{B^2 R^6}{I} \sin^2(\alpha) \quad (2.11)$$

where  $n$  is often called the “braking index” and would be expected to be  $n = 3$  for pure electromagnetic dipolar spin-down.

<sup>14</sup>We note that our definition differs by a factor of 2 from the definition  $m \approx \pi BR^3 / \mu_0$  used elsewhere in the literature.

As pointed out above, this calculation assumed a rotating dipole magnet in vacuo. As already described, the lighthouse model assumes a plasma-filled magnetosphere around the pulsar. Thus, not surprisingly the braking index of  $n = 3$  is not observed for most pulsars. Other sources of energy dissipation can exist, the most prominent example of which is a wind of particles outflowing from the pulsar. A remarkable observation of this effect has been demonstrated in the pulsar B1931+24 (Kramer et al., 2006a).

### 2.2.2 The characteristic age

Equation (2.11) can be used to obtain a rough estimate of the pulsar age, assuming its spin period has followed this relation over its complete past. Then, the differential Equation (2.11) can be integrated by separation of variables from time  $t_0$  in the past to the present time  $t$  and expressing  $\gamma_{\text{dip}}$  in terms of  $P$  and  $\dot{P}$  to yield

$$t - t_0 = \frac{P(t)}{(n-1)\dot{P}(t)} \left[ 1 - \left( \frac{P(t)}{P(t_0)} \right)^{n-1} \right]. \quad (2.12)$$

Assuming pulsars are born spinning much faster than at the present time  $P(t_0) \ll P(t)$ , the expression in the square brackets on the right-hand side of Equation (2.12) is of order unity and Equation (2.12) simplifies to

$$t - t_0 = \frac{P}{(n-1)\dot{P}}, \quad (2.13)$$

which defines the *characteristic age*  $\tau_c^{(n)}$  of a pulsar, assuming a braking index  $n$ :

$$\tau_c^{(n)} \equiv \frac{P}{(n-1)\dot{P}} \approx \frac{31.7 \text{ Myrs}}{n-1} \times \left( \frac{P}{1 \text{ s}} \right) \left( \frac{10^{-15} \text{ s s}^{-1}}{\dot{P}} \right), \quad (2.14)$$

This is the time it takes a pulsar born at an infinitely low period to spin down to period  $P$  at the present time. It is a rough estimate of the age of a pulsar, not to be taken literally because of the assumptions going into this estimate; also, the braking index can vary between pulsars. Different examples are the Crab pulsar with  $\tau_c^{(3)} = 1270 \text{ yrs}$ <sup>15</sup>, while the known age of the pulsar is 957 yrs in 2011. Here, the known age from the supernova recorded in 1054, and the estimate from the spin-down age agree well. A counter-example is PSR J0358+2817; Kramer et al. (2003) showed that the characteristic age is  $\tau_c^{(3)} = 620 \text{ kyrs}$ ; due to precise proper motion measurements the pulsar could be shown to be associated with the supernova remnant S147 with an age of only 30 kyrs. Here, the two ages differ by a factor of 20!

These two examples are to illustrate that the characteristic age may be useful as a *rough* estimate and should not be interpreted as the real age of the pulsar.

### 2.2.3 Magnetic field strength

The direct measurement of neutron star magnetic field strengths is possible through the observation of features in the X-ray spectrum. A thermal spectrum is emitted from the hot neutron star and sometimes contains additional features from the cyclotron radiation of

<sup>15</sup><http://www.jb.man.ac.uk/~pulsar/crab.html>

electrons in the neutron star's magnetic field. Observations of these features were used to infer the magnetic field strength for the isolated neutron star 1E1207.4-5209 (Bignami et al., 2003). Other observations are possible in spectral features of X-ray binaries like Her X-1 (Truemper et al., 1978) and 4U 0115+63 (Wheaton et al., 1979). These direct measurements indicate magnetic field strengths in the range of  $8 \times 10^6$  T to  $5.3 \times 10^8$  T.

For radio pulsars, no such measurements have been possible. An order-of-magnitude estimate of the magnetic field strength can however be extracted from assuming the spin-down is dominated by dipolar electromagnetic emission. In that case we can solve Equation (2.10) for the magnetic field strength to obtain

$$B = \sqrt{\frac{3c^3 \mu_0}{8\pi^3} \frac{I}{R^6 \sin^2(\alpha)} P \dot{P}}. \quad (2.15)$$

Since the inclination angle  $\alpha$  as well as moment of inertia  $I$  and the radius  $R$  are usually unknown, we call this magnetic field strength the characteristic magnetic field. Furthermore, as already pointed out above, other processes can contribute to the observed pulsar spin down  $\dot{P}$ . Thus, Equation (2.15) is useful to obtain an order-of-magnitude estimate of the magnetic field strength at the neutron star surface; with the canonical values of  $I$ ,  $R$ , and  $\alpha = \frac{\pi}{2}$  we find

$$B = 2.0 \times 10^8 \text{ T} \times \left( \frac{\dot{P}}{10^{-15} \text{ s s}^{-1}} \right)^{\frac{1}{2}} \left( \frac{P}{\text{s}} \right)^{\frac{1}{2}} \quad (2.16)$$

for the magnetic field on the pulsar surface.

---

## 2.3 Magnetosphere, beam geometry and polarisation

---

The simple toy model introduced above allows for a simple description of many observed pulsar properties such as pulsar spin period evolution, energetics, and magnetic fields. Above, we simply explained the observed pulses from radio pulsars by the sweep of a conical beam over the observer's line of sight. Here, we illustrate the emission processes in the pulsar magnetosphere with the help of the Goldreich-Julian model (Goldreich and Julian, 1969). We further introduce a more complete picture of the geometrical factors describing the pulsar beam and its polarisation.

### 2.3.1 Goldreich-Julian model

To derive the formalism describing the simple toy model of a pulsar above we have always assumed that the pulsar is a highly-magnetised rotating neutron star in vacuo. In fact, this ad-hoc model is not consistent with Maxwell's equations as was realised by Goldreich and Julian (1969). Constructing the simple toy model and assuming vacuum outside the neutron star is inconsistent: the strong rotating magnetic fields induce electric fields strong enough to pull out charges from the neutron star surface which then will form a plasma-filled magnetosphere around the neutron star.

The *Goldreich-Julian model* (Goldreich and Julian, 1969) is the simplest model of the pulsar magnetosphere. It is not a fully realistic model of a neutron star and its magnetosphere, yet some basic principles can be readily understood with its help. In this model, the pulsar is assumed to be an aligned rotator, i.e. the magnetic and the rotation axis are pointing in the same direction. The magnetic field is assumed to be a simple dipole field. Further, the

pulsar is assumed to be a superconducting sphere inside vacuum. Goldreich and Julian (1969) show that this simple constellation of a highly-magnetised, rapidly-rotating, superconducting neutron star in vacuum is inconsistent as it leads to a discontinuity in the radial electric field at the surface of the neutron star, much stronger than local gravity. This results in the extraction of charged particles from the neutron star that form a plasma-filled magnetosphere around the neutron star. A full derivation of the equations given here can be found in Section 8.3.2

For the magnetic field  $\vec{B}$  in spherical coordinates we find

$$\vec{B} = \frac{B_R R^3}{2r^3} (2 \cos(\theta) \vec{e}_r + \sin(\theta) \vec{e}_\theta). \quad (2.17)$$

with a magnetic field  $B_R$  at the stellar surface. Assuming a rotation of the pulsar around an axis  $\vec{\Omega}$ , points inside the pulsar are moving with a velocity  $\vec{v} = \vec{\Omega} \times \vec{r}$ . As pointed out above, the Goldreich-Julian model (Goldreich and Julian, 1969) for sake of simplicity assumes that the pulsar rotation axis coincides with its magnetic field axis. Note, that in practice small deviations from the alignment must be allowed to observe a pulsing radio signal.

The neutron star is assumed to be a super-conducting sphere. Thus, an electric field  $\vec{E}$  is induced by the rotating magnetic field. Inside the super-conduction neutron star, the charge distribution will be re-arranged such that the inside of the sphere is force-free. The force  $\vec{F}$  acting on the charges is the Lorentz force, which in equilibrium vanishes inside the star. This implies

$$\vec{E}_< = -\vec{v} \times \vec{B} = \frac{\Omega B_R R^3}{2r^2} (\sin^2(\theta) \vec{e}_r - \sin(2\theta) \vec{e}_\theta) \quad (2.18)$$

for the induced electric field  $\vec{E}_<$  in the stellar interior. Note, that the electric field is symmetric under rotation in the azimuthal direction.

The exterior of the neutron star we assume to be charge-free. The exterior charge density  $\rho_>$  thus vanishes everywhere  $\rho_> \equiv 0$ , and from Maxwell's equations  $\nabla\Phi_> \equiv 0$  follows for the exterior electrostatic potential. The electrostatic potential has to be continuously connected to the potential in the interior at the stellar surface  $r = R$ . Also, we impose the boundary condition that the exterior electrostatic potential vanishes at infinity. Solving this equation system, see Section 8.3.2, we can compute the electric field inside and outside of the neutron star as:

$$\vec{E}(\vec{r}) = \begin{cases} \frac{\Omega B_R R^3}{2r^2} [\sin^2(\theta) \vec{e}_r - \sin(2\theta) \vec{e}_\theta] & \text{for } r \leq R \\ \frac{\Omega B_R R^3}{2r^4} [(3 \sin^2(\theta) - 2) \vec{e}_r - \sin(2\theta) \vec{e}_\theta] & \text{for } r > R \end{cases}. \quad (2.19)$$

As expected, the tangential component of  $\vec{E}$  along the  $\theta$ -direction is continuous at the stellar surface, since otherwise it would be compensated for by surface currents re-arranging the surface density. The radial component however has a discontinuity at the stellar surface. It jumps by

$$\Delta E_r(\theta) = \Omega B_R R \cos^2(\theta), \quad (2.20)$$

which leads to a surface charge density of

$$\sigma(\theta) = \epsilon_0 \Delta E_r(\theta) = \epsilon_0 \Omega B_R R \cos^2(\theta). \quad (2.21)$$

Is the solution described so far a stable solution? To answer this question, consider the electric field strength at the stellar surface parallel to the magnetic field lines. This component is interesting because it can accelerate charges out of the neutron star's crust. The

parallel  $E_{\parallel}$  component of  $\vec{E}$  at the stellar surface is given by

$$E_{\parallel} = \left. \frac{\vec{E} \cdot \vec{B}}{|\vec{B}|} \right|_{r=R} = -2\Omega B_R R \frac{\cos^3(\theta)}{\sqrt{3 \cos^2(\theta) - 1}}. \quad (2.22)$$

The numerical pre-factor determining the order of magnitude for the electrical field strength in the previous equation has the value

$$2\Omega B_R R = 4\pi P^{-1} B_R R \approx 1.26 \times 10^{13} \text{ V m}^{-1} \left( \frac{1 \text{ s}}{P} \right) \left( \frac{B_R}{10^8 \text{ T}} \right) \left( \frac{R}{10 \text{ km}} \right), \quad (2.23)$$

which means that the electrostatic forces on charged particles exceed those of gravity by up to ten orders of magnitude. In turn, charged particles will be ripped out of the neutron star surface by the induced electric fields, accelerated along the magnetic field lines and form a plasma-filled magnetosphere surrounding the neutron star. The initially assumed vacuum condition outside the neutron star cannot be stable.

Assume now, that outside the star a charge distribution is allowed to form. Because charged particles can move freely subject to the Lorentz force, the exterior charge distribution  $\rho_{>}$  in static equilibrium follows from Maxwell's equations and the vanishing Lorentz force, Equation (8.63) (for details see Section 8.3.2) as

$$\begin{aligned} \rho_{>}(r, \theta) &= -2\epsilon_0 (\vec{B} \cdot \vec{\Omega}) \\ &= -\frac{\epsilon_0 \Omega B_R R^3}{r^3} (3 \cos^2(\theta) - 1). \end{aligned} \quad (2.24)$$

This also implies that the surface defined by  $\vec{B} \cdot \vec{\Omega} = 0$  separates space into regions with differing signs of the charge density.

Then the number density of charges at the magnetic poles, also known as the *Goldreich-Julian density*  $n_{\text{GJ}}$  is given by assuming a complete separation of charges and dividing the charge density by the charge of an electron,  $-e$ .

$$n_{\text{GJ}} = -\frac{1}{e} \rho_{>}(r = R, \theta = 0) = \frac{2\epsilon_0 \Omega B_R}{e} = \frac{4\pi \epsilon_0 B_R}{eP} \quad (2.25)$$

$$= 6.95 \times 10^{16} \text{ m}^{-3} \left( \frac{B_R}{10^8 \text{ T}} \right) \left( \frac{1 \text{ s}}{P} \right) \quad (2.26)$$

This high plasma density is a theoretical maximum value unless other processes contribute to the charge density (Lorimer and Kramer, 2005).

The plasma in the stellar exterior co-rotates rigidly with the stellar interior. This follows from the condition of vanishing Lorentz force in equilibrium, Equation (8.63), applied to both stellar interior and exterior. More details can be found in Section 8.3.2. The co-rotation can only be maintained until the rotational velocity reaches the speed of light. The cylinder inside which this condition is fulfilled, is called the *light cylinder* and its radius  $R_{\text{lc}}$  is obtained from the condition  $R_{\text{lc}} \Omega = c$ :

$$R_{\text{lc}} = \frac{c}{\Omega} = \frac{cP}{2\pi} = 4.77 \times 10^7 \text{ m} \left( \frac{P}{1 \text{ s}} \right), \quad (2.27)$$

much larger than the typical diameter of a neutron star, about the size of a large planet<sup>16</sup>. As the magnetic field drops off with  $r^{-3}$ , the magnetic field strength at the light cylinder is given by

$$B_{\text{lc}} = B_R \left( \frac{R}{R_{\text{lc}}} \right)^3 = B_R \left( \frac{R\Omega}{c} \right)^3 = B_R \left( \frac{2\pi R}{cP} \right)^3 \quad (2.28)$$

$$= 9.2 \times 10^{-4} \text{ T} \left( \frac{B_R}{10^8 \text{ T}} \right) \left( \frac{R}{10 \text{ km}} \right)^3 \left( \frac{1 \text{ s}}{P} \right)^3. \quad (2.29)$$

The light cylinder divides the neutron star magnetosphere into two regions: inside the light cylinder, the magnetic field lines close, while outside the light cylinder the field lines do not close. The first region contains *closed field lines*, while the latter contains *open field lines*. The regions with open field lines determine the *polar cap* on the neutron star surface (Lorimer and Kramer, 2005). The size of the polar cap is defined by the *last open field line*; this field line is the one tangential to the light cylinder. This can be used to define the boundary of the polar cap on the neutron star surface at spherical coordinates  $r = R$ ,  $\theta = \theta_{\text{pc}}$ , and  $\phi \in [0, 2\pi)$ . On any magnetic field line in the assumed dipole field, the expression  $\sin(\theta) r^{-1}$  is constant. Therefore, the polar cap opening angle follows from:

$$\frac{\sin^2(\theta)}{r} = \frac{\sin^2\left(\frac{\pi}{2}\right)}{R_{\text{lc}}} = \frac{2\pi}{cP} = \frac{\sin^2(\theta_{\text{pc}})}{R} \quad (2.30)$$

### 2.3.2 Radio emission from acceleration gaps

In the previous section we have shown that the simple Goldreich-Julian model predicts that a highly-magnetised, rapidly-rotating neutron star must be surrounded by a dense, plasma-filled magnetosphere. Theoretical modelling of the pulsar radio emission (see Section 3.6 in Lorimer and Kramer (2005) for an overview), requires plasma densities much larger than the Goldreich-Julian density, Equation (2.26), calculated in the previous section. Therefore, other mechanisms increasing the number of available plasma particles must exist. Possible mechanisms include the so-called *magnetospheric gaps regions* or *acceleration gaps*. Inside these gaps the condition of the rigidly co-rotating magnetosphere is no longer maintained, the force free state in the stellar exterior is no longer given, and thus, residual electric fields will arise, as described before Equation (2.24).

These gap regions are expected to occur in parts of the magnetosphere depleted of plasma. Two of these regions are thought to occur likely in nature: the open field line region above the polar cap, the so-called *polar gap* (Daugherty and Harding, 1986; Ruderman and Sutherland, 1975; Sturrock, 1971), and the region in between the field lines running close to the light cylinder, the so-called *outer gap* (Daugherty and Harding, 1986; Romani, 1996). Here, we will only consider the polar gap.

In the open field line region above the magnetic poles, the particles from the neutron star surface are easily extracted and then accelerated by the strong residual electric fields, Equation (2.23), parallel to the magnetic field lines up to relativistic energies with Lorentz factors  $\gamma \lesssim 10^7$  (Lorimer and Kramer, 2005). As these charges move on curved, accelerated orbits they emit curvature radiation in form of  $\gamma$ -photons; another possible process is the production of  $\gamma$ -photons from inverse Compton scattering between relativistic charged particles and photons at lower energy.

<sup>16</sup>For comparison, the radius of Jupiter is  $r_{\text{jup}} = 7.14 \times 10^7 \text{ m}$ .

Since the generated  $\gamma$ -photons move in presence of the strong magnetic field near the pulsar, they can either split into two  $\gamma$ -photons (Adler, 1971) or be converted into a pair of an electron and a positron (Daugherty and Harding, 1983). This obviously requires the energy of the  $\gamma$ -photon to exceed that of the particle pair (Erber, 1966). The resulting particles are then accelerated again by the electric fields in the polar gap. They themselves may then produce a second generation of photons, which again create particles from pair creation processes. This process is called an avalanche of *secondary pair plasma* and was pointed out already by Sturrock (1971). It is possible that further (tertiary etc.) generations of photons and created pairs continue this avalanche. Hibschan and Arons (2001b,c) find theoretical values of pair production multiplicities<sup>17</sup> in the range from 10 to  $10^4$ , depending on the magnetic field of the pulsar and the energy of the first-generation photon. Thus, this process could increase the initial plasma density by the same factor. Recently, de Jager (2007) has derived lower limits on the pair production multiplicity from H.E.S.S.<sup>18</sup> measurements of the high-energy emission from pulsar wind nebulae; extrapolations of these measurements indicate that the pair production multiplicities are well above the theoretically predicted values from Hibschan and Arons (2001c). The observable radio emission finally is believed to be produced by the secondary or tertiary plasma at some distance from the stellar surface.

Note, that the polar gap model also predicts the shut-down of pulsar radio emission if the accelerating electric fields are not strong enough. The acceleration is determined by the difference in the electrostatic potential difference at the stellar exterior; if this difference is not large enough to exceed an assumed critical value for the efficient production of multiple photons and pair generations, its dependence on  $B_R$  can be translated into a dependence on  $P$  and  $\dot{P}$  via Equation (2.15). The values of  $P$  and  $\dot{P}$  where radio emission is expected to cease, define the *pulsar death line* and the *graveyard* shown in Figure 2.9.

Similarly, if the magnetic field strength exceeds a certain critical value ( $B_c = 4.4 \times 10^9$  T, according to Daugherty and Harding (1983)), other competing processes besides pair production limit the radio emission; this condition can again be converted into limits on  $P$  and  $\dot{P}$ . The corresponding region is also shown in Figure 2.9

### 2.3.3 Beam geometry

A more detailed description involves the geometrical factors, shown in Figure 2.4, which we adapted from Lorimer and Kramer (2005).

The emission cone is centred on the magnetic axis and has an angular radius (or *half opening angle*) of  $\varrho$ . It is inclined by the *inclination angle*  $\alpha$  with respect to the rotation axis of the pulsar. The observer's line of sight intersects under the angle  $\beta$  (the *impact parameter*). The rotation of the pulsar carries the emission cone across the observer's line of sight. With spherical geometry one can show that the observed pulse width  $W$  measured along the rotation phase can be expressed as a function of  $\varrho$  and the other angles as

$$\sin^2\left(\frac{W}{4}\right) = \frac{\sin^2\left(\frac{\varrho}{2}\right) - \sin^2\left(\frac{\beta}{2}\right)}{\sin(\alpha)\sin(\alpha + \beta)}, \quad (2.31)$$

<sup>17</sup>i.e. how many pairs are produced from a single photon in the first generation

<sup>18</sup>H.E.S.S. is the High Energy Stereoscopic System, a system of four Imaging Atmospheric Cherenkov Telescopes in Namibia. It is designed to detect cosmic  $\gamma$ -rays in the 100 GeV to TeV energy range by air showers.

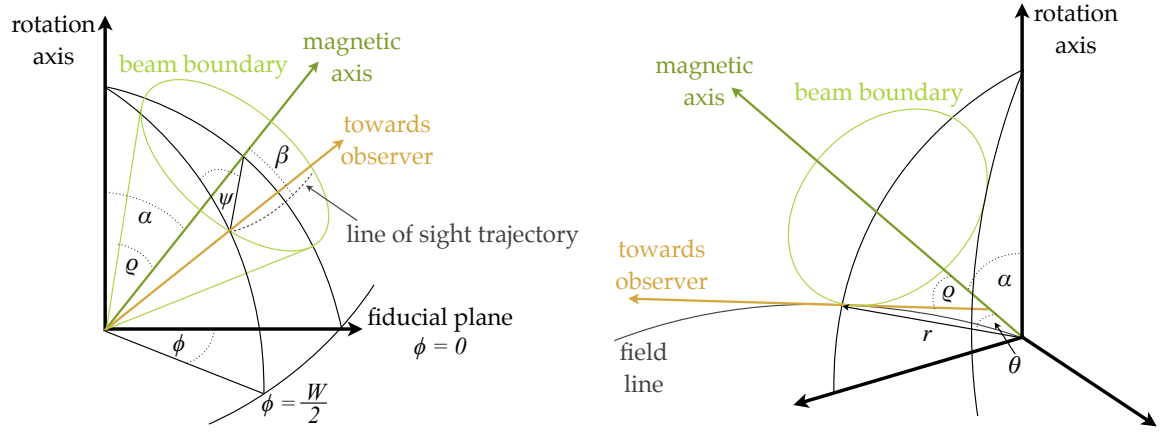


**Figure 2.4:** The geometry of beamed pulsar emission. **(Left)** The emission cone orientation is determined by the inclination angle  $\alpha$  and the impact parameter  $\beta$ . The half opening angle of the cone is  $\varphi$ . **(Right)** The relationship between the polar coordinates of the emission cone and the angular radius of the emission cone. This figure was adapted from Lorimer and Kramer (2005).

as shown in Gil et al. (1984). In some cases (see Section 8.3.1) the equivalent form

$$\cos(\varphi) = \cos(\alpha) \cos(\alpha + \beta) + \sin(\alpha) \sin(\alpha + \beta) \cos\left(\frac{W}{2}\right) \quad (2.32)$$

with  $\varphi$  as a function of  $W$  is more useful.

From the geometry it is clear that a pulse can only be visible if  $|\beta| \leq \varphi$ . Depending on where the line of sight passes with respect to the magnetic and the rotation axis, one distinguishes between two scenarios: the *inner line of sight*, and the *outer line of sight*, respectively. The inner line of sight happens for  $\beta < 0$  ( $\alpha < 90^\circ$ ) or for  $\beta > 0$  ( $\alpha > 90^\circ$ ), respectively. The outer line of sight then is given for  $\beta > 0$  ( $\alpha < 90^\circ$ ) or for  $\beta < 0$  ( $\alpha > 90^\circ$ ), respectively.

Assuming confinement of the emission cone by the last open field lines, one can relate the cone opening angle  $\varphi$  to the polar coordinates (radius  $r$  and angle  $\theta$  in the plane perpendicular to the rotation axis, see Figure 2.4) of these field lines (Lorimer and Kramer, 2005). Gangadhara and Gupta (2001) show that this relation is given by

$$\tan(\theta) = -\frac{3}{2 \tan(\varphi)} \pm \sqrt{2 + \left(\frac{3}{2 \tan(\varphi)}\right)^2}. \quad (2.33)$$

The solution with the plus sign can be approximated by

$$\theta \approx \frac{2}{3}\varphi \quad (2.34)$$

for small  $\theta$  and  $\varphi$  ( $\lesssim 30^\circ$ ), i.e. for regions close to the magnetic axis. Let us now assume that Equation (2.34) describes the last open magnetic field lines. We can then insert the coordinate relation for the last open field lines at the light cylinder from Equation (2.30) to obtain

$$\varphi \approx \frac{3}{2} \sqrt{\frac{2\pi r}{cP}} = 1.24^\circ \left(\frac{1 \text{ s}}{P}\right)^{\frac{1}{2}} \left(\frac{r}{10 \text{ km}}\right)^{\frac{1}{2}} \quad (2.35)$$

This equation indicates a simple relationship between cone opening angle  $\varphi$  and the inverse of the square root of the spin period  $P$ . The opening angle  $\varphi$  can be inferred from the

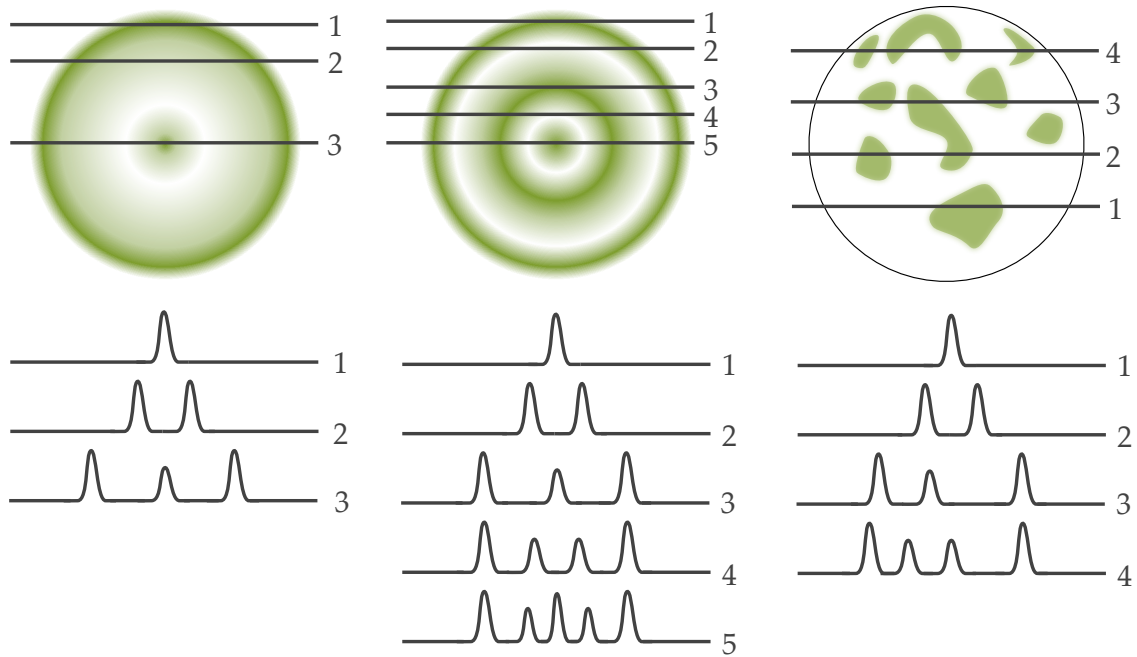


**Figure 2.5:** Schematics of different beam structure models and their resulting pulse profiles. The left panel shows the simplest model with a hollow cone and a core component by Backer (1976), an augmentation of the model by Komesaroff (1970). The panel in the middle shows the model of nested cones by Rankin (1993a). On the right, the patchy-beam model by Lyne and Manchester (1988). Possible pulse profiles are below, labeled by the line of sight intersection above.

measured pulse width via Equation (2.32), given that  $\alpha$  and  $\beta$  are known. The latter two angles can be obtained from polarisation measurements of the pulse profile (for details on this method, see Section 2.3.4). Various authors indeed report this predicted relationship for slow pulsars (Gil et al., 1993; Kramer et al., 1994; Rankin, 1993a,b). Millisecond pulsars do not seem to follow this relation (Lorimer and Kramer, 2005).

### Beam structure

The structure of the beam itself might deviate from the simple filled-cone picture assumed here. A hollow cone emission follows from the early model proposed by Komesaroff (1970): there, the emission is caused by the curvature (synchrotron) emission of electrons accelerated along the curved magnetic field lines. The smaller the radius of curvature of the field line, the higher the emitted power. The strongest emission is expected at the last open field line, tangential to the light cylinder, while the emission should vanish completely at the centre of the beam along the magnetic axis. This naturally leads to the emission along a hollow cone in which the opening angle is defined by the last open field lines (see above). This model can easily explain single or two-component pulse profiles: a single-component profile is seen when the line of sight grazes along the shell of the hollow cone; a two-component profile is seen for an intersection of the hollow cone, where the separation of the components varies with the impact parameter angle  $\beta$ . The two cases are illustrated in the leftmost panel of Figure 2.5.

More complex pulse profiles with more than two components have been observed in nature. In order to explain their existence and origin, two different main models have

been proposed: a) a nested cone-structure along with a central core component and b) a patchy beam structure. We briefly review both models here and illustrate them as well in Figure 2.5.

Backer (1976) introduced a central *pencil beam*, also referred to as a *core* component (Lorimer and Kramer, 2005) to the earlier hollow cone model. The additional core component then explains the occurrence of three-component pulse profiles. A further addition to this model is another emission cone, so that the emission beam is composed of two nested hollow emission cones and a central pencil beam. In a series of papers a very detailed analysis of this idea and its validity by analysis of (polarisation) observations of pulsars is presented by Mitra and Rankin (2002); Radhakrishnan and Rankin (1990); Rankin (1983a,b, 1986, 1990, 1993a,b); Rankin and Ramachandran (2003). This paper series also analyses other observed phenomena in radio pulsar emission on grounds of the same model, namely mode changing, drifting sub-pulses, and pulse nulling, see e.g. Lyne and Graham-Smith (2005).

Various pulsars exhibit asymmetries between the peaks in multi-component profiles or a displacement of the “core” component from the centre of the pulse profile; both effects are not expected from and not explained straightforwardly from the nested cone model. This could imply a large variation of emission intensity around the cone. A more detailed analysis by Lyne and Manchester (1988) indicated that in fact the pulsar beam might consist of randomly distributed patches within an envelope, which defines the overall pulse shape. This could be due to only certain parts of the field lines being active at any given time; this could be explained by localised plasma discharges in the polar gap region (see Section 2.3.2). This model is illustrated in the rightmost panel of Figure 2.5.

As of today, the interpretation of measured pulse profiles exclusively by one of the above models is still not clear and under debate: Kijak and Gil (2002) find observations to agree well with the nested cone model but not with patchy-beam model, while Han and Manchester (2001) draw the opposite conclusion. New models have been developed recently, that combine a partially active (somewhat patchy) beam, where the activity pattern changes as a function of the emission height in the magnetosphere (Karastergiou and Johnston, 2007). It seems to reproduce the observed variety of pulse profiles well.

### 2.3.4 Rotating vector model

Measurements of the polarisation of pulse profiles have shown a remarkably simple structure; in many cases the polarisation angle is characterised by a simple S-shaped sweep over one pulse period. Radhakrishnan and Cooke (1969) showed that the observable sweep of the polarisation angle can be explained by a remarkably simple model of the pulsar beam geometry, polarisation the so-called rotating vector model (RVM). It relates the polarisation vector of the radio emission to a the magnetic field line at the emission point in a radiating cone of emission. As this vector crosses the line of sight, its projected position angle (the polarisation angle) changes smoothly in a S-shaped way. This is shown schematically in Figure 2.6.

If the pulse profile consists of multiple components, it will be possible that each component will have its own related field line and the components will be emitted from different small regions in the magnetosphere. In this case the position angle curve has to be interpreted as the series of multiple emission sources crossing the line of sight. (Blaskiewicz et al., 1991) have shown that apart from some limiting cases the original rotating vector model geometry may still be applied.

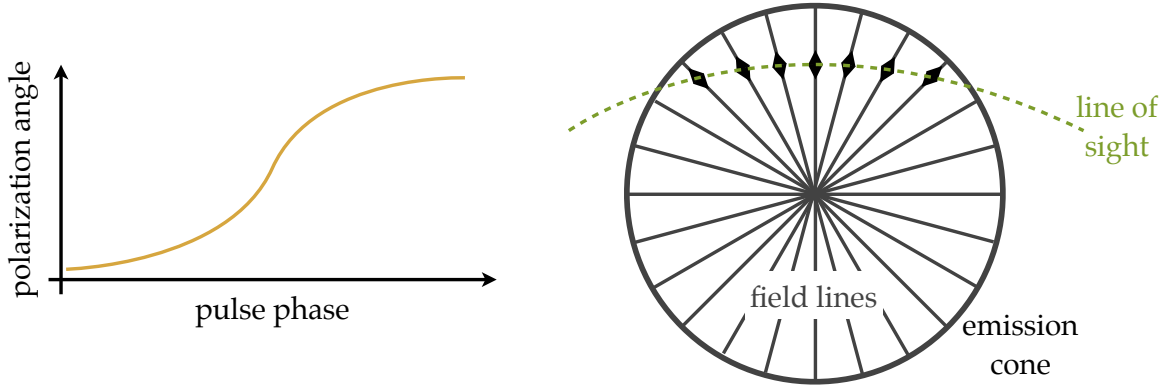


**Figure 2.6:** Schematic of the rotating vector model by Radhakrishnan and Cooke (1969), adapted from Lorimer and Kramer (2005). The right hand picture shows a view down the emission cone along the magnetic axis. The radial lines are the magnetic field lines. As the emitting field line is swept across the line of sight (green), the angle between the two lines, the polarisation angle, varies smoothly. The variation of the polarisation angle as a function of the rotation (pulse) phase is shown schematically on the left.

In the rotating vector model, the polarisation angle  $\psi$  is given by the relation

$$\tan(\psi - \psi_0) = \frac{\sin(\phi + \phi_0) \sin(\alpha)}{\sin(\alpha + \beta) \cos(\alpha) - \cos(\alpha + \beta) \sin(\alpha) \cos(\phi + \phi_0)}, \quad (2.36)$$

where  $\phi$  is the pulsar's spin (or pulse) phase,  $\alpha$  is the angle between the pulsar's rotation and magnetic axes,  $\beta$  is the angle between the line of sight and the pulsar's magnetic axis (the so-called impact parameter), and  $\psi_0$  is the projected direction of the rotation axis (Lyne and Graham-Smith, 2005).

The steepest ascent of the S-shaped curve of polarisation angle over pulse phase can readily be determined as the derivative of Equation (4.3) at  $\phi = \phi_0$  and is found to be

$$\max_{0 \leq \phi \leq 2\pi} \left( \frac{d\psi}{d\phi} \right) = \frac{\sin(\alpha)}{\sin(\beta)} \quad (2.37)$$

and is related to the inclination angle and the impact parameter only. For fixed  $\alpha$ , the steepest ascent is found for  $\beta = 0$  when the beam is cut centrally by the line of sight.

In the literature, there are various improvements to the initial RVM model to include relativistic effects or, for example, plasma currents (Blaskiewicz et al., 1991; Hibschan and Arons, 2001a). Here we do not describe these, as for the scope of this thesis, the simple model is sufficient. It is noteworthy, however, that the corrections and shifts resulting from the more advanced models, allow a determination of the emission height in the pulsar magnetosphere

## 2.4 Pulse broadening in the interstellar medium

The sharp radio pulse emitted from the radio pulsar does not arrive this way at the terrestrial detector. On its way through the interstellar medium, two main effects effectively broaden the pulse. Dispersion is caused by the interaction of radio waves with the free electrons from ionised hydrogen gas, and can be fully corrected for with proper observing

hardware and software. Multi-path scattering of radio waves causes a part of the radio waves to take a slightly longer way, introducing an extra delay, which cannot be corrected for directly in observing hardware and software.

### 2.4.1 Dispersion

Already at the discovery of pulsars by Hewish et al. (1968) it was found that the arrival time of the pulsar's pulses depends on the radio frequency at which they are emitted. Hewish et al. (1968) correctly interpreted this effect being caused by the presence of free electrons from ionised hydrogen gas in the interstellar medium which causes a frequency dependence of the group velocity of radio waves.

The refractive index  $\mu$  (neglecting small corrections from the Galactic magnetic field) for a radio wave of frequency  $\nu$  is given by

$$\mu = \sqrt{1 - \left(\frac{\nu_p}{\nu}\right)^2}, \quad (2.38)$$

where  $\nu_p$  is the resonance frequency of the plasma and is given by

$$\nu_p = \frac{1}{2\pi} \sqrt{\frac{n_e e^2}{m_e \epsilon_0}} = 8.979 \text{ kHz} \times \sqrt{\frac{n_e}{1 \text{ cm}^{-3}}}, \quad (2.39)$$

where  $n_e$  is the electron number density,  $e$  the elementary charge,  $m_e$  the mass of the electron and  $\epsilon_0$  the vacuum permittivity.

It follows from Equation (2.38) that  $\mu < 1$  and thus for the group velocity  $v_g = c\mu < c_0$ . The delay relative to a signal at infinite frequency over a distance  $d$  is then given by

$$\Delta t = \int_0^d \frac{dl}{v_g} - \frac{d}{c}. \quad (2.40)$$

Substituting  $v_g \approx c \left(1 + \frac{v_p^2}{2\nu^2}\right)$  for  $\nu_p \ll \nu$  we find

$$\Delta t = \frac{e^2}{8\pi^2 m_e \epsilon_0 c} \frac{DM}{\nu^2} \quad \text{with} \quad DM = \int_0^d dl n_e, \quad (2.41)$$

where the integrated electron number density along the line of sight is called the dispersion measure (DM). The pre-factor has a numerical value of

$$\frac{e^2}{8\pi^2 m_e \epsilon_0 c} \approx 4148.8 \text{ MHz}^2 \text{ pc}^{-1} \text{ cm}^3 \text{ s}. \quad (2.42)$$

From Equation (2.41) we find the delay between two frequencies  $\nu_1$  and  $\nu_2$  as:

$$\Delta t \approx 4149 \text{ s} \left( \left(\frac{1 \text{ MHz}}{\nu_1}\right)^2 - \left(\frac{1 \text{ MHz}}{\nu_2}\right)^2 \right) \frac{DM}{1 \text{ pc cm}^{-3}}. \quad (2.43)$$

The effect is illustrated in Figure 2.7. It shows an observation from the PALFA survey of PSR J1922+1722 ( $P_0 \approx 236$  ms, discovered in the Deep Multibeam Survey Processing Camilo et al. (2004)) folded at the pulsar spin period. Successive pulses are coherently added or

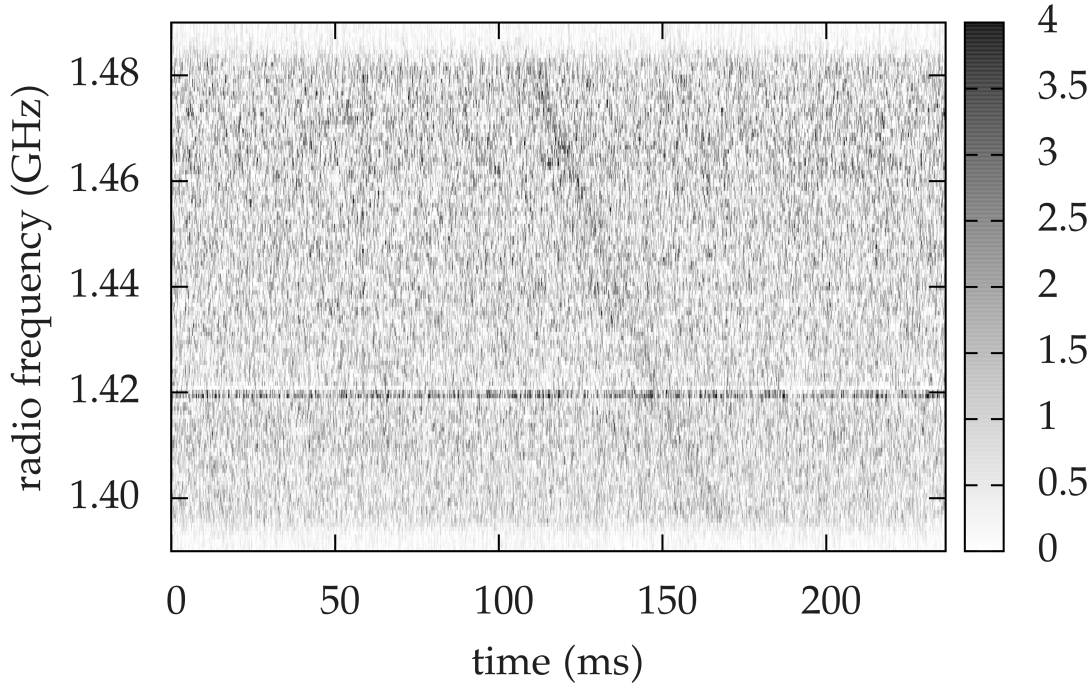


**Figure 2.7:** Dispersion in the interstellar medium: higher radio frequencies arrive earlier than lower radio frequencies. The graph shows an observation of PSR J1922+1722 folded at the spin period to coherently add successive single pulses. The summed dispersed pulse can be seen between 100 ms and 170 ms. The grey-scale shows the radio flux in arbitrary units. The line at 1.42 GHz is the 21-cm hydrogen line.

“stacked” to increase signal-to-noise ratio. The sweep over the radio frequency band is clearly visible between 100 ms and 170 ms. The delay between the highest and the lowest frequency of 1.49 GHz and 1.39 GHz, respectively is  $\Delta t \approx 66$  ms. This corresponds to a  $DM \approx 236 \text{ pc cm}^{-3}$  for this pulsar.

Consider a small frequency range  $[\nu - \Delta\nu/2, \nu + \Delta\nu/2]$ ; with  $\Delta\nu \ll \nu$ . This is fulfilled by a single frequency channel of the filterbank or for many pulsar surveys also by the complete radio frequency observation band<sup>19</sup>. The smearing by dispersion over this frequency range is given by  $\delta t = \Delta\nu \times \frac{d(\Delta t)}{d\nu}$ , or using Equation (2.41):

$$\delta t = -8298 \text{ s} \left( \frac{1 \text{ MHz}}{\nu} \right)^3 \left( \frac{DM}{1 \text{ pc cm}^{-3}} \right) \left( \frac{\Delta\nu}{1 \text{ MHz}} \right). \quad (2.44)$$

Measuring the time delay from Equation (2.43) over a range of radio frequencies allows to determine the dispersion measure and thereby the amount of free electrons along the line of sight. With a numerical model of the distribution of electrons in our Galaxy, this information can be used to infer the distance to the pulsar. The most recent model (NE2001) including the spiral arm structure of our Galaxy is due to Cordes and Lazio (2002). It also features a web-interface<sup>20</sup> for distance computations (among others) based on the NE2001 model.

<sup>19</sup>For example for the PALFA survey  $\Delta\nu = 100$  MHz and  $\nu = 1400$  MHz still is well described by this relation.

<sup>20</sup>[http://rsd-www.nrl.navy.mil/7213/lazio/ne\\_model/](http://rsd-www.nrl.navy.mil/7213/lazio/ne_model/)

### 2.4.2 Multi-path propagation

Another fundamental limit to the temporal resolution of pulses arises from an increasing amount of free electrons along the line of sight with larger DM; this leads to multi-path scattering and stochastic broadening of the pulse not removable by de-dispersion (Lorimer and Kramer, 2005). The pulse broadening by multi-path scattering manifests itself in form of an exponential tail at the pulse profile, see e.g. Figures in Bhat et al. (2004).

A multi-frequency study of 98 low Galactic latitude pulsars at Arecibo Observatory (Bhat et al., 2004) derived a relationship between the dispersion measure DM and the pulse broadening time  $\tau_d$ . This quantity measures the time scale of the exponential tail at the scattered pulse profile

$$\log_{10} \left( \frac{\tau_d}{1 \text{ ms}} \right) = -6.46 + 0.154 \log_{10} (\text{DM}) + 1.07 (\log_{10} (\text{DM}))^2 - 3.86 \log_{10} (\nu), \quad (2.45)$$

where the dispersion measure DM is in  $\text{pc cm}^{-3}$  and the radio frequency  $\nu$  is in GHz.

This fundamental limit can also be used as a figure of merit when generating trial DMs for the de-dispersion in an analysis pipeline to search for unknown pulsars, compare Section 3.7.2. The step size usually is given by constraints on the observer's side, i.e. inherent instrumental limits on time resolution or de-dispersion. If, however, these effects become much smaller than the expected scattering time scale from Equation (2.45), the step size can be further increased; this can save a little, although unlikely much, computation time. See Section 3.7.2 for some more detail.

## 2.5 The Galactic population of pulsars

---

The most complete catalogue of all known pulsars with published parameters is the ATNF catalogue (Manchester et al., 2005) with a fully searchable and freely available online interface at <http://www.atnf.csiro.au/people/pulsar/psrcat/>. At the time of this writing 1880 radio pulsars, anomalous X-ray pulsars, and soft  $\gamma$ -ray repeaters exhibiting coherent pulsed emission are listed in the ATNF.

Although the catalogue presents the world's largest collection of pulsars, the known population only is a small fraction of all Galactic pulsars; Lorimer et al. (2006) find a number of  $30000 \pm 1100$  pulsars beam towards Earth and a total number of  $155000 \pm 6000$  active Galactic radio pulsars. The various selection effects leading to the much smaller number of detected pulsars and the correction to be applied to the known pulsar sample are studied in Sec. 3.1 of Lorimer (2008).

### 2.5.1 Spatial distribution of Galactic pulsars

Let us now characterise the known population of Galactic radio pulsars based on the ATNF catalogue by their distribution in the Galaxy, their spin properties, and their spin-downs. The simplest, and most obvious selection effect is the dilution of the observed flux density with distance; this effects is also referred to as the *inverse-square law* since the flux density  $S$  is proportional to the inverse square of the distance  $d$

$$S(d) = \mathcal{L}d^{-2}, \quad (2.46)$$

where  $\mathcal{L}$  is the intrinsic pseudo-luminosity of the pulsar; this term applies because  $\mathcal{L}$  does not account for the emission geometry, nor the emission in narrow beams. Thus, the known

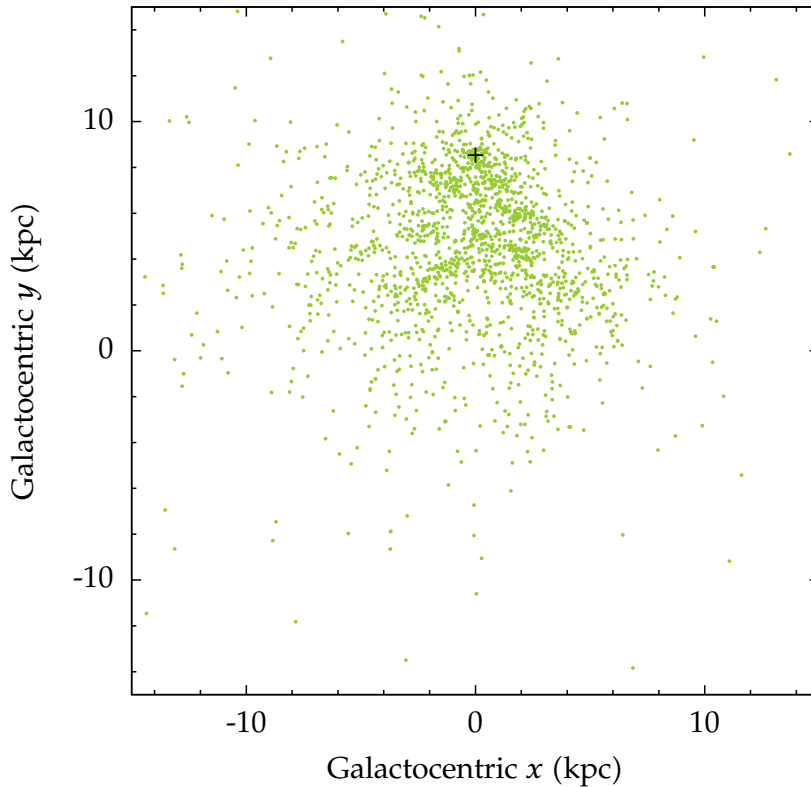


**Figure 2.8:** Positions of the known Galactic pulsars projected onto the Galactic plane. The Sun's position is marked by the black cross, the Galactic centre is in the centre of the plot. Note the strong concentration of pulsars close to the Sun and the Galactic spiral arm structure visible in the pulsar distribution.

pulsar sample will be dominated by the near-by and/or luminous pulsars. This effect can be clearly seen in Figure 2.8, which shows the known pulsars in Galactic cartesian coordinates projected onto the Galactic plane. A clear concentration of sources close to the Sun is apparent in contrast to that of other stellar populations that are radially symmetric with respect to the Galactic centre. The positions of the pulsars also exhibit a correlation with the Galactic spiral arms; most pulsars are young sources born in the spiral arms not having travelled far away from their birth sites. A more detailed study can be found in Lorimer (2008).

### 2.5.2 The $P-\dot{P}$ diagram

One of the cornerstones of visualising the Galactic pulsar population and discriminating various sub-groups of pulsars is the aptly named  $P-\dot{P}$  diagram, which plots the pulsar's spin period derivative  $\dot{P}$  (if measured) as a function of the pulsar spin period  $P$ . Its importance for pulsar astronomy is comparable to that of the Hertzsprung-Russel diagram for the classification of star types in stellar astronomy. Figure 2.9 shows the pulsar sample from the ATNF catalogue plotted in this manner. As we have shown in Section 2.2, the measurable

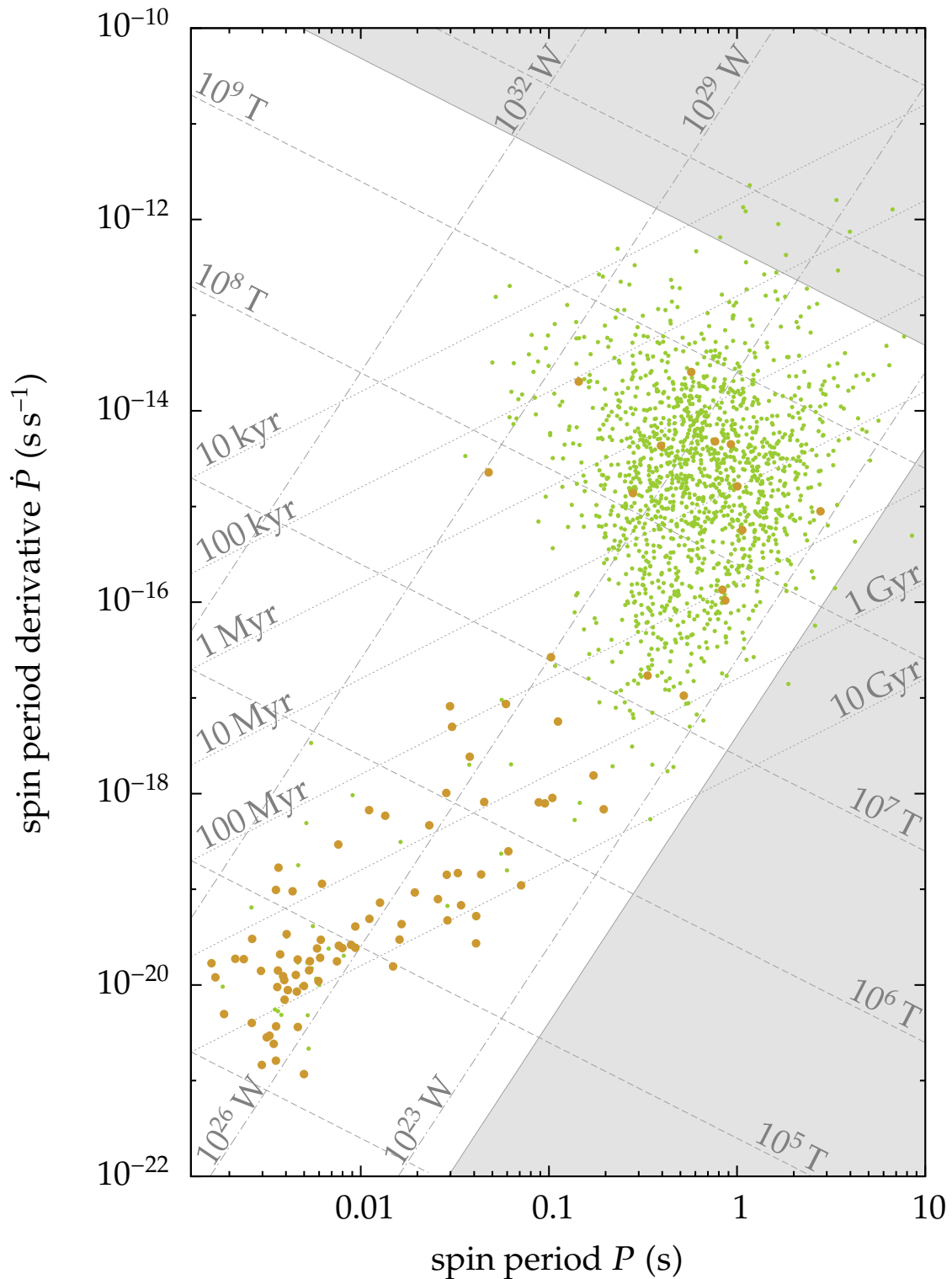


**Figure 2.9:** The  $P$ - $\dot{P}$  diagram. The measured period  $P$  and its derivative  $\dot{P}$  allow estimates of energy emission, characteristic age, and magnetic field strength (grey lines in the background). Green dots are isolated pulsars, orange dots are binary pulsars. The shaded area at the bottom right is the so-called *graveyard*, where pulsars end up when their radio emission switches off. The shaded area at the top right is where strong magnetic fields enable processes competing with the pair cascades assumed to produce the radio emission.

period and period derivative can be used in simple pulsar models to infer a set of system properties. The total energy emission, the characteristic age, and the surface magnetic field can be estimated from our pulsar toy model (Section 2.1.2) by Equations (2.6), (2.14), and (2.16), respectively. Lines of constant energy emission, characteristic age, and magnetic field are shown and labeled in Figure 2.9.

Two groups can immediately be seen in the  $P-\dot{P}$  diagram: the larger of them in the upper right corner of the region not shaded in grey, and the smaller set in at lower left. These are the non-recycled (mostly isolated young) pulsars and the recycled pulsars, respectively; the latter have been spun up by accretion of matter from a companion star.

### 2.5.3 Isolated young pulsars

The larger group are the regular pulsars born from a supernova. In the  $P-\dot{P}$  diagram they reside at high magnetic fields and intermediate spin periods of around 0.1 s. They spin down continuously losing energy by the emission of radio waves and move to higher spin periods along lines of constant magnetic field, crossing the lines of constant characteristic age. At some point the radio emission switches off when a pulsar crosses the *death line* and enters the pulsar *graveyard* (the shaded region in the bottom right). Pulsars visible in the graveyard challenge the theoretical models predicting these regions.

Several young pulsars have been associated with supernova remnants; for the older pulsars at longer spin periods this has not been possible, because the remnants dissipate and become invisible within  $10^5$  years, a relatively short time compared to the typical pulsar ages.

One way of forming an isolated young pulsars is from stars born isolate; in this case a progenitor star with a main sequence mass of more than 8 solar masses explodes in a supernova at the end of its active stellar life; it leaves behind a neutron star, that can be visible as a pulsar under favourable conditions.

Isolated young pulsar can also form from binary stellar systems via different pathways, depicted in figure 2.10. Firstly, the binary system is disrupted when the primary component undergoes its supernova explosion, creating a young isolated pulsar and a runaway star. Secondly, the system has two initially high mass stars such that the secondary one will also undergo a supernova which can disrupt the system at a late stage in its evolution, creating a young pulsar and a mildly recycled pulsar (which is called a disrupted recycled pulsar). Finally, the first star is initially massive enough to end its life in a supernova if it were isolated; in the binary system, however, it loses enough mass due to mass transfer becoming finally a white dwarf. The secondary star is now massive enough to become a He star that ends in a supernova and produces a neutron star. This supernova of the secondary star can disrupt the system and lead to the formation of a young pulsar; no recycling of the secondary star happens in this pathway because the primary turns into a compact object *first*.

### 2.5.4 Recycled pulsars

The smaller group on the bottom left has the same or larger characteristic ages as the oldest regular pulsars; their magnetic fields are order of magnitudes smaller than the ones of regular pulsar. Also, their spin periods are comparable to that of young pulsars or even shorter by up to two orders of magnitude. These pulsars are called *recycled pulsars*, since they have been raised from dead pulsars in the graveyard by accreting matter and angular

momentum from a companion star. This process lowers the surface magnetic field but also spins the dead pulsar up until it starts emitting again despite its lower magnetic field.

As can be seen from the  $P-\dot{P}$  diagram, recycled pulsars are spread over a wide range of spin frequencies between tens and hundreds of Hertz. Recycled pulsars around a few ten Hertz are usually called *mildly recycled* pulsars; in these systems typically only a small amount of accretion happened because of short and/or less efficient accretion phases. This led to a mild spin-up and recycling. Pulsars at the higher frequencies ( $f > 100$  Hz) are referred to as *fully recycled* (or sometimes simply *recycled*) *millisecond pulsars*.

Again, figure 2.10 shows the pathways leading to the different types of recycled pulsars. Fully recycled millisecond pulsars are formed in pathways with a long accretion phase. This happens in systems where the primary star undergoes a supernova explosion first, which the system survives, and which is followed by a Roche lobe overflow of the secondary that leads to accretion of matter onto its neutron star companion. During this phase, the system can emit X-rays (see Section 2.5.5). When accretion stops the neutron star can be visible as a millisecond pulsar in a wide orbit around a low-mass white dwarf. Mildly recycled pulsars are formed in pathways where no accretion disk is formed and the mass transfer from the secondary happens in form of a less efficient common envelope phase or stellar winds. In the common envelope phase, the neutron star formed from the primary supernova spirals into and expels the envelope of the developed secondary star. Depending on the mass of the secondary it will then either form a massive white dwarf or another neutron star.

### 2.5.5 X-ray pulsars

On its way to become a recycled pulsar, the accreting system can be visible as an X-ray pulsar: the accreted material is heated up by differential rotation and friction within an accretion disk and produces X-rays. The matter accreted onto the surface of the neutron star is directed to the polar caps by the magnetic field where it heats up and produces a spot on the neutron star surface hot enough to emit X-rays. This spot spins around and can cause periodic variations in the observed X-ray flux superimposed to the background from the accretion disk.

### 2.5.6 Isolated and binary pulsars

Two other important sub-groups have been plotted in different colours in Figure 2.9: the green dots are the isolated pulsars while the orange dots are binary pulsars. This agrees well with the scenarios described in the previous sections. We have seen that for the recycling process a secondary companion is necessary, thus most of the binary pulsars are among the recycled systems. In these systems the binary system survived the first supernova forming the pulsar, the pulsar then was spun up by its companion. If the companion became a white dwarf, the observed orbits are mostly circular or almost so; if the companion is another second neutron star, the orbits are typically far more eccentric because the second supernova nearly disrupted the system.

## 2.6 Neutron stars as gravitational-wave sources

---

Neutron stars are expected to emit continuous gravitational waves by two main processes: orbital motion in a binary system and mechanisms related to the spin of an isolated neutron star. Continuous gravitational radiation refers to the quasi-monochromatic spectrum of the

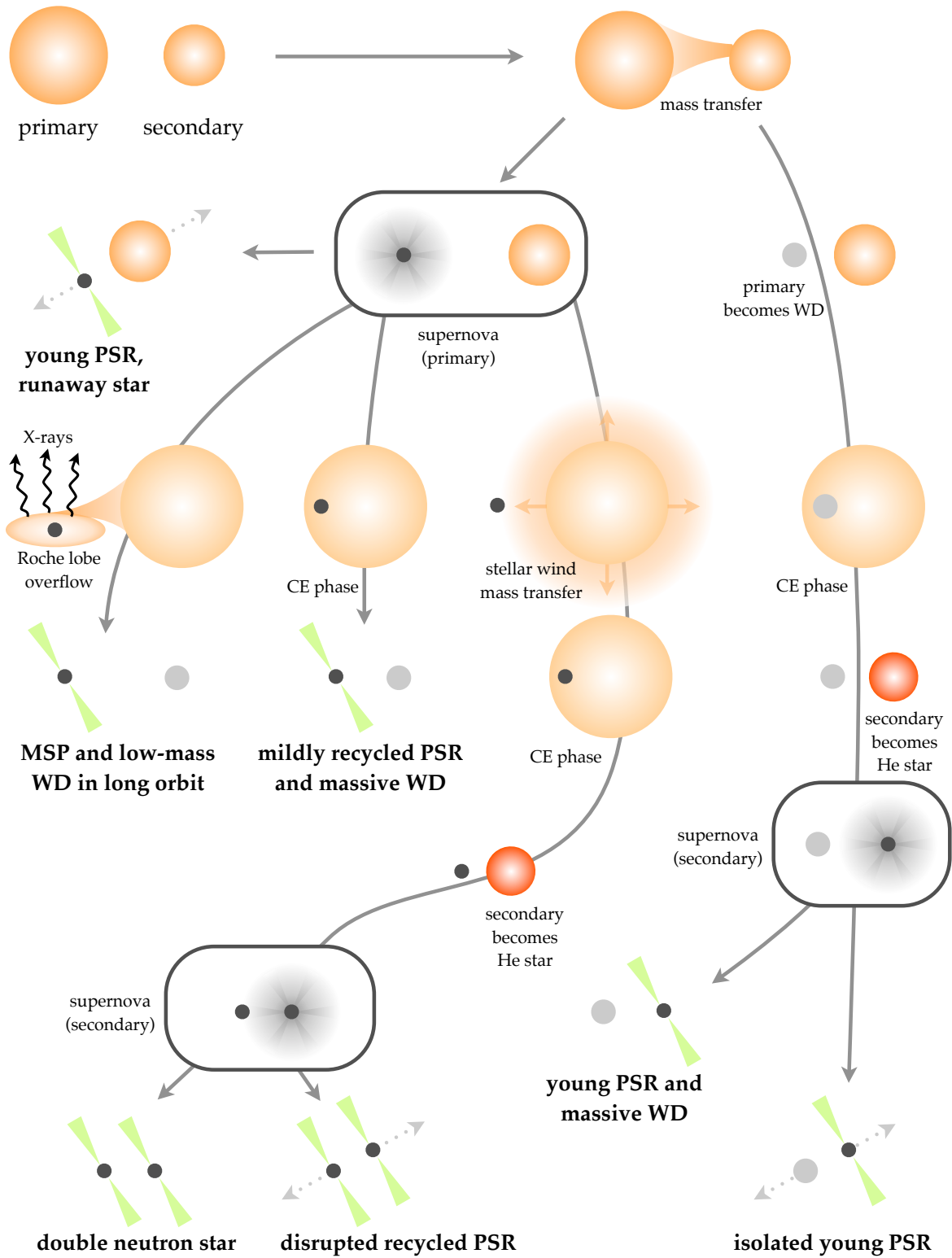


**Figure 2.10:** The schematic evolution of pulsars (adapted from Stairs (2004) and Lorimer (2008)). Grey arrows indicated different paths, depending on the initial stellar masses; intermediate stages are labeled, the final stages are labeled in bold font. *CE phase* stands for *common envelope phase*, in which the compact star spirals into and expels the envelope of the other star. A *He star* is the exposed stellar helium core after stripping of the hydrogen envelope.

emitted signals changing intrinsic frequency only on very long time scales compared to the observation time.

The binary system are expected to be rarer as we have seen from the known pulsar sample above; also, the emission of gravitational waves from the binary motion is expected to happen at frequencies accessible only to space-based detectors like the planned LISA satellite mission (Danzmann, 2003; Danzmann and Rüdiger, 2003; Hughes, 2007; Shaddock, 2008) with the route to LISA being prepared by the LISA Pathfinder mission (Armano et al., 2009) expected to be launched in 2013.

For the isolated pulsars a variety of mechanism leading to the emission of continuous gravitational waves has been proposed in the literature, which we will review in the following section. We orient our review on a more exhaustive overview of gravitational wave sources in Pletsch (2009).

### 2.6.1 Gravitational-wave emission mechanisms

Rapidly rotating, isolated neutron stars are expected to emit continuous gravitational waves in the frequency range where ground-based detectors are most sensitive, between roughly 10 Hz and  $10^3$  Hz. Three different classes of emission mechanisms have been proposed to be responsible for this emission:

1. excited oscillations in the fluid component of the neutron star
2. precession of the neutron star about its spin axis
3. non-axisymmetric deformations of the neutron star

It is of course also possible that yet unknown processes lead to the emission of continuous gravitational waves.

#### Excited oscillations in the fluid component of the neutron star

Excited oscillations in the fluid component of the neutron star can happen during the birth of the neutron star or an accretion phase. A review of these emission mechanisms is given in Stergioulas (2003) and Andersson (2003); a well-studied example are the so-called r-modes which are oscillations of the superfluid restored by the Coriolis force from the rotation of the neutron star. Andersson (1998); Friedman and Morsink (1998); Stergioulas (2003) find that the r-mode oscillation might be unstable because of gravitational back-reaction. This instability has been proposed as a source of continuous gravitational waves at four thirds the rotation frequency. This emission might be found in newborn neutron stars (Owen et al., 1998) and accreting systems (Bildsten, 1998). Prediction of the emission strength is highly uncertain because of the modelling of the neutron star interior involved. In the accreting systems, the emission might last up to thousands of years (Andersson et al., 2001; Wagoner, 2002), while in young neutron stars r-mode excitations are expected to be damped within months (Andersson et al., 2001).

#### Precession of neutron stars

Precession of neutron stars about the spin axis occurs if the neutrons star's rotation axis is not aligned with its symmetry axis. The precessing motion is defined by the angle between the rotation axis and the symmetry axis; this angle usually is called the *wobbling angle*. Free

precession with a wobbling angle  $\alpha_w$  will cause gravitational waves (Jones and Andersson, 2002; Van Den Broeck, 2005; Zimmermann and Szedenits, 1979) of amplitude

$$h_0 = 2 \times 10^{-28} \left( \frac{\alpha_w}{0.1 \text{ rad}} \right) \left( \frac{1 \text{ kpc}}{r} \right) \left( \frac{\nu}{100 \text{ Hz}} \right) \quad (2.47)$$

at frequencies  $\nu - \nu_w$ ,  $\nu + \nu_w$ , which are sidebands due to the precessing motion, and at  $2\nu$  due to non-axisymmetric rotation of the neutron star (Zimmermann and Szedenits, 1979). Cutler and Jones (2001) showed that earlier calculations were underestimating the emission time scale by a factor of up to  $10^5$ . Nonetheless, precession in the known pulsar population seems to be very unlikely and emission from this mechanism is thought to be too weak to be detectable in first-generation detectors.

Recently Jones (2010) showed that a frequency component at exactly the rotation frequency  $\nu$  can be emitted in non-precessing motion. This is related to the “pinned” superfluid in the neutron star interior; it rotates by forming an array of vortices, where the rotation rate is proportional to the area density of vortices. These vortices can interact with the charged component of the neutron star resulting in a pinning of the vortices<sup>21</sup>. The pinning of the superfluid might happen along an axis that is not one of the principal axis of the moment of inertia tensor. Jones (2010) shows that the moment of inertia of the pinned superfluid is much larger than other asymmetries, which in turn means that the non-precessing motion corresponds to a rotation around the pinning axis and not around one of the principal axes, finally leading to emission at  $2\nu$  and  $\nu$ .

### Non-axisymmetric deformations of neutron stars

Non-axisymmetric deformations of neutron stars are the most promising mechanism for the generation of gravitational waves detectable by ground-based detectors. A detection in first-generation detectors might be possible, although the second-generation detectors will improve chances dramatically.

Deformations can arise in the formation of the neutron star; when it settles down and separates into a superfluid interior with an exterior crust, crystallisation in the crust can lead to local, non-axisymmetric deformations of the crust. The superfluid interior cannot build up deformations. The deformation typically is measured in terms of an *ellipticity*  $\varepsilon$ , which is defined by the asymmetry in the moments of inertia:

$$\varepsilon = \frac{I_{xx} - I_{yy}}{I_{zz}}, \quad (2.48)$$

where rotation around the z-axis is assumed. An example of a deformation leading to a non-vanishing ellipticity is a “mountain” or “hill” on the neutron star surface supported by elastic stresses in the neutron star crust or by magnetic fields. Note, however, that due to the strong gravity on the surface of the neutron star and even though the crystalline crust has a breaking strength roughly  $10^{10}$  times larger than man-made engineering materials (Horowitz and Kadau, 2009), a mountain might not rise much higher than centimetres at best!

<sup>21</sup>This pinning prevents the vortices from participating in the spin-down of the rest of the neutron star with the spin rate of the vortices remaining constant. Thus, a difference in spin period between the pinned areas and the remaining neutron star builds up. If that difference is large enough, it gets released in a simultaneous unpinning event at all sites, that spins up the neutron star’s charged component. This is believed to be a possible explanation for the well known pulsar glitches.

The gravitational wave signal is emitted at  $f = 2\nu$ , where  $\nu$  is the rotation frequency of the neutron star, and has an amplitude<sup>22</sup> of

$$h_0 = 4\pi^2 \frac{GI \varepsilon f^2}{c^4 r} \quad (2.49)$$

$$= 1.06 \times 10^{-26} \times \left( \frac{I}{10^{38} \text{ kg m}^2} \right) \left( \frac{\varepsilon}{10^{-6}} \right) \left( \frac{f}{100 \text{ Hz}} \right)^2 \left( \frac{1 \text{ kpc}}{r} \right), \quad (2.50)$$

where  $r$  is the distance to the neutron star, and all variables have been scaled to typical values. While typical neutron star distances are well known from pulsar observations (Manchester et al., 2005), and the canonical neutron star moment of inertia varies only by a factor of two depending the equation of state (Lattimer and Prakash, 2001), the typical ellipticities for neutron stars are completely unknown. Recent molecular dynamics simulations by Horowitz and Kadau (2009) of the neutron star crust have shown that it could support ellipticities<sup>23</sup> as large as  $4 \times 10^{-6}$ . Owen (2005) studied exotic stellar models such as solid quark stars, hybrid quark-baryon or meson-condensate stars; these objects replace the canonical neutron star with either a solid star made from strange quarks or a hybrid stars with mixture of baryonic and charged quark or condensed meson matter concentrated towards the stellar core. Owen (2005) finds that these exotic objects might sustain ellipticities as high as  $6 \times 10^{-4}$  for the quark stars and  $9 \times 10^{-6}$  for hybrid stars.

Targeted searches of gravitational waves from known neutron stars (seen as radio pulsars) (Abbott et al., 2005, 2007a; Abbott et al., 2008b) obtain upper limits on the ellipticities in the range between a few times  $10^{-7}$  and  $10^{-4}$ , which agree well with the theoretically predicted values. The fact that these measurements are upper limits could indicate that the typical ellipticities are of order  $10^{-7}$  or smaller. The exotic models (quark and hybrid stars) do not seem to be common among the known pulsars.

Accreting neutron star might also emit gravitational waves by non-axisymmetric deformations. Bildsten (1998) showed that the temperature differences induced by the accreting matter can lead to a non-vanishing non-axisymmetric quadrupole moment. The accreting matter is funnelled by the magnetic fields to the magnetic poles where it heats up as it gets piled onto the neutron star surface. These hot spots then induce density variations and cause a misaligned quadrupole moment that finally leads to the emission of continuous gravitational waves as long as the hot spot exists. Bildsten (1998) finds ellipticities of  $10^{-7}$  are induced by this process. Melatos and Payne (2005) further showed that the accreted matter could be magnetically confined to build up larger “mountains” leading to even larger ellipticities.

Note, that the gravitational wave amplitude from non-axisymmetric deformations in Equation (2.50) is almost two orders of magnitude larger than the value predicted from free precession in Equation (2.47). In the work presented in Chapters 6 and 7 in this thesis we therefore concentrate on the emission of continuous gravitational waves by non-axisymmetric deformations of isolated pulsars as the most promising source. Isolated neutron stars outnumber the accreting systems by far (Manchester et al., 2005), thus the accreting binary systems emitting gravitational waves due to non-axisymmetric deformation may be neglected here for simplicity.

<sup>22</sup>assuming optimal mutual orientation (gravitar sky position given by the unit vector orthogonal to the plane of the detector arms; gravitar spin axis parallel to this vector)

<sup>23</sup>for the canonical neutron star

Note, that of any of these emission mechanisms also can happen in a neutron star in a binary system. There, the Doppler effect from binary motion will lead to additional frequency modulation in the signal received at the detector.

### 2.6.2 Gravitars

As detailed above, continuous emission from spinning neutron stars is a promising source of gravitational waves, but so far no detections have been reported. This begs the question “what is the largest expected amplitude of the continuous signal from non-axisymmetric neutron stars?” There might exist a (so far undetected) population of spinning neutron stars whose dominant energy loss goes into the production of gravitational waves, rather than into electromagnetic radiation. These are often called *gravitars* (Palomba, 2005); we show later in this thesis that gravitars set an upper limit on the amplitude of gravitational waves from spinning neutron stars that are also emitting electromagnetic radiation.

We stress that while this work studies the behaviour of a population of Galactic gravitars, it does not make a plausibility case for the possible existence of such objects, or study their potential astrophysical implications. The study itself is nevertheless interesting, because even if gravitars do *not* exist, they provide a relevant upper bound on the gravitational-wave emission by objects (such as rapidly-spinning neutron stars) that *do* exist.

### 2.6.3 Simulating the galactic gravitar population

In order to estimate the total emission of gravitational waves from Galactic gravitars one needs to set up a realistic model of the Galactic gravitar population to predict the present day distribution of these sources. The strain amplitude of the gravitational waves from gravitars depends on the distance, frequency, and deformation (ellipticity) of the gravitar. Thus, a realistic simulation must include the following functions that describe different aspects of the gravitar population. The parameters can naturally be split into two groups:

**spatial distribution parameters:** what is the present time distribution of gravitars in the Galaxy? This is governed by the initial spatial distribution of gravitars, their initial velocity, the Galactic gravitational potential, the birth rate as a function of time, and their age.

**frequency distribution parameters:** what is the present day distribution of pulsars as a function of their spin frequency? This only depends on the birth frequency distribution, the distribution of ellipticities, the birth rate as a function of time, and their age.

The distribution of present day gravitational wave strains then depends on the combination of both of these groups, but each can be simulated independently. They are only connected by the birth rate and age they both share. This simplifies the simulation process and obtaining a picture of the present day gravitar population.

The necessary birth distributions used as input to the simulations are borrowed from the known distributions of pulsars; we assume that these distributions may as well be used for gravitars. In the literature a range of reconstructed birth distributions for position, velocity, and spin frequency from likelihood analysis of pulsar population synthesis as well as from the study of pulsar proper motion samples are available. The Galactic gravitational potential has been well studied in the literature as well.

### **Blandford's argument**

In 1984 Blandford found a simple analytic relationship between the expected maximum amplitude of gravitational waves emitted by gravitars and their average Galactic birthrate. This argument was not published but it is documented by a citation in (Thorne, 1987). The argument was revised in (Abbott et al., 2007b).

Work presented in this thesis in Chapter 6 revises both the original and the revised Blandford arguments, and shows that two key assumptions of these arguments do not hold in a realistic Galactic model of gravitars. This work corrects the assumptions of the argument, and then investigates how the conclusions are affected by this change.

### **Gravitator detection predictions**

A full model of the present day gravitar population can further be used to predict detection probabilities for today's and future gravitational wave detectors. So far, only one example of this can be found in the literature (Palomba, 2005). The predictions found in this reference however suffer from one flaw: in the simulation unrealistically high sensitivity was assumed. In this work we first present results assuming a realistic sensitivity curve for the complete detection pipeline. This for the first time allows to constrain the putative Galactic gravitar population, and to estimate detection rates with current and future searches.

### **Search optimisation**

Work presented here also addresses the problem of optimising a search pipeline with limited computational power based on simulations of the population to be searched for. This is similar to the problem of maximising the amount of money won in a casino (detections made by a search) given a fixed initial amount of money to spend (a fixed amount of computation cycles to spend) on different gambling tables (in different parts of the search parameter space). From the gambling example it is clear, that one should maximise the ratio of pay-off and costs (winning chances) over the tables and gamble only where this ratio is maximal<sup>24</sup>.

For gravitar searches a similar approach is possible: assuming the simulated population reliably represents the actual gravitar population, it can be used to predict the detectability of gravitars in a small search parameter space volume. This detectability can then be compared with the costs for searching this small parameter space volume. Their ratio yields a pay-off-to-cost ratio by which one can decide whether or not to search the given parameter space volume. We show by applying the Neyman-Pearson criterion that thresholding on this ratio is the optimal procedure to determine the part of parameter space that will maximise the number of detections for a fixed amount of computation cycles.

This approach can be used to improve future blind searches to semi-targeted searches in the sense that certain parts of the parameter space are excluded, that would be searched in a fully blind search. The computation cycles saved can be used to either a) speed up the search or b) to re-invest the computation cycles saved to search deeper in the remaining parameter space.

---

<sup>24</sup>if gamble one must

# 3

## Einstein@Home Radio Pulsar Search

### 3.1 Overview and context

---

Einstein@Home (Abbott et al., 2009) is a volunteer distributed computing project, which exploits idle compute cycles donated by volunteers from the general public, to carry out compute-intensive searches for unknown, spinning neutron stars. Einstein@Home is one of the large of the in total  $\sim 100$  such volunteer distributed computing projects. Einstein@Home was launched in February, 2005 as part of the World Year of Physics and since then more than 290,000 volunteers have signed up their home, office computers, and laptops.

The main goal of Einstein@Home is the discovery of new, unknown neutron stars either by detection of their gravitational wave emission or by their emission of radio waves as radio pulsars. In both cases the expected signals are weak and the signal parameters are unknown; thus, finding these signals requires searching a wide parameter space. These searches are limited by the available computing power, not by the sensitivity of the instruments used for the data collection.

This chapter provides an overview over distributed computing in general and more specific about Einstein@Home. We present the Einstein@Home infrastructure for the radio pulsar search with a detailed description of the search pipeline: from data acquisition at the Arecibo Observatory, over the data preparation to the data analysis on the computers of the general public, and finally the post-processing of the data analysis products. The radio pulsar search is the central topic of this thesis.

### 3.2 PALFA survey

---

The Arecibo telescope in Puerto Rico with its 305-m spherical primary reflector is the world's largest single-dish radio telescope and thus an instrument providing superb sensitivity to survey the sky for pulsars. Large-scale pulsar surveys have proved to be an efficient way of detecting new pulsars. Early surveys focused on slow pulsars, while large-scale survey also capable of detecting fast (millisecond) pulsars were first conducted in the early 1990 years.

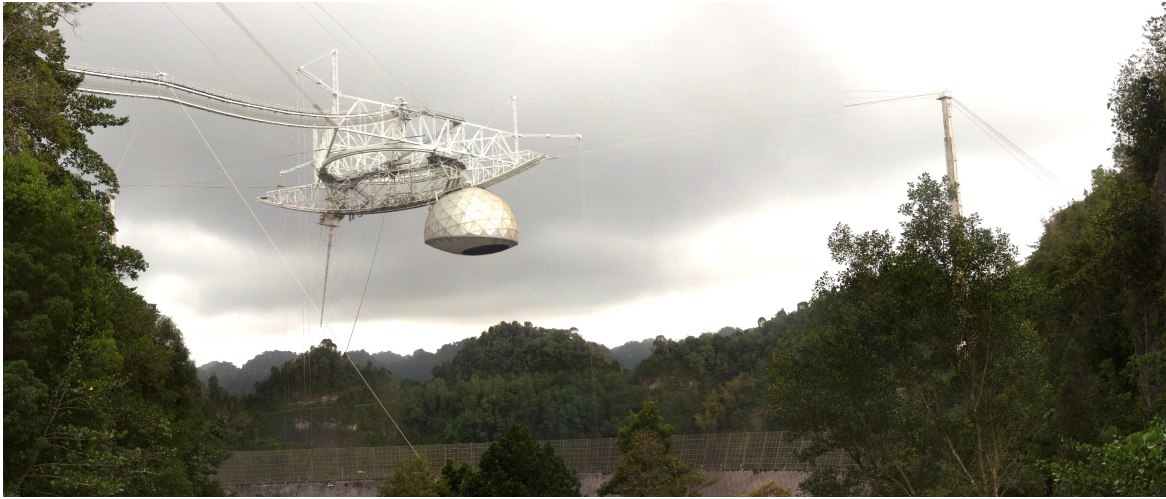


**Figure 3.1:** View of the Arecibo telescope from the terrace in front of the control room facing South. The 305-m dish is at the bottom of the photograph, the western tower can be seen on the right, the eastern tower on the left behind the trees (the northern tower is on top of the hill to the left). Left of the middle, the platform with the 430-MHz line feed and the Gregorian dome housing the ALFA receiver is visible.

The sky accessible to the Arecibo telescope has been surveyed multiple times in the past 35 years. Arecibo Observatory itself has been used repeatedly for different systematic pulsar surveys of the sky available (see Section 3.2.2) to the telescope. Some of these mostly early surveys were at radio frequencies of 430 MHz:

**Hulse and Taylor (1975b)** conducted a survey near the Galactic plane ( $|b| \leq 5^\circ$ ) at 430 MHz, discovering 40 new pulsars.

**Stokes et al. (1986)** surveyed near the Galactic plane ( $|b| \leq 10^\circ$ ) with high time resolution to increase sensitivity to fast spinning pulsars. Five new pulsars were found, one of them (B1855+09) a millisecond pulsar.

**Nice et al. (1995)** searched near the Galactic plane ( $|b| \leq 8^\circ$ ), finding 24 new pulsars, two of them previously unknown millisecond pulsars.

Surveys at low radio frequency suffer from selection effects due to higher Galactic radio background, stronger multi-path scattering (see Section 2.4.2), and dispersion in the interstellar medium (see Section 2.4.1). The latter two decrease sensitivity to fast-spinning pulsars because they effectively broaden the pulses, smear out the signal, and thus lower signal-to-noise ratio. Therefore, surveys at higher frequencies (L-band, around 1.4 GHz) were also conducted in parts of the sky accessible to the Arecibo telescope, but not using the Arecibo Observatory:

**Clifton et al. (1992)** surveyed with the 76-m telescope at Jodrell Bank. Observations were very close the Galactic plane ( $|b| \leq 1.1^\circ$ ), also covering Galactic longitudes ( $-5^\circ < \ell < 95^\circ$ ), which are partly accessible to Arecibo (compare Section 3.2.2). 40 new pulsars were found in this survey.

**Manchester et al. (2001)** with the Multibeam survey at 64-m Parkes radio telescope (Australia) have discovered hundreds of new pulsars; the sky area searched over has an

overlap with the Arecibo sky. There are also parts of the northern sky visible exclusively from Arecibo but not from Parkes.

The PALFA survey is designed to probe the Galaxy much more deeply than any of these previous surveys with highest sensitivity to fast-spinning pulsars over a wide range of dispersion measures, allowing to detect these objects even at large distances. This sensitivity is achieved by an unmatched temporal resolution over a wide radio frequency observation bandwidth (Cordes et al., 2006).

### 3.2.1 Data acquisition

The observations use an instrument, called Arecibo L-band feed array (ALFA), described in full detail in Cordes et al. (2006). Here, we will give a short overview of the observation system features.

ALFA is a seven feed-horn, dual-polarisation radio receiver capable of operating in a 300 MHz band from 1.2 GHz to 1.5 GHz. For the PALFA survey (until early 2009), a 100 MHz wide band around 1.4 GHz was used. ALFA is placed at the Gregorian focus of the Arecibo telescope; its seven feed horns are arranged in a filled hexagon shape with the central beam exactly at the middle of the Gregorian focus. The incoming radio signals are converted into electric signals by orthomode transducers; these provide dual, linearly polarised signals to cooled receivers. The receiver signals are transported via optical fibre to intermediate electronics and back-end spectrometers in the control building. There, autocorrelation spectrometers, the Wideband Arecibo Pulsar Processors (WAPPs; Dowd et al., 2000) sum the polarisations and provide a 100 MHz of bandwidth with 256 time lags and a time resolution of  $64 \mu\text{s}$ .

The fast sampling time of  $64 \mu\text{s}$  is necessary to fully recover the signals from millisecond pulsars. Most pulsars have small duty cycles (the ratio  $W/P \ll 1$  of pulse width  $W$  to spin period  $P$ ); this leads to signal contributions at multiples of the fundamental spin frequency, the so-called “harmonics”. For a signal with duty cycle  $W/P$ , typically  $\approx P/W$  harmonics are expected (Lorimer and Kramer, 2005). The fast sampling allows to resolve up to eight harmonics for a pulsar of  $P = 1 \text{ ms}$ .

The data stream for each feed horn is called a *beam*. Each WAPP collects the data from two beams and interleaves the data streams into a single data set. Seven physical beams (the data streams from the feed horns) make up one *pointing*; one dummy beam, containing either zeros or a copy of another beam, is added to allow all four WAPPs to interleave data).

The seven beams are elliptically shaped; the equivalent circular beam diameter (full width at half maximum) is  $3.35'$ . The centres of the outer beams lie on an ellipse of  $11.0'$  by  $12.8'$ . Figure 3.3 shows the coverage of the sky by three interleaved PALFA pointings, each in a different colour. Note the elliptical beam shape and relative position of the beams in a pointing. For more details on the sky coverage see the next section.

### 3.2.2 Sky coverage

The goal of the PALFA survey is to cover the regions of the sky close to the Galactic plane visible for the Arecibo telescope. Because the telescope can only observe with a zenith angle  $\leq 19.7^\circ$ , only a  $39.4^\circ$  wide stripe in the sky is available. Because of the inclination of the Earth’s rotation axis with respect to the Galactic plane this allows for two “windows” near the Galactic plane.

### Visible sky from Arecibo observatory

The “Arecibo sky” (i.e. the part of the sky visible from Arecibo Observatory) is shown in Figure 3.2. The top plot uses Galactic coordinates and the bottom plot equatorial coordinates. The part of the sky visible for Arecibo is in between the two light-green lines. The light-grey lines in the background show the the equatorial coordinate grid in the top plot and the Galactic coordinate grid in the bottom plot.

In the top plot, the equator ( $\delta = 0^\circ$ ) and the line of zero right ascension ( $\alpha = 0^h$ ) are shown by slightly wider lines in a darker shade of grey. Close to the plane of the Galaxy two sky areas (in dark-green) are visible at  $30^\circ \lesssim \ell \lesssim 70^\circ$  and  $170^\circ \lesssim \ell \lesssim 210^\circ$ . The two areas are used for the PALFA survey. They lie in the declination range accessible from Arecibo observatory:

$$\varphi - 19.7^\circ \leq \delta \leq \varphi + 19.7^\circ, \quad (3.1)$$

where  $\varphi = 18^\circ 20' 39''$  is the geographic latitude of Arecibo Observatory, thus yielding a range in declination of

$$-1.36^\circ \lesssim \delta \lesssim 38.04^\circ. \quad (3.2)$$

Furthermore, the largest number of pulsar per unit solid angle on the sky is expected near the Galactic plane, where pulsars are born and spend most of their lifetime. Thus, in Galactic coordinates the PALFA search area is restricted to Galactic latitudes  $|b| \leq 5^\circ$ . Combining these two constraints defines the sky search area for the PALFA survey. Note, that the Galactic centre (on the right border of the top plot of Figure 3.2 at  $\ell = 0^\circ$ ) is not visible for the Arecibo Observatory. At the centre of the top plot is the Galactic anti-centre ( $\ell = 180^\circ$ ), which lies in one of the PALFA survey sky regions.

The bottom panel in Figure 3.2 shows the Arecibo sky in equatorial coordinates. The colour code is the same as in the top panel. The grey coordinate lines now show Galactic coordinates, in dark-grey lines of  $b = 0^\circ$  and  $\ell = 0^\circ$  are displayed.

### Covering the Arecibo sky

The filled hexagonal beam pattern presented in Section 3.2.1 consists of seven *beams*. The collected seven data streams of these seven beams form one *pointing*. For each beam, sky coordinates are recorded; the coordinates of the central beam are used to reference the complete pointing, e.g. for naming of data files).

The complete solid angle of the sky search region has to be covered in such a way, that each point on the sky is covered by at least one beam at a certain fraction of the central sensitivity. For the PALFA survey, the design goal is to cover all of the sky with at least half the sensitivity of the central beam. The resulting tiling strategy for the PALFA has been derived in Freire (2003) and consists of three adjacent pointings interleaved in the way as depicted in Figure 3.3. Note, that this tiling has holes with slightly higher loss in the sensitivity than the initially required value; this was balanced against the otherwise much higher overlap between the beams and the resulting increase in observation time Freire (2003).

### 3.2.3 Observation setup and data volume

The PALFA survey utilises different observation set-ups. Until early 2009, all survey observations used the WAPPs, after that new observation backends, the Mock spectrometers<sup>1</sup>,

<sup>1</sup><http://www.naic.edu/~astro/mock.shtml>

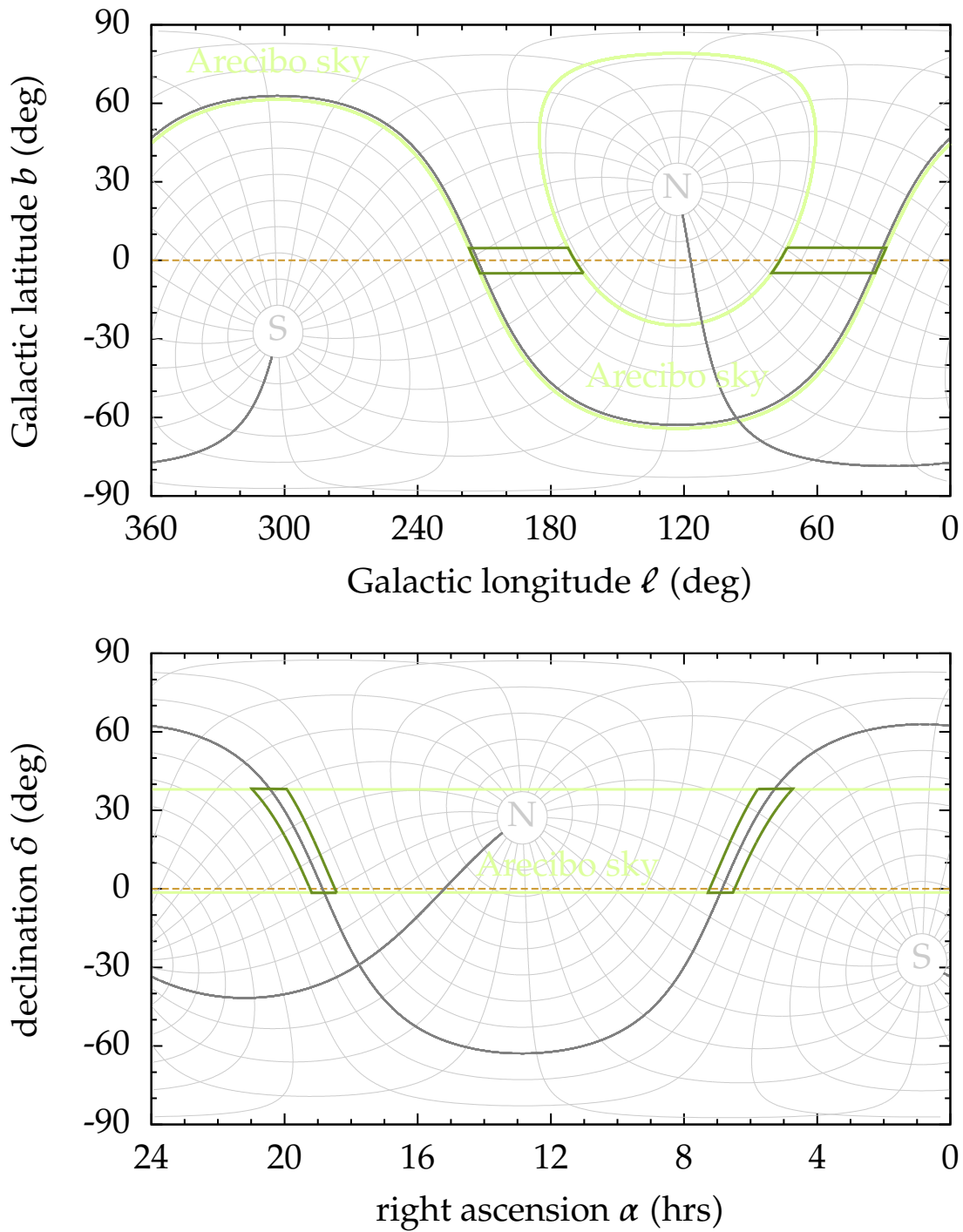


**Figure 3.2:** The “Arecibo sky” is between the thick light-green lines. The PALFA survey windows close to the Galactic plane are shown in darker green. **(Top)** The Galactic centre is located on the left and right border of the map, the Galactic anti-centre in the centre. The grey letters N and S denote the equatorial north and south pole, respectively. Lines of  $\delta = 0^\circ$  and  $\alpha = 0^h$  are shown in dark-grey. **(Bottom)** The colour code is the same as above. The grey letters N and S denote the Galactic north and south pole, respectively. Lines of  $b = 0^\circ$  and  $l = 0^\circ$  are shown in dark-grey.

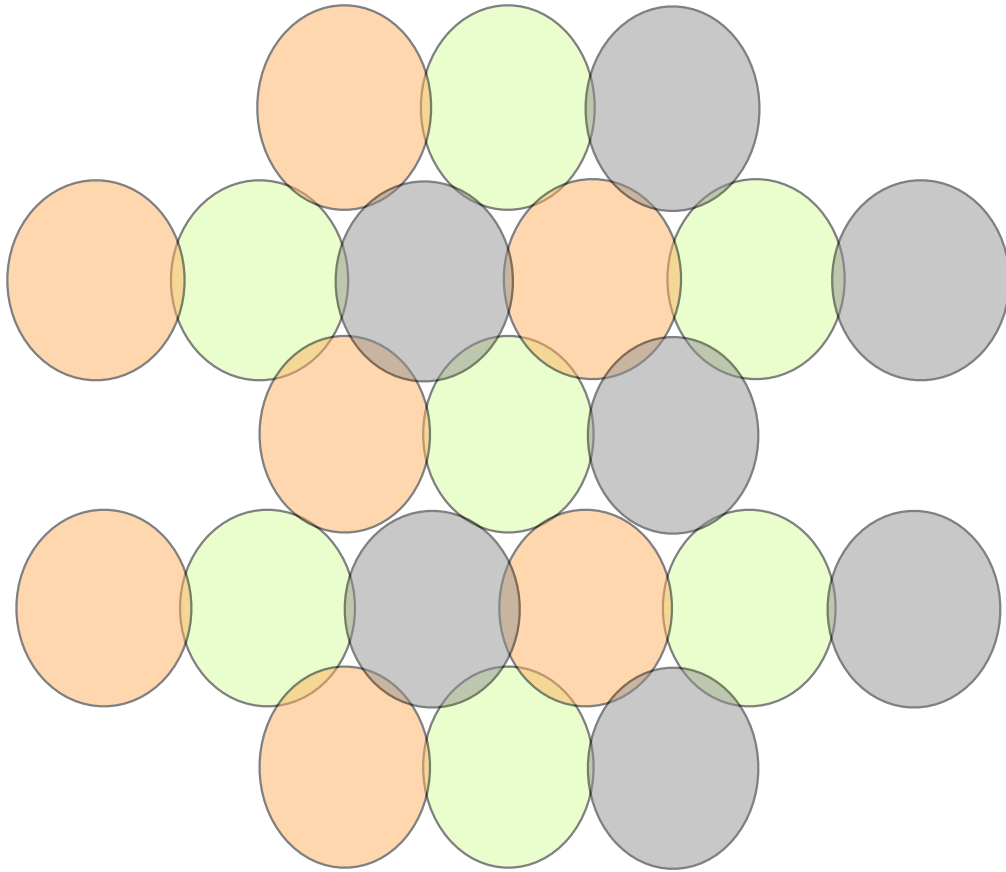


**Figure 3.3:** Tiling strategy for the PALFA survey. Each ellipse shows the  $-3$  dB sensitivity contour relative to the centre of the corresponding beam. Beam colours denote the three different pointings used to achieve the required coverage. The figure was adapted from Freire (2003).

were used. So far, Einstein@Home has only analysed data taken with the WAPPs. Observations obtained with the Mock spectrometers will be processed by Einstein@Home in the near future.

All observations with the WAPPs always observe a bandwidth of 100 MHz around 1.4 GHz and sample the data every  $64 \mu\text{s}$  (see Section 3.2.1 for details).

The total observation time is varied depending on the sky position (Cordes et al., 2006). Regular pointings into the inner Galaxy, the dark-green window at  $30^\circ \lesssim \ell \lesssim 80^\circ$  in Figure 3.2, have an observation time of 268.435 456 s; this observation time is given by obtaining  $2^{22}$  time samples<sup>2</sup>. Due to file system limitations, each data set consists of three files, two of them 2 GB in size, and one smaller “spill-over” file. These files with a total volume of 4 GB contain the autocorrelation functions, sampled at 2 bytes per sample; it is 256 lags sampled at 2 bytes for a total of  $2^{22}$  time samples and 2 beams, yielding  $2^{32}$  bytes, or 4 GB.

Regular pointings into the outer Galaxy, the dark-green window at  $160^\circ \lesssim \ell \lesssim 220^\circ$  in Figure 3.2, have an observation time of 134.217 728 s; this observation time is given by obtaining  $2^{21}$  time samples. There are additionally inner Galaxy pointings with a shorter observation time of 134.217 728 s from the beginning of the PALFA survey. Due to the same

<sup>2</sup>Having data sets with  $2^n$  points is advantageous when using Fourier algorithms for the analysis. Fast Fourier transforms are particularly efficient for these sizes.

file system limitations as above, here each data set consists of two files, one 2 GB in size, and one smaller “spill-over” file.

Data from two beams are interleaved in the files produced by a single WAPP; there are in total four WAPPs, each creating a set of three files for two interleaved beams. Thus, each pointing results in twelve files, which have to be de-interleaved and combined afterwards; furthermore, the autocorrelation functions in the data sets have to be converted into radio frequency dynamic spectra to obtain the data streams for each single of the seven beams. For the Einstein@Home search, this is part of the data pre-processing on dedicated servers at the AEI Hannover, see Section 3.7 for details.

There also are data from a precursor survey to the PALFA survey (Cordes et al., 2006), mostly with observation times shorter by another factor of two, which were not analysed by Einstein@Home

In total there are 91.0 TB of data for inner Galaxy pointings and 37.4 TB of data for outer Galaxy pointings. From these, there are 32760 beams with  $\sim 268$  s observation time and 5649 beams with  $\sim 134$  s observation time of the inner Galaxy; for the outer Galaxy observations, there are 29670 beams with  $\sim 134$  s observation time.

In the total data volume cited here there is a small fraction of pointings with shorter or longer observation times, observations of known pulsars and follow-up observations of pulsar discoveries, which were not searched by Einstein@Home.

### 3.2.4 Data storage and movement

The raw data are recorded to RAID storage systems at the Arecibo Observatory computer facilities. Disks containing the raw data are shipped to the Center for Advanced Computing (CAC) at Cornell University. There, the data are stored in RAID systems. Also, the CAC hosts web and database servers for the upload and download of data and various processed data products to and from the different institutions in the PALFA collaboration.

For Einstein@Home, data are transferred from CAC to the Albert Einstein Institute, Hannover, via high-speed internet connections. The gridFTP protocol from the Globus toolkit (Foster, 2006) is used to achieve average speeds of more than  $60 \text{ MByte s}^{-1}$ . Data are stored on spinning media in file servers at the AEI. For permanent storage, data are stored on a Hierarchical Storage Management (HSM) system. The HSM consists of a Fibre-Channel disk array backed by a large capacity tape robot.

### 3.2.5 Data analysis

Obtained data are processed by different pipelines, targeting complementary parameter space parts. The pipelines fall into two main categories: a) single pulse searches and b) periodicity searches, both of which are described briefly here.

#### Single pulse searches for intermittent radio sources

The single pulse searches are optimised to detect pulsars and other radio sources that do not emit periodically but rather intermittently, e.g. nulling pulsars (Lorimer and Kramer, 2005) or the recently discovered rotating radio transients (RRATs; McLaughlin et al., 2006). From RRATs only occasional radio burst are detected. A detailed description of the radio transient search algorithms, results, and statistics from the PALFA survey can be found in Deneva et al. (2009).

Two main methods are applied to identify single pulse candidates; the first method is a matched filtering method convolving the de-dispersed time series with pulse templates. The matched filtering is done sub-optimally in an approximative fashion by adding up to  $2^7$  neighbouring time samples and thresholding after each summing step. Asymmetric pulses (due to scattering in the ISM) are not well-matched by the templates and scattered pulses can be wider than the range covered by  $2^7$  samples.

In order to complement the sub-optimal matched-filtering approach the second method detects time-domain clusters. This is a hierarchical process in which all samples above a certain threshold are chosen as cluster centres in the first step. In the following step, the cluster is augmented by including all nearby samples above a certain (other) threshold. This method also allows for gaps in between samples of a single cluster. This method does not assume symmetry of the pulses, but it also has an upper limit on the maximum number of samples per cluster.

In both approaches, data are analysed (and relevant statistics are generated) in blocks much shorter than the observation time to minimise effects of baseline variations in between single pulses on time scales much longer than the pulse width. This however also limits the maximum pulse width and decreases sensitivity to longer pulses.

These single pulse search pipelines are run at different PALFA collaboration sites on computer clusters based on different software suites. At Cornell University's CAC, and the Swinburne University of Technology a pipeline<sup>3</sup> developed at Cornell University is run, using both methods described above and in full detail in Deneva et al. (2009). A pipeline based on PRESTO (Ransom et al., 2002) is run independently at West Virginia University, University of British Columbia, McGill University and the University of Texas at Brownsville. The PRESTO search code implements a similar matched-filtering approach.

### Periodicity searches

The second class of searches done on the PALFA data are periodicity searches. Here, the inherent assumption is that the pulsar is emitting (pulsing) continuously. Thus, the signal is a periodic signal plus additional noise and can be analysed optimally with Fourier methods. There is an overlap between the single pulse searches and the periodicity searches: a single pulse search algorithm may detect a continuously emitting pulsar and a periodicity search may detect an intermittently emitting pulsar. The overlap between the two methods has been studied in detail in Deneva et al. (2009), see e.g. Figure 7 therein. The PALFA survey data are analysed in the collaboration using periodicity searches with three different pipelines, reviewed in the following.

### Cornell pipeline

At Cornell University a periodicity search is run that performs the simplest periodicity analysis on the de-dispersed time series: the time series are Fourier transformed, and harmonic summing (see Section 3.8.5) to improve the sensitivity to a narrow pulses is applied. Candidates are selected by comparing the detection statistic to a threshold. The computational demands for this analysis guarantee a relatively quick completion and can enable fast discoveries. A drawback is that this method's low sensitivity to pulsars in binary systems. In binary systems, the pulsar spin frequency is modulated by the orbital frequency of the

---

<sup>3</sup><http://arecibo.tc.cornell.edu/PALFA/>

binary system, smearing the pulsar signal over several frequency bins in a Fourier analysis, effectively reducing the signal-to-noise ratio.

#### **PRESTO pipeline**

A different pipeline based on the PRESTO software suite (Ransom et al., 2002) runs at various sites in the PALFA collaboration. The PRESTO pipeline includes the search for isolated pulsars (comparable to the pipeline at Cornell) as a subset of a search for binary pulsars. The search method applied here is called an acceleration search because it assumes a constant orbital acceleration along the line of sight during the observation. The search parameters are reduced from the full set of Keplerian orbital parameters to the single value of acceleration, greatly reducing the computational needs to perform such a search. An acceleration search can in principle be achieved by re-sampling the de-dispersed time series with a set of trial accelerations and Fourier analysing each re-sampled time series. This approach becomes computationally dominated by the Fourier analysis for long time series. The details of a computationally efficient form of acceleration search are described in Ransom et al. (2002). There, the Fourier transform is only computed a single time, after which the correction for trial acceleration values is applied in the frequency domain.

Acceleration searches perform with a reasonably low loss in signal-to-noise ratio for orbital periods longer than  $\approx 10T_{\text{obs}}$ , where  $T_{\text{obs}}$  is the total time spanned by the time series. For a more detailed examination, see Johnston and Kulkarni (1991) and Ransom et al. (2003) as well as Section 8.8 of this thesis.

#### **Quicklook analysis at Arecibo observatory**

For most of the survey, a “quicklook” analysis was also run at Arecibo Observatory to guarantee an almost real-time analysis of data at reduced resolution. This allowed for the quick detection of slow pulsars during the course of the survey. With various upgrades of software and receivers, the quicklook pipeline became non-functional; investigations to revive use of this pipeline are underway at the time of this writing.

#### **Einstein@Home radio pulsar search**

The third periodicity search is the Einstein@Home radio pulsar search, the set-up of which is described in full detail in the following sections of this chapter. This search pipeline tackles the computationally challenging task of a blind pulsar search over a wide parameter space of Keplerian orbital parameters: the set consists of four parameters describing a pulsar signal in a circular orbit. This brute-force approach allows to detect pulsars in much shorter orbits with periods  $P_{\text{orb}} \approx T_{\text{obs}}$ . It is enabled by tapping into the enormous computing power provided by volunteers from the general public worldwide.

### **3.3 Volunteer distributed computing**

---

The basic idea of volunteer distributed computing is a simple one. Members of the general public own two or three orders more aggregate computing power than universities and research institutions. The computing power is distributed in people’s private homes and/or offices in desktop computers and laptops. With only a small fraction of this computing power new data analysis or simulation problems, out of reach before, can be tackled

and solved, as many scientific research projects are limited by the available computing resources. Typical problems are, on the one hand, Monte-Carlo simulations and explorations of large parameter spaces that do not analyse observational data or, on the other hand, the sensitive, deep analysis of observational data, covering large, previously inaccessible parameter space regions. Note: this section is partly adapted from Allen et al. (2011).

To put the prospects of volunteer distributed computing into perspective: there are of order *one billion* desktop computers and laptops with internet connection worldwide. Most of these computers contain Intel or AMD manufactured central processing units (CPUs). Most of the modern CPUs contain two, four, or even more cores, each of which can perform four floating points operations per clock cycle, and are clocked at a few GHz. On average, each computer has one Gigabyte (GB) of random-access memory (we will refer to this in short by *RAM* or *memory*). Furthermore, each computer comes with hard-drives or solid-state disks for data storage with typical capacities of hundreds of GB. These personal computers are in fact very similar to the building blocks for modern high-throughput computer clusters like the ATLAS cluster at the AEI in Hannover, Germany; using consumer marketplace computers guarantees that parts are readily available and come at a low price. The important difference in scale is that typical computing farms, computer clusters, or supercomputers contain of order thousands of compute nodes and cores, while in volunteer distributed computing there are hundreds of thousands or millions of compute cores, which still is a very small fraction of the one billion CPUs worldwide.

The practical implementation of modern volunteer distributed computing projects is simple and requires only minimal attention from the volunteers deciding to donate computing time on their private computers. Members of the general public (*volunteers*) can register (*sign up*) their home or office computers (*hosts*) for a particular project like Einstein@Home, SETI@Home, Folding@Home, and so on. When the computers are idle, they do computing work for the project, download any data and executables that are needed over an internet connection and, after finishing the computations, upload results back to the server.

The economics of volunteer computing projects are compelling. The total computing power collectively available to these projects corresponds to millions of CPUs. This is more computing power than is available to all but the very largest of the “big science” projects. The equivalent value of the electrical power for Einstein@Home donated computing power alone is tens of thousands of dollars *each day*.

In the next section we review why not all research problems limited by the available computing power are suited for volunteer distributed computing. Limits arise from the fundamental structure of the research problem and technical constraints due to the distribution of hosts all over the world. Furthermore, there are social and psychological components, because computation time is donated voluntarily.

### 3.3.1 Constraints on suitable problems

Volunteer distributed computing is not a “magic bullet” for all large-scale scientific data analysis or simulation type problems. Constraints arise on suitability arise from psychological and/or social and technical reasons.

Psychological constraints arise from the fact that people must sign up their hosts voluntarily; thus the science goals of the volunteer distributed computing project must pique their interests. If the project aims to acquire a large as possible group of volunteers, the science goals must be formulated clear and understandable to volunteers without much background in the respective area of science. Interest in the topic must be excited and kept

over longer times; the latter can be supported by active communication with interested project volunteers over message boards, newsletters, etc. Judging by the topics covered by large volunteer distributed computing projects<sup>4</sup>, a handful of science areas fulfils these requirements: astronomy and astrophysics, humanitarian and/or medical research, climate science, and mathematics.

Technical constraints arise from the dispersion of volunteer distributed computing hosts all over the world. The necessary data transfer over the internet via a few central project servers limits the transfer bandwidth; further, the sporadic availability (say, a few times each week) of host machines means host-to-host communication must not be central to the scientific problem in question. Assuming the project server is connected through a  $100 \text{ MB s}^{-1}$  connection to the internet and is trying to serve of order  $10^5$  hosts, for each host only  $100 \text{ kB s}^{-1}$  bandwidth is available. Compare this to the typical value of few  $\text{GB s}^{-1}$  for computer cluster, where nodes also are always available with very low latencies in the nanosecond range. This means that in volunteer distributed computing, the bandwidth is six orders of magnitude lower, and the latency is  $\sim 14$  orders of magnitude larger than in “traditional” cluster computing!

A further important constraint on such analysis, compared to carrying out the analysis on a traditional supercomputer or compute farm, is that the ratio of data to compute time must be very small. All data for the analysis with volunteer distributed computing has to be transferred to the host over internet connections and stored on the hosts storage devices; none of these steps must interfere with the owner’s usage of the computer. This excludes transferring very large data sets, i.e. many Gigabytes of observational data to a single host to avoid usage of large amounts of disk-space on the volunteer’s host and excessively long download times. Furthermore, the amount of processing time spent on a certain amount of observational data has to be large compared to the data volume to avoid frequent downloads of large amounts of data.

All these constraints lead to a five main requirements for distributed volunteer computing:

1. the scientific problem to solve must belong to the class of *embarrassingly parallel problems*. This means that the problem can be broken with little to no effort into smaller sub-problems that can be solved independently of each other. No communication between sub-processes solving each of the sub-problems is necessary.
2. The ratio between data volume downloaded and uploaded and total computation time on this data volume must be small. Typical values of about 1 MB per CPU hour or smaller nowadays work well in practice.
3. The scientific application on the host must only use a small fraction of the host memory; otherwise the operating system cannot quickly suspend or restart tasks without interfering with the owner’s usage of the computer. In practice few hundred MB of memory can be used on modern computers.
4. The scientific application also must be capable of frequent and lightweight *checkpointing*, that is: saving the current state of the computation in a small file, which allows resuming it at a later point in time without loss of information or the need to restart from the beginning. This is needed to allow the computer owner to interrupt the computation whenever wanted.

---

<sup>4</sup><http://boincstats.com/>

5. Adapting a science problem to volunteer computing is a elaborate and time-consuming process. The science problem must be mature enough so that months of development can be invested safely into porting the application to various operating systems and/or hardware platforms, and in tuning and optimising the code.

### 3.3.2 GPUs and future volunteer computing

For over forty years, the development of computing hardware was well described by a heuristic fit known as “Moore’s Law”. Moore (1965) observed that the number of transistor on integrated circuits grew exponentially with time, in turn doubling the computing power at fixed cost every 18 months. This trend has continued over the last decades by shrinking the sizes of the components on integrated circuits following Moore’s prediction very well. Along the shrinking component sizes, clocking speeds could be increased while decreasing operating voltages at the same time.

Within the next decade, this trend will come to an end for two main reasons. The operating voltages cannot be decreased further. They already are close to the band-gap energy<sup>5</sup> in the semiconductors used for the fabrication of integrated circuits. The smallest typical component size (also called “process size”) is also hitting a fundamental limit: it currently is 32 nm and is expected to decrease to about 10 nm at most. Fundamentally, it cannot get much smaller since silicon crystallises in a diamond cubic lattice with a lattice constant of 0.357 nm (Andrew, 1990).

To overcome these fundamental problems, there is a relatively simple solution: one has to increase the number of computing cores per chip. This trend is reflected in the multi-core CPUs manufactured today, which are common in modern desktop computers and laptops. The consumer market also has a high demand for multi-core systems in a different form: graphics processing units (GPUs), used for high-detail rendering of computer graphics, for example for computer gaming. Modern, high-end GPUs have core numbers in access of 500, each of which can perform one floating point operation per clock cycle. Modern GPUs cannot only be used for graphics-rendering: leading manufactures provide programming interfaces to use GPUs as all-purpose computing machines.

### 3.3.3 Einstein@Home

Einstein@Home is a volunteer distributed computing project which was publicly launched on February 19, 2005, and searches data from the LIGO and VIRGO gravitational-wave (GW) detectors. Starting on March 24, 2009, Einstein@Home also began, in parallel with the GW searches, to analyse radio survey data from Arecibo Observatory, searching for radio pulsars.

Volunteers of the general public sign up their computers by visiting the project website at <http://einstein.phys.uwm.edu/> and following the instructions. This includes downloading and installing a small executable, available for Linux, Mac, and Windows operating systems. The installation procedure does not take longer than a few minutes and allows the volunteer to attach the computer (*host*) to Einstein@Home. After this initial setup, the program does not require further attention from the volunteer. Every time the host would be idle, scientific data analysis of astrophysical data is run on the CPU or GPU with the results of the running analysis being presented in a screensaver (if activated). All data and scientific executable download and result upload happens fully automatically.

---

<sup>5</sup>The band-gap energy for silicon is 1.12 eV, and 1.46 eV for GaAs, respectively

### Project dimensions

For Einstein@Home, at the time of writing, hosts from more than 290,000 individual volunteers have been signed up and successfully returned scientific results. The participants are from all 192 countries recognised by the United Nations<sup>6</sup>. Each week, the Einstein@Home project servers are contacted by around 80,000 different hosts from 50,000 different volunteers to request new work from the servers or to report finished work. On average, each host is running Einstein@Home jobs for 35% of the time. The estimated aggregate sustained computing power<sup>7</sup> currently is about 400 TFlop s<sup>-1</sup>, which, at the time of writing, is among the fastest twenty super-computers worldwide<sup>8</sup>. This is an enormous amount of computational power donated by volunteers from the general public.

To put this into perspective, this means that that each week Einstein@Home contributes about *five million* CPU hours. Assuming an average power consumption of 150 W, this means that the sustained electrical power contributed and donated by the Einstein@Home volunteers is of order

$$P_{\text{tot}} = 80000 \times 0.35 \times 150 \text{ W} = 4.2 \text{ MW}. \quad (3.3)$$

Using the current typical German electricity costs of  $\approx 0.2$  Euro kWh<sup>-1</sup>, this scales to 7.4 million Euros donated annual costs for electrical power alone. The additional costs for hardware and administration of a similarly-sized cluster would be substantially greater, as can be seen by comparing to the prices for cloud computing offered by the Amazon Elastic Compute Cloud (Amazon EC2)<sup>9</sup>; for Einstein@Home the provision and administration of the hardware is donated by the volunteers as well.

About 25% of all hosts on Einstein@Home have GPUs to date, and we expect this fraction to rise substantially within the next years. The Einstein@Home search for radio pulsar has been ported to NVidia GPUs, see Section 3.8.8 and Bock (2010) for more details.

### Science goals

The initial and still long-term goal of Einstein@Home is the detection of continuous gravitational waves in the data of ground-based gravitational wave detectors. Continuous gravitational waves could be emitted by rapidly-spinning neutron stars through a variety of mechanisms, see Section 2.6. The search for this type of gravitational waves is part of the world-wide effort towards the first direct detection of gravitational waves. Predicted by Albert Einstein in 1916, no direct detection has been achieved yet, but the latest generation of world-wide distributed ground-based detectors offers for the first time a realistic chance of detection. The currently operating laser interferometric detectors are LIGO at the two sites in Hanford, Washington and Livingston, Louisiana in the USA (Abramovici et al., 1992), Virgo in Cascina, Italy (Caron et al., 1997), and GEO 600 near Hannover, Germany (Danzmann et al., 1995).

The continuous gravitational wave signals from spinning neutron stars are expected to be very weak and buried deep in detector noise. Furthermore, the source parameters like sky position, spin frequency, spin frequency derivative are unknown, search sensitivities for this type of signal are limited by the available amount of computational resources (Brady and Creighton, 2000; Brady et al., 1998). Since the parameter space can be split up into small

<sup>6</sup><http://www.un.org/News/Press/docs/2006/org1469.doc.htm>

<sup>7</sup>[http://einstein.phys.uwm.edu/server\\_status.html](http://einstein.phys.uwm.edu/server_status.html)

<sup>8</sup><http://www.top500.org/list/2010/11/100>

<sup>9</sup><http://aws.amazon.com/ec2/>

disjunct patches, each requiring only a relatively small amount of detector data to analyse, this science problem however fulfils the requirements formulated above, making the search for continuous gravitational waves a problem well-suited for volunteer computing.

So far, no direct detections of continuous gravitational waves have been achieved by Einstein@Home; it is however the most sensitive blind all-sky search for this type of gravitational waves using data from the most sensitive ground-based detectors. Upper limits using results from Einstein@Home analysis runs have been published (Abbott et al., 2009; Abbott et al., 2009). Currently, Einstein@Home is analysing the data set from the fifth data run (S5) of the LIGO instruments using an improved method (Pletsch and Allen, 2009), which has been shown to be optimal under the standard assumptions for the noise sources and which increases the search sensitivity by a factor six at reduced computational costs.

Einstein@Home's second science goal is the detection of unknown radio pulsars in tight binary systems, which we motivate and review in the following section.

### 3.3.4 Einstein@Home's search for radio pulsars in tight binaries

Since March 24, 2009, Einstein@Home has also been analysing data in the radio-frequency spectrum from the Arecibo Observatory, Puerto Rico. This development of this new search is the central topic of this thesis. The sources of interest here are radio pulsars, highly magnetised and rapidly spinning neutron stars that emit beams of radio waves into space. If the beam intersects the line of sight of a terrestrial observer, a regularly pulsating radio source, a pulsar, is detectable with large radio telescopes. The 305-m Arecibo Observatory is the world's largest single-dish radio telescope, with high sensitivity due to high-end receivers and backends. A substantial fraction of all known radio pulsars and some of the most interesting specimen have been discovered with Arecibo Observatory.

Pulsars are the compact remnants of massive stars at super-nuclear densities, which provide the opportunity to study matter unavailable in terrestrial laboratories. They further can provide information about their formation history and therefore about the processes occurring in supernovae. Pulsars exhibit magnetic fields much stronger than those accessible under terrestrial conditions, which open up another laboratory of the extremes. Because pulsars are compact objects with their Schwarzschild radius only a third of the physical radius, they have extremely high surface gravity, which enables test of General relativity in the strong-field regime. Thus, already isolated pulsars can provide new input to a wide range of scientific fields.

The pulsars which have yielded the most interesting results in the past, are binary pulsars; these pulsars orbit the common centre of mass with a companion, which can be another neutron star, a white dwarf, or a main sequence star. Most of these binary pulsars spin faster than their isolated kin because of a phase of matter transfer in the common past of the binary system, which spins up the pulsar. The very fast spinning pulsars enable new test of the equation of state of neutron stars and General Relativity. The binary motion of the pulsar, which can serve as a very precise clock, can be monitored with exquisite precision to allow very stringent tests of Einstein's theory of gravity. Also, the measurement of relativistic effects can allow to obtain precise mass measurements of the neutron star and its companion.

Only a small fraction of the currently known pulsars are in binary systems, which also makes them useful tests of stellar population synthesis models: these model must be able to explain their sometimes finely tuned formation pathways.

Relativistic effects become more pronounced and therefore easier to measure the shorter

the orbital period is. Thus, finding binary radio pulsars with short orbital periods is one of the main goals of current radio pulsar research. This subclass of radio pulsars is one of the most interesting as it can effect various areas of science.

Starting from a longer, maybe eccentric orbit, the emission of gravitational waves shrinks and, and especially circularises, the orbit rapidly. Unfortunately, the decay of the binary separation also progresses faster, the closer the companions are, so that a binary pulsar only spends the very last short bit of its time before coalescence in short period orbits. From the fact that we know of the existence of binary radio pulsars which will coalesce in time scales short compared to the age of the universe, we can infer that there could be radio pulsars in very tight binaries in our Galaxy. The argument is as follows.

By emission of gravitational radiation, the merger time for a binary system with masses  $m_1$  and  $m_2$  in an initially circular orbit with radius  $r$  is (Peters, 1964)

$$T_{\text{merge}} = \frac{5}{256} \frac{c^5 r^4}{G^3 m_1 m_2 (m_1 + m_2)} = 7.06 \text{ Myr} \left( \frac{P}{1 \text{ hr}} \right)^{\frac{8}{3}} \left( \frac{1.4 M_{\odot}}{m_1} \right)^{\frac{5}{3}} \frac{(1 + \mu)}{2^{\frac{1}{3}} \mu}, \quad (3.4)$$

where  $\mu = m_2/m_1$  is the mass ratio of the binary system and the last factor is unity for equal masses. For initially eccentric orbits, the merger time is significantly shorter (Peters, 1964).

A figure of merit of the shortest expected orbital period can be obtained from the estimated merger rate of, e.g. Galactic double neutron star systems. Kalogera et al. (2004a) and Kalogera et al. (2004b) estimate the merger rate to be  $\Gamma_{\text{merge}} = 83_{-66}^{+209} \text{ Myr}^{-1}$ . The equation

$$\Gamma_{\text{merge}} T_{\text{merge}} = 1 \quad (3.5)$$

defines the orbital period at which there is on average a single Galactic double neutron star system merging within the time defined by  $\Gamma_{\text{merge}}^{-1}$  (Allen and Cordes, 2008). Using the values from the above equation we find for the corresponding shortest orbital period  $P_{\text{min}} = 5.5_{-2.1}^{+4.5} \text{ min}$ . In other words: there could be at least one Galactic double neutron star binary with an orbital period as short as six minutes. We can further infer that the orbits of these tight binary systems most likely are almost circular, see Section 3.4.5 for a justification.

The data analysis to discover these objects is currently limited by the available computational power; the presence of a binary companion and resulting orbital accelerations strongly modulate the apparent spin frequency by the Doppler effect. If this effect is not corrected for, the sensitivity to pulsars in binary systems is massively degraded. As the orbital parameters of the binary system are unknown a priori, a wide parameter space has to be searched, especially for tight binaries with the additional unknown orbital parameters. Einstein@Home's enormous computing power is used to search for radio pulsars in very tight binary orbits, exploring a region of orbital parameter space not available to other search methods, which significantly lose sensitivity in this highly interesting part of parameter space.

### 3.3.5 The Berkeley Open Infrastructure for Network Computing

The Berkeley Open Infrastructure for Network Computing, or in short "BOINC" was created in 2002 as a middleware system toolkit for distributed volunteer computing. BOINC was mainly developed by David P. Anderson and is based at the Space Sciences Laboratory, University of California, Berkeley, USA. The BOINC software toolkit is an open source project, licensed under GNU Lesser General Public License (LGPL). BOINC provides an infrastructure for the project server side (i.e. the part of volunteer computing accessible to

project developers), the client side (i.e. the part of volunteer computing owned by the volunteers from the general public), and project community features, such as message boards, project web pages, etc. The server side is responsible to manage the distribution of the scientific work to the computers of hundreds of thousands volunteers, while the BOINC client side enables the communication with the server side and conducts the scientific computation or data analysis, as for Einstein@Home.

There are a few big differences between distributed volunteer computing and traditional scientific computing on large clusters or computer grids. On dedicated clusters or grids the computing hardware is controlled and administered by project staff, the hardware is continuously available and reliable, and hardware problems can be fixed readily. In volunteer computing, the computing hardware resides in homes and offices of the general public, can contain faulty hardware and / or software, is not continuously available, and there are no means for the project staff of actively fixing occurring hardware problems. This dictates the central assumption behind all distributed computing projects: nothing is reliable except the project servers under direct control of the project staff. This further implies the need for redundant computations to minimise the influence of client side faults on the scientific results; see below and Section 3.9 for details on redundant computation in the Einstein@Home project.

We now present more details on the two sides (server and client, respectively) any BOINC project is composed of.

### 3.3.6 BOINC server side and client side

Einstein@Home, like any BOINC project, has two sides. One side is fully controlled and owned by the project (the *server side*), while the other side is not owned and not under control of the project (the *client side*).

The *server side* are computers designed to serve as the central project beacon: all data are prepared for analysis on this side, sent out to the volunteers' computers, and all processing products are collected on this side.

The *client side* is the collection of all volunteer computers attached to the BOINC project. It receives data, search codes and search instruction from the server side via the internet, conducts the scientific analysis as instructed and uploads the resulting data products via the internet to the server side.

#### Server side

The BOINC project server side is represented by a set of computer servers. These computers are owned, configured, and administered by the project scientists and run various BOINC programs and processes. The physical location of the BOINC project server for Einstein@Home is at the University of Wisconsin- Milwaukee, USA. The BOINC upload and download servers for the radio pulsar search on Einstein@Home is located at the Albert Einstein Institute in Hannover, Germany. For the gravitational wave search, download servers are located at the Albert Einstein Institute in Golm and Hannover, Germany, at the University of Glasgow, UK, at the MIT, Boston, USA, at The Pennsylvania State University, State College, USA at the Caltech LIGO Lab, USA, and at the University of Wisconsin-Milwaukee, USA<sup>10</sup>

---

<sup>10</sup> <http://einstein.phys.uwm.edu/contributors.php>

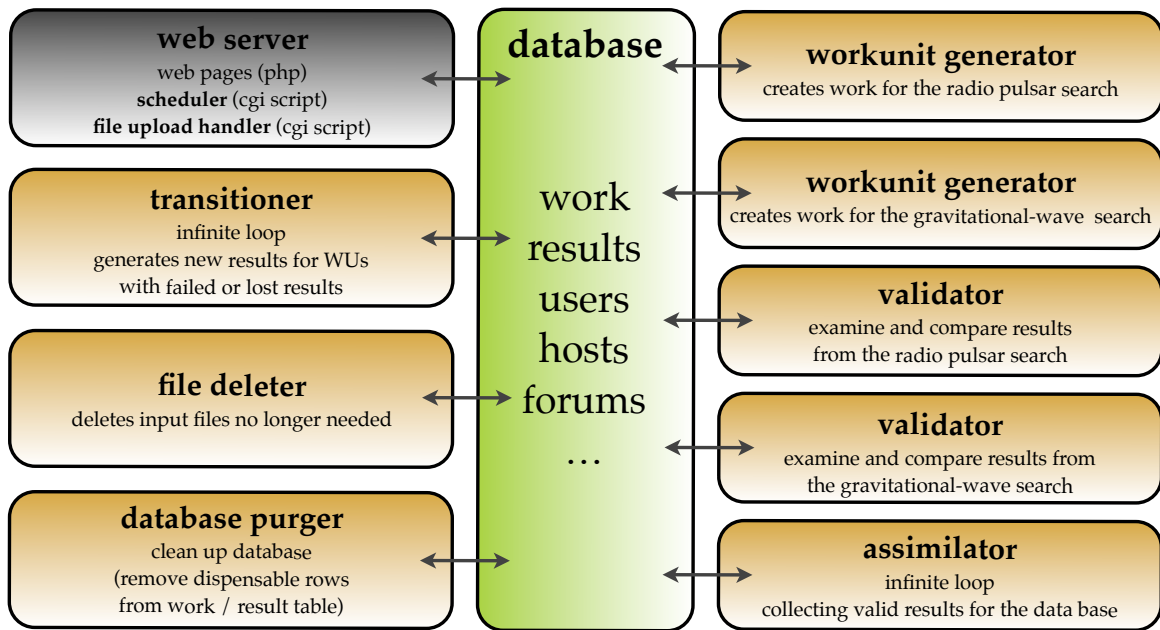


**Figure 3.4:** Program and process structure of the BOINC server side. Each box is a different process or program running on the Einstein@Home BOINC servers; orange boxes are daemon processes, grey boxes are Apache processes. All processes are coordinated via communication through a central data base in the middle of the diagram. Processes on the left are taken without major modification from the BOINC framework (Anderson et al., 2006); processes on the right have been written specifically for Einstein@Home. Figure adapted from Allen et al. (2011).

The BOINC programs and processes used by Einstein@Home are shown in Figure 3.4, which was adapted from Allen et al. (2011). Each box in the diagram is a different process or program running on the Einstein@Home BOINC servers; orange boxes are daemon processes (explained below), grey boxes are Apache processes (see also below). All processes are coordinated via communication through a central data base in the middle of the diagram. Processes on the left are taken without major modification from the BOINC framework (Anderson et al., 2006); processes on the right have been written specifically for Einstein@Home.

The core part of the Einstein@Home BOINC project server side is the central mysql database, shown in green in the middle of Figure 3.4, which is running on a state-of-the-art high-end server. As shown in the figure it collects information relevant to the project in different tables, the most important of which are the user, the host, the work, and the result table, respectively. The user table contains one row for each volunteer registered with Einstein@Home. The host table contains one row for each computer that has contacted the Einstein@Home project server at least once. The work table list the workunits (described below), one per row. The result table contains one row per result, that is each instance of a workunit. One workunit can give rise to multiple results, since results are sent out redundantly for validation purposes (see Section 3.9), can be in process, or not sent to client machines, for example. The database also contains a forum table for the message boards posts that volunteers and developers can post in the boards at [http://einstein.phys.uwm.edu/forum\\_index.php](http://einstein.phys.uwm.edu/forum_index.php). The database contains further tables, which are not relevant here.

Most of the important processes on the BOINC server side, Figure 3.4, are so-called *daemon processes*. These processes run for a long time in the background, independent of direct user control. A typical daemon process action is the issue a query on the database, checking for a particular condition, execute some action depending on the query result, and then return to sleep for a pre-defined time interval (seconds or minutes). An example is the validator daemon process, which is described in detail for the radio pulsar search in Section 3.9; the validator checks the database to evaluate whether there is a pre-defined number of successful<sup>11</sup> results. If the appropriate number of results is found, the validator then compares the results by an algorithm described in Section 3.9 to check for agreement; if the results are indeed found to agree, they are marked as valid results, and one of them is marked as the canonical result. *Credits*, a number representing the amount of volunteer computing done, are then granted to the volunteers, whose computer ran the respective workunits. If the results are not found to agree, a flag in the database is set that will be read by the transitioner (see Figure 3.4), which will then generate a new result for the workunit. When this new result is returned later to the project, the validator will compare the new set of results with one another.

A very important daemon process is the workunit generator, which creates the meta information needed to run the science application on the volunteers' computer attached to the BOINC project. Each row in the work table specifies the application and its version to run; it further specifies the command line arguments to use and which input files have to be downloaded for this workunit. In order to run the workunit only on computers with hardware capable to do so, the row in the work table also contains the required memory size, the estimated runtime, and for the radio pulsar search the credits to be granted. In the Einstein@Home radio pulsar search the main data preparation steps done by the workunit generator are described in Sections 3.7.2-3.7.4.

Apart from the daemon processes, there are also a couple of cgi processes run by the Apache webserver (grey box in Figure 3.4). The first important cgi process is the file upload handler, which receives completed results from the BOINC client running on the client side (see below). This uses the normal Hypertext Transfer Protocol (HTTP) via port 80 and enables any host with web access to run Einstein@Home. The scheduler reads scheduler request files issued from the BOINC client. These can contain requests for new work, for example because the volunteer's computer will soon have depleted its currently available amount of work. To fulfil the request for new work, the scheduler then queries the database to find workunits suitable for the host. The same pathway also is used to report completed work. In this case, the scheduler updates the database by marking the respective result as uploaded.

### Client side

The BOINC client side is the collection of all volunteer computers attached to the BOINC project and the BOINC processes and scientific project applications running on these computers- Usually, none of these machines is owned or administered by the project.

The central BOINC process on the client side is the so-called *BOINC client*. This program does not run any scientific data analysis or computation itself; it coordinates the launch, possible interruption, and exit of the scientific application of any BOINC project the computer is attached to. It further coordinates the data download and upload. The communi-

---

<sup>11</sup>the science application ran without reported errors and the results were successfully uploaded to the project servers

cation medium with the possible various BOINC project servers are short XML files. The files sent by the BOINC client are called *scheduler requests* (see above) while the files sent in reply from the project server are called *scheduler replies*. These scheduler messages are used to request new work from the server or to report finished work.

When the BOINC client detects that the volunteer computer is idle<sup>12</sup>, it starts a task from one of the BOINC projects; if it has not done so earlier, it will now download necessary science application executables for the computer's operating system, as well as the necessary input data from the project server. Veracity of these files is checked by the md5 checksums and the digital signature issued by the project. Then, the BOINC client runs the tasks from start or from available *checkpoints*, i.e. an earlier saved partial task results and task status. The user-definable balance between different projects and the coordination of timing the task execution to meet upload deadlines is kept by scheduling algorithms within the BOINC client. Furthermore, the BOINC client collects information about the exit and possible error status of the science application, and makes sure the science application does not exceed the allocated limits on disk space, memory consumption, or CPU runtime.

The science applications run by the BOINC client are the part of the BOINC project doing the scientific computation, be it Monte-Carlo like simulations, or as for Einstein@Home the data analysis of detector output data. The data files downloaded from the project servers contain output from the gravitational wave detectors, or the Arecibo Observatory in the case of the radio pulsar search. The science application analyses these data, writes the statistically most significant candidates to a file, which then is uploaded to the project servers as the result.

The BOINC client requests the science application to write checkpoints on a regular basis. These checkpoint files contain an image of the current computation state so that loading this checkpoint at a later time allows to resume the computation from the saved state without restarting from the beginning and without loss of information. For the Einstein@Home radio pulsar search, the checkpoint file contains the position in the hot loop of the science application (see Figure 3.22) at the interruption and the current five top lists of the candidates found so far. When a task is started, it will first look for checkpoint files, load them and resume the computation in the hot loop from existing checkpoints. If no checkpoint is found, the computation is started from the beginning of the hot loop.

For the Einstein@Home radio pulsar search, the science application codes are written in standard C/C++ programming language, linked to standard open source libraries for special types of calculations (FFTW (Frigo and Johnson, 2005) for Fourier analysis, functions from the Gnu Scientific Library (GSL; Galassi, 2009) for various statistical evaluations). For communication with the BOINC client, the science application is also linked against the BOINC application library. This library provides essential replacements for the standard IO routines, like `FILE * boinc_fopen()` for the standard `FILE * fopen()` to ensure consistent opening of files on different operating systems<sup>13</sup>. `boinc_time_to_checkpoint()` can be called by the science application, returning a non-zero value if it is time to write a checkpoint file. In the radio pulsar search, this is checked after each iteration in the hot loop (Figure 3.22), i.e. after each orbital template. The successful writing of a checkpoint is signalled to the BOINC client by `boinc_checkpoint_completed()`. Progress of the scientific computation is communicated via `boinc_fraction_done()` to the client and describes the

<sup>12</sup>i.e. the CPU usage falls below a user-definable value

<sup>13</sup>For example, `FILE * boinc_fopen()` opens files non-exclusively on Windows operating system to avoid blocking by other processes like, e.g. virus scanners

fraction of total work done for a task; this information then is needed to estimate the remaining task runtime and to schedule tasks such that they meet the project deadlines. For the Einstein@Home radio pulsar search, this simply is the current loop counter in the hot loop divided by the total amount of loop iterations (orbital templates). `boinc_finish()` finally is called by the properly exit the science application and to report the exit status (and possible error codes) to the BOINC client

### 3.3.7 Validation workflow

The only safe assumption in the universe of a distributed volunteer computing project is that nothing is reliable except the project servers. The volunteer computers are not owned, nor administered by the project scientists; thus, any machine attached to the project should be considered unreliable. A machine could return a correct result, an incorrect result, or even a forged “fake” result. Other possibilities are that the computer does not finish the computation within the deadline (see below), or is detached from the distributed computing project forever.

To increase the robustness of volunteer distributed computing against this type of problems, the *same* task is sent out to multiple attached computers and the returned result files are checked for mutual consistency (*validated*). This is achieved on the BOINC server side (see Section 3.3.6 and Figure 3.4) by the transitioner creating a *quorum* of unsent results in the result table of central database from the workunits in the work table of the central database. Workunits are inserted into the database by the workunit generator, which for Einstein@Home reads data files, prepares them by splitting them into smaller amounts of work suitable for computation on the volunteer computers, and enters corresponding entries into the database. The unsent results then are assigned to volunteer computers, marked with the computer identity and with a deadline, within which the result has to be returned to the project servers. The deadline for Einstein@Home currently is two weeks. The result then is uploaded if the computation finished successfully, and validated for individual correctness and mutual consistency based on pre-defined, project-specific metrics. The quorum for Einstein@Home currently is to obtain two agreeing results. If the validation fails, the transitioner generates a new row in the results table of the central database which will be assigned to a different host by the scheduler. The validation process for the radio pulsar search is described in detail in Section 3.9.

## 3.4 Phase model and parameter space

---

This section contains the theoretical background to describe the signal from a radio pulsar in a circular orbit by means of a phase model. It further provides the metric for the search for these signals on the space of physical binary system parameters. The ansatz presented here and the metric were first described and derived by Messenger (2008).

### 3.4.1 The fully coherent search

The Einstein@Home search for radio pulsars presented in this thesis differs in key aspects from other searches for binary pulsars. The description of the binary motion is not approximated, it is fully included in the parameter space description: where a single value of acceleration is used in the acceleration searches to *approximate* a small part of the binary

orbit, three parameters of a circular Keplerian orbit apply in the Einstein@Home search that *correctly and fully* describe the pulsar signal at any point in the orbit.

This complete description of the orbit comes at the price of higher computational costs and a higher-dimensional parameter space but offers to detect signals from pulsars in much shorter orbits. While the validity of acceleration searches breaks down at the point where more than about 10% of the orbit are visible in an observation, there is, in principle, no constraint<sup>14</sup> to detect pulsars in orbits arbitrarily short compared to the observation time with the Einstein@Home search.

Other binary pulsar search methods divide a longer observation into smaller pieces, analyse each of it with the approximation of an acceleration search, and then combine the results incoherently (Chandler, 2003); this approach however is an *incoherent* combination of *approximatively* analysed data segments. The Einstein@Home search is a *fully coherent* data analysis: the data are analysed in a single piece and no major approximations are used to described the signal.

A rough comparison between non-acceleration searches, acceleration searches, acceleration searches with an additional jerk term, and a fully coherent search like the Einstein@Home search is presented in Section 8.8.

In the remaining part of this section we will describe the parameter space of pulsar orbital and spin parameters for the Einstein@Home search for binary radio pulsars. We further describe, which part of the space of all possible circular orbits we constrain the search to. We then define a measure of distance on the parameter space, the *metric*, which is based on the loss of squared signal-to-noise ratio for small deviations from a parameter space point. We then review the resulting metric in some detail.

In Section 3.5 we describe how the information from the metric can be used to construct a finite set of test signal waveforms against which the data have to be compared in order to detect any possible signal. This finite set of test waveforms is called a *template bank*. We review the construction process of recently developed methods of simple and efficient template banks (Harry et al., 2009; Messenger et al., 2009) and show a novel way to efficiently construct some of these template banks.

Equipped with this knowledge, we then tackle the inner workings of the part of the search pipeline that conducts the data analysis for circular orbits and runs on the client machines attached to the Einstein@Home project. The preparation of the data into workunits on the Einstein@Home server side is described in Section 3.7. The client search code is described in full detail in Section 3.8.

### 3.4.2 Phase model for circular orbits

For a general orbit, the phase model can be described as

$$\Phi(t) = 2\pi f \left( t - \frac{d(t)}{c} \right) + \Phi_0 + \mathcal{O} \left( \frac{v^2}{c^2} \right), \quad (3.6)$$

where  $d(t)$  is the varying distance between observer and pulsar in the binary system and  $f$  is the intrinsic spin frequency of the pulsar (and  $c$  the speed of light). This description is approximate because the time  $t$  denotes detector time and this description does not take into effect retardation effects. These effects are of order  $v^2/c^2$ , and can be neglected here.

<sup>14</sup>other than the available computing power

The apparent frequency seen by an external observer changes because of the pulsar's motion along the observer's line of sight, which causes a frequency shift by the Doppler effect. The apparent frequency is given by

$$f(t) = \frac{1}{2\pi} \frac{d\Phi(t)}{dt} = f \left( 1 - \frac{v(t)}{c} \right), \quad (3.7)$$

where  $v$  is the velocity of the pulsar along the line of sight.

For an elliptic orbit (see Section 8.4), the distance  $d(t)$  is given by

$$d(t) = d(\theta(t)) = d_0 - r(\theta(t)) \sin(i) \sin(\theta(t) + \omega) \quad (3.8)$$

and the velocity along the line of sight by

$$v(\theta(t)) = \frac{a \sin(i) \Omega_{\text{orb}}}{\sqrt{1-e^2}} (\cos(\theta(t) + \omega) + e \cos(\omega)) \quad (3.9)$$

In the case of a circular orbit with  $e = 0$ , we have  $r(\theta(t)) = r = \text{const}$  and  $\theta(t) + \omega = \Omega t + \psi$ , so that Equation (3.8) for a circular orbit simplifies to:

$$d(t) = d_0 - r \sin(i) \sin(\Omega t + \psi), \quad (3.10)$$

where  $d_0$  is the distance to the binary system's barycentre,  $r \sin(i)$  is the projected radius of the system (with orbital inclination  $i$ ) along the line of sight,  $\Omega = \frac{2\pi}{P_{\text{orb}}}$  is the angular velocity on the orbit of period  $P_{\text{orb}}$ , and  $\psi$  is the initial orbital phase. Inserting the distance into the phase model yields

$$\Phi(t; \Lambda) = 2\pi f (t + \tau \sin(\Omega t + \psi)) + \Phi'_0, \quad (3.11)$$

where we have defined  $\tau = \frac{r \sin(i)}{c}$  and absorbed the constant term in the distance to the pulsar in the initial phase  $\Phi'_0$ .  $\Lambda$  is the collection of the parameters  $f, \tau, \Omega, \psi$  describing the system. Thus, any blind search without prior information about the parameters will have to search over the four-dimensional space of  $f, \tau, \Omega, \psi$

### 3.4.3 Parameter space description

The physical parameter space for the Einstein@Home radio pulsar search has four dimensions: the intrinsic spin frequency of the pulsar,  $f$ , the orbital angular velocity,  $\Omega_{\text{orb}} = 2\pi P_{\text{orb}}^{-1}$ , the projected orbital radius,  $\tau$ , and the initial orbital phase,  $\psi$ , compare Equation (3.11). The physical meaning of these coordinates is shown in the left panel of Figure 3.5.

The coordinates are labeled at an example orbit shown by a dashed dark-grey line. The pulsar (solid black circle) and the companion (light grey circle) orbit the common center of mass (c.o.m). An observer in the orbital plane will experience changes in the line of sight (l.o.s.) velocity through changes of the apparent frequency. In the blue region the apparent frequency is higher than the intrinsic frequency, and vice versa in the red region. The schematic shows the orbital parameter space coordinates and an example orbit in dashed dark-grey. Not shown is the orbital inclination  $i$ , which is the angle between the orbital plane normal vector and the line of sight. The projected orbital radius is then  $\tau = r \sin(i) / c$ .

The multiples of  $\pi$  at the circular orbit show the value of the orbital phase. Orbital phase of  $\Phi_{\text{orb}} = \frac{\pi}{2}$  is the point closest to the observer in our convention,  $\Phi_{\text{orb}} = \pi$  is the point with the highest redshift in apparent frequency.  $\Phi_{\text{orb}} = \frac{3\pi}{2}$  is the point most distant to

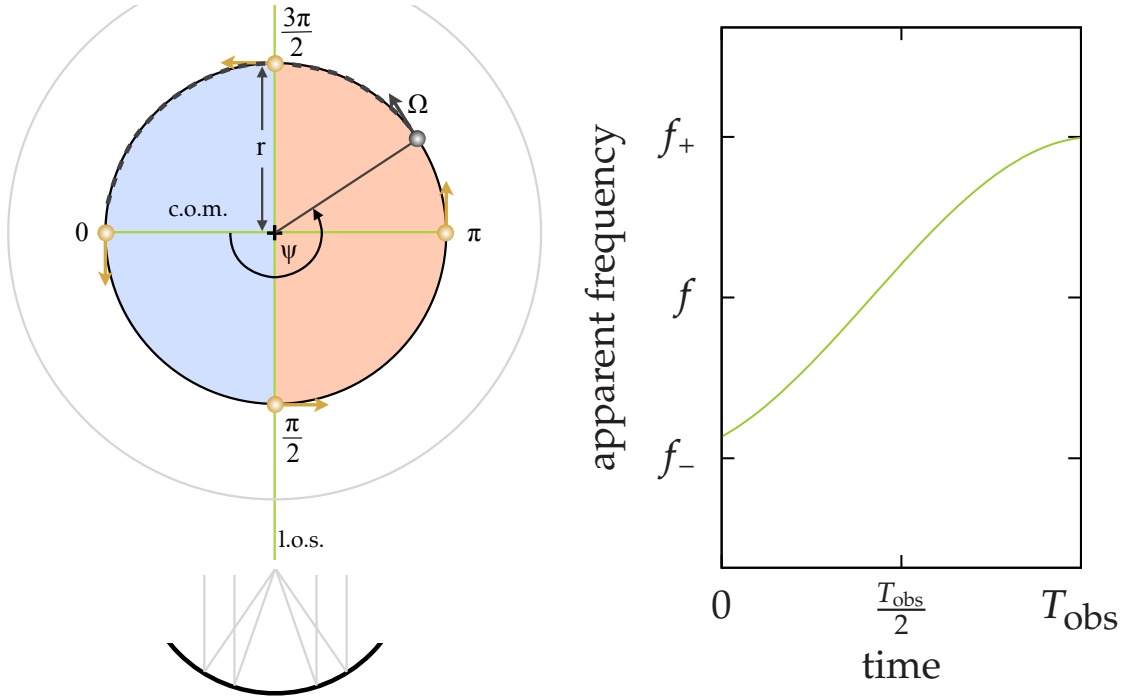


**Figure 3.5:** (Left) Schematic of circular binary motion. An observer in the orbital plane will see changes in the line of sight (l.o.s.) velocity in form of changes of the apparent frequency. In the blue region the apparent frequency is higher than the intrinsic frequency, and vice versa in the red region. The schematic shows the orbital parameter space coordinates and an example orbit in dashed dark-grey. (Right) The apparent frequency as a function of the observation time for the example orbit (dashed dark-grey in the left panel). The values of maximum and minimum apparent frequency are  $f_+ = f(1 + \Omega\tau)$  and  $f_- = f(1 - \Omega\tau)$ , respectively.

the observer without apparent frequency change, and  $\Phi_{\text{orb}} = 0$  is the point with the highest blueshift in apparent frequency. The orbital phase  $\psi$  is measured in mathematically positive sense from the line connecting the pulsar with the observer. The sense of direction of the orbital motion is determined by the value of the initial phase  $\psi$ , since defining  $\psi' = \psi + \pi$  in the phase model (3.11) is equivalent to defining  $\tau' = -\tau$ , which is equivalent to flipping the orbit upside down.

The right panel of Figure 3.5 shows the apparent frequency as a function of the observation time for the indicated example orbit. The values of maximum and minimum apparent frequency are  $f_+ = f(1 + \Omega\tau)$  and  $f_- = f(1 - \Omega\tau)$ , respectively. The example signal starts off near an orbital phase where the frequency is maximally redshifted, crosses the most distant point of the orbit with zero frequency modulation near the middle of the observation; close to the end, the signal reaches almost maximum blueshift in frequency.

### 3.4.4 Constraining the parameter space for Einstein@Home

Any signal from a pulsar in a circular orbit is described by the parameter tuple  $\{f, \Omega, \tau, \psi\}$ . With limited computing resources, one cannot analyse data for any possible circular orbit. The parameter space has to be constrained using astrophysically motivated constraints for likely orbital parameters and spin frequencies and constraints from the available computing resources.

**PALFA observations with 268 s observation time**

The parameter space searched by Einstein@Home is constrained in the frequency by searching for frequencies

$$0 \text{ Hz} \leq f \leq 400 \text{ Hz}. \quad (3.12)$$

This is the frequency, the orbital template bank is constructed for; in other words: we can recover frequency components with  $f \leq 400 \text{ Hz}$  with the chosen nominal mismatch (see below). In the frequency analysis part of the search code we search up to frequencies of 250 Hz. This choice allows to obtain up to sixteen summed harmonics for each pulsar candidate, as the Nyquist frequency is 3.9 kHz. As we will see below, the number of necessary templates grows with  $f_{\text{max}}^3$ , which makes searching for higher spin frequencies very expensive. Searching up to the chosen frequency still allows to detect a large number of possible regular pulsars and millisecond pulsars.

Other constraints are used on the orbital parameters. For the orbital angular velocity  $\Omega$  the constraint at the lower end<sup>15</sup> comes from the acceleration search pipelines, to which the Einstein@Home pipeline was designed to be complementary. Acceleration searches over an observation time  $T_{\text{obs}}$  lose sensitivity to orbits with periods  $P_{\text{orb}} \lesssim 10T_{\text{obs}}$ . For the observation time of the PALFA survey pointings with  $T_{\text{obs}} \approx 268 \text{ s} \approx 4.5 \text{ min}$ , we choose  $P_{\text{orb}} \leq 45 \text{ min}$ . The upper limit is again dictated by the available computing resources. As we will see below, the number of necessary templates grows drastically with larger  $\Omega$  (or smaller  $P_{\text{orb}}$ ), so that for this reason we choose  $P_{\text{orb}} \geq 11 \text{ min}$  for the Einstein@Home search on the 268-s PALFA survey data sets. Moreover, from the estimates in Section 3.3.4 we know that the shortest expected orbital for a DNS binary in our galaxy is of order five to ten minutes. Thus, the constraints for orbital period and orbital angular velocity are

$$11 \text{ min} \leq P_{\text{orb}} \leq 45 \text{ min} \quad (3.13)$$

$$9.5200 \times 10^{-3} \text{ rad s}^{-1} \geq \Omega_{\text{orb}} \geq 2.3271 \times 10^{-3} \text{ rad s}^{-1}. \quad (3.14)$$

For the orbital radius we motivate constraints from the component and pulsar masses system we wish to obtain sensitivity to (Messenger, 2008). Rather than fixing, say an upper limit on the projected radius  $\tau = r \sin(i)$ , we allow for a maximum projected radius that depends on the orbital period. From Kepler's laws we can relate the orbital radius  $r$  and the orbital angular velocity  $\Omega$  via

$$r^3 \Omega^2 = \frac{G m_c^3}{(m_p + m_c)^2}, \quad (3.15)$$

where  $m_p$  is the pulsar mass and  $m_c$  is the companion mass. For the projected radius  $\tau$  we find

$$\tau = \sin(i) \frac{G^{\frac{1}{3}} m_c}{c(m_p + m_c)^{\frac{2}{3}}} \Omega^{-\frac{2}{3}} =: \alpha_i \frac{G^{\frac{1}{3}} m_c}{c(m_p + m_c)^{\frac{2}{3}}} \Omega^{-\frac{2}{3}}. \quad (3.16)$$

The mass-dependent factor is maximised when  $m_p$  is minimal and  $m_c$  is maximal<sup>16</sup>. We define  $\alpha_i := \sin(i)$ . The maximum projected radius for given masses and orbital angular velocity is obtained for  $\alpha_i = 1$ , which corresponds to an observer in the orbital plane, or

<sup>15</sup>low values of  $\Omega$  and large values of  $P_{\text{orb}}$

<sup>16</sup>This is also intuitively clear: the less mass the pulsar has the more it is accelerated; the higher the mass of the companion, the larger the gravitational acceleration of the pulsar.

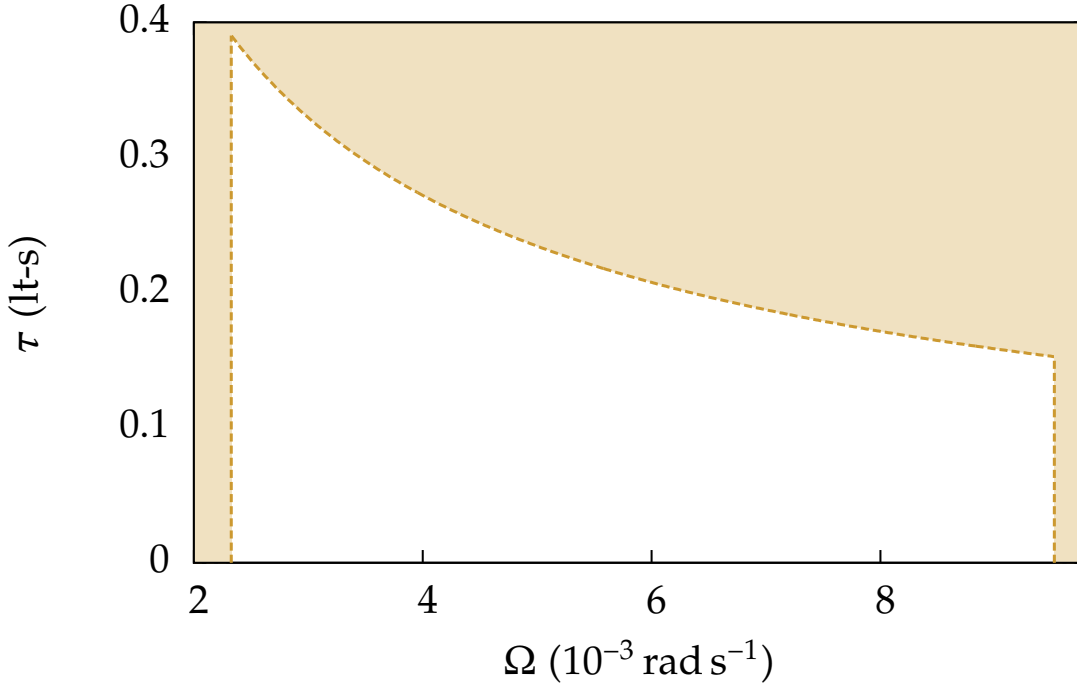


**Figure 3.6:** Constraining the Einstein@Home orbital parameter space: the semi-transparent orange region is the part of parameter space excluded by Equations (3.14) and (3.17), the white region is the Einstein@Home orbital parameter space for the 268-s PALFA observations.

$i = \frac{\pi}{2}$ . For  $\alpha_i = 0$ , or  $i = 0$ , the projected radius vanishes and no frequency modulation is visible; this case is degenerate with an isolated pulsar. As we will see below, the number of necessary templates grows with the maximum value  $\tau_{\max}$ . Thus, we can use restrictions on  $\tau_{\max}$  as another mean to tune the number of templates. The constraint on  $\tau$  chosen for the Einstein@Home search is defined by choosing  $\alpha_{i,0}$  for maximum companion mass  $m_{c,\max}$  and minimum pulsar mass  $m_{p,\min}$  and inserting into Equation (3.16)

$$0 \leq \tau \leq \alpha_{i,0} \frac{G^{\frac{1}{3}} m_{c,\max}}{c(m_{p,\min} + m_{c,\max})^{\frac{2}{3}}} \Omega^{-\frac{2}{3}} \quad (3.17)$$

For the Einstein@Home search we have chosen  $\alpha_{i,0} = 0.5$  for  $m_{c,\max} = 1.6 M_{\odot}$  and  $m_{p,\min} = 1.2 M_{\odot}$ . The resulting constraints on the projected orbital radius  $\tau$  and angular velocity  $\Omega$  are shown in Figure 3.6. The semi-transparent orange region is the part of parameter space excluded by Equations (3.14) and (3.17), the white region is the Einstein@Home orbital parameter space. The third parameter space dimension is the initial orbital phase  $\psi$ , measured along the orbit as shown in Figure 3.5. No other constraint than the reduction to the periodicity interval  $[0, 2\pi)$  apply in this coordinate. The coordinate  $\psi$  is not shown in Figure 3.6; it can be visualised as an extension of the white parameter space wedge parallel to the paper normal vector.

#### PALFA observations with 134 s observation time

For the shorter, 134-s, PALFA survey observations the parameter space constraints were modified. The shorter observation time allowed to search for even shorter orbital periods.

The constraints on orbital period and orbital angular velocity, respectively, were

$$5.5 \text{ min} \leq P_{\text{orb}} \leq 22.5 \text{ min} \quad (3.18)$$

$$19.0400 \times 10^{-3} \text{ rad s}^{-1} \geq \Omega_{\text{orb}} \geq 4.6542 \times 10^{-3} \text{ rad s}^{-1}. \quad (3.19)$$

Because of the shorter observation time, the data analysis was sped up and allowed to re-invest that speed-up into searching for higher spin frequencies:

$$0 \text{ Hz} \leq f \leq 660 \text{ Hz}. \quad (3.20)$$

Again, this is the frequency the orbital template bank is constructed for; in other words: we can recover frequency components with  $f \leq 660 \text{ Hz}$  with the chosen nominal mismatch (see below). In the frequency analysis part of the search code we search up to frequencies of 250 Hz. This choice allows to obtain up to sixteen summed harmonics for each pulsar candidate, as the Nyquist frequency is 3.9 kHz.

The constraint on the projected radius was kept unchanged as given in Equation (3.17)

### Conservative probabilistic interpretation

As orbital inclinations in nature will be randomly distributed, we can interpret setting an upper limit on the projected radius as a probabilistic limit on the number of systems detectable in the parameter space. The orbital inclination unit vectors are randomly distributed on the surface of the unit sphere, thus the distribution in the inclination angle is uniform in  $\cos(i)$ . The fraction  $p$  of systems with an inclination angle between 0 and  $i_{\text{max}}$  is

$$p = \int_0^{i_{\text{max}}} di \sin(i) = 1 - \cos(i_{\text{max}}) = 1 - \sqrt{1 - \alpha_i^2}, \quad (3.21)$$

so that (with  $\alpha_i = \sin(i)$  as before)

$$\alpha_i = \sqrt{1 - (1 - p)^2}, \quad (3.22)$$

if we want to the search to be sensitive to a fraction  $p$  of all systems. Not all systems will have favourable inclinations so that some systems, depending on the mass ratio can be outside the constrained parameter space.

We note, that the probability  $p$  is lowest at the extreme mass ratio case. For other mass ratios, the probability of detection  $p$  is in fact much larger. Assume the parameter space constraints  $m_c \leq m_{c,\text{max}}$ ,  $m_p \geq m_{p,\text{min}}$ , and  $\alpha_i = \alpha_{i,0}$  have been chosen for the Einstein@Home radio pulsar search, where  $\alpha_{i,0}$  is the value of  $\alpha_i$  for the extreme mass ratio case. We can then define  $\alpha$  as a function of the masses as

$$\alpha(m_p, m_c) = \alpha_{i,0} \frac{m_{c,\text{max}} (m_c + m_p)^{\frac{2}{3}}}{m_c (m_{c,\text{max}} + m_{p,\text{min}})^{\frac{2}{3}}}, \quad (3.23)$$

from which we can define the fraction of detectable systems as a function of the masses in the constrained parameter space by

$$p(m_p, m_c) = 1 - \sqrt{1 - \alpha^2(m_p, m_c)}. \quad (3.24)$$

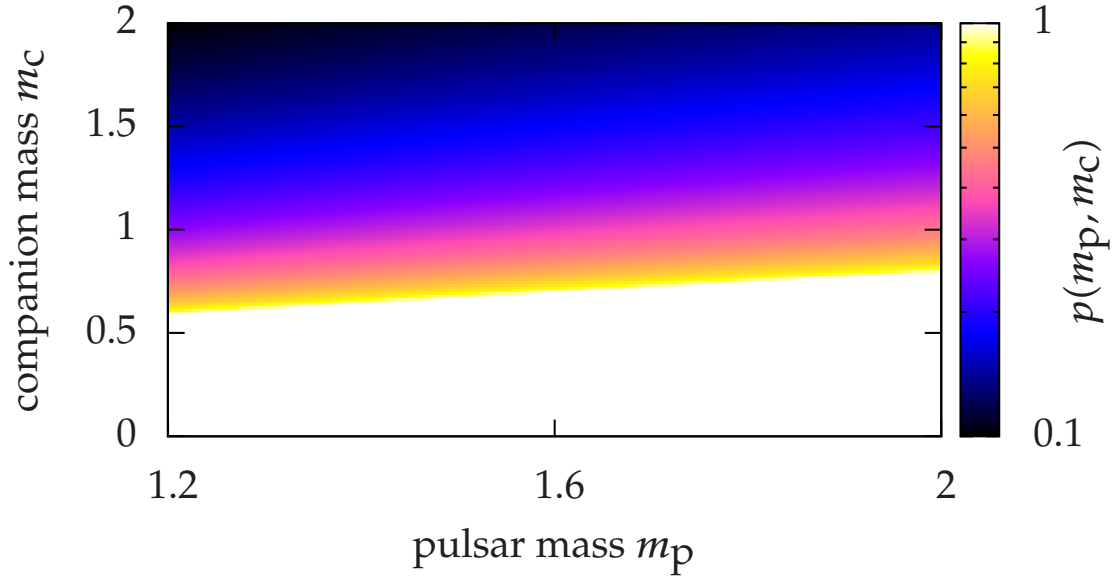


**Figure 3.7:** The probability  $p(m_p, m_c)$ , Equation (3.24), for the Einstein@Home radio pulsar search with  $\alpha_{i,0} = 0.5$  for  $m_{c,\max} = 1.6 M_\odot$  and  $m_{p,\min} = 1.2 M_\odot$ . The horizontal axis shows the pulsar mass and the vertical axis the companion mass. The colour code shows the value of  $p$ . All systems in the white area are detectable at any orbital orientation and at any point in their orbit, in the other coloured areas only a fraction  $p$  has guaranteed favourable orbital inclinations.

Figure 3.7 shows this function plotted for the Einstein@Home radio pulsar search. The horizontal axis shows the pulsar mass  $m_p$ , the vertical axis the companion mass  $m_c$ , and the colour code shows the value of  $p(m_p, m_c)$ .

We further note that this argument is a conservative estimate of the detectability for a given system. It assumes that the system can be detected *everywhere* along the orbit. On the other hand, even if the inclination is not favourable, i.e. the value of  $\tau$  is too large for the given  $\Omega$  in the parameter space, there are still parts of the orbit where the signal can be well enough described by parameters *inside* the parameter space although its physical parameters are *outside* the parameter space. This effectively means that the Einstein@Home search has non-vanishing sensitivity to signals outside its parameter space. We detail this further in Section 3.4.7.

### 3.4.5 Justification of the circular approximation

For the parametrisation of the Einstein@Home search parameter space we assumed circular orbits. This is motivated by the following reasons. Firstly, the parametrisation of a Keplerian circular orbit needs only three parameters and is straightforward to implement. The parametrisation of an arbitrary Keplerian orbit with non-zero eccentricity needs five parameters (the eccentricity and the length of the periastron) and requires solving Kepler's equation iteratively (Meeus, 1991). Searching the circular parameter space is already constrained by available computing power, and searching the full Keplerian parameter space

increases the computational demands by adding two extra dimensions to the parameter space and for the iterative solving of Kepler’s equation. For future extensions of the Einstein@Home search pipeline, a search over arbitrary orbits is conceivable as volunteers donate growing amounts of compute cycles to the project.

Secondly, the extrapolation from known pulsars shows that the orbits will have strongly circularised by the time they reach the very short orbital periods, the Einstein@Home search is designed for. The majority of the known pulsar-WD binaries is in orbits with very small eccentricity, that is  $e \lesssim \text{few} \times 10^{-4}$  (Lorimer, 2008). Thus, they are already very well described by a circular phase model. If these systems evolve further to shorter orbital periods, their orbits get circularised even further and would be almost perfectly described by a circular phase model.

Let us evolve the known DNS systems from Lorimer (2008) by the equations describing the orbital evolution due to emission of gravitational waves (Peters, 1964). We find that the eccentricities  $e_{11 \text{ min}}$  at orbital periods of 11 min are very small compared to the present-day values. We find  $e_{11 \text{ min}} = 0.00579$  for PSR J0737-3039,  $e_{11 \text{ min}} = 1.67 \times 10^{-4}$  for PSR J1518+4904,  $e_{11 \text{ min}} = 0.00475$  for PSR B1534+12,  $e_{11 \text{ min}} = 0.00371$  for PSR J1756-2251,  $e_{11 \text{ min}} = 0.00161$  for PSR J1811-1736,  $e_{11 \text{ min}} = 4.99 \times 10^{-5}$  for PSR B1820-11,  $e_{11 \text{ min}} = 7.10 \times 10^{-4}$  for PSR J1829+2456,  $e_{11 \text{ min}} = 0.00326$  for PSR J1906+0746,  $e_{11 \text{ min}} = 0.0302$  for PSR B1913+16, and  $e_{11 \text{ min}} = 0.0416$  for PSR B2127+11C. With the exception of the last two pulsars, we find that always  $e_{11 \text{ min}} \lesssim 0.005$ , which means that pulsars in such orbits will be detectable without significant additional mismatch as we will show in Section 3.5.5.

Apart from circularisation of initially elliptical orbits by emission of gravitational waves, another pathway can lead to the formation of tight circular binary radio pulsars. It has been long proposed and recently observed by Archibald et al. (2009) that X-ray binaries can become visible as binary radio pulsars. This can happen as soon as the accretion stops and radio waves from the pulsar can escape the system and reach Earth. The orbits of these systems are very quickly circularised during the phase of mass transfer (Stairs, 2004).

The X-ray binary with the shortest known orbital period is X1820-303 (Smale et al., 1987), which has an orbital period of about 11 minutes. If the accretion in this system would stop, a radio pulsar in an almost perfectly circular 11-min orbit could emerge, being by far the pulsar in the shortest period orbit. Such an object would be unlikely detected by acceleration searches, but could possibly be an easy target for the Einstein@Home radio pulsar search.

The sensitivity of the Einstein@Home pipeline to eccentric orbits (with  $e \leq 0.1$ ) is examined in more detail in Section 3.5.5

### 3.4.6 Parameter space metric

The phase model in Equation (3.11) contains the time domain description of any signal at a point in the parameter space. This is the well-known case of a modelled signal waveform which is described by a set of parameters, where the exact parameter values are unknown. A *matched filtering* process of convolving the data with multiple waveforms (so-called templates), each described by a different  $n$ -tuple of parameters, is a widely used approach to this problem in gravitational wave data analysis, see e.g. Abbott et al. (2007a, 2009); Abbott et al. (2009); Abbott et al. (2007b); Owen and Sathyaprakash (1999).

Since not every possible of the infinitely many points in the parameter space can be tested, we need to define a way of testing only a finite set of parameter space points. This can be achieved by defining a measure of distance on the parameter space by the so-called

*parameter space metric* (Balasubramanian et al., 1996; Owen, 1996; Owen and Sathyaprakash, 1999). Here, we summarise the general derivation of the metric from any phase model, see Section 8.5 for details. We then apply it to the specific case of the phase model in Equation (3.11).

### Definition of metric and mismatch

Assume, the signal is described by a phase model  $\Phi(\Lambda; t)$  depending on a tuple of signal parameters  $\Lambda = \{\lambda_i\}$  and time  $t$ . Let the signal be defined by

$$S(\Lambda_1; t) = \mathcal{A} \exp(i\Phi(\Lambda_1; t)), \quad (3.25)$$

where  $\mathcal{A}$  is the complex amplitude of the signal. One can also define the signal as the real part of  $S(\Lambda_1; t)$ , but the derivation of the metric does not depend on this specific choice. We then define the coherent detection statistic  $\mathcal{D}(\Lambda_1, \Lambda_0)$  (demodulated power) assuming a template at  $\Lambda_0$  for signal recovery as

$$\begin{aligned} \mathcal{D}(\Lambda_1, \Lambda_0) &= \left| \frac{1}{T} \int_0^T dt S(\Lambda_1; t) \exp[-i\Phi(\Lambda_0; t)] \right|^2 \\ &= \left| \frac{\mathcal{A}}{T} \int_0^T dt \exp[i(\Phi(\Lambda_1; t) - \Phi(\Lambda_0; t))] \right|^2. \end{aligned} \quad (3.26)$$

This is the detection statistic if a signal with parameters  $\Lambda_1$  is recovered at a parameter space point  $\Lambda_0$ ; the vice versa statement is equivalent because of the symmetry of  $\mathcal{D}$ . If  $\Lambda_1 = \Lambda_0$  (i.e. the signal is recovered with the correct parameters), we find  $\mathcal{D}(\Lambda_0, \Lambda_0) = |\mathcal{A}|^2$ .

From the detection statistic we can define the *mismatch* between two parameter space points  $\Lambda_0$  and  $\Lambda_1$  by

$$m(\Lambda_1, \Lambda_0) = 1 - \frac{\mathcal{D}(\Lambda_1, \Lambda_0)}{\mathcal{D}(\Lambda_0, \Lambda_0)} = m(\Lambda_0, \Lambda_1), \quad (3.27)$$

which is symmetrical in its arguments, because the symmetry of  $\mathcal{D}$  with respect to exchange of the arguments is inherited. This expression of the metric is exact and valid for any pair of points in the parameter space. However, it is necessary to compute the detection statistic integral by Equation (3.26), which in principle can be computationally very expensive. For detection purposes it is not necessary to compare two points in parameter space with a large mismatch.

Thus, it is useful to study the mismatch for small deviations in the parameter space coordinates. One can show (see Section 8.5 for details) that the mismatch for these small deviations  $\Delta\Lambda$  in the parameter space coordinates can be written as

$$m(\Lambda + \Delta\Lambda, \Lambda) = (\langle \partial_\alpha \Phi \partial_\beta \Phi \rangle_T - \langle \partial_\alpha \Phi \rangle_T \langle \partial_\beta \Phi \rangle_T) \Delta\Lambda^\alpha \Delta\Lambda^\beta, \quad (3.28)$$

where we have defined the short-hand notation for the time-average of a function  $\mathcal{G}(t)$  as

$$\langle \mathcal{G}(t) \rangle_T \equiv \frac{1}{T} \int_0^T dt \mathcal{G}(t). \quad (3.29)$$

Equation (3.28) inspires the definition of the parameter space metric  $g_{\alpha\beta}$  by identifying

$$\begin{aligned} m(\Lambda + \Delta\Lambda, \Lambda) &= g_{\alpha\beta} \Delta\Lambda^\alpha \Delta\Lambda^\beta, \\ g_{\alpha\beta} &= \langle \partial_\alpha \Phi \partial_\beta \Phi \rangle_T - \langle \partial_\alpha \Phi \rangle_T \langle \partial_\beta \Phi \rangle_T. \end{aligned} \quad (3.30)$$

The elements of metric described by Equation (3.30) can thus be straightforwardly computed from the chosen phase model by differentiation and integration.

### The metric for the full phase model

Using the method described in the previous section it is straightforward to compute the metric elements for the phase model from Equation (3.11). The results is a four-by-four matrix, which we give in full detail in Section 8.6.

### Projected metric

If one of the coordinates of parameter space can be searched very efficiently independent of the others, it can be useful to exclude it (project it out) from the metric that is used to cover the parameter space. In the case here, the frequency dimension can be very efficiently analysed by means of the Fast Fourier Transform (FFT). Thus, conducting all analysis in the frequency dimension in an independent FFT and covering the parameter space of orbital parameters only, yields different advantages: the search in the frequency dimension is very efficient; the remaining parameter space has only three dimensions and is thus easier to describe; the implementation of a search separated in orbital parameters and frequency analysis is straightforward to implement.

To project out the frequency dimension from the metric  $g_{ij}$  for the full phase model, we construct the *projected metric*  $\gamma_{ij}$  on the subspace orthogonal to the frequency direction. In general, if we want to project out the  $\alpha$ -th dimension, we define the projected metric (Messenger, 2008) via

$$\gamma_{ij} := g_{ij} - \frac{g_{\alpha i} g_{j \alpha}}{g_{\alpha \alpha}}, \quad (3.31)$$

where  $\alpha, \beta \in \{1, 2, 3, 4\}$  denotes coordinates in the full parameter space and  $i, j \in \{1, 2, 3\}$  denotes coordinates in the parameter space where frequency has been projected out. From this definition it is clear that  $\gamma_{i\alpha} = \gamma_{\alpha i} = 0$ , so, as expected, any component in  $\alpha$  direction is set to zero in the projected metric and the number of dimensions is reduced by one.

The projected metric is constructed for a specific frequency  $f_0$  at which it is valid. This frequency has to be the maximum frequency of signal components we desire our search to be sensitive to. The projected metric for  $f_0$  can also be used to construct templates banks to recover signals at lower frequencies  $f < f_0$ . With the projection in frequency direction, Equation (3.31) is specified to

$$\gamma_{ij} := g_{ij} - \frac{g_{fi} g_{jf}}{g_{ff}}. \quad (3.32)$$

The full parameter space is a cartesian product of a regular grid in frequency (given by the FFT) and the non-uniform set of orbital templates constructed from the projected metric. For each orbital template, the full FFT has to be searched.

The result of the full computation of the projected metric is a three-by-three matrix, which we give in Section 8.7.

From the explicit expressions for the metric elements in Section 8.7 we see that each element is quadratic in  $f_0$ . Therefore, the determinant of the projected metric has a prefactor  $\propto f_0^6$ . The scaling in the other parameters is not that easily described.

### 3.4.7 Isomismatch surfaces

To explore the properties of the projected metric, let us now consider isomismatch surfaces, i.e. surfaces in parameter space on which the mismatch from a given template is constant. We will not consider the approximation of the mismatch by the metric, but rather the full expression from Equation (3.27) using the detection statistic defined by Equation (3.26). The isomismatch surfaces then demonstrate the *size of a template*, i.e. in what part of parameter space are signals detectable with less than the given mismatch  $m_0$  if one searches only with the parameter values  $\Lambda$  of the template. The larger the extent of the isomismatch surface, the less templates are needed to search a given volume of parameter space, and the smaller the extent of the isomismatch surface, the more templates are necessary for the same volume.

For the three-dimensional orbital parameter space, the isomismatch surfaces will be two-dimensional, enclosing a three-dimensional volume covered by the template for which the surface is defined. For simplicity, we will consider here a slice through such a volume by another one-dimensional hyper-surface of constant  $\psi$ . If the metric is a good approximation of the exact mismatch, these slices are ellipses. If higher than quadratic terms in the coordinate offsets contribute, the shape will differ from an ellipse.

For a demonstration of the isomismatch surfaces in the parameter space of pulsars in circular orbits, we have chosen the following set-up. We fixed  $\psi = 0$ ,  $f = 400$  Hz, and  $T = 268$  s for all signals considered in the following; we varied  $\Omega$  and  $\tau$ . Each tuple  $\{\Omega_0, \tau_0, \psi_0 = 0; f_0 = 400 \text{ Hz}\}$  defined a point  $\Lambda_0$  at the center of a template. We then found points  $\{\Omega_1, \tau_1, \psi_1 = 0; f_1\} =: \Lambda_1$  around  $\Lambda_0$  at which the mismatch is constant  $m_0 = 0.3$ ; this defines the slice through the isomismatch surface for  $m_0 = 0.3$ . We numerically maximized the integral definition of the detection statistic in Equation (3.26) over  $f_1, \Omega_1, \tau_1$ , at  $\psi_1 = 0$ ; this is analogous to how the Einstein@Home search code in the real search works, see Section 3.8.

The results are shown in Figure 3.8. As before, the orange parameter space region is excluded by the constraints for the Einstein@Home search on the longer PALFA survey pointings, see Section 3.4.4; the white region is the Einstein@Home orbital parameter space, where we suppressed the third dimension,  $\psi$ . The black “+”-signs mark the locations of the templates  $\Lambda_0$  chosen. The size of each template is shown by a light-grey area around the template location and is enclosed by a thin dark-grey line.

The template areas are clearly not ellipsoidal, indicating that for a mismatch of  $m_0 = 0.3$  the approximation of the metric breaks down, see also the next section. The metric is not a valid approximation under these circumstances. Especially the templates at lower  $\Omega$  and/or  $\tau$  are strongly curved and not symmetric around the centre of the template. At low  $\Omega$  and/or  $\tau$  the total variation of phase, from Equation (3.11), is small and allows for large offsets in the signal parameters from the correct values at low mismatch. In other words, in this part of the parameter space the parameters are not well determined from a single observation.

We would like to emphasize that templates at the boundaries of the parameter space cover a significant fraction of parameter space outside the region defined in Section 3.4.4. Therefore, the Einstein@Home search is sensitive to signals outside the defined part of parameter space. This effect increases at lower spin frequencies  $f$ . As shown above, the square root of the projected metric determinant  $\gamma$  scales with  $f^3$ . Below, we show that proper volume  $dV$  is linked to parameter space volume  $d^n\lambda$  via  $d^n\lambda = \sqrt{\gamma}^{-1} dV$ , see Equation (3.33) and thereafter. Therefore, the parameter space volume for a fixed proper volume (template

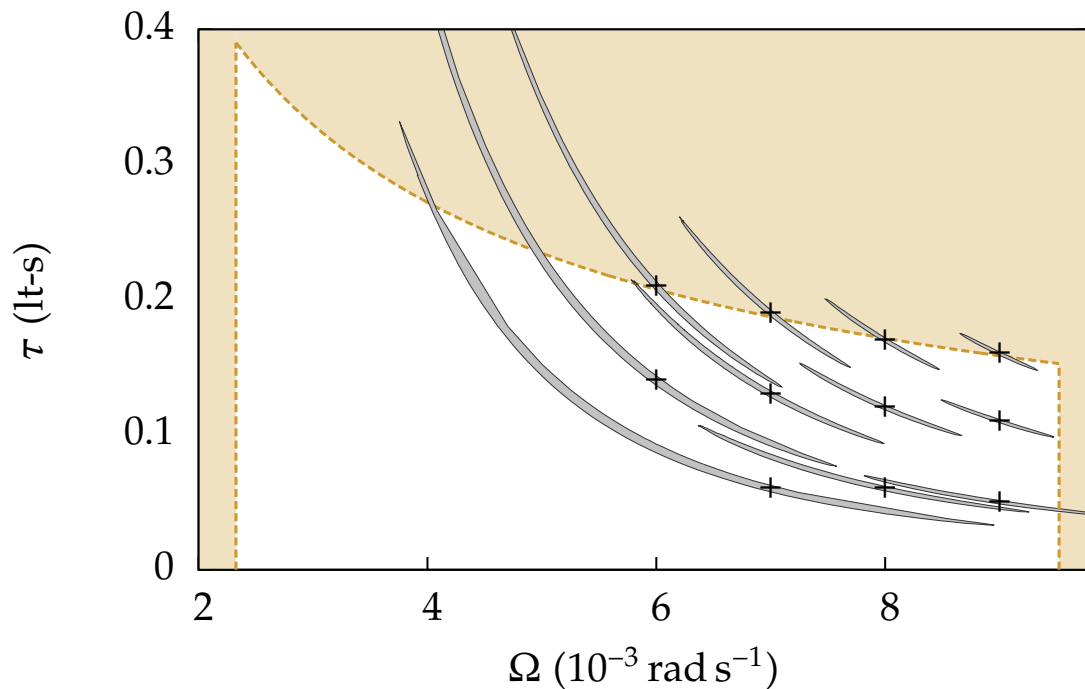


**Figure 3.8:** Slices through isomismatch surfaces at  $\psi = 0$  and  $f = 400$  Hz. +-signs mark the location of templates, grey areas show the area covered by each template. Deviations from an elliptic form and asymmetry around the template centre indicate that the metric is not a valid approximation to the exact mismatch. The large extent of the surfaces beyond the Einstein@Home parameter space shows sensitivity to signals outside the constrained space.

size) is proportional to  $f^{-3}$ . Lowering  $f$  thus drastically increases the template size: the template sizes shown in Figure 3.8 would be twice as large in each dimension (volume increasing by a factor eight) for signals at half the frequency, i.e. 200 Hz.

### Limits to the metric approximation

The metric defines a measure of distance on the parameter space; it measures the relative loss in detection statistic if a signal is recovered at a different point. Note, that this description is only valid up to second order in the deviations of the coordinates. The metric does not give typical scales to which this approximation is valid; these depend on the coordinates chosen for the parameter space description and have to be examined in detail independently. A typical problem that can arise when higher order terms contribute is that the metric approximation *overestimates* the mismatches. Thus, parameter space points with an in fact small mismatch appear to have a much larger mismatch computed from the metric. In other words: point that seem to be separated by a large mismatch are actually “close together” in terms of mismatch. When covering the parameter space with a set of templates in order to recover any unknown signal in it, this overestimation will lead to a higher number of templates than actually required; templates will be correlated stronger with each other. This correlation or additional overlap can be cured if for the covering of the parameter space not the mismatch as metric approximation is used but if the actual mismatch is computed by means of Equation (3.26).

That the approximative metric description of the parameter space for the Einstein@Home radio pulsar search is indeed an approximation can also be appreciated from Figure 3.8. The slices through the surfaces of constant mismatch are clearly curved and cannot not be described a metric, which is quadratic in the coordinate offsets. The visible curvature comes from higher order contributions. Using the metric to generate a lattice-based template bank for the Einstein@Home search would be impossible in the currently used coordinates. It is unclear how to transform the coordinates so that the lattice-based approach would be feasible.

For the Einstein@Home search, however, we do not have to consider the limits of the metric approximation. In this search, a so-called “stochastic template bank” was implemented (see Section 3.5), using the computation of the mismatch by the full integral expression, Equation (3.26), not the metric approximation. Thus, the stochastic template bank for the Einstein@Home search is not affected negatively by limits of the metric approximation. On the contrary, the large extent of mismatch surfaces means that the search also is sensitive to signals outside the part of the parameter space covered with a template bank.

---

### 3.5 Orbital parameter template bank construction

---

This section describes the construction of the template banks used for the Einstein@Home radio pulsar search. As described above, the parameter space in total has four dimensions: pulsar spin frequency  $f$ , orbital angular velocity  $\Omega_{\text{orb}} = 2\pi/P_{\text{orb}}$ , projected radius along the line of sight  $\tau$  and initial orbital phase  $\psi$ . The frequency is projected out, because efficient fast searches in this dimension are possible by use of the Fast Fourier Transform (FFT). This leaves the parameter space of the three orbital parameters to be searched independently.

By use of the metric, a template bank, “classically” in form of a lattice, can be generated to cover the signal parameter space in such a way that the loss in signal-to-noise ratio between any signal and (at least) one template is less than a value a priori deemed as acceptable. From gravitational wave studies it is known that even in low-dimensional spaces, generating lattice-based template banks is a complicated problem, see e.g. Abbott et al. (2009, 2007b).

It has been shown in Prix (2007) that the template placement problem can be described equivalently as a sphere covering problem. Thus, methods from this field can be applied to assist lattice-based template bank construction. Practical problems arise in the lattice-based construction in curved parameter spaces, the necessary coordinate transformations and at the boundaries of the (transformed) parameter space.

New, recently developed methods like random (Messenger et al., 2009) and stochastic (Harry et al., 2009) template banks can overcome part of these difficulties at the price of yielding only probabilistic coverage of each point in parameter space. Each point in parameter space is then close enough to at least a single template with a certain probability  $\eta < 1$ . For a “classical” lattice-based template bank, we would have  $\eta = 1$  for a certain (small) nominal mismatch: no matter where in parameter space a signal would be, there is at least a single template that recovers this signal with the nominal mismatch. If  $\eta < 1$ , this coverage with the nominal mismatch is only given a fraction  $\eta$  of the parameter space.

In the construction of these new kinds of template banks one thus allows for probabilistic holes in the final template bank. It has been shown that the size of these holes can be theoretically well described (Messenger et al., 2009). This new type of template bank not only reduces the number of required templates by a large amount but it also simplifies (for

random template banks more than for stochastic template banks) the process of generating a template bank.

### 3.5.1 Random template banks

The main idea in the construction of random template banks is to give up on the complete coverage  $\eta = 1$  of the parameter space by randomly placing templates in the parameter space. The number density of random templates is varied according to the properties of the parameter space. A related approach, discussed in Section 3.5.3, are stochastic template banks. There, the randomly placed templates are pruned in a subsequent step to remove overlapping templates not contributing significantly to the coverage of the parameter space.

For the details of random template banks we refer the reader to Messenger et al. (2009) and Manca and Vallisneri (2010). We will review only the most important results from these papers needed for the practical construction of a random template bank.

#### Total number of random templates

A random template bank for a given signal parameter space  $\mathcal{S}_n$  is described by the nominal mismatch  $m_*$  that is achieved over a fraction  $\eta < 1$  of the parameter space. That is, a template bank with  $m_* = 0.2$  and  $\eta = 0.9$  will have a mismatch of 0.2 or less on 90% of the signal parameter space. We can describe the parameter space by a metric  $g_{\alpha\beta}(\lambda_1, \lambda_2, \dots, \lambda_n)$  as a function of  $n$  the collection of all signal parameters  $\{\lambda_i\}$ . The proper volume of the parameter space  $V_{\mathcal{S}_n}$  is given by

$$V_{\mathcal{S}_n} = \int_{\mathcal{S}_n} dV = \int_{\mathcal{S}_n} d^n \lambda \sqrt{g}, \quad (3.33)$$

where  $g = \det(g_{\alpha\beta})$  is the determinant of the parameter space metric. We define the volume of an  $n$ -dimensional ball as

$$C_n = \frac{\pi^{\frac{n}{2}}}{\Gamma(\frac{n}{2} + 1)}. \quad (3.34)$$

This is the  $n$ -dimensional volume enclosed by a  $(n - 1)$ -dimensional sphere. These objects are also referred to as an  $n$ -ball and a  $(n - 1)$ -sphere, respectively. The  $n$ -dimensional volume covered by a single template of mismatch  $m_*$  is then

$$V_T = C_n m_*^{\frac{n}{2}}. \quad (3.35)$$

Now, we can write the number of random templates required to achieve coverage  $\eta$  with nominal mismatch  $m_*$  of a parameter space  $\mathcal{S}_n$  as

$$N_{\mathcal{R}}(\eta, m_*, \mathcal{S}_n) = \frac{\ln(1 - \eta)}{\ln\left(1 - m_*^{\frac{n}{2}} \frac{C_n}{V_{\mathcal{S}_n}}\right)}. \quad (3.36)$$

For details and a derivation of this formula, see Sections II and III in Messenger et al. (2009). In most cases we will have the case of templates that are much smaller than the extent of the parameter space and thus  $m_*^{\frac{n}{2}} C_n / V_{\mathcal{S}_n} \ll 1$ . Then we can Taylor-expand Equation (3.36) to obtain

$$N_{\mathcal{R}}(\eta, m_*, \mathcal{S}_n) \approx \frac{m_*^{-\frac{n}{2}} V_{\mathcal{S}_n}}{C_n} \ln\left(\frac{1}{1 - \eta}\right). \quad (3.37)$$

Given a signal parameter space and desired values of coverage and nominal mismatch, Equation (3.37) allows us to compute the total number of random templates we need to place on the parameter space.

### Distributing the random templates

The correct distribution in parameter space can be achieved by different methods. Two different methods were applied to generate a random template bank for the Einstein@Home search on PALFA data.

Measured in proper volume the templates have to be distributed uniformly; proper and parameter space volume are related by Equation (3.33) via the square root of the determinant of the metric  $dV = d^n \lambda \sqrt{g}$ . It can be shown from (see Equations (40) and (41) in Messenger et al. (2009)) that the template pseudo-density in signal parameter space is given by

$$\hat{\rho}_{\mathcal{R}}(\{\lambda_i\}) = \frac{dN_{\mathcal{R}}}{d^n \lambda} = \sqrt{g(\{\lambda_i\})} \rho_{\mathcal{R}}, \quad (3.38)$$

where  $\rho_{\mathcal{R}}$  is the constant density specified by Equation (3.37) from

$$\rho_{\mathcal{R}} = \frac{N_{\mathcal{R}}}{V_{S_n}} = \frac{dN_{\mathcal{R}}}{dV} = \frac{1}{\sqrt{g}} \frac{dN_{\mathcal{R}}}{d^n \lambda}. \quad (3.39)$$

In other words: the pseudo-density  $\hat{\rho}_{\mathcal{R}}$  that governs the distribution of templates in signal parameter space is up to the constant factor  $\rho_{\mathcal{R}}$  proportional to the square root of the determinant of the metric. The computation of the metric elements and its determinant is – unlike the diagonalisation of the metric – easily achieved even in curved parameter spaces.

For the sampling of random templates from the pseudo-density function different methods are available:

- a) Markov Chain Monte Carlo (MCMC) methods
- b) importance resampling and rejection resampling
- c) decomposition of the parameter space into small contiguous hyper-cubes of nearly constant  $\sqrt{g}$

In cases a) and b) the probability distribution function to sample from must be known only up to a constant factor, thus here the square root of the determinant may be used without further adjustments. We implemented a MCMC sampling method and the decomposition method, described in more detail below.

### Random template placement by parameter space decomposition

The orbital parameter space for the Einstein@Home search is the three-dimensional space of  $\Omega_{\text{orb}}$ ,  $\tau$ , and  $\psi$ . Its parameter space metric is derived and described in Section 3.4.6. To cover the parameter space with random templates we first implemented an algorithm that decomposes the parameter space into smaller cubes in which the determinant of the metric can be assumed constant. Consider a set of contiguous patches  $\mathcal{S}_n^{(i)} \subseteq \mathcal{S}_n$ , such that

$$\mathcal{S}_n = \bigcup_i \mathcal{S}_n^{(i)} \quad \text{and} \quad \mathcal{S}_n^{(i)} \cap \mathcal{S}_n^{(j)} = 0 \quad \forall j \neq i. \quad (3.40)$$

We further assume that the determinant  $g$  of the parameter space metric is nearly constant over each  $\mathcal{S}_n^{(i)}$ ; let the determinant in the  $i$ -th patch be denoted by  $g^{(i)}$ . Then, the number of random templates in the  $i$ -th patch is

$$\begin{aligned} dN_{\mathcal{R}}^{(i)} &= \sqrt{g^{(i)}} d^n \lambda \\ &= \sqrt{g^{(i)}} d\Omega_{\text{orb}} d\tau d\psi. \end{aligned} \quad (3.41)$$

So, placing  $dN_{\mathcal{R}}^{(i)}$  templates<sup>17</sup> with uniform probability in coordinate space in  $\mathcal{S}_n^{(i)}$  for all  $i$  will achieve a random template over  $\mathcal{S}_n$ . The uniform probability in each cube is achieved by sampling from a uniform probability density function in each coordinate.

We chose a regular grid in all parameter space coordinates for simplicity. To guarantee a conservative implementation that would not underestimate the number of required templates, several measures were taken. Firstly, we identified the variation of the metric determinant inside the cube by computing the metric on a number of sub-points inside each cube, recording the maximum determinant  $g_{\text{max}}^{(i)}$ . If the necessary number of templates in any cube fulfilled

$$dN_{\mathcal{R}}^{(i)} < 1 \quad \text{with} \quad dN_{\mathcal{R}}^{(i)} = \sqrt{g_{\text{max}}^{(i)}} d\Omega_{\text{orb}} d\tau d\psi \quad (3.42)$$

still a single random template was generated in the respective cube.

This method turned out to be *very* conservative with respect to the number of templates generated and was soon replaced by MCMC sampling in the signal parameter space to obtain a the same coverage using less templates.

### Random template placement by MCMC sampling

To generate a random template bank in a curved parameter space  $\mathcal{S}_n$  one needs to sample from a probability density function proportional to the determinant of the metric  $g$  on the parameter space.

A straightforward way to implement this is the use of Markov Chain Monte Carlo Methods, more specifically, the Metropolis-Hastings algorithm (Hastings, 1970; Metropolis et al., 1953), which we will describe briefly here.

The Metropolis-Hastings algorithm can be used to draw random samples from probability distributions and is especially useful if the distribution  $p$  to sample from is not accessible directly<sup>18</sup>. In our case, we know the density only up to a constant factor, which in principle could be computed from normalisation but might introduce other numerical errors. Also,  $p$  must only be known up to a constant factor for the Metropolis-Hastings algorithm. The algorithm generates a Markov Chain (Gregory, 2005) in which each the  $(n + 1)$ -th state,  $x_{n+1}$ , depends only on the previous state  $x_n$  but not on other earlier states. This usually assumes a general proposal density function  $q(x_n, x_{\text{prop}})$ ;  $q$  depends on the current state  $x_n$  and is used to generate a new proposed state  $x_{\text{prop}}$ . The decision whether the proposal is

---

<sup>17</sup>where the value was rounded up to the next integer

<sup>18</sup>In the case of the Einstein@Home search for binary pulsars, the metric has a complicated form, compare Sections 8.6 and 8.7, which makes it difficult to implement a pdf to sample with the available software libraries.

“accepted” ( $x_{n+1} = x_{\text{prop}}$ ), or “rejected” ( $x_{n+1} = x_n$ ) is made using the general prescription:

$$x_{n+1} = \begin{cases} x_{\text{prop}} & \text{if } \varkappa < \frac{p(x_{\text{prop}})}{p(x_n)} \times \frac{q(x_n, x_{\text{prop}})}{q(x_{\text{prop}}, x_n)} \\ x_n & \text{else} \end{cases} \quad (3.43)$$

where  $\varkappa$  is from a uniform random distribution on the interval  $[0, 1]$ . In other words, the proposal is accepted if the product of the ratios between a) the probability of the proposal state and the probability of the current state and b) the ratio between the proposal density in the two directions is large enough. Thus, proposed states with higher  $p$  than the current state are more likely to be accepted unless the proposal density  $q$  shifts preference to other states. Because Equation (3.43) only depends on the ratio of the probability density  $p$  for two states, constant normalisation factors cancel out.

### Independence chain Metropolis Hastings algorithm

A special case of the Metropolis Hasting algorithm is the choice of a proposal density  $q$  that does not depend on  $x_n$  at all. This case is called the “Independence Chain Metropolis Hastings algorithm”. Then, the acceptance criterion becomes

$$x_{n+1} = \begin{cases} x_{\text{prop}} & \text{if } \varkappa < \frac{p(x_{\text{prop}})}{p(x_n)} \\ x_n & \text{else} \end{cases} \quad (3.44)$$

and only depends on the probability distribution we want to sample, where again  $\varkappa$  is from a uniform random distribution on the interval  $[0, 1]$ .

### Practical implementation

We adapted the MCMC sampling method for the construction of a random and a stochastic template bank on the parameter space of the orbital templates  $\Omega$ ,  $\tau$ , and  $\psi$ . The parameter space is described in detail in Section 3.4.3.

Let us first described the construction of a random template bank for this parameter space. The construction of a stochastic template bank will be initially the same, but will feature additional steps that we will describe later.

Firstly, the total number of random templates necessary to cover the parameter space is computed from Equation (3.36). The proper volume of the parameter space  $V_{S_n}$  is computed from the integral

$$V_{S_n} = \int_{S_n} dV = \int_0^{\tau(\Omega)} d\tau \int_{\Omega_{\min}}^{\Omega_{\max}} d\Omega \int_0^{2\pi} d\psi \sqrt{g(\Omega, \tau, \psi)}, \quad (3.45)$$

where the upper and lower limits of the integrals come from the chosen parameter space to cover. The integral is approximated as a Riemannian sum in the practical implementation. For the parameter space described in Section 3.4.4 we find  $V_{S_n} = 1967.45$ . With the coverage  $\eta = 0.9$  and a nominal mismatch<sup>19</sup>  $m_* = 0.2$  we find the total number of orbital templates as  $N_{\mathcal{R}} = 12091$ .

<sup>19</sup>We require  $m_* = 0.2$  in the orbital parameters. The frequency analysis will add its own mismatch of  $m_f = 0.088$ , so that the total nominal mismatch  $m_*^{\text{tot}} < m_* + m_f < 0.3$ .

For each proposal template, random values  $\{\Omega', \tau', \psi'\}$  are drawn from uniform distributions on the complete range in the orbital parameters, independently of the current template  $\{\Omega, \tau, \psi\}$ . The probability density function  $p$  here is proportional to the determinant of the metric  $p(\Omega, \tau, \psi) = k\sqrt{g(\Omega, \tau, \psi)}$  with some normalisation constant  $k$ . The acceptance of the proposal template is decided by means of Equation (3.44). All random number draws used the `gs1_rng_taus2` random number generator from THE GSL with implementations of the appropriate distributions from the GSL (Galassi, 2009). If the proposed template is accepted, a new random template independent of the previous one is generated. This procedure is repeated until the number of accepted templates reaches  $N_{\mathcal{R}}$ .

### 3.5.2 Determinant of the projected metric for the Einstein@Home search

In Figure 3.9 we show the value of the square root of the determinant  $\gamma = \det(\gamma_{ij})$  of the frequency-projected metric,  $\sqrt{\gamma}$ , Equation (3.31), on the constrained parameter space of the Einstein@Home search (Section 3.4.4). This plot indicates the density of random templates to be distributed in the orbital parameter space.

In the top plot we show the value of  $\sqrt{\gamma}$  as a function of  $\Omega$  and  $\tau$ . Further, we have chosen  $f = 400$  Hz which is the maximum frequency in the Einstein@Home search and  $T_{\text{obs}} = 268$  s, which is the observation time for the long PALFA survey pointings. We also have fixed  $\psi = 0$  for all  $\Omega$  and  $\tau$ . A rise in template density towards higher values of  $\tau$  and  $\Omega$  is clearly visible. More templates are necessary to detect signals from pulsars in shorter period orbits with larger projected radius with any given loss in signal-to-noise ratio. In the Einstein@Home parameter space, the template density values range roughly over eight orders of magnitude.

In the bottom plot we show the value of  $\sqrt{\gamma}$  as a function of  $\Omega$  and  $\psi$  for fixed  $\tau = 0.15$  lt-s. Again,  $f = 400$  Hz and  $T_{\text{obs}} = 268$  s. The value of  $\sqrt{\gamma}$  increases with growing  $\Omega$  and is almost constant as a function of  $\psi$ . Two “streaks” of lower template density can be clearly identified. They lie at  $\psi = \pi - \frac{1}{2}\Omega T_{\text{obs}}$  and  $\psi = 2\pi - \frac{1}{2}\Omega T_{\text{obs}}$ . At these points, the midpoint of the observation at  $t_{\text{mid}} = \frac{1}{2}T_{\text{obs}}$  takes place at orbital phases of  $\Omega t_{\text{mid}} + \psi = \pi$  or  $\Omega t_{\text{mid}} + \psi = 2\pi$ , where the Doppler effect is maximal, compare Figure 3.5. Fewer templates are necessary to detect pulsar signals at these parts of the orbit.

As we have noted above, the determinant of the projected metric has a prefactor  $\propto f_0^6$ , which in turn means that its square root and therefore, the template density, scale with  $f_0^3$ . Increasing the frequency range by a factor of two, increases the number of necessary templates by a factor of eight!

### 3.5.3 Stochastic template banks

As pointed out above, stochastic template banks are related to the random template banks in the sense, that the latter can be used as a starting point to construct the first. Any random template bank can be used to construct a stochastic template bank. The templates from the random template bank are used as proposal templates for the generation of a stochastic template bank. A stochastic bank could be generated from any proposal templates; it is however an advantage if the proposals already are distributed according to the pseudo-density from Equation (3.38). This speeds up the generation process of the stochastic template bank because proposal are more frequent where more templates are needed.

The advantage of a stochastic template bank is that it does not contain overlapping templates, which can be present in random template banks. Thus, depending on the parameter

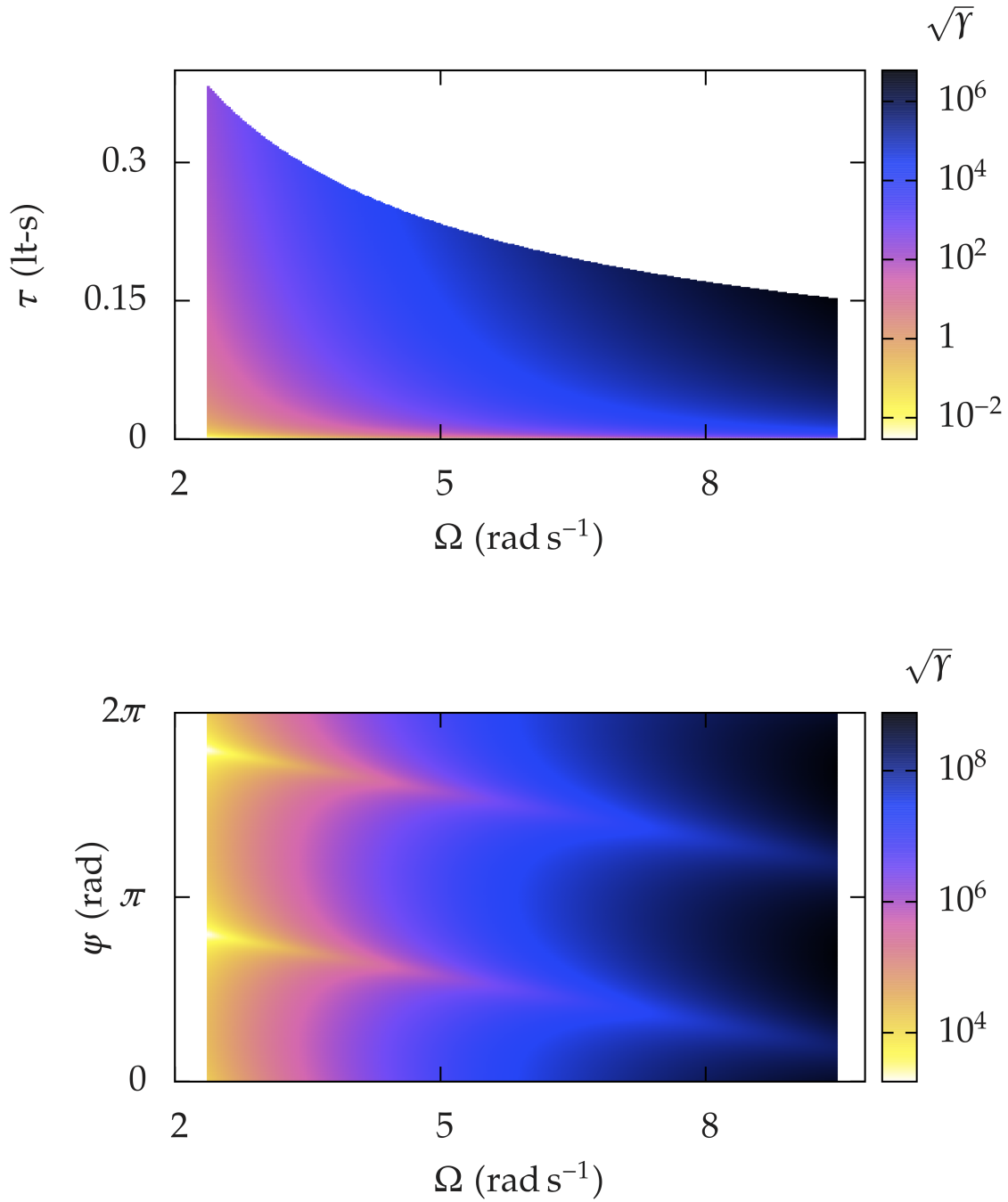


**Figure 3.9:** Square root of the projected metric determinant  $\sqrt{\gamma}$ . The value of  $\sqrt{\gamma}$  is a measure for the template pseudo-density, Equation (3.38). For both plots we assume  $f = 400$  Hz. **(Top)** the value of  $\sqrt{\gamma}$  as a function of  $\Omega$  and  $\tau$  for  $\psi = 0$ . The template density rises towards shorter orbital periods and larger projected radii. **(Bottom)** the value of  $\sqrt{\gamma}$  as a function of  $\Omega$  and  $\psi$  for  $\tau = 0.15$  lt-s. Two “streaks” of lower template density are visible: they lie at  $\psi = \pi - \frac{1}{2}T_{\text{obs}}\Omega$  and  $\psi = 2\pi - \frac{1}{2}T_{\text{obs}}\Omega$ , such that the orbital phase at the midpoint of the observation is  $\pi$  or  $2\pi$ , respectively, where the Doppler effect is maximal.

space and the structure of the iso-mismatch surfaces, large computation time savings are possible. This comes at the price of spending a large amount of computation time for the generation of the stochastic template bank compared to the negligibly small computation time needed to create a random template bank. This has to be weighed against the computation time savings from re-using the stochastic template bank for a large number of analyses.

### 3.5.4 Efficient parallel construction of stochastic template banks

The biggest challenge in constructing a stochastic template bank is the efficient use of available computing resources. The process of pruning overlapping templates can be very time-consuming if the metric as a measure of an exact distance computation is not available or cannot be used because of curvature properties of the parameter space. Thus, the total CPU time necessary can easily reach dimensions not feasible for computation on a single workstation. Here we describe how to parallelise the construction process of a stochastic template bank for execution on a large computer cluster with thousands of computing nodes without fast inter-node communication.

#### Serial construction

In the default setup, a single template is proposed at each step, its correlation with all templates in the template bank is computed and the proposed template is accepted to the bank if the correlation is less than a pre-defined threshold value. Since each proposed template's acceptance depends on all templates proposed before it, this is a serial process. The total number of comparisons that has to be made is

$$N_{\text{comp}} \leq N(N-1)/2, \quad (3.46)$$

if in total  $N$  templates are proposed and compared with each other. This is the upper limit on the accurate value, because not all templates are accepted. Therefore not each proposed template is compared to each other one.

Parallelisation is possible by splitting the existing template bank into smaller subsets and comparing the proposed template in parallel to each subset. The computation can be stopped as soon as in one subset a correlation higher than the pre-defined threshold is found; then the proposed template will be rejected. In a computer cluster environment like condor however, the inter-process communication necessary for this stopping is difficult to achieve. Also, in other cases *all processes* must finish to decide about acceptance or rejection of a *single template*. Overall, the efficiency of this parallelisation method on computer clusters with slow inter-node communication is low.

#### Parallelisation of the construction process

We will now describe an improved parallelisation algorithm that makes full use of a large computer cluster's possibilities. The central idea is to circumvent the dependence of the  $(n+1)$ -th proposed template on the  $n$ -th proposed template in an early stage. The complete process is illustrated in Figure 3.10.

We begin with a set of  $2^n$  coarse random template banks with few (i.e. hundreds of) templates. "Coarse" means that the nominal mismatch  $m_*^{(i)}$  for fixed coverage for each random template bank is much higher than the nominal mismatch  $m_*$  at the same coverage finally to be achieved. The standard pruning step that would require much larger computational

### 3.5. ORBITAL PARAMETER TEMPLATE BANK CONSTRUCTION

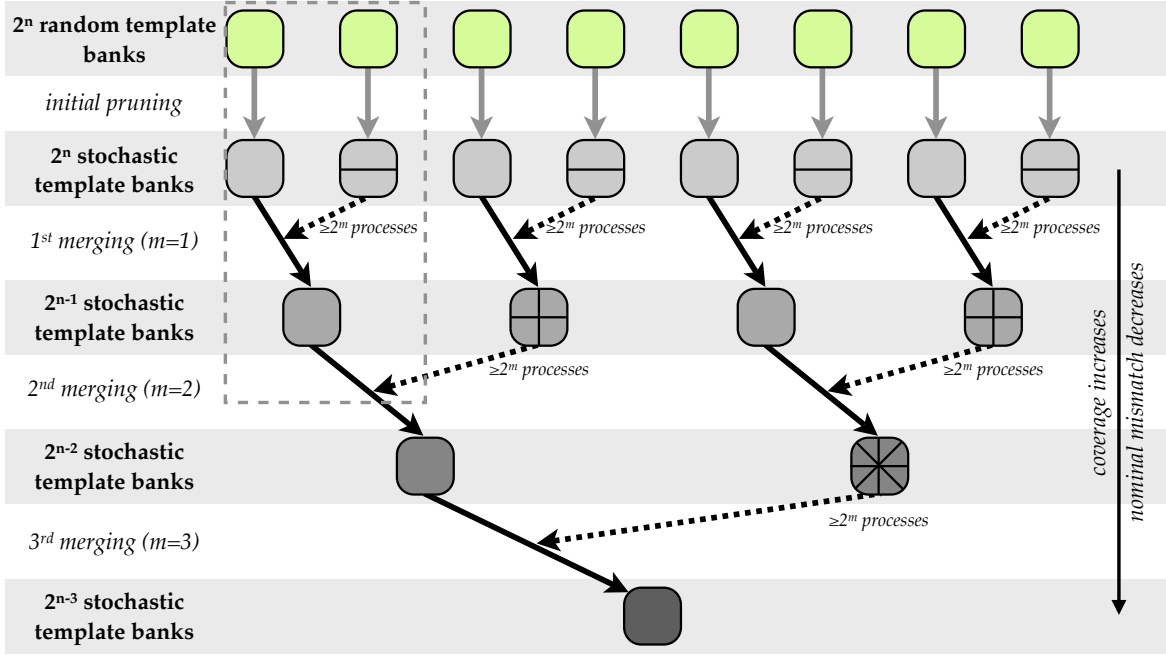


**Figure 3.10:** Efficient parallelisation of stochastic template bank generation: successive massive parallel merging of stochastic template banks of increasing coverage follows an initial step of pruning coarse random template banks. The area enclosed in the grey dashed rectangle is shown in detail in Figure 3.11.

capacities for the complete template bank is feasible on a single cluster node for the few templates. The mismatch used for the pruning decision at this stage is the final nominal mismatch  $m_*$ . In the pruning step all template pairs overlapping by more than  $1 - m_*$  are identified; one template of the pair is removed from the template bank. This initial pruning yields a set of  $2^n$  coarse *stochastic* template banks. Thus, after the pruning step, in each of the  $2^n$  coarse template banks no template overlaps by more than  $1 - m_*$  with any other template in the bank.

Pairwise merging of two of those coarse stochastic templates is easily parallelisable now. The templates from one bank are used as proposal templates to be added to the other bank. The proposal templates only have to be checked for overlap with templates in the target bank but not with each other, since this was done in the initial pruning step. Thus, the set of proposal templates can be split into subsets, each of which can be compared in parallel to all templates in the target bank. One only needs to keep track of accepted templates for each subset independently of all other subsets. All accepted templates are added to the target bank (ideally after computations for all subsets have finished) to form a finer stochastic template bank. “Finer” here means that the nominal mismatch of the template bank for fixed coverage is smaller. Note, that in principle, it is not necessary to wait for all subsets to be tested; since the subsets are independent of each other, proceeding with part of the subsets merged is possible as well. The merging process is shown in some more detail in Figure 3.11.

The described method is applied in parallel to all  $2^n$  coarse stochastic template banks. Thus, this first merging step yields  $2^{n-1}$  finer stochastic template banks. Then, these can be merged iteratively and pairwise using the same algorithm outlined here. In the next stage the number of templates is reduced to  $2^{n-2}$ . For maximum efficiency, the number of subsets

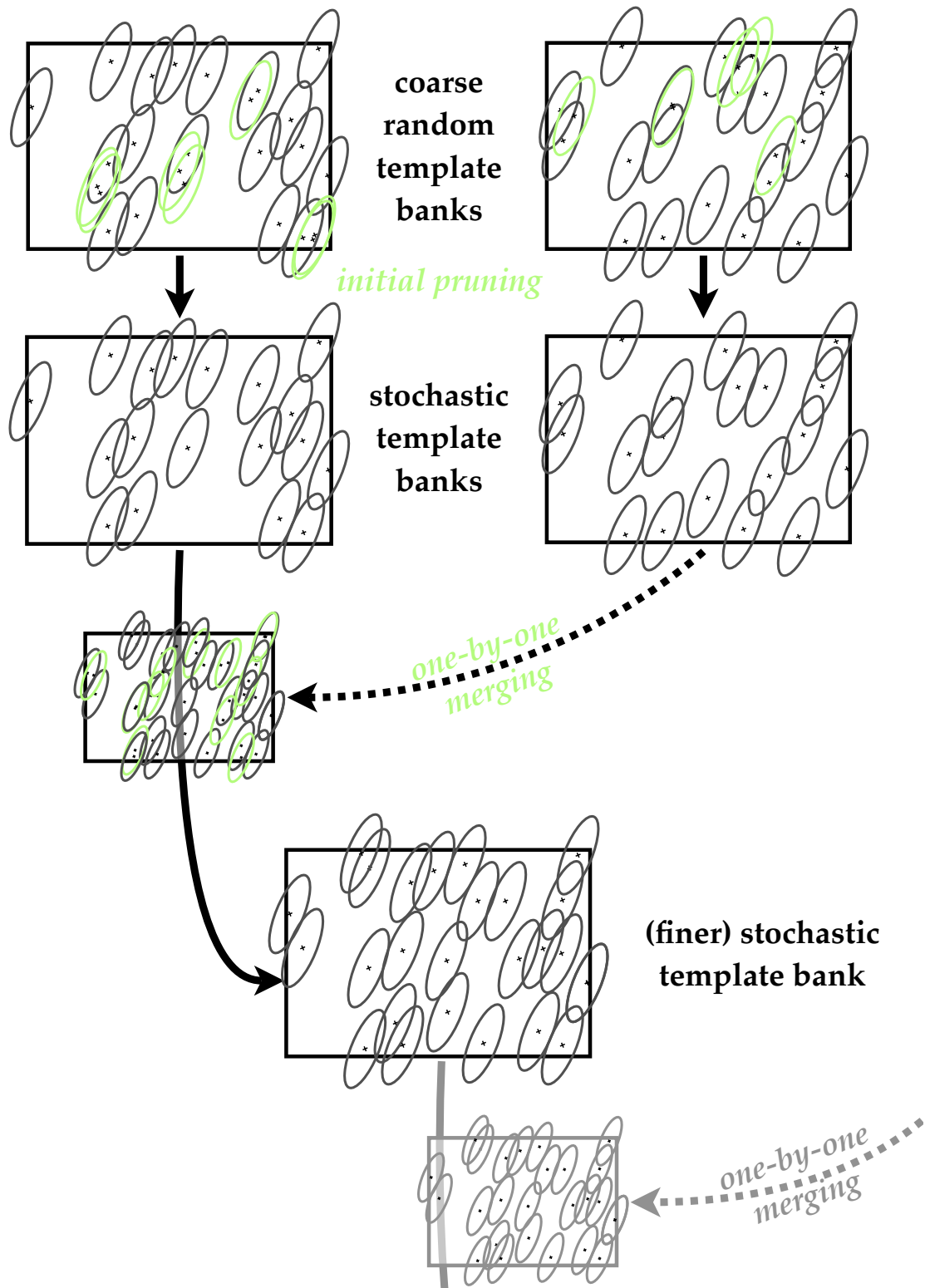


**Figure 3.11:** Illustration of the initial pruning and the merging process: detailed view of the grey dashed box on the top left in Figure 3.10. The green templates in each box are removed by the pruning process because they overlap.

into which the template banks are divided should be adjusted so that the total number of processes is of the same order as the number of compute nodes available. Note, that this can also be adaptively used to make most efficient use of computing resources by balancing between few longer running jobs or many small fast jobs.

### Number of template comparisons for serial and parallel implementation

Let us now count the number of template comparisons for this method to show that it is the same order of magnitude as for the serial method described above. Assume there are  $n_{\text{banks}} = 2^n$  coarse random template banks at the first stage, in total we have  $n_{\text{template}} = N$  templates at the beginning. Each coarse bank therefore contains  $2^{-n}N$  templates, the total number of comparisons in the first pruning step is

$$\begin{aligned} n_{\text{comp}}^{\text{first}} &= n_{\text{banks}} n_{\text{template}} (n_{\text{template}} - 1) / 2 \\ &= 2^n \times 2^{-n} N (2^{-n} N - 1) / 2 \\ &= N (2^{-n} N - 1) / 2, \end{aligned} \quad (3.47)$$

assuming all templates are tested pairwise against each other. Accordingly we will assume for each further merging stage that no templates are rejected. Thus the number of comparisons we obtain is an upper limit on the number of comparisons.

The number of templates in each template bank after the  $i$ -th merge is  $n_{\text{templates}}^{(i)} = 2^{-n+i}N$ , the number of comparisons between two template banks is given by

$$\begin{aligned} n_{\text{comp}}^{(i)} &\leq n_{\text{templates}}^{(i)} \times n_{\text{templates}}^{(i)} \\ &\leq 2^{-2n+2i} N^2, \end{aligned} \quad (3.48)$$

because each template from one bank is compared to each template from the other bank. There are  $n_{\text{pairs}}^{(i)} = 2^{n-i-1}$  pairs of banks at the  $i$ -th level. There will be at most  $i_{\text{max}} = n$  merging processes until a single template bank results from the merging process. The number of comparison operations at the  $i$ -th level (for  $i \leq n - 1$ , because no comparison happens for the last stage at  $n = i$ ) therefore is

$$\begin{aligned} N_{\text{comp}}^{(i)} &\leq n_{\text{pairs}}^{(i)} \times n_{\text{comp}}^{(i)} \\ &\leq 2^{n-i-1} 2^{-2n+2i} N^2 \\ &\leq 2^{-n+i-1} N^2. \end{aligned} \quad (3.49)$$

Then, the total number of comparisons is

$$\begin{aligned} N_{\text{comp}} &\leq n_{\text{comp}}^{\text{first}} + \sum_{i=0}^{n-1} N_{\text{comp}}^{(i)} \\ N_{\text{comp}} &\lesssim \frac{N}{2} (2^{-n} N - 1) + \sum_{i=0}^{n-1} 2^{-n+i-1} N^2 \\ &\lesssim 2^{-n-1} N^2 - \frac{N}{2} + 2^{-n-1} N^2 \frac{2^n - 1}{2 - 1} \\ &\lesssim \frac{N}{2} (N - 1), \end{aligned} \quad (3.50)$$

in agreement with Equation (3.46). The exact number of comparisons (as above) might be less since not all templates are accepted. This calculation was to show that the comparisons are re-shuffled, not saved.

### Stopping condition for the stochastic template bank construction

An important question in the construction of a stochastic template bank is how to find the point at which the template bank has reached the desired coverage of the parameter space, i.e. at which point the adding of new templates can be stopped.

One possible way of measuring this is to keep track of the rejection rate, i.e. which fraction of the recently proposed templates has not been accepted as a new template for the stochastic template bank. If one wants to compute this fraction “on the fly”, this requires averaging over a large enough number of proposed templates, so that a reliable estimator is obtained. However, the number of proposed templates to average over must not be too large in order to obtain a sufficiently “local” average.

A computationally more expensive but much more exact and reliable estimator of the covering can be obtained by creating a large number of fake signals with random parameters and recovering them with the so far constructed stochastic template bank. Then, the coverage can be obtained by examining the distribution of mismatches. If the coverage is reached, i.e. if a certain fraction of the mismatches is below a pre-defined threshold, the template bank construction can be stopped. If this criterion is not fulfilled, additional templates have to be added<sup>20</sup>, additional tests with fake signal injections have to be run until the stopping criterion is fulfilled.

We describe the use of injecting a large ensemble of fake signals and recovering them with the search pipeline in more detail in Section 3.5.5 in the context of verifying the constructed stochastic template banks for Einstein@Home.

### 3.5.5 The Einstein@Home template banks

The Einstein@Home search is the first large-scale search to implement the recently developed methods of random and stochastic template banks (Harry et al., 2009; Messenger et al., 2009). We required a coverage of 90% of the orbital parameter space with a mismatch of less than 20%. Then, the total mismatch over the whole parameter space (orbital + frequency) is less than 30%, since the maximum mismatch in frequency was chosen to be smaller than 8.8%, see Section 3.8.6. The initial requirement for the mismatch in the complete search was to have a mismatch of less than 30% over 90% of the orbital parameter space, which we will denote by  $\eta_{0.3} \geq 0.9$  (more than 90% of the parameter space covered with a mismatch of 0.3 or less, or equivalently by:  $m_{0.9} \leq 0.3$ ).

#### Implemented template banks

The Einstein@Home search initially (for the first few months) used a random template bank to cover the parameter space described in Section 3.4.4.

The random template bank was obtained with the method of parameter space decomposition into smaller subspaces. This initial template bank used  $\sim 24000$  orbital templates. It was soon realised that the conservative implementation of this method of generating

---

<sup>20</sup>In fact once can use the signal parameters from the fake injections that have a mismatch larger than required as additional proposal templates

the random template bank significantly overestimated the necessary number of templates. Setting up a random template bank for the same parameter space with the independence chain Metropolis Hastings algorithm requires only 12091 orbital templates, see below Equation (3.45), and achieves the same coverage of the parameter space.

As shown above, the step from the random to the stochastic template banks is simple. We therefore implemented the parallel efficient generation of stochastic template banks as described in Section 3.5.4 on the ATLAS cluster at the AEI Hannover. We were able to construct a stochastic template bank with 6661 orbital templates that covered the parameter space at the same coverage as the random template bank with only 55% of the templates in a comparable random template bank. This stochastic template bank has been used for the largest part of the Einstein@Home search on the PALFA survey data and sped up the search significantly. Further speedup came from different code optimisations.

A similar stochastic template bank was constructed using the same methods for the analysis of the shorter PALFA data sets from the outer Galaxy pointings and some short inner Galaxy observations; it contains 7113 orbital templates.

The orbital template bank for the 268-s long pointings is visualised in Figure 3.12, where we plot all orbital templates in the parameter space and view the three-dimensional parameter space from different angles. The increase of the template density towards larger  $\tau$  and  $\Omega$  is clearly visible.

### Verification of the stochastic template bank for circular orbits

In order to verify that the constructed random template bank fulfils the requirements from above, we tested it against signals injected at random points in the orbital parameter space, measured the mismatch for each of these signals, and evaluated the results for the whole ensemble. We show here only tests for the template bank constructed for the 268-s observations.

The test was conducted using a code to generate fake signals for given signal parameters and feeding the fake data into the search code used for the Einstein@Home search. The injected signal parameters were chosen at random in the parameter space. They were drawn from a density distribution proportional to the square root of the determinant of the metric. The fake data generation code generated a de-dispersed time series containing a signal with the given random orbital parameters; no noise was added. The signals were single sinusoids at the highest frequency the orbital template bank was constructed for,  $f = 400$  Hz. In total, we tested the stochastic template bank with 20,000 random injections.

The fake de-dispersed time series was analysed by the Einstein@Home search code with the stochastic orbital template bank and the actual search setup. The search code did not whiten the data or apply a zap list because the fake data are noise-free. From the results of the search code we then extracted the strongest candidate from the search using the stochastic orbital template bank. We then computed the mismatch by comparing the detection statistic to the theoretically expected value. As a reference point, we also searched the data with the orbital parameters of the injected template to ensure the signal was reconstructed correctly, if the parameters are exactly known.

Because the full search also searches over frequency, the additional mismatch in frequency applies and we have to compare the results from these tests to the the figures of merit  $\eta_{0.3}$  or  $m_{0.9}$ ; the quantity  $\eta_{0.3}$  is the fraction of signals recovered with a mismatch of 0.3 or less, and  $m_{0.9}$  is the 90%-quantile of all measured mismatches. We require  $\eta_{0.3} \geq 0.9$  or  $m_{0.9} \leq 0.3$ .

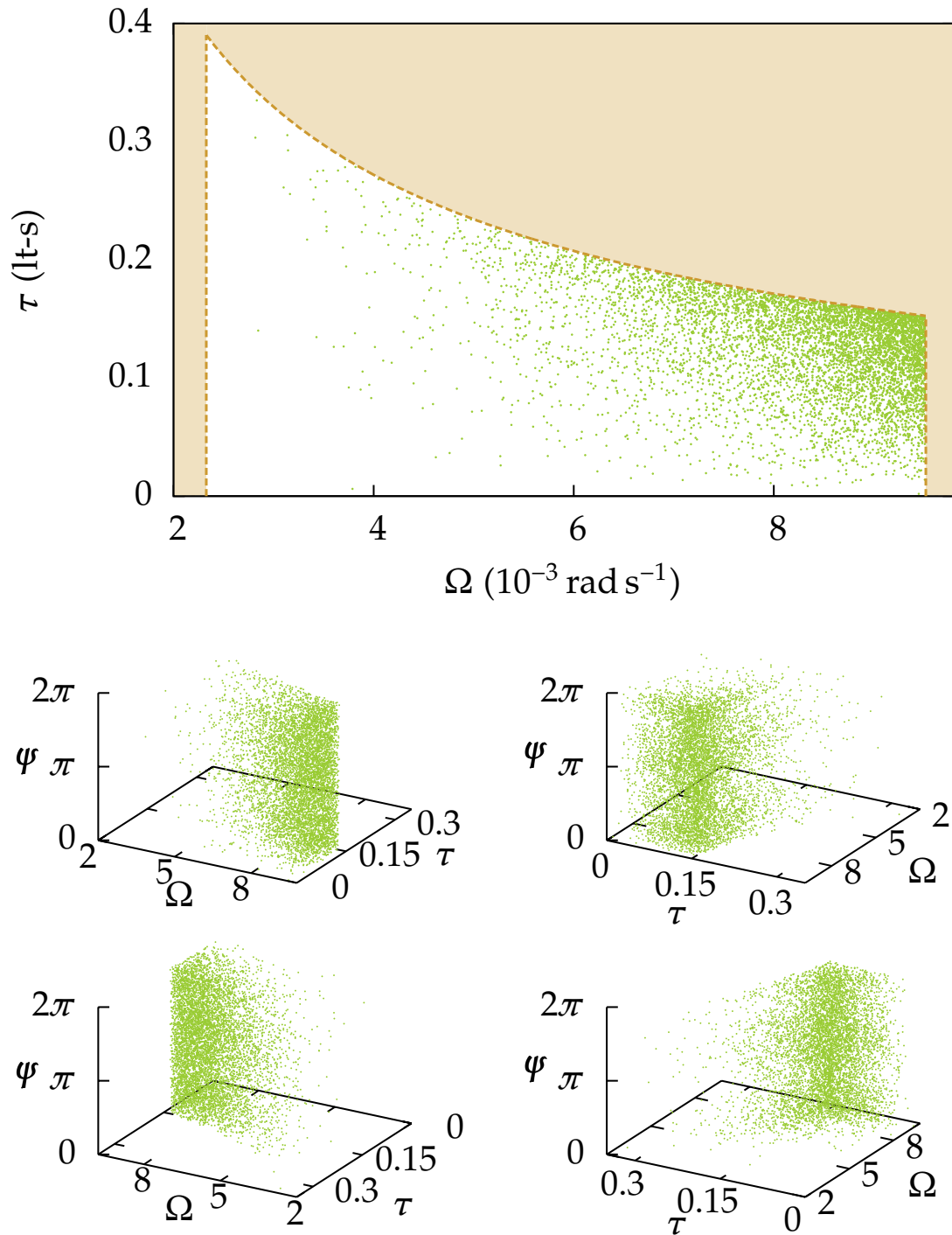


**Figure 3.12:** The Einstein@Home orbital template bank for the 268-s PALFA observations. **(Top)** the orbital templates (green dots) projected onto the space of  $\Omega$  and  $\tau$ . As in Figure 3.6, the orange part of the parameter space is excluded by Equations (3.14) and (3.17). **(Bottom)** the orbital templates in the three-dimensional space of  $\Omega$  (in  $10^{-3} \text{ rad s}^{-1}$ ),  $\tau$  (in lt-s) and  $\psi$  (in rad). From the top left, the plots in clockwise direction are rotated by additional  $90^\circ$  around the  $\psi$ -axis. In the top right plot, the two “streaks” with lower template density are visible, compare Section 3.5.2.

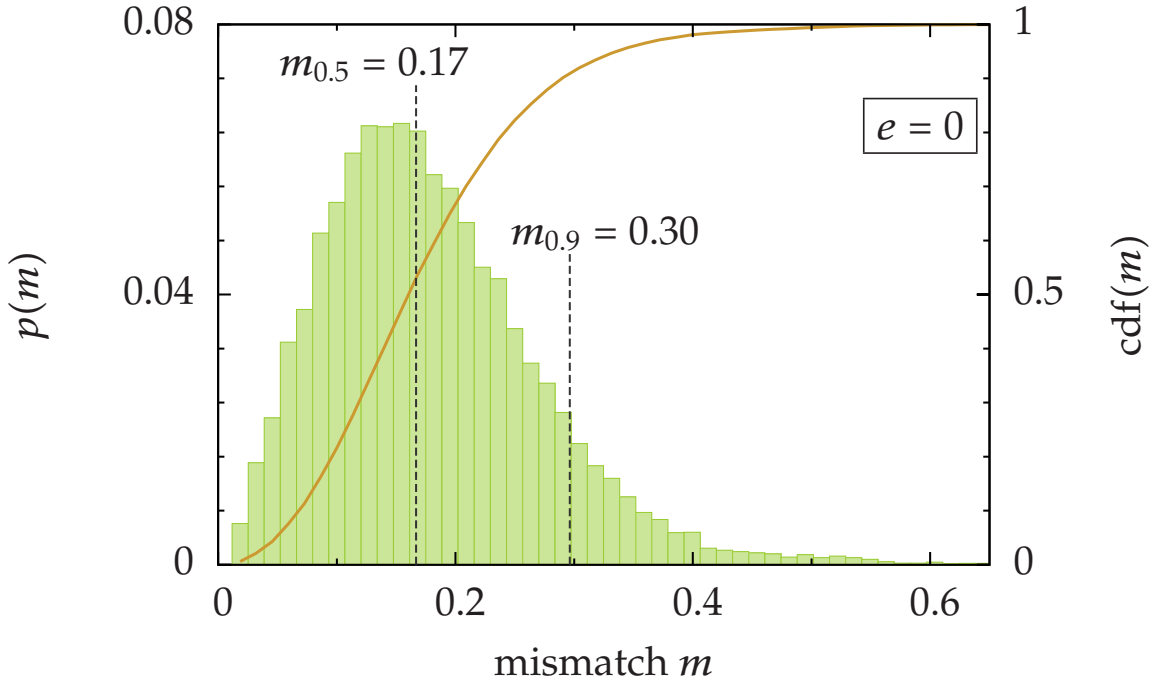


**Figure 3.13:** Template bank test results for circular orbits. The figure shows a normalised histogram (in green) of the mismatch distribution from each 20,000 random injections; the histogram values can be read off on the left vertical axis, the horizontal axis displays the mismatch. The orange graph shows the cumulative distribution function of the mismatch, the values can be read off on the right-hand side. The median  $m_{0.5}$  and the 90%-quantile  $m_{0.9}$  of the mismatch distribution have been highlighted.

For the circular orbits (see Figure 3.13) we find  $m_{0.9} = 0.30$  and  $\eta_{0.3} = 0.91$ . The requirements for the template bank are fulfilled, in 90% of the cases any signal is recovered with a mismatch of less than 30%. The figure shows a normalised histogram (in green) of the distribution of the mismatches from the 20,000 random injections; the axis for the histogram is the left vertical axis. The horizontal axis displays the mismatch. The orange graph shows the cumulative distribution function of the mismatch, the values can be read off on the right-hand side. We have highlighted the median  $m_{0.5} = 0.17$  and the 90%-quantile,  $m_{0.9}$ , of the mismatch distribution.

The same tests were conducted to verify the initially used *random* template bank for circular orbits. Virtually the same results of  $m_{0.9} = 0.30$  and  $m_{0.5} = .17$  were found.

### Tests of the stochastic template bank for eccentric orbits

As we have motivated in Section 3.4.5, it is physically justified to assume that the short-period orbits of binary pulsars are likely almost perfectly circularised. It is useful, however, to explore the sensitivity of the Einstein@Home search to orbits with non-zero eccentricity.

We employ the same mechanism of generating fake data and searching those with the Einstein@Home search codes and the stochastic template bank to test the sensitivity to pulsars in circular orbits. The setup is the same as the one described in the previous section. The key difference is that the injected signals now have non-zero eccentricity, which makes them signals *outside* the modeled parameter space, Equation 3.11. We have injected each

20,000 signals for eccentricities of  $e = 10^{-4}$ ,  $e = 10^{-3}$ ,  $e = 10^{-2}$ ,  $e = 5 \times 10^{-2}$ , and  $e = 10^{-1}$ .

Figure 3.14 shows the results for  $e = 10^{-4}$  and  $e = 10^{-3}$ . In both cases, no significant change in the overall mismatch distribution is visible. We find  $m_{0.9} = 0.30$  and  $m_{0.5} = 0.17$  in both non-zero eccentricity cases which is identical to the values obtained for the circular orbits.

Figure 3.15 shows the results for  $e = 10^{-2}$  and  $e = 2.5 \times 10^{-2}$ . For  $e = 10^{-2}$ , no significant change in the overall mismatch distribution is visible; we find  $m_{0.9} = 0.30$  and  $m_{0.5} = 0.17$ . For  $e = 2.5 \times 10^{-2}$ , a slight overall shift of the mismatch distribution towards higher values is noticeable with  $m_{0.9} = 0.31$  and  $m_{0.5} = 0.18$ .

Figure 3.16 finally shows the results for  $e = 5 \times 10^{-2}$  and  $e = 10^{-1}$ . In both cases the unmodelled influence of the eccentricity on the signal is clearly visible as a degradation in the overall template bank performance; the mismatch distribution broadens significantly. We find  $m_{0.5} = 0.20$  and  $m_{0.9} = 0.37$  for  $e = 5 \times 10^{-2}$ ; analogously,  $m_{0.5} = 0.27$  and  $m_{0.9} = 0.48$  for  $e = 10^{-1}$ .

### Conclusion

Pulsars in orbits with eccentricities  $e < 10^{-2}$  are detectable by the Einstein@Home search without measurable additional mismatch. The search maintains nearly full sensitivity to these objects. From our estimates in Section 3.4.5, we have seen that for most currently known binary pulsars this condition is fulfilled as soon as their orbital periods are of order 11 min. For larger eccentricities, the sensitivity is reduced, especially in the very short period orbits. Although non-zero eccentricity is unmodelled by our circular orbit phase model, the search is able to detect pulsars in slightly eccentric orbits. If the search sensitivity were to be extended to higher eccentricities, a different parameter space description had to be chosen.

## 3.6 Einstein@Home radio pulsar search overview

---

This section provides a brief overview of the Einstein@Home search for binary pulsars in Arecibo Observatory radio data. We briefly review the the data movement, the server setup, the generation of work for Einstein@Home hosts, the data analysis on the host machines and, and the final validation and post-processing of the scientific results. This will provide the reader with an overview of the most important steps in and components of the search pipeline and references to the later sections that give a full account of each single step.

### Data movement

Data disks from Arecibo Observatory are sent to Cornell University's Center for Advanced Computing, (CAC) where data are archived and distributed to other processing sites in an international collaboration. They are also searched for isolated pulsars and single pulses (Section 3.2.5) at the CAC.

For Einstein@Home, data are transferred from CAC to the Albert Einstein Institute, Hannover, via high-speed internet connections. The gridFTP protocol from the Globus toolkit (Foster, 2006) is used to achieve average speeds of more than  $60 \text{ MByte s}^{-1}$ . Data are stored on spinning media in file servers at the AEI. For permanent storage, data are stored on a Hierarchical Storage Management system on tape.

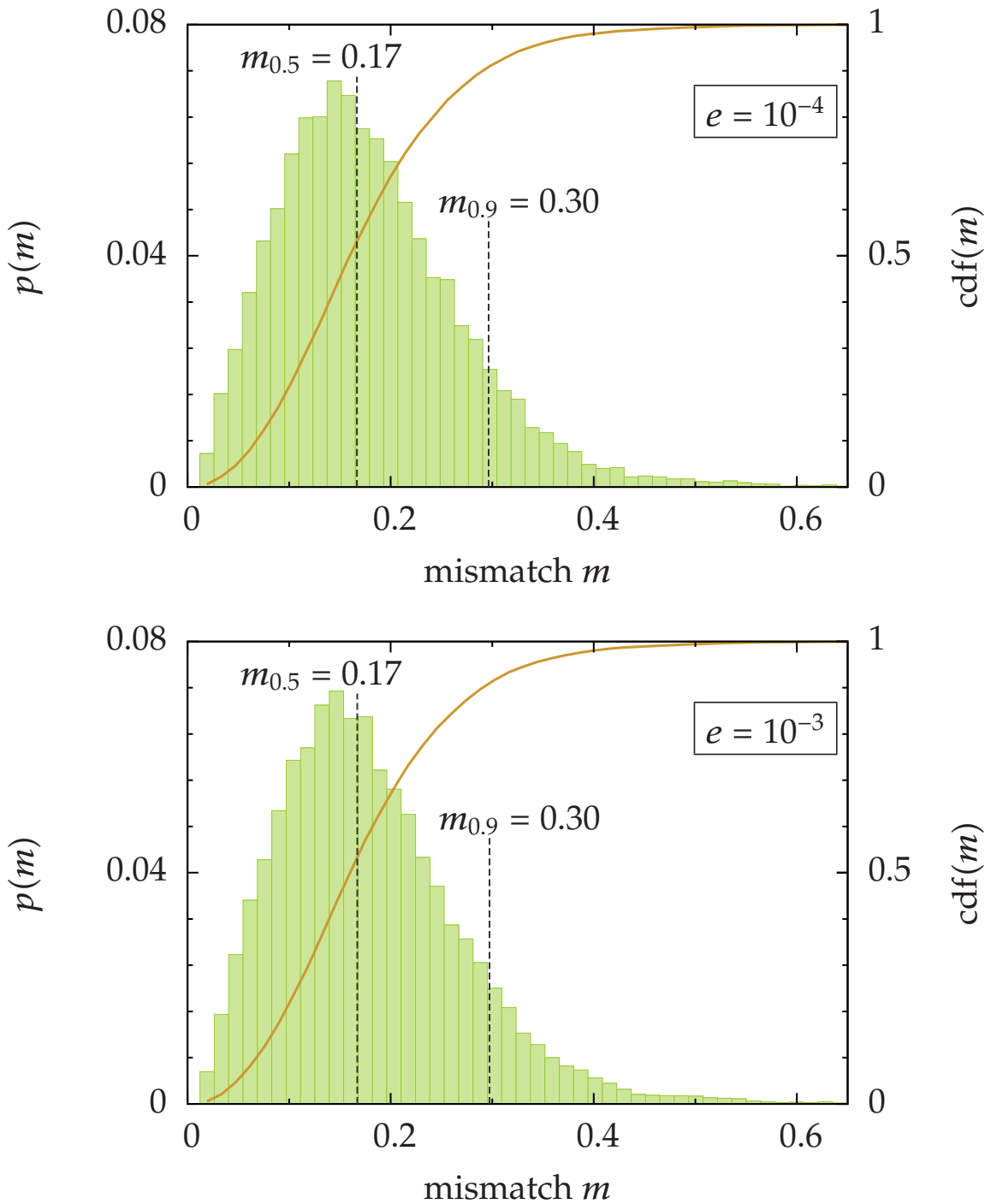


**Figure 3.14:** Template bank test results for eccentric orbits with **(top)**  $e = 10^{-4}$  and **(bottom)**  $e = 10^{-3}$ . The figure shows normalised histograms (green) mismatch distribution from each 20,000 random injections; the histogram values can be read off on the left vertical axis, the horizontal axis displays the mismatch. The orange graph shows the cumulative distribution function of the mismatch, the values can be read off on the right-hand side. The median  $m_{0.5}$  and the 90%-quantile  $m_{0.9}$  of the mismatch distribution have been highlighted.

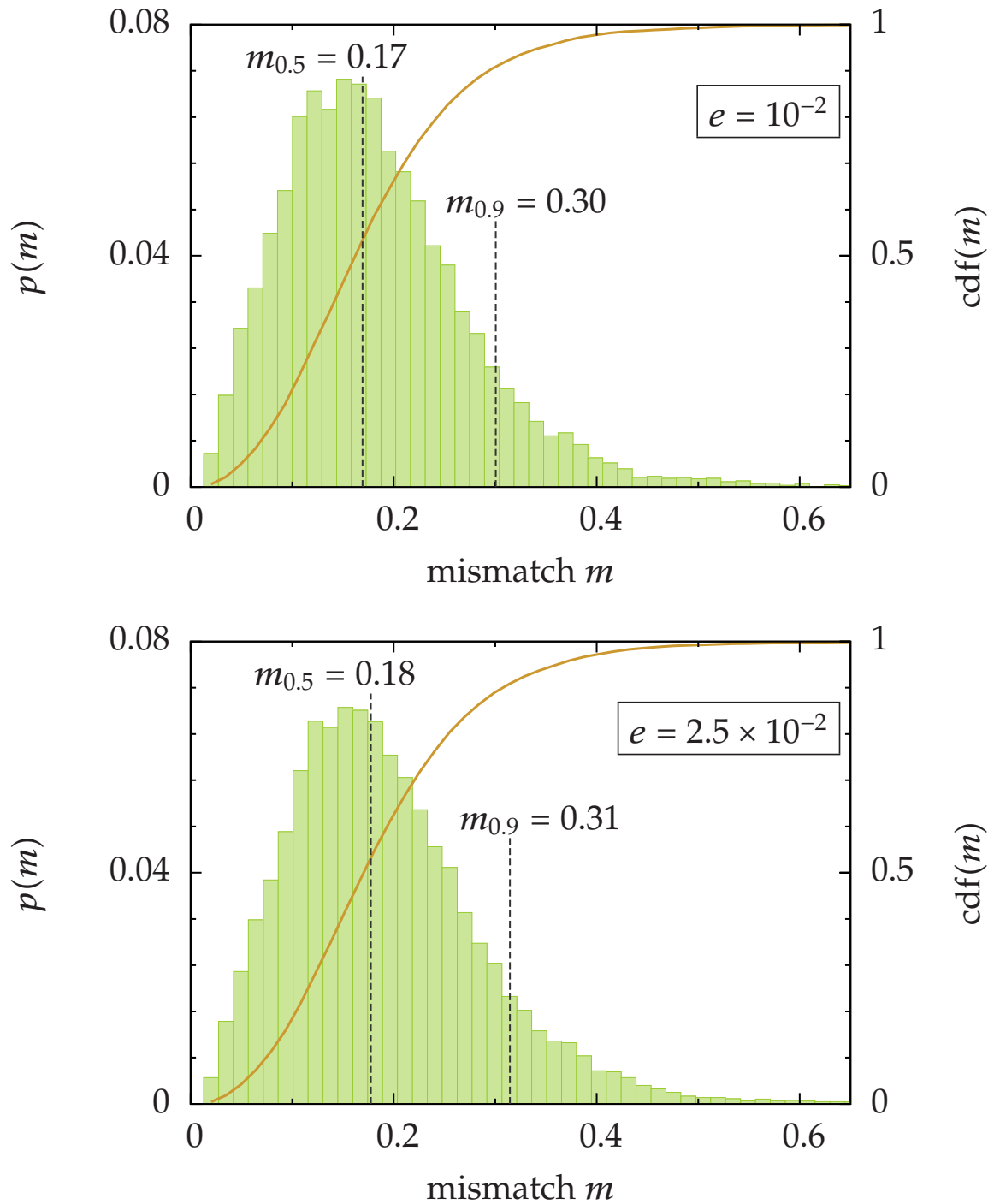


**Figure 3.15:** Template bank test results for eccentric orbits with **(top)**  $e = 10^{-2}$  and **(bottom)**  $e = 2.5 \times 10^{-2}$ . The figure shows normalised histograms (green) mismatch distribution from each 20,000 random injections; the histogram values can be read off on the left vertical axis, the horizontal axis displays the mismatch. The orange graph shows the cumulative distribution function of the mismatch, the values can be read off on the right-hand side. The median  $m_{0.5}$  and the 90%-quantile  $m_{0.9}$  of the mismatch distribution have been highlighted.

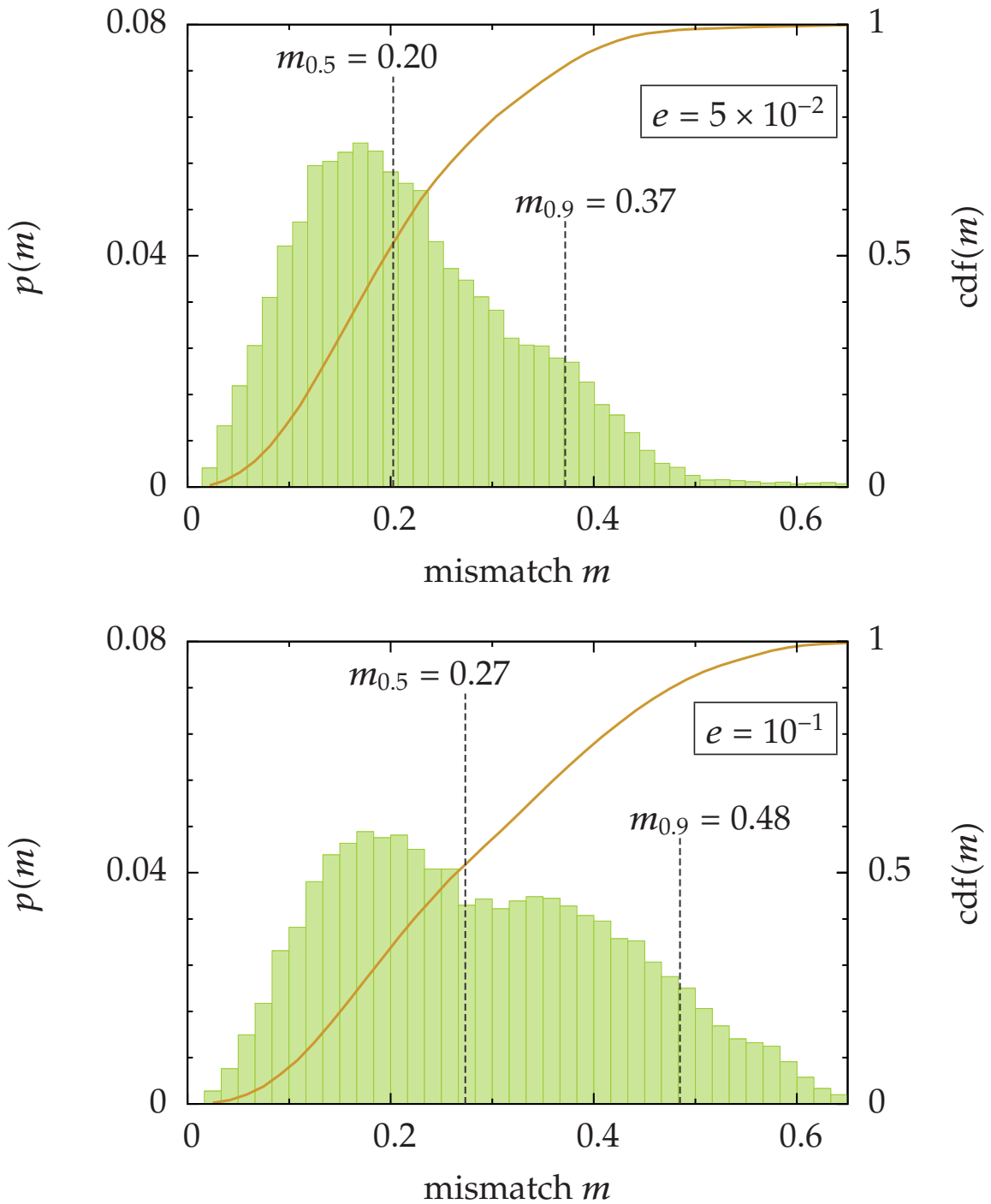


**Figure 3.16:** Template bank test results for eccentric orbits with **(top)**  $e = 5 \times 10^{-2}$  and **(bottom)**  $e = 10^{-1}$ . The figure shows normalised histograms (green) mismatch distribution from each 20,000 random injections; the histogram values can be read off on the left vertical axis, the horizontal axis displays the mismatch. The orange graph shows the cumulative distribution function of the mismatch, the values can be read off on the right-hand side. The median  $m_{0.5}$  and the 90%-quantile  $m_{0.9}$  of the mismatch distribution have been highlighted.

### Server and hardware setup

Data from Cornell University's CAC are first stored on a 16 disk RAID-6 server with a total net capacity of 28 TByte. Another server retrieves data from this machine to preprocess the data files into a more suitable format for the Einstein@Home workunit generation, see Section 3.7. This preprocessed data is then read by many independent tasks running on the work unit generation computer; up to 11 tasks are run in parallel. Each task needs about one hour (wall clock time) to generate 630 workunits suitable to be sent out to Einstein@Home hosts.

The generated work units are finally written to a download server hosting again 16 disks in RAID-6 configuration. Each work unit is then sent out to at least two Einstein@Home participants for processing and is finally deleted from the download server after the results for the work unit are returned and found to be valid.

### Workunit generation

For Einstein@Home, the generation of the workunits uses different software packages, some of which are standard pulsar processing tools, some of which were tailor-made for Einstein@Home. The raw data are converted into filterbank format (a radio-frequency spectrum at high temporal resolution) using tools from the SIGPROC software package; see Section 3.7.1 for details. The filterbank data are de-dispersed, down-sampled, and compressed in dynamic range using tools developed specifically for the Einstein@Home radio pulsar search, see Section 3.7.2. The last step yields 630 de-dispersed time series, each 2 MB in size. Hosts attached to Einstein@Home download workunits containing multiple time series for one beam from the Einstein@Home download server at the AEI Hannover.

### Computation on client machines

Each host attached to Einstein@Home downloads workunits, that consists of multiple time series. Then, each time series is separately analysed for signals from pulsars in binary systems with orbital periods longer than 11 minutes. The time series are re-sampled in time domain (Section 3.8.3) for each orbital template, analysed by Fourier techniques (Section 3.8.4) and incoherent harmonic summing (Section 3.8.5) to increase the sensitivity to pulsed signals. Then, candidates are generated based on their false alarm probability in Gaussian noise, Section 3.8.7. A top list of the 100 most significant candidates is the final processing product of the data analysis of each time series.

### Validation and post-processing

After completion of the computation, the host uploads its result (a list of the 100 most significant candidates) to the Einstein@Home upload server. For each workunit, initially two results are generated. The results are validated (details in Section 3.9) to ensure scientific correctness of the results. If the two initial results do not agree within the pre-defined metrics, additional results are generated by sending out the corresponding workunit to one other client machine at a time until two results are found to agree.

After correct results have been retrieved for all 630 de-dispersed time series, results are collected via cron jobs on a daily basis (Section 3.10.1) into files containing the candidates for one telescope beam. These are inspected visually via overview plots (Section 3.10.2) to quickly identify promising candidates. Further automated post-processing is used to

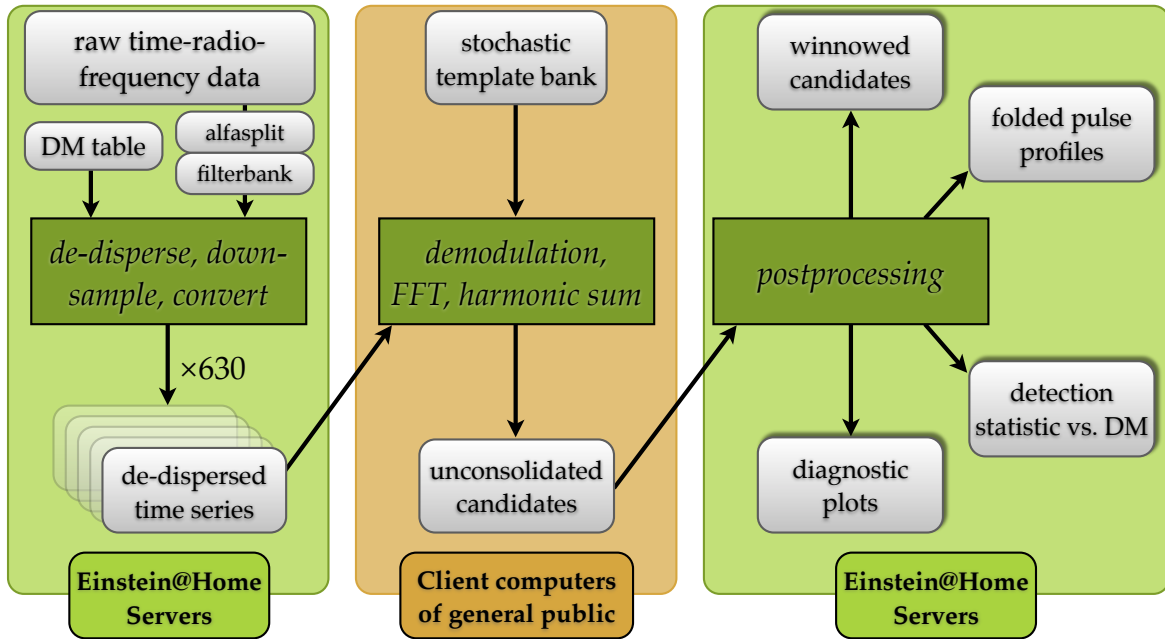


**Figure 3.17:** Overview of the processing steps in the Einstein@Home search for radio pulsars. Section 3.7 describes the left-most part of this Figure, while Section 3.8 describes the middle part. Section 3.10 finally describes the post-processing illustrated on the right hand side.

identify fainter pulsar candidates; new coordinates are used in a clustering algorithm to reduce the number of candidates to follow up (Section 3.10.3).

### 3.7 Data preparation on the server side

First the raw data are transferred from the CAC at Cornell University, New York (USA) to the Albert Einstein Institute, Hannover (Germany), see Section 3.6. The the first processing step is the preparation of the data on dedicated servers at the Albert Einstein Institute; in this step the data are split into smaller chunks that together with the scientific application form the workunits. These are then sent to the volunteer’s computers, where the computations are done and results are sent back to other Einstein@Home servers. A schematic overview of the complete pipeline can be found in Figure 3.17. This section describes the left-most part of the Figure.

The data preparation consists of four steps: the conversion of the raw telescope data, the removal of the dispersion caused by the presence of free electrons in the interstellar medium, the down-sampling of the data to reduce the time resolution by a factor of two and finally, the compression of the data from 16-bit to 8-bit resolution.

#### 3.7.1 Data preprocessing and data format conversion

The raw data taken at the telescope are correlator functions which are converted into the filterbank format for de-dispersion and further processing. Moreover, each raw data set contains the correlator functions from *two beams* in an interleaved manner. Each raw data set consists of three files, each of which covers a fraction of the observation time.

The de-interleaving is done with a software called *alfasplit* which was developed at

Cornell University. Each of the three files is de-interleaved independently, yielding two files each. These files are then the correlator functions for each of the two beams in the initial raw data set. An example use is

```
$ alfasplit p2030.G46.08-00.81.C.wapp2.53910.0082
opening p2030_53910_21544_0082_G46.08-00.81.C_2.wapp
opening p2030_53910_21544_0082_G46.08-00.81.C_3.wapp
```

```
$ alfasplit p2030.G46.08-00.81.C.wapp2.53910.0083
opening p2030_53910_21544_0083_G46.08-00.81.C_2.wapp
opening p2030_53910_21544_0083_G46.08-00.81.C_3.wapp
```

```
$ alfasplit p2030.G46.08-00.81.C.wapp2.53910.0084
opening p2030_53910_21544_0084_G46.08-00.81.C_2.wapp
opening p2030_53910_21544_0084_G46.08-00.81.C_3.wapp
```

The correlator functions can be converted into filterbank format with tools from the SIG-PROC software suite (Lorimer, 2002) using the program called `filterbank`. One can think of the filterbank format as a 2D stream of radio frequency versus time or a collection of radio frequency spectra recorded at each time sample. The conversion of three of the files obtained in the example above is done by calling

```
$ filterbank p2030_53910_21544_0082_G46.08-00.81.C_2.wapp \
p2030_53910_21544_0083_G46.08-00.81.C_2.wapp \
p2030_53910_21544_0084_G46.08-00.81.C_2.wapp -floats -headerfile > \
p2030_53910_21544_0082_G46.08-00.81.C_2.fil,
```

where `-floats` sets the output to 8-bit format, and `-headerfile` writes the header information for this observation into an ascii file called `head`.

The filterbank file now is simply a list of 8-bit numbers, each of which represents a radio frequency spectral channel at a given time sample. To be read by the de-dispersion code, a program called `addheader.c` reads in the header file, parses its contents and writes it in front of the filterbank file. Merging header file and filterbank file into a single file reduces the number of files to be handled in the subsequent processing steps and avoids confusion of header files and filterbank files that do not belong together. `addheader.c` was written from scratch for the Einstein@Home search.

### **PALFA survey WAPP files naming convention**

The naming convention for the PALFA survey WAPP files is as follows. Each file ends on `.wapp` to indicate the proprietary WAPP data format. The underscore divides the file name into six groups of letters. The first, in the above example `p2030`, is the Arecibo wide survey number. For the PALFA survey it is `p2030`; we note there there are some files starting with a capital letter: `P2030`. The survey name is entered by the observer and varied between the two variants. The second group, here `53910`, is the modified Julian date, MJD, at the time of the observation. The third field, here `21544` is the number of seconds since midnight UT at the start of the observation. The fourth field, here `0084` is a running file number reset at the start of each observing session. The fifth field, here `G46.08-00.81.C`, denotes the observing position or object. For survey observations it shows Galactic coordinates of the central beam, indicated by the capital letter `G`; in our example the coordinates are  $\ell = 46.08^\circ$ ,

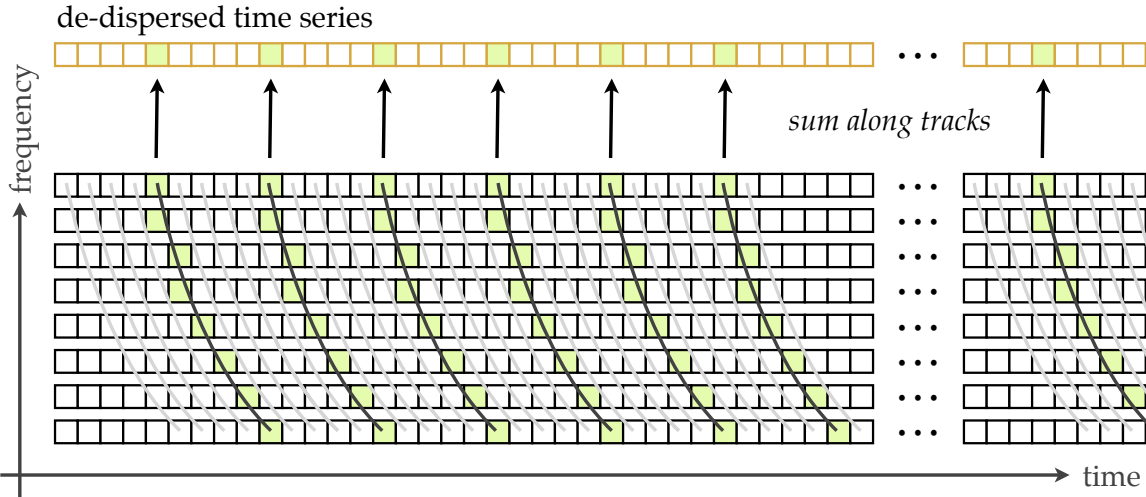


**Figure 3.18:** Schematic of the de-dispersion process. The bottom part of the figure shows schematic filterbank data (with eight channels). For a given DM trial value, the corresponding track  $\Delta t(\nu, \text{DM})$  from Equation (2.43) is computed and all bins along the tracks (here shown in light-grey) starting at the fiducial frequency (highest here) are summed. Here, each fifth track is highlighted in dark-grey and the summed bins in light-green. At the top, the resulting de-dispersed time series is shown, its bin given by the sums along the tracks.

$b = -00.81^\circ$ . The capital letter after the position, here C, can be N, S, or C, each indicating one of three interleaved tiling grids used in the PALFA survey, compare Figure 3.3. The final field, here 2 and 3, respectively, is the beam number and can take values between 0 and 7, the last beam being the dummy beam.

### 3.7.2 De-dispersion

As detailed in Section 2.4.1, the radio signal from the pulsar undergoes dispersion when travelling through the interstellar medium. The interaction with the free electrons along the line of sight causes a radio-frequency dependent delay in the arrival time of the radio waves. The amount of dispersion is determined by the dispersion measure which is the integrated column density of free electrons between the observer and the pulsar.

The process of removing this delay is called de-dispersion. Since the distance to the pulsar is unknown, the amount of free electrons and thus the amount of dispersion is unknown. Thus, the de-dispersion is conducted using a grid of trial values (see below). For each trial value, we can compute the delay  $\Delta t(\nu, \text{DM})$  for each frequency channel in the filterbank data by Equation (2.43) relative to a fiducial frequency, e.g. that of the filterbank channel with the highest frequency. We then use this frequency dependent delay to define tracks in the plane of time and radio frequency along which single channel data are summed. The sum from this track is then assigned to a time sample at the fiducial frequency at which the track starts. This process is repeated for the next time sample to obtain a full de-dispersed time series. Alternatively, one can shift each frequency channel by  $-\Delta t(\nu, \text{DM})$  and then sum all shifted time samples that are at the same time after shifting. The de-dispersion process is shown schematically in Figure 3.18.

As visible in Figure 3.18, in this summing scheme, the number of channels summed decreases with higher DM value at the end of the time series. This results in a window function applied to the end of the data stream. Note, however that the time delay from disper-

sion, which determines the window size is much smaller than the observation time; thus, no significant loss of data results.

### Trial DM values

The dispersion has to be corrected for a number of dispersion measure trial values. The necessary spacing  $\Delta\text{DM}$  in dispersion measure DM is given by equating the dispersive delay  $\delta t$  over the observed radio frequency bandwidth from Equation (2.44) with the sampling time  $t_{\text{samp}}$

$$\Delta\text{DM} = 1.205 \times 10^{-4} \text{ pc cm}^{-3} \left( \frac{t_{\text{samp}}}{\text{s}} \right) \left( \frac{\nu}{1 \text{ MHz}} \right)^3 \left( \frac{1 \text{ MHz}}{\Delta\nu} \right) \quad (3.51)$$

For the PALFA survey set up ( $\Delta\nu = 100 \text{ MHz}$ ,  $\nu = 1400 \text{ MHz}$ ), this yields a DM spacing of  $\Delta\text{DM} = 0.2 \text{ pc cm}^{-3}$ . Thus, a grid of trial values  $\text{DM}_i$  is set up by

$$\text{DM}_i = i \times \Delta\text{DM}, \quad (3.52)$$

where  $\Delta\text{DM}$  is given by Equation (3.51). When  $i$  equals the number of filterbank channels,  $n_{\text{chan}}$ , the total delay across  $\Delta\nu$  is  $n_{\text{chan}} \times t_{\text{samp}}$ , and the delay across a single channel is  $t_{\text{samp}}$ ; the corresponding DM is called the ‘‘diagonal DM’’. For  $i > n_{\text{chan}}$ , the total delay is dominated by the smearing in the single filterbank channels.

The dispersion smearing hampers the detection of fast-spinning pulsars if the smearing time is larger than the sampling time. Further computations can be saved by down-sampling the time series to lower sampling times; this step decreases the number of operations for the further processing and does not further lower sensitivity to fast-spinning pulsars. Typical pulsar search pipelines therefore down-sample the data by factors of  $M$  at dispersion measures for which  $i = M \times n_{\text{chan}}$ , for integer  $M$ .

For distributed computing, the workunit runtimes should not vary over a large range; too short workunits can cause data base problems on the server side problems, while too long workunits can cause problems with deadlines to be met by the client machines. Thus, for Einstein@Home this short-cut is not taken in order to obtain a set of workunits with homogeneous runtimes.

The trial DMs for the Einstein@Home search are based on the trial DMs for the Cornell pipeline (Cordes et al., 2006). The original list was modified slightly in two ways: a) the spacing of the DMs was increased by a factor of two. This is because the sampling time of the data for Einstein@Home is twice as large. From Equation (3.51) it is clear that  $\Delta\text{DM}$  is linear in the sampling time, justifying our modification. b) For  $\text{DM} > 431 \text{ pc cm}^{-3}$  the spacing was increased by another factor of two compared to the Cornell pipeline to reduce the number of necessary DM trials. This is justified from the fact that the main pulse broadening contribution at high DMs is the multi-path scattering which cannot be removed by de-dispersion (see below and Figure 3.20). The trial DMs used in the Einstein@Home pipeline are shown in Figure 3.19

We used 630 trial different trial values, covering the range from  $0 \text{ pc cm}^{-3}$  to  $1010.4 \text{ pc cm}^{-3}$ . The spacing was  $0.6 \text{ pc cm}^{-3}$  for  $0 \text{ pc cm}^{-3} \leq \text{DM} \leq 212.4 \text{ pc cm}^{-3}$ ,  $1.0 \text{ pc cm}^{-3}$  for  $213.4 \text{ pc cm}^{-3} \leq \text{DM} \leq 348.4 \text{ pc cm}^{-3}$ ,  $2.0 \text{ pc cm}^{-3}$  for  $350.4 \text{ pc cm}^{-3} \leq \text{DM} \leq 432.4 \text{ pc cm}^{-3}$ , and  $6.0 \text{ pc cm}^{-3}$  for  $438.4 \text{ pc cm}^{-3} \leq \text{DM} \leq 1010.4 \text{ pc cm}^{-3}$ , respectively.

The fundamental limit to the time resolution arising from multi-path scattering, see Section 2.4.2, can also be exploited when generating trial DMs for the de-dispersion. The step size usually is given by constraints on the observer’s side, i.e. inherent instrumental limits on time resolution or de-dispersion, see above. If, however, these effects become much

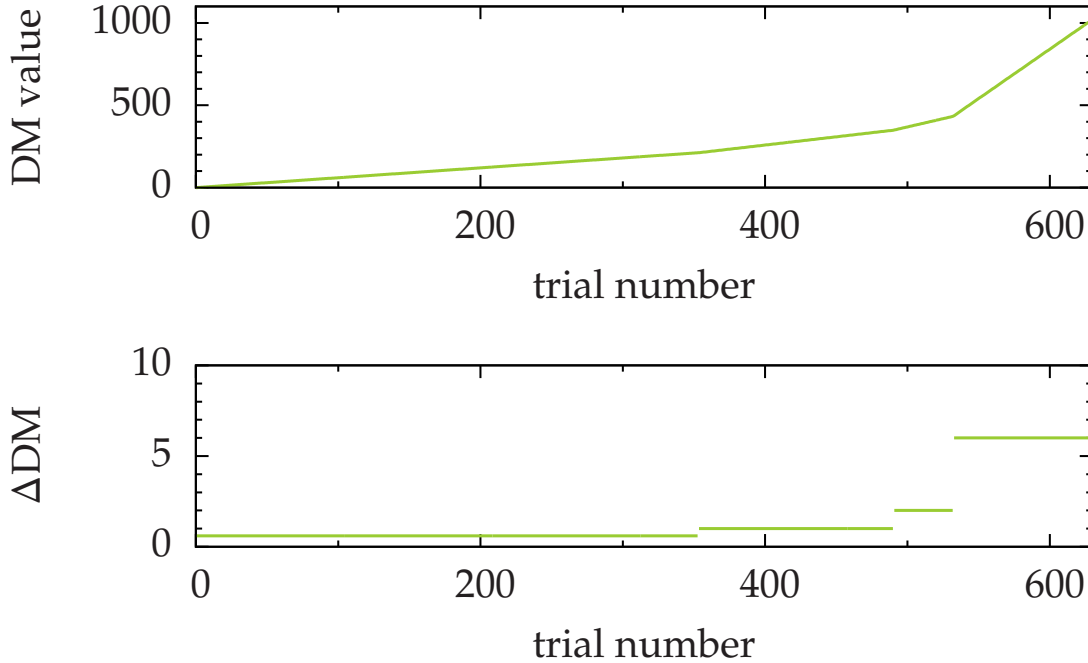


**Figure 3.19:** The Einstein@Home trial DMs, modified from the Cornell pipeline trial list (Cordes et al., 2006). **(Top)** The dispersion measure value as a function of the trial number. Four ranges with differing step sizes from Equations (3.51) and (2.45) (at high DMs) are visible. **(Bottom)** The step sizes  $\Delta\text{DM}$  as a function of the trial number, again showing the four different ranges.

smaller than the expected scattering time scale from Equation (2.45), the step size can be further increased; this can save a little, although unlikely much, computation time. Figure 3.20 shows the scattering timescale as a function of the dispersion measure in a double-logarithmic plot in a green curve. It further shows the corresponding step-size in DM from Equation (3.51) and for PALFA survey parameters as an orange curve. This is the step-size to be chosen if the delay over the complete observed radio bandwidth is to be less than the sampling time, or in this case scattering time scale.

The de-dispersion along with other preparation steps of the data (see Sections 3.7.3 and 3.7.4) in the Einstein@Home pipeline is managed by a C program called `dedisperse.c`, written from scratch for this purpose.

### 3.7.3 Down-sampling

As detailed in Section 3.3.3, it is necessary to reduce the data volume served by the Einstein@Home servers to the volunteers' computers by a factor of a few to a manageable amount. In the Einstein@Home radio pulsar search, the raw data and pre-processed data volumes are reduced by two means: down-sampling the time resolution (explained in this section) and decreasing the dynamical range (explained in Section 3.7.4).

The down-sampling step is applied at the filterbank data stage. There, each radio frequency channel is down-sampled independently in memory and the resulting half as long frequency channels are combined to down-sampled filterbank data.

First, each channel of  $n_{\text{samp}}$  real-valued samples with sampling time  $t_{\text{samp}}$  is Fourier trans-

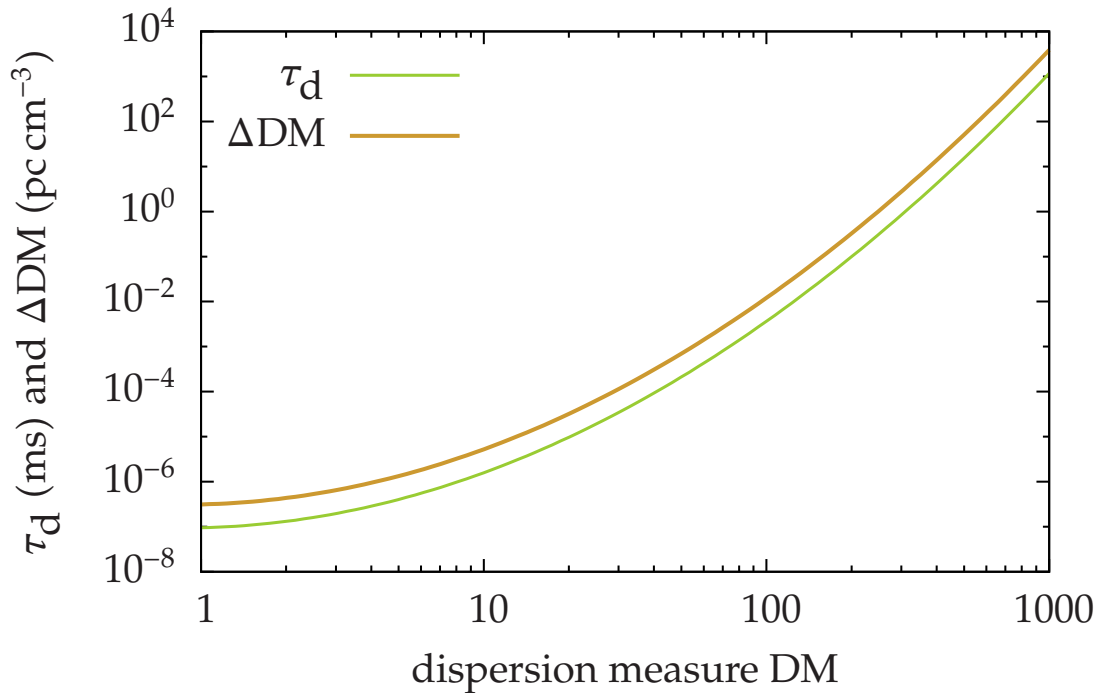


**Figure 3.20:** The typical time scale of multi-path scattering fitted from observations reported in Bhat et al. (2004). The green curve is the best fitting model for  $\tau_d$  from Bhat et al. (2004), also in Equation (2.45). The orange curve shows this time scale value  $\tau_d$  converted into a step size  $\Delta DM$  in dispersion measure using Equation (3.51) and the parameters of the PALFA survey. This DM step-size is the dispersive delay over the complete observation radio bandwidth.

formed by use of algorithms from the “Fastest Fourier Transform in the West” (FFTW; Frigo and Johnson., 2010). In frequency domain  $\frac{1}{2}n_{\text{samp}} + 1$  complex-valued samples are obtained, and a low-pass filter with a cut-off at half the Nyquist frequency  $f_{\text{Ny}} = \frac{1}{2t_{\text{samp}}}$  of the original data is applied. The filter has a simple top-hat shape. In other words: all frequency components with  $f \in [f_{\text{Ny}}/2, f_{\text{Ny}}]$  are set to zero, all other frequency components are left unchanged. This filtering process is necessary to avoid aliasing when down-sampling the time resolution in the next step.

Then, the inverse Fourier transform is applied to the low-pass filtered radio frequency channel of  $\frac{1}{2}n_{\text{samp}} + 1$  complex-valued samples. In the resulting radio frequency channel of  $n_{\text{samp}}$  real-valued samples every other sample is chosen for the down-sampled time series. The radio channel data resulting from the last step will then have  $\frac{1}{2}n_{\text{samp}}$  real samples; this is the down-sampled radio frequency channel we wanted to achieve. The sampling time of the down-sampled data is  $t'_{\text{samp}} = 2t_{\text{samp}}$ . Repeating this process for each channel, a down-sampled filterbank file with a sampling time twice as large as the initial sampling time is obtained.

Figure 3.21 illustrates the down-sampling process for a single radio frequency channel with its intermediate steps. For this purpose a fake sinusoidal signal with an amplitude of 0.05 was injected in Gaussian stationary noise with unit variance, generating a time series of  $2^{16}$  samples. The top panel in Figure 3.21 shows the original time series in green and the down-sampled time series in orange. The bottom panel shows the moduli of the Fourier transforms of the original data (green) and the down-sampled data (orange, on top).

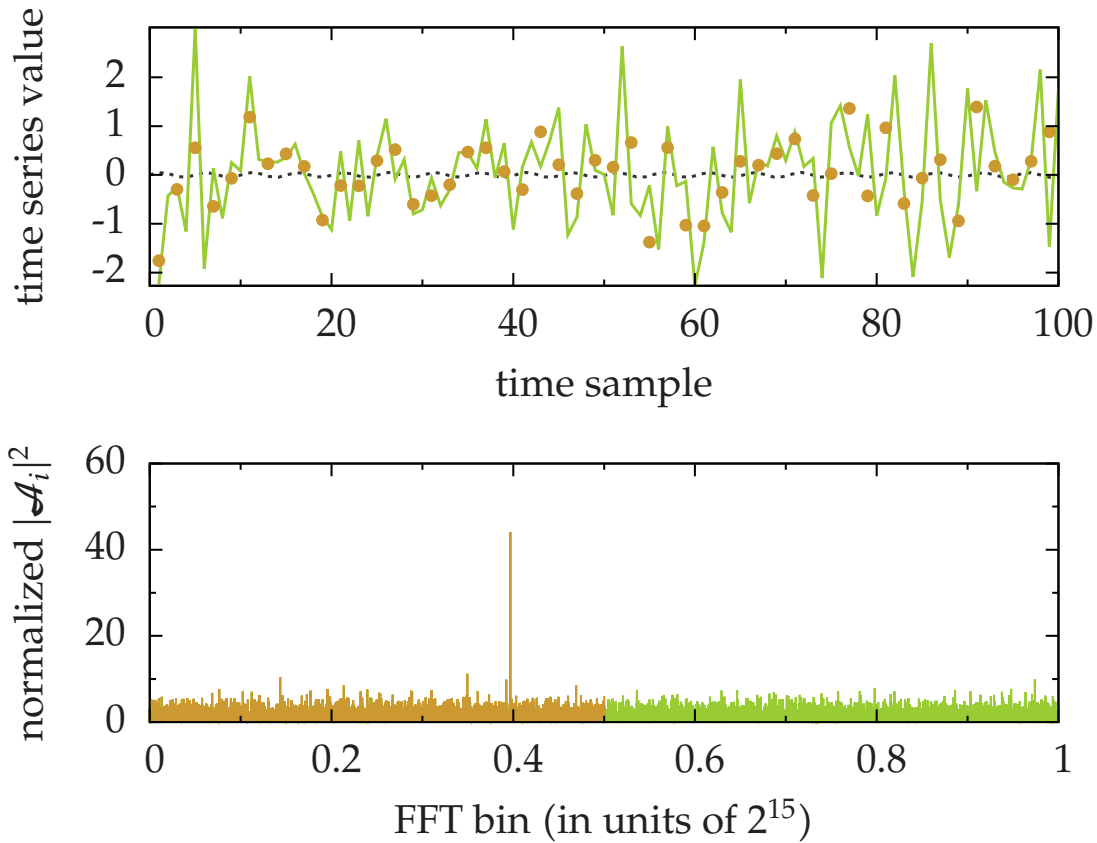


**Figure 3.21:** Illustration of the down-sampling process used to reduce the data size. **(Top)** the first 100 samples from a time series containing a sinusoidal signal (dark-grey dashed line) in Gaussian, stationary noise of unit variance with zero mean. The green line is the signal at the initial sampling time, the orange points are the data points from the down-sampled time series obtained after low-pass filtering and picking every other sample. Note that this is different from simply picking every other sample without low-pass filtering or simple linear interpolation between the points. **(Bottom)** the moduli of the Fourier transform of the initial time series (green) and the down-sampled time series (orange, on top). The Fourier amplitudes have been normalised to the number of samples in the time series. The signal peak is of equal signal-to-noise ratio in both cases.

Note the conservation of signal-to-noise ratio between the initial time series and the down-sampled time series at the end of the process. Further note the difference between the original data points and the points from the down-sampled time series. The latter are *not* simply every other point from the initial data set or a linear interpolation between two points of the initial data set. Simply choosing every other point from the initial data set results in aliasing, which must be counteracted by a low-pass filter. Linear interpolation between two points is a low-pass filter, although with a very soft cut-off that passes higher frequencies as well. The combination of low-pass filtering and down-sampling by a factor of two achieves very good anti-aliasing. More detailed studies comparing the Fourier power in the initial data and the down-sampled data showed that the error made by the resampling is less than 0.5% in Fourier power.

### 3.7.4 Data type conversion

To further reduce the data volume, the dynamic range of the de-dispersed time series is reduced as a final step. As explained in Section 3.7.3, limited internet bandwidth makes it necessary to optimise the ratio between computation time and data volume transferred. A further reduction in the data volume can be achieved by reducing the dynamic range of the data. The raw data for the PALFA survey are recorded with 16 bits (or 2 byte) per time sample. A time series of  $N_{\text{samp}} = 2^{22}$  samples would take  $2^{23}$  byte = 8 Mbyte.

The data are mainly Gaussian distributed noise; most pulsars are not bright enough so that single pulses could be seen in the de-dispersed time series, which would skew the Gaussian statistics. Thus, there is no immediate need for a high dynamic range to correctly map strong variations in signal strength. An analysis in the PALFA collaboration has shown that the possible loss in signal-to-noise ratio is less than a few percent even if the dynamic range is reduced to 8-bit or even single-bit resolution (Cordes, 2009). As an example, the very successful Parkes Multibeam Survey (Lyne et al., 2000) uses 1-bit digitisation from the filterbank stage on. 1-bit sampling proved to be very robust against strong, intermittent bursts of RFI (Lorimer and Kramer, 2005). Brinklow (1989) showed that for 1-bit sampling the loss in signal-to-noise ratio is less than  $1 - \sqrt{1/\pi} \approx 20.2\%$  compared to perfect sampling, which for usual surveys is less than other losses in the pipeline. In searches where the signal is dominated by noise, a sampling with low dynamic range is well suited; this holds true for the observations of most pulsars, which will not be clipped by the reduction in dynamic range.

The dynamic range reduction is the last step in `dedisperse.c`. For each de-dispersed time series, the 16-bit samples  $t_i^{(16)}$  are sorted by their value; the median  $m$ , the 1% ( $q_{0.01}$ ) and the 99% ( $q_{0.99}$ ) quantile are obtained. Then, a scale factor

$$s = \frac{127}{q_{0.99} - m} \quad (3.53)$$

is computed. Each sample is multiplied with the scale factor  $s$  and rounded to the nearest integer to obtain samples  $t_i^{(8)}$  in the 8-bit dynamic range:

$$t_i^{(8)} = \text{int} \left( s \times \left( t_i^{(16)} - m \right) \right), \quad (3.54)$$

where  $\text{int}(x)$  is the function that yields the nearest integer value of  $x$ . Values  $t_i^{(8)}$  that fall below or above the 8-bit range of  $[-127, +127]$  are set to the minimum of  $-127$  or the maximum  $+127$ , respectively. The `int` values are cast into `signed char` values which are 8-bit data types. The scale factor  $s$  is recorded in the header of the de-dispersed time series for the later reconstruction of the de-dispersed time series in floating point resolution.

Finally, the file header information and the de-dispersed, down-sampled, dynamic-range compressed time series is written to file. In total a set of 630 de-dispersed time series is obtained for each telescope beam, each file  $\approx 2$  Mbyte in size, yielding a total data volume of 1.3 Gbyte to distribute. For the observations with shorter observation times, these numbers are halved.

De-dispersed time series are bundled for the Einstein@Home search in workunits. A single workunit contained up to ten de-dispersed time series in order to get acceptable processing times per workunit and ease stress on the central data base by lowering the number of total workunits.

## 3.8 Client search code

The search code, running on the volunteers' hosts, consists of five main steps. After data conditioning, the de-dispersed time series is demodulated for signals in circular orbits in the time domain. It is Fourier transformed and up to 16 harmonics from the signal are incoherently summed in Fourier power domain; finally, a list of the most significant candidates is generated. We will give a brief overview over the main steps here, detailed descriptions are available in sections 3.8.1 to 3.8.9.

Each client receives one or multiple de-dispersed time series, which are searched for signals from binary pulsars by time-domain demodulation and subsequent frequency analysis. In first, preparatory steps, the de-dispersed time series is converted from 8-bit dynamic range back into single floating point precision (32 bits), see Section 3.8.1 for details.

Next, the time series' power spectrum is spectrally normalised and frequency bands known to be contaminated by radio frequency interference are removed from the de-dispersed time series. The spectral normalisation, RFI mitigation, and the method employed to generate the zap list is described in Section 3.8.2.

In the next step, the whitened and cleaned time series is demodulated in time domain for a set of orbital templates and analysed in frequency domain subsequently. An internal top list of the most significant candidates is updated after the analysis for each orbital template. The time demodulation method and the frequency analysis are described in Sections 3.8.3 and 3.8.4. The parameter space and the construction of the template bank was described in full detail in Section 3.5.

After finishing the main demodulation loop, a significance ( $\mathcal{S} = -\log_{10}(p)$ , with  $p$  the false-alarm probability in Gaussian noise) is calculated for each of the accumulated candidates. Finally, the top 100 candidates with highest  $\mathcal{S}$  are written to a file and uploaded to the project servers for post processing.

Figure 3.22 displays these main steps in a flow chart for quick reference. With orange boxes data files are shown, light green boxes display internal variables, arrays or structures in the search code. Green boxes illustrate processes of central importance for the search. The thick dark-grey line encloses the hot loop of the code, executed for each orbital template in the template bank; comments on the left refer to execution dates.

### 3.8.1 Data type conversion

As detailed in Section 3.7.4, the dynamic range of the de-dispersed time series is reduced for reasons of data transfer bandwidth. While the raw data have a dynamic range of 2 byte (16 bits, or 65536) values, the de-dispersed time series are delivered in 8 bit resolution (256 values), saving a factor of two in data volume with little reduction in signal-to-noise ratio (Brinklow, 1989; Lorimer and Kramer, 2005).

As shown in Section 3.7.4, the 8-bit sampled data are described by an integer in the range  $[-127, +127]$  and a scale factor, which is used to convert 8-bit data to 32-bit range (single precision) to get the proper scaling of the values in the de-dispersed time series. The conversion from 8-bit samples  $t_i^{(8)}$  to 32-bit samples  $t_i^{(32)}$  is

$$t_i^{(32)} = \frac{1}{s} t_i^{(8)}, \quad (3.55)$$

where  $s$  is the scaling factor from the header information of the datafile. Note that the median  $m$  used for the scaling of the time series data in Equation (3.54) is not used here.

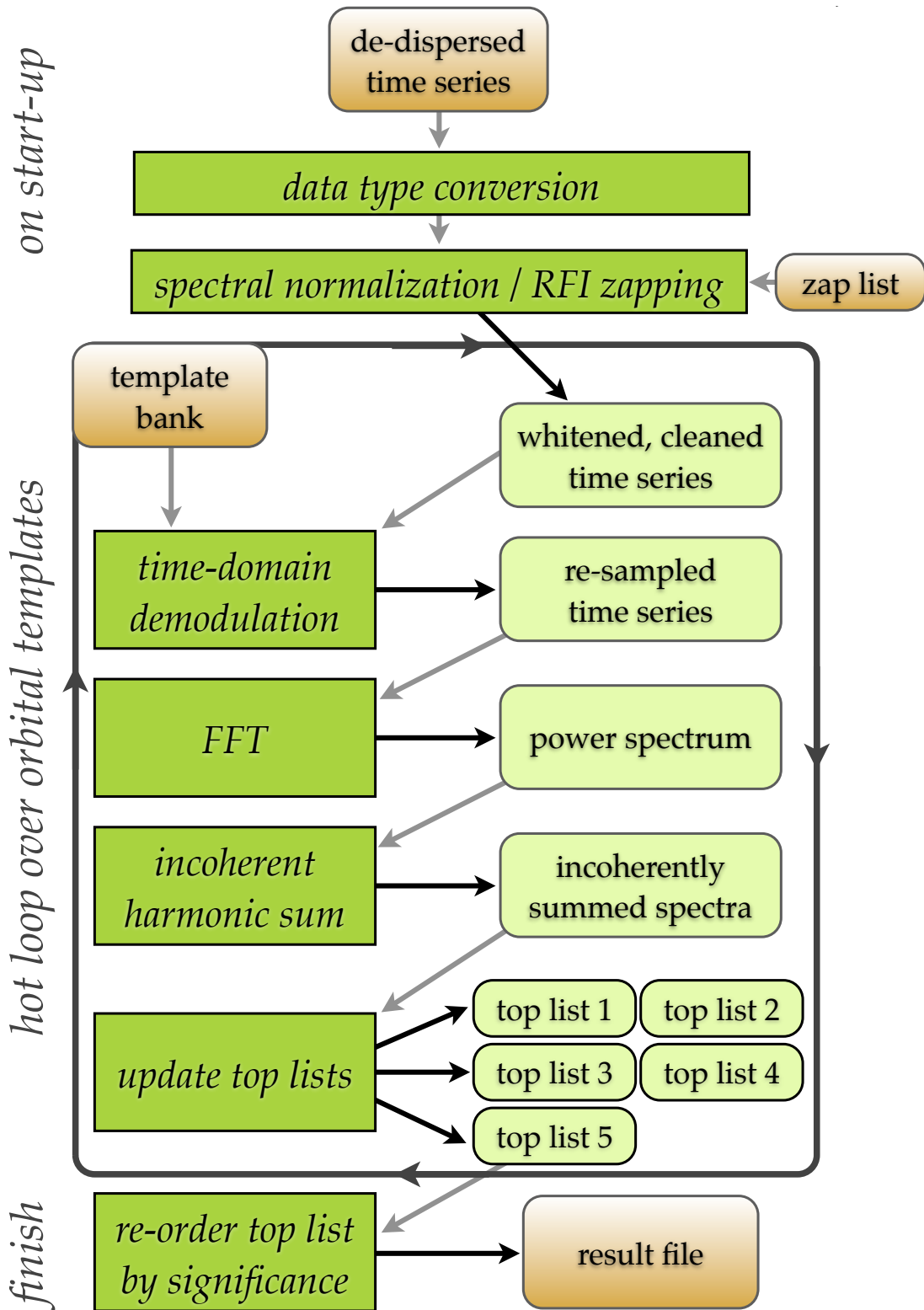


**Figure 3.22:** The main steps of the search code. With orange boxes data files are shown, light green boxes display internal variables, arrays or structures in the search code. Green boxes illustrate processes of central importance for the search. The thick dark-grey line encloses the hot loop of the code, executed for each orbital template in the template bank; comments on the left refer to execution dates.

This is equivalent to applying a constant offset to all samples such that the median equals zero. This can be done without loss of generality since a constant offset will only influence the DC-term in the frequency analysis which is discarded anyway later on.

### 3.8.2 Spectral normalisation and RFI mitigation

Fluctuations in the receiver and/or data acquisition systems can lead to an excess of noise at low frequencies, so-called “instrumental red noise” (Lorimer and Kramer, 2005). In order to obtain an unbiased weighting of signal significances at all frequencies it is necessary to normalise the spectrum by dividing it by its local median (Ransom, 2001).

The statistical analysis for periodic signals can be further skewed by the presence of periodic terrestrial signals, so-called radio frequency interference (RFI). RFI can sometimes be discriminated from celestial signals by the missing dispersion; thus, any periodic signal at, or close to  $DM = 0$  should not be considered as potential celestial signal. This turns out not to be correct for all RFI: there are RFI signals that are dispersed, mimicking a pulsar signal very well.

Other periodic RFI are present at multiple narrow radio frequency bands. These appear as pulsar-like signals at multiple non-zero trial DM values, since an apparent dispersion can be described by a set of different DMs, connecting different subsets of the narrow bands.

Other RFI signals appear as relatively broad-band radio emission and can be discriminated from celestial signals by two main means: a) re-observation or b) identification of the same apparent signal in multiple beams of the same pointing and/or occurrence on multiple days. The latter motivates the generation of a *zap list*, a catalogue of known recurring periodic, terrestrial signals. This approach was used for the Einstein@Home radio pulsar search and is described below. Narrow frequency bands described by a zap list are replaced by random noise in the Fourier transform of the de-dispersed time series.

#### Spectral normalisation

The uncompressed (see Section 3.8.1) de-dispersed time series is zero-padded<sup>21</sup>, to increase the spectral resolution and minimise the loss of sensitivity of discrete Fourier transforms for signals in between Fourier bins. For the search on PALFA data the padding extends the length of the time series from initially  $n_{\text{unpad}}$  samples to  $n_{\text{pad}} = 3n_{\text{unpad}}$  samples. The zero-padded time series is Fourier transformed via a Fast Fourier Transform (FFT), details in Section 3.8.6.

If the time series were represented by Gaussian noise only, each sample  $t_i$  would be drawn from a Gaussian random distribution. In Fourier domain, each bin’s real  $\Re(\mathcal{A}_i)$  and imaginary  $\Im(\mathcal{A}_i)$  component would then also follow a Gaussian distribution. The noise power spectrum would thus look flat, since all frequency bins followed the same distribution. This case is called *white Gaussian noise*.

In this ideal case, the estimation of significances is relatively easy and straightforward (see Section 3.8.7). Only a global normalisation to adjust the variance of the distribution has to be applied to yield comparable results independent of the level of noise.

Significances in the Einstein@Home search are inferred from the power spectrum; sometimes, also the Fourier amplitudes  $|\mathcal{A}_i|$  are used to estimate significances (Lorimer and

<sup>21</sup>see Section 3.8.6 in this thesis and Section 6.1.3.2 in Lorimer and Kramer (2005)

Kramer, 2005). The bins  $\rho_i$  of the power spectrum are given by

$$\rho_i = |\mathcal{A}_i|^2 = (\Re(\mathcal{A}_i))^2 + (\Im(\mathcal{A}_i))^2. \quad (3.56)$$

If the  $\mathcal{A}_i$  follow Gaussian distribution of zero mean and unit variance  $\sigma^2 = 1$ , one can show (see Section 8.2) that the  $\rho_i$  follow a simple exponential distribution

$$p(\rho_i) = e^{-\rho_i}, \quad (3.57)$$

which also corresponds to chi-square distribution with two degrees of freedom of  $2\rho_i$ , i.e.  $p(\rho_i) = \chi_2^2(2\rho_i)$ . The median of the above distribution is  $m_\rho = \ln(2) \approx 0.693$ , while the mean value  $\mu_\rho = 1$ .

If the noise was ideal white, Gaussian noise, one would simply compute (measure) the mean  $\mu_{\text{mes}}$  of all the power spectrum bins, and scale the complex Fourier amplitudes  $\mathcal{A}_i$  by a factor  $\sqrt{\mu_\rho / \mu_{\text{mes}}}$  to normalise the noise spectrum. In reality this comes with two caveats: a) the noise likely is not white, but contains “red” components and b) the mean is prone to biases from single strong outliers.

The latter can be cured by using the median rather than the mean. Further, one does not compute the median of the whole ensemble but instead over smaller contiguous blocks or a running median in a window around the frequency bin to normalise. The block-size or window-size, respectively, has to be small enough to match the typical scale of the red noise component, but large enough to yield a reliable estimate of the median.

The Einstein@Home search code computes for each frequency bin in the power spectrum the running median  $m_{\rho, \text{run}}$  over a window of  $n_{\text{window}}$  power spectrum bins around this bin. For the search on PALFA data, this adjustable window size is set to 1000 bins. This corresponds to a width of  $\Delta_{\text{window}} = \frac{n_{\text{window}}}{n_{\text{pad}} t_{\text{samp}}} \approx 1.24$  Hz. The central bin’s complex amplitude is scaled by the factor  $\sqrt{\ln(2) / m_{\rho, \text{run}}}$  to set the median locally to the required value for white noise.

This process is repeated for all bins in the Fourier spectrum of the time series. However, it cannot be applied strictly to the first and the last  $\frac{1}{2}n_{\text{window}}$  frequency bins, because for these less than the full window size is available for the running median computation. In the search code, these bins at the lowest and highest frequency band are set to zero to suppress any influence from them. Also, they are not used in the later stages of the analysis.

### Generating the zap list

To identify recurring periodic RFI from terrestrial origin, a large ensemble of beams observed over a longer timescale (days to months) has to be considered. Pulsar signals will only show up in a handful beams, assuming there are no multi-pass observations of the sky region of interest; recurring RFI can however be detected in a) multiple beams of the same pointing and b) on multiple observation days over the time interval considered. Thus, selecting the most common periodicity candidates from a large ensemble of candidates is a simple and effective measure to create a *global zap list* for a survey. The global zap list is a straightforward-to-implement, but very conservative approach; it contains frequency ranges around recurring periodicity candidates that will be replaced by random noise<sup>22</sup> in the de-dispersed time series for any DM before the Fourier analysis. This process is

<sup>22</sup>the advantage of replacing RFI with random noise rather than with zeros is in the smaller resulting skew of the statistics

called “zapping”, hence the list name. Since it will be applied to *all* data sets, independent of whether the RFI is present in the data set or not, real signals could potentially also be zapped out. Given that a pulsar signals consists of many harmonics at different frequencies over a wide range it is unlikely that the removal of pulsar signals happens.

The zap list creation can be improved by going from a global zap list to a *local zap list*, considering periodicity candidates from shorter stretches of observation time, e.g. a single observation day. This approach avoids the potential problems from zapping frequency bands unnecessarily, but is slightly more complicated to set up. In a distributed computing environment this would mean to distribute an individual zap list for each workunit compared to simply always distributing the same file.

Another possibility is a two-pass approach that will generate a *beam-specific zap list*; the first pass is the processing without any sophisticated zap lists<sup>23</sup>; in the second pass the periodic signals found in the first pass are subtracted (or masked) to reveal potentially weaker signals masked in the first pass. This approach has the advantage of being able to identify also the weakest signals by iterative subtraction of possibly masking signals. It comes with the drawback of at least doubling the total computation time, though. It might also be possible to run the first stage at lower resolution (larger sampling time, shorter time series, fewer trial DMs) to obtain a beam-specific zap list. Care has to be taken not to falsely discard any pulsar signals from the first pass as RFI.

Note that the generation of a global zap list has to be done only once for the complete survey data. This requires that large amounts of periodicity candidates by a quick running pipeline (therefore, no acceleration or more complicated search) are available. If local or beam-specific zap lists are generated, this can be done as part of the pre-processing, always assuming that the necessary ensembles of data sets are fully available.

For the Einstein@Home search, the frequency bands to be zapped were selected from a list of periodicity candidates generated from the Cornell pipeline, Section 3.2.5, by J. Cordes. A total of 2,030,604 periodicity candidates up to 7.8125 kHz and over the complete range of trial DMs up to  $1000 \text{ pc cm}^{-3}$  from all processed beams were collected from the Cornell pipeline database. 654,468 of these periodicity candidates were flagged previously as caused by RFI. These periodicity candidates were binned in frequency, assuming a frequency resolution of  $\Delta f = (2 \times 300 \text{ s})^{-1} = 0.00167 \text{ Hz}$ . Any frequency bin containing more than 200 candidates was selected for further processing.

Each frequency bin was broadened to a frequency interval to account for the native frequency resolution and the Doppler shift in frequency due to Earth’s orbital motion<sup>24</sup>. Overlap between the resulting frequency ranges was consolidated in a second step to obtain disjunct frequency bands. In total a frequency range of 226.059 Hz was covered by recurring RFI in 332 different frequency bands up to 7.786 kHz.

For the Einstein@Home search, only frequency ranges below 3.90625 kHz were used, because of the down-sampling by a factor of two and the correspondingly lowered Nyquist frequency. RFI around multiples of the power line frequency 60 Hz was consolidated, and half-Hertz wide frequency intervals around power line harmonics up to 180 Hz were manually inserted into the zap list. The final zap list contains a total of 233 bands, covering 72.383 Hz; this is 1.85% of the total bandwidth of 3.9 kHz. Table 8.1 in Section 8.1 shows the full zap list used for the Einstein@Home radio pulsar search on Arecibo PALFA data.

<sup>23</sup>using a zap list only for power line harmonics and other known instrumental artefacts

<sup>24</sup>Doppler effect induced frequency shift:  $\Delta f = f \left| \frac{v}{c} \right|$  and  $\left| \frac{v}{c} \right| < 10^{-4}$  for the Earth’s orbital motion

### RFI zapping

After the spectral normalisation (see above), a total of 233 bands (1.85% of the power spectrum) contaminated by well-known sources of RFI are removed. The corresponding frequency bins are replaced by samples from random Gaussian noise of the appropriate variance. The zap list and its generation process are described above as well.

The zap list is delivered with the scientific application to the volunteer's computers. It resides on these machines as long as they run the Einstein@Home radio pulsar search or until it is superseded by an updated zap list. As a global zap list it is used for any de-dispersed time series, independent of the beam it was derived from and the trial DM.

The zap list is a simple two-column ascii text file with 233 lines in total, each line containing a frequency band to clean. The first column contains the lower frequency each frequency band, the second column the upper frequency of the frequency band. The first ten lines of the zap list file are (compare to Table 8.1):

```
0.002500000 0.034166667
0.040016668 0.041684029
0.081675002 0.083341839
0.833334185 0.835000853
0.836667515 0.838334184
0.840000846 0.841667514
1.198333941 1.200000609
1.413333858 1.415000525
8.216666955 8.218333622
8.343332510 8.345001343
```

The science application reads in the file line by line, converts the frequencies into integer frequency bins, and replaces the required bins in the Fourier transform of the de-dispersed time series with random Gaussian noise. After the whitening step, the bins in the Fourier transform follow a Gaussian distribution with zero mean and unit variance in the noise-only case.

Finally, the whitened and cleaned Fourier spectrum is inverse Fourier transformed to obtain the whitened and cleaned time series. Because the time series was zero-padded to increase the frequency resolution before the transform, only the first  $n_{\text{unpad}}$  samples of the back-transformed time series are obtained as *whitened, cleaned, and de-dispersed time series* for further analysis. The extra step back to time domain is necessary to apply the time-domain demodulation (see Section 3.8.3).

The data conditioning described above is done only once per de-dispersed time series at science code startup. The whitening and zapping only requires about a second on a modern computer. If the code is started from a checkpoint, the whitening and zapping is repeated from the beginning, since the whitened and cleaned time series is not stored on the Einstein@Home client machines.

### 3.8.3 Time domain demodulation

The binary motion of the pulsar modulates the arrival time of the radio pulses. When the pulsar is close to Earth, the pulses arrive earlier than from the distant side of its orbits. When it is receding from Earth, the pulses arrive at a slightly lower rate, when it is approaching Earth, the pulses arrive at a slightly higher rate, for a detailed description see

Section 3.4.3. Both of these effects are caused by the binary motion and can be corrected for by time- shifting single time series bins.

For each template, a nearest-neighbour demodulation in time domain re-samples the time series to a fiducial time at the binary system's barycenter. Let the time at the system's barycenter be  $t$ . From the system geometry described in Section 3.4.3 a signal emitted at  $t$  from the pulsar arrives at the detector at a time  $t'$  given by

$$t'(t; \Lambda) = t - \tau \sin(\Omega t + \psi) + \Phi'_0 + \frac{d}{c} \quad (3.58)$$

with the orbital parameters  $\tau$ ,  $\Omega$ , and  $\psi$ . The constant phase contribution  $\Phi'_0 + \frac{d}{c}$  from the initial phase of the signal and the constant light travel time over a distance  $d$  from the pulsar system barycentre to the detector can be neglected: the detection statistic in Equation (3.26) is insensitive to constant phase shifts.

The signal is recorded in samples  $s'_i = s'(t'_i)$  at the detector in regular time steps  $t'_i = i \times t_{\text{samp}}$ . To obtain the signal at the pulsar system barycenter in regular samples  $s_j = s(t_j)$  with  $t_j = j \times t_{\text{samp}}$ , we have to solve the equation (obtained by inserting the discrete sampling times into Equation (3.58) and diving both sides by  $t_{\text{samp}}$ )

$$i(j; \Lambda) = j - \frac{\tau}{t_{\text{samp}}} \sin(j \times \Omega t_{\text{samp}} + \psi) + \text{const}. \quad (3.59)$$

In our search method the solution is obtained by first shifting the start times of one of the time scales to match up both. This is achieved by subtracting or adding an appropriate offset, constant for each orbital template.

Then, for each  $j$  we compute the right-hand side of Equation (3.59), which usually will not be an integer number. We then take the nearest integer of the obtained value. We here denote by  $[x]_{\text{int}}$  the closest integer to a real-valued number  $x$ . Therefore, the signal sent out at integer barycentric time step  $j$  arrives at the detector at integer barycentric time step  $i_{\text{int}}$  given by

$$i_{\text{int}}(j; \Lambda) := \left[ j - \frac{\tau}{t_{\text{samp}}} \sin(j \times \Omega t_{\text{samp}} + \psi) + \text{const} \right]_{\text{int}}. \quad (3.60)$$

This equation relates each sample  $j$  at barycentric time to a sample  $i_{\text{int}}$  in the measured time series at the detector. Therefore, to obtain the time series at the pulsar system barycenter, we compute for each  $j$  the corresponding  $i_{\text{int}}$  and define the samples of the re-sampled time series  $s_j^{\text{rs}}$  by

$$s_j^{\text{rs}} = s_{i_{\text{int}}(j; \Lambda)}. \quad (3.61)$$

This method is the *nearest-neighbour time-domain resampling*, illustrated in Figure 3.23.

The figure depicts schematically the steps of the time-domain resampling. For each time sample in the barycentred time series (labeled "barycenter time series"), the correspond instant in time is computed by Equation (3.58) at which that time sample would arrive at the detector (axis labeled "continuous time"). For this instant we then find the nearest neighbour in the detector time series (labeled "observed time series") and assign the observed bin value at this sample to the bin value in the barycenter time series we initially started from.

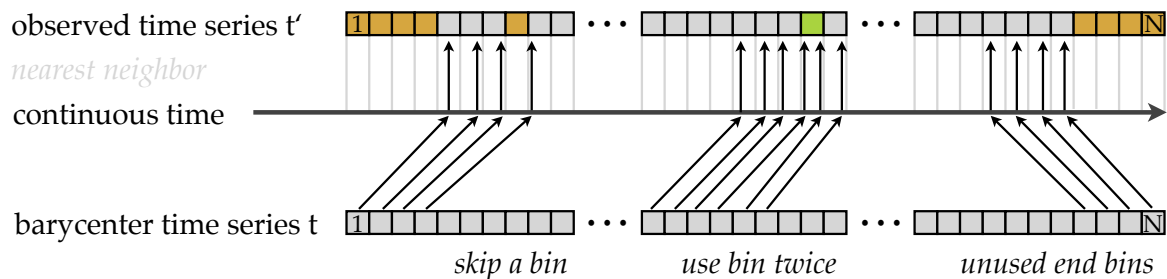


**Figure 3.23:** Schematic of the time-domain resampling showing special cases. For simplicity, the first few bins of the detector time series might be not used for the barycentred time series, the loss is of order  $\tau \ll T_{\text{obs}}$ . Due to the nearest neighbour resampling, a single bin from the detector time series might be skipped and not appear in the barycentered time series at all, or get used for two subsequent bins. In analogy to the beginning of the time series, bins at the end might also be unused.

For each orbital template the de-dispersed time series is re-sampled with this algorithm. For any orbital template similar enough<sup>25</sup> to the actual orbital parameters of a binary system present in the data, the re-sampled time series at the pulsar system barycenter then contains a periodic signal following a simple phase model

$$\Phi(t; \Lambda) = 2\pi ft, \quad (3.62)$$

which can be detected very efficiently with Fourier methods described in Section 3.8.4.

In order to minimise possible losses in the Fourier analysis step (see Section 3.8.4), we pad the re-sampled time series by bins containing no signal but the mean of the previous samples. This is the so-called *mean-padding*<sup>26</sup>, which is used to increase the frequency resolution of the Fourier analysis in order to minimise the losses in signal-to-noise ration in discrete Fourier transforms.

The mean value for the padding is computed on the fly for each re-sampled time series by adding the sample value into a buffer which at the end of the resampling is divided by the number of time samples in the re-sampled time series.

### 3.8.4 Fourier analysis

After the de-dispersed time series has been properly re-sampled by the algorithm described in Section 3.8.3 to correct for the Doppler effect caused by a binary orbit, it needs to be analysed for the presence of periodic signals. We employ one of the most widely used concepts for this, the Fourier analysis, which decomposes the information represented in the time series in frequency domain. Periodic signals then can be identified in the Fourier domain more readily. We here described the features of this analysis method important for our pipeline. A good and more detailed overview over various aspects of Fourier analysis can be found in e.g. Ransom (2001) or in the description of one widely used software library (FFTW; Frigo and Johnson. (2010)).

<sup>25</sup>“similar” here means that the loss in the detection statistic from Equation (3.26) is small. It does not mean that the errors in the parameter space coordinates are small, since small deviations in one coordinate can be absorbed in deviations from the true value in other coordinates.

<sup>26</sup>see footnote on page 27 of Ransom (2001)

### Basics

The data to be analysed are discretely sampled de-dispersed and re-sampled time series. Let  $s_i$  denote the value of the  $i$ -th real-valued sample in the time series. Since the data are discrete, we cannot compute the continuous Fourier transform but rather the *discrete Fourier transform* (DFT). We define the  $k$ -th bin of the DFT of our time series  $s_i$  by

$$\mathcal{A}_k = \sum_{j=0}^{N-1} s_j e^{-2\pi i k \frac{j}{N}}, \quad (3.63)$$

where  $i^2 = -1$ , and  $N$  is the number of samples in the time series. This definition is called the “un-normalized” DFT, as applying the transform and its inverse multiplies the result by a factor  $N^2$ . The normalisation can be achieved either by multiplying the result of the DFT with  $\sqrt{N \langle s_i^2 \rangle}$  (Lorimer and Kramer, 2005; Ransom, 2001), or use a variation of this method employing the median rather than the mean, see Section 3.8.2. As detailed below, a proper normalisation is needed to estimate statistical significances.

Let the regular sampling time in the time series be denoted by  $t_{\text{samp}}$ . Then, the  $k$ -th frequency bin is at a frequency

$$f_k = \frac{k}{N t_{\text{samp}}} = \frac{k}{T_{\text{obs}}} \quad (3.64)$$

with the observation time  $T_{\text{obs}}$  (the total time spanned by the time series). The frequency index  $k$  runs from 1 to  $\frac{N}{2}$ . Each  $k$  defines a single *frequency bin* of width

$$df = \frac{1}{T_{\text{obs}}}, \quad (3.65)$$

which is the fundamental frequency resolution of the DFT. The highest resolvable frequency is the *Nyquist frequency* at

$$f_{\text{Ny}} = \frac{1}{2t_{\text{samp}}}. \quad (3.66)$$

While the brute-force approach for the calculation of the DFT would apparently require  $\mathcal{O}(N^2)$  operations (compare Equation (3.63)), cleverly designed algorithms, so-called fast Fourier transforms (FFT), break the computation down to  $\mathcal{O}(N \log_2(N))$ ; this allows to compute even very long FFTs of, say  $N = 2^{25}$  samples in relatively short time (seconds) on modern CPUs. For our analysis we make use of the algorithms provided in the open source software library “Fastest Fourier Transform in the West” (FFTW; Frigo and Johnson (2005)).

Another simplification that speeds up the computation of the DFT further comes for real-valued time series. In that case,  $s_i^* = s_i$ , and we find

$$\mathcal{A}_k^* = \sum_{j=0}^{N-1} s_j^* e^{2\pi i k \frac{j}{N}} = \sum_{j=0}^{N-1} s_j e^{-2\pi i (N-k) \frac{j}{N}} = \mathcal{A}_{N-k} \quad \text{or} \quad \mathcal{A}_k = \mathcal{A}_{N-k}^*, \quad (3.67)$$

where the star denotes the complex conjugate. So, for real-valued time series the DFT is symmetric around the Nyquist frequency at  $k = \frac{N}{2}$  and only half of the frequency bins have to be computed. FFTW provides specific algorithms that make use of these symmetries for real time series and speed up the computation by about a factor of two.

### Examples

We now look in more detail at the response of a DFT to signals with frequencies that do not lie in the middle of the Fourier bins, but rather in between two bins. We then show some techniques that can be employed to improve the response of the DFT to such signals.

The finite frequency resolution of the DFT implies that natural signals, occurring at any possible frequency, will not always lie at the center of a frequency bin  $f_k = kT_{\text{obs}}^{-1}$ . They can also occur in between bins, with consequences for the response of the DFT to such a signal. Assume the signal has a frequency  $f_r = rT_{\text{obs}}^{-1}$ , we can then write  $f_r$  as a combination of the nearest Fourier frequency  $f_k = kT_{\text{obs}}^{-1}$  with  $k \in \mathbb{N}$  and a fractional residual  $-\frac{1}{2} \leq k - r < \frac{1}{2}$  such that

$$f_r = \frac{k}{T_{\text{obs}}} + \frac{(k-r)}{T_{\text{obs}}} \quad (3.68)$$

One can readily show (compare Section 2.3.2 in Ransom (2001)) that the general DFT response to such a signal at  $f_r$  can be written in terms of the Fourier amplitudes  $\mathcal{A}_k$  and the Fourier powers  $\mathcal{D}_k$  as

$$\mathcal{A}_r = \mathcal{A}_k e^{-i\pi(k-r)} \text{sinc}(\pi(k-r)) \quad (3.69)$$

$$\mathcal{D}_r = \mathcal{D}_k \text{sinc}^2(\pi(k-r)) \quad (3.70)$$

with normalisation factors  $\mathcal{A}_k$  and  $\mathcal{D}_k = |\mathcal{A}_k|^2$  as the responses to the same signal at  $f_k$  and the sinc-function defined by

$$\text{sinc}(x) := \frac{\sin(\pi x)}{\pi x}. \quad (3.71)$$

What does that imply, say, for signals at frequencies most distant from any frequency bin, that is: exactly in between two Fourier bins? For this case,  $k-r = \frac{1}{2}$ ,  $\text{sinc}\left(\frac{1}{2}\right) = \frac{2}{\pi} \approx 0.64$ , and  $\text{sinc}^2\left(\frac{1}{2}\right) = \frac{4}{\pi^2} \approx 0.41$ . This means that the DFT response to signals in between two Fourier bins is reduced to 64% (in amplitude) to 41% (in power) compared to the response to signals at the middle of the bin. This effects is known as *scalping* and is further illustrated in Figure 3.24.

### Improving the Fourier response

There are several ways to overcome the loss of sensitivity from scalping. **a)** *brute force calculation* at many points in between Fourier bins. **b)** *Fourier interpolation*, a method that allows to compute the Fourier response in between bins by using the neighbouring few bins; **c)** *interbinning*, a special case of the Fourier interpolation using only the two neighbouring bins that allows one to compute the Fourier response in the middle between two bins. **d)** *padding the time series* with zeros or the mean adds no power to signal components but increases the frequency resolution.

**Method a)** is very costly and for long time series not a practical approach in most cases. Therefore, we will not discuss it further here.

**Method b)** relies on the known Fourier response to an arbitrary signal given by Equation (3.70). For a previously known frequency, the full response  $\mathcal{A}_r^{\text{full}}$  can be reconstructed by multiplying the DFT bins with the inverse of the response function and summing this over a set of neighbouring bins

$$\mathcal{A}_r^{\text{full}} \approx \sum_{k=[r]-n}^{k=[r]+n} \mathcal{A}_k e^{-i\pi(r-k)} \text{sinc}(\pi(r-k)), \quad (3.72)$$

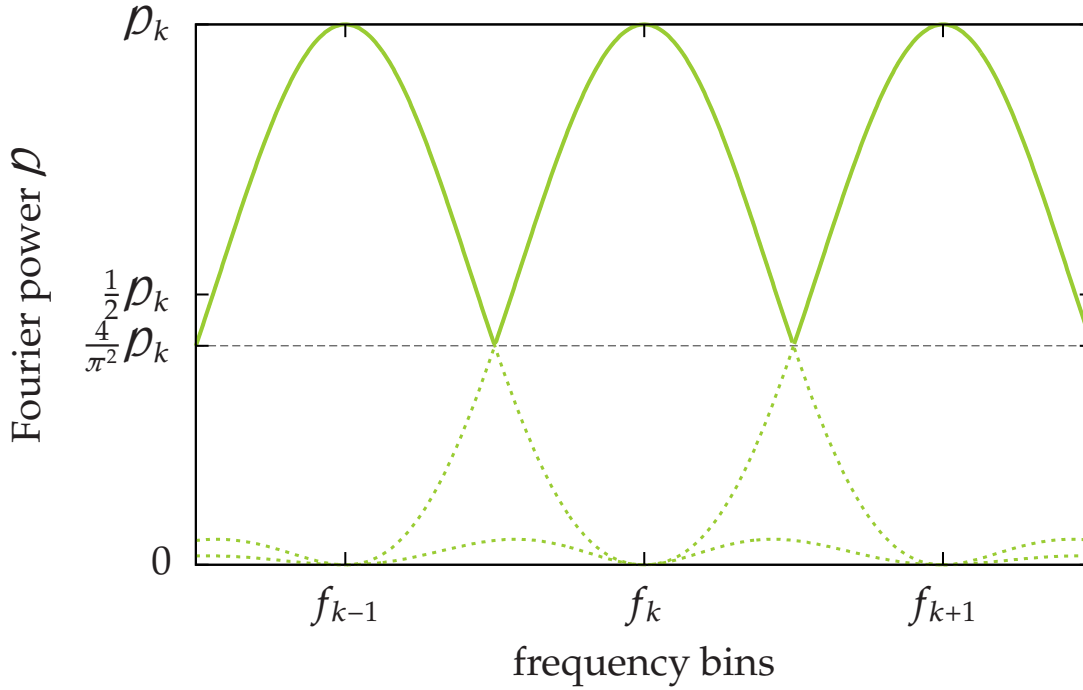


**Figure 3.24:** Illustration of scalloping in Fourier domain. The three curves shows the sinc-function power responses from Equation (3.70) of three Fourier bins to a sinusoidal signal. The thick curve is the envelope of all responses and shows the overall DFT response to a signal at any frequency. The worst response of  $\frac{4}{\pi^2} \approx 0.41 P_k$  in power is in the middle between two Fourier bins.

see Equations (2.28) to (2.30) in Ransom (2001). Typical values for  $n$  are of order 16. Since the frequency must be known in advance, the use of this method is restricted to special cases.

**Method c)** is the special case of Equation (3.72) for  $n = 1$ ; one finds, see Equation (2.31) in Ransom (2001),

$$\mathcal{A}_{k+\frac{1}{2}} \approx \frac{\pi}{4} (\mathcal{A}_k - \mathcal{A}_{k+1}) \quad \text{and} \quad \rho_{k+\frac{1}{2}} = \left| \mathcal{A}_{k+\frac{1}{2}} \right|^2. \quad (3.73)$$

This is a cheap way of reducing the power loss from 59% in the unmodified DFT to only 14.3%<sup>27</sup>. It comes however with drawbacks: the computed “interbinned” Fourier bins (interbins) are no longer statistically independent, making the reliable estimates of statistical significances more difficult; there is a correlation between each interbin and the two initial independent Fourier bins it was computed from. The distribution of the power values in the presence of noise alone also is changed. Furthermore, if phase information is needed, interbinning is less useful as it does not correctly retain phase information. A variation of the interbinning scheme from Lorimer and Kramer (2005) is

$$\rho_k = \frac{1}{2} \max \left\{ 2|\mathcal{A}_k|^2, |\mathcal{A}_{k-1}|^2 + |\mathcal{A}_k|^2, |\mathcal{A}_k|^2 + |\mathcal{A}_{k+1}|^2 \right\}. \quad (3.74)$$

Here, each Fourier power is maximised over the three possible combinations involving the central bin and its two neighbours. Any signal spread over two bins can be recovered with

<sup>27</sup>Ransom (2001) cites a value of 7.4% in amplitude, which translates to the given value in power

this method. It has to be kept in mind, that the same comments about introduced statistical dependence and changes in the distributions in the noise-only case apply as well.

**Method d)**, the padding of time series is straightforward to understand and apply. Here, the initial time series of  $N$  bins is extended to in total  $k_{\text{pad}}N$  bins, where we call  $k_{\text{pad}} > 1$  the *padding factor*. The additional bins are filled with a constant value and the DFT of the padded time series is computed. This increases the number of necessary computations, but it has the advantages compared to the methods above: here, all frequency bins have the same statistical properties. Its practical implementation also is straightforward as one does not need to implement any maximisation or additional steps; the DFT algorithm simply is run on the padded time series.

Depending on what value is chosen for the padding constant, there are two often-used cases: if all additional bins are filled with zeros, this is called *zero-padding*, if they are filled with the mean of the others bins in the time series, the method is called *mean-padding*.

For the mean-padding, the constant value contributes effectively no power to the frequency components for non-zero frequency. However, since the number of bins has been increased by a the padding factor  $k_{\text{pad}}$ , the effective observation time is increased to  $T_{\text{obs}}^{\text{eff}} = k_{\text{pad}}T_{\text{obs}} > T_{\text{obs}}$ . Thus, the initial frequency resolution  $df$  is improved by the padding factor to

$$df_{\text{pad}} = \frac{1}{T_{\text{obs}}^{\text{eff}}} = \frac{df}{k_{\text{pad}}}. \quad (3.75)$$

This further means that this effectively adds frequency bins in between the initial Fourier bins and mitigates the effects of DFT scalloping. This is illustrated in Figure 3.25 where we show the effect of mean padding with a padding factor of  $k_{\text{pad}} = 3$ . Then, the frequency resolution is increased by a factor of three, and two additional bins are computed in between two of the initial Fourier bins. In the Figure, the initial Fourier bin responses are shown in dashed green lines, and the additional bins gained from the padding in dashed grey lines. The envelope of all of those, which is the overall padded DFT response, is shown in a thick green line. The worst case power loss is now only  $1 - \text{sinc}^2\left(\frac{\pi}{6}\right) = 1 - \frac{9}{\pi^2} \approx 8.8\%$ , compared to the 59.5% for the unpadded case.

In fact, we use mean padding with a padding factor of three for the Einstein@Home search. This way, the maximum loss in frequency is the above quoted 8.8%, which is below the target value of 10%. In general, for a padding factor  $k_{\text{pad}}$ , the maximum overall loss in Fourier power due to DFT scalloping is given by

$$\frac{\rho_r}{\rho_k} = 1 - \text{sinc}^2\left(\frac{\pi}{2k_{\text{pad}}}\right). \quad (3.76)$$

This translates into 18.9% for  $k_{\text{pad}} = 2$ , 8.8% for  $k_{\text{pad}} = 3$ , 5.0% for  $k_{\text{pad}} = 4$ , and 3.2% for  $k_{\text{pad}} = 5$ .

Moreover, for the mean padding there is a continuous transition of the time series to the constant mean value. In the case of *zero* padding and non-zero mean, padding the time series with zeros would introduce a step in the padded time series. A discontinuous step has frequency contributions at high frequencies which could interfere with the actual signal frequency components present in the data. Therefore, mean padding is in general to be preferred to zero-padding (Ransom, 2001). Another possibility is to subtract a constant value from all initial time series bins such that the mean is zero.

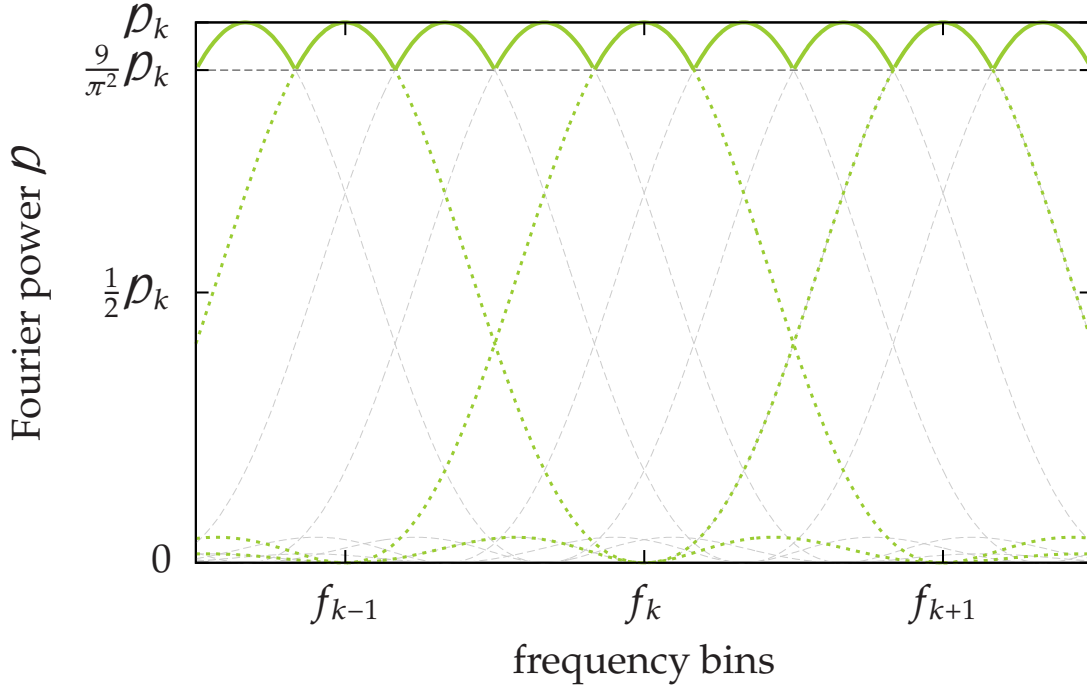


**Figure 3.25:** Illustration of mean-padding with a padding factor  $k_{\text{pad}} = 3$  to mitigate scalloping in DFTs. The initial Fourier bin responses are shown in dashed green lines, and the additional bins gained from the padding in dashed grey lines. The envelope of all of those, which is the overall padded DFT response, is shown in a thick green line.

### Periodic signal in white noise

In almost all practical applications, the data stream consist of a periodic signal and added white noise. The sensitivity of Fourier methods to periodic signals can be used to efficiently detect weak periodic signals buried deeply in the noise given a long enough time series. If the signal is consistently present in the time series, it adds coherently to a *single* Fourier bin<sup>28</sup>, while the white noise randomly adds to *all* bins in the DFT (Ransom, 2001).

Consider a periodic signal of the form

$$s(t) = \mathcal{A}_0 \sin(2\pi f_k t), \quad (3.77)$$

with the frequency  $f_k$  at the center of a Fourier bin. Rewriting in the discrete form for a time series of  $N$  samples

$$s_i = \mathcal{A}_0 \sin\left(2\pi f_k \frac{i}{N}\right), \quad (3.78)$$

covering an observation time  $T_{\text{obs}}$ . This signal causes a (unnormalized) Fourier power as defined by Equation (3.63) of

$$\rho_k = |\mathcal{A}_k|^2 = \frac{|\mathcal{A}_0|^2 N^2}{4} = \frac{|\mathcal{A}_0|^2 N^2}{4} \quad (3.79)$$

<sup>28</sup>that is: if the signal is at the center of a Fourier bin, in the other cases, it can be almost perfectly reconstructed to a single bin using the methods described above to improve the Fourier response.

Normalising the  $\mathcal{A}_k$  by  $\sqrt{N\langle s_i^2 \rangle}$  (Lorimer and Kramer, 2005; Ransom, 2001) in the presence of noise yields  $\rho_k^{\text{norm}} = \frac{|\mathcal{A}_0|^2 N}{4\langle s_i^2 \rangle}$  for the normalised power. Replacing  $N = T_{\text{obs}}/t_{\text{samp}}$ , we arrive at

$$\rho_k^{\text{norm}} = \frac{|\mathcal{A}_0|^2 T_{\text{obs}}}{4\langle s_i^2 \rangle t_{\text{samp}}}. \quad (3.80)$$

The normalised power increases linearly with observation time for a periodic signal in white noise. The Fourier amplitudes accordingly increase with the square root of the observation time. The noise on the other hand has a normalised power spectrum that follows a chi-square distribution, described in more detail in Section 3.8.7, i.e. its distribution properties do not change with longer integration times. Therefore, the signal-to-noise ratio, defined as the Fourier power normalised by the standard deviation of the noise distribution also increases linearly with the observation time. If we require that  $\rho_k > \rho_{\text{min}}$  for a minimum threshold  $\rho_{\text{min}}$  on power, we find

$$|\mathcal{A}_0|^2 T_{\text{obs}} > 4\rho_{\text{min}} \langle s_i^2 \rangle t_{\text{samp}}. \quad (3.81)$$

This inequality defines the minimum observation time  $T_{\text{obs}}$  necessary to detect a signal with an amplitude  $\mathcal{A}_0$  in white noise; we can also read it as a definition of the smallest amplitude of a periodic signal detectable in a given observation.

All the discussion so far assumed that the signal was at the center of a Fourier bin. If it lies in between Fourier bins, the equations have to be augmented by the sinc-function response derived in Equation (3.70). In practice for that case, one of the methods described above to improve the Fourier response has to be applied. This and the relations derived in this section are demonstrated in Figure 3.26.

Here, a weak periodic signal with an amplitude  $\mathcal{A}_0 = 4 \times 10^{-2}$  was “injected”, i.e. added, into random white noise with unit variance  $\langle s_i^2 \rangle = 1$  to generate a situation similar to reality. The generated time series has  $N = 2^{15}$  bins, and the signal was injected at the center of the bin  $n_{\text{sig}} = 15000$ . The panel at the top left shows the first 500 bins of the generated time series in green and the signal without noise in orange. Because the noise amplitude is a factor of 25 below the variance of the noise, the signal cannot be recognised in time domain. The panel labeled “a)” shows the complete DFT of the time series, the signal can be seen with a DFT power close to the expected value of  $\rho \approx 26.2$ , from Equation (3.79); the random noise here has increased the power by a small amount. The panel labeled “b)” shows the loss from scalloping: the signal now was injected at  $n_{\text{sig}} = 15000.5$ , in between two Fourier bins. The expected value would be  $\rho \approx 23.9$ , but in the presence of noise, random fluctuations can lower this value further as demonstrated here. The signal has the almost the same Fourier power as two other random noise fluctuations visible in this panel. For the panel labeled “c)”, the signal was padded with a padding factor  $k_{\text{pad}} = 3$  to improve the Fourier response; the signal is well recovered at the expected level.

### 3.8.5 Harmonic summing

Because a pulsar signal has a duty cycle of typically a few percent, higher harmonics contribute signal power at integer multiples of the spin frequency. Thus, signal-to-noise ratio can be increased by summing up these harmonics. The Einstein@Home search code sums up to 16 harmonics (see Section 3.8.6).

In time domain, the signal of a pulsar consists of short radio pulses, which typically cover a few percent of the pulse period  $P_0$ ; one usually defines the duty cycle  $w = W/P_0$

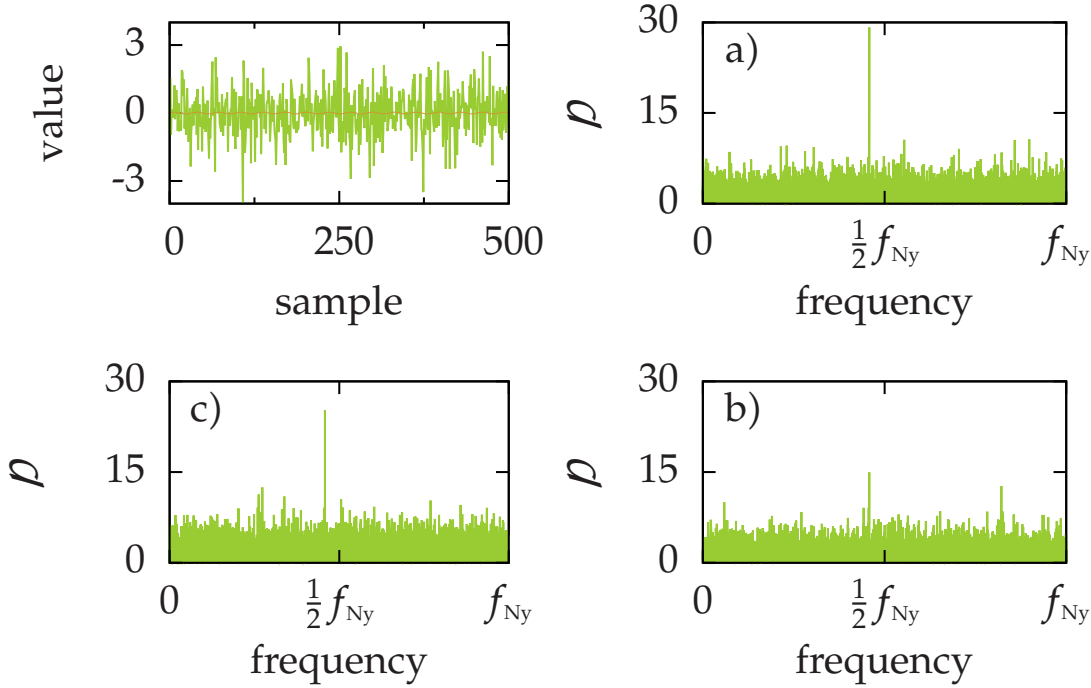


**Figure 3.26:** Illustration of DFT sensitivity and mean padding using a time series of  $2^{15}$  samples containing white noise and a weak periodic signal. The panel at the top left shows the first 500 bins of a time series in green and the signal without noise in orange. a) shows the complete DFT of the time series, if the signal is injected at the center of a Fourier bin. b) shows the loss from scalloping and random noise fluctuations, the signal was added in between two bins. In c) the signal was padded with a padding factor  $k_{\text{pad}} = 3$  to improve the Fourier response; the signal is well recovered at the expected level.

for the pulse width  $W$ . In the frequency domain this leads to the appearance of  $1/w$  *higher harmonics*, that is: signal power at integer multiples  $n f_0$  of the pulse frequency  $f_0 = 1/P_0$ . This is illustrated in Figure 3.27, where we have injected a top-hat shaped pulsed signal with a duty cycle of 5% into white noise to generate a time series of  $2^{16}$  samples. We then have computed the Fourier power spectrum which exhibits the comb of harmonics above the fundamental frequency  $f$ . We also computed the noise-free case to show the structure of the harmonics more clearly.

This can be seen as follows: assume the signal in time domain follows a top-hat shape with duty cycle  $w \in [0, 1]$ , an amplitude  $\mathcal{A}$  and a period  $P_0$

$$S(t) = \begin{cases} \mathcal{A} & \text{if } t \in [t_0, t_0 + wP_0] \\ 0 & \text{else} \end{cases} \quad \text{periodic with } P_0 \quad (3.82)$$

This  $P_0$ -periodic function can be represented in a Fourier series:

$$S(t) = \sum_{n=-\infty}^{\infty} c_n e^{in \frac{2\pi}{P_0} t} \quad \text{with} \quad c_n = \frac{1}{P_0} \int_0^{P_0} dt e^{-in \frac{2\pi}{P_0} t} S(t), \quad (3.83)$$

where the  $|c_n|^2$  carry the information about the Fourier power content of the fundamental frequency  $f_0$  and the higher harmonics. In the simple example above, it is straightforward

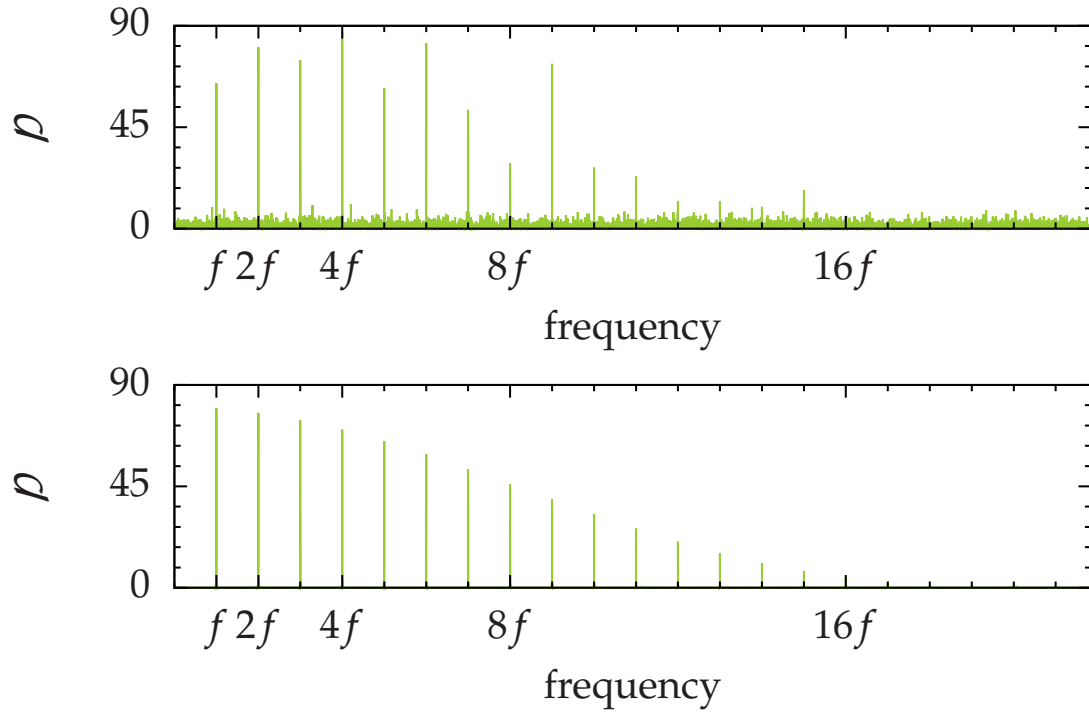


**Figure 3.27:** Illustration of comb of harmonics for a pulsed periodic signal. A top-hat shaped pulsed signals with a duty cycle of 5% was injected into white noise. **(Top)** shows the comb of harmonics in the presence of noise. **(Bottom)** shows the clean comb of harmonics in the noise-free case.

to show that

$$c_n = w \mathcal{A} e^{-i\pi\alpha} \frac{\sin(\pi n\omega)}{\pi n\omega} \quad \text{with} \quad \alpha = 2t_0 \frac{n}{P_0} + \omega n \quad (3.84)$$

and therefore

$$|c_n|^2 = w^2 \mathcal{A}^2 \frac{\sin^2(\pi n\omega)}{(\pi n\omega)^2} =: w^2 \mathcal{A}^2 \text{sinc}^2(\pi n\omega). \quad (3.85)$$

From Parseval's theorem

$$\sum_n |c_n|^2 = \frac{1}{P_0} \int_0^{P_0} dt |S(t)|^2, \quad (3.86)$$

follows for our example the total Fourier power (excluding the  $c_0 = \mathcal{A}^2 w^2$  coefficient which determines a constant offset) in all harmonics  $c_{\text{tot}}$ :

$$c_{\text{tot}} = \sum_{n \neq 0} |c_n|^2 = \mathcal{A}^2 w (1 - w) \quad (3.87)$$

and the relative power contribution of each harmonic  $c_n/c_{\text{tot}}$

$$\frac{c_n}{c_{\text{tot}}} = \text{sinc}^2(\pi n\omega) \frac{w}{(1 - w)}. \quad (3.88)$$

The duty cycle for a typical pulsar is of order  $w = 0.05$ , which means that detecting the fundamental frequency recovers only a fractional power of 10.4%, summing two harmonics 20.6%, summing four harmonics 39.6%, summing eight harmonics 68.8%, and summing 16 harmonics recovers 89.5%, respectively. Thus, summing harmonics will increase the

sensitivity to narrower pulses dramatically. This example was to illustrate the necessity of harmonics summing for the detection of weak pulsed signals. A more detailed study can be found in (Lorimer and Kramer, 2005) and (Ransom, 2001).

### 3.8.6 Einstein@Home search Fourier techniques

For the Einstein@Home search, we make use of some of the techniques described above: mean-padding and incoherent harmonic summing, the latter of which was implemented from scratch for Einstein@Home. A third technique is the maximisation of the detection statistic in each frequency bin over all orbital templates. Here, we summarize which of the previously presented Fourier techniques are implemented in the Einstein@Home search.

#### Mean-padding

To improve the response of the DFT to signals in between the discrete Fourier bins we mean-pad the de-dispersed demodulated time series with a padding factor of  $k_{\text{pad}} = 3$ . After the time-domain resampling, the time series is padded to three times its initial length by filling the remaining bins with the mean computed from the re-sampled bins. With the mean-padding we lose less than 8.8% in Fourier power in any signal frequency component from performing the DFT.

We compute the DFT of each mean-padded, re-sampled de-dispersed time series and compute from it the power spectrum by squaring and adding the imaginary and real part of the DFT. Using the Fourier power instead of the Fourier amplitude saves the relatively expensive computations of the square root and is statistically equivalent, if the correct noise distributions are used for the evaluation of candidate significance.

#### Incoherent harmonic summing

To improve the sensitivity of the search algorithm to pulsed periodic signals we employ the technique of incoherent harmonic summing. For each possible signal we sum one, two, four, eight, or sixteen harmonics and maximise the statistical significance over the number of summed harmonics. For each number of harmonics summed, the code constructs an internal top-list. Each of the 5 lists contains the 100 candidates with the highest summed Fourier power for the given number of harmonics. Each list entry moreover contains the orbital template, and the spin frequency.

The incoherent harmonic sum is implemented in a loop over the bins of the Fourier power spectrum. For each bin, we assume consecutively that it is the fundamental, the second, the fourth, the eighth, or the sixteenth harmonic of a possible signal. If the current bin is  $i$  and the  $n$ -th higher harmonic is considered we compute the power spectrum bin of the sub-harmonics at  $m \frac{i}{n}$  with  $m \in \mathbb{N}$  and  $m \leq n$ . We then add the power values at all respective sub-harmonics and consider the result a candidate with  $n$  harmonics at the lowest sub-harmonic  $\frac{i}{n}$ . This process is repeated for each frequency bin  $i$ .

This computation can be sped up efficiently by computing values only for  $n = 1, 2, 4, 8, 16$  and realising that the subharmonics of higher  $n$  are part of the sub-harmonics of the smaller  $n$ . Therefore, for each frequency bin  $i$  we first assume that the signal has only a single harmonic at  $i$ . We then assume that the signal has two harmonics at  $[i/2]$  (square brackets indicate nearest integer to this value) and  $i$  and sum the power values in these bins. Next, we assume that the signal has four harmonics at  $[i/4]$ ,  $[2i/4] = [i/2]$ ,  $[3i/4]$ , and  $i$ ; since we already have summed the second and the last value for the computation of the case with

two harmonics, we only need to add the remaining two values to obtain the summed power for four harmonics from the fundamental at  $i/4$ . The cases for eight harmonics from  $[i/8]$  and sixteen harmonics from  $[i/16]$  follow analogously. The resulting candidate is stored as a candidate with  $n$  harmonics at the lowest sub-harmonic  $\frac{i}{n}$  if it is more significant than the current candidate at the same frequency bin with the same number of harmonics. This last step maximises the candidate significance in each frequency bin for each number of summed harmonics.

In the computation of the sub-harmonics we round the values of  $m\frac{i}{n}$  to the nearest integer. This means that sub-harmonics of two neighbouring bins  $i$  and  $i+1$  repeat. Because we maximise over the candidate significance, this means that by the repetition of bins in the incoherent harmonic summing we obtain the most significant incoherent harmonic sum that is consistent with the trail of harmonics for any signal.

### Updating the top-lists – maximising detection statistic in frequency bins over orbital templates

Because of the correlations in the parameter space and the split of the parameter space into a frequency part and the perpendicular subspace, a single strong signal or RFI can appear as a candidate signal in the *same* frequency bin in *different* orbital templates. This increases the number of potential candidates for each physical signal present in the data.

Since the number of candidates stored internally and reported back to the Einstein@Home servers is limited, we perform a further check on each possible candidate to mitigate this effect. For each candidate generated from the search algorithm we check if there is already a candidate in the same frequency bin. If there is none, the new candidate is stored; if there is already a candidate, the new one is only stored in the internal top lists if it is statistically more significant than the existing candidate.

This check is done after performing the computations for each orbital template, so that it maximises the candidate significance in each frequency bin over all orbital templates.

#### 3.8.7 Detection statistic

The search algorithm detailed in the previous sections yields candidates for each orbital template, fundamental frequency, and number of summed harmonics. Because of the limited data volume that can be uploaded by the client machines to the Einstein@Home servers, candidates have to be selected by their statistical significance on the client machines *before* they are reported back and uploaded. Since candidates differ in their number of summed harmonics, a detection statistics has to be defined that equalises possible differences between different candidates to allow for a fair comparison.

Simply choosing the summed harmonics FFT power would introduce a strong bias for a high number of harmonics; the FFT power is always non-negative, thus adding more harmonics, even if they are noise contributions, would increase this detection statistic.

#### Basic detection statistic

To construct an estimate of statistical significance from the detection statistic value we will assume that the noise in the time series is Gaussian and stationary with unit variance and zero mean. Let the time series consist of the sum of signal  $s(t)$  and noise  $n(t)$ :

$$x(t) = s(t) + n(t) \tag{3.89}$$

If there is no signal in the de-dispersed time series ( $s(t) \equiv 0$ ), each time series bin will follow a Gaussian distribution. We define the normalised power (see Section 8.2.2)

$$\rho_i = \frac{p_i}{\sigma_n} = \frac{|\tilde{x}_i|^2}{\sigma_n}. \quad (3.90)$$

as our *detection statistic for a single harmonic*, where  $\sigma_n$  is the variance of the noise. This simplifies to

$$\rho_i = p_i = |\tilde{x}_i|^2 \quad (3.91)$$

in the case of unit variance of the noise. In practice, the unit variance of the noise for all bins is enforced by the spectral normalisation process detailed in Section 3.8.2.

If multiple harmonics are summed, our detection statistic is modified to

$$\rho_\Sigma = \sum_{i \in \mathcal{H}} \rho_i, \quad (3.92)$$

where  $\mathcal{H} = \{i_1, i_2, \dots, i_N\}$  is the set of all indices of the  $N$  harmonics to be summed.

One can show (see Section 8.2.2 for details) that in the noise-only case  $2\rho_i$  follows a chi-square distribution with two degrees of freedom. Then,  $2\rho_\Sigma$  follows a chi-square distribution with  $2N$  degrees of freedom, accordingly. A chi-square distribution with  $n$  degrees of freedom is given by

$$\chi_n^2(x) = \frac{1}{2^{\frac{n}{2}} \Gamma(\frac{n}{2})} x^{\frac{n}{2}-1} \exp\left(-\frac{x}{2}\right), \quad (3.93)$$

see Section 8.2.3 for a derivation of this general expression and the more specific cases for  $n = 1$  and  $n = 2$ , the latter being the distribution of the  $2\rho_i$ .  $\Gamma$  is the Gamma function, see Section 8.2.3. Figure 3.28 shows the distribution functions as a function of the  $2\rho$  value.

### Estimating the significance

The statistical significance of any candidate is obtained by comparing the summed harmonic power  $\rho_\Sigma$  with the *false alarm probability* from the noise-only case. The false alarm probability is the probability that a candidate is due to random fluctuations of noise alone and is used as a measure of the statistical significance.

When  $N$  harmonics are summed for a candidate, the power spectrum bins in the noise-only case (assumed as ideal white Gaussian noise) follow the distribution

$$p(\rho_\Sigma) d\rho_\Sigma = \chi_{2N}^2(2\rho_\Sigma) d(2\rho_\Sigma) = \frac{1}{2^{N-1} \Gamma(N)} x^{N-1} e^{-\rho_\Sigma} d\rho_\Sigma. \quad (3.94)$$

The complement of the cumulative distribution function of a chi-square distribution  $\chi_n^2(x)$  is given by the incomplete upper Gamma function, Section 8.2.3

$$\begin{aligned} Q_n(x) &= \Gamma\left(\frac{x}{2}; \frac{n}{2}\right), \\ &= \frac{1}{\Gamma(\frac{n}{2})} \int_{\frac{x}{2}}^{\infty} dy y^{\frac{n}{2}-1} e^{-y}. \end{aligned} \quad (3.95)$$

Then, the false-alarm probability  $p_{\text{fa}}$  of a candidate with  $N$  summed harmonics and a summed power  $\rho_\Sigma$  is

$$p_{\text{fa}} = Q_{2N}(2\rho_\Sigma) \quad (3.96)$$

$$= \frac{1}{\Gamma(N)} \int_{\rho_\Sigma}^{\infty} dy y^{N-1} e^{-y}, \quad (3.97)$$

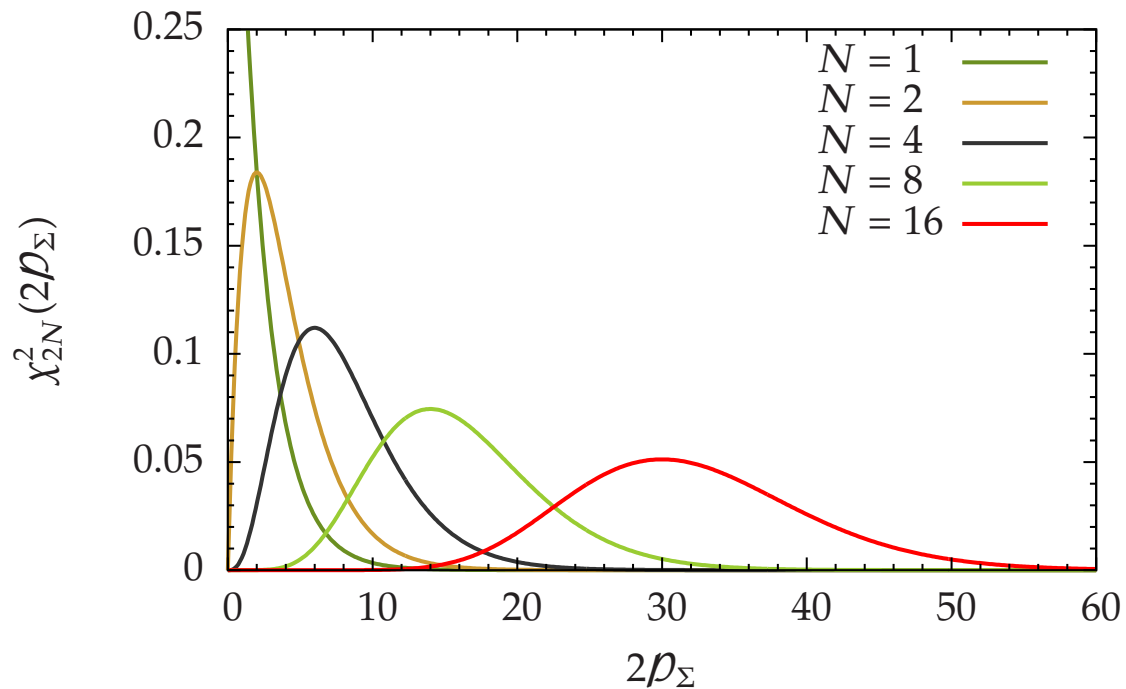


**Figure 3.28:** The probability distribution functions  $\chi_{2n}^2$  for  $n = 1, 2, 4, 8, 16$ . These are the distributions of  $2\rho_\Sigma$  arising when summing 1, 2, 4, 8, and 16 harmonics in the power spectrum, respectively.

where the integral can be readily computed by means of numerical methods implemented in software libraries like the GSL (Galassi, 2009).

In practice it is useful to consider a monotonic function of  $p_{fA}$  to translate the in most cases very small false alarm probabilities into a more useful range of values. We define the *significance*  $\mathcal{S}$  of a candidate with  $N$  summed harmonics and a summed power  $\rho_\Sigma$  by

$$\mathcal{S}(\rho_\Sigma, N) = -\log_{10}(p_{fA}) = -\log_{10}(Q_{2N}(2\rho_\Sigma)). \quad (3.98)$$

Figure 3.29 shows the significance as a function of  $2\rho_\Sigma$  for a range of summed harmonic power values and the assumption that  $N = 1, 2, 4, 8$ , and 16 harmonics are summed.

### Asymptotic significance

From Figure 3.29 an asymptotic behaviour of the defined significance  $\mathcal{S}$  is apparent. From formula (26.4.12) in Abramowitz and Stegun (1984) we find the asymptotic behaviour of the false alarm probability from Equation (3.96) as

$$p_{fA} = Q_{2N}(2\rho_\Sigma) \approx \frac{\rho_\Sigma^{N-1} e^{-\rho_\Sigma}}{\Gamma(N)}, \quad (3.99)$$

and thus the asymptotic significance as

$$\mathcal{S}_a(\rho_\Sigma, N) \approx \log_{10}(e) \rho_\Sigma - (N-1) \log_{10}(\rho_\Sigma) + \log_{10}(\Gamma(N)). \quad (3.100)$$

For large  $\rho_\Sigma$ , the asymptotic significance grows linearly with logarithmic corrections in  $\rho_\Sigma$ . This can be used to extend the computation of  $\mathcal{S}$  to very large values of  $\rho_\Sigma$ , for which the numerical computation used for  $Q$  in Equation (3.98) breaks down. Figure 3.30 shows the relative error of the asymptotic approximation  $\mathcal{S}_a$  as a function of  $\mathcal{S}$ .

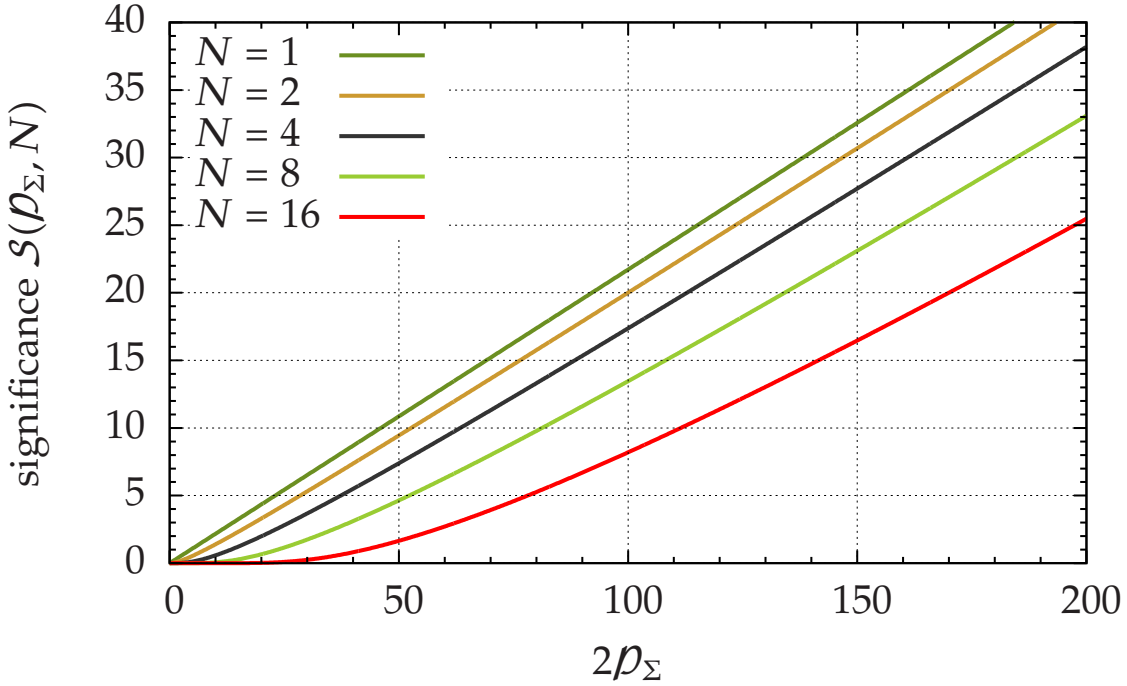


**Figure 3.29:** Significance  $\mathcal{S}(\rho_\Sigma, N)$  from Equation (3.98) as a function of summed harmonic power  $\rho_\Sigma$  and number of harmonics  $N$ . Note, that the significance is a logarithmic scale to base 10.

### Candidate selection by significance

For the selection of candidates from the analysis, their statistical significance is estimated by the method detailed in the previous section. The most significant candidates from the analysis of each de-dispersed time series are chosen. The number of candidates that can be reported back from the volunteer’s computers is limited by the bandwidth capacity and the total amount of data that can be post-processed on the Einstein@Home servers subsequently.

Further, a large enough number of candidates has to be generated to ensure a *validation* of the results (see Section 3.9); results returned from a single volunteer’s computer must not be trusted for different reasons, therefore each results is computed by at least two different computers, and compared for agreement afterwards. A minimum number of  $n_{\text{ret}}$  candidates to be returned is required for successful validation.

For the Einstein@Home search on PALFA data, these two constraints result in returning the 100 most significant candidates for each de-dispersed time series, thus yielding 63,000 unconsolidated candidates per observed telescope beam for post-processing on Einstein@Home servers.

Candidates have to be selected based on their statistical significance  $\mathcal{S}$  on the side of the client machines before upload. This goal can be achieved by applying thresholds on the significance a candidate has to reach to be accepted and uploaded. The computation of significances by Equation (3.98), however, is computationally expensive due to the computation of the  $Q$ -value.

Therefore, the search algorithm internally uses five independent top lists (of  $n_{\text{ret}}$  candidates each), for the optimised sum of 1, 2, 4, 8, and 16 harmonics. These top lists are sorted

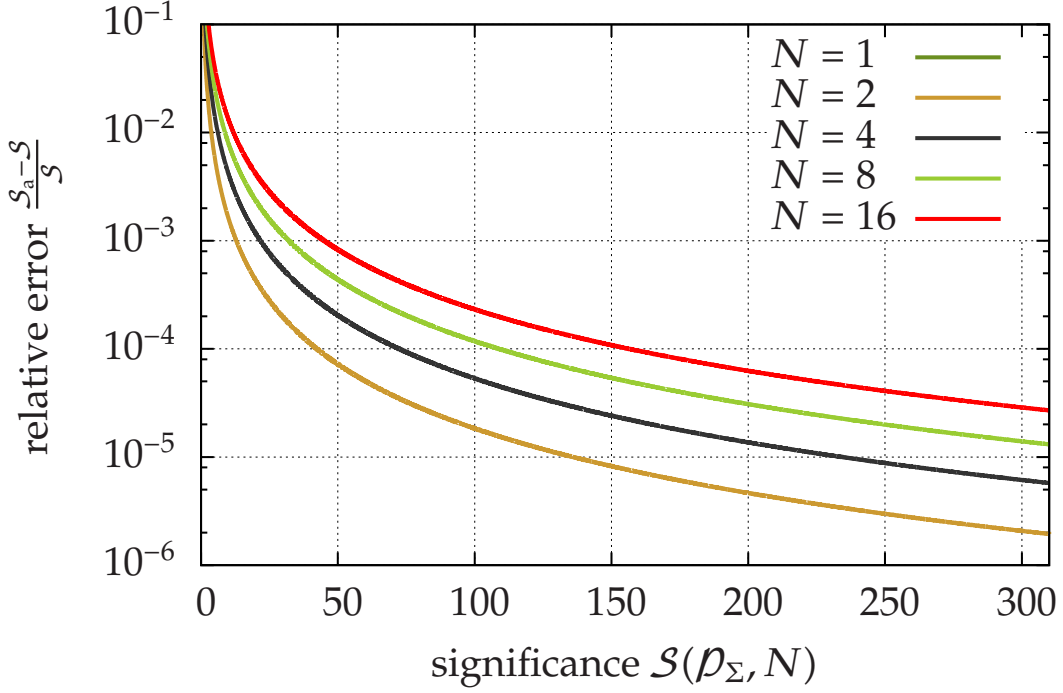


**Figure 3.30:** The relative error of the asymptotic significance  $S_a(\rho_\Sigma, N)$  from Equation (3.100) as a function of the exact significance  $S(\rho_\Sigma, N)$  from Equation (3.98).

by the summed harmonic power, which is a valid proxy for the significance  $S$  as long as only candidates with the same number of summed harmonics are compared. These five top lists are updated after the analysis for each orbital template. When the computation for all orbital templates is finished, the significances for the  $5n_{\text{ret}}$  candidates are computed. Then, a list of *all* candidates is generated and ordered by their significance. Finally, the most significant (top)  $n_{\text{ret}}$  candidates out of the  $5n_{\text{ret}}$  total candidates are returned to the Einstein@Home servers.

### Computation of thresholds on significance

To meet the need of a minimum number of candidates per analysed de-dispersed time series, the thresholds on candidate summed power and significance are computed as follows.

Assume the  $N_{\text{cand}}$  most significant candidates (independent of the number of harmonics summed for each one) should be obtained for each de-dispersed time series. Let the orbital template bank contain  $N_{\text{templ}}$  templates. Given a total false alarm probability  $p_{\text{fa}}$  per analysed Fourier spectrum (i.e. for a single orbital template), we then expect

$$N_{\text{fa}} = N_{\text{templ}} p_{\text{fa}} \quad (3.101)$$

false alarm candidates from noise alone in the analysis of  $N_{\text{templ}}$  orbital templates. If a minimum number of candidates to be returned is required  $N_{\text{fa}} \geq n_{\text{ret}}$ , we find

$$p_{\text{fa}} \geq \frac{n_{\text{ret}}}{N_{\text{templ}}}. \quad (3.102)$$

We assume here that the orbital templates are independent from each other; in reality this might not be true, templates can be correlated, and the *effective* template number is lower.

In this case, Equation (3.101) underestimates the number of false alarms; a safety factor  $> 1$  should be applied to the wanted false alarm rate to correct for this effect. In the absence of a signal, the “false alarm candidates” can be used for the validation of the results. To ensure a large enough number of these candidates, a low enough threshold on the values of the power spectrum bins has to be set. The threshold should not be set too low, since this will cause more candidates to be tested against the internal top lists, potentially slowing down the analysis.

For the construction of the threshold on the power spectrum bins,  $p_{\text{fa}}$  has to be converted into a *single-bin* false alarm probability  $\rho$ . Assume that  $N_f$  independent frequency bins are used in the Fourier analysis; then, the probability that none out of these bins causes a false alarm is given by  $(1 - \rho)^{N_f}$  and the probability that one bin causes a false alarm is  $1 - (1 - \rho)^{N_f}$ . Equating this with the per Fourier-analysis false alarm probability  $p_{\text{fa}}$  and solving for  $\rho$  yields

$$\rho = 1 - (1 - p_{\text{fa}})^{\frac{1}{N_f}}. \quad (3.103)$$

This false alarm probability can be converted into a minimum significance by

$$\mathcal{S}_{\text{min}} = -\log_{10}(\rho). \quad (3.104)$$

From Equation (3.96) the single-bin false alarm probability is equivalent to a threshold  $2\mathcal{D}_{\text{min}}$  on  $2\mathcal{D}_{\Sigma}$  for a candidate from  $N$  summed harmonics via

$$\begin{aligned} \rho &= Q_{2N}(2\mathcal{D}_{\text{min}}) \\ &= \frac{1}{\Gamma(N)} \int_{\mathcal{D}_{\text{min}}}^{\infty} dy y^{N-1} e^{-y}. \end{aligned} \quad (3.105)$$

This requires solving this implicit equation for  $\mathcal{D}_{\text{min}}$  for given  $\rho$  and  $N$ . Numerical software libraries like the GSL (Galassi, 2009) contain pre-defined functions for a relatively fast yet still expensive computation of inverse  $Q$ -values for chi-square distributions.

By setting the per template false alarm probability  $p_{\text{fa}}$  in dependence on the size of the orbital template bank we ensure to obtain (even in the noise-only case) at least  $n_{\text{ret}}$  candidates. The search code then computes thresholds on  $\mathcal{D}_{\Sigma}$  for the different harmonic sums from Equation (3.105) and only considers candidates for the internal top lists that exceed the corresponding threshold and the minimum power of the candidate with the smallest  $\mathcal{D}_{\Sigma}$  in the list.

As an example, consider the Einstein@Home search on PALFA data, where  $N_f = 3 \times 2^{21}$  and  $N_{\text{templ}} = 6661$ ; at least  $n_{\text{ret}} = 100$  candidates are to be returned for validation purposes. Then,  $p_{\text{fa}} \geq \frac{100}{6661} \approx 0.015$ . The search used  $p_{\text{fa}} = 0.04$ , which is equivalent to a single-bin false alarm probability of  $\rho = 1.30 \times 10^{-8}$ , a significance  $\mathcal{S}_{\text{min}} = 7.89$ , and thresholds on  $\mathcal{D}$  of 18.1, 21.3, 26.3, 34.7, and 49.0 for 1, 2, 4, 8, and 16 summed harmonics, respectively.

The set of thresholds for an unrealistically high false alarm probability  $\rho = 0.075$  is illustrated in Figure 3.31.

### 3.8.8 GPU search code

After the successful launch of the search code on Einstein@Home in March 2009, it became soon clear that the program might benefit in terms of speed from parallelisation in several parts of the code. A version of the code running on NVidia Graphics Processing Units

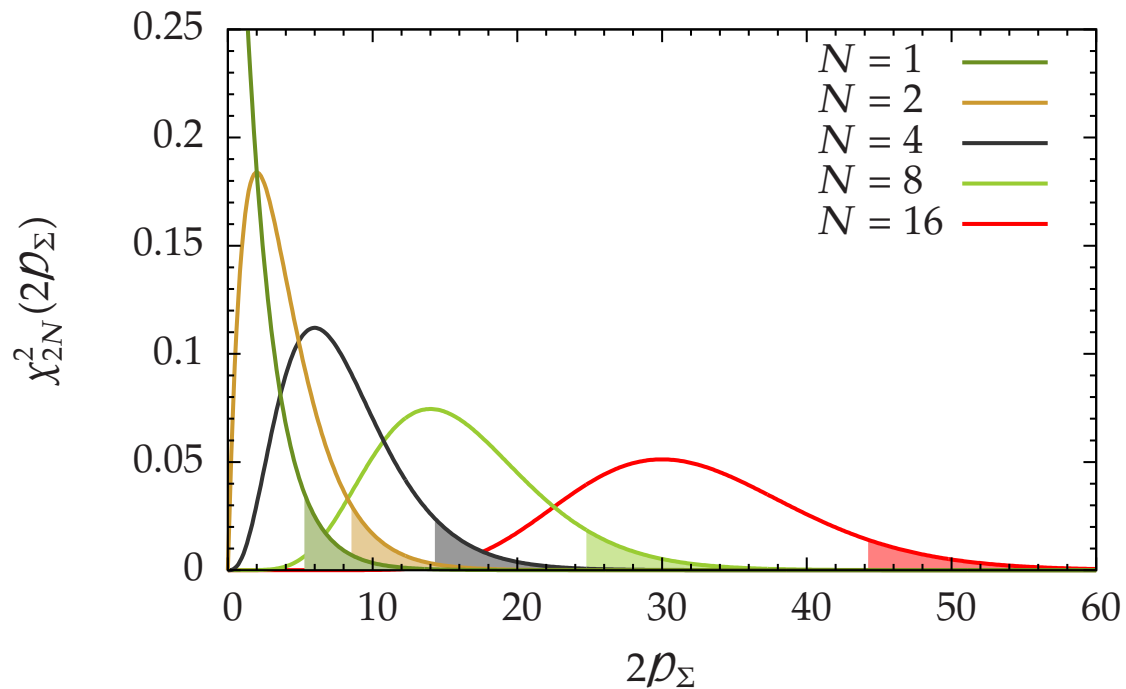


**Figure 3.31:** Illustration of thresholds on  $2\rho_\Sigma$ . This graph shows the noise-only distributions of power spectra values for different numbers of harmonics summed. The shaded areas indicate the upper 7.5%-quantile of the distribution function, thus any candidate in the shaded area for the corresponding number of summed harmonics would have a significance of  $\mathcal{S} \geq -\log_{10}(0.075) \approx 1.12$ .

(GPUs) was developed by Bock (2010). Here, we briefly review GPU computing and the implementation of the Einstein@Home search.

In contrast to regular CPUs with about a dozen processor cores at most, GPUs have up to many hundred processing cores that can run computations in parallel, allowing for potential speed-ups in parallelisable computation problems. GPUs are used in addition to a CPU and can speed up certain kinds of computations enormously. Modern GPUs reach peak performances of more than  $\sim 1$  TeraFlop/s, e.g. for the Tesla C2070<sup>29</sup>. Compare this for example to the ATLAS computing cluster: it reached 52 TFlop/s peak performance in the Linpack benchmark test with 5420 CPU cores<sup>30</sup>; under ideal circumstances, the same peak performance could be achieved by only 52 GPUs. This is only an order-of-magnitude estimate, the actual speed-up achievable with GPUs can be much smaller. Limits to the speed-up come from the amount of fast memory accessible to the cores on the GPU or non-parallelisable parts of the problem.

The GPU implementation of the Einstein@Home radio pulsar search by Bock (2010) uses the “Compute Unified Device Architecture” (CUDA) software framework<sup>31</sup> for the parallel computing implementation. CUDA provides a C/C++ framework to develop, compile and run specific codes, so-called “kernels”, on NVidia GPUs. This framework allows for easy transfer of kernels and data to and from the main memory to GPU memory, and to execute the kernels on the GPU cores. Special care has to be taken to make optimal use of the large

<sup>29</sup>[http://www.nvidia.de/docs/I0/43395/NV\\_DS\\_Tesla\\_C2050\\_C2070\\_jul10\\_lores.pdf](http://www.nvidia.de/docs/I0/43395/NV_DS_Tesla_C2050_C2070_jul10_lores.pdf)

<sup>30</sup><http://www.top500.org/system/performance/9234>

<sup>31</sup>[http://www.nvidia.com/object/cuda\\_home\\_new.html](http://www.nvidia.com/object/cuda_home_new.html)

amount of available computing power and to exploit the possibilities of many computation threads running in parallel.

NVidia further developed libraries for the computation of Fast Fourier Transform on NVidia GPUs. The necessary library (CUFFT) can be linked into CUDA kernels to speed up the computation of FFTs. Because the Einstein@Home radio pulsar search relies heavily on this type of computation, the first step in the porting of the search code to GPUs was the replacement of the use of FFTW on the CPU by CUFFT on the GPU. All other computations were still conducted on the CPU at this point. Because the CPU code spends about two thirds of its runtime computing FFTs, this sped up the code by a factor of about three; It used a full CPU core and made only minor use of the full capacities of a GPU.

In the next step, further steps of the computation were ported to the GPU and implemented with CUDA. The current code conducts for each orbital template the time-domain resampling, the computation of the Fourier transform, and the harmonic summing on the GPU. The only parts of the code remaining completely on the GPU are the initial spectral normalisation and zapping of known RFIs, the collection of candidates after each the computation is finished for each orbital template, and the final result file construction. Different orbital samples are done serially; working on multiple time-domain re-samplings, and FFTs of them is prohibited for the radio pulsar search by the amount of fast memory available on typical GPUs.

For typical workunits, the average speed-up was about a factor of 15 for the Einstein@Home radio pulsar search running on NVidia GPUs compared to the corresponding CPU workunit.

### 3.8.9 Result file format

For each analysed de-dispersed time series, one result file is generated. Note, that bundling multiple de-dispersed time series into a single workunit means that a single workunit can produce multiple result files. The result files from the CPU and the GPU search code are ascii text files in a fixed format. Each result file contains 100 lines, each representing one of the 100 most significant candidates found in the analysis of the given de-dispersed time series.

Each line contains seven values, representing different properties of the candidate; the quantities reported are in order as they appear in each line: spin frequency  $f$  in Hertz, orbital period  $P_{\text{orb}}$  in seconds, projected orbital radius  $\tau$  in light-seconds, initial orbital phase  $\psi$  in radians, summed harmonic power  $\mathcal{P}_{\Sigma}$  in sigma of the underlying distribution for the given number of harmonics summed, significance  $\mathcal{S}$  given the distribution for the given number of harmonics summed, and the number of harmonics summed,  $N_{\text{harm}}$ .

The result file may also contain comment lines for additional information. Comment lines are marked by starting with a percent sign (%). For the radio pulsar search on Einstein@Home comment lines are used to mark the end of a complete result file by a “done” marker (%DONE%). Comment lines are further used to obtain information about the volunteer name, the host, and the date the result was reported; these are used to associate volunteers and hosts, respectively, in the case of new pulsar discoveries and re-detections of known pulsars.

Below lines from an example result file (from the first of the two results that contain the second pulsar discovered by Einstein@Home with highest significance) are shown for illustration; the majority of the result lines in the result file body have been suppressed for brevity and are indicated by . . . .

```
% User: Vit-MIPT
% Host: 7d05eb94b34ac74f6d268955f8920849
% Date: 2010-07-02T13:34:50+00:00

48.237542311351 664.955627441406 0.001925377408 0.026667248458 34.2915 39.5784 16
24.121254682541 925.369506835938 0.018978450447 2.043694257736 33.0581 37.6724 16
48.243751128515 925.369506835938 0.018978450447 2.043694257736 39.3057 37.6344 8
24.118771155675 664.955627441406 0.001925377408 0.026667248458 32.8844 37.4046 16
48.242509365082 757.630065917969 0.011681836098 1.945477485657 37.1321 35.1357 8
...
...
48.218915859858 702.119323730469 0.046159762889 5.746006011963 18.6922 16.3869 16
%DONE%
```

Note that this pulsar is so strong that all of the 100 candidates reported are caused by the pulsar; they are either harmonically related (at half the fundamental spin frequency) or have triggered other orbital templates.

### 3.9 Validation

---

The scientific computations run on computers of the general public which cannot be controlled directly at the hardware nor system software level for integrity. Thus, any returned result could be partially or completely corrupt and incorrect. Causes for these errors can occur at the hardware, software and user level and include over-clocked hardware, defective operating system libraries, and the maliciousness of volunteers uploading faked results without computation. BOINC is also able to catch certain types of common errors during program runtime, e.g. insufficient memory or disk space, errors reported by the science application, BOINC internal inconsistencies, missing input or output files, or the manual abortion of a workunit by the volunteer. If BOINC detects such a problem, the corresponding workunit is marked as *unsuccessful* because of a *client error*, and another instance of the same workunit is generated and sent to a different client machine. This is repeated as long as at least *two* successful results are returned to the Einstein@Home servers.

At this stage it is still possible that any of the successful results still is afflicted with errors that did not cause the computation to fail or report an error. Einstein@Home's radio pulsar search software is available for different operating systems (Windows, Mac OSX on Intel processors, and GNU/Linux) and the science application on different volunteer's computers can use different floating point libraries, compiler instructions, and CPU hardware. All of this leads to minor numerical differences (acceptable to a certain level of computational accuracy) in the results of the computations that impede simple byte-by-byte comparisons of the result files. An automatic validator compares results and rejects results that do not agree within pre-defined acceptable ranges with each other. This validation process is set up in two steps, first checking the consistency of each single file then ensuring the consistency of the two results with each other.

In the first step, each result is tested to conform to the fixed seven-column output format with 100 result lines in the output file, see Section 3.8.9. Each line is scanned and each entry is confirmed to lie in pre-defined ranges. Failing any of these tests causes the result to be marked as *invalid* and causes another copy of the corresponding workunit to be sent to a different volunteer's computer.

Assuming both files have passed the first stage and are found to be valid individually, they are checked for mutual consistency in the second step. The validator tries to match

each line from one result to a line in the other result. Two lines are considered consistent and matching when the individual values for the DM, the frequency, the three orbital parameters, the summed harmonic power, and the significance agree within less than a factor of  $10^{-5}$  with the values in the second result's candidate line. The candidate's number of harmonics as integer value has to be exactly equal in both lines. Since the candidate lines are sorted by their significance, the small numerical differences can cause the order of candidate lines to vary between the results; the validator therefore searches for matching lines in the complete result file. The metric of the validation is the number of unmatched lines, if there is more than one unmatched line, both results are marked as *inconclusive*. Unmatched lines at the end of the result file (at low significances), can be excepted from the validation metric; they can be unmatched if the small numerical differences kept the matching line from appearing in the result file. Again, another instance of the workunit is generated and sent to a different client machine.

Assuming, the third result is returned to the Einstein@Home servers and passes the first stage of validation, it is compared to both inconclusive results. If it matches with one of them, these two results are marked *valid*, the result not matching the two others is marked *invalid*. If the third result does not match any of the two inconclusive results, the process of generating further instances of the workunit is repeated until two matching and therefore valid results are found. Credits are only granted for valid results.

### 3.10 Post-processing

---

When all workunits for a given beam are complete, the results are post-processed on Einstein@Home servers at Hannover. The post-processing takes place in three main steps: a) collection of the result files for each beam into a single file, b) creation of overview plots for visual inspection, and c) automated post-processing using different heuristic algorithms on the collected result files to sift through the huge number of candidates.

Keep in mind that each beam will result in 100 top candidates from 630 different dispersion measure trials, thus yielding 63,000 candidates in total. Plotting all these candidates in a handful of plots is an easy way to visualise to complete data set and even detect most of the possible pulsar signals or identify RFI contamination. This first stage is detailed in Section 3.10.1. It is possible that weak pulsars are missed in the visual inspection of these plots, therefore a more complete, automated post-processing (currently under development) is necessary as a second step.

Not all of the 63,000 candidates will be real pulsar signals, they can arise from random fluctuations of the noise or radio frequency interference. The first can be excluded to a certain fraction by thresholding on the detection statistic, making it less likely for noise fluctuations to be selected as candidates for further investigations; the latter can in some cases be identified by a peak of the signal at low dispersion measures (because of their terrestrial origin) or simultaneous occurrences in several beams of the same pointing, which is less likely to happen for pulsars (unless they are extremely bright).

Also, a strong pulsar signal will show up not only at a single dispersion measure trial value or at a single orbital template, or frequency. If a signal is strong enough it will trigger other templates with high enough significance, causing additional detections of the same pulsar. These correlations can be used in (heuristic) algorithms to discriminate pulsar signals from RFI and to reduce the number of candidates by orders of magnitude. We have implemented and used three different heuristic algorithms. They rely on reducing the

number of candidates by hierarchical identification of the strongest candidates in narrow frequency bands over a certain range in DM, matching the significance as a function of DM in narrow frequency bands, or clustering in coordinates using a first order approximation<sup>32</sup> of detection statistic coordinate correlations.

For each of these methods, harmonic relations between candidates are also exploited to further reduce the number of candidates: because of the harmonic summing step (Section 3.8.5), a pulsar can also be detected at integer multiples  $nf_0$ ,  $n \in \mathbb{N}$  and rational fractions  $\frac{n}{m}f_0$ ,  $n, m \in \mathbb{N}$  of the fundamental frequency  $f_0$ , again causing additional detections of the same pulsars. Exploiting these harmonics relations reduces the number of candidates and can be used to discriminate RFI and random noise fluctuations from pulsar signals.

As soon as a promising candidate is identified it is closer inspected by use of different tools from the PRESTO software package (Ransom et al., 2002) to fold the time series, refine spin period, spin period derivative, and dispersion measure (Section 3.10.4).

### 3.10.1 Result collection

As first step all result files for a given beam are collected into a single file. Comment lines and empty lines are removed from each individual result file for the different 630 dispersion measure trials. The result files are augmented by an additional column in the first place of each line, which contains the integer running number of the dispersion measure trial. A table of all values is used to translate this integer into the value of dispersion measure in physical units. For plotting and post-processing purposes, the running number is advantageous, because differing spacing in DM, see Section 3.7.2, causes stretching the plots. All cleaned and augmented result files are then concatenated into a single larger file which is then sorted by DM trial number. The following lines are the first ten lines from the result file containing the pulsar J1952+2630 as an example:

```
0 115.796923637390 1658.437377929688 0.006059269421 4.781784057617 41.0891 50.2176 16
0 130.229940017064 1399.123046875000 0.074442118406 5.412323474884 36.0069 42.2428 16
0 130.241115887960 1063.657348632813 0.041680149734 5.896464824677 42.5741 41.4086 8
0 130.251049995422 936.209411621094 0.024923810735 5.475196838379 50.808 50.9895 8
0 130.252291758855 1359.708496093750 0.032824844122 6.000621318817 45.5546 57.3069 16
0 130.253533522288 1359.708496093750 0.032824844122 6.000621318817 57.0367 58.2916 8
0 130.257258812586 799.355102539063 0.015022451058 5.442821502686 42.985 53.2191 16
0 130.258500576019 799.355102539063 0.015022451058 5.442821502686 49.508 49.4709 8
0 130.269676446915 1658.437377929688 0.006059269421 4.781784057617 42.6285 52.6536 16
0 130.270918210348 1658.437377929688 0.006059269421 4.781784057617 63.4139 86.1876 16
...
```

This result collection is done by a set of scripts running on daily basis controlled by a cron job to eliminate the need for regular human intervention.

### 3.10.2 Overview plots

For the visualisation, overview plots for a quick inspection are created. Useful indicators to recognise pulsars and discriminate them from RFI include

**DM peak:** any dispersed signal will show a characteristic peak if its significance is plotted as a function of the dispersion measure (Cordes and McLaughlin, 2003).

**harmonic structure:** due to the incoherent harmonic summing in the code, a signal with contributions from integer multiples of the fundamental frequency will also have

<sup>32</sup>This approximation might break down for signal from pulsars in the shortest orbits, but we expect it work well for all other cases.

highly significant candidates at integer multiples or fractions of the fundamental frequency.

**structures in parameter space:** the mismatch structures caused by correlations in the detection statistic between parameter space coordinates can also be used to quickly inspect the veracity of a candidate signal. This is similar to the correlations described by Pletsch (2008) for the gravitational-wave case.

These characteristics inspire the use of overview plots to quickly inspect the results (i.e. all 63,000 candidates) from a complete beam. This does not replace the need to identify related candidates in the complete set and to further examine the most promising and/or significant among these. The overview plots can however be used to inspect a large amount of data in short time and to detect most pulsars efficiently.

The plots found to be most useful were the following five:

1. a three-dimensional plot of significance as a function of dispersion measure and spin frequency. In this plot the DM peak as well as the harmonic structure are visible. The points are colour-coded by a measure of the spin frequency derivative.
2. a two-dimensional plot of colour-coded significance as a function of dispersion measure and spin frequency. In this plot the DM peak as well as the harmonic structure are visible. This is a version of the first plot, projected onto the DM- $f$  plane. It can avoid possible visual confusion in the three-dimensional plot.
3. a two-dimensional plot of colour-coded significance as a function of dispersion measure and spin frequency derivative.
4. a two-dimensional plot of colour-coded significance as a function of the orbital angular velocity  $\Omega = \frac{2\pi}{P_{\text{orb}}}$  and the projected radius  $\tau$ .
5. a two-dimensional plot of colour-coded significance as a function of the orbital angular velocity  $\Omega = \frac{2\pi}{P_{\text{orb}}}$  and the initial orbital phase  $\Psi$ .

Figure 3.32 shows the overview plots for the pulsar J1850+01 discovered in the PALFA survey, the numbers in the plot correspond to the numbering above.

### Plotting and clustering coordinates

For the generation of the overview plots and the automated post-processing algorithms described below, a new set of coordinates is used. The physical coordinates used for the description of the parameter space induce correlations in the detection statistic function. These correlations can be partly resolved by switching to a new coordinate system.

Pletsch (2008) has shown the use of this technique for the search for continuous gravitational waves, where the new set of coordinates can be used for the search itself, allowing to reduce the amount of necessary computation by exploiting the correlations. A similar step can be applied here for the post-processing, were we introduce new coordinates akin to the ones from Pletsch (2008).

Consider the phase model from Equation (3.11)

$$\Phi(t; \Lambda) = 2\pi f [t + \tau \sin(\Omega t + \psi)] + \Phi'_0, \quad (3.106)$$

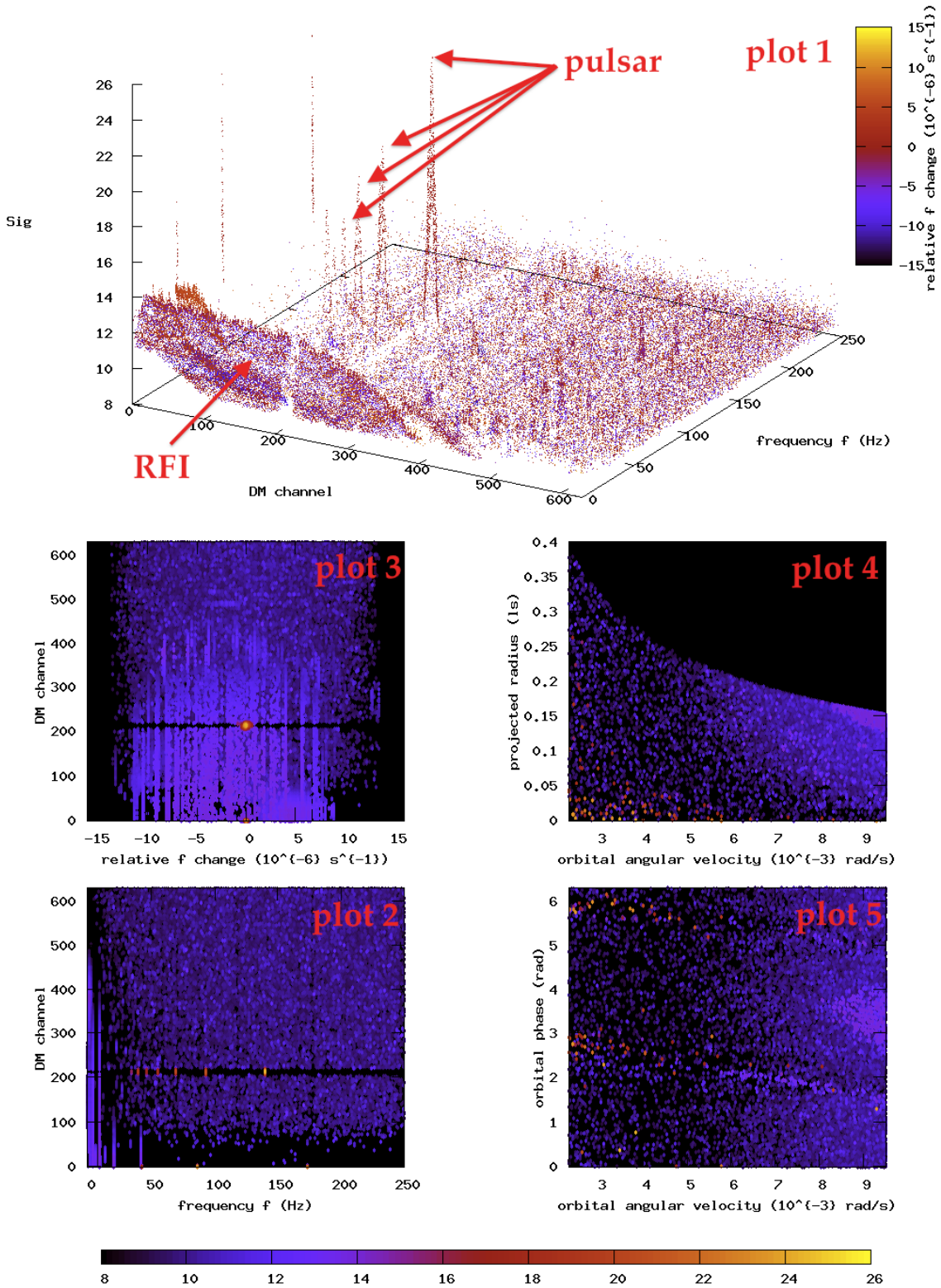


**Figure 3.32:** An example of the overview plots used for quick inspection of all the 63,000 candidates from a single beam. (Top) the harmonic structure and the DM peak are clearly visible in the three-dimensional plot of significance as a function of dispersion measure and spin frequency. (Bottom) mismatch and harmonic structures in other dimensions of the parameter space.

which we can rewrite as

$$\Phi(t; \Lambda) = 2\pi f \left( t(1 + \tau\Omega \cos(\psi)) - \frac{\tau\Omega^2}{2} \sin(\psi) t^2 - \frac{\tau\Omega^3}{6} \cos(\psi) t^3 + \mathcal{O}(t^4) \right) \quad (3.107)$$

for  $\Omega t \ll 1$ . We further define

$$v_1 := f(1 + \tau\Omega \cos(\psi)) \quad (3.108)$$

$$v_2 := -\frac{\tau\Omega^2 \sin(\psi)}{2} f \quad (3.109)$$

$$v_3 := -\frac{\tau\Omega^3 \cos(\psi)}{6} f \quad (3.110)$$

and rewrite the phase model as

$$\Phi(t; \Lambda_v) = 2\pi \left( v_1 t + v_2 t^2 + v_3 t^3 + \mathcal{O}(t^4) \right). \quad (3.111)$$

We refer the reader to sections 8.8.1 and 8.8.2 for details. The importance of these coordinates can be seen by inserting this approximation into the detection statistic from Equation (3.26):

$$\rho(\Lambda^{(t)}, \Lambda^{(s)}) = \left| \frac{\mathcal{A}}{T} \int_0^T dt \exp \left[ i \left( \Phi(\Lambda^{(t)}; t) - \Phi(\Lambda^{(s)}; t) \right) \right] \right|^2, \quad (3.112)$$

where  $\Lambda^{(s)} = \{f^{(s)}, \Omega^{(s)}, \tau^{(s)}, \psi^{(s)}\}$  and  $\Lambda^{(t)} = \{f^{(t)}, \Omega^{(t)}, \tau^{(t)}, \psi^{(t)}\}$  are the coordinate tuples for the template and the signal in parameter space, respectively. Using the approximation of the phase model from Equation (3.111), the detection statistic up to second order in  $\Omega t$  approximates to

$$\rho(\Lambda^{(t)}, \Lambda^{(s)}) \approx \left| \frac{\mathcal{A}}{T} \int_0^T dt \exp \left[ 2\pi i \left( v_1^{(s)} t + v_2^{(s)} t^2 + \dots - \left( v_1^{(t)} t + v_2^{(t)} t^2 + \dots \right) \right) \right] \right|^2 \quad (3.113)$$

The argument of the exponential is zero if and only if

$$v_i^{(s)} - v_i^{(t)} = 0 \text{ for all } i \in \mathbb{N}. \quad (3.114)$$

This follows from the fact that  $(1, t, t^2, \dots)$  is a basis of the vector space of real polynomials. Thus, the argument of the exponential can only be zero if all coefficients, thus all  $v_i^{(s)} - v_i^{(t)}$  vanish. This defines the family of “hyper-surfaces” introduced in Pletsch (2008) for the continuous gravitational wave case.

These hyper-surfaces describe the correlations between points in the parameter space. Points with a low mismatch lie on the intersection of all hyper-surfaces; if points lie far away from one of the hyper-surfaces, the corresponding coefficient  $v_i^{(s)} - v_i^{(t)}$  will deviate from zero, causing an oscillatory term in the approximated detection statistic Equation (3.113) and a deviation from the high value of the detection statistic.

Thus, plotting the coordinates  $v_1$  and  $v_2$  instead of  $f$  and a frequency derivative  $\dot{f}$  (computed from the phase model parameters) has the advantage of grouping templates triggered by the same physical signal closer together than plotting the physical parameters. In

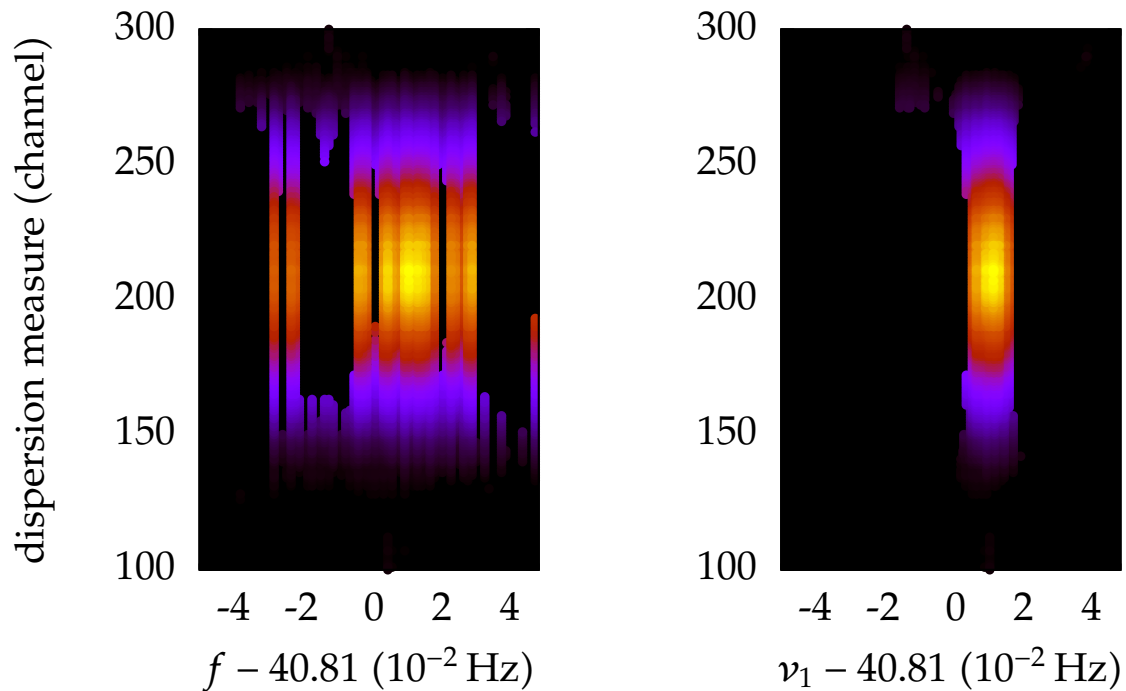


**Figure 3.33:** The use of hyper-surface coordinates for plotting reduces the spread in the plotted parameter, grouping physically related candidate signals closer together. **(Left)** Significance  $\mathcal{S}(f, \text{DM})$  as a function of spin frequency and dispersion measure. **(Right)** Significance  $\mathcal{S}(\nu_1, \text{DM})$  as a function of  $\nu_1$ , Equation (3.108), and dispersion measure. Note, the reduction of data point spread.

other words: an offset from the true value in one of the physical parameters can be compensated for in terms of detection statistic by also applying an offset in one of (or multiple) the other parameters. If, however, only a single physical parameter is plotted, this will result in an apparent spread of the parameters values. Plotting the variables defined by the hyper-surface equations mitigates this effect, since all hyper-surface equations have to be fulfilled independently.

This is demonstrated in Figure 3.33, where we show the significance  $\mathcal{S}$  as a function of spin frequency and dispersion measure for the detection beam of PSR J2007+2722. We have zoomed into a narrow frequency band around the most significant peak of candidates in the beam. The left panel shows  $\mathcal{S}(f, \text{DM})$ , while the right-hand panel shows  $\mathcal{S}(\nu_1, \text{DM})$ . Note, how much the spread in the measure of frequency is reduced by this choice.

The plots shown in Figure 3.32 in fact show  $\nu_1$  and  $\frac{\nu_2}{f}$  from Equations (3.108) and (3.109), respectively, and are referred to as “frequency” and “relative frequency change” in the axis labels.

### 3.10.3 Candidate number reduction

For each telescope beam, the Einstein@Home pipeline generates 63,000 candidates. In principle, it would be possible to consider each of these independently, follow up and refine it with other software tools. However, resulting from the set-up of the pipeline it is possible that a single real signal (depending on its strength) can cause a large number of the 63,000 candidates. In other words, seemingly “different” candidates in the collected result files are

in fact caused by the same physical signal.

This effect comes from different necessary steps in the analysis pipeline. Corrections for some of these effects could be included into the pipeline at the level of the volunteer's computers, other can only be done at the post-processing stage with the pipeline in its current set-up.

The first step causing multiple appearances of a real signal is the harmonic summing. The pipeline optimises the detection statistic by incoherently summing signal contribution at integer multiples  $n$  of the fundamental frequency  $f$ . Thus, it is possible to obtain a significant signal by starting at, say  $2f$ , and only sum signal contributions at even multiples  $2nf$  of the fundamental frequency. The same holds true for other multiples of the fundamental frequency; this means however an increasing loss in significance. It is also possible to start the harmonic summing at rational fractions  $\frac{n}{m}f$  of the fundamental frequency. Then, also a subset of the signal contributions will be summed along contributions of noise at fractional multiples in between genuine signal contributions. In both cases, only a subset of the harmonics is summed so that the highest significance should be obtained at the correct fundamental frequency; noise can skew this simple picture in the case of weak signals. As a consequence of this effect, a pulsar signal can show up at rational multiples of the fundamental frequencies of the fundamental frequency, leading to additional candidates from the same physical signal.

The second step causing multiple candidate appearances is the grid of trial dispersion measure values. It is set up fine enough so that dispersion delay is less than or equal to the full sampling time resolution. The full time resolution however, is unnecessary for the detection of slower pulsars, whose signals do not contain frequency contribution up to the Nyquist frequency. For these, the time resolution effectively could be strongly reduced; therefore, the spacing of the DM trial values, Equation (3.51), could be increased accordingly. Since this would massively reduce the sensitivity to faster spinning pulsars, this cannot be applied in general to the pipeline, and slow pulsars will be searched with effectively too many trial DMs. This means, that most bright enough pulsars will appear with a high significance at a larger set of neighbouring trial DMs. As mentioned above, this leads to a specific peak shape if the significance as a function of DM is considered (Cordes and McLaughlin, 2003). Again, this leads to additional candidates from the same physical signal.

Correlations between the parameter space coordinates in the detection statistic function also lead to additional candidates caused by the same physical signal. For example, a small offset in frequency can be compensated by an offset in the orbital parameters; similarly, there are correlations between the orbital parameters. In consequence, signal can be recovered with slightly offset physical parameters, leading to additional candidates caused by the same physical signal.

The effect of the harmonic summing could in principle be corrected for in the search code running on the volunteer's computers. This is currently not implemented, since it does not lead to a loss of signals unless very bright pulsars are in the examined beam. In this case, the beam will be examined further anyway, and additional pulsars possibly masked by the strongest one can be detected in that step. Also, the appearance of the harmonic structure is a useful feature in discriminating pulsar signals from RFI.

The spread of a signal over multiple trial DMs also is a very useful feature in the discrimination from RFI. It also cannot be corrected for in the current Einstein@Home pipeline since each volunteer's machine has access to a small subset of the trial DMs only. Consolidation of the candidates can therefore only be conducted at the post-processing stage when results

from all trial DMs are available.

In the ideal case, the correlations between the coordinates in the detection statistics could be used to define new search coordinates as in the continuous gravitational wave case (Pletsch, 2008; Pletsch and Allen, 2009). The same approximations necessary for the implementation of this approach are not possible for the most interesting case of very short orbital periods, rendering this approach very difficult here. It can however be used as a tool for the post-processing in the form of coordinates for plotting (Section 3.10.2) and clustering (see below in this section).

For the implementation of these candidate consolidation and candidate number reduction schemes, three simple ad-hoc algorithms have been implemented in software. All algorithms are available in the same piece of software, `reduce.c`; they can be run on the collected result files and process the result file by the methods described below, reduce the number of candidates, generate additional metrics for the consolidated candidates and return a shorter list of candidates which then can be followed up more extensively.

### Top-Down candidate consolidation

The simplest approach to the consolidation of candidate is a simple hierarchical approach starting at the most significant candidates and stepping down to lower significances.

Each significant candidate defines regions of frequency-DM parameter space that are assumed to belong to this candidate and blocked from further analysis; this follows the assumption that a set of candidates from the same physical signal is represented by its most significant (*top*) candidate and all associated candidates (*down*) at lower significances can be consolidated with the top one.

The iterative algorithm starts at the candidate with the highest significance in the result file. Frequency bands around rational multiples of its frequency are generated and a window in dispersion measure of fixed width is generated. Candidates inside the DM window and these frequency bands are marked as associated to the candidate this search step was initiated from. All candidates not marked as associated to some other more significant candidate are checked for association with the current top candidate. The number of associated candidates is used as an additional measure of significance for this candidate. This procedure is iterated until no candidates without association are left.

The widths of the frequency bands are chosen as the Doppler width given by the maximum Doppler modulation from templates in the orbital template bank. The width in DM is chosen fixed ad-hoc in the current implementation of the code. This could be improved by adapting the the width according to the estimated pulse width from the spin frequency and the number of summed harmonics and using formula (12) in Cordes and McLaughlin (2003).

Figure 3.34 demonstrates this candidate consolidation algorithm on the example of the discovery observation of the pulsar J2007+2722. In red we plot the candidates remaining after the consolidation process on top of all initial candidates (in grey). Only eight out of 63,000 candidates with  $S > 15$  remain after the consolidation; this threshold on  $S$  comes allowing for of order one false alarm candidate in the complete survey analysis. More than a single candidate remains in this example, because this strong pulsar exhibits candidates at fractional multiples of the fundamental frequency that are not consolidated in the algorithm.

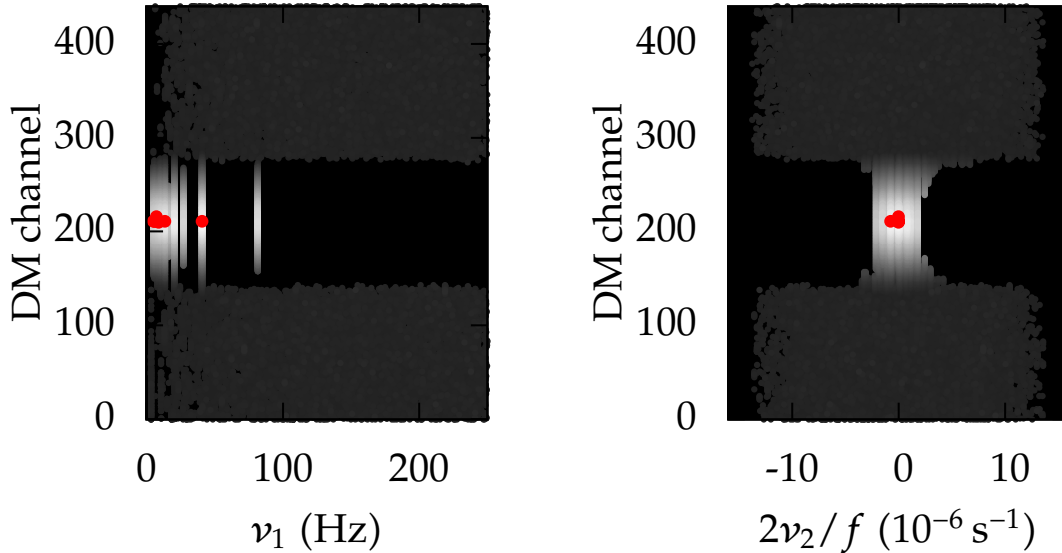


**Figure 3.34:** Candidate consolidation with the top-down algorithm, shown in  $\nu_1$  (frequency equivalent),  $2\nu_2/f$  (relative frequency change equivalent), and DM. In grey-scale all candidates in the discovery beam of the pulsars J2007+2722 before consolidation are shown. Red dots are the candidates after the consolidation procedure.

### Clustering candidate consolidation

The most developed consolidation algorithm is a clustering algorithm in the space of new coordinates for spin frequency, its derivative, and the dispersion measure. These coordinates are the hyper-surface coordinates  $\nu_1$  and  $\nu_2$ , defined in Equation (3.108) and (3.109), respectively. Real signals must lie on both hyper-surfaces, and all candidates caused by the same physical signal have to lie on the hyper-surfaces of the same two values of  $\nu_1$  and  $\nu_2$ .

Thus, defining a clustering algorithm in these coordinates is a straightforward procedure to reduce the number of candidates to that of the real signals present in the data above a certain significance threshold.

We set up an ad-hoc grid in the two-dimensional space of  $\{\nu_1, \nu_2\}$ , compute these coordinates for each candidate in the result file, and fill the grid with these candidates. Each candidate will then be associated to a *cluster*, i.e. a grid cell in the two-dimensional space. Each cluster is denoted by a single unique integer number constructed from the position in the grid.

Then, an iterative loop over all candidates is run: each candidate is checked for association with the specific cluster given by the most significant (top) candidate currently not associated with any other cluster. A counter of the number of candidates in this cluster as, a measure of the spread in dispersion measure, and the mean dispersion measure of candidates in this cluster is obtained. All candidates found to be associated with the top cluster are marked as to be ignored by the following iterations so that they cannot give rise to a new cluster with them as top candidate. This step is iterated until no candidate is left unassociated with any cluster.

Then, harmonically related clusters are identified in a second iterative loop. From now on, only *clusters* are considered in the analysis, no single candidates exist, because they have all been associated with one of the cluster that is assumed to represent it. The iterative

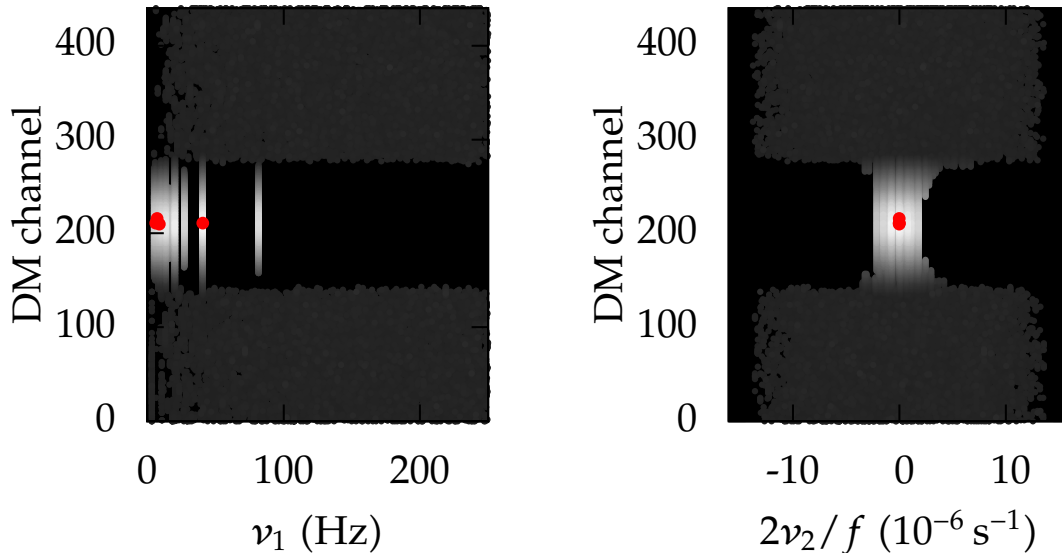


**Figure 3.35:** Candidate consolidation with the clustering algorithm, shown in  $\nu_1$  (frequency equivalent),  $2\nu_2/f$  (relative frequency change equivalent), and DM. In grey-scale all candidates in the discovery beam of the pulsars J2007+2722 before consolidation are shown. Red dots are the candidates after the consolidation procedure.

loop starts at the most significant cluster, identifies harmonically related clusters by their unique number identifier, adds candidates from the related cluster to the top cluster, and marks the clusters added as to be ignored in further iterations. This loop is repeated until no unrelated cluster or single cluster (i.e. without harmonically related clusters) is left over. The dispersion measure statistic are kept as those of the top cluster; additional checks at this stage could further ensure that no clusters unrelated in DM are clustered together. A coincidental relation in frequency is unlikely, though because of the small frequency width possible because of the clustering hyper-surface coordinates.

Finally, the remaining clusters are re-clustered with possible neighbouring clusters. An iterative loop runs through all clusters, identifies neighbouring clusters in the two-dimensional grid and adds them to the top cluster among the neighbouring set. Again, added clusters are marked not to be considered in the next iterations of the loop. This last loop is continued until all neighbouring clusters have been identified and re-clustered.

Figure 3.35 demonstrates this candidate consolidation algorithm on the example of the discovery observation of the pulsar J2007+2722. In red we plot the candidates remaining after the consolidation process on top of all initial candidates (in grey). Only four out of 63,000 candidates with  $\mathcal{S} > 15$  remain after the consolidation; this threshold on  $\mathcal{S}$  comes allowing for of order one false alarm candidate in the complete survey analysis. More than one candidate remains in this example, because this strong pulsar exhibits candidates at fractional multiples of the fundamental frequency that are not consolidated in the algorithm.

### Shape-matching candidate consolidation

The last ad-hoc algorithm further relies on the detecting the typical peak shape in the curve of significance as a function of dispersion measure. It is iterative in the same way as the

previous algorithm, looping over candidates with decreasing significance, and associating less significant ones with those at the top.

The iteration again starts at the most significant candidate in the collected result file. Here, again a Doppler window in frequency is computed, and only candidates within this frequency window are considered in the next step. Now, the width of dispersion measure however is varied over a range of typical values, allowing for more flexibility and optimisation over this free parameter. For each DM range, a least squares fit to a parabola with a width given by the DM range and peak at the top candidate is conducted. Only points with significances of at least 60% of the significance of the top candidate are considered so that the peak still closely resembles a parabola. The squared residual is recorded as a measure for the goodness of the fit. The best fitting DM range is chosen after a loop over all DM ranges for a top candidate has been completed.

Further optimisation of this algorithm is necessary to including a step that looks for harmonic relations between the obtained candidates.

This ad-hoc algorithm is currently still experimental and might not work with the same success as the clustering approach. Especially for weak signals where the top 60% candidates can lie well within the noise floor and the least-squares fit will be increasingly skewed by random contributions from the noise.

#### 3.10.4 Candidate refinement

After a candidate has been identified either by visual inspection of the overview plots (Section 3.10.2) or by the candidate reduction methods (Section 3.10.3), its parameters are refined with tools from the PRESTO software package (Ransom et al., 2002).

The subroutine `prepfold` is used to fold the raw radio telescope data at their full resolution to avoid the down-sampling necessary in the Einstein@Home pipeline. `prepfold` is provided with the spin frequency  $f$  and dispersion measure DM; it then searches an adjustable cube in the space of  $f$ ,  $\dot{f}$ , and DM around the given central position and optimises the candidate's parameters. It finally prompts the best fitting values found in the optimisation and presents a set of diagnostic plots similar to the ones described on Section 3.10.2, but constrained to a much smaller part of the parameter space. It further provides plots for the specific candidate not available for the global overview: a phase plot showing the radio emission over the observation band, a phase plot showing the consistency of the signal over the observation time, a chi-squared statistic map in  $f$ - $\dot{f}$  space and one-dimensional cuts along  $f$  and  $\dot{f}$  through the chi-square maximum (compare Figures 4.3 and 5.2).

The plots and information provided by `prepfold` allow further discrimination of real celestial signals from RFI. Pulsars are expected to emit over a wide range of radio wavelength, while RFI typically covers only a fraction of the observation band. Most pulsars also tend show continuous emission over the whole observation time, while RFI can be burst-like and very intermittent<sup>33</sup>.

In the future, the implementation of improved discrimination techniques like neural networks (Bishop, 1995) is conceivable as an additional step to the automated candidate identification. Neural networks have been successfully applied in a re-analysis of the Parkes Multibeam survey by Eatough et al. (2010) and lead to the detection of a previously unidentified pulsar.

<sup>33</sup>A prominent exception are the *nulling* pulsars, which exhibit an intermittent radio emission, sometimes switching on and off during an observation. They still do emit over a wide range of wavelength, though.

### 3.10.5 Total amount of data analysed

At the time of writing the post-processing of the results from the Einstein@Home search is under way and not yet fully completed. So far, 66162 PALFA survey beams have been successfully and completely processed by the Einstein@Home project. The overview plots from 64491 beams have been visually inspected and visually searched for pulsars. 273 detections of 137 pulsars have found by this inspection of the results. Among these are 3 detections of the two pulsars discovered by Einstein@Home.

The attentive reader will notice that the number of PALFA survey beams (68079) from Section 3.2.3 is larger than than the number of fully processed beams given here. Investigations are under way to resolve the difference and process all available PALFA survey pointings on Einstein@Home. There are several reasons for this difference.

About 700 beams suffered from data quality issues (e.g., buffer overflows in the WAPPs), which made it impossible to run these beams through the data preparation on the Einstein@Home server side. Recently, a new scheme for the data preparation has been developed, using tools from the PRESTO software suite (Ransom et al., 2002) that should be more robust against such problems in data quality and should enable successful processing of these remaining beams.

Another reason for beams not being processed by Einstein@Home is that they were not copied from the data storage facilities at the Arecibo Observatory to the CAC at Cornell University. Since all the data used by Einstein@Home were only copied from what was available at the CAC, this also contributes beams that could not be processed by Einstein@Home.

A third, and last, reason is that for some beams, there were workunits that failed to give valid results, generating repeated errors on the client machines. After a certain number of errors had been accumulated for these workunits, they were manually cancelled, i.e. no valid result had to be generated for those workunits. Likely reasons for those faulty workunits are again data quality issues that did pass the data preparation on the server side unnoticed.

All available PALFA survey beams not successfully or completely processed on Einstein@Home will be identified and re-run on Einstein@Home or the ATLAS cluster at the AEI Hannover using the improved data preparation scheme .

## 3.11 Mini mock data challenge

---

A test of the complete search pipeline was conducted with a small scale “mock data challenge” (MDC). In an MDC, fake data sets are generated, which contain possible signals with signal parameters unknown to the data analyst. Then, the data sets are fed into the pipeline and analysed using the methods described in this chapter. For each data set, the data analyst decides if a signal was present in the data and if so, at which parameters. We note, that the main goal of this test is to evaluate the detection abilities of the pipeline, signal parameter estimation is a secondary goal and not as important<sup>34</sup>.

For our MDC, ten fake data sets were generated with the code `makefakedata.c`. For each of the data sets, the following parameters were randomly chosen from a uniform distribution in the ranges indicated: spin frequency  $f \in$

---

<sup>34</sup>In the case of a promising real pulsar candidate, a confirmation observation has to be conducted, which in the case of a confirmation would be followed by a regular timing observation program to obtain orbital and spin parameters.

**Table 3.1:** Injected and recovered signals in the mini MDC. Each pair of lines shows in the first line the injected, and (if recovered) in the second line the recovered signal parameters.

| #  | injected | frequency (Hz) $f$ | DM ( $\text{pc cm}^{-3}$ ) | $\Omega$ ( $10^{-3} \text{ rad s}^{-1}$ ) | $\tau$ (lt-s) | $\psi$ (rad) |
|----|----------|--------------------|----------------------------|---|---------------|--------------|
| 1  | no       | 183.490694756      | 395.5                      | 8.065                                     | 0.060325      | 3.772151     |
|    | —        | —                  | —                          | —   | —             | —            |
| 2  | no       | 138.174455386      | 391.7                      | 9.247                                     | 0.080058      | 0.918219     |
|    | —        | —                  | —                          | —   | —             | —            |
| 3  | yes      | 154.83095568       | 304.8                      | 2.801                                     | 0.299922      | 2.805281     |
|    | yes      | 154.77339427       | 304.4                      | 3.699                                     | 0.126698      | 2.730068     |
| 4  | no       | 155.584863361      | 318.5                      | 3.304                                     | 0.042734      | 5.307378     |
|    | —        | —                  | —                          | —   | —             | —            |
| 5  | no       | 185.151335953      | 243.9                      | 3.406                                     | 0.203154      | 3.797398     |
|    | —        | —                  | —                          | —   | —             | —            |
| 6  | yes      | 100.35588174       | 346.8                      | 8.392                                     | 0.070857      | 1.860731     |
|    | yes      | 100.36677122       | 347.4                      | 7.358                                     | 0.094691      | 2.014825     |
| 7  | no       | 45.6579424118      | 303.9                      | 7.341                                     | 0.067895      | 3.886451     |
|    | —        | —                  | —                          | —   | —             | —            |
| 8  | yes      | 164.549709177      | 672.2                      | 5.472                                     | 0.017818      | 2.237935     |
|    | yes      | 164.548556010      | 672.4                      | 8.293                                     | 0.011682      | 1.945477     |
| 9  | yes      | 130.631532411      | 708.1                      | 8.821                                     | 0.122242      | 3.097706     |
|    | yes      | 130.634754896      | 708.4                      | 8.001                                     | 0.146078      | 3.227635     |
| 10 | no       | 64.9407680821      | 264.3                      | 6.743                                     | 0.182294      | 4.137015     |
|    | —        | —                  | —                          | —   | —             | —            |

[1 Hz, 250 Hz], dispersion measure  $\text{DM} \in [0 \text{ pc cm}^{-3}, 800 \text{ pc cm}^{-3}]$ , orbital angular velocity  $\Omega \in [2.33 \times 10^{-3} \text{ rad s}^{-1}, 9.52 \times 10^{-3} \text{ rad s}^{-1}]$ , projected orbital radius  $\tau \in \left[0, 6.9 \times 10^{-3} \left(\frac{\Omega}{1 \text{ rad s}^{-1}}\right)^{-\frac{2}{3}} \text{ lt-s}\right]$ , initial orbital phase  $\psi \in [0, 2\pi)$ , duty cycle  $w \in [0.04, 0.16]$ , and signal amplitude (in Gaussian noise of unit variance in each frequency channel)  $\mathcal{A}_0 \in [3 \times 10^{-3}, 5.5 \times 10^{-3}]$ . The observation time, observation frequency and bandwidth were kept fixed at the PALFA search values of  $\sim 268 \text{ s}$ ,  $1.4 \text{ GHz}$ , and  $100 \text{ MHz}$ , respectively.

For each signal, a fake filterbank file containing a signal with the randomly chosen parameters was created using `makefakedata.c`. Additionally, for each signal, it was randomly decided (in 1:1 ratio) whether to inject the signal or not. Therefore, the first step of the MDC yielded ten data sets out of which an unknown number contained each a signal with unknown parameters. The signal parameters and information about whether the signal was injected was stored in an ascii file, which was printed, and then kept under seal by a third person. The data analyst was not to gain access to this information before the analysis was completed and results were formulated.

The data sets were then analysed by the Einstein@Home search pipeline codes on the ATLAS cluster at the AEI Hannover and post-processed using methods described in this chapter.

The result of the data analysis was that four of the ten data sets contain fake signals with orbital and frequency parameters as described in Table 3.1. Comparing with the previously printed out and sealed information about injected signals revealed that the pipeline indeed performed as expected: indeed there were four signals injected at parameters that agree with the recovered parameters. Because of the influence of random noise, the discreteness of the orbital template bank, and the discrete frequency bins in the FFT, perfect parameter reconstruction is not expected. The injected parameters are also given in Table 3.1.

All injected signals were found. No signal detection was claimed in the data sets that did not contain a signal. The reconstructed signal parameters agree within the expected deviations from the injected parameters. Follow-ups on finer grids (instead of the relatively coarse template banks, designed for detection) could be used to obtain improved estimates of the orbital parameters. Therefore, this MDC demonstrates the detection ability of the Einstein@Home search pipeline.

Figure 3.36 shows the Einstein@Home result plots as introduced in Section 3.10.2 for the fake signals from injections #6 and #8. Note the pronounced offset of the relative frequency derivative from zero.

A different test conducted when running the search on real observational data is the comparison of the results from different pipelines. As we have already described in Section 3.10.5, the Einstein@Home pipeline results agree with those from the other pipelines analysing the PALFA survey data.





# 4

## Discovery of PSR J2007+2722

---

*partly appeared in Science, 329, 5997 (2010)*

---

### 4.1 Overview and context

---

Einstein@Home (Abbott et al., 2009) is a volunteer distributed computing project (Anderson et al., 2006). Members of the public “sign up” their home or office computers (“hosts”), which automatically download “workunits” from the servers, carry out analyses when idle, and return results. These are automatically validated by comparison with results for the *same* workunit, produced by a different volunteer’s host. More than 250,000 individuals have contributed; each week about 100,000 different computers download work. The aggregate computational power ( $0.25 \text{ PFlop s}^{-1}$ ) is on par with the largest supercomputers. Einstein@Home’s primary goal is to detect gravitational waves from rapidly-spinning neutron stars in data from LIGO and VIRGO (Abbott et al., 2009).

Since 2009, about 35% of Einstein@Home compute cycles have also been used to search for pulsars in radio data from the PALFA project at the 305 m Arecibo Telescope. Data disks are sent to Cornell University’s Center for Advanced Computing, where data are archived. For Einstein@Home, data are transferred to Hannover, de-dispersed for 628 different dispersion measures ( $\text{DM} \in [0, 1002.4] \text{ pc cm}^{-3}$ ), and resampled at  $128 \mu\text{s}$ . Hosts receive workunits containing time series for four DM values for one beam. Each is 2 MB in size, covering 268.435456 s. A host demodulates each time series (in the time domain) for 6661 different circular orbital templates with periods greater than 11 minutes (our Galaxy has even shorter period binaries). The grid of templates is spaced so that for pulsar spin-frequencies below 400 Hz, less than 20% of signal-to-noise ratio is lost. Fourier algorithms sum up to 16 harmonics. A total of 1.85% of the power spectrum is removed to eliminate well-known sources of radio frequency interference. A significance ( $\mathcal{S} = -\log_{10} p$ ,

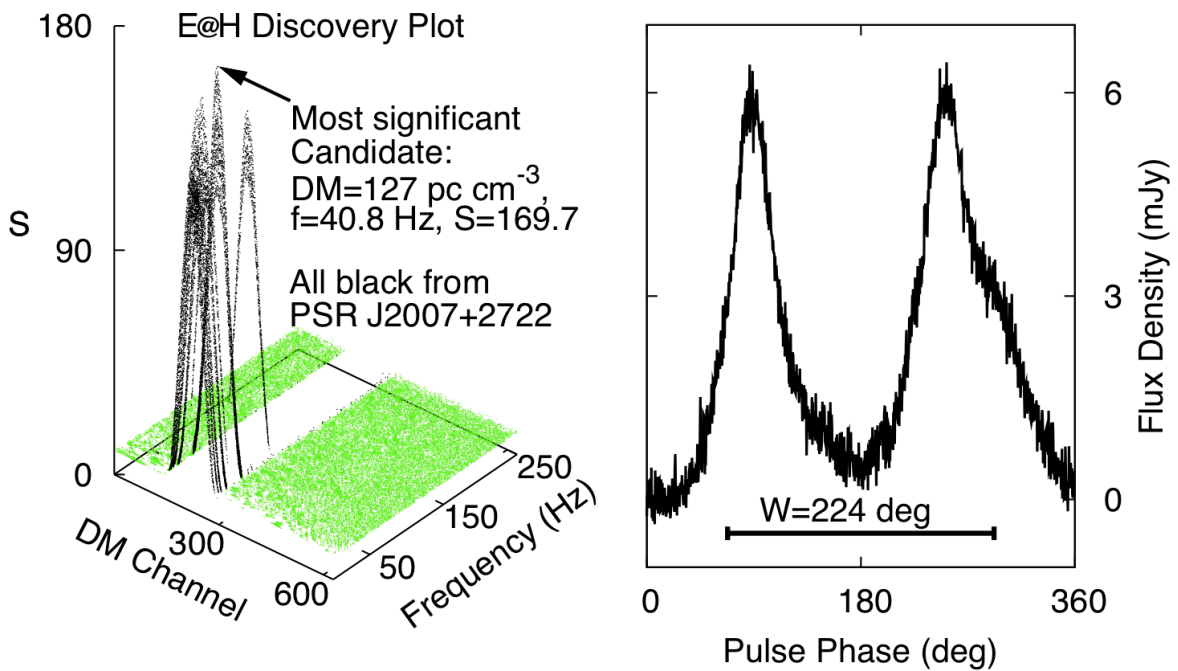


**Figure 4.1:** (Left) significance  $S$  as a function of DM and spin frequency (all Einstein@Home results for the discovery beam). (Right) the pulse profile at 1.5 GHz (GBT). The bar illustrates the extent of the pulse.

with  $p$  the false-alarm probability in Gaussian noise) is calculated at each grid-point. After  $\sim 2$  CPU-hours, the host uploads the 100 most significant candidates to the server.

When all workunits for a given beam are complete, the results are post-processed on servers at Hannover. Candidates with  $S > 15$  are identified by eye, then optimised with PRESTO (see SOM). To date (July 2010) Einstein@Home has searched 27,000 of 68,000 observed beams. It has re-detected 120 pulsars, most in the past four months, because code and algorithm optimisations sped-up the search by a factor  $\sim 7$ .

## 4.2 Discovery of PSR J2007+2722

On 11 July, the 24-ms PSR J2007+2722 was discovered with a significance of  $S = 169.7$ . Figure 4.1 displays the discovery plot from the Einstein@Home search results in the left panel.

The overview plot for all Einstein@Home candidates from the discovery beam is shown in Figure 4.2. The coordinates used in this discovery plot are explained in Section 3.10.2. The harmonic structure from detections at rational fractions and integer multiples of the spin frequency is clearly visible as well as the peak in significance as a function of dispersion measure.

The discovery plot created using the PRESTO software package (Ransom et al., 2002) is shown in Figure 4.3, which displays various useful diagnostic information: the top left plot is the folded pulse profile over two rotations of the pulsar; below it a pulse phase vs. observation time plot shows the emission of the pulsar over the observation. The grey-scale plot in the centre shows the broad-band radio emission as a function of the pulse phase and below it, the peak in  $\chi^2$  as a function of dispersion measure is displayed. In the right panel,

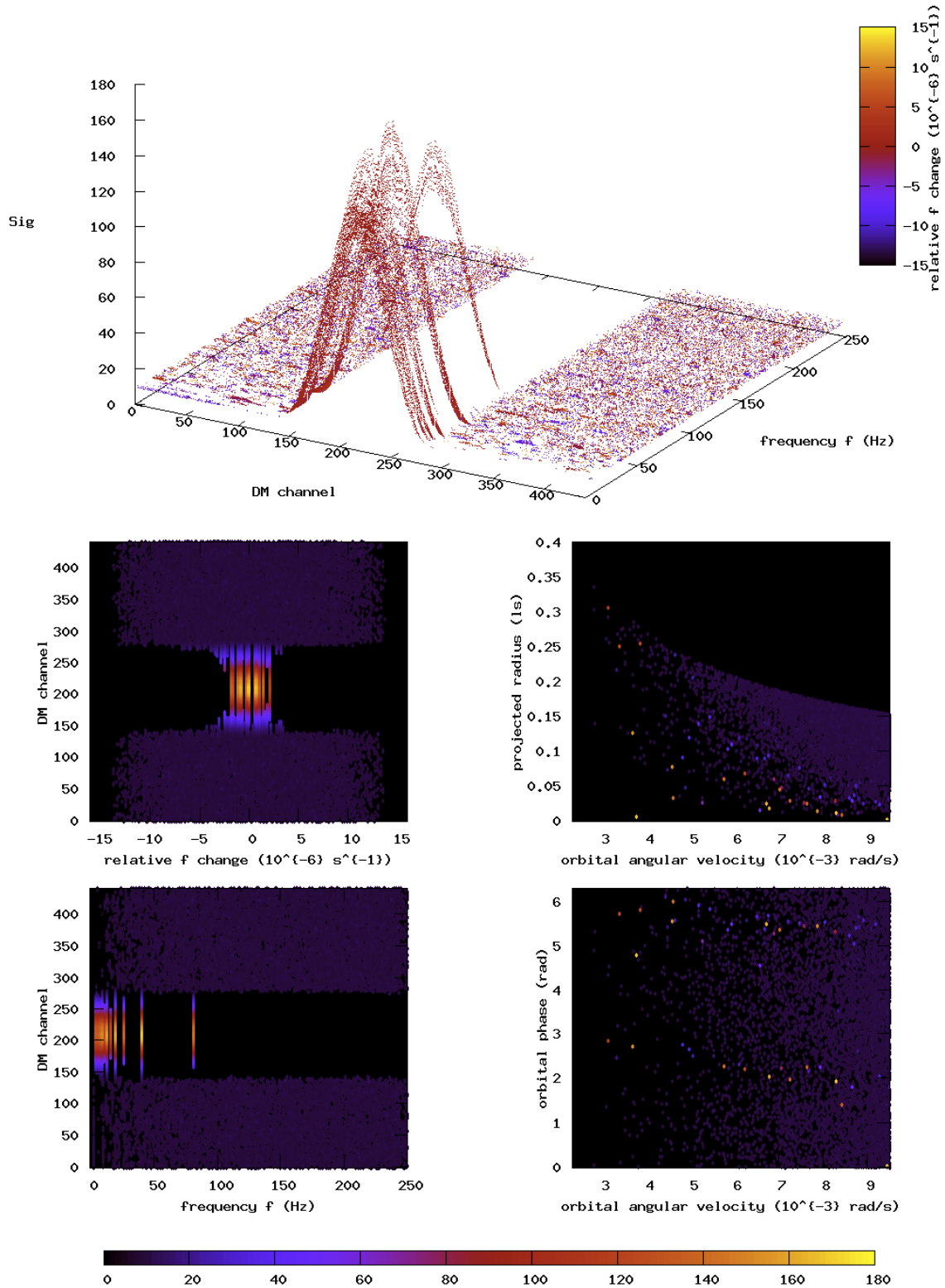


**Figure 4.2:** Einstein@Home result overview plots from the J2007+2722 discovery beam. **(Top)** the harmonic structure and the DM peak are clearly visible in the three-dimensional plot of significance as a function of dispersion measure and spin frequency. **(Bottom)** mismatch and harmonic structures in other dimensions of the parameter space.

a  $\chi^2$ -map in  $P$  and  $\dot{P}$  along with two cuts is shown.

On the early morning of July 13, 2010, the candidate sky position was observed by the Green Bank Telescope (GBT, USA) and the pulsar was confirmed. The pulsar was also later re-detected in another PALFA survey observation beam. Further follow-up observations were done by the GBT, the Lovell Telescope at Jodrell Bank Observatory (UK), the radio telescope at Effelsberg (Germany), the Westerbork Synthesis Radio Telescope (WSRT, Netherlands), and Arecibo, see Section 4.3.

The period-averaged flux density<sup>1</sup> is 2.1 mJy at 1.5 GHz. Gridding observations using Arecibo and WSRT unambiguously associate the pulsar with a source in an archival VLA C-array observation, having 1.2 mJy flux density at 4.86 GHz, at RA 20<sup>h</sup>07<sup>m</sup>15<sup>s</sup>.77 DEC 27°22'47".7 (J2000) with uncertainty  $\lesssim 1''$ . The pulsar is not in a supernova remnant or globular cluster and has no counterpart in X-ray or gamma-ray point-source catalogs. The DM of 127 pc cm<sup>-3</sup> implies a distance of 5.3<sup>+0.8</sup><sub>-0.7</sub> kpc (Cordes and Lazio, 2002).

### 4.3 Improving sky position accuracy

---

The discovery sky position from the PALFA survey data has an accuracy of about 2', which is given by the size of the Arecibo telescope ALFA beams (compare Figure 3.3). By observations over periods longer than one year, one can determine pulsar positions much more accurately by pulsar timing (Lorimer and Kramer, 2005); typical errors are fractions of an arcsecond. Developing a timing model that predicts the times of arrival (TOA) for each single radio pulse allows to estimate the position up to an error  $\varepsilon$  (in radians) of order

$$\varepsilon \approx \frac{\Delta_{\text{TOA}}}{\Delta_{\text{R}}^{\text{max}}} = \frac{\delta_{\text{TOA}} P}{x_{\oplus} \cos(\beta)}, \quad (4.1)$$

where  $\Delta_{\text{TOA}}$  is the average error of the measured TOAs and  $\Delta_{\text{R}}^{\text{max}}$  is the amplitude of the Römer delay over the course of a year. With  $\delta_{\text{TOA}}$  we denote the TOA error as a fraction of the pulsar spin period  $P$ .  $x_{\oplus} \approx 500$  s is the light travel time across the Earth's orbit and  $\beta$  is the ecliptical longitude. Typical values for pulsars with sharply peaked profiles or sharp features in the profile are  $\delta_{\text{TOA}} \approx 10^{-2}$ . Assuming the period  $P \approx 24$  ms and  $\beta \approx 46^\circ$  of PSR J2007+2722, we find an error of  $\varepsilon \approx 7 \times 10^{-7}$  rad  $\approx 0.1''$ .

Observing PSR J2007+2722 for a year was not an option since the first discovery of an astronomical object by a distributed volunteer computing project was an important milestone, and thus quickly publishing the discovery was necessary. Obtaining a more accurate sky position was nonetheless very important: only smaller error boxes allow to check for associations with astronomical observations in other wavelengths, such as X-rays and  $\gamma$ -rays; measuring or setting an upper limit on the intrinsic pulsar spin down  $\dot{P}$  also is only possible for an accurate enough sky position. For observations spanning times much shorter than a year, period changes are degenerate with errors in sky position.

For PSR J2007+2722, different options to improve the sky position were used, which luckily allowed a very accurate determination of the sky position (error of about  $\lesssim 1''$ ); the pulsar could be identified through a combination of observations at two telescopes with a source in archival Very Large Array (VLA) data, which naturally come with very high accuracy.

We note that this section is partially based on work to appear in an upcoming more detailed paper on PSR J2007+2722 (Allen et al., 2011).

---

<sup>1</sup>The unit of the flux density is "Jansky", short Jy; 1 Jy = 10<sup>-26</sup> W m<sup>-2</sup> Hz<sup>-1</sup>.

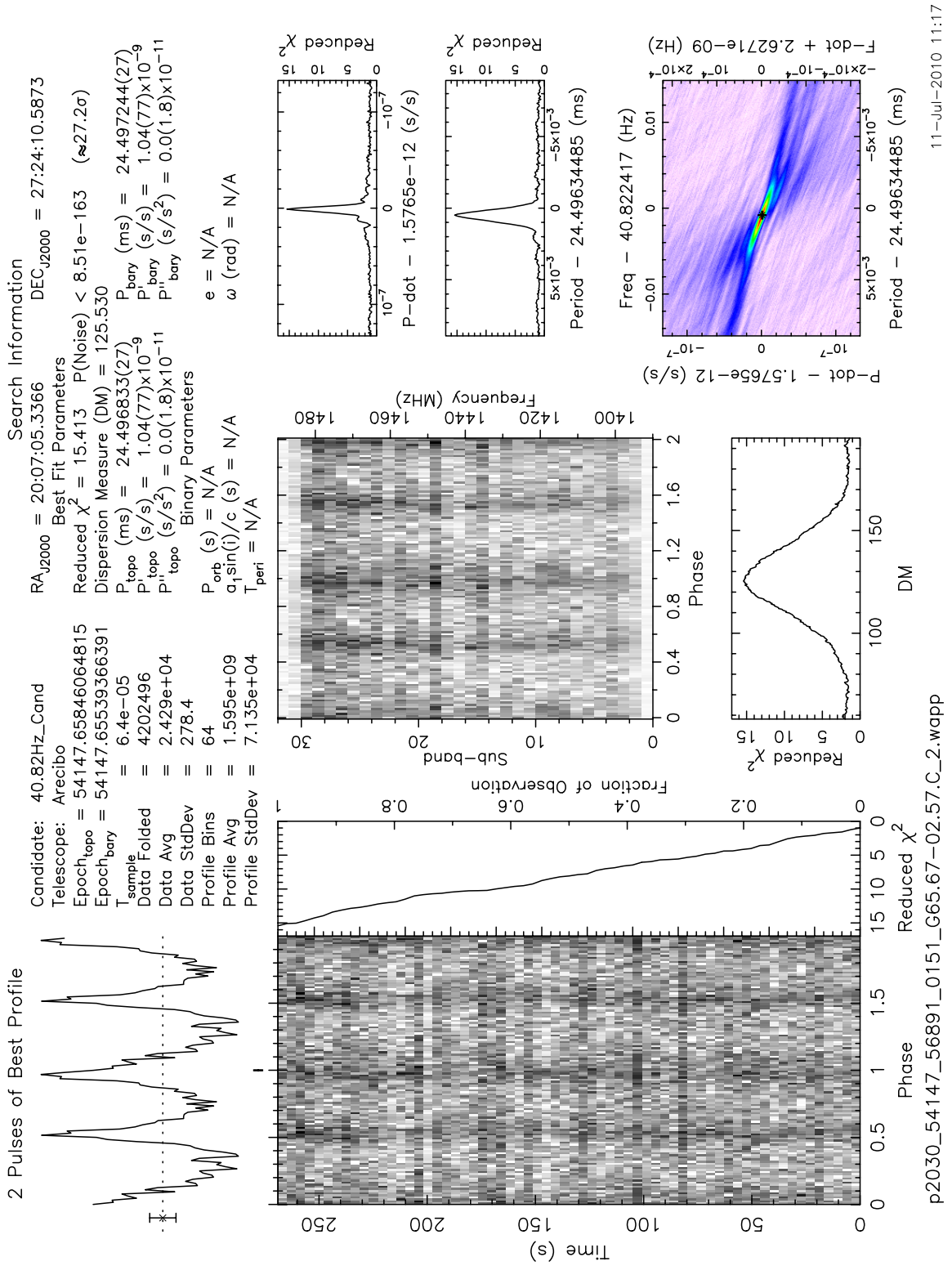


**Figure 4.3:** PSR J2007+2722 diagnostic PRESTO plots from the discovery observation. The top left plot is the folded pulse profile over two rotations of the pulsar; below it a pulse phase vs. observation time plot shows the emission of the pulsar over the observation. The grey-scale plot in the centre shows the broad-band radio emission as a function of the pulse phase and below it, the peak in  $\chi^2$  as a function of dispersion measure is displayed. In the right panel, a  $\chi^2$  in  $P$  and  $\dot{P}$  along with two cuts is shown.

### 4.3.1 Gridding observations with the Arecibo telescope

The first option used was a gridding observation of the pulsar with the Arecibo telescope. On July 19, 2010, a square of nine gridding pointings around the discovery sky position was carried out. The observations used the L-wide receiver<sup>2</sup> and the Mock spectrometer backends. The offset between the individual pointings from the gridding was  $1'$  and the pulsar was detected in five out of the nine beams with signal-to-noise ratios of 2.9, 15.6, 19.8, 22.5, and 97.9, respectively. A weighted average using only the two pointings with the two largest signal-to-noise ratios yielded an estimated position at RA  $20^{\text{h}}07^{\text{m}}12.^{\text{s}}7$  and DEC  $27^{\circ}23'26''$  with an estimated error of  $1'$ . As a consistency check, a second sky position estimate was obtained using all five beams, in which the pulsar was detected; the sky position obtained this way differed by  $\sim 25''$  from the discovery position.

### 4.3.2 Gridding observations with the WSRT

The estimated accuracy of one arcminute after the Arecibo gridding observations was not good enough to obtain measurements of, or upper limits on, the pulsar spin down. Therefore, further observations were conducted with the Westerbork Synthesis Radio Telescope (WSRT; north of Westerbork in the Netherlands). The WSRT consists of fourteen 25-m radio telescopes, arranged on a straight 2.7 km East-West line. The observations of PSR J2007+2722 were made on the late evening of July 19, 2010 at an observation frequency of 1380 MHz over a bandwidth of 160 MHz.

Aperture synthesis using the fourteen East-West arranged telescopes generates a fan-beam with an elliptical<sup>3</sup> beam shape of approximately  $12'' \times 30'$ ; the beam are oriented in North-South direction with the longer axis. The complete Arecibo beam of  $2'$  in diameter was covered with ten observations, each of which lasted for 1180 s. The highly elongated elliptical fan-beams are shown schematically in Figure 4.4. The upper panel shows the ten very elongated WSRT fan-beams (grey ellipses) used to cover the Arecibo beam (orange circle) in the correct scale. The lower left panel is a zoom into the centre.

For each of the ten observations (i.e. also for each fan-beam) the data were de-dispersed with the previously obtained DM of PSR J2007+2722 and folded at the period with the PuMa-II backend (Pulsar Machine II; Karuppusamy et al., 2008). PuMa-II provides near real-time coherent de-dispersion for pulsar observations with the WSRT. The pulsar was detected in two (number 7 and 8) of the ten beams, with signal-to-noise ratios of  $\sim 24$  and  $\sim 21.0$ , respectively. These two beams are highlighted by a green filling in both panels of Figure 4.4. The two graphs on the right in Figure 4.4 show the two folded pulse profiles for these two beams.

Overlapping the two fan-beams containing the pulsar, weighting them by signal-to-noise ratio, and combining this with the Arecibo beam allows to construct a combined error ellipse for the position of the pulsar. The ellipse is centred on RA  $20^{\text{h}}07^{\text{m}}14.^{\text{s}}5$  and DEC  $27^{\circ}23'36''$ , has a semi-major axis of  $51''$ , a semi-minor axis of  $7''$  and its major axis is rotated  $20^{\circ}$  westwards from the North direction. The ellipse is shown in red in Figure 4.5.

### 4.3.3 Imaging and NVSS Catalog Identification

The data obtained from the WSRT observations were also imaged to produce a radio image of the observed sky region. If data are only obtained over a short observation time, the

<sup>2</sup><http://www.naic.edu/~astro/RXstatus/Lwide/Lwide.shtml>

<sup>3</sup>Note that these ellipses are very elongated with a ratio of 1 : 150 between the two axes.

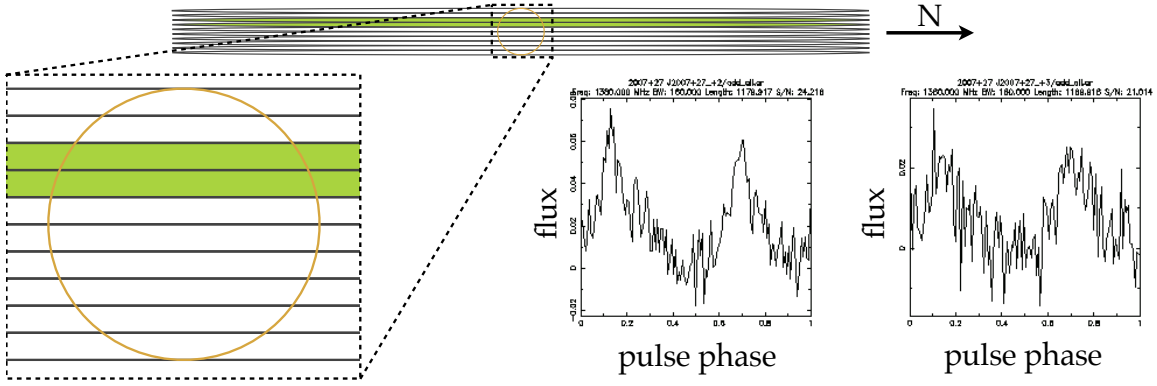


**Figure 4.4:** Schematic of the gridding observations with the WSRT and the folded pulse profiles for the two fan-beams in which PSR J2007+2722 was detected. The upper panel shows the ten very elongated WSRT fan-beams (grey ellipses) used to cover the Arecibo beam (orange circle) in the correct scale. The lower left panel is a zoom into the centre; in both panels, the two fan-beams highlighted by a green filling are the ones in which PSR J2007+2722 was detected. The two graphs on the right show the two folded pulse profiles for these fan-beams; graphs adapted from (Allen et al., 2011).

highly elongated fan-beam shape would not be able to discriminate sources even at potentially large angular distances (of order of the longer side of the beam). If the total amount of available data covers several hours, the rotation of the fan-beams relative to the sky reduces this degeneracy and the effective point spread function gets increasingly concentrated onto a small point. The observations of PSR J2007+2722 covered a total time of six hours, which rotates the beams only far enough to reduce the point spread functions to ellipses, however, much less elongated than the initial beam. The result of the imaging process is shown in Figure 4.5. The imaging data are shown in grey-scale and the cyan circle is the error region obtained from the Arecibo gridding observation. The red ellipse is the error region from the WSRT observations, which detected the pulsar in two fan-beams.

The imaging process reveals a single radio source consistent with the error regions obtained from the Arecibo gridding observations and the WSRT detection of the pulsar in two fan-beams. The source is visible at the southern edge of the Arecibo and the WSRT error regions in Figure 4.5. The source is also recorded in the 1.4 GHz National Radio Astronomical Observatory (NRAO) Very Large Array (VLA) Sky Survey (NVSS) catalog (Condon et al., 1998): the source NVSS 200715+272243 is at sky position RA  $20^{\text{h}}07^{\text{m}}15.^{\text{s}}86$  and DEC  $27^{\circ}22'43.5''$ . It has a catalogued flux density of 2.3 mJy at 1.4 GHz.

#### 4.3.4 VLA archival data

It was possible to obtain archival VLA data for a sky region close to the position of the pulsar, large enough to contain the pulsar. The VLA data archive contains an observation of the stellar cluster IRAS 20050+2720, see e.g. (Guenther et al., 2010), from August 14, 1997, with an observation time of 1600 s. Data were obtained in full Stokes mode with the VLA operating at 4.86 GHz over a bandwidth of 50 MHz. An image generated from these archival data in the right panel of Figure 4.5; eight point sources with flux densities larger than  $200 \mu\text{Jy}$ , and one extended source can be identified. Data were obtained in B1950.0 coordinates and converted to J2000.0 coordinates, errors in the coordinate conversion are  $\lesssim 1''$ .

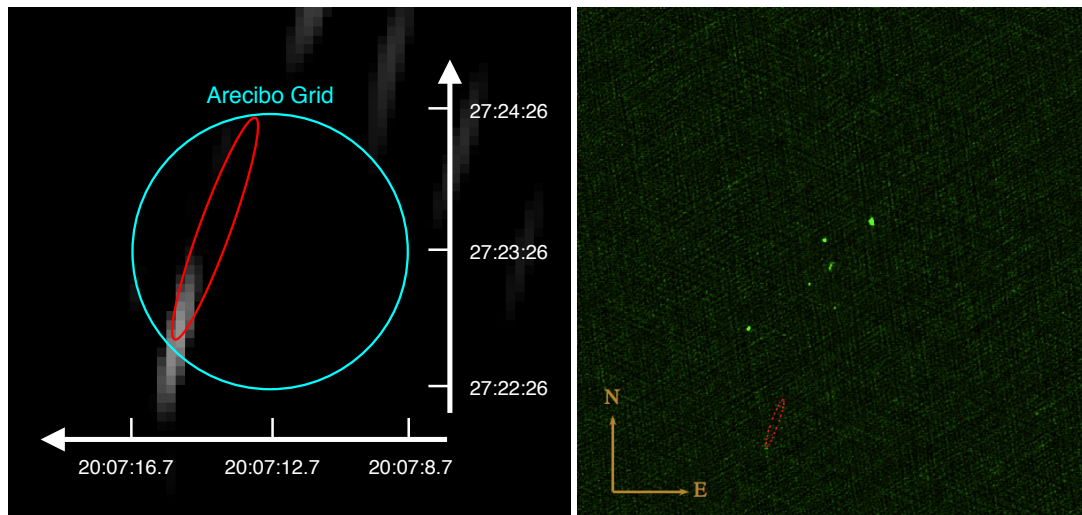


**Figure 4.5:** (Left) Imaging observations of PSR J2007+2722 with the WSRT. The imaging data are shown in grey-scale and the cyan circle is the error region obtained from the Arecibo gridding observation. The red ellipse is the error region from the WSRT observations, which detected the pulsar in two fan-beams. The imaged source is PSR J2007+2722. This figure is adapted from Allen et al. (2011). (Right)  $16' \times 16'$  image of archival VLA data at 4.8 GHz from a 1600-s observation containing the sky position of PSR J2007+2722, the intensity has been corrected by a model for primary beam response. A VLA source can be seen on the southern corner of the red ellipse, which is the combined WSRT-Arecibo error region from the left panel

Only one of the point sources lies within both the WSRT and the Arecibo error regions and is consistent with the imaging obtained from the WSRT observations. The consistent point source has a primary beam-corrected flux density of 1.2 mJy at 4.86 GHz and is located at coordinates RA  $20^{\text{h}}07^{\text{m}}15.^{\text{s}}77$  and DEC  $27^{\circ}22'47.68''$  (J2000.0). The flux density value has an error of about 10% from uncertainties in the primary beam correction, since the source is close to the edge of the beam; the measured flux density is consistent with the spectrum of radio pulsars, therefore we conclude that the source in the VLA archival data is PSR J2007+2722.

The VLA source is shown in more detail in Figure 4.6: the left panel shows an overview of the region zoomed into the error regions from WSRT and Arecibo observation, while the right panel also shows an error region for the position of the source from the VLA archival data. The error region is a circle with a radius of  $1''$  corresponding to the uncertainty from the coordinate conversion from B1950.0 to J2000.0.

### 4.3.5 High-Energy and optical counterparts

With the final sky position obtained from the VLA archival data, we checked X-ray and  $\gamma$ -ray catalogues for high-energy counterparts. No counterpart in the Fermi Large Area Telescope Point Source Catalog (Abdo et al., 2010) was found. There are three archival Chandra X-ray observations<sup>4</sup> (ObsID 6438, 7254, and 8492 with observation times of 23.2 ks, 21.1 ks, and 51.2 ks, respectively); from these, no X-ray counterpart could be identified. The pulsar is not in any known globular cluster or in a supernova remnant.

<sup>4</sup><http://heasarc.gsfc.nasa.gov/docs/archive.html>

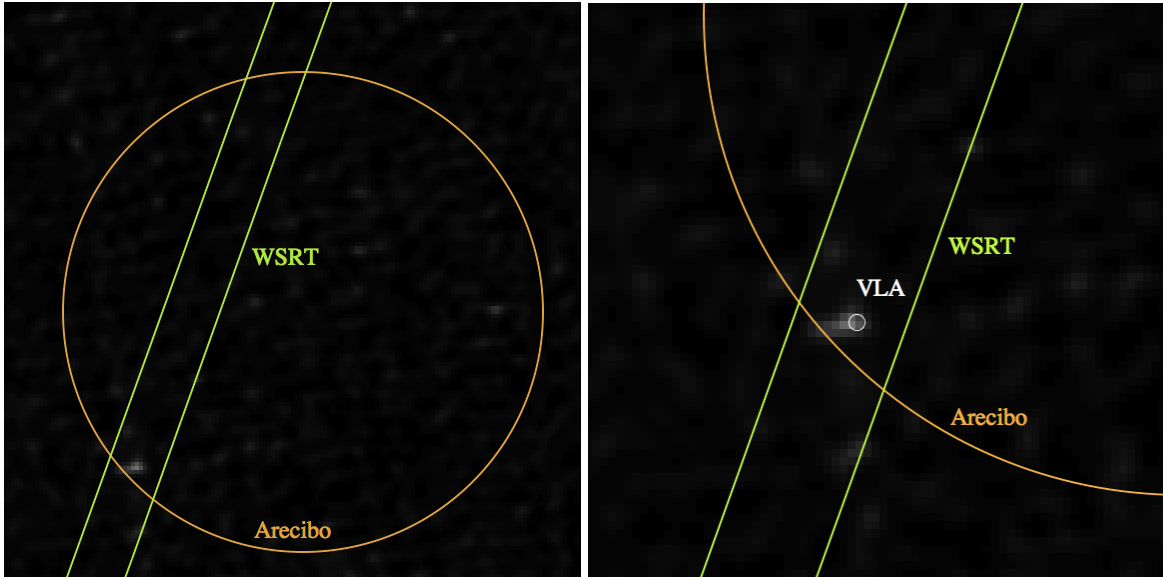


**Figure 4.6:** VLA archival data at 4.86 GHz. **(Left)** Overview of the error regions from Arecibo gridding and WSRT observations. Only a single point source with 1.2 mJy flux density at 4.86 GHz is consistent with both error regions and the WSRT imaging, compare Figure 4.5. **(Right)** Zoom to the single source, also showing a 1'' circle as the VLA observation uncertainty. Figure adapted from Allen et al. (2011)

#### 4.3.6 Spectrum from multifrequency GBT observations

In order to further characterise PSR J2007+2722 quickly for the publication, the pulsar was observed with the GBT on July 21, 2010. The pulsar was observed at five different frequency bands, centred at 430 MHz, 820 MHz, 1.5 GHz, 2 GHz, and 8.9 GHz. The pulsar was detected at all frequencies with the exception of 430 MHz.

Full Stokes data were obtained for the observations at 1.5 GHz and 2 GHz. We use the data from 1.5 GHz, which have the best signal-to-noise ratio to fit the orbital geometry with the rotating vector model (RVM) in Section 4.5 below.

For all frequencies at which the pulsar was detected, pulse-averaged flux densities were obtained from the GBT observations; in combination with the flux density from the NVSS catalog and the VLA archival data, the pulsar's flux density has been measured at six different frequencies. The NVSS and the VLA data are measurements of the *total flux density*, which measures the complete emission from the source, not only the pulsed emission. The GBT measurements are of *pulsed flux density* and exclude the non-pulsed emission; on the other hand, the very wide pulse profile of PSR J2007+2722 means that the contribution from non-pulsed emission is minor compared to the pulsed emission. Table 4.1 lists all measured flux densities for PSR J2007+2722.

To obtain an estimate of the spectrum and its properties, we fitted a power law to the observed spectrum using only the measurements of pulsed flux density for frequencies above 1 GHz. We constrain ourselves to pulsed flux densities to ensure that the un-pulsed components do not skew the measurements. We choose the frequencies  $> 1$  GHz, since pulsars can show a turnover at lower frequencies which cannot be fitted by a simple single-component power law (Lorimer and Kramer, 2005). We therefore fit the parameters  $S_{1400}$

**Table 4.1:** Measured flux densities for PSR J2007+2722

| Frequency | Flux density $S$ (pulsed / total) | Observation   |
|-----------|-----------------------------------|---------------|
| 820 MHz   | 1.6 mJy ( $p$ )                   | GBT           |
| 1400 MHz  | 2.3 mJy ( $t$ )                   | NVSS          |
| 1500 MHz  | 2.1 mJy ( $p$ )                   | GBT           |
| 2000 MHz  | 1.7 mJy ( $p$ )                   | GBT           |
| 4860 MHz  | 1.2 mJy ( $t$ )                   | VLA-C archive |
| 8900 MHz  | 0.3 mJy ( $p$ )                   | GBT           |

and  $\zeta$  in the power law

$$S(\nu) = S_{1400} \left( \frac{\nu}{1400 \text{ MHz}} \right)^{\zeta} \quad (4.2)$$

using the measurements at 1500 MHz, 2000 MHz, and 8900 MHz. From a least-squares fit using the software tool `gnuplot` and coordinates  $\log_{10}(S)$  and  $\log_{10}(\nu)$  find the best-fitting values  $S_{1400} = 2.4(2)$  mJy and  $\zeta = -1.12(6)$ ; estimated asymptotic errors are from the least-squares fitting with `gnuplot`. The result of the fit along with all measurements from Table 4.1 is shown in Figure 4.7. The scaling of the flux density with a low power of the observation frequency means that PSR J2007+2722 has a relatively flat spectrum. The majority of pulsars has spectral indices (that is the scaling exponent)  $0 \geq \zeta \geq -4$  with a mean value of around  $-1.8 \pm 0.2$  (Lorimer and Kramer, 2005). More measurements of pulsed flux density over the complete range of radio frequencies are necessary to obtain a more accurate spectrum and spectral index.

#### 4.4 Obtaining the spin parameters

Observations of PSR J2007+2722 were carried out with the Green Bank Telescope, the Arecibo Telescope, the Lovell Telescope at Jodrell Bank, and the Effelsberg Telescope. For each observation, TOAs were obtained using standard methods. The TOAs were analysed using the `tempo` software package (Taylor et al., 2010) with the JPL DE405 solar system ephemeris. TOAs were referred to the local observatory clock standards. For the timing analysis, the sky position obtained from the VLA archival data ( $20^{\text{h}}07^{\text{m}}15.^{\text{s}}77$  and DEC  $27^{\circ}22'47.7''$ ) was assumed and kept fixed.

Under these assumptions, the analysis of the TOAs obtained over the 18 days in July and August 2010 gives the following results for the spin parameters of PSR J2007+2722: the pulsar's barycentric spin frequency is  $40.820677620(6)$  Hz at MJD 55399.0. With the VLA position, the data give an upper limit on the spin period derivative of  $|\dot{f}| < 3 \times 10^{-14} \text{ s}^{-2}$ . This corresponds to an estimated surface magnetic field  $B < 2.1 \times 10^6$  T, and characteristic age  $\tau_c > 21$  Myr.

These limits and lack of a companion mean that J2007+2722 is likely the fastest-spinning disrupted recycled pulsar yet found (Belczynski et al., 2010). However we cannot rule out it having been born with low  $B$  (Halpern and Gotthelf, 2010). Either way, PSR J2007+2722 is a rare, isolated low- $B$  pulsar which contributes to our understanding of pulsar evolution.

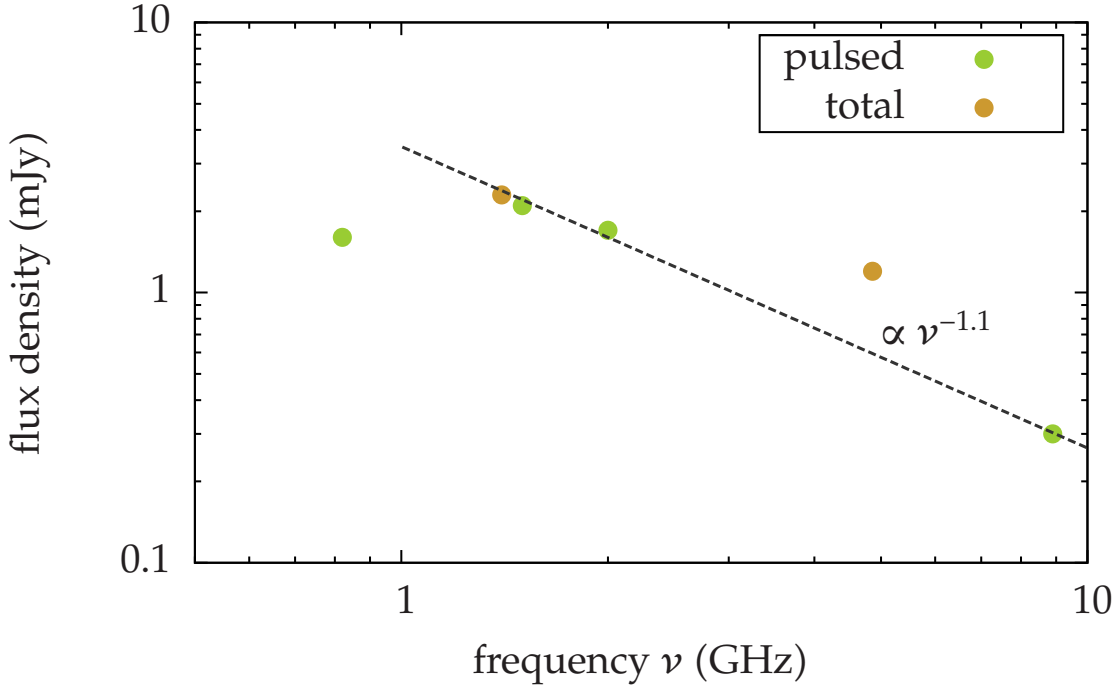


**Figure 4.7:** Spectrum of PSR J2007+2722, based on the flux density measurements in Table 4.1. Orange filled circles are the measurements of total flux density from the NVSS catalog and the VLA-C archival data. Green filled circles are the measurements of pulsed flux density from the GBT observations. The dashed line is a power-law fit to the pulsed flux density at frequencies above 1 GHz. With a spectral index  $\zeta \approx -1.1$ , the spectrum is relatively flat.

## 4.5 Emission geometry

Observational data in full Stokes mode from the GBT taken on July 21, 2010, provide full polarisation information for the observed wide pulse profile. The rotating vector model is a simple model predicting the sweep of polarisation angle over the pulse profile as a function of the emission geometry, see Section 2.3.3. In turn, one can infer the emission and beam geometry from polarisation measurements. We use the GBT observation at 1.5 GHz to examine the geometry of PSR J2007+2722.

### 4.5.1 Rotating vector model

PSR J2007+2722 has a very wide pulse profile (right panel of Figure 4.1). The full pulse width between the outer half-maxima is  $W \approx 224^\circ$ . The wide pulse could indicate that the pulsar has nearly aligned magnetic and spin axes.

As shown in Section 2.3.3, the polarisation properties of the pulsar beam can be explained by a very simple model, called the rotating vector model (RVM). The polarisation angle  $\psi$  is given by the relation

$$\tan(\psi - \psi_0) = \frac{\sin(\phi + \phi_0) \sin(\alpha)}{\sin(\alpha + \beta) \cos(\alpha) - \cos(\alpha + \beta) \sin(\alpha) \cos(\phi + \phi_0)}, \quad (4.3)$$

where  $\phi$  is the pulsar's spin (or pulse) phase,  $\alpha$  is the angle between the pulsar's rotation and magnetic axes,  $\beta$  is the angle between the line of sight and the pulsar's magnetic axis

(the so-called impact parameter), and  $\psi_0$  is the projected direction of the rotation axis (Lyne and Graham-Smith, 2005).

Given a polarisation measurement, it is straightforward to find the best-fitting model parameters  $\alpha$ ,  $\beta$ ,  $\psi_0$ ,  $\phi_0$  for the pulsar and to examine the beam geometry of the pulsar in question.

#### 4.5.2 Polarisation data reduction

On July 22, 2010 a L-band polarisation observation of PSR J2007+2722 with the Green Bank Telescope was made. Stokes parameters  $I$ ,  $Q$ ,  $U$ , and  $V$  were recorded. In the bottom panel, Figure 4.8 shows the measured unnormalized radio flux  $S_{1500}$  at 1.5 GHz; the total flux  $I$ , the linear polarised content  $L = \sqrt{U^2 + Q^2}$  and the circularly polarised content  $V$  are displayed over one rotation of the pulsar. The top panel in Figure 4.8 also shows the polarisation angle  $\psi$  computed from

$$\psi = \frac{1}{2} \arctan\left(\frac{U}{Q}\right). \quad (4.4)$$

The orange points in the top panel are chosen for further analysis; they have been selected by the criterion that their estimated standard deviation in  $\psi$  is less than  $8^\circ$ . This is a proxy for choosing data points from the two peaks in the pulse profile where the pulsed emission is strongest and where the estimated error is smallest. The estimated standard deviation  $\sigma_{\psi_i}$  of the  $i$ -th measurement of polarization angle  $\psi$  is given by

$$\sigma_{\psi_i} = \frac{1}{2(Q_i^2 + U_i^2)} \sqrt{\sigma_U^2 Q_i^2 + \sigma_Q^2 U_i^2}, \quad (4.5)$$

where  $\sigma_U$  and  $\sigma_Q$  are the standard deviation of  $U$  and  $Q$ , respectively, computed from the off-pulse region of the pulse profile.

To examine the beam geometry based on the polarisation measurements, the best-fitting RVM configuration for the chosen data points is obtained. For each selected data point  $i$  we compute the pulse phase  $\phi_i$  and the polarisation angle  $\psi(\phi_i)$ , from Equation (4.4) and the estimated standard deviation of  $\sigma_{\psi_i}$  from Equation (4.5).

We then choose a rotating vector model configuration by fixing the parameters  $\alpha$ ,  $\beta$ ,  $\psi_0$ ,  $\phi_0$ . From this model, we compute the expected model sweep of the polarisation angle as a function of the pulse phase  $\psi_{\text{mod}}(\phi; \alpha, \beta, \psi_0, \phi_0)$ . We then obtain the reduced chi-squared statistic of this model from

$$\chi^2(\alpha, \beta, \psi_0, \phi_0) = \frac{1}{n_{\text{dof}}} \sum_{i=0}^{n_{\text{points}}} \left( \frac{\psi_{\text{mod}}(\phi_i; \alpha, \beta, \psi_0, \phi_0) - \psi(\phi_i)}{\sigma_{\psi_i}} \right)^2, \quad (4.6)$$

where the number of data points  $n_{\text{points}} = 548$  from our data selection criterion and the number of degrees of freedom is  $n_{\text{dof}} = n_{\text{points}} - n_{\text{param}} = 544$ , because we fit for  $n_{\text{param}} = 4$  parameters.

The main beam geometry is determined by the  $\alpha$  and  $\beta$  alone, while  $\phi_0$  and  $\psi_0$  are fiducial values. Thus, to map the parameter space of beam geometry, we minimise for each point  $(\alpha, \beta)$  the  $\chi^2$  from Equation (4.6) over  $(\psi_0, \phi_0)$ . We choose a step-width of  $1^\circ$  in  $\alpha$  and  $\beta$  and  $2^\circ$  wide steps in  $\psi_0$  and  $\phi_0$ , respectively.

All models have to fulfil the additional constraint of

$$|\beta| \leq \rho, \quad (4.7)$$

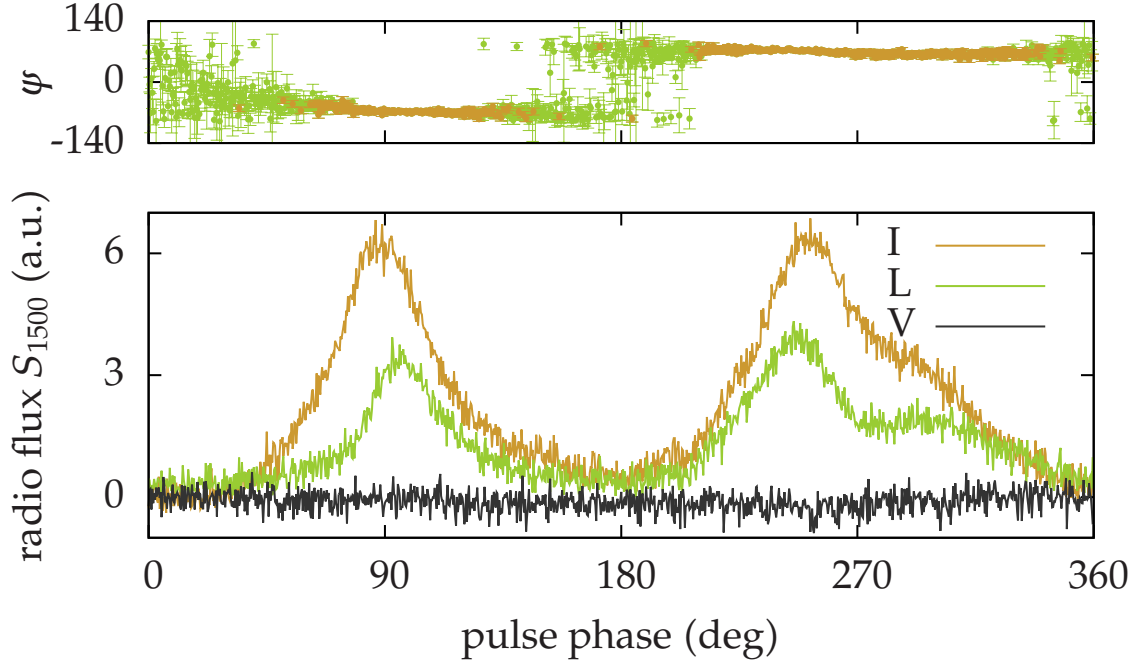


**Figure 4.8:** Polarisation measurement of PSR J2007+2722 at 1.5 GHz with the Green Bank Telescope. **(Bottom)** the total flux  $I$ , the linear polarised content  $L = \sqrt{U^2 + Q^2}$  and the circularly polarised content  $V$  are shown over one rotation of the pulsar. **(Top)** the polarisation angle  $\psi$  as a function of the pulse phase. Shown are all measurements with estimated 1-sigma error bars. Orange points are chosen for further analysis

where  $\rho$  is the half-opening angle of the pulsar's beam or of the emission cone, respectively. If the constraint is not met, the line of sight misses the pulsar's beam or cone, respectively. We can use this inequality to further constrain the models. Assuming the two peaks are caused by the intersections of the line of sight with the walls of the emission cone, the outer full pulse width at half maximum  $W$  and the half-opening angle  $\rho$  are related from simple spherical geometry by (Gil et al., 1984; Lorimer and Kramer, 2005)

$$\cos(\rho) = \cos(\alpha) \cos(\alpha + \beta) + \sin(\alpha) \sin(\alpha + \beta) \cos\left(\frac{W}{2}\right). \quad (4.8)$$

One can show (see Section 8.3.1) that combining the constraint from Equation (4.7) and the previous equation results in a constraint

$$-\alpha \leq \beta \leq 180^\circ - \alpha \quad (4.9)$$

that does not depend on  $W$ . We note that one can also write this constraint using the angle  $\zeta = \alpha + \beta$  as  $0^\circ \leq \zeta \leq 180^\circ$  (Lyne and Graham-Smith, 2005). This is also clear from the symmetry of Equation (4.3) under the simultaneous substitution

$$\alpha \rightarrow 180^\circ - \alpha \quad \text{and} \quad \beta \rightarrow 180^\circ - \beta. \quad (4.10)$$

For reasons of clearness we will stick to not using  $\zeta$  for the remaining analysis. We then

vary the rotating vector model parameters over the full available ranges:

$$0 \leq \alpha \leq 180^\circ \quad \text{and} \quad -\alpha \leq \beta \leq 180^\circ - \alpha \quad (4.11)$$

$$-180^\circ \leq \psi_0 \leq 180^\circ \quad \text{and} \quad 0 \leq \phi_0 \leq 360^\circ. \quad (4.12)$$

### 4.5.3 Three possible polarisation models

We consider three different polarisation models that could explain the observed sweep of  $\psi$ , all of which are possible given the data.

The first model is the pure rotating vector model as described above in Section 4.5.2 without any additional assumptions. The data reduction and analysis is done exactly as described above.

In the second model we allow for the existence of orthogonal polarisation modes (Backer et al., 1976; Weisberg et al., 1999) in the second peak of the pulse profile. This assumption might seem somewhat arbitrary here, but cannot be ruled out in general. To test all possible configurations we also allow for this possibility. Then, the polarisation angle of the second peak (where  $\psi \geq 0$ , compare Figure 4.8) is lowered by  $90^\circ$  by the condition

$$\psi' = \begin{cases} \psi & \text{if } \psi < 0 \\ \psi - 90^\circ & \text{if } \psi \geq 0 \end{cases}, \quad (4.13)$$

and the minimisation of  $\chi^2$  over the parameter space is repeated for the set of modified data points  $\psi'$ . We make use of the proxy condition on  $\psi$  to discriminate between the pulse components.

Finally, we further assume the possibility of a full  $180^\circ$  polarisation angle wrap between the two pulse components. In this case, the polarisation angle of the second component is lowered by  $180^\circ$  following

$$\psi'' = \begin{cases} \psi & \text{if } \psi < 0 \\ \psi - 180^\circ & \text{if } \psi \geq 0 \end{cases}, \quad (4.14)$$

where we again make use of the fact that  $\psi \geq 0$  in the second pulse component. Then, the minimisation of  $\chi^2$  over the parameter space is repeated for the set of modified data points  $\psi''$ .

### 4.5.4 Results for the three models

The results of these three parameter space mappings are shown in Figures 4.9 and 4.10. In the figures each panel shows the minimised  $\chi^2$  in colour code on a logarithmic scale over the complete  $(\alpha, \beta)$  parameter space. Note that all three plots cover the same range of  $\chi^2$ .

The results for the best-fitting parameter combinations are given in Table 4.2. The best-fitting points obtained from the mapping process on the grid was refined by a least-squares fitting with a Levenberg-Marquardt algorithm. We also computed the corresponding half opening angle  $\rho$  for the best-fitting parameters from Equation (4.8) and the measured value for the profile width  $W = 224^\circ$ . All models have reduced  $1.54 \leq \chi^2 \leq 3.53$  which indicate a sub-optimal fit to the data, see Table 4.2.

The rotating vector model without any assumptions has the largest  $\chi^2 = 3.53$  and is shown in Figure 4.9. The best fitting parameters ( $\alpha = 69.13(32)^\circ$ ,  $\beta = 10.32(71)^\circ$ ) indicate a

**Table 4.2:** The best-fitting rotating vector model parameters for the three possible models considered here. “Pure RVM” is the rotating vector model without further assumptions, “OPM” stands for orthogonal polarisation modes and “phase wrap” assumes the complete phase wrap between the two peaks. The best parameter combinations are also shown as black crosses in Figures 4.9-4.11. The numbers in parentheses are the estimated 1-sigma errors in the last two digits.  $\rho$  was computed from Equation (4.8) and the peak-to-peak pulse width  $W_{pp} = 164^\circ$ .

| model      | $\alpha$ (deg) | $\beta$ (deg) | $\phi_0$ (deg) | $\psi_0$ (deg) | $\chi^2_{\min}$ | $\rho$ (deg) |
|------------|----------------|---------------|----------------|----------------|-----------------|--------------|
| pure RVM   | 69.13(32)      | 10.32(71)     | 186.7(14)      | 1.22(37)       | 3.53            | 78.9         |
| OPM        | 0.79(48)       | 1.02(62)      | 175.2(18)      | -42.85(25)     | 1.95            | 1.9          |
| phase wrap | 0.38(10)       | 0.47(13)      | 1.5(30)        | -89.56(62)     | 1.54            | 0.9          |

fairly strongly inclined emission cone that intersects the emission cone close to centrally in an *outer line of sight* (Lorimer and Kramer, 2005). The emission cone is *very* wide ( $\rho = 78.9^\circ$  for full peak-to-peak pulse width  $W_{pp} = 164^\circ$  and  $\rho = 106.2^\circ$  for full half-maximum pulse width  $W = 224^\circ$ ) in this model; because  $\rho > \alpha$ , the rotation axis lies inside the cone and the pulsar is an aligned rotator in this model.

Slightly better fits are achieved by the model with the additional assumptions of orthogonal polarisation modes. This model has a smaller  $\chi^2 = 1.95$  at the price of a very unlikely geometries of very narrow emission cones and very closely aligned axes. The results are shown in Figure 4.10. This model has best-fitting parameters ( $\alpha = 0.79(48)^\circ$ ,  $\beta = 1.02(62)^\circ$ ) that would indicate an aligned rotating pulsar. The emission cone also has to be *very* narrow ( $\rho = 1.9^\circ$ ) for the observed pulse width  $W_{pp}$ . Note however, that this would still mean aligned rotation and magnetic axes. We also note that solution with larger positive  $\alpha$  and  $\beta$  exist, that have only slightly higher  $\chi^2$ , compare the  $\chi^2$ -map in Figure 4.10. These solutions also have larger cone opening angles and avoid the problem of the unlikely geometry.

The model allowing for a full phase wrap between the two pulse components is shown in Figure 4.11. Here, the results are similar as for the previous one: the  $\chi^2$ -value of 1.54 is the smallest of all three models, but the emission geometry is very unlikely: the best-fitting parameters ( $\alpha = 0.38(10)^\circ$ ,  $\beta = 0.47(13)^\circ$ ) indeed indicate an aligned rotating pulsar, but the emission cone is with  $\rho = 0.9^\circ$  even narrower than in the previous model, rendering this even more unlikely. The same remark as in the previous also applies here: from the  $\chi^2$ -map in Figure 4.11 solutions with only slightly higher  $\chi^2$  exist, that have wider cone opening angles and avoid the problem of the unlikely geometry.

In conclusion, all models predict a pulsar with aligned magnetic and rotation axes. The RVM fits with further assumptions have smaller  $\chi^2$  than the model without additional assumptions; the beam geometry in all three cases is unusual. No clear conclusion can be drawn based on the available data. This pulsar promises to be an interesting object with respect to its emission geometry. Further observations are necessary to clearly discriminate between the possible models.

## 4.6 Future Work

The pulsar has been regularly observed with the Lovell telescope at Jodrell Bank observatory over the last months. A second paper describing a detailed timing solution and further details is in preparation by Allen et al. (2011).

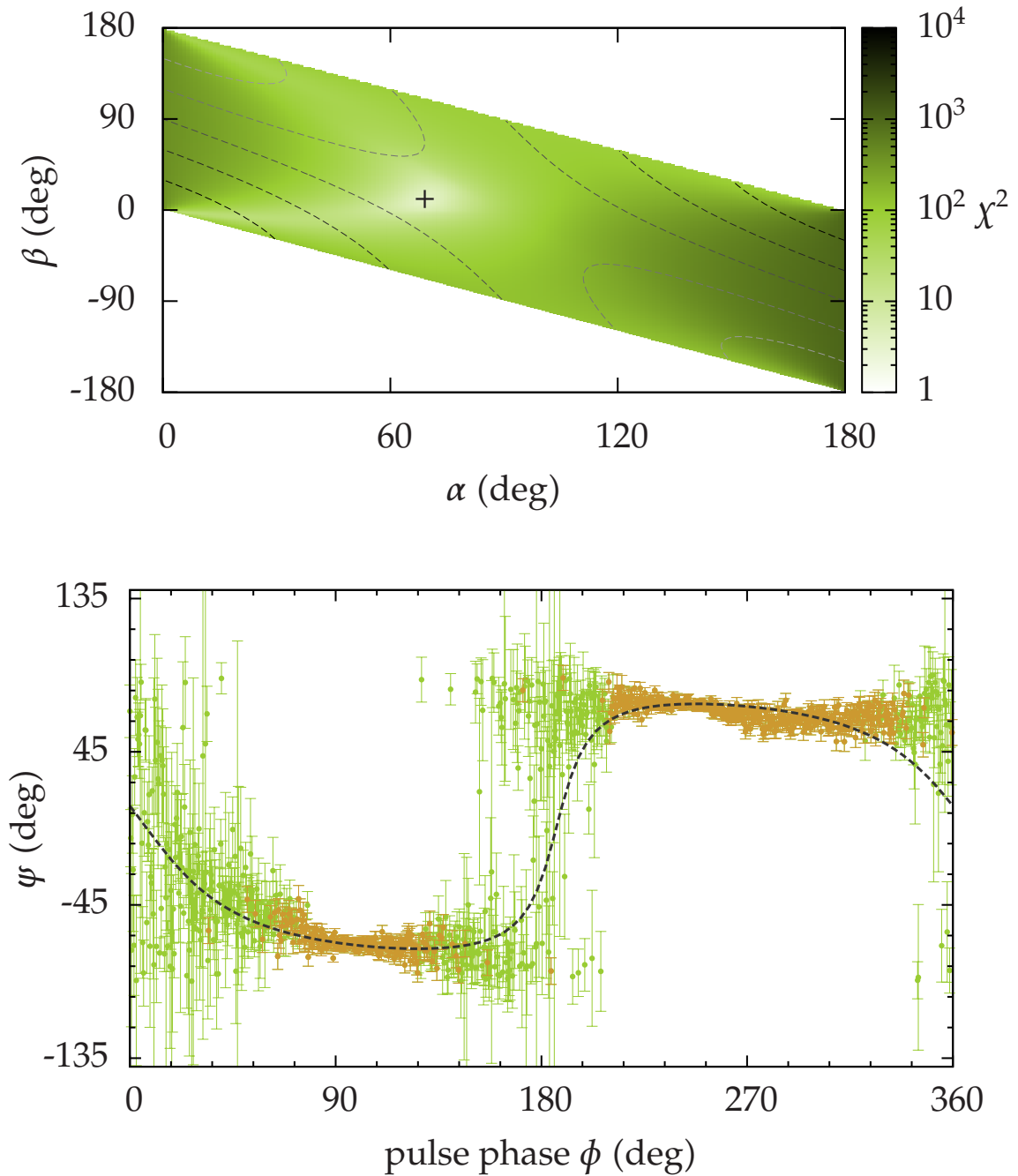


**Figure 4.9:** (Top): minimised  $\chi^2$  in colour code as a function of inclination angle  $\alpha$  and impact parameter  $\beta$  for the model without additional assumptions. The black crosses mark the best-fitting combinations of  $\alpha$  and  $\beta$  (see also Table 4.2). The dashed lines are the contours of the half-opening angle computed from Equation (4.8). The contour levels from black to lighter grey are  $30^\circ$ ,  $60^\circ$ ,  $90^\circ$ ,  $120^\circ$ , and  $150^\circ$ . (Bottom): the best fit polarisation angle sweep as predicted by the RVM (dashed line) compared to the measured polarisation angle (data points with error bars).

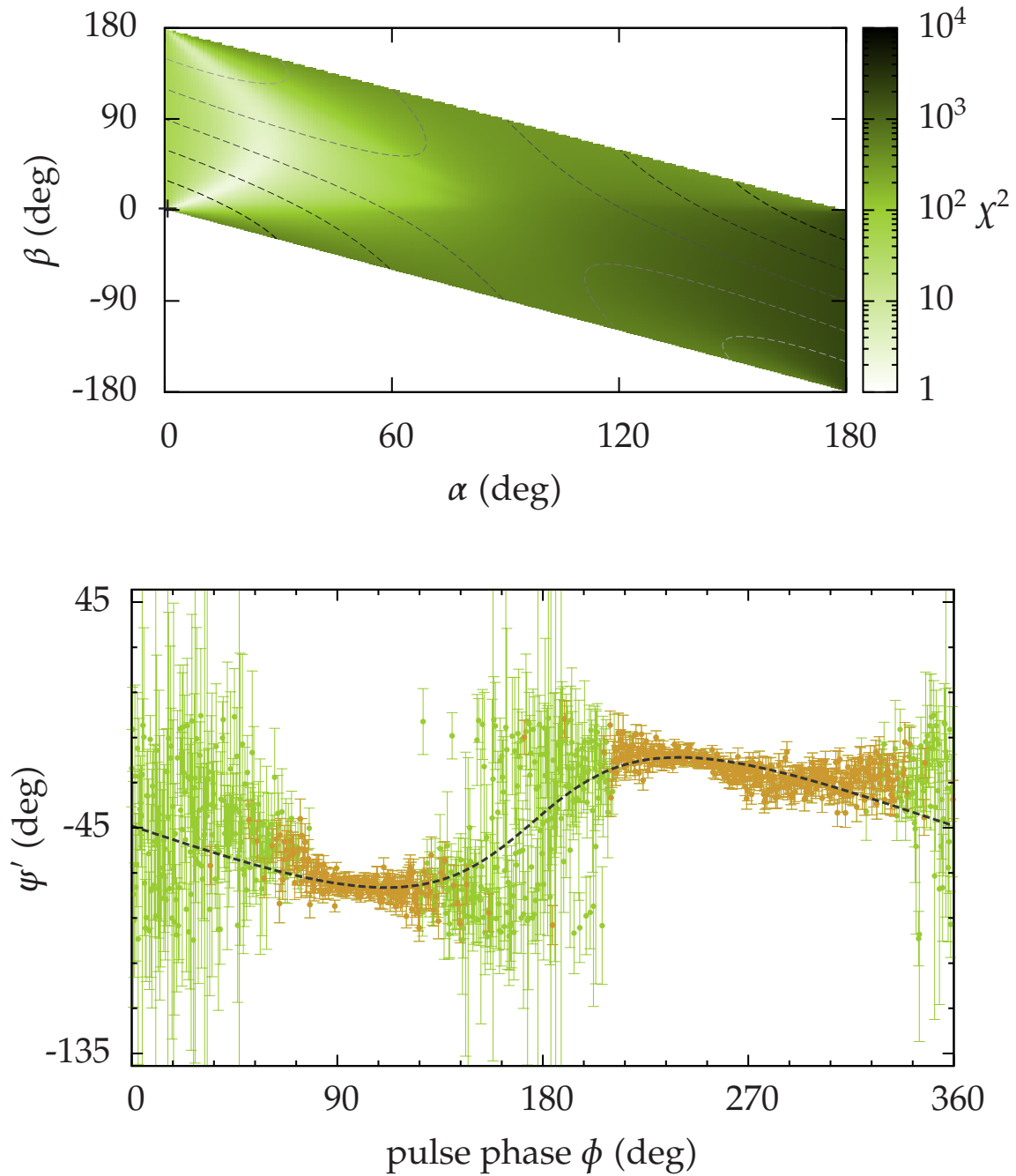


**Figure 4.10: (Top):** minimised  $\chi^2$  in colour code as a function of inclination angle  $\alpha$  and impact parameter  $\beta$  for the model with OPM in the second pulse peak. The black crosses mark the best-fitting combinations of  $\alpha$  and  $\beta$  (see also Table 4.2). The dashed lines are the contours of the half-opening angle computed from Equation (4.8). The contour levels from black to lighter grey are  $30^\circ$ ,  $60^\circ$ ,  $90^\circ$ ,  $120^\circ$ , and  $150^\circ$ . **(Bottom):** the best fit polarisation angle sweep as predicted by the RVM (dashed line) compared to the modified polarisation angle (data points with error bars) from Equation (4.14).

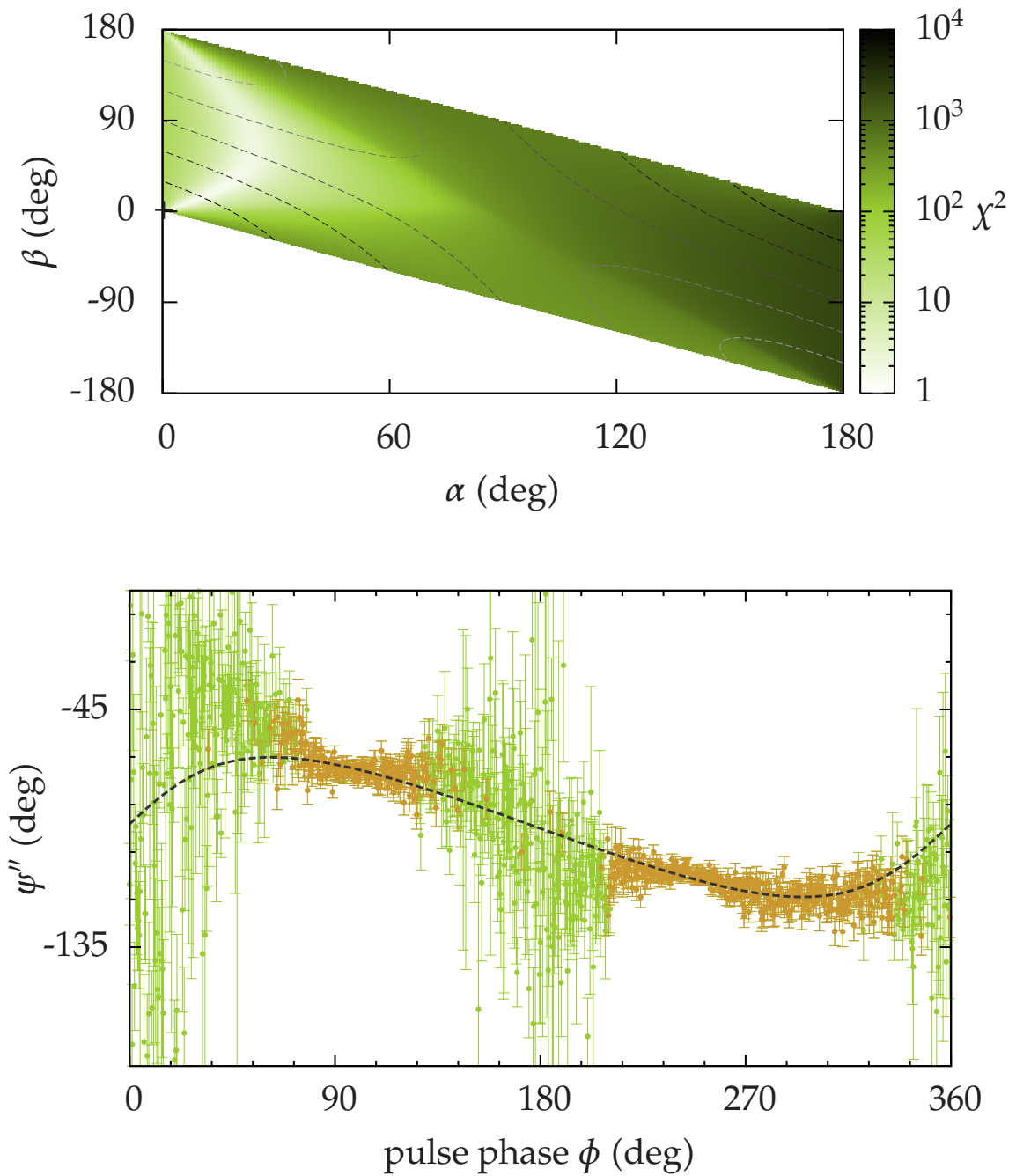


**Figure 4.11: (Top):** minimised  $\chi^2$  in colour code as a function of inclination angle  $\alpha$  and impact parameter  $\beta$  for the model with full phase wrap between the pulse peaks. The black crosses mark the best-fitting combinations of  $\alpha$  and  $\beta$  (see also Table 4.2). The dashed lines are the contours of the half-opening angle computed from Equation (4.8). The contour levels from black to lighter grey are  $30^\circ$ ,  $60^\circ$ ,  $90^\circ$ ,  $120^\circ$ , and  $150^\circ$ . **(Bottom):** the best fit polarisation angle sweep as predicted by the RVM (dashed line) compared to the modified polarisation angle (data points with error bars) from Equation (4.14).

# 5

## Discovery of PSR J1952+2630

---

*appeared in ApJ Letters, 732, 1, L1 (2011)*

---

### 5.1 Overview and Context

---

Pulsars in short-period orbits with neutron stars or white dwarfs are invaluable tools for diverse areas of science. Pulsars are precise clocks and enable very stringent tests of Einstein's theory of general relativity (e.g. Taylor and Weisberg, 1989 and Kramer and Wex, 2009). These binary systems also provide unique opportunities to studying their properties as stellar-evolution endpoints (see review by Stairs (2004)). The detection of relativistic effects like the Shapiro delay, most easily measured for highly-inclined binary systems with a massive companion, can reveal the orbital geometry as well as the masses of the pulsar and its companion (Ferdman et al., 2010). Precise mass measurements of the pulsar further our understanding of matter at (super)nuclear densities by providing constraints on the possible equations of state, e.g. Demorest et al. (2010).

Here, we report the discovery and the orbital parameters of PSR J1952+2630. This pulsar is in an almost circular 9.4-hr orbit with a massive companion of at least  $0.95 M_{\odot}$ , assuming a pulsar mass of  $1.4 M_{\odot}$ . Thus, this new binary system is a good candidate for the measurement of relativistic effects like the Shapiro delay and could have an impact on all science areas listed above.

### 5.2 Discovery of PSR J1952+2630

---

PSR J1952+2630 was discovered in Pulsar ALFA (PALFA) survey observations taken in August 2005 with the 305-m Arecibo telescope. The survey observations cover two sky regions close to the Galactic plane ( $|b| \leq 5^{\circ}$ ). One region is in the inner Galaxy ( $32^{\circ} \lesssim \ell \lesssim$

77°) and is observed with 268 s dwell time per observation; the other in the outer Galaxy ( $168^\circ \lesssim \ell \lesssim 214^\circ$ ) with 134 s long observations. The observations use ALFA, a cooled seven feed-horn, dual-polarisation receiver at 1.4 GHz (Cordes et al., 2006). Signals are amplified, filtered, and down-converted. Then, autocorrelation spectrometers, the Wideband Arecibo Pulsar Processors (WAPPs) (Dowd et al., 2000), sum polarisations and generate spectra over 100 MHz of bandwidth with 256 channels every  $64 \mu\text{s}$ .

Data are archived at the Center for Advanced Computing (CAC), Cornell University. They are searched for isolated and binary pulsars in three independent pipelines: (1) a pipeline at the CAC searching for isolated pulsars and single pulses; (2) a pipeline using the PRESTO<sup>1</sup> software package operating at several PALFA Consortium member sites, searching for isolated pulsars and binary pulsars with orbits longer than  $\approx 1$  hr, and single pulses; and (3) Einstein@Home, searching for isolated or binary pulsars with orbits longer than 11 minutes.

Einstein@Home<sup>2</sup> is a distributed computing project. Its main goal is the detection of gravitational waves from unknown rapidly-spinning neutron stars in data from the LIGO and VIRGO detectors (Abbott et al., 2009). Since March 2009, about 35% of Einstein@Home compute cycles have been used to search for pulsars in radio data from the PALFA survey. For Einstein@Home, volunteer members of the public sign up their home or office computers, which automatically download work units from project servers over the internet, carry out analyses when idle, and return results. These are automatically validated by comparison with results for the *same* work unit, produced by a different volunteer's computer. As of today, more than 280,000 individuals have contributed; each week about 100,000 different computers download work. The aggregate sustained computational power of 0.38 PFlop/s is comparable to that of the world's largest supercomputers<sup>3</sup>.

For Einstein@Home, raw data are transferred from the CAC to the Albert Einstein Institute, Hannover, Germany, via high-speed internet connections. There, servers de-disperse the raw data into time series with 628 trial dispersion measure (DM) values up to  $1002.4 \text{ pc cm}^{-3}$ . For bandwidth and throughput reasons, the time resolution of the raw data is reduced by a factor of two to  $128 \mu\text{s}$ . The de-dispersed and down-sampled time series are downloaded by the volunteers' computers over the internet and coherently searched for signals from pulsars in circular orbits longer than 11 minutes. A detection statistic, the significance  $\mathcal{S} = -\log_{10}(p)$ , is evaluated on a grid of parameter space points, where  $p$  is the false-alarm probability of the signal in Gaussian noise. A list of the 100 most significant candidates for each de-dispersed time series is returned. After completion of all work units for a given observation, the results are post-processed on servers in Hannover, visually inspected and optimised using tools from the PRESTO software package and finally uploaded to a central database at Cornell. A more detailed account of the Einstein@Home pipeline is available in Allen et al. (2011).

The 20.7-ms pulsar J1952+2630 was found with a maximum significance of  $\mathcal{S} = 39.6$  by visual inspection of the Einstein@Home results from a 268-s survey pointing with beam center at equatorial coordinates (J2000.0)  $\alpha = 19^{\text{h}}52^{\text{m}}34.^{\text{s}}5$ ,  $\delta = +26^\circ 31' 14''$ . The pulsar is detected most significantly at a dispersion measure of  $\text{DM} = 315.4 \text{ pc cm}^{-3}$ . The NE2001 model of Cordes and Lazio (2002) with the given sky position implies a distance of  $9.4^{+2.1}_{-1.4}$  kpc. The discovery observation exhibits a marginally significant, but large, barycen-

<sup>1</sup><http://www.cv.nrao.edu/~sransom/presto/>

<sup>2</sup><http://einstein.phys.uwm.edu/>

<sup>3</sup><http://www.top500.org/list/2010/11/100>

tric period derivative  $\dot{P} = 1.1(7) \times 10^{-9} \text{s s}^{-1}$  over the short observation time and indicates that PSR J1952+2630 is in a short-period binary system.

The overview plot for all Einstein@Home candidates from the discovery beam is shown in Figure 5.1. The coordinates used in this discovery plot are explained in Section 3.10.2. The harmonic structure from detections at rational fractions and integer multiples of the spin frequency is clearly visible as well as the peak in significance as a function of dispersion measure.

Figure 5.2 shows a collection of diagnostic plots generated with a part of the PRESTO software package.

### 5.3 Follow-up observations

To obtain the orbital parameters of the binary system, follow-up observations with the Arecibo telescope were carried out between 2010 July 29 and 2010 November 24. They were conducted mostly in coincidence with PALFA survey observations and used the central beam of the ALFA receiver with the Mock spectrometers<sup>4</sup>. These observations provide a total spectral range of 300 MHz in two overlapping bands of 172 MHz with 512 channels each, centred on 1.4 GHz at a time resolution of 65.476  $\mu\text{s}$ . For our analysis, we use data from the upper band ranging from 1.364 GHz to 1.536 GHz, since the lower band tends to show more radio frequency interference from terrestrial sources. Most follow-up observations cover an observation time  $T_{\text{obs}} \approx 600 \text{ s}$ , though a few are of shorter duration. On 2010 July 29 and 2010 July 30 two longer ( $T_{\text{obs}} \approx 4200 \text{ s}$ ) follow-up observations with a time resolution of 142.857  $\mu\text{s}$  covering the same frequency range in 2048 channels were carried out. The epochs of the follow-up observations range from MJDs 55407 to 55525.

On 2010 August 19, gridding observations of the pulsar position were performed at 2.1 GHz to improve the uncertainty of the discovery sky position. We used a square grid centred on the discovery position with 9 observation pointings. The pulsar was found with equal signal-to-noise ratio in two of the gridding pointings. The improved sky position half-way between these two pointings is  $\alpha = 19^{\text{h}}52^{\text{m}}34.^{\text{s}}4$ ,  $\delta = +26^{\circ}30'14''$  with an uncertainty of  $\approx 1'$  given by the telescope beam size.

Figure 5.3 shows the folded pulse profile of PSR J1952+2630 obtained from the 576-s follow-up observation on 2010 September 19. The full width at half maximum duty cycle is 6%, corresponding to a width of the pulse of  $w_{50} = 1.3 \text{ ms}$ . The dispersive delay across a frequency channel is 0.3 ms for the given DM, frequency resolution and central frequency. We calibrate the profile using the radiometer equation to predict the observation system's noise level. Since the sky position is known to  $1'$  accuracy, we can only derive limits on the flux density. We obtain a system equivalent flux density  $S_{\text{sys}}$  of 3.0 Jy to 3.8 Jy, depending on the precise pulsar position within the beam<sup>5</sup>. The observation bandwidth is 172 MHz, the observation time is 576 s, and the folded profile has  $N = 128$  bins; then the expected off-pulse noise standard deviation used for calibration is 76  $\mu\text{Jy}$  to 98  $\mu\text{Jy}$ . The estimated period-averaged flux density of the pulsar at 1.4 GHz is  $70 \mu\text{Jy} \leq S_{1400} \leq 100 \mu\text{Jy}$  (depending on its position within the beam).

<sup>4</sup><http://www.naic.edu/~astro/mock.shtml>

<sup>5</sup>The unit of the flux density is "Jansky", short Jy;  $1 \text{ Jy} = 10^{-26} \text{ W m}^{-2} \text{ Hz}^{-1}$ .

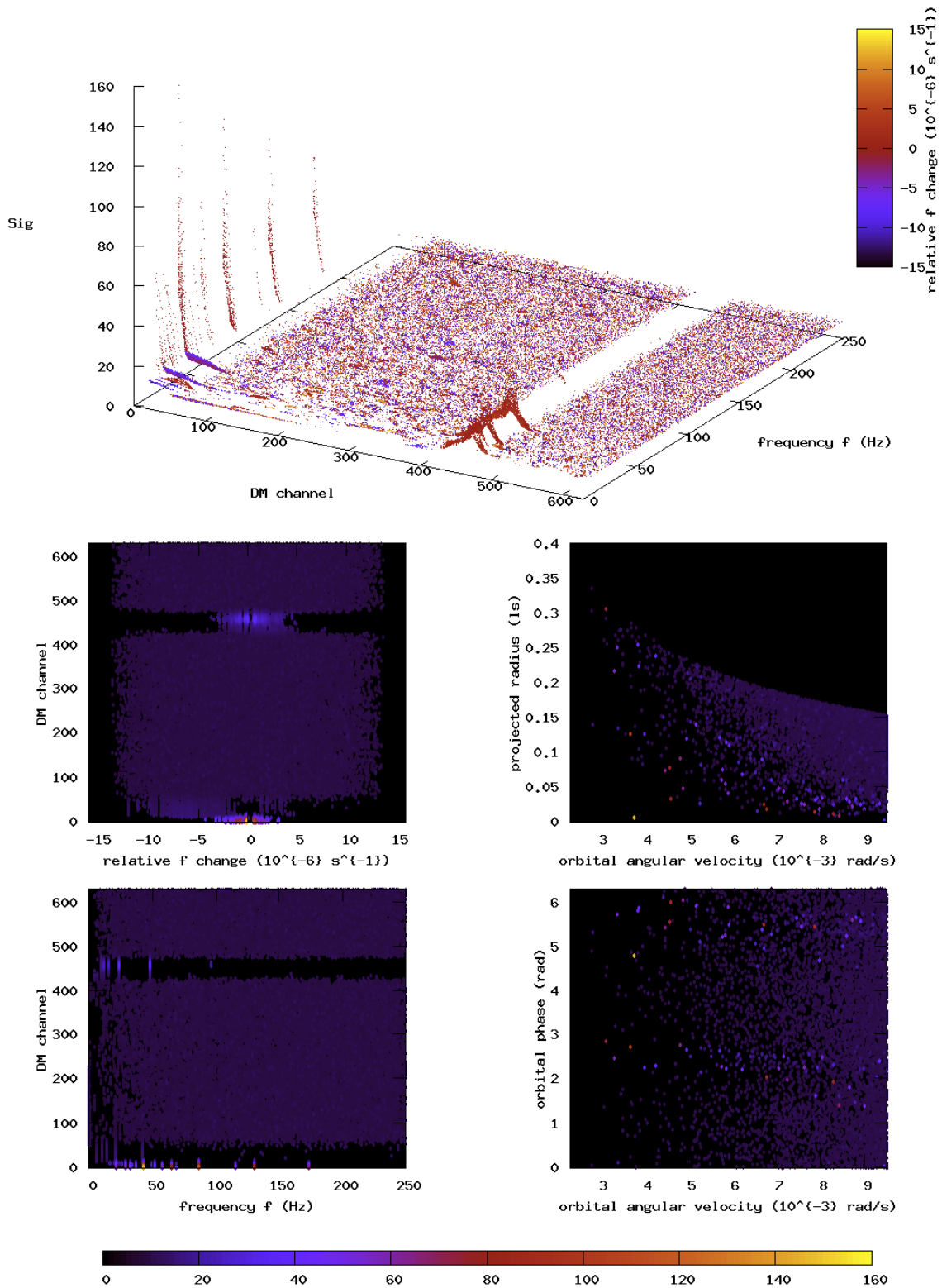


**Figure 5.1:** Einstein@Home result overview plots from the J1952+2630 discovery beam. **(Top)** the harmonic structure and the DM peak are clearly visible in the three-dimensional plot of significance as a function of dispersion measure and spin frequency. **(Bottom)** mismatch and harmonic structures in other dimensions of the parameter space.

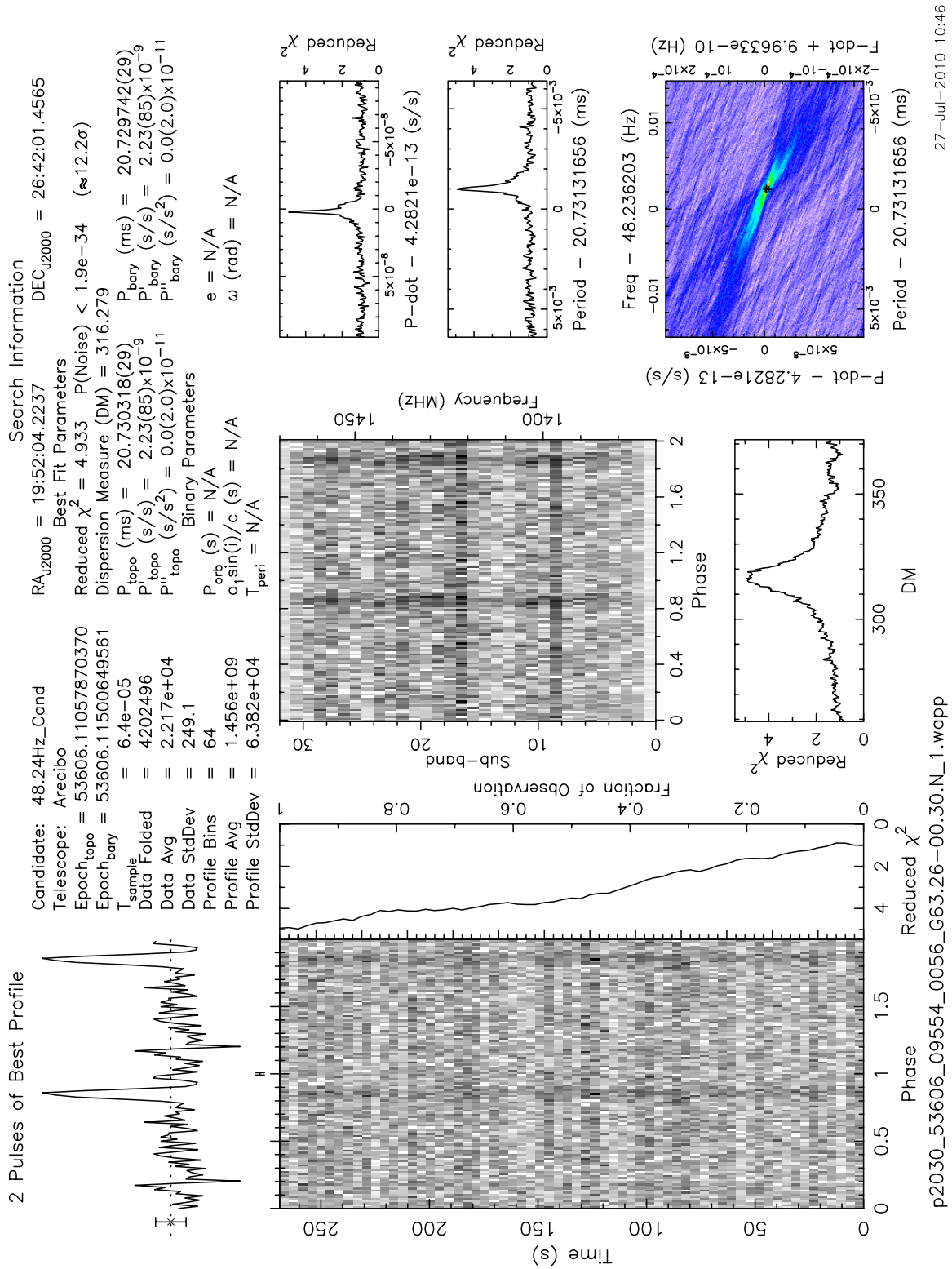


**Figure 5.2:** PSR J1952+2630 diagnostic PRESTO plots from the discovery observation. The top left plot is the folded pulse profile over two rotations of the pulsar; below it a pulse phase vs. observation time plot shows the emission of the pulsar over the observation. The grey-scale plot in the center shows the broad-band radio emission as a function of the pulse phase and below it, the peak in  $\chi^2$  as a function of dispersion measure is displayed. In the right panel, a  $\chi^2$  in  $P$  and  $\dot{P}$  along with two cuts is shown. Note the high value of barycentric period derivative indicating acceleration of the pulsar due to binary motion.

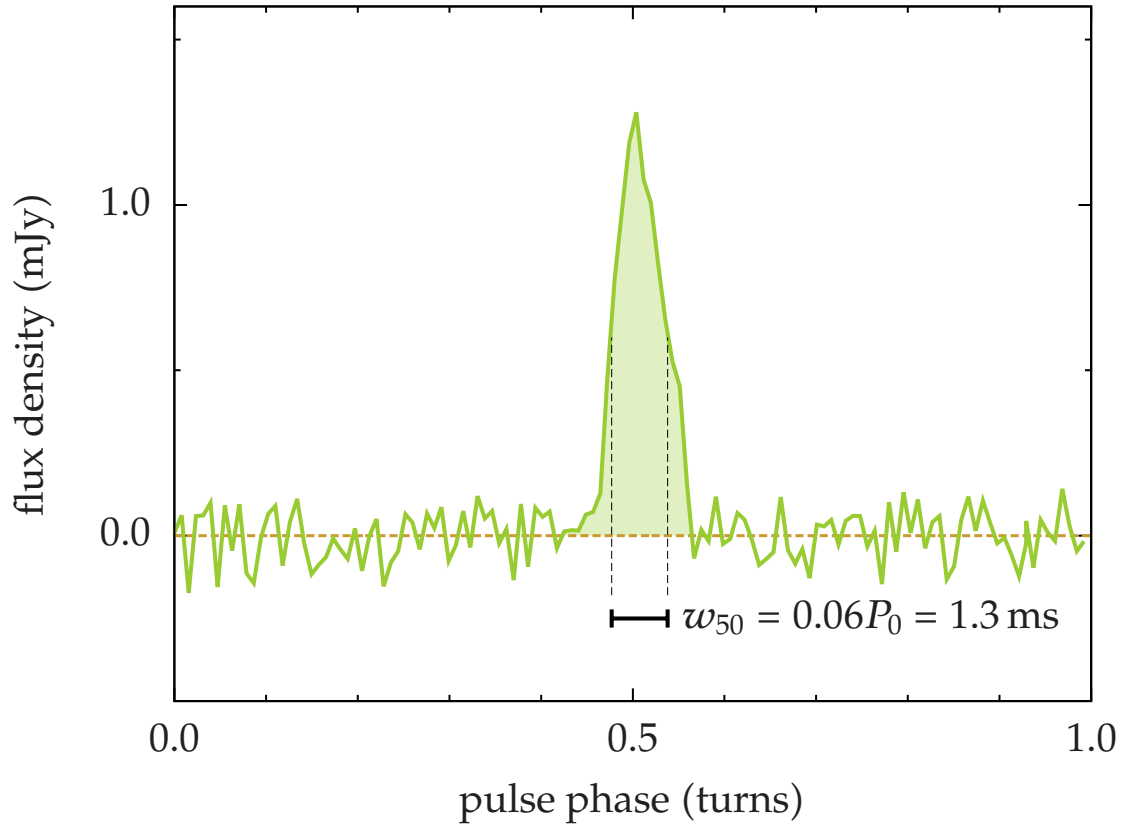


**Figure 5.3:** The folded pulse profile of PSR J1952+2630 at 1.4 GHz from the 576-s follow-up observation on 2010 September 20. The resulting period-averaged flux density is  $70 \mu\text{Jy} \leq S_{1400} \leq 100 \mu\text{Jy}$  (depending on the precise pulsar position within the beam). The duty cycle is 6% of the pulsar period  $P_0$ . The dispersive delay across a frequency channel is 0.3 ms.

## 5.4 Spin period-based orbital solution

We now describe how to obtain a solution for the orbital parameters of a binary pulsar system based on measurements of the barycentric spin period and spin period derivative. For this spin period-based analysis we closely follow the method described in (Freire et al., 2001a).

The pulsar's orbital motion in a binary system causes changes of the apparent barycentric spin frequency over time due to the Doppler effect. For a pulsar in a circular orbit, the barycentric spin period  $P$  and the acceleration  $a$  as a function of the orbital phase  $\theta = \Omega_{\text{orb}}(t - T_{\text{asc}})$  measured from the time of passage of the ascending node  $T_{\text{asc}}$  are given by

$$P(\theta) = P_0(1 + x\Omega_{\text{orb}} \cos(\theta)) = P_0 + P_1 \cos(\theta) \quad (5.1)$$

and

$$a(\theta) = -c\Omega_{\text{orb}}^2 x \sin(\theta) = -A_1 \sin(\theta), \quad (5.2)$$

respectively. The quantities on the right-hand sides are defined as  $P_1 \equiv P_0 x \Omega_{\text{orb}}$  and  $A_1 \equiv -c\Omega_{\text{orb}}^2 x$ .  $P_0$  is the intrinsic barycentric spin period of the pulsar,  $x = r \sin(i) / c$  is the projected orbital radius in units of light-seconds.  $r$  is the radius of the pulsar orbit,  $i$  the

orbital inclination, and  $c$  the speed of light. The orbital angular velocity is  $\Omega_{\text{orb}} = 2\pi/P_{\text{orb}}$  for an orbital period  $P_{\text{orb}}$ . The acceleration is calculated from the measured barycentric spin period  $P$  and spin period derivative  $\dot{P}$  via

$$a = \frac{c\dot{P}}{P}. \quad (5.3)$$

Finding the unique orbital solution by least-squares fitting of the orbital parameters  $(P_{\text{orb}}, x, T_{\text{asc}})$  and the intrinsic spin period  $P_0$  from Eqs. (5.1) and (5.2) can be very difficult with a given set of  $(P, a)$  measurements. If the measurements are separated by gaps larger than one orbital period, deriving  $P_{\text{orb}}$  is hindered by the unknown number of complete orbits in the gaps. Eliminating the time  $t$  breaks the degeneracy and enables first reliable estimates that can serve as initial values for a refinement we describe in Section 5.4.2.

#### 5.4.1 First estimates of the orbital parameters

From the right-hand sides of Eqs. (5.1) and (5.2) it is clear that a circular orbit traces out an ellipse in counter-clockwise direction in the plane of  $P$  and  $a$ , centred on  $(P_0, 0)$  with semi-major axes  $P_1$  and  $A_1$ , respectively independent of  $t$ . The defining equation of this ellipse is given by

$$\frac{(P - P_0)^2}{P_1^2} + \frac{a^2}{A_1^2} = 1 \quad (5.4)$$

We rewrite this as a parabola in the coordinates  $a^2$  and  $P$ :

$$a^2 = A_1^2 - \frac{A_1^2}{P_1^2} (P - P_0)^2. \quad (5.5)$$

In these coordinates it is now straightforward to apply a least-squares fitting algorithm. From the best-fit values of  $P_0$ ,  $P_1$ , and  $A_1$  first estimates of the orbital parameters are calculated using

$$P_{\text{orb}} = \frac{2\pi c P_1}{P_0 A_1} \quad \text{and} \quad x = \frac{c P_1^2}{A_1 P_0^2}, \quad (5.6)$$

compare Eqs. (7) and (8) from (Freire et al., 2001a).

For each follow-up observation of length  $T_{\text{obs}} \gtrsim 600$  s, we obtain a pair of values, the barycentric spin period  $P$  and the spin period derivative  $\dot{P}$ , using the PRESTO software package. For the two longer follow-up observations of  $T_{\text{obs}} \approx 4200$  s, we obtain  $(P, \dot{P})$  pairs over seven contiguous stretches of approximately 600 s each. The acceleration is computed from  $a = c\dot{P}P^{-1}$ , yielding in total 34  $(P, a)$  pairs. From these, we compute the best-fitting orbital parameters with the method described above. We employ the Levenberg-Marquardt algorithm included in the gnuplot plotting software<sup>6</sup> for the least-squares fitting. The data points are weighted by their inverse variance. The best-fitting parameters are

$$P_0 = 20.732361(32) \text{ ms}, P_1 = 0.010772(61) \text{ ms}, \text{ and } A_1 = 29.33(30) \text{ m s}^{-2}. \quad (5.7)$$

The numbers in parentheses show the estimated 1-sigma errors in the last two digits. The error estimates are from the least-squares fitting algorithm. The derived orbital parameters are

$$x = 2.760(43) \text{ lt-s and } P_{\text{orb}} = 9.27(11) \text{ h} \quad (5.8)$$

<sup>6</sup><http://www.gnuplot.info/>

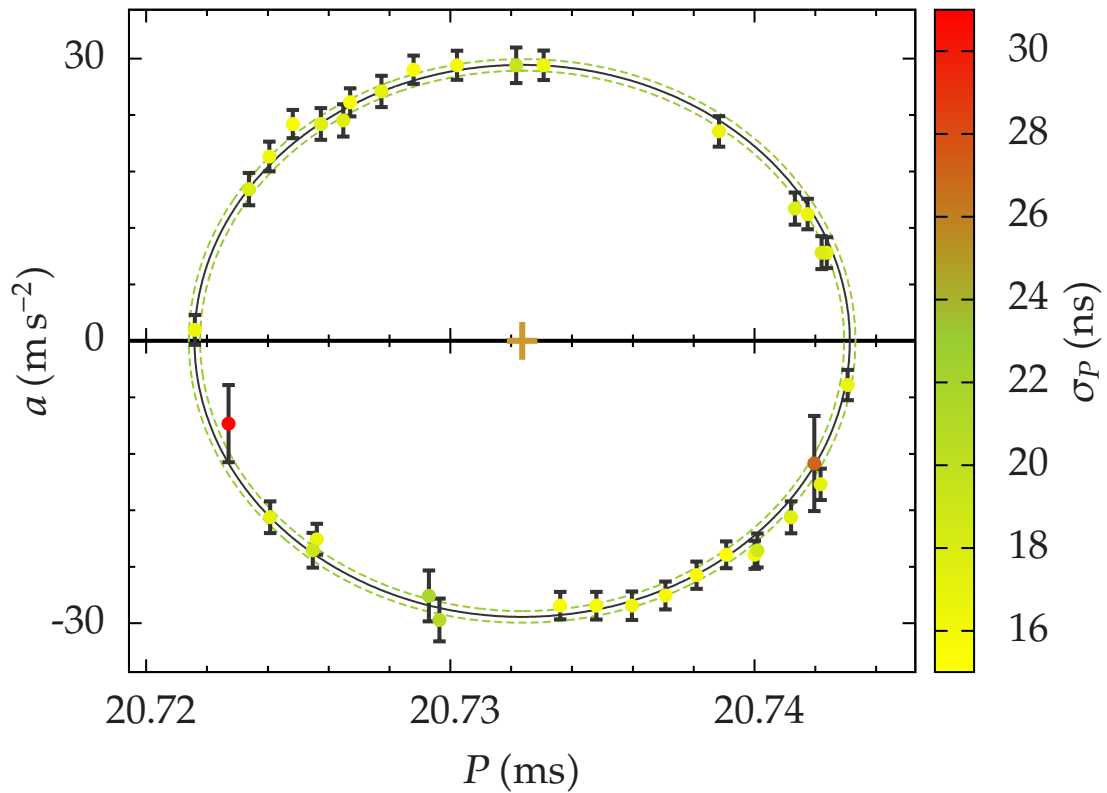


**Figure 5.4:** The measured barycentric spin periods  $P$  and derived barycentric accelerations  $a$ . Error bars indicate the estimated 1-sigma errors in acceleration, while the colour code of the dots shows the estimated 1-sigma spin period error in ns for each measurement. The dark-grey ellipse shows the best-fitting circular orbital solution, while the dashed green ellipses show the 1-sigma confidence region. The orange cross marks the center of the best fit ellipse.

with the errors defined as above. Note that the errors are relatively large. Figure 5.4 shows the measured spin periods and accelerations and the best fitting ellipse for a circular orbit.

Since the time dependence was eliminated we do not to obtain  $T_{\text{asc}}$  by fitting the ellipse alone.

### 5.4.2 Refining the orbital parameters

The initial set of orbital parameters can be extended and its errors reduced by exploiting the full information provided by Equation (5.1) and all spin period measurements. We perform a least-squares fit (Levenberg-Marquardt algorithm, data weighted by inverse variances) in the full parameter set of  $\Omega_{\text{orb}}$ ,  $T_{\text{asc}}$ ,  $x$  and  $P_0$ <sup>7</sup>. The barycentric spin period as a function of time  $t$  for a circular orbit is given by writing out Equation (5.1):

$$P(t) = P_0(1 + x\Omega_{\text{orb}} \cos(\Omega_{\text{orb}}(t - T_{\text{asc}}))). \quad (5.9)$$

<sup>7</sup>We note that for reasons of numerical stability we fit for  $\psi$  in the modified expression  $\cos(\Omega_{\text{orb}}(t_{\text{MJD}} - 55407) + \psi)$  for the cosine instead of fitting for  $T_{\text{asc}}$ . Then,  $T_{\text{asc}} = 55407 - \frac{\psi}{2\pi} P_{\text{orb}}$

Fitting  $P(t)$  over the complete set of available observations provides tighter constraints on the orbital parameters and breaks some of the parameter degeneracies in the ellipse parameters. The starting values for the fitting procedure are the initial estimates from Section 5.4.1. To achieve convergence of the fitting process, increasingly larger sets of data points and parameters have to be included and multiple re-fitting steps are necessary.

### 5.4.3 Markov Chain Monte Carlo sampling

After the fit has converged, the parameters are further refined and their errors estimated by Markov chain Monte Carlo (MCMC) sampling. With the MCMC sampling, the results of the least-squares fitting are verified and better estimates of the errors are obtained.

Proposal points for the chain are randomly chosen from uniform distributions in  $P_0$ ,  $x$ ,  $P_{\text{orb}}$ ,  $\varphi$ ,  $e$ , and  $\omega$ . The intervals centred on the best-fit value found by the refinement process; the size of the intervals is eight times as the size of the estimated error from the least-squares fitting to guarantee coverage of a wide enough parameter space. We use a Independence Chain Metropolis-Hastings approach; here, the proposal density does not depend on the current state of the chain. The sampling process itself still is a chain because the choice of the  $n + 1$ -th sample depends on the  $n$ -th sample.

In total we obtain  $4 \times 10^6$  MCMC samples from the distribution; they were split up in 800 cluster jobs each generating 5000 samples. The resulting histograms in each dimension are shown in Figure 5.5. Table 5.1 shows the refined orbital parameters for PSR J1952+2630 obtained in this manner.

This simple model does not take into account the intrinsic spin-down of the pulsar. Fitting for the spin down rate is not yet possible with the data reported here, because of the degeneracy with an offset in sky position, which itself is not known to high enough accuracy. This effect results in a systematic error of the best-fit results at an unknown level.

With the improved orbital parameters we reduce the spin period measurements to the interval of one orbital period to show the varying barycentric spin period as a function of the orbital phase. Each measurement  $(t, P(t))$  is mapped to  $(\theta(t), P(t))$ , where  $\theta(t)$  is the orbital phase as defined before Equation (5.1). Figure 5.7 shows all measured spin periods  $P$  as a function of the orbital phase  $\theta$  in the upper panel and the residuals in spin period in the lower panel. No clear structure is visible in the residuals and thus no striking evidence of non-zero eccentricity is apparent. The choice of the circular orbital model is therefore justified.

### 5.4.4 Upper limit on orbital eccentricity

To set an upper limit on the eccentricity of PSR J1952+2630's orbit, we modify the circular orbital model used above. We use a spin-period model based on the ELL1 timing model by (Lange et al., 2001) which was developed for orbits with small eccentricity  $e$ . Then, Equation (5.1) in first order in  $e$  is modified to

$$P(\theta) = P_0 [1 + x\Omega_{\text{orb}} (\cos(\theta) + \varepsilon_1 \sin(2\theta) + \varepsilon_2 \cos(2\theta))], \quad (5.10)$$

where the additional constants are given by  $\varepsilon_1 = e \sin(\omega)$  and  $\varepsilon_2 = e \cos(\omega)$ , respectively. The angle  $\omega$  is the longitude of the periastron measured with respect to the ascending node of the orbit. We now fit for the complete set of parameters  $(P_0, x, \Omega_{\text{orb}}, T_{\text{asc}}, \varepsilon_1, \varepsilon_2)$  using the measured  $P(t)$ . Following the same method as described in Section 5.4.2, we find the best fitting orbital solution including the additional eccentricity parameters. An MCMC

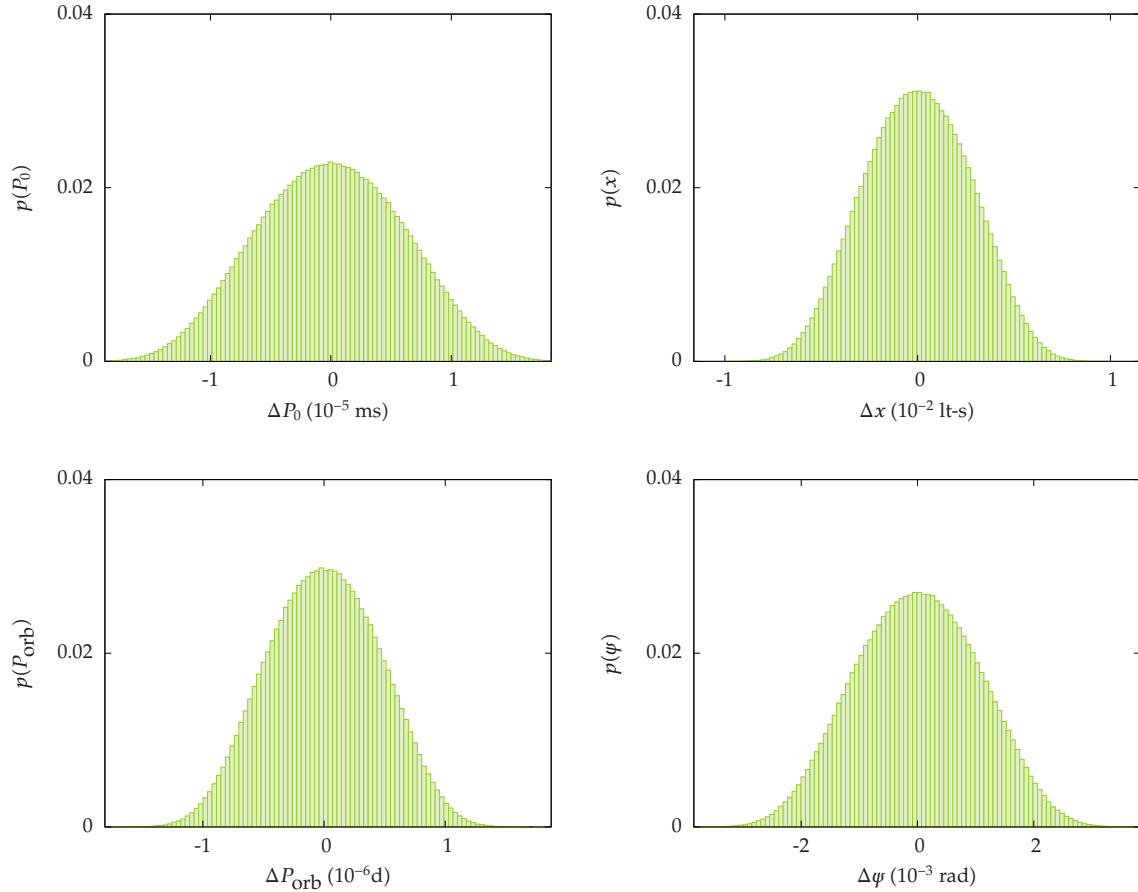


**Figure 5.5:** Histograms of the marginalised posterior distributions for the pulsar parameters  $P_0$ ,  $x$ ,  $P_{\text{orb}}$ , and  $\psi$  from an MCMC sampling of the parameter space. In total  $4 \times 10^6$  samples were generated, here we only show  $4 \times 10^5$  samples per plot. Each plot shows the deviations from the best-fit values from Table 5.1.

sampling of the parameters space is also conducted for this spin period model (5.10). Figure 5.8 shows the marginalised posterior distribution for the eccentricity  $e$  while Figure 5.9 shows the correlations of eccentricity with the other model parameters. The parameters ( $P_0, x, \Omega_{\text{orb}}, T_{\text{asc}}$ ) only change slightly within the confidence regions obtained from the circular fit. The posterior probability distribution function (pdf) of the eccentricity is consistent with a circular ( $e = 0$ ) orbital model; from the posterior pdf we obtain a  $2\sigma$  upper limit on the eccentricity of  $e \lesssim 1.7 \times 10^{-3}$

## 5.5 Discussion

The mass function is defined by

$$f = \frac{4\pi^2 c^3}{G} \frac{x^3}{P_{\text{orb}}^2} = \frac{(m_c \sin(i))^3}{(m_p + m_c)^2} \quad (5.11)$$

where  $m_p$  and  $m_c$  are the pulsar mass and the companion mass, respectively. Inserting the orbital parameters yields  $f = 0.15360(1) M_\odot$  for PSR J1952+2630. Assuming a pulsar mass

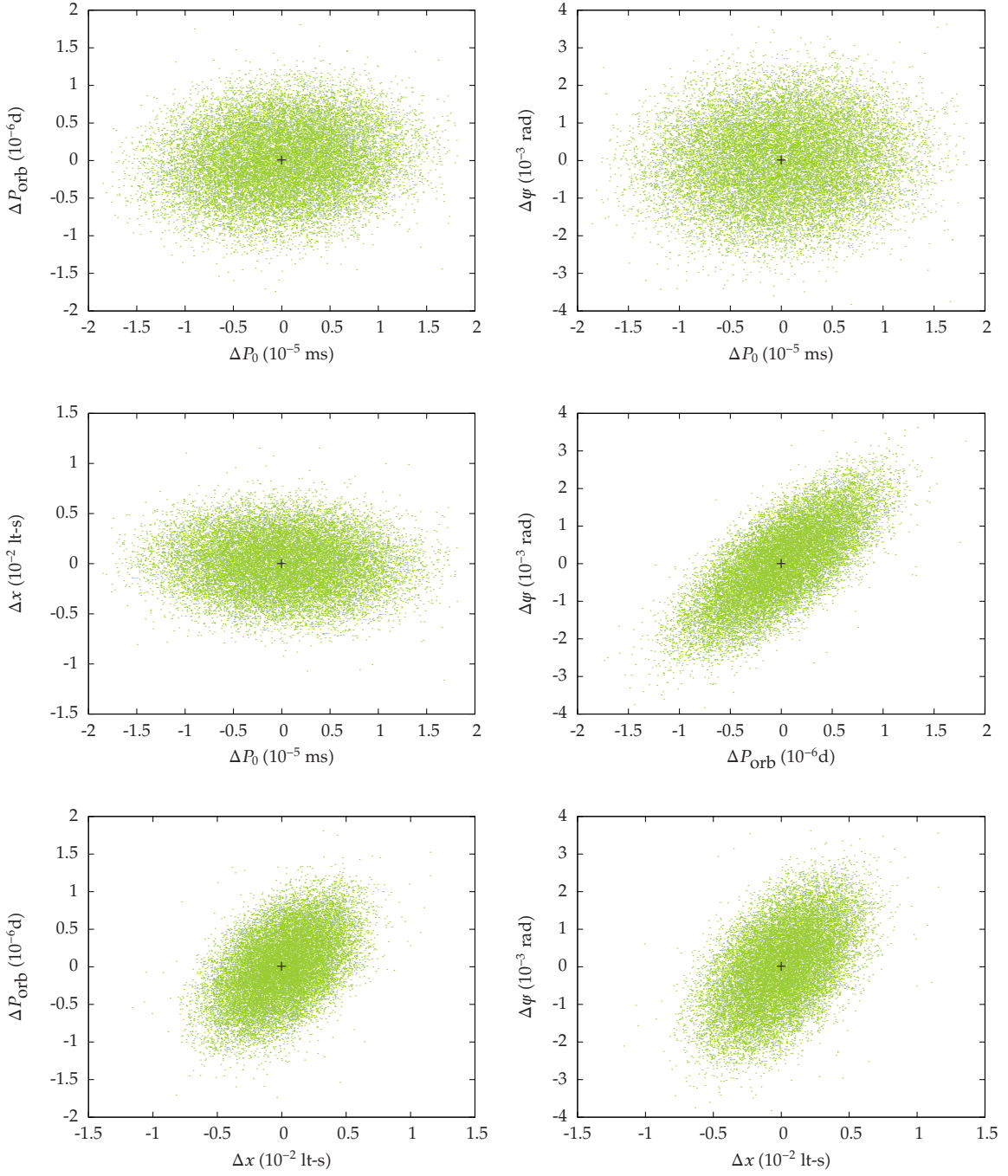


**Figure 5.6:** Scatter plots of the marginalised two-dimensional posterior distributions for the pulsar parameters  $P_0$ ,  $x$ ,  $P_{\text{orb}}$ , and  $\psi$  from an MCMC sampling of the parameter space. In total  $4 \times 10^6$  samples were generated, here we only show  $4 \times 10^5$  samples per plot. Each plot shows the deviations from the best-fit values from Table 5.1.

Table 5.1: PSR J1952+2630 Parameters from a Spin-period based Analysis

| Parameter  | Value   |
|--|---|
| Right ascension, $\alpha$ (J2000.0) .....                        | 19 <sup>h</sup> 52. <sup>m</sup> 6 <sup>a</sup> |
| Declination, $\delta$ (J2000.0) .....                            | +26°30' <sup>a</sup>                            |
| Galactic longitude, $\ell$ (deg) .....                           | 63.25 <sup>a</sup>                              |
| Galactic latitude, $b$ (deg) .....                               | -0.37 <sup>a</sup>                              |
| Distance, $d$ (kpc) .....  | 9.4 <sup>+2.1</sup> <sub>-1.4</sub>             |
| Distance from the Galactic plane, $ z $ (kpc) .....              | 0.06  |
| Dispersion measure, DM (pc cm <sup>-3</sup> ) .....              | 315.4   |
| Period averaged flux density, $S_{1400}$ ( $\mu$ Jy) .....       | $\leq 100, \geq 70$                             |
| FWHM duty cycle (pulse width, $w_{50}$ (ms)) .....               | 6% (1.3)  |
| Intrinsic barycentric spin period, $P_0$ (ms) .....              | 20.732368(6)                                    |
| Projected orbital radius, $x$ (lt-s) .....                       | 2.801(3)  |
| Orbital period, $P_{\text{orb}}$ (d) .....                       | 0.3918789(5)                                    |
| Time of ascending node passage, $T_{\text{asc}}$ (MJD) .....     | 55406.91066(7)                                  |
| Orbital eccentricity, $e$ .....                                  | $\lesssim 1.7 \times 10^{-3}$ ( $2\sigma$ )     |
| Mass function, $f$ ( $M_{\odot}$ ) .....                         | 0.15360(1)                                      |
| Minimum companion mass, $m_c$ ( $M_{\odot}$ ) .....              | 0.945   |
| Median companion mass, $m_{c, \text{med}}$ ( $M_{\odot}$ ) ..... | 1.16  |

<sup>a</sup>The sky position was obtained from a gridding observation and has an accuracy of 1' given by the telescope beam size.

Thirty-four measurements of  $P$  and  $\dot{P}$  between MJDs 55407 and 55525 are used. The numbers in parentheses show the estimated  $1\sigma$  errors in the last digits.

$m_p = 1.4 M_{\odot}$ , we obtain a minimum companion mass  $m_c \geq 0.945 M_{\odot}$  for  $i = 90^\circ$ . With  $i = 60^\circ$  we obtain the median companion mass  $m_{c, \text{med}} = 1.16 M_{\odot}$ . For a companion mass  $m_c = 1.25 M_{\odot}$  (smallest measured neutron star mass (Kramer et al., 2006b), we obtain an inclination angle of  $i = 55.1^\circ$ .

No evidence of eccentricity  $e > 1.7 \times 10^{-3}$  is found from this analysis. A common envelope phase with mass transfer in the system's past can explain the almost circular orbit and the short orbital period. Also, the companion's progenitor most likely was not massive enough to undergo a supernova explosion; the supernova would have likely kicked the companion which almost guarantees a much higher orbital eccentricity. Thus, a neutron star companion is conceivable but unlikely. The companion most likely is a massive white dwarf. The high white dwarf companion mass, the compactness of the orbit, and the moderate spin period, indicate that the pulsar most likely survived a common envelope phase (Ferdman et al., 2010).

Low eccentricity, spin period, and high companion mass most likely place this system in the rare class of intermediate mass binary pulsars (IMBPs) (Camilo et al., 2001). The

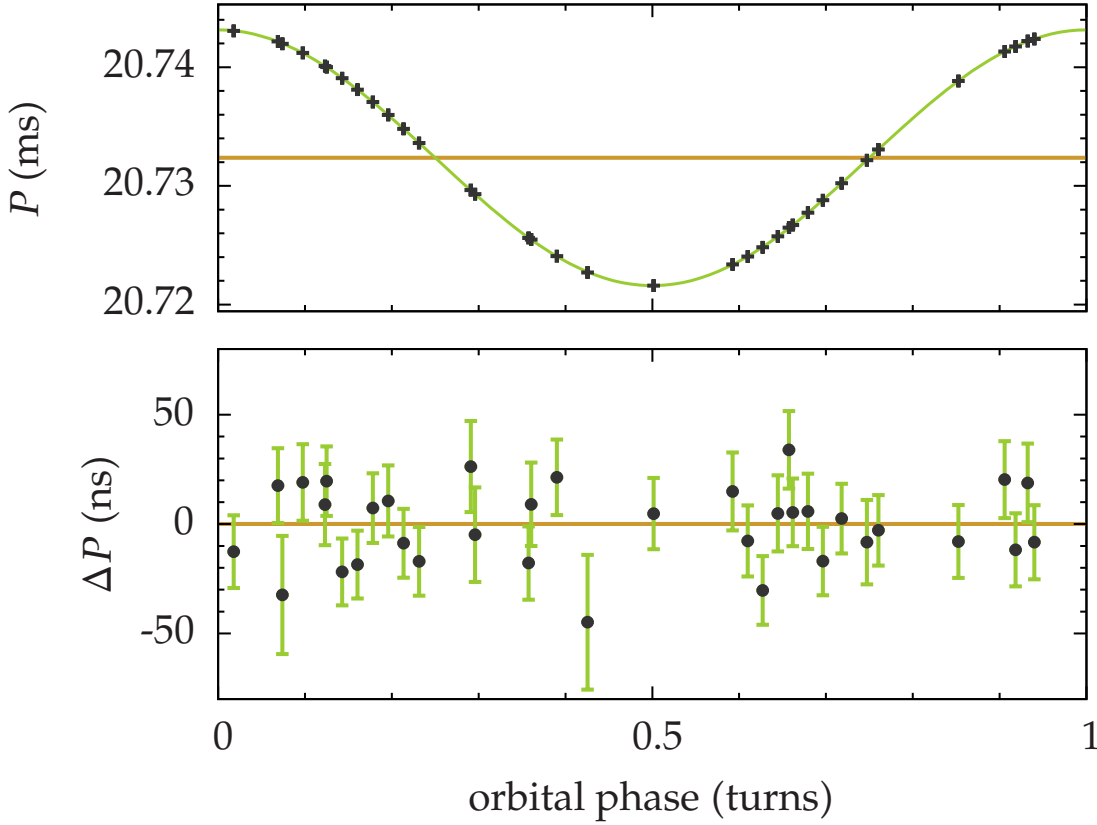


**Figure 5.7:** (Top) Points (with error bars, too small to see) are the measured spin periods  $P$  as a function of the orbital phase computed from the orbital model in Table 5.1. The curve is the expected model spin frequency, the thin orange line is at  $P_0$ . (Bottom) The residual difference between expected and measured spin frequency as a function of the orbital phase. No clear trend indicating non-zero eccentricity is evident.

distance of PSR J1952+2630 to the Galactic plane,  $|z| \approx 0.06$  kpc, is comparable to that of the other five IMBPs (Ferdman et al., 2010); this low scale height of the known IMBP population might be due to observational selection effects from deep surveys along the Galactic plane (Camilo et al., 2001).

Phinney (1992) derived a relation between the orbital period and eccentricity of low mass binary pulsars (LMBPs with companion mass  $0.15 M_\odot \lesssim m_c \lesssim 0.4 M_\odot$ ). Figure 4 in Camilo et al. (2001) displays this relation for LMBPs and IMBPs. The LMBPs follow the theoretically predicted relation very well, while the IMBPs do not follow the same relation; they have higher eccentricities than LMBPs with the same orbital period. The slope however, seems to be very similar to the one for the LMBPs. This might suggest that there exists a similar relation for this class of binary pulsars. An exact measurement of the orbital eccentricity of PSR J1952+2630 from a coherent timing solution will add another data point that could help to test this hypothesis at short orbital periods.

Detection of the Shapiro delay in PSR J1952+2630 might allow precision mass estimates and strong constraints on the orbital geometry of the binary. Figure 5.10 shows the measurable Shapiro delay amplitude for PSR J1952+2630 as a function of the pulsar mass and the companion mass; this is the part not absorbed by Keplerian orbital fitting (peak-to-peak

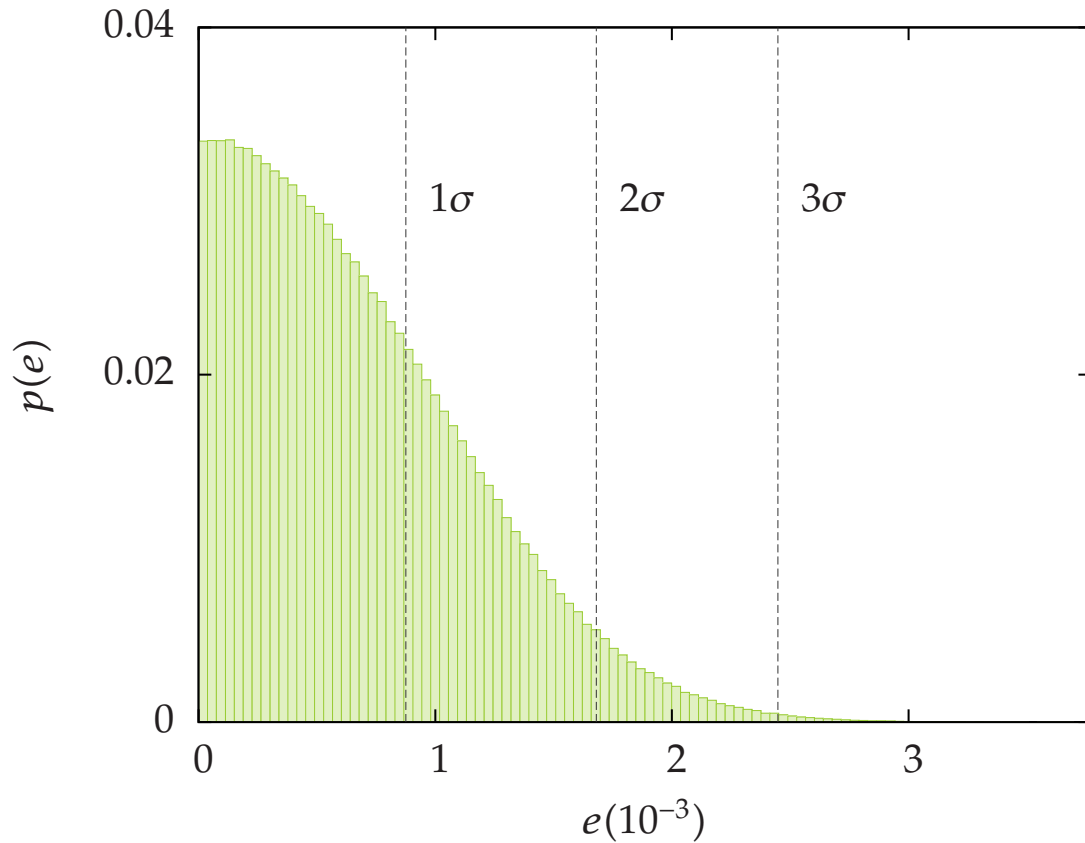


**Figure 5.8:** Histograms of the marginalised posterior distribution of eccentricity  $e$ . Three upper limits on  $e$  are shown by dashed vertical lines.

amplitude of Equation (28) in Freire and Wex (2010)).

Preliminary timing observations using the Mock spectrometers at the Arecibo telescope have TOA uncertainties of approximately  $20 \mu\text{s}$ . These are currently unconstraining, because no dedicated, deep observations at superior conjunction are available. Observations over a larger bandwidth and use of coherent de-dispersion techniques with new instrumentation could improve TOA uncertainties further to  $10 \mu\text{s}$ . Thus, a detection of Shapiro delay requires relatively high inclination angles. If no Shapiro delay is detected, this will enable more stringent lower limits on the companion mass. These alone promise to be interesting, given the already known high minimum companion mass.

## 5.6 Conclusions and future work

We have presented a spin-period based analysis of the orbital parameters of the newly discovered binary pulsar PSR J1952+2630. The pulsar has an orbital period of 9.405 h in an almost circular orbit with a projected radius of 2.80 lt-s. The mass function of  $f = 0.154 M_{\odot}$  implies a minimum companion mass of  $0.946 M_{\odot}$ . Most likely, the companion is a massive white dwarf, although a neutron star companion cannot be excluded.

The above described observations and further follow-up observations will be used to derive a coherent timing solution for PSR J1952+2630. This will provide a more precisely

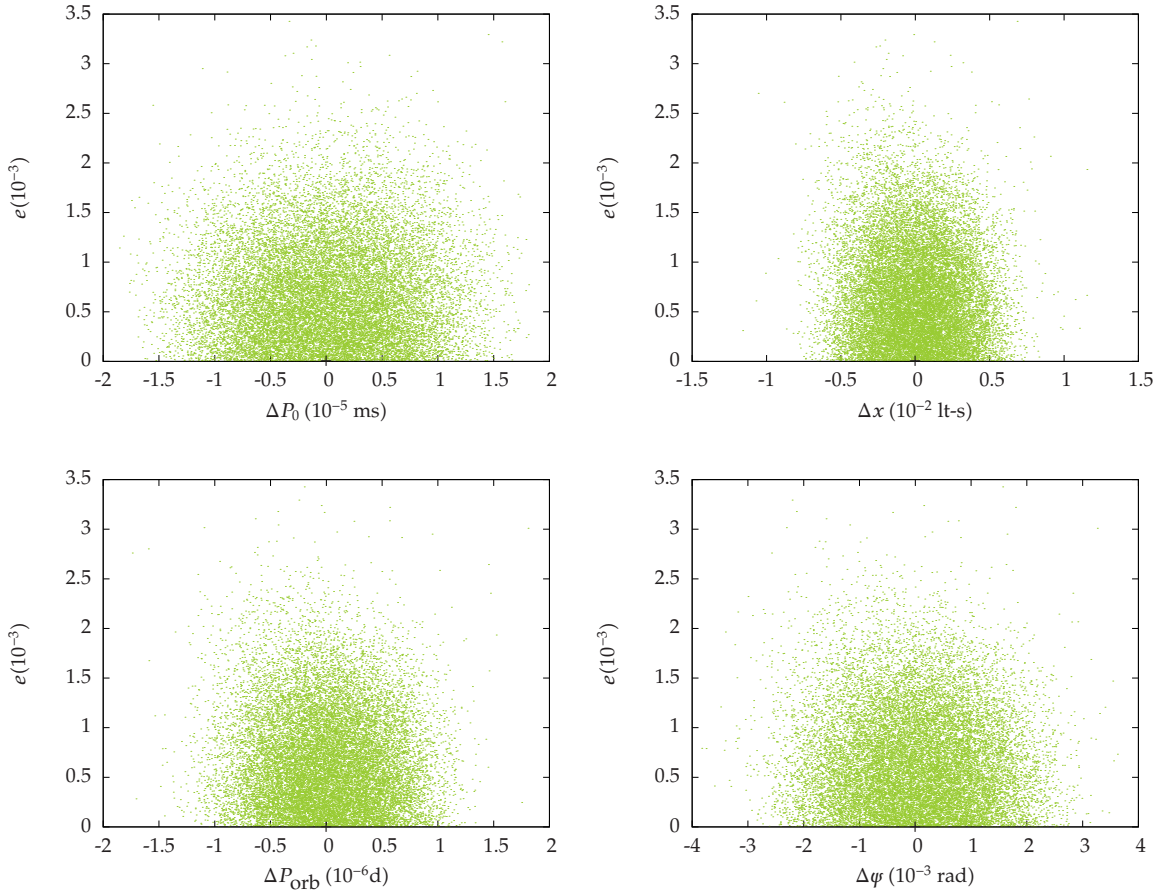


**Figure 5.9:** Scatter plots of the marginalised two-dimensional posterior distributions for the pulsar parameters  $P_0$ ,  $x$ ,  $P_{\text{orb}}$ , and  $\psi$  in combination with eccentricity  $e$  from an MCMC sampling of the parameter space. In total  $4 \times 10^6$  samples were generated, here we only show  $4 \times 10^5$  samples per plot.

measured sky position, orbital parameters, and values for the orbital eccentricity and the intrinsic spin-down of the pulsar. This should enable a detailed description of this binary system and constrain its possible formation.

Detection of the Shapiro delay in this binary pulsar will allow precision mass estimates and strong constraints on the orbital geometry of the binary. If no Shapiro delay is detected, this will enable more stringent lower limits on the companion mass, which alone promise to be interesting given the already known high minimum companion mass.

This pulsar is the second pulsar discovered by the global distributed volunteer computing project Einstein@Home (Knispel et al., 2010). This further demonstrates the value of volunteer computing for discoveries in astronomy and other data-driven science.

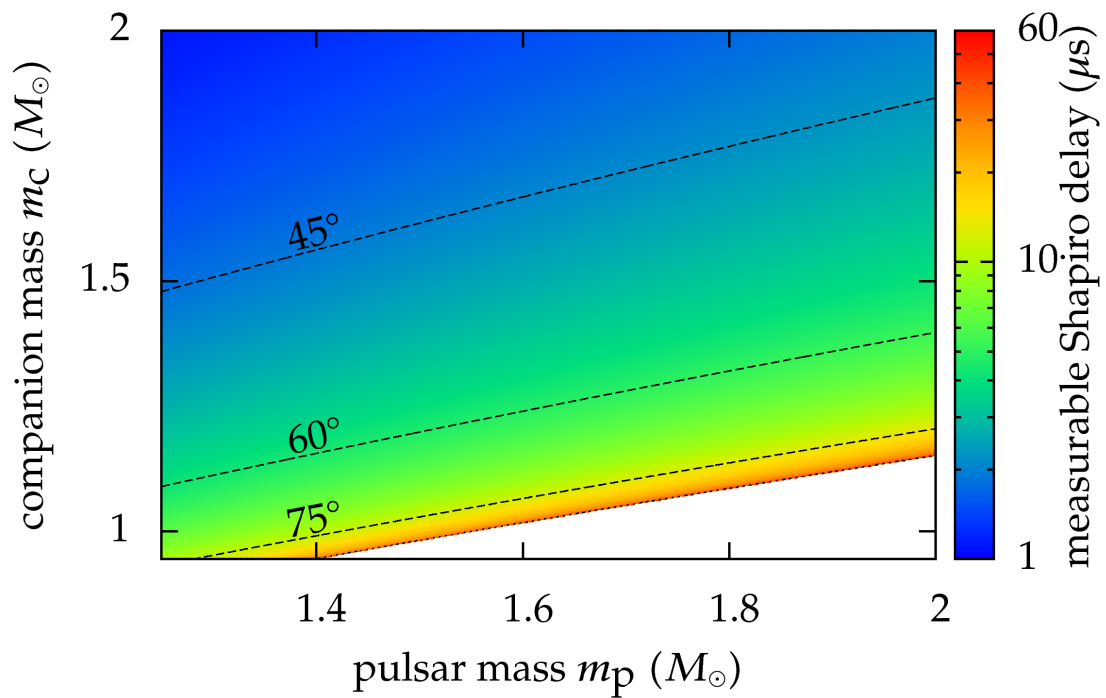


**Figure 5.10:** Measurable Shapiro delay amplitude (not absorbed by Keplerian orbital fitting) for PSR J1952+2630 as a function of the pulsar mass and the companion mass. The dashed lines show constant inclination angles of  $45^\circ$ ,  $60^\circ$ ,  $75^\circ$ , and  $90^\circ$  at the bottom.

# 6

## The Strongest Continuous Gravitational Wave Signal

---

*appeared in Phys. Rev. D 78, 044031 (2008)*

---

### 6.1 Overview and context

---

Continuous emission from spinning neutron stars is a promising source of gravitational waves, however so far no detections have been reported. This could be due to the insufficient sensitivity of detectors and search methods or due to the amplitudes of the present signals. This begs the question “what is the largest expected amplitude of the continuous signal from non-axisymmetric neutron stars?” For the most optimistic look at this, we assume the existence of a (so far undetected) population of spinning neutron stars whose dominant energy loss goes into the production of gravitational waves, rather than into electromagnetic radiation. These are called “gravitars” (Palomba, 2005); we show later in this chapter that gravitars set an upper limit on the amplitude of gravitational waves from spinning neutron stars that are also emitting electromagnetic radiation.

In 1984 Blandford found a simple analytic relationship between the expected maximum amplitude of gravitational waves emitted by gravitars and their average Galactic birthrate. This argument was not published but it is documented by a citation in Thorne (1987). The argument was recently revised in Abbott et al. (2007b). This work revises both the original and the revised Blandford arguments, and shows that two key assumptions of these arguments do not hold in a realistic Galactic model of gravitars. This work corrects the assumptions of the argument, and then investigates how the conclusions are affected by this change.

We stress that while our work studies the behaviour of a population of Galactic gravitars, it does not make a plausibility case for the possible existence of such objects, or study their

potential astrophysical implications. The study itself is nevertheless interesting, because even if gravitars do *not* exist, they provide a relevant upper bound on the gravitational-wave emission by objects (such as rapidly-spinning neutron stars) that *do* exist.

This chapter is organised as follows. Section 6.2 reviews Blandford's argument and its assumptions. A simple analytic calculation is used to derive the frequency-space distribution of the sources. This allows a sharper statement of the conclusion and clarifies the dependence upon the assumptions. The aim of this paper is to test whether these assumptions are fulfilled in a realistic model of our galaxy and, if the assumptions do not hold, what the consequences are. Section 6.3 describes a numerical simulation of the Galaxy, and Section 7.3 presents results for the simulated spatial and frequency distribution of gravitars at the present time. The simulated spatial distributions do not satisfy the assumptions of Blandford's argument: they are not two-dimensional and uniform. Section 6.5 uses these simulated distributions to recompute the expected maximum gravitational-wave amplitudes from gravitars. As shown in Abbott et al. (2007b), the maximum expected gravitational wave amplitudes from gravitars are upper limits for the gravitational wave amplitudes from neutron stars spinning down through combined electromagnetic and gravitational-wave emission. Previous work assumed that all neutron stars are formed with the same (high) birth-frequency. Here, the argument is generalised to cover a continuous distribution of initial frequencies. This is followed by a short conclusion.

For realistic models of neutron stars, the general upper limit on gravitational-wave emission set by considering the gravitar case applies for gravitational-wave frequencies  $f \gtrsim 250$  Hz. The reader who wants to skip all the details and just see the final result is advised to look at Figure 6.6 which is the main result of the paper.

## 6.2 Blandford's argument: an analytic description

### 6.2.1 Frequency evolution and a first analysis

If a rotating neutron star has a nonaxisymmetric shape, it will radiate away rotational energy by the emission of gravitational waves. It is straightforward to derive the equations describing the frequency evolution of gravitars. Their spin-down due to their nonaxisymmetric shape is given by

$$\dot{f} = -\frac{32\pi^4}{5} \frac{GI}{c^5} \varepsilon^2 f^5, \quad (6.1)$$

where  $f$  is the frequency of the emitted gravitational waves, which is twice the spin frequency of the gravitar.  $G$  is Newton's gravitational constant,  $I$  is the momentum of inertia with respect to the rotational axis,  $c$  is the speed of light and  $\varepsilon = \frac{I_1 - I_2}{I}$  is the ellipticity of the gravitar. Integrating (6.1) gives the frequency of gravitational waves emitted at time  $t$  as

$$f(t) = \left( f_B^{-4} + \beta^{-1} \varepsilon^2 t \right)^{-\frac{1}{4}} \quad \text{with } \beta = \frac{5}{128\pi^4} \frac{c^5}{GI}, \quad (6.2)$$

assuming an initial (birth) gravitational-wave frequency  $f_B = f(0)$ . The constant  $\beta$  is approximately

$$\beta^{\frac{1}{3}} = 5.3 \times \left( \frac{10^{38} \text{ kg m}^2}{I} \right)^{\frac{1}{3}} \text{ kHz}. \quad (6.3)$$

We infer from (6.2) the spin-down timescale

$$\tau_{\text{GW}}(\varepsilon, f) := \beta \varepsilon^{-2} f^{-4} \approx 4.6 \text{ Gyr} \left( \frac{10^{-7}}{\varepsilon} \right)^2 \left( \frac{100 \text{ Hz}}{f} \right)^4, \quad (6.4)$$

which is the time for a gravitar born at a gravitational wave frequency  $f_{\text{B}} \gg f$  with ellipticity  $\varepsilon$  to spin down to gravitational-wave frequency  $f$  via the emission of gravitational waves. These equations allow one to calculate the gravitational-wave frequency at the present time for any gravitar given its birth frequency, ellipticity, and age. This in turn allows one to determine the frequency distribution of a population of gravitars.

The strain amplitude  $h$  of gravitational waves emitted by a gravitar at distance  $r$  to the detector and assuming optimal mutual orientation (gravitar sky position given by the unit vector orthogonal to the plane of the detector arms; gravitar spin axis parallel to this vector) is given by

$$h = 4\pi^2 \frac{GI}{c^4} \frac{\varepsilon f^2}{r}. \quad (6.5)$$

Given a model for the spatial distribution of gravitars, this allows one to determine the distribution of gravitational-wave amplitudes.

Let us begin by giving Blandford's original argument in a more complete form than the single-paragraph version given in Thorne (1987).

Assume there is a population of Galactic gravitars, which remain undetected because they do not emit electromagnetic waves. Palomba (2005) (particularly Section 6 and the appendix) shows the conditions necessary for a neutron star to be a gravitar. Popov et al. (2000) is a simulation of a population of isolated neutron stars accreting matter from the interstellar medium and demonstrates that quite a few neutron stars may in fact meet these conditions. Taken together, these two papers establish a detailed plausibility argument for the possible existence of a population of gravitars.

Assume the neutron stars are uniformly distributed in a thin two dimensional Galactic disk with radius  $R$  and assume that the time between gravitar births in our galaxy is constant:  $\tau_{\text{B}} \approx 30 \text{ yrs}$ . Assume that all gravitars are born with the same ellipticity  $\varepsilon$  and high birth frequency  $f_{\text{B}}$ . The frequency of each gravitar will then evolve according to (6.2).

Consider an interval  $[f_1, f_2]$  of gravitational wave frequencies with  $f_1, f_2 \ll f_{\text{B}}$ . Let us consider wide ranges of frequencies corresponding to the broad-band sensitivity of modern interferometric detectors. Then, from (6.2) the time a gravitar will spend in this interval of frequencies is

$$t_{12} = \left[ 1 - \left( \frac{f_1}{f_2} \right)^4 \right] \tau_{\text{GW}}(\varepsilon, f_1). \quad (6.6)$$

The number of sources in this frequency interval is given by  $N_{12} = \frac{t_{12}}{\tau_{\text{B}}}$  if  $t_{12} \geq \tau_{\text{B}}$  and depends on the choice of the frequency band. Because of the assumed two dimensionality and uniformity of the spatial distribution the average distance  $r_{\text{cl}}$  to the closest gravitar in this range of frequencies can be written as

$$r_{\text{cl}} = \frac{R}{\sqrt{N_{12}}} = R \sqrt{\frac{\tau_{\text{B}}}{\tau_{\text{GW}}(\varepsilon, f_1)}} \left[ 1 - \left( \frac{f_1}{f_2} \right)^4 \right]^{-\frac{1}{2}}. \quad (6.7)$$

The formula given in Thorne (1987) agrees with Equation (6.7) if one assumes that the factor in square brackets is of order unity, which is the case for the latest generation of broad-band interferometric gravitational-wave detectors.

To estimate the gravitational-wave amplitude of the strongest source requires a bit of care. To get the flavour of the original argument, consider a one-octave frequency band  $[f, 2f]$ . The quantity in square brackets in (6.7) is  $15/16$  which we approximate as unity. Substituting the distance to the closest source (6.7) into (6.5) and neglecting the fact that  $f^2$  can vary by up to a factor of four within the octave, gives the amplitude of the strongest source in this one-octave frequency band to be

$$h = 4\pi^2 \frac{GI}{c^4} \frac{\varepsilon f^2 \sqrt{\tau_{\text{GW}}}}{R\sqrt{\tau_{\text{B}}}} = 4\pi^2 \frac{GI}{c^4} \frac{\sqrt{\beta}}{R\sqrt{\tau_{\text{B}}}} = \sqrt{\frac{5GI}{8c^3 R^2 \tau_{\text{B}}}}. \quad (6.8)$$

The Blandford argument is simply the observation that this amplitude is (1) independent of the population's deformation  $\varepsilon$  and (2) independent of frequency  $f$ .

Blandford's argument may also be stated in terms of a comparison between two different model Galaxies, each containing a similar populations of gravitars but each having a different (but constant) value of the ellipticity.

### 6.2.2 Restating Blandford's argument

The previous paragraph is a rigorous version of Blandford's original argument. We now generalise this, building on the methods first presented in Abbott et al. (2007b).

Let us first define useful quantities to describe a population of gravitars. As before  $r$  denotes the distance between gravitar and detector,  $f$  is the frequency of gravitational waves emitted, and  $\varepsilon$  is the ellipticity of the gravitar.

In this section  $t$  measures the age of the gravitars. A gravitar with age  $t = 0$  is born at the present time, whereas  $t > 0$  for a gravitar born in the past.

Because optimal mutual orientation of the gravitar's spin and the detector's normal axis is assumed, the gravitational-wave amplitude depends only on the distance  $r$  but not on the sky position. Therefore, it is useful to define the probability  $dP_r$  of finding a gravitar born time  $t$  ago at the present time in a spherically symmetric shell  $[r, r + dr]$  around the Sun<sup>1</sup>. The probability can be written in terms of a probability density  $q_r(r, t)$  as

$$dP_r = q_r(r, t) dr. \quad (6.9)$$

Moreover, let us define the probability  $dP_f$  of finding gravitars born time  $t$  ago with ellipticity  $\varepsilon$  in a present-time frequency band  $[f, f + df]$ .  $dP_f$  can be written in terms of a probability density  $q_f(\varepsilon, f, t)$  as

$$dP_f = q_f(\varepsilon, f, t) df. \quad (6.10)$$

Note, that the probability densities are normalised by  $\int_0^\infty dr q_r(r, t) = 1 \quad \forall t$  and  $\int_0^\infty df q_f(\varepsilon, f, t) = 1 \quad \forall \varepsilon, t$ .

For further generalisation consider a continuous distribution of gravitational wave frequencies at birth instead of a single, high value. Let  $dP_{f_0}$  be the probability of the birth frequency being in a band  $[f_0, f_0 + df_0]$ . The corresponding probability density  $q_{f_0}(f_0)$  is defined by

$$dP_{f_0} = q_{f_0}(f_0) df_0, \quad (6.11)$$

normalised as before. Frequency change by redshift from cosmological evolution is neglected since all gravitars considered are within our galaxy.

<sup>1</sup>Detector and Sun can be assumed collocated on Galactic scale.

To link the initial frequency distribution  $q_{f_0}$  to the present-time distribution  $q_f$ , consider a gravitar with ellipticity  $\varepsilon$  whose current frequency is  $f$ , and let  $f_0(\varepsilon, f, t)$  denote the gravitar's frequency at time  $t$  in the past. Solving (6.2) for the birth frequency yields

$$f_0(\varepsilon, f, t) = \left(f^{-4} - \beta^{-1}\varepsilon^2 t\right)^{-\frac{1}{4}}. \quad (6.12)$$

The probability density  $q_f$  can be rewritten in terms of the initial frequency distribution  $q_{f_0}$  by a change of variables. The fraction of gravitars in a birth frequency band  $[f_0, f_0 + df_0]$  is the same as the fraction in a present time frequency band  $[f, f + df]$ , so the identity  $q_f df = q_{f_0} df_0$  yields

$$q_f(\varepsilon, f, t) df = q_{f_0}(f_0(\varepsilon, f, t)) \frac{\partial f_0(\varepsilon, f, t)}{\partial f} df \quad (6.13)$$

$$= q_{f_0}(f_0(\varepsilon, f, t)) \frac{f_0^5(\varepsilon, f, t)}{f^5} df, \quad (6.14)$$

from which

$$q_f(\varepsilon, f, t) = q_{f_0}(f_0(\varepsilon, f, t)) \frac{f_0^5(\varepsilon, f, t)}{f^5} \quad (6.15)$$

immediately follows.

To allow for a time-dependent birthrate of Galactic gravitars, let  $\dot{n}(t)$  be the birthrate as a function of  $t$ . The number of gravitars  $dN$  formed during a short time interval  $[t, t + dt]$  is then  $dN = \dot{n}(t) dt$ .

The number  $d\tilde{N}$  of gravitars in a thin spherical shell  $[r, r + dr]$  around the position of the Sun, with frequencies in  $[f, f + df]$ , with fixed ellipticity  $\varepsilon$ , formed in a time interval  $[t, t + dt]$  ago is then given by

$$\begin{aligned} d\tilde{N} &= dP_r \times dP_f \times dN \\ &= q_r(r, t) dr \times q_f(\varepsilon, f, t) df \times \dot{n}(t) dt. \end{aligned} \quad (6.16)$$

From (6.5) it follows that for fixed  $\varepsilon$  and  $f$  there is a unique, invertible mapping  $r(h)$  from the amplitude of gravitational waves  $h$  to the distance  $r$  of the gravitar from the Sun. A change of variables from  $r$  to  $h$  yields

$$d\tilde{N} = q_r(r(h), t) \left| \frac{dr(h)}{dh} \right| dh \times q_f(\varepsilon, f, t) df \times \dot{n}(t) dt \quad (6.17)$$

and the number  $M(f_1, f_2, h_{\max})$  of gravitars with a gravitational wave amplitude  $h \geq h_{\max}$  in a frequency band  $[f_1, f_2]$  and ages  $t \leq \bar{t}$  is given by integration as

$$\begin{aligned} M(f_1, f_2, h_{\max}) &= \\ &= \int_0^{\bar{t}} dt \dot{n}(t) \int_{f_1}^{f_2} df q_f(\varepsilon, f, t) \int_{h_{\max}}^{\infty} dh q_r(r(h), t) \left| \frac{dr(h)}{dh} \right|. \end{aligned} \quad (6.18)$$

Here, the integral over  $h$  is performed for a fixed  $\varepsilon$  (assuming the same ellipticity for every gravitar) and fixed  $f$  and  $t$ . After integrating out the dependence on  $h$  the follow-up integration over  $f$  weights the previous integral by the frequency density. The last integration sums the distributions from different birth times weighted by the Galactic neutron star birthrate at that time.

Before Equation (6.18) is used to re-derive Blandford's result, let us prove that the frequency distribution from a single birth frequency has reached a steady state ( $\partial_t \varrho_f = 0$ ) at frequency  $f$ , if  $f(t) < f < f_B$ , where  $f(t)$  is given by (6.2). Consider a frequency band  $[f, f + df]$  which is wide enough to contain at least one gravitar at all times  $t$ . If  $f(t) < f < f_B$ , the constancy of the birthrate guarantees that if and only if a gravitar leaves the frequency band by the lower boundary another gravitar will enter the frequency band from higher frequencies. The assumption of a steady state is crucial. If the distribution has not reached a steady state in a certain frequency band there will be no sources in that band and there is no contribution to the integral in (6.18).

Let us now re-derive Blandford's result by using a density function  $\varrho_r(r, t) = 2r/R^2$  which describes a population of Galactic gravitars uniformly distributed in a flat two-dimensional disk with radius  $R^2$ . Further, assume a constant birthrate  $\dot{n}(t) = \frac{1}{\tau_B}$  and a single high birth frequency  $f_B$  such that  $\varrho_{f_0}(f_0) = \delta(f_0 - f_B)$ . Inserting  $r(h)$  into (6.18) by solving (6.5) for  $r$  we find after a slightly technical but straightforward calculation

$$M(f_1, f_2, h_{\max}) = \frac{5GI}{\tau_B c^3 R^2} \int_{f_1}^{f_2} \frac{df}{f} \int_{h_{\max}}^{\infty} \frac{dh}{h^3}. \quad (6.19)$$

The integrations are trivial and yield

$$M(f_1, f_2, h_{\max}) = \frac{5GI}{2\tau_B c^3 R^2} h_{\max}^{-2} \ln\left(\frac{f_2}{f_1}\right). \quad (6.20)$$

Let us follow Abbott et al. (2007b) and assume a 50% chance of detection, corresponding to  $M = 1/2$ . One finds a maximum gravitational-wave strain (Abbott et al., 2007b)

$$h_{\max} = \sqrt{\frac{5GI}{\tau_B c^3 R^2} \ln\left(\frac{f_2}{f_1}\right)}. \quad (6.21)$$

This result can also be directly compared with the earlier result (6.8) from the cruder analysis, by setting  $f_2 = 2f_1$  and setting  $M = 1$ . The values of  $h_{\max}$  obtained by these two different analyses disagree by about 40%, but are independent of deformation and frequency  $f_1$ .

For a broad band search performed today we assume  $\ln(f_2/f_1) \approx 1$ . Then (6.21) gives the largest amplitude expected under the assumptions<sup>3</sup> from Galactic gravitars as  $h_{\max} \approx 4 \times 10^{-24}$ .

For later comparison with the realistic Galactic model, let us calculate the dimensionless averaged fractional frequency density  $\hat{\varrho}_f(\varepsilon, f)$  in the population. It is defined by  $d\hat{P}_f = \hat{\varrho}_f(\varepsilon, f) \frac{df}{f}$  being the probability to find gravitars with a fixed ellipticity  $\varepsilon$  in a frequency band  $[f, f + df]$ ,

$$\hat{\varrho}_f(\varepsilon, f) = \frac{f}{N_{\text{tot}}} \int_0^{\bar{t}} dt \dot{n}(t) \varrho_f(\varepsilon, f, t), \quad (6.22)$$

where  $N_{\text{tot}} = \int_0^{\bar{t}} dt \dot{n}$  is the number of gravitars formed during the timespan  $\bar{t}$ . Using the same assumptions as for the derivation of (6.20) yields

$$\hat{\varrho}_f(\varepsilon, f) = \frac{4\beta}{\tau_B} \varepsilon^{-2} f^{-4}. \quad (6.23)$$

<sup>2</sup>This assumes that the Sun is farther from the edge of the disk than the closest expected source. Since the expected loudest sources are very close to the Sun this assumption is justified.

<sup>3</sup> $R = 10$  kpc,  $\tau_B = 30$  yrs,  $I = 10^{38}$  kg m<sup>2</sup>.

For fixed ellipticity the averaged fractional frequency density falls off with  $f^{-4}$  and scales for fixed frequency as  $\varepsilon^{-2}$ .

Let us summarise the assumptions made for this analytic calculation of the strongest gravitational-wave signal from Galactic gravitars. Assume all gravitars are born at a single high birth frequency with fixed ellipticity and constant birthrate, and reside in a two-dimensional, uniform distribution, i.e. in a thin Galactic disk. Assume their spin-down is governed by the emission of gravitational waves as described by Equation (6.2). Adopting these assumptions and a 50% chance of actual detection, the largest amplitude  $h_{\max}$  of gravitational waves emitted by Galactic gravitars in a frequency band  $[f_1, f_2]$  is given by (6.21). Thus, a precise statement about  $h_{\max}$  is the following

**Result:** *Assume the existence of a population of Galactic gravitars with uniform, two-dimensional spatial distribution, single, high birth frequency, fixed ellipticity  $\varepsilon$ , and constant birthrate. Choose a frequency band  $[f, sf]$  with scale  $s > 1$  large enough such that there is at all times at least one gravitar in this band. Then the largest amplitude  $h_{\max}$  of gravitational waves emitted by Galactic gravitars in this band is independent of  $f$  and  $\varepsilon$  and depends only on the scale  $s$ .*

Searching wider ranges of frequencies increases the value of  $h_{\max}$  because the absolute number of gravitars in wider ranges of frequency increases. However, in (6.21) the gain from going to higher frequencies grows slowly, as the square root of the logarithm, because the gravitars spend less time at higher frequencies.

### 6.2.3 A natural limit to the result

Because of the crucial assumption of a steady-state distribution in frequency there are obvious limits to this simple model. The time to reach a steady state in a given narrow frequency band  $[f, f + df]$  must be at least of the same order of magnitude as the spin-down timescale (6.4), because otherwise no gravitar will have spun down to frequencies contained in the band.

If all gravitars are born at the same high frequency the time to reach a steady state is exactly the spin-down age. If on the other hand there is a continuous distribution of initial frequencies, then reaching a steady state in a certain frequency band requires longer evolution times. Only then most of the gravitars in that band are ones that have spun down from higher frequencies. Over time this effect “washes out” any effects of the initial frequency distribution.

There is a natural limit to the result due to the finite age of the Universe, since no gravitar can be older than the Universe itself. An even better limit would be the age of the Galaxy, or rather that of the Galactic neutron star population. However, since the age of the Universe is known much more accurately than the age of the Galaxy, and since they differ only by a factor of order 2, we will use the age of Universe in all of our estimates below.

The age of the Universe  $t_0$  can be calculated from Hubble's constant  $H_0$  as  $t_0 = \frac{2}{3}H_0^{-1}$ . Then the finiteness sets limits on the values of  $\varepsilon$  and  $f$  for which the population has reached a steady state. We easily find from (6.4) that the population is in a steady state for gravitational-wave frequencies that satisfy

$$\varepsilon^2 f^4 > \frac{3}{2} H_0 \beta. \quad (6.24)$$

Fixing the ellipticity, one can calculate a frequency

$$\tilde{f}(\varepsilon) = \left( \frac{3H_0\beta}{2\varepsilon^2} \right)^{\frac{1}{4}} = 76 \text{ Hz} \left( \frac{10^{-7}}{\varepsilon} \right)^{\frac{1}{2}} \quad (6.25)$$

above which the population can be assumed to be close to a steady state.

We would like to stress that a realistic population with a continuous distribution of initial frequencies has to have evolved over a time  $T \approx \text{few} \times \tau_{\text{GW}}$  to be in steady-state. Thus the true value of  $\tilde{f}(\varepsilon)$  is larger by a factor of a few, and falls into the frequency range of highest sensitivity in modern interferometric gravitational-wave detectors (between 100 Hz and 300 Hz).

The range of ellipticities for which the assumption of steady state breaks down is then given by

$$\tilde{\varepsilon}(f) \lesssim 5.8 \times 10^{-8} \left( \frac{100 \text{ Hz}}{f} \right)^2. \quad (6.26)$$

In general it is not valid to assume that the frequency distribution in our galaxy is in steady-state.

We postpone further discussion of a uniform two-dimensional spatial distribution to Section 6.4.3 after presenting the setup of our numerical Galactic model.

### 6.3 Numerical model

The second section of this paper gave a precise analytic formulation of Blandford's argument including the extensions and improvements of Abbott et al. (2007b). To understand if this argument holds in a more realistic model of our galaxy, we set up a numerical simulation of the time evolution of a population of Galactic gravitars. This follows Palomba (2005), using a more recently published result from Hobbs et al. (2005) for the initial velocity distribution of neutron stars. To compute the spatial distribution, the equations of motion following from the Galactic potential given in Section 6.3.1 are evolved over time. The assumed initial conditions for the differential equations (i.e. initial positions and velocities of the gravitars) are described in Sections 6.3.2 and 6.3.3, respectively. Section 6.3.4 describes the adopted distributions for the initial spin period. The results of the simulations will be presented afterwards in Sections 6.4.1 and 6.4.2.

#### 6.3.1 Galactic potential and equations of motion

The motion of Galactic gravitars is governed by the Galactic gravitational potential. The potential first given by Paczynski (1990) is adopted. This potential describes our galaxy as axisymmetric with respect to the rotation axis. Thus, cylindrical coordinates  $\rho$ ,  $z$  and  $\varphi$  are used.  $\rho$  denotes the distance to the Galactic rotation axis, and  $z$  is the distance perpendicular to the disk.

The adopted potential represents our galaxy as composed of three different mass components. The most massive is a nonuniform flat disk with a radial scale of 3.7 kpc and a  $z$ -direction scale of 0.2 kpc. The component with the second highest mass is the halo, which is described by a density distribution  $\varrho_{\text{H}} \propto (r^2 + r_{\text{H}}^2)^{-1}$ , where  $r_{\text{H}} = 6$  kpc is called the halo core radius. The central bulge of our galaxy is represented by a spheroidal lower mass component with a density  $\varrho_{\text{S}} \propto (r^2 + b_{\text{S}}^2)^{-\frac{5}{2}}$ , where  $b_{\text{S}} = 0.277$  kpc.

**Table 6.1:** Mass and scale parameters for the Galactic potential

| structure       | mass                                | typical radii   |                   |
|-----------------|-------------------------------------|-----------------|-------------------|
| <i>Disk</i>     | $M_D = 8.07 \times 10^{10} M_\odot$ | $a_D = 3.7$ kpc | $b_D = 0.200$ kpc |
| <i>Spheroid</i> | $M_S = 1.12 \times 10^{10} M_\odot$ | $a_S = 0$ kpc   | $b_S = 0.277$ kpc |
| <i>Halo</i>     | $M_H = 5.00 \times 10^{10} M_\odot$ | $r_H = 6.0$ kpc |                   |

The corresponding potential therefore consists of three terms

$$\Phi(\rho, z) = \Phi_S(r) + \Phi_D(\rho, z) + \Phi_H(r). \quad (6.27)$$

describing, respectively, the potential energy per unit mass of the spheroid, the disk and the halo in our galaxy. The first two components ( $i = S, D$ ) are given by

$$\Phi_i(\rho, z) = -GM_i \left[ \rho^2 + \left( a_i + \sqrt{z^2 + b_i^2} \right)^2 \right]^{-\frac{1}{2}}. \quad (6.28)$$

For the potential of the halo  $r^2 = \rho^2 + z^2$  is substituted and the following spherical symmetric expression is used

$$\Phi_H(r) = \frac{GM_H}{r_H} \left[ \frac{1}{2} \ln \left( 1 + \frac{r^2}{r_H^2} \right) + \frac{r_H}{r} \arctan \left( \frac{r}{r_H} \right) \right]. \quad (6.29)$$

The parameter values are shown in Table 6.1.

The axial symmetry of the Galactic model leads to conservation of the  $z$ -component of the angular momentum  $L_z$ . Thus, the effective potential is

$$\Phi_{\text{eff}}(\rho, z) = \Phi(\rho, z) + \frac{L_z^2}{2\rho^2}. \quad (6.30)$$

The equations of motion that are evolved are

$$\ddot{\rho} = -\frac{\partial \Phi_{\text{eff}}}{\partial \rho} \quad \text{and} \quad \ddot{z} = -\frac{\partial \Phi_{\text{eff}}}{\partial z}. \quad (6.31)$$

The equation of motion for  $\varphi$  is given by  $\rho^2 \dot{\varphi} = L_z$ . In the simulation this equation is not used because  $\varphi$  is not evolved, but drawn from a uniform random distribution  $\varphi \in [0, 2\pi)$ .

### 6.3.2 Initial spatial distribution

The initial spatial distribution of gravitars is proportional to the density of massive progenitor stars of neutron stars. While there is quite good agreement about the initial distribution in  $z$ -direction, the initial distribution along the radial direction is unknown.

In the  $z$ -direction the initial position is drawn from a Laplacian distribution with scale factor  $z_0 = 0.075$  kpc. The probability of a gravitar's birth in an interval  $[z, z + dz]$  is given by

$$p_z(z) dz = \frac{1}{2z_0} \exp\left(-\frac{|z|}{z_0}\right) dz. \quad (6.32)$$

We considered three different models for the initial radial distribution together with the given initial  $z$ -distribution.

The simplest radial distribution from Palomba (2005) is an exponential fall off with a scale factor  $\rho_1 = 3.2$  kpc. The probability of a gravitar's birth in a distance interval  $[\rho, \rho + d\rho]$  is then

$$p_1(\rho) d\rho = \frac{1}{\rho_1} \exp\left(-\frac{\rho}{\rho_1}\right) d\rho. \quad (6.33)$$

The spatial distribution of  $10^4$  newborn neutron stars using this model is shown in Figure 6.1(a).

Note however that this distribution leads to an extreme concentration of neutron stars towards the Galactic center. These are not seen in pulsar surveys (Yusifov and Kucuk, 2004). So following Paczynski (1990) a gamma distribution given by

$$p_2(\rho) d\rho = a_\rho \frac{\rho}{\rho_2^2} \exp\left(-\frac{\rho}{\rho_2}\right) d\rho, \quad (6.34)$$

is also considered, where gravitar formation in the disk is allowed for  $\rho \leq 25$  kpc, and the constants are given by  $\rho_2 = 4.78$  kpc and  $a_\rho = 1.0345$ . The spatial distribution of  $10^4$  newborn neutron stars using this model is shown in Figure 6.1(b).

A third distribution

$$p_3(\rho) d\rho = \frac{\rho^5}{120\rho_3^6} \exp\left(-\frac{\rho}{\rho_3}\right) d\rho, \quad (6.35)$$

with  $\rho_3 = 1.25$  kpc taken from Yusifov and Kucuk (2004) is also considered. It is fitted to the radial distribution of Population I stars which are considered to be likely progenitors of neutron stars. Again, gravitar birth events are allowed for  $r \leq 25$  kpc. On average, only one gravitar out of 14 thousand is born with  $\rho > 25$  kpc, so the normalisation constant  $a_\rho \approx 1$ . The spatial distribution of  $10^4$  newborn neutron stars using this model is shown in Figure 6.1(c).

### 6.3.3 Initial velocity

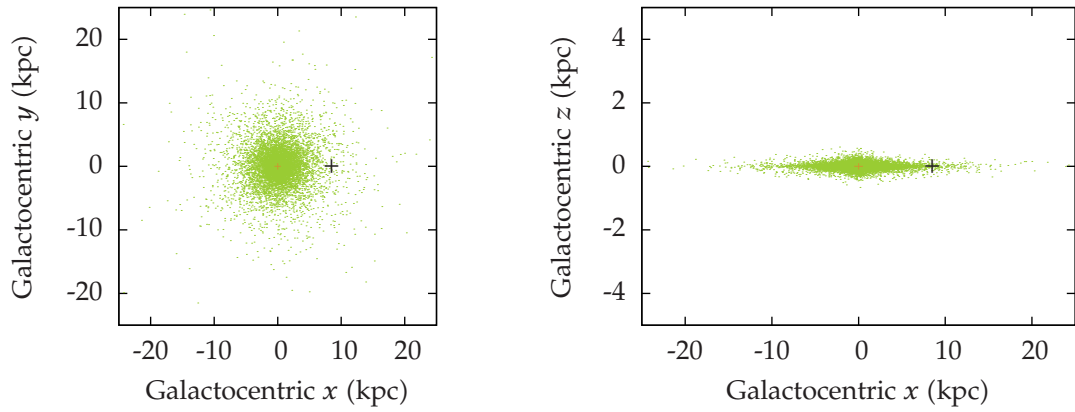
The Galactic rotation determines the velocity of the supernova progenitors and therefore also that of the newborn neutron stars.

From classical mechanics the rotational speed of a body on a circular orbit in the axisymmetric potential (6.27) is given by  $v_{\text{rot}} = \sqrt{\rho \partial_\rho \Phi(\rho, z)}$ . From the initial coordinate of a gravitar the corresponding  $v_{\text{rot}}$  on a tangential circular orbit is calculated (neglecting initial rotation velocities perpendicular to the Galactic disk, because all gravitars are born with low initial values of  $z$ ). Looking down on the Galaxy from positive  $z$ -values the Galaxy is chosen to rotate counterclockwise.

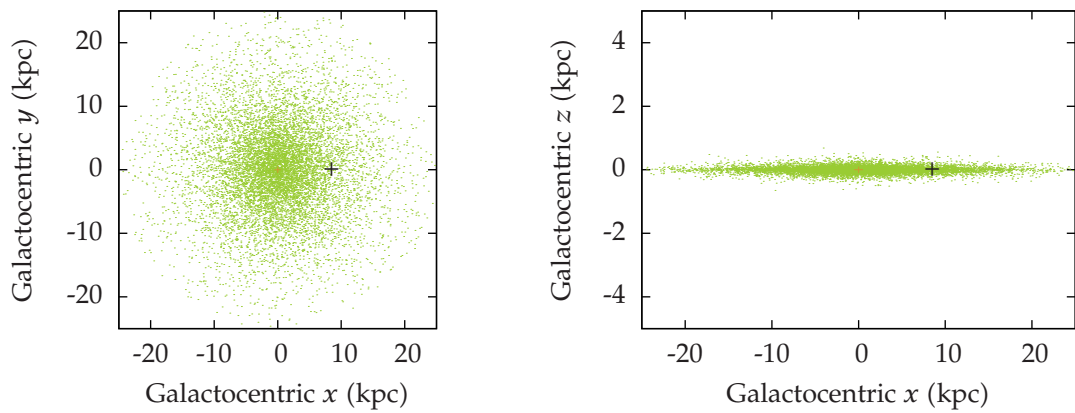
Furthermore, it is assumed that gravitars are born in a supernova explosion that will kick the newborn star. The direction of that kick is assumed to be isotropic. The kick speed is drawn from a Maxwellian distribution with a mean velocity  $\bar{v} = 430$  km/s. The probability for the kick speed to be in an interval  $[v_{\text{kick}}, v_{\text{kick}} + dv_{\text{kick}}]$  is

$$p_v(v_{\text{kick}}) dv_{\text{kick}} = \frac{32v_{\text{kick}}^2}{\pi^2 \bar{v}^3} \exp\left(-\frac{4v_{\text{kick}}^2}{\pi \bar{v}^2}\right) dv_{\text{kick}}. \quad (6.36)$$

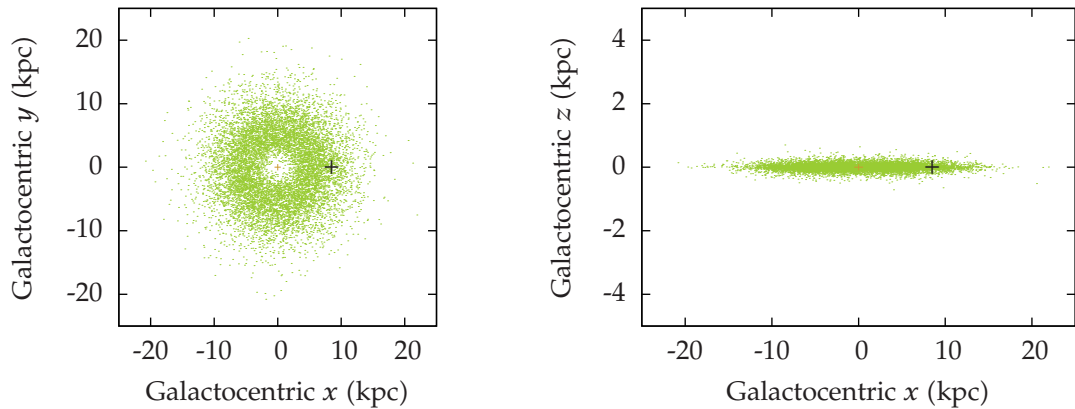
It is assumed that this distribution from Hobbs et al. (2005) may be used for gravitars as well as for pulsars.



(a) The spatial distribution of newborn neutron stars from Palomba (2005).



(b) The spatial distribution of newborn neutron stars from Paczynski (1990).



(c) The spatial distribution of newborn neutron stars from Yusifov and Kucuk (2004).

**Figure 6.1:** The initial spatial distributions considered in the simulations. **(Left)** viewed from above the Galactic disk. **(Right)** viewed from the side of the Galactic disk. Note, that in the right-hand side panels the  $z$ -axis covers a five times smaller range than the  $x$ -axis. The orange cross marks the center of the Galaxy, the black cross the position of the Sun, respectively.

### 6.3.4 Initial period distribution

Because of the conservation of angular momentum in the supernova event and the much smaller radius of the gravitar compared with its progenitor, newborn neutron stars will spin rapidly.

We considered three models for the distribution of the initial rotation periods following the models given in Palomba (2005). The existence of three different models reflects our ignorance of the actual distribution of initial periods.

The first model is described by a lognormal distribution

$$p_{P_0}(P_0) = \frac{1}{\sqrt{2\pi}\sigma P_0} \exp\left[-\frac{1}{2\sigma^2} \left(\ln(P_0) - \ln(\overline{P_0})\right)^2\right] \quad (6.37)$$

where  $P_0$  is measured in seconds and where the values  $\sigma = 0.69$  and  $\overline{P_0} = 5$  ms are taken from Arzoumanian et al. (2002). Gravitars with  $P_0 < 0.5$  ms are excluded.

The second model is using the same probability distribution as the first model but every initial period  $P_0 < 10$  ms is set to 10 ms exactly. In this way the possible presence of r-modes in young neutron stars is mimicked. These modes can dissipate rotational energy of the newborn neutron star and increase its initial period to about 10 ms within 1 yr.

The third model considered is a further extension of the second one. It includes the effects of matter fall-back after the supernova explosion. The increase of angular momentum by the accreting matter could counteract the r-mode induced deceleration. The resulting initial period will approach an intermediate value. The choice from Palomba (2005) to draw the initial period from a uniform distribution between 2 ms and 15 ms is adopted

### 6.3.5 Coding and implementation

With the initial distributions from Sections 6.3.2 and 6.3.3 and the equations of motion (6.31) at our disposal, it is a straightforward problem to find the spatial distribution of a population of gravitars at the present time.

The code for the simulation is written in C. The equations of motion (6.31) are integrated via a Burlisch-Stoer method in combination with Stoermer's rule for the direct discretisation of a system of second-order differential equations using routines described in Press et al. (1992). Over the integration time the total energy is conserved to one part in  $10^6$ .

For the derivation of the frequency distributions (6.15) the probability distributions are implemented by random number generators and functions from the GNU Scientific Library (GSL; Galassi, 2009). The fractional frequency density (6.22) is obtained via a Monte-Carlo integration using  $2 \times 10^{12}$  random values of initial frequency and a uniform distribution of ages.

Depending on the model of the initial spatial distribution the integration of  $10^6$  neutron star trajectories over a time of 200 Myrs takes 2.5 mins to 13.3 mins on an AMD Opteron 185 processor. Most of the simulations were done on the Morgane cluster at the AEI in Potsdam.

## 6.4 Results

---

### 6.4.1 Frequency distributions

In the derivation of the generalised result (6.19) the assumption of a steady-state frequency distribution (6.23) is (along with the two-dimensional uniform spatial distribution) the key

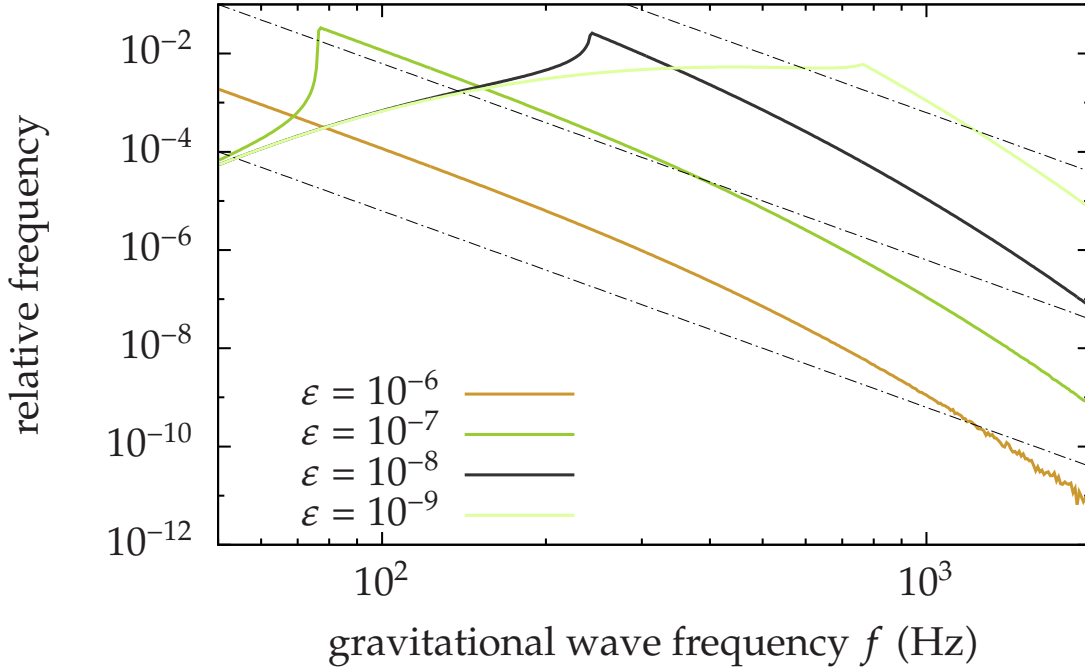


**Figure 6.2:** The distribution  $\hat{\varrho}_f(\varepsilon, f)$  in frequency after  $\bar{t} = 13.6$  Gyrs for varying ellipticity using a lognormal distribution of initial periods in the range  $f \in [50 \text{ Hz}, 2000 \text{ Hz}]$ . The dashed lines correspond to a slope  $f^{-4}$ , as Equation (6.23) would predict for a single high birth frequency. The kink in the graphs for  $\varepsilon \lesssim 10^{-7}$  is at the frequency given by Equation (6.25).

to the independence of the maximum amplitude on ellipticity and frequency. Let us therefore first have a look at the frequency distributions that result from a continuous distribution of initial frequencies and compare them with the corresponding density resulting from a single birth frequency (6.23).

Figure 6.2 shows the results of the Monte Carlo integration for  $\bar{t} = 13.6$  Gyrs using a lognormal distribution of initial periods and a fixed ellipticity for each run in the frequency range  $f \in [50 \text{ Hz}, 2000 \text{ Hz}]$ . The ellipticity varies over 3 orders of magnitude from  $10^{-9}$  to  $10^{-6}$ . The dashed lines correspond to a scaling proportional to  $f^{-4}$ , which results from a single birth frequency and shows a steady-state distribution as calculated in Equation (6.23). For  $\varepsilon = 10^{-6}$  the population is close to a steady state at the present time because the scaling is nearly proportional to  $f^{-4}$ . For smaller ellipticities one can identify a kink in the density function at a frequency  $\tilde{f}$  as given by (6.25). The kink is due to gravitars born at high frequencies that are too young to have spun down to lower frequencies. The frequency distribution for  $\varepsilon \lesssim 10^{-7}$  is not in a steady state in the frequency range of highest sensitivity for modern interferometric detectors, which is between 100 Hz and 300 Hz.

We also note that  $\hat{\varrho}_f(\varepsilon, f)$  does not scale as  $\varepsilon^{-2}$  in all frequency bands. It only scales as  $\varepsilon^{-2}$  at high frequencies.

Let us now compare the fractional frequency densities that result from different models of initial frequency distributions for a fixed ellipticity. Figure 6.3 shows the distribution in frequency space after an evolution time of  $\bar{t} = 13.6$  Gyrs for  $\varepsilon = 10^{-7}$ . Each graph corresponds to one of the models for the initial frequency distribution. If the evolution time is long compared with the spin-down time  $\tau_{\text{GW}}$  (6.4), most of the gravitars will have spun

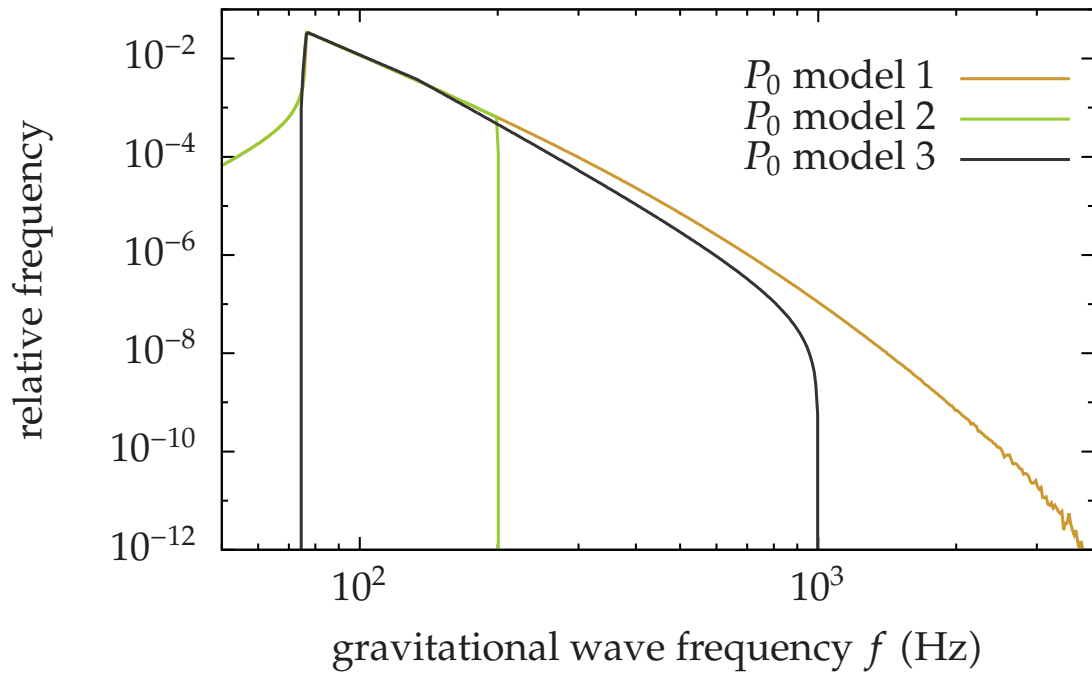


**Figure 6.3:** The distribution in frequency space in the range  $f \in [50 \text{ Hz}, 4000 \text{ Hz}]$  after  $\bar{t} = 13.6 \text{ Gyrs}$  for  $\varepsilon = 10^{-7}$  for three different models of the initial gravitar frequency distribution.

down to low frequencies, and the distribution will be dominated by those older sources. Yet, if the respective model has upper or lower limits on the birth frequencies one cannot expect the fractional densities to agree near these boundaries. However, in frequency bands of interest for modern interferometric detectors (100 Hz to 300 Hz) the distributions only show minor differences between the different models.

#### 6.4.2 Spatial steady-state distribution and timescales

Since the gravitars are born in a thin disk and receive an isotropic kick by the supernova, they tend to leave the disk after some Myrs. They either escape the Galactic gravitational potential, or are bound to the Galaxy on some “orbit”. The numerical simulation is used to find the timescale on which these processes wash out the imprint of the initial spatial distribution.

Let us introduce the function  $\hat{M}(r, t)$ , which is the number of gravitars in a ball of radius  $r$  around the position of the Sun that were formed a time  $t$  ago. The radial probability distribution  $q_r(r, t)$  as introduced in Section 6.2.2 is related to  $\hat{M}$  via the derivative with respect to  $r$

$$q_r(r, t) dr = \frac{1}{N_{\text{tot}}} \partial_r \hat{M}(r, t) dr. \quad (6.38)$$

To obtain a dynamical picture,  $\hat{M}(r, t)$  is computed in steps of 1 Myr from 0 Myrs to 200 Myrs. For each of the 201 values of integration time the trajectories of  $N_{\text{tot}} = 10^9$  Galactic gravitars are evolved using the numerical integration methods described in Section 6.3.5 and the radial distance distribution is derived from their final positions. The radial resolution is chosen as 2.5 pc for  $0 \text{ kpc} \leq r < 12 \text{ kpc}$  and as 100 pc for  $12 \text{ kpc} \leq r \leq 20 \text{ kpc}$

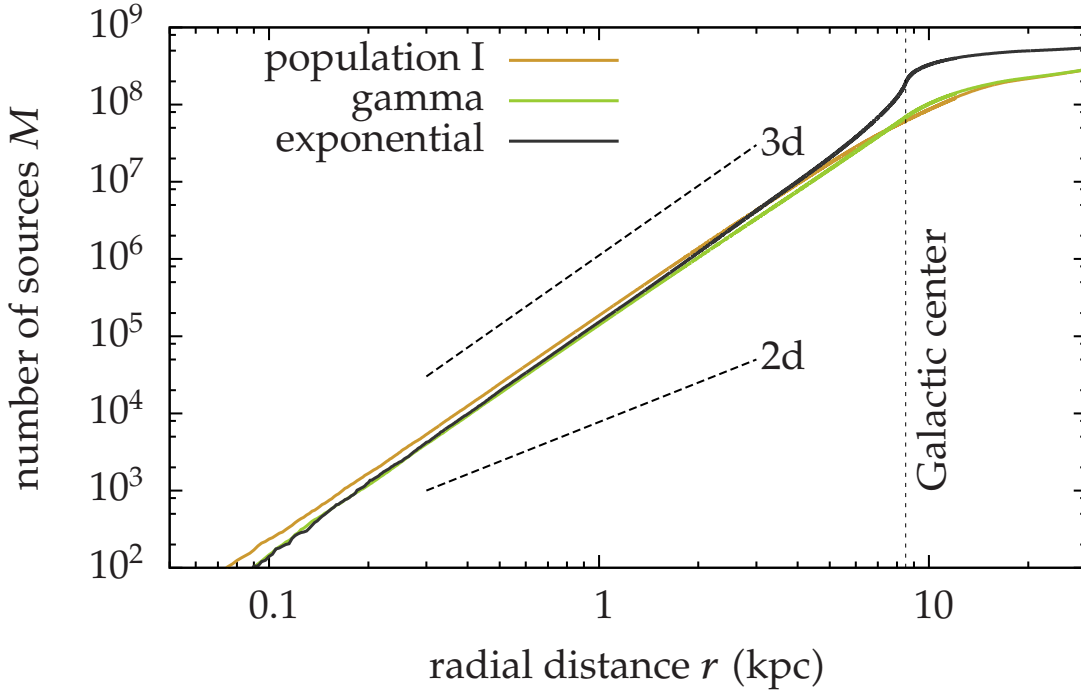


**Figure 6.4:** The distribution of gravitars as a function of radial distance from the Sun. The graphs show the number of gravitars inside spheres of radius  $r$  plotted against  $r$ . The age of all sources is  $t = 200$  Myrs. The scaling dimension of these graphs is shown in Figure 6.5. The straight (dashed) lines show the corresponding slope for a uniform two- (three-) dimensional distribution.

Figure 6.4 shows the number of gravitars inside balls of radius  $r$  around the position of the Sun, which were formed  $t = 200$  Myrs ago, for the different initial radial distributions. The saturation near  $r = 8.5$  kpc is due to the high density of gravitars near the Galactic center. The simulations show that the spatial distribution settles into a state of equilibrium for  $t \approx 200$  Myrs. There is no significant difference between the distributions for  $t = 200$  Myrs and  $t = 2$  Gyrs. By the age of 200 Myrs the initial distribution is washed out; evolution over longer times no longer changes the radial distribution  $\hat{M}(r)$ .

### 6.4.3 Scaling dimension of the spatial distribution

The assumption of a two-dimensional and uniform spatial distribution of gravitars at the present time is crucial for Blandford's argument. The numerical simulation can test if these assumptions are valid or not.

A useful concept is that of the *scaling dimension*. To obtain the scaling dimension, the function  $\hat{M}(r)$  as introduced in the previous section is used. Assume a uniform distribution, and describe the number of sources inside each ball as a function of its radius  $r$  by a simple power law

$$\hat{M}(r) \propto r^D. \quad (6.39)$$

$D$  is called the *scaling dimension* of the distribution.

Even an exactly two-dimensional spatial distribution of gravitars (e.g. the Galactic disk) can effectively scale as a  $D$ -dimensional object due to density gradients. Note, that the scaling dimension is a local quantity depending on the position of evaluation.

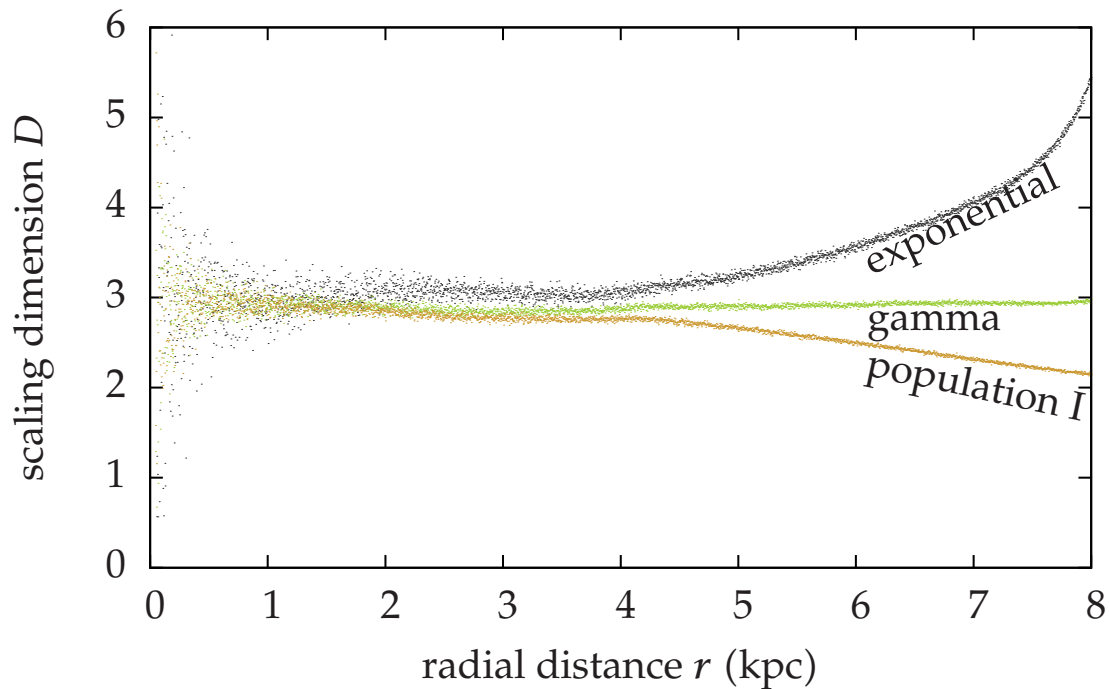


**Figure 6.5:** The local scaling dimension  $D(r)$  of the spatial distribution of gravitars around the position of the Sun as calculated by (6.40). The corresponding radial distributions of sources are shown in Figure 6.4. Note, that here the graphs are only shown for  $r \leq 8$  kpc.

To illustrate the scaling properties of the evolved Galactic spatial distribution of gravitars, the local scaling dimension is computed for  $r \leq 8$  kpc and is shown in Figure 6.5. From (6.39) the scaling dimension  $D(r)$  can be derived via

$$D(r) = \frac{r \partial_r \hat{M}(r)}{\hat{M}(r)} \quad (6.40)$$

The differentiation is computed numerically using a cubic splining on the tabulated values. The scattering of points for  $r \lesssim 1$  kpc is due to the small number of sources at short distances and resulting numerical noise.

The scaling dimension at every distance to the Sun is greater than 2. For the first model of initial radial distributions it even reaches values  $D \geq 5$ . For the second model there is a slight increase in the scaling dimension towards the Galactic center where the scaling dimension  $D \approx 3$ . For the last model the scaling dimension decreases with larger radial distance but always  $D > 2$ .

We conclude that the scaling dimension of the population of gravitars in the model of our galaxy is significantly larger than 2. More precisely averaging  $D$  over distances  $r \leq 2$  kpc – where  $D$  is nearly constant and independent of the initial radial distribution – yields  $D \approx 2.95$ .

## 6.5 The strongest continuous gravitational-wave signal

Using the frequency and spatial distributions obtained from our Galactic simulation, it is straightforward to derive the maximum expected amplitude of continuous gravitational

waves from gravitars.

### 6.5.1 Numerical method

Let us first describe the numerical method for computing the maximum expected amplitude of the gravitational waves using the distributions in space and frequency as presented in Sections 6.4.1 and 6.4.2.

Equation (6.18) is used to obtain the value of  $M(f_1, ef_1, h_{\max})$  for a given frequency band  $[f_1, ef_1]$  ( $\ln(e) = 1$ ) and a trial value of  $h_{\max}$ . To compare the results with Abbott et al. (2007b)  $h_{\max}$  is tuned via a bisection method within  $\pm 2.5\%$  to the target value  $M_{\text{tar}} = 0.5$  such that  $0.4875 \leq M(f_1, ef_1, h_{\max}) \leq 0.5125$ .

As described in Section 6.4.2 the function  $\hat{M}(r, t)$  giving the number of gravitars with a solar radial distance less than  $r$  is tabulated. From these values  $\varrho_r(r, t) = \partial_r \hat{M}(r, t) / N_{\text{tot}}$  is numerically computed via a cubic splining method.

The distribution in frequency space  $\varrho_f(\varepsilon, f, t)$  is taken from Equation (6.15) with distributions of initial periods as described in Section 6.3.4.

Given a frequency band a high value of  $h_{\max}$  is chosen as trial value. Then the frequency is chosen fixed at the lower boundary of the band and the integration over  $h \in [h_{\max}, h_{\text{up}}]$  in (6.18) is conducted by calculating from (6.5) the corresponding  $r(h)$  and inserting into the interpolated  $m(r, t)$ . For the upper limit  $h_{\text{up}}$  of the integration the value that would be obtained if the gravitar was at the closest possible distance is taken. Then no contribution to the integral is lost. After integrating over  $h$  the integration over frequency in the chosen band  $[f_1, ef_1]$  is done and weighted by  $\varrho_f(\varepsilon, f, t)$ .

The result of these two integrations is then integrated over all times  $t \in [0, \bar{t} = 13.6 \text{ Gyrs}]$  where the time-step between two evaluations is chosen as  $dt = \min\{1 \text{ Myr}, \frac{\tau_{\text{GW}}}{10}\}$  to obtain a sufficiently fine time-step to track both spatial and frequency evolution. This integration over time is weighted by a constant birthrate of  $\dot{n}(t) = (30 \text{ yrs})^{-1}$ .

### 6.5.2 Maximum expected amplitude

Using the results of the simulation, one can see if the value of  $h_{\max}$  (obtained by the method described in the previous section) differs from the one predicted by Blandford's result as extended and improved in Abbott et al. (2007b).

To avoid boundary effects, from now only the first model for the distribution of initial frequencies is considered. In all frequency bands, the other models always give a smaller maximum amplitude of gravitational waves  $h_{\max}$ .

Figure 6.6 shows the resulting value of  $h_{\max}$  for different values of the ellipticity and all spatial distribution models. The graphs are to be understood as follows: the maximum amplitude of gravitational waves is calculated as described in the previous section for every choice of initial spatial distributions and for frequency bands  $[f, ef]$ . The graphs show the value  $h_{\max}$  obtained in such a band as a single point at  $(f, h_{\max})$ . From Figure 6.6 it is obvious that the assumptions of Blandford's argument are not fulfilled for a realistic model of our galaxy. The graphs for different values of ellipticity do not line up, and each single graph is curved. Thus, the maximum amplitude of gravitational waves from Galactic gravitars does depend on both the ellipticity and frequency.

For highly deformed gravitars the graphs are nearly flat indicating a weak dependence on  $f$ , while for low values of  $\varepsilon$  the previously-discussed kink appears.

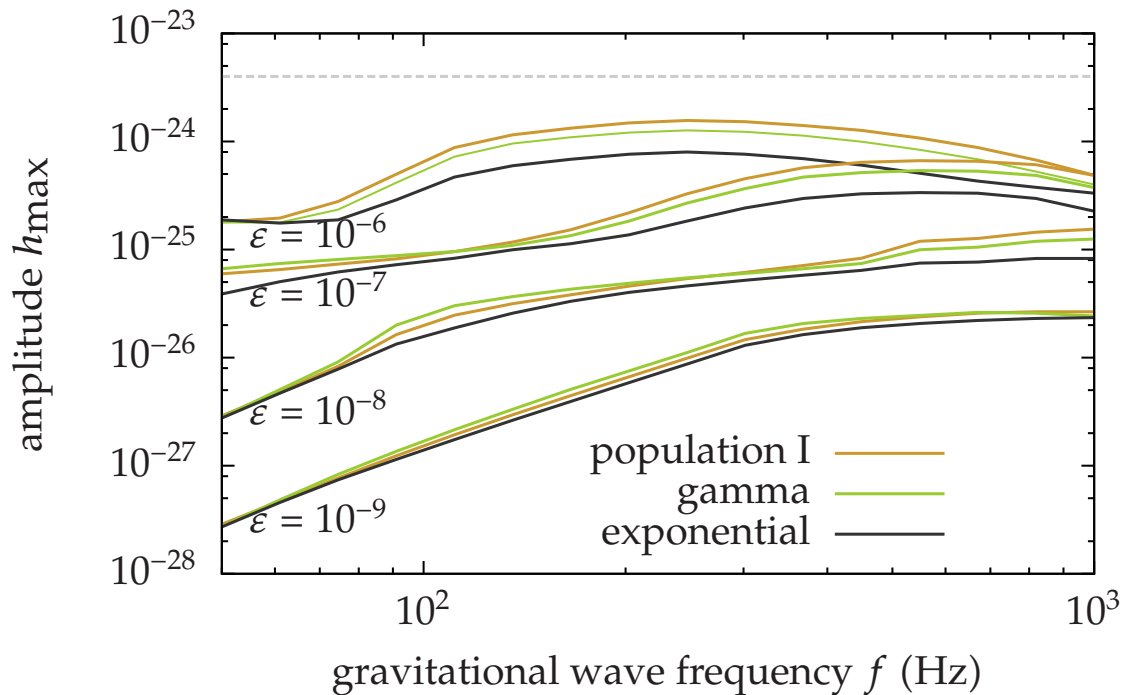


**Figure 6.6:** The maximum strain amplitude of gravitational waves  $h_{\max}$  from Galactic gravitars in frequency bands  $[f, ef]$  in the range  $f \in [50 \text{ Hz}, 1000 \text{ Hz}]$ . Each plotted point  $h_{\max}(f)$  is the value  $h_{\max}$  calculated for a frequency band  $[f, ef]$  which is one natural-logarithmic-octave wide. The three curves show different initial spatial distribution models. For contrast, the dotted, straight line (independent of frequency and ellipticity  $\varepsilon$ ) shows the value of  $h_{\max}$  from Abbott et al. (2007b), which improved and extended Blandford’s argument.

The choice of the initial radial distribution causes only small differences. The inter-model differences are usually of the order of 10%, and in the worst case are about 50% for a particular ellipticity and frequency. This is because the strongest gravitational waves are emitted by gravitars at very small distances<sup>4</sup>. As can be seen from Figure 6.4, the distribution for radial distances  $r \lesssim 5 \text{ kpc}$  from the Sun is nearly the same independent of the initial radial distribution.

Assuming the highest possible ellipticity  $\varepsilon = 10^{-6}$  for the gravitars, the strongest signal has an amplitude of  $h_{\max} \approx 1.6 \times 10^{-24}$  in the band  $[250 \text{ Hz}, 680 \text{ Hz}]$  which is improved (strengthened) by a factor of  $\approx 3$  compared with the value given in Abbott et al. (2007b). Note that this improvement factor would be smaller if larger values of  $\varepsilon$  were considered. In any case, the improvement factor is substantially larger at other frequencies.

In the case of the more realistic value  $\varepsilon = 10^{-7}$ , the estimate is  $h_{\max} \approx 6.6 \times 10^{-25}$  in the band  $[550 \text{ Hz}, 1500 \text{ Hz}]$  and is lower than the simple analytic estimate by a factor of 6.

Table 6.2 lists the maximum values for the amplitude of the strongest gravitational waves for all adopted values of the ellipticity and the frequency band in which the maximum amplitude is expected.

To illustrate the expected distance to the strongest gravitars we used the results of Figure 6.6 together with Equation (6.5) to compute the distance to these sources as a function of the gravitational-wave frequency interval and the ellipticity. The result is shown in Fig-

<sup>4</sup>E. g. a gravitar with  $f = 2 \text{ kHz}$ ,  $\varepsilon = 10^{-6}$  must be as close as  $r = 1 \text{ kpc}$ .

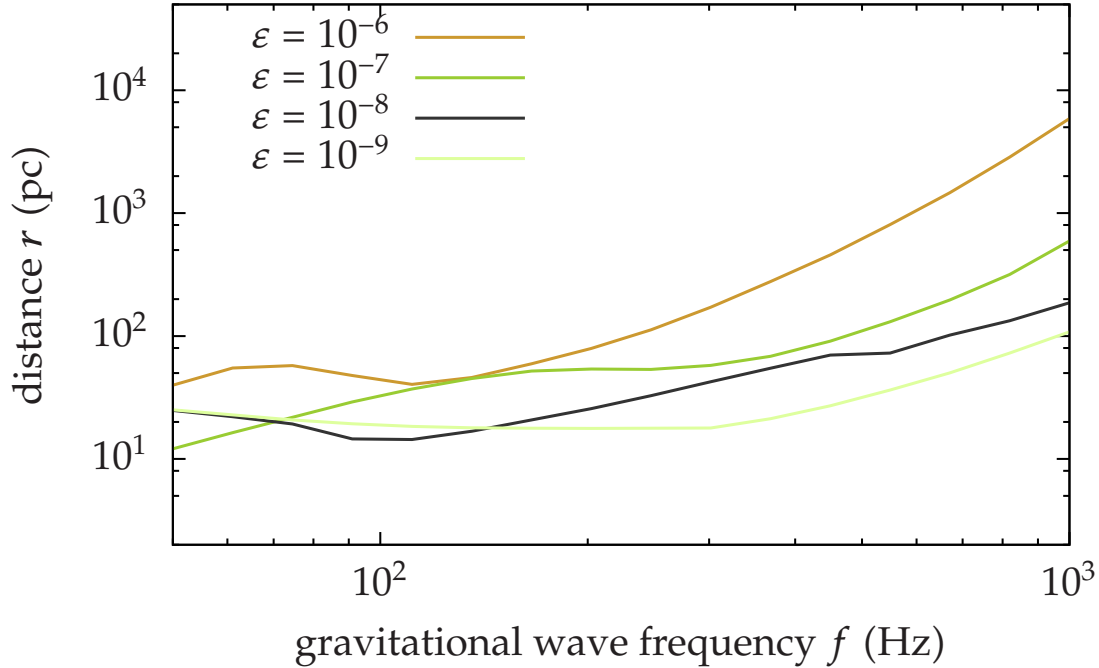


**Figure 6.7:** The expected distance to the strongest gravitar, corresponding to Figure 6.6. Because each frequency axis value of Figure 6.6 refers to an entire logarithmic octave  $\ln(f_2/f_1) = 1$  range, in principle the plots should show a range of distances which is two logarithmic octave wide:  $\ln(h_2/h_1) = 2$ . To simplify the appearance of this plot, we show only a single curve at the central value. The expected range of distances ranges from a factor of  $1/e$  below this plot to  $e$  above this plot.

ure 6.7

We conclude that the assumptions of Blandford’s argument do not hold in our Galactic model. The expected gravitar spatial distribution is not a two-dimensional uniform thin disk, and the expected gravitar frequency distribution is not yet in a steady state for realistic values of neutron star ellipticity.

### 6.5.3 Remarks on an upper limit

In the previous section we obtained the expected maximum amplitude of a gravitational-wave signal from a deformed neutron star spinning down purely by gravitational waves. Let us now address the question whether this value poses an upper limit on the gravitational-wave amplitude from objects that spin down partly by gravitational waves and partly by electromagnetic dipolar emission. It must be stressed that recycled millisecond pulsars are not covered here, since spin-up is *not* considered.

Abbott et al. (2007b) gave a clever argument about why the expected maximum gravitational-wave strain from gravitars sets an upper limit for all neutron stars that have not gone through an accretion-powered spin-up phase. However that argument implicitly assumes only birth frequencies *above* the observed frequency band for the pulsars, and also assumes that the pulsar population frequency-space distribution is in steady-state in the observed frequency band. Here, we do not make either of these assumptions.

**Table 6.2:** Maximum values for the amplitude  $h_{\max}$  of gravitational waves in dependence on the ellipticity  $\varepsilon$ .

| $\varepsilon$ | $h_{\max}$            | frequency band     |
|---------------|-----------------------|--------------------|
| $10^{-6}$     | $1.6 \times 10^{-24}$ | [250 Hz, 680 Hz]   |
| $10^{-7}$     | $6.6 \times 10^{-25}$ | [550 Hz, 1500 Hz]  |
| $10^{-8}$     | $1.5 \times 10^{-25}$ | [1000 Hz, 2800 Hz] |
| $10^{-9}$     | $2.7 \times 10^{-26}$ | [1000 Hz, 2800 Hz] |

In this section we show that the results from Figure 6.6 are a strict upper limit for frequencies  $f > 250$  Hz. This is related to the distribution of initial frequencies which has its maximum at  $f_0 = 250$  Hz and is decreasing monotonically for larger values of initial frequency. To maximise the number of sources in a frequency band at a given time in this regime, the slowest possible spin-down is required. Any faster spin-down only would remove sources from this frequency band without adding more new ones from higher frequencies. Since the slowest possible spin-down without weakening the gravitational-wave signal is attained by switching off dipolar emission, the results from Figure 6.6 are a strict upper limit on the gravitational-wave amplitude for  $f > 250$  Hz.

To formulate a rigorous proof of this claim, we characterise the generalised spin-down such a “mixed” neutron star will experience with a spin-down parameter  $\hat{y}$ . As shown in Section 2.2 the spin-down from electromagnetic dipolar emission in terms of the rotation frequency  $\nu$  is given by

$$\dot{\nu}_{\text{dip}} = -\frac{2\pi^2 B_p^2 R^6 \sin^2(\alpha)}{3c^3 I} \nu^3 =: \gamma_{\text{dip}} \nu^3, \quad (6.41)$$

where  $B_p$  is the magnetic field strength at the neutron star’s magnetic pole,  $\alpha$  is the angle between the rotation axis and the magnetic field, and  $R$  is the radius of the neutron star. Rewriting Equation (6.1) the spin-down from gravitational waves is

$$\dot{\nu}_{\text{gw}} = -\frac{512\pi^4 G}{5c^5} I \varepsilon^2 \nu^5 =: \gamma_{\text{gw}} \nu^5. \quad (6.42)$$

A neutron star emitting energy by both mechanisms at once will experience a total spin-down

$$\dot{\nu} = \gamma_{\text{gw}} \nu^5 + \gamma_{\text{dip}} \nu^3. \quad (6.43)$$

This differential equation cannot (in contrast to (6.1)) be solved analytically for  $\nu(t)$ , yet it can be integrated to give the time  $t(\nu, \nu_0)$  in which a neutron star spins down from rotation frequency  $\nu_0$  to  $\nu$ :

$$t(\nu, \nu_0) = \frac{1}{2|\gamma_{\text{dip}}|} \left[ \frac{\nu_0^2 - \nu^2}{\nu_0^2 \nu^2} + \hat{y} \ln \left( \frac{\nu^2}{\nu_0^2} \left( \frac{1 + \hat{y} \nu_0^2}{1 + \hat{y} \nu^2} \right) \right) \right], \quad (6.44)$$

where  $\hat{y} := \gamma_{\text{gw}}/\gamma_{\text{dip}}$  is the *general spin-down parameter*. Note, that  $\hat{y} \rightarrow 0$  corresponds to switching off gravitational wave emission, while  $\hat{y} \rightarrow \infty$  leads to pure gravitational-wave spin-down. Taking these limits in (6.44), one easily recovers the equations for pure dipolar and gravitational-wave spin-down, respectively, which can be solved analytically for  $\nu(t)$ .

Let us now turn to the derivation of the expected maximum gravitational wave amplitude from such neutron stars. The derivation given in Section 6.2.2 is straightforwardly modified to incorporate the generalised spin-down. The generalisation of the present-time gravitational-wave frequency distribution  $q_f$  is obtained by writing Equation (7.26) for fixed  $t$  and  $\hat{y}$  as

$$q_f(f, t, \hat{y}) df = q_{f_0}(f_0(f, t, \hat{y})) \frac{\partial f_0(f, t, \hat{y})}{\partial f} df. \quad (6.45)$$

Note, that (6.44) cannot be solved analytically for  $f_0(f, t, \hat{y}) = 2\nu_0(f, t, \hat{y})$ . Care has to be taken to evaluate the partial derivative. Taking the total derivative of  $t(\nu, \nu_0) = \text{const}$  with respect to  $\nu$  and application of the chain rule yields by a straightforward calculation

$$\frac{\partial f_0}{\partial f} = \frac{\partial \nu_0}{\partial \nu} = -\frac{\partial t}{\partial \nu} \cdot \left( \frac{\partial t}{\partial \nu_0} \right)^{-1}. \quad (6.46)$$

Evaluation of this expression by use of (6.44) finally leads to

$$\frac{\partial f_0}{\partial f} = \frac{f_0^3 (4 + \hat{y} f_0^2)}{f^3 (4 + \hat{y} f^2)}. \quad (6.47)$$

It is easy to see that  $\hat{y} \rightarrow \infty$  implies  $\frac{\partial f_0}{\partial f} \rightarrow \frac{f_0^5}{f^5}$ , reproducing Equation (6.15).

However, there is no conceptual difference between a spin-down governed by  $\varepsilon$  and one governed by  $\hat{y}$ . One can write Equation (6.18) giving the number of neutron stars with fixed spin-down parameter  $\hat{y}$  in a frequency band  $[f_1, f_2]$  and gravitational-wave amplitude  $h \geq h_{\max}$  as

$$M(f_1, f_2, h_{\max}, \hat{y}) = \int_0^{\bar{t}} dt \dot{n}(t) \int_{f_1}^{f_2} df q_f(f, t, \hat{y}) \int_{h_{\max}}^{\infty} dh q_r(r(h), t) \frac{dr(h)}{dh}. \quad (6.48)$$

The fact that  $h_{\max}$  for given  $\hat{y}$ ,  $f_1$ ,  $f_2$  and  $M$  is an upper limit on the gravitational-wave amplitude from a population of neutron stars, whose spin-down is governed by  $\hat{y}$ , can be rephrased as follows:  $h_{\max}$  is an upper limit, if  $M(f_1, f_2, h_{\max}, \hat{y})$  is maximal as a function of  $\hat{y}$ . If  $M$  is not maximal as a function of  $\hat{y}$ , then a larger value of  $h_{\max}$  in the same frequency band could be found for a different value of  $\hat{y}$  giving the same  $M$ . Thus, it is necessary to identify maxima of  $M(f_1, f_2, h_{\max}, \hat{y})$  in  $\hat{y}$ . These satisfy

$$\frac{d}{d\hat{y}} M(f_1, f_2, h_{\max}, \hat{y}) = 0. \quad (6.49)$$

From Equation (6.48) it is clear, that the only term affected by the derivative is  $q_f(f, t, \hat{y})$ . Applying the chain rule to (6.45) after inserting (6.47) one obtains

$$\frac{d}{d\hat{y}} q_f = \frac{\partial q_{f_0}}{\partial f_0} \cdot \frac{\partial f_0}{\partial \hat{y}} \cdot \frac{f_0^3 (4 + \hat{y} f_0^2)}{f^3 (4 + \hat{y} f^2)} + q_{f_0} \cdot \frac{f_0^3 (f_0^2 - f^2)}{f^3 (4 + \hat{y} f^2)^2}, \quad (6.50)$$

where the arguments of the functions are suppressed.

Let us show that the last equation implies that the maximum expected amplitude as given in Section 6.5.2 is a rigorous upper limit for frequencies  $f_0$  for which

$$\left. \frac{\partial \varrho_{f_0}}{\partial f_0} \right|_{f_0(f,t,\hat{y})} \leq 0 \quad \forall f, t. \quad (6.51)$$

The second summand on the right-hand side of (6.50) is positive  $\forall f, t, \hat{y}$ . The last factor in the first summand is always positive. It is also clear, that  $\partial_{\hat{y}} f_0 < 0 \quad \forall f, t$  for a fixed value of  $\varepsilon$ <sup>5</sup>. Therefore, if (6.51) holds true, it follows  $\frac{d}{d\hat{y}} \varrho_f > 0 \quad \forall f, t, \hat{y}$  and  $\frac{d}{d\hat{y}} M > 0 \quad \forall \hat{y}$ . Thus, if (6.51) is fulfilled, the global maximum of  $M$  as a function of  $\hat{y}$  is reached for  $\hat{y} \rightarrow \infty$ , that is for pure gravitational wave spin-down.

As mentioned earlier, for the model distribution of initial frequencies adopted to produce Figure 6.6 has its maximum at  $f_0 = 250$  Hz and is monotonically decreasing for larger values of initial frequencies. Therefore, Equation (6.51) is fulfilled for  $f \geq 250$  Hz in Figure 6.6, and the graphs shown there are a strict upper limit on the gravitational-wave amplitude from neutron stars spinning down by gravitational waves and electromagnetic dipolar emission for  $f > 250$  Hz.

## 6.6 Conclusions

We have used analytical arguments and the results of a numerical simulation to show that the assumptions of Blandford's argument do not hold in a realistic model of our galaxy.

The assumptions (both in the original and in revised formulations of the argument) cannot be fulfilled for realistic values of ellipticity. The spatial scaling dimension  $D$  of an evolved neutron star distribution fulfils  $D > 2$  making a simple two-dimensional model invalid. The distribution in frequency will not be in a steady state at the present time for realistic values of ellipticity.

Because these two assumptions do not hold, the simple geometrical reasoning behind Blandford's argument is not valid. The numerical simulations provide an improved estimate of the expected maximum amplitude of gravitational waves from gravitars. We also showed that for frequencies  $f > 250$  Hz this maximum amplitude is an upper limit for gravitational waves from neutron stars that spin down by gravitational waves and electromagnetic dipole emission.

Although the expected maximum amplitude is lower by about 1 order of magnitude compared to the previous estimates, we would like to stress that in all of the models so far the influence of the Gould belt has been neglected. This young star-forming region (age  $\sim 40$  Myrs) near the Sun is characterised by an abundance of massive O- and B-type stars enriching the solar neighbourhood with young neutron stars. If there exists a population of gravitars born in the Gould belt, their gravitational-wave signals are more likely to be the first ones to be detected.

<sup>5</sup>Increasing  $\hat{y}$  for fixed  $\varepsilon$  and therefore fixed  $\gamma_{\text{gw}}$  is only possible by decreasing  $\gamma_{\text{dip}}$ , that is reducing the amount of energy radiated away by dipolar spin-down. Accordingly, the total spin-down is slower and  $f_0$  less.

# 7

## Gravitar Population Modelling

---

*to be submitted to Phys. Rev. D*

---

### 7.1 Overview and context

---

Rapidly spinning neutron stars are expected to emit continuous gravitational waves if they are non-axisymmetrically deformed. Most such stars could belong to an electromagnetically invisible population of objects that lose their energy predominantly in gravitational waves. Previous papers have coined the name “gravitars” for this class of electromagnetically silent yet gravitational-wave emitting neutron stars, see e.g. Palomba (2005). Recent statistical simulations suggest that these gravitational waves could be detected by instruments like LIGO for the most optimistic models (Knispel and Allen, 2008). However, international efforts have not yet made a successful detection (Abbott et al., 2009; Abbott et al., 2009). New methods have been explored recently, that promise to improve the sensitivity of blind searches by about an order of magnitude (Cutler, 2011; Pletsch and Allen, 2009).

This paper refines previous simulations in a key aspect: for the first time realistic sensitivity curves of actual searches are used to simulate detectabilities. Previously, either non-realistic, optimal assumptions for the search sensitivity were made (Palomba, 2005), or statistical upper limits on signal strength alone were obtained (Knispel and Allen, 2008). Here, we also describe the distribution of gravitars in search parameter space in better detail than before by using more extensive simulations. We further introduce an analytical way of evolving the frequency distribution over time, where previously only a Monte-Carlo approach was available.

Moreover, we identify the most promising regions of parameter space to search, which provides useful information to design future searches. We present a general framework for the optimisation of blind searches using population synthesis results as model input.

We present an analytical toy model of an optimisation process for blind searches. From the general framework we show how existing blind searches can be prioritised to minimise the time to a first detection. We also describe the concept of inexpensive semi-targeted searches: this is similar to the prioritisation process and can provide computationally much less expensive searches with almost the same sensitivity as completely blind searches to the modelled source population.

Finally, we apply the optimisation process to a specific example and show how to construct an inexpensive semi-targeted search for gravitars from an existing Einstein@Home blind all-sky search for continuous gravitational waves.

## 7.2 Methods

---

Population synthesis is a widely used method to explore the properties of a stellar population given some prior knowledge about birth properties and evolution. A large number of single objects with a set of properties drawn randomly from predefined distributions is generated and evolved over time according to evolution equations. In this paper, a population of isolated neutron stars evolving by the emission of gravitational waves and moving in the gravitational potential of our Galaxy is studied.

Our population study consists of three separable parts: firstly, the numerical simulation of Galactic gravitar orbits, and secondly, the semi-analytical frequency evolution. Both can be evolved independently, they are connected by the evolution time alone. As a third step the detectability of the gravitar population with previous, current, and future realistic searches for these objects is studied by combining the results of the first two steps.

Let us now consider in more detail the three steps of this study, beginning with the numerical simulation of the Galactic orbits. In the following we will look at these defining components: the gravitational potential of the Galaxy, the initial distribution in the Galaxy, the initial distribution of velocities, and the birthrate as a function of time.

### 7.2.1 Galactic potentials and equations of motion

The galactic gravitational potential governs the motion of Galactic gravitars by defining the equations of motion. We consider two potentials widely-used throughout literature. We will describe the gravitational potentials and derive the equations of motion.

Both potentials describe our galaxy as axisymmetric with respect to the rotation axis. Thus, cylindrical coordinates  $R$ ,  $z$  and  $\varphi$  are used.  $R$  denotes the distance to the Galactic rotation axis,  $z$  is the distance perpendicular to the disk, and  $\varphi$  is the angle measured in the direction of Galactic rotation from a line joining the Sun with the Galactic center. The spherical distance between two points is denoted by  $r = \sqrt{R^2 + z^2}$ .

The first potential was first given by Paczynski (1990). It represents our galaxy as composed of three different mass components: a nonuniform flat disk, a halo, and a spheroidal bulge component.

The corresponding potential energy per unit mass consists of three terms

$$\Phi_1(R, z) = \Phi_s(r) + \Phi_d(R, z) + \Phi_h(r). \quad (7.1)$$

describing, respectively, the spheroid, the disk and the halo in our galaxy. The first two

**Table 7.1:** Parameters of the Galactic gravitational potential  $\Phi_1 (R, z)$ 

| Constant      | Disk (d)              | Spheroid (s)          | Halo (h)              |
|---------------|-----------------------|-----------------------|-----------------------|
| $M (M_\odot)$ | $8.07 \times 10^{10}$ | $1.12 \times 10^{10}$ | $5.00 \times 10^{10}$ |
| $b$ (kpc)     | 0.200                 | 0.277                 | ...                   |
| $a$ (kpc)     | 3.7                   | 0.0                   | 6.0                   |

**Table 7.2:** Parameters for the Galactic gravitational potential  $\Phi_2 (R, z)$  with  $\vec{h} = (h_1, h_2, h_3)$  and  $\vec{\beta} = (\beta_1, \beta_2, \beta_3)$ .

| Constant        | Disk-Halo (dh)        | Bulge (b)            | Nucleus (n)       |
|-----------------|-----------------------|----------------------|-------------------|
| $M (M_\odot)$   | $1.45 \times 10^{11}$ | $1.0 \times 10^{10}$ | $9.3 \times 10^9$ |
| $b$ (kpc)       | 5.5                   | 1.5                  | 0.25              |
| $a_G$ (kpc)     | 2.4                   | ...                  | ...               |
| $\vec{h}$ (kpc) | (0.325, 0.090, 0.125) | ...                  | ...               |
| $\vec{\beta}$   | (0.4, 0.5, 0.1)       | ...                  | ...               |

components are given by

$$\Phi_{s,d} (R, z) = -\frac{GM_{s,d}}{\sqrt{\left(a_{s,d} + \sqrt{z^2 + b_{s,d}^2}\right)^2 + R^2}}. \quad (7.2)$$

For the potential of the halo the following spherical symmetric expression is used

$$\Phi_h (r) = \frac{GM_H}{a_h} \left[ \frac{1}{2} \ln \left( 1 + \frac{r^2}{a_h^2} \right) + \frac{a_h}{r} \arctan \left( \frac{r}{a_h} \right) \right]. \quad (7.3)$$

The parameter values are shown in Table 7.1.

The second potential was initially proposed by Carlberg and Innanen (1987) and later modified by Kuijken and Gilmore (1989). This fit consists of a disk-halo, a bulge, and a nucleus component:

$$\Phi_2 (R, z) = \Phi_{dh} (R, z) + \Phi_b (r) + \Phi_n (r). \quad (7.4)$$

The disk-halo component is axisymmetric and described by

$$\Phi_{dh} (R, z) = -\frac{GM_{dh}}{\sqrt{\left(a_G + \sum_{i=1}^3 \beta_i \sqrt{z^2 + h_i^2}\right)^2 + b_{dh}^2 + R^2}}, \quad (7.5)$$

while the bulge and nucleus components are given by the spherical symmetric expressions

$$\Phi_{b,n} (r) = -GM_{b,n} \left( b_{b,n}^2 + r^2 \right)^{-\frac{1}{2}}. \quad (7.6)$$

The values of the constants are given in Table 7.2.

Due to the axial symmetry of  $\Phi_1$  and  $\Phi_2$ , the  $z$ -component of the angular momentum  $L_z$  is conserved. An effective potential is given by

$$\Phi_{\text{eff}}(R, z) = \Phi(R, z) + \frac{L_z^2}{2R^2}. \quad (7.7)$$

The equations of motion are

$$\ddot{R} = -\frac{\partial\Phi_{\text{eff}}}{\partial R}, \quad \ddot{z} = -\frac{\partial\Phi_{\text{eff}}}{\partial z} \quad \text{and} \quad \dot{\varphi} = \frac{L_z}{R^2}. \quad (7.8)$$

These equations of motion have a unique solution when supplied with initial conditions. Here, initial conditions are the initial velocities and positions drawn from distributions described below.

### 7.2.2 Initial velocity

The Galactic rotation determines the velocity of the supernova progenitors and therefore also that of the newborn neutron stars.

The rotational speed of a body on a circular orbit in the axisymmetric potentials (7.1) and (7.4) is given by  $v_{\text{rot}} = \sqrt{R\partial_R\Phi_{1,2}(R, z)}$ . For each gravitar the corresponding  $v_{\text{rot}}$  on a tangential circular orbit is calculated from the initial coordinates (neglecting rotation velocities perpendicular to the Galactic disk, because of the low initial values of  $z$  for all gravitars at birth). Looking down on the Galaxy from positive  $z$ -values the rotation is chosen to be counterclockwise.

Furthermore, it is assumed that gravitars are born in a supernova explosion imparting a kick to the newborn neutron star. The direction of the kick is assumed to be isotropic. The kick's magnitude is drawn from a Maxwellian distribution with a mean velocity  $\bar{v} = 430$  km/s. The probability for the kick speed to be in an interval  $[v, v + dv]$  is then

$$p_v(v) dv = \frac{32v^2}{\pi^2\bar{v}^3} e^{-\frac{4v^2}{\pi\bar{v}^2}} dv. \quad (7.9)$$

This distribution from Hobbs et al. (2005) was obtained from pulsar observations. We assume it may be used for gravitars as well.

### 7.2.3 Initial spatial and age distribution

We consider the Galactic disk and the Gould Belt, a region in the Galactic solar neighbourhood abundant in neutron star progenitors, as birth sites for neutron stars.

#### Galactic disk

The initial spatial distribution of gravitars in the Galactic disk is proportional to the density of massive progenitor stars of neutron stars. While there is quite good agreement about the initial distribution in  $z$ -direction, the initial distribution along the radial direction is unknown. In the  $z$ -direction the initial position is drawn from a Laplacian distribution with scale factor  $z_0 = 0.075$  kpc. The probability of a gravitar's birth in an interval  $[z, z + dz]$  is given by

$$p_z(z) dz = \frac{1}{2z_0} e^{-\frac{|z|}{z_0}} dz. \quad (7.10)$$

We consider two different models for the initial radial distribution together with the above given initial  $z$ -distribution. Following Paczynski (1990) a gamma distribution given by

$$p_1(R) dR = a_R \frac{R}{R_1^2} e^{-\frac{R}{R_1}} dR, \quad (7.11)$$

is first considered, where gravitar formation in the disk is allowed for  $R \leq 25$  kpc, and the constants are given by  $R_1 = 4.78$  kpc and  $a_R = 1.0345$ . A second distribution

$$p_2(R) dR = \frac{R^5}{120R_2^6} e^{-\frac{R}{R_2}} dR, \quad (7.12)$$

with  $R_2 = 1.25$  kpc taken from Yusifov and Kucuk (2004) is also considered. It is fitted to the radial distribution of Population I stars which are considered to be likely progenitors of neutron stars. Again, gravitar birth events are allowed for  $r \leq 25$  kpc. On average, only one gravitar out of  $1.4 \times 10^4$  is born with  $R > 25$  kpc, so the normalisation constant  $a_R \approx 1$  is dropped in the definition of  $p_2$

We assume a constant birthrate of  $2 \times 10^4 \text{ Myr}^{-1}$  for the Galactic disk. We allow for ages up to at most 500 Myrs. With hindsight, this choice is justified by the fact that in our simulations we find that most of the detectable sources ( $> 99\%$  for all models considered, compare the inset in Figure 7.7 as well) have ages smaller by two orders of magnitude. This is because gravitars rapidly escape the solar neighbourhood due to high spatial velocity or leave the most sensitive frequency band of the detectors due to frequency evolution. Only young rapidly spinning gravitars close to the Sun<sup>1</sup> can be detected.

### The Gould belt

We describe the Gould Belt as a torus with rectangular cross-section. The outer radius is 0.3 kpc, while the inner radius is 0.15 kpc. Its thickness is 0.06 kpc. The belt is centred on a point 0.1 kpc in anti-Galactic-center direction from the Sun and tilted by  $18^\circ$  such that the belt lies below the Galactic plane at larger distances from the Galactic center. The belt is assumed co-rotating with the Sun. Figure 7.1 shows a schematic cut through our model of the Gould belt along a plane containing the Galactic centre and the Sun and perpendicular to the plane of the Galaxy.

Following Palomba (2005), we assume a birthrate of  $27 \text{ Myr}^{-1}$  and uniform birth probability in the belt volume described above. According to Palomba (2005) the age of the belt is 40 Myrs. In our simulation birth events from the Gould belt start 40 Myrs in the past, no sources are born before that point in time.

### 7.2.4 Coding and implementation

With the initial distributions from Sections 7.2.3 and 7.2.2 and the equations of motion (7.8) known, it is straightforward to evolve a population of Galactic gravitars in time and study their spatial distribution.

The code for the simulation is written in C using standard libraries. The equations of motion (7.8) are integrated by re-writing them as first-order differential equations and using the variables  $\varphi, R, \dot{R}, z, \dot{z}$  as independent variables. The integration is done via an

<sup>1</sup>We consider the detector on Earth and the Sun for our purposes as collocated.

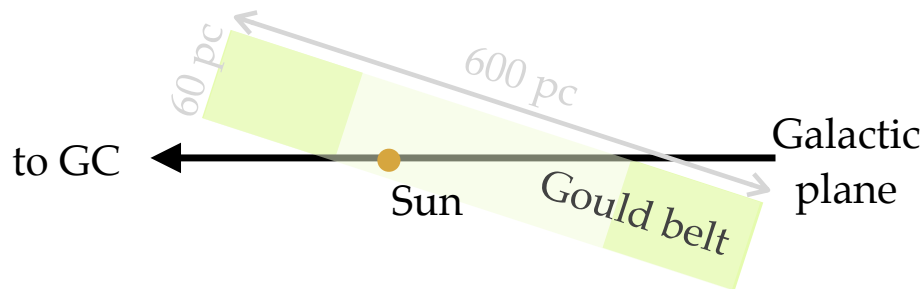


**Figure 7.1:** Schematic showing a cut through our model of the Gould belt along a plane containing the Galactic centre and the Sun and perpendicular to the plane of the Galaxy. The belt is inclined by  $18^\circ$  with respect to the Galactic plane and its centre is offset from the Sun by 100 pc.

eighth-order Runge-Kutta algorithm with adaptive step-size from the GNU Scientific Library (GSL; Galassi, 2009). We chose the step-size in such a way that over the integration time the total energy is always conserved to better than one part in  $10^6$ , in most cases to better than one part in  $10^7$ . Depending on the model of the initial spatial distribution and the Galactic gravitational potential the integration of  $10^6$  neutron star trajectories over a random time between 0 and 500 Myrs takes 2.3 mins to 13.3 mins on a modern processor. Most of the simulations were done on the ATLAS cluster at the AEI in Hannover.

### 7.2.5 Frequency evolution

The frequency evolution of a single gravitar and a population of such objects is determined by three parameters: the spin-down from gravitational-wave emission, the distribution of spin frequencies at birth, and the distribution of their deformation (ellipticity).

A non-axisymmetric deformed neutron star will radiate away rotational energy by the emission of gravitational waves. It is straightforward to derive the equations describing the frequency evolution of gravitars. Their instantaneous spin-down due to their nonaxisymmetric shape is given by

$$\dot{f} = -\frac{32\pi^4 GI}{5c^5} \varepsilon^2 f^5, \quad (7.13)$$

where  $f$  is the frequency of the emitted gravitational waves, which is twice the spin frequency of the gravitar.  $G$  is Newton's gravitational constant,  $I$  is the moment of inertia with respect to the rotational axis,  $c$  is the speed of light and  $\varepsilon = \frac{I_1 - I_2}{I}$  is the ellipticity of the gravitar. Integrating (7.13) gives the frequency of gravitational waves emitted at time  $t$  as

$$f(t) = \left( f_0^{-4} + \beta^{-1} \varepsilon^2 t \right)^{-\frac{1}{4}} \quad \text{with } \beta = \frac{5}{128\pi^4} \frac{c^5}{GI}, \quad (7.14)$$

assuming an initial (birth) gravitational-wave frequency  $f_0 = f(0)$ . The constant  $\beta$  is approximately

$$\beta^{\frac{1}{3}} = 5.3 \times \left( \frac{10^{38} \text{ kg m}^2}{I} \right)^{\frac{1}{3}} \text{ kHz}. \quad (7.15)$$

The above equations describes the gravitational-wave frequency at the present time for a gravitar given its birth frequency, ellipticity, and age.

### 7.2.6 Initial frequency distribution

Because of the conservation of angular momentum in the supernova and the much smaller radius of the compact remnant compared with its progenitor, newborn neutron stars will spin rapidly.

We considered two models for the distribution of the initial spin frequencies following the models used in Palomba (2005). We convert the distributions for initial spin periods from that paper into distribution for initial gravitational-wave frequencies. The fact, that we use different models reflects our ignorance of the actual distribution of initial frequencies and allows us to test their impact on the results.

The first model is motivated from pulsar observations and found as the maximum likelihood model by population synthesis (Arzoumanian et al., 2002). It is described by a log-normal distribution

$$p_{f_0}(f_0) df_0 = \frac{1}{\sqrt{2\pi}\sigma f_0} \exp\left[-\frac{1}{2\sigma^2} \left(\ln(f_0) - \ln(\bar{f}_0)\right)^2\right] df_0 \quad (7.16)$$

where  $f_0$  is measured in Hz and where the values  $\sigma = 0.69$  and  $\bar{f}_0 = 400$  Hz are taken from Arzoumanian et al. (2002). Gravitars with  $f_0 > 4$  kHz are excluded.

The second model considered is a physical extension of the first one. It includes the effects of matter fall-back after the supernova as well as the (possible) existence of r-modes in young neutron stars. An increase angular momentum by accreting matter could counteract the r-mode induced deceleration. The resulting initial frequency will approach an intermediate value. The choice from Palomba (2005) is to draw the initial period from a uniform distribution between 2 ms and 15 ms. Therefore the initial gravitational-wave frequency will follow a power law distribution:

$$p_{f_0}(f_0) df_0 = \begin{cases} a f_0^{-2} & \text{if } f_0 \in I_{f_0} \\ 0 & \text{else} \end{cases}, \quad (7.17)$$

where  $I_{f_0} = [133.\bar{3} \text{ Hz}, 1 \text{ kHz}]$  is the range of initial frequencies and  $a = 153.85 \text{ Hz}^2$  is the normalising constant.

### 7.2.7 Ellipticity distribution

The typical ellipticity of neutron stars is unknown, and also the maximum value depending on the unknown equation of state is not well known. For exotic models, maximum values of  $10^{-5}$  to  $10^{-4}$  might be possible, while  $10^{-9}$  to  $10^{-6}$  are considered more reasonable. Our only assumptions are a mean value  $\bar{\epsilon}$  and a maximum value  $\epsilon_{\max}$ . Following Palomba (2005), we will use the probability distribution function  $p$ , which maximises the entropy functional

$$\mathcal{S}[p] = \int_{-\infty}^{\infty} dy p(y) \ln(p(y)) \quad (7.18)$$

to get the pdf with the largest uncertainty under the given constraints. We find

$$p_{\epsilon}(\epsilon) = a(\tau) e^{-\frac{\epsilon}{\tau}} \text{ with } a(\tau) = \frac{1}{\tau \left(1 - e^{-\frac{\epsilon_{\max}}{\tau}}\right)}. \quad (7.19)$$

**Table 7.3:** The value of  $\tau$  solving Equation (7.20) for  $\varepsilon_{\max} = 2.5 \times 10^{-6}$  and varying mean  $\bar{\varepsilon}$ .

| $\bar{\varepsilon}$ | $10^{-6}$                  | $10^{-7}$                  | $10^{-8}$                  |
|---------------------|----------------------------|----------------------------|----------------------------|
| $\tau$              | $2.032\,63 \times 10^{-6}$ | $1.000\,00 \times 10^{-7}$ | $1.000\,00 \times 10^{-8}$ |

The value of  $\tau$  is computed numerically by solving

$$\tau = \bar{\varepsilon} + \frac{\varepsilon_{\max}}{\exp\left(\frac{\varepsilon_{\max}}{\tau}\right) - 1} \quad (7.20)$$

for  $\tau$ . We always assume  $\varepsilon_{\max} = 2.5 \times 10^{-6}$ . The value of  $\tau$  for different values of  $\bar{\varepsilon}$  is shown in Table 7.3.

### 7.2.8 Analytical frequency distribution evolution

Previous papers studied the frequency evolution fully by a Monte-Carlo approach. Given values for ellipticity, birth frequency and age (all three drawn from the respective assumed distribution), it is straightforward to calculate the present-day spin frequency from Equation (7.14) for a single gravitar. Repeating this process with many random samples from the three-dimensional parameter space, one can numerically arrive at the evolved frequency distribution; the latter is the distribution of gravitars in spin frequency, assuming random distribution for birth frequency, ellipticity, and age. Compare, for example, Figure 4 in Palomba (2005). Figures 1 and 2 in Knispel and Allen (2008) are special cases when the ellipticity is fixed and not drawn from a distribution.

Here, we show how the evolved frequency distribution can be derived fully analytically, assuming random distributions in birth frequency, ellipticity, and age. This eliminates the need for costly Monte-Carlo simulations to explore this parameter space and enables one to easily obtain the evolved frequency distributions for a variety of different random distributions as well as special cases as in Palomba (2005) and Knispel and Allen (2008).

#### Parameter distributions

Consider a continuous distribution of gravitational-wave frequencies at birth. Let  $dP_{f_0}$  be the probability of the birth frequency being in a band  $[f_0, f_0 + df_0]$ . The corresponding probability density  $p_{f_0}(f_0)$  is defined by

$$dP_{f_0} = p_{f_0}(f_0) df_0. \quad (7.21)$$

A frequency change by redshift from cosmological evolution is neglected since all gravitars considered are within the Galaxy.

Assume a birthrate  $p_t(t)$  of Galactic gravitars which is defined by the probability  $dP_t$  for a gravitar to be born in the time interval  $[t, t + dt]$  being

$$dP_t = p_t(t) dt. \quad (7.22)$$

A gravitar with age  $t = 0$  is born at the present time, whereas  $t > 0$  means birth in the past.

Moreover, consider the probability  $dP_\varepsilon$  for each source having an ellipticity in the range  $[\varepsilon, \varepsilon + d\varepsilon]$  defining a distribution of ellipticities  $p_\varepsilon(\varepsilon)$  by

$$dP_\varepsilon = p_\varepsilon(\varepsilon) d\varepsilon. \quad (7.23)$$

All previously defined probability distributions are assumed to be properly normalised, such that  $\int_0^\infty dx p_x(x) = 1$ .

### The evolved frequency distribution

We now show how to obtain an evolved distribution in frequency, given an initial distribution of frequency, birth rate and ellipticity. Define the conditional present-time frequency distribution  $p_f(f|\varepsilon, t)$  such that

$$dP_f = p_f(f|\varepsilon, t) df \quad (7.24)$$

is the probability of finding a gravitar in the frequency band  $[f, f + df]$ , assuming an ellipticity  $\varepsilon$  and an age  $t$ . To compute  $p_f(f|\varepsilon, t)$  from the initial  $p_{f_0}(f_0)$ , consider a single gravitar with ellipticity  $\varepsilon$  whose current frequency is  $f$ , and let  $f_0(\varepsilon, f, t)$  denote the gravitar's frequency at time  $t$  in the past. Solving (7.14) for the birth frequency yields

$$f_0(f, \varepsilon, t) = \left(f^{-4} - \beta^{-1}\varepsilon^2 t\right)^{-\frac{1}{4}}. \quad (7.25)$$

The probability density  $p_f$  can be rewritten in terms of the initial frequency distribution  $p_{f_0}$  by a change of variables. The fraction of gravitars in a birth frequency band  $[f_0, f_0 + df_0]$  is the same as the fraction in a present time frequency band  $[f, f + df]$ , so the identity  $p_f df = p_{f_0} df_0$  yields

$$p_f(f|\varepsilon, t) df = p_{f_0}(f_0(f, \varepsilon, t)) \frac{\partial f_0(f, \varepsilon, t)}{\partial f} df \quad (7.26)$$

$$= p_{f_0}(f_0(f, \varepsilon, t)) \frac{f_0^5(f, \varepsilon, t)}{f^5} df, \quad (7.27)$$

from which

$$p_f(f|\varepsilon, t) = p_{f_0}(f_0(f, \varepsilon, t)) \frac{f_0^5(f, \varepsilon, t)}{f^5} \quad (7.28)$$

immediately follows. The probability  $dP$  of finding a gravitar in a small parameter cube  $[f, f + df] \times [\varepsilon, \varepsilon + d\varepsilon] \times [t, t + dt]$  is

$$dP = p_f(f|\varepsilon, t) p_t(t) p_\varepsilon(\varepsilon) df d\varepsilon dt. \quad (7.29)$$

The evolved frequency distribution is obtained by marginalising over  $t$  and  $\varepsilon$  as

$$p_f^{\text{ev}}(f) df = \int_0^T dt \int_0^\infty d\varepsilon p_f(f|\varepsilon, t) p_t(t) p_\varepsilon(\varepsilon) df. \quad (7.30)$$

Note, that this expression of the evolved frequency distribution can be computed directly without need for Monte-Carlo simulations for any given set of initial distributions from Section 7.2.8 by use of Equation (7.28).

Another important quantity is the evolved frequency distribution for a fixed age of all sources, which is obtained by marginalising Equation (7.29) over ellipticity only:

$$p_f^{\text{ev}}(f|t) df = \int_0^\infty d\varepsilon p_f(f|\varepsilon, t) p_\varepsilon(\varepsilon) df, \quad (7.31)$$

which is shown in Figure 7.2 for both of our initial frequency distributions and a range of evolution times  $t$ .

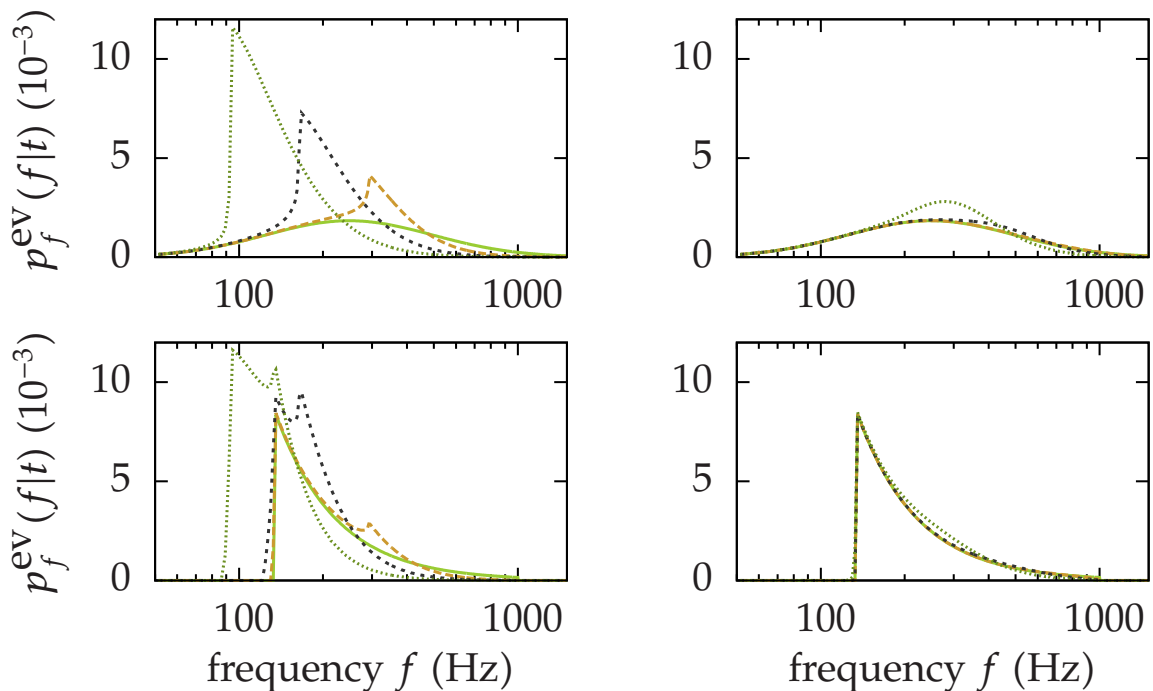


**Figure 7.2:** The evolved frequency distribution  $p_f^{\text{ev}}(f|t)$  for fixed ages  $t$  from Equation (7.31). The top panel shows the evolution of the lognormal initial frequency distribution, Equation (7.16), for  $\bar{\epsilon} = 10^{-6}$  on the left-hand side and for  $\bar{\epsilon} = 10^{-7}$  on the right-hand side. The bottom plots show the according evolution of the power-law initial frequency distribution, Equation (7.17). The colour code is:  $t = 0$  Myr, solid light-green line;  $t = 0.1$  Myr, dashed orange line;  $t = 1.0$  Myr, dashed dark-grey line;  $t = 10$  Myr, dashed dark-green line.

### 7.2.9 Search sensitivity modelling

Sections 7.2.1 to 7.2.3 describe how to compute the *spatial* distribution of an evolved Galactic gravitar population by numerical integration. Sections 7.2.5 to 7.2.8 showed how to analytically obtain the evolved frequency distribution. In this section we show how to combine both distributions with search sensitivity modelling to assess the detectability of a given population with a given search.

We first rewrite the sensitivity as a lower bound on ellipticity depending on frequency and distance. We then use this bound to formulate the detectability of a gravitar population in the most general case of continuous spatial distribution and for the case of the simulation where the spatial distribution is described by an ensemble of discrete sources.

We assume the search sensitivity may be described by only a frequency dependence. We neglect sensitivity variations in the sky because typical searches are carried out over time baselines of order a year so that these variations average out. Then, the search sensitivity is fully described by a sensitivity curve  $h_{\text{min}}(f)$ . This is the minimum gravitational-wave strain  $h$  detectable with that search at frequency  $f$ . The strain amplitude  $h$  of gravitational waves emitted by a gravitar at distance  $r$  to the detector and assuming optimal mutual

orientation<sup>2</sup> is given by

$$h(f, \varepsilon, r) = 4\pi^2 \frac{GI}{c^4} \frac{\varepsilon f^2}{r} =: \alpha \frac{\varepsilon f^2}{r}. \quad (7.32)$$

For a source to be detectable the source strain needs to exceed the minimum detectable strain  $h(f, \varepsilon, r) \geq h_{\min}(f)$  and we can use (7.32) to obtain in turn a lower bound on  $\varepsilon$  for given  $r, t$ , and  $f$ :

$$\varepsilon \geq \frac{r h_{\min}(f)}{\alpha f^2} =: \varepsilon_{\min}(f, r). \quad (7.33)$$

Given a distance, age, and spin frequency of a gravitar, and the sensitivity of the search method at the spin frequency, this equation determines the minimum necessary ellipticity of the gravitar to be detectable. Thus, we can use Equation (7.33) to determine the probability that any pulsar from the Galactic population is detectable. We will now compute these *detectabilities* for the continuous case (assuming we can obtain a continuous number density of Galactic gravitars), and the for the discrete case (assuming we obtain positions and ages for discrete Galactic gravitars from a Monte-Carlo simulation).

### Detectabilities for a continuous spatial distribution

For the continuous case let us assume that the spatial distribution is described by  $n_r(r|t)$ , such that

$$dN_r = n_r(r|t) dr \quad (7.34)$$

is the number of gravitars in a spherical shell  $[r, r + dr]$  around the detector, given an evolution time  $t$ . Note that this is now a number density and normalised such that  $\int dN_r = N_{\text{tot}} \forall t$  is the total number of gravitars. Then, by Equation (7.29) the number  $dN_{\text{tot}}$  of gravitars in the small parameter space volume  $[f, f + df] \times [\varepsilon, \varepsilon + d\varepsilon] \times [t, t + dt] \times [r, r + dr]$  is

$$dN_{\text{tot}} = p_f(f|\varepsilon, t) p_t(t) p_\varepsilon(\varepsilon) n_r(r|t) df d\varepsilon dt dr. \quad (7.35)$$

Thus, by integration and normalisation with  $N_{\text{tot}}$  we get the probability of detecting any source from a given population by means of a given search as

$$P_{\text{tot}}^{\text{det}} = \frac{1}{N_{\text{tot}}} \int_0^\infty df \int_0^T dt p_t(t) \int_0^\infty dr n_r(r|t) \int_{\varepsilon_{\min}(f,r)}^\infty d\varepsilon p_f(f|\varepsilon, t) p_\varepsilon(\varepsilon). \quad (7.36)$$

This quantity describes the detectable fraction of the gravitar population. The expectation value for the number of gravitars is  $\langle N_{\text{tot}}^{\text{det}} \rangle = P_{\text{tot}}^{\text{det}} N_{\text{tot}}$ . The total number of gravitars has to be obtained from integrating the birthrate over age of the Galaxy.

The corresponding probability distribution function for the distribution of the detectable sources in frequency is obtained by not integrating Equation (7.35) over  $f$  and is

$$p_{\text{tot}}^{\text{det}}(f) df = \frac{1}{N_{\text{tot}}} \int_0^T dt p_t(t) \int_0^\infty dr n_r(r|t) \int_{\varepsilon_{\min}(f,r)}^\infty d\varepsilon p_f(f|\varepsilon, t) p_\varepsilon(\varepsilon) df. \quad (7.37)$$

<sup>2</sup>gravitar sky position given by the unit vector orthogonal to the plane of the detector arms; gravitar spin axis parallel to this vector

### Detectabilities for a discrete spatial distribution

Equation (7.36) and (7.37) assume a continuous spatial distribution  $n_r(r|t)$ . This distribution is not directly available from the simulations described in Sections 7.2.1 to 7.2.4. The result of such a Monte-Carlo simulation of Galactic gravitar orbits is a set of  $N_{\text{tot}}$  discrete single sources, each labeled by a distance  $r_i$  and an age  $t_i$ . We can define a pseudo-density

$$p_t(t) n_r(r|t) = \sum_{i=1}^{N_{\text{tot}}} \delta(t - t_i) \delta(r - r_i) \quad (7.38)$$

with  $\delta(x)$  the Dirac Delta function and the sum running over all  $N_{\text{tot}}$  simulated gravitars. Then, by using Equation (7.38) in Equation (7.36) the detectable fraction of a given population is

$$P_{\text{tot}}^{\text{det}} = \frac{1}{N_{\text{tot}}} \sum_{i=1}^{N_{\text{tot}}} P_i^{\text{det}}, \quad (7.39)$$

which is the normalised sum of the detectabilities  $P_i^{\text{det}}$  given by

$$P_i^{\text{det}} = \int_0^\infty df \int_{\varepsilon_{\min}(f, r_i)}^\infty d\varepsilon p_f(f|\varepsilon, t_i) p_\varepsilon(\varepsilon). \quad (7.40)$$

In other words,  $P_i^{\text{det}}$  is the probability (given the chosen distributions for ellipticity and initial frequency) that a source of age  $t_i$  and in distance  $r_i$  is detectable with a search characterised by  $h_{\min}(f)$ . Again, the probability density function in frequency for the discrete case is given by dropping the  $f$ -integration as

$$p_{\text{tot}}^{\text{det}}(f) = \frac{1}{N_{\text{tot}}} \sum_{i=1}^{N_{\text{tot}}} p_i^{\text{det}}(f) \quad (7.41)$$

with

$$p_i^{\text{det}}(f) = \int_{\varepsilon_{\min}(f, r_i)}^\infty d\varepsilon p_f(f|\varepsilon, t_i) p_\varepsilon(\varepsilon). \quad (7.42)$$

### Weighted histograms of other quantities

Equations (7.41) and (7.39) describe the distribution in frequency and the absolute number of detectable sources, respectively. If the distribution in some other parameter is to be considered, a weighted histogram in the respective parameter can be constructed where the weights are given by the  $P_i^{\text{det}}$  from Equation (7.40) for each simulated source.

More specific, assume each gravitar is assigned a parameter  $\phi$ , which for the  $i$ -th gravitar has the value  $\phi_i$ . For simplicity we assume that if the gravitar is detectable, its parameter value  $\phi_i$  can be determined without error; this might not be true for actual measurements where parameter can be correlated and are subject to measurement uncertainties. This concept is useful, however, if we want to study the underlying distribution of a parameter in the detectable population of gravitars. We then can construct a weighted histogram of the parameter  $\phi$  by incrementing the bins of the histograms by the detectabilities  $0 \leq P_i^{\text{det}} \leq 1$  instead by unity for the  $i$ -th gravitar with parameter value  $\phi_i$ .

In this manner, distance distribution, age distributions, and sky maps for the detectability can readily be constructed. We employ this method in sections 7.3 below for this purpose.

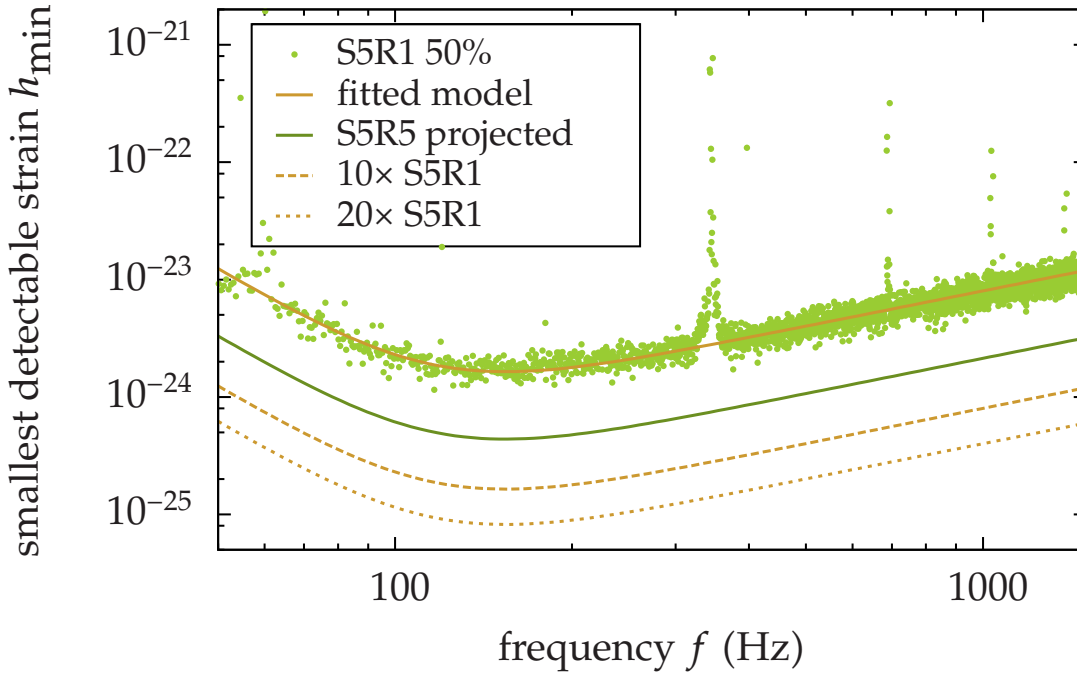


**Figure 7.3:** The different sensitivity curves  $h_{\min}(f)$  used to determine which of the simulated gravitars were detectable with which probability. The dots show the actual sensitivity of the Einstein@Home search in the S5R1 run, the curves show fits according to Equation (7.43)

### 7.2.10 Simulated search sensitivity

In order to simulate existing search pipelines, we will use the sensitivity of the most sensitive search for continuous gravitational waves. This is the most recent, completely processed Einstein@Home search (Abbott et al., 2009) for which we have plotted the sensitivity curve from the S5R1 run in Figure 7.3. The curve shown is the minimum gravitational-wave strain as a function of frequency that would have led to a detection of 50% of all sources. For more detail we refer the reader to Abbott et al. (2009). We have fitted a simple model to the sensitivity curve with a rise  $\propto f$  for high frequencies and a rise  $\propto f^{-3}$  at the low frequency end. Fitting to the S5R1 50% sensitivity we find

$$h_{\min}(f) = 1.5 \times 10^{-18} \left( \frac{f}{1 \text{ Hz}} \right)^{-3} + 0.8 \times 10^{-26} \left( \frac{f}{1 \text{ Hz}} \right) \quad (7.43)$$

This fit are shown in Figure 7.3. In the same figure we also show sensitivity curves scaled to the projected sensitivity of a more recent Einstein@Home run, the S5R5 run (Pletsch, 2010), and a hypothetical search assuming 10 times higher sensitivity than in S5R1 and 20 times higher sensitivity than in S5R1. These sensitivities might be achievable with newly developed methods (Pletsch and Allen, 2009) or better observational data in the future. The fitting smoothes out the less sensitive frequency bands polluted by the violin modes of the mirror suspension in the detector and effectively increases sensitivity in these bands. This leads to a slightly higher probability of detection than with the real sensitivity curve. Given other uncertainties in the modelling process, we neglect this effect.

### 7.3 Results

---

In this section we present the results from various simulation runs and study the distribution of gravitars in parameter space. We considered in total 108 different models. Each model results from choosing one of three initial spatial distribution models, one of two Galactic gravitational potential models, one of three ellipticity distribution models, one of three sensitivity models, and one of two initial frequency distributions as described in Section 7.2.

For each spatial distribution model we firstly computed  $3 \times 10^9$  gravitar orbits. For each of the resulting final positions the detectability  $P_{\text{tot}}^{\text{det}}$  was computed for all of the 108 combinations to yield the expected total number of detections.

Moreover, The frequency distribution  $p_{\text{tot}}^{\text{det}}(f) df$  was computed for each model as well as histograms in distance and age, and a sky-map. These results allow a detailed enough study of the theoretically detectable population of Galactic gravitars to, for example, enable searches which concentrate deeper searches on the most “cost-efficient” parts of the parameter space; see Section 7.4 for a definition of cost-effectiveness in this context.

Each model assumed a search in the frequency range between 50 Hz and 1.5 kHz gravitational-wave frequency. The sensitivity was assumed to depend on the gravitational-wave frequency only and to be given by the form described in Section 7.2.10 and in Figure 7.3. We considered the projected S5R5 sensitivity, and hypothetical searches with sensitivities ten times and twenty times higher than the S5R1 50% sensitivity, respectively.

The main results in short are

- a) A detection within the next years is possible only for the most optimistic models. Details can be found in Section 7.3.1 and table 7.4.
- b) For high ellipticities ( $\bar{\epsilon} = 10^{-6}$ ), the frequency distribution of detectable sources is relatively sharply peaked around  $f = 200$  Hz and falls off quickly to higher and lower frequencies. For  $\bar{\epsilon} = 10^{-7}$  the distribution broadens and the peak shifts to  $f = 500$  Hz for the Gould belt. There are still much fewer sources at high frequencies than at the peak<sup>3</sup>. Details on are in Section 7.3.5 and figures 7.9 and 7.10.
- c) Most detectable sources from the Gould belt are younger than 1 Myr, and younger than a few Myr for Galactic disk sources. Details are in Section 7.3.3 and figure 7.7.
- d) Most detectable sources from the Gould belt are within  $\sim 0.5$  kpc of the Sun and most of the Galactic disk sources are within  $\sim 1$  kpc of the Sun. Details are in Section 7.3.4 and figure 7.8.

#### 7.3.1 Expected number of detections

We first consider the total expected number of detections. A detection within the next years is possible for the optimistic models only. Tables 7.4 and 7.5 show the resulting expected numbers of detections for all models. Each cell contains a value of the expected number of detections for the given model  $\langle N_{\text{tot}} \rangle = P_{\text{tot}}^{\text{det}} N_{\text{tot}}$ . The first column of the table denotes the spatial model used, where “Pac” stands for the Galactic potential from Equation (7.1), and “KaG” for the potential from Equation (7.4), respectively. “Gam” denotes the initial

---

<sup>3</sup>This is important in the design of searches on the most cost-efficient parts of the parameter space, as the search costs scale with a high power in  $f$ .

spatial distribution from Equation (7.11), “PnI” denotes the spatial distribution from Equation (7.12), and “GdB” denotes sources from the Gould belt as described in Section 7.2.3.

The values are always referred to the fraction  $\gamma$  of newborn neutron stars born as gravitars. If only a fraction  $\gamma$  of sources becomes gravitars, the expectation values are scaled accordingly. In the table, we normalise by division by  $\gamma$ . **Note:** the values in the table for  $\bar{\varepsilon} = 10^{-7}$  and  $\bar{\varepsilon} = 10^{-8}$  are scaled by an overall factor of  $10^{-2}$  and  $10^{-5}$ , respectively. For clarity we have marked cells in the table with a coloured background when  $\langle N_{\text{tot}} \rangle \gamma^{-1} > 0.5$ , i.e. where we would expect at least 50% summed probability of a single detection.

There are no expected detections at this 50%-level, if  $\bar{\varepsilon} = 10^{-8}$  even assuming a hypothetical search with twenty times the S5R1 50% sensitivity. Differences between results for sources from the Gould belt and the Galactic disk are more than one order of magnitude for the lognormal frequency distribution and much larger for the flat frequency distribution. This large difference is addressed in more detail below. Between the different models of the Galactic disk, the results agree within a factor of a few for a given sensitivity. This is due to the different local probability densities in the initial spatial and frequency distributions, since at low ellipticities only the near and young sources have non-vanishing detectabilities.

For  $\bar{\varepsilon} = 10^{-7}$ , our models require at least ten times S5R1 50% sensitivity and in most cases rather twenty times S5R1 50% sensitivity. Even then, only up to slightly less than five total detections are expected. For a given sensitivity, the results agree within a factor of two. This is much smaller than the range spanned by the results at  $\bar{\varepsilon} = 10^{-8}$ , since now the local differences are washed out by source migration and frequency evolution. For the lognormal frequency distribution (Table 7.4) results from the Gould belt and the disk agree within a factor of five or less, while for the flat frequency distribution (Table 7.5) the difference is as large as two orders of magnitude, see below for more details on this difference.

For the largest ellipticity ( $\bar{\varepsilon} = 10^{-6}$ ) considered in our simulations, detections are expected for all sensitivities and models, although only at a marginal level for the projected S5R5 sensitivity. The results for sources from the Galactic disk for a given sensitivity agree always within a factor of two or less if other parameters are varied. The values for sources from the Gould belt are smaller by about an order of magnitude, which is due to a saturation effect (as there are no more additional sources detectable from increasing sensitivity to larger distances). This effect is addressed in more detail below.

### 7.3.2 Sky maps

We computed sky density maps for all models. The sky was split into  $4^\circ \times 2^\circ$  cells: 90 cells in right ascension  $\alpha$  and 45 cells in declination  $\delta$ . Each cell’s density value was determined by the summed detectabilities for the sources located in the respective cell. Finally, each cell’s total count was normalised by  $1/\cos(\delta_{\text{center}})$  to correct for the varying surface element on the celestial sphere. Each cell’s value is the expected number of sources to be detectable in the cell.

The plots in Figures 7.4-7.6 show the skymaps for some of the models. Each plot shows the complete celestial sphere in Galactic coordinates with the Galactic center at the center of the map, North up, in a Hammer-Aitoff projection. The colour code shows the detectability density of sources in units of  $10^{-4} \text{ sqdeg}^{-1}$ . Note the change in scale between different plots. For smooth plotting of the maps the  $4^\circ \times 2^\circ$  cells were interpolated into 25 smaller cells.

For all plots shown we chose the most optimistic combination of the Galactic gravitational potential and initial spatial distribution. This is the Kuijken and Gilmore (KaG) potential, Equation (7.4), with the initial spatial distribution fitted to Population I stars (PnI)

**Table 7.4:** Expected total number of detections ( $\langle N_{\text{det}} \rangle$ ) for different models for mean ellipticity, initial spatial distribution, gravitational potential, and search sensitivity. All models here use the *lognormal distribution of initial spin frequency*. The number of detections is obtained by multiplying with the gravitar fraction  $\gamma$  of newborn neutron stars. Cells in green are models with at least 0.5yr predicted detections.

| model   | $\bar{\epsilon} = 10^{-6}$ (per $\gamma$ )     |  |  | $\bar{\epsilon} = 10^{-7}$ (all in $10^{-2}/\gamma$ ) |  |  | $\bar{\epsilon} = 10^{-8}$ (all in $10^{-5}/\gamma$ ) |  |  |
|---------|--|--|--|---|--|--|---|--|--|
|         | $\langle N_{\text{det}}^{\text{SSR5}} \rangle$ | $\langle N_{\text{det}}^{10^\times} \rangle$ | $\langle N_{\text{det}}^{20^\times} \rangle$ | $\langle N_{\text{det}}^{\text{SSR5}} \rangle$        | $\langle N_{\text{det}}^{10^\times} \rangle$ | $\langle N_{\text{det}}^{20^\times} \rangle$ | $\langle N_{\text{det}}^{\text{SSR5}} \rangle$        | $\langle N_{\text{det}}^{10^\times} \rangle$ | $\langle N_{\text{det}}^{20^\times} \rangle$ |
| Pac/Gam | 1.045  | 11.99  | 62.84  | 2.571   | 47.07  | 315.9  | 1.493   | 237.0  | 2770   |
| Pac/Pnl | 1.743  | 20.12  | 103.8  | 4.903   | 73.75  | 496.2  | 66.29   | 752.3  | 4788   |
| KaG/Gam | 1.105  | 12.15  | 62.79  | 3.366   | 50.07  | 323.8  | 9.870   | 372.8  | 3333   |
| KaG/Pnl | 1.839  | 19.82  | 102.6  | 4.679   | 74.47  | 483.4  | 6.678   | 432.7  | 4234   |
| Pac/GdB | 0.7132   | 4.270  | 9.180  | 1.071   | 20.28  | 86.95  | 1.219   | 30.51  | 161.0  |
| KaG/GdB | 0.7054   | 4.294  | 9.016  | 1.049   | 20.37  | 88.07  | 1.123   | 28.99  | 143.4  |

**Table 7.5:** Expected total number of detections ( $\langle N_{\text{det}} \rangle$ ) for different models for mean ellipticity, initial spatial distribution, gravitational potential, and search sensitivity. All models here use the *flat distribution of initial spin period*. The number of detections is obtained by multiplying with the gravitar fraction  $\gamma$  of newborn neutron stars. Cells in green are models with at least 0.5yr predicted detections.

| model   | $\bar{\epsilon} = 10^{-6}$ (per $\gamma$ )     |  |  | $\bar{\epsilon} = 10^{-7}$ (all in $10^{-2}/\gamma$ ) |  |  | $\bar{\epsilon} = 10^{-8}$ (all in $10^{-5}/\gamma$ ) |  |  |
|---------|--|--|--|---|--|--|---|--|--|
|         | $\langle N_{\text{det}}^{\text{SSR5}} \rangle$ | $\langle N_{\text{det}}^{10^\times} \rangle$ | $\langle N_{\text{det}}^{20^\times} \rangle$ | $\langle N_{\text{det}}^{\text{SSR5}} \rangle$        | $\langle N_{\text{det}}^{10^\times} \rangle$ | $\langle N_{\text{det}}^{20^\times} \rangle$ | $\langle N_{\text{det}}^{\text{SSR5}} \rangle$        | $\langle N_{\text{det}}^{10^\times} \rangle$ | $\langle N_{\text{det}}^{20^\times} \rangle$ |
| Pac/Gam | 0.6890   | 8.381  | 45.35  | 1.229   | 25.52  | 178.6  | 0.2015  | 84.98  | 1058   |
| Pac/Pnl | 1.143  | 14.01  | 74.68  | 2.656   | 39.33  | 274.1  | 27.79   | 371.6  | 2220   |
| KaG/Gam | 0.7328   | 8.523  | 45.23  | 1.742   | 26.98  | 183.5  | 2.520   | 147.6  | 1474   |
| KaG/Pnl | 1.219  | 13.83  | 73.76  | 2.206   | 38.44  | 265.9  | 1.226   | 170.6  | 1828   |
| Pac/GdB | 0.3052   | 1.093  | ...  | 0.1035  | 0.6544                                       | 1.538  | 0.01094   | 0.01705                                      | 0  |
| KaG/GdB | 0.3174   | 1.283  | ...  | 0.1235  | 0.8830                                       | 1.131  | 0.05009   | 0.02335                                      | 0  |

from Equation (7.12). Differences from choosing other combinations are small compared to varying the initial frequency distribution or the mean value of ellipticity.

For the plots Figure 7.4(a), Figure 7.5(a), and Figure 7.6(a) we assumed the lognormal initial frequency distribution. Under this assumption the relative detectability of the younger Gould belt population is high and the Gould belt is visible as a faint, broad band in the Figures with  $18^\circ$  inclination to the Galactic plane.

Increased sensitivity in Figure 7.5(a) exhibits a stronger contribution from the Galactic plane because sources at larger distances are more likely to be detected; still some contribution from the belt is visible.

For the more realistic  $\bar{\epsilon} = 10^{-7}$  in Figure 7.6(a) no clear structure in the sky is visible since only the closest almost uniformly distributed gravitars in the solar neighbourhood are detectable. The Gould belt contributes weakly to the structure and is visible as the band described above.

The plots in the bottom panels of the figures, i.e. Figure 7.4(b), Figure 7.5(b), and Figure 7.6(b), are the counterparts of the sky maps in the top column and assume in contrast the power-law initial frequency distribution. For all of them it is clear that the contribution of the younger Gould belt population is suppressed compared to the lognormal frequency distribution model. This lowers the total number of expected detected sources and evens out sky structure. Only for higher sensitivity and at high mean ellipticity the Galactic disk becomes visible as clear structure in Figure 7.5(b).

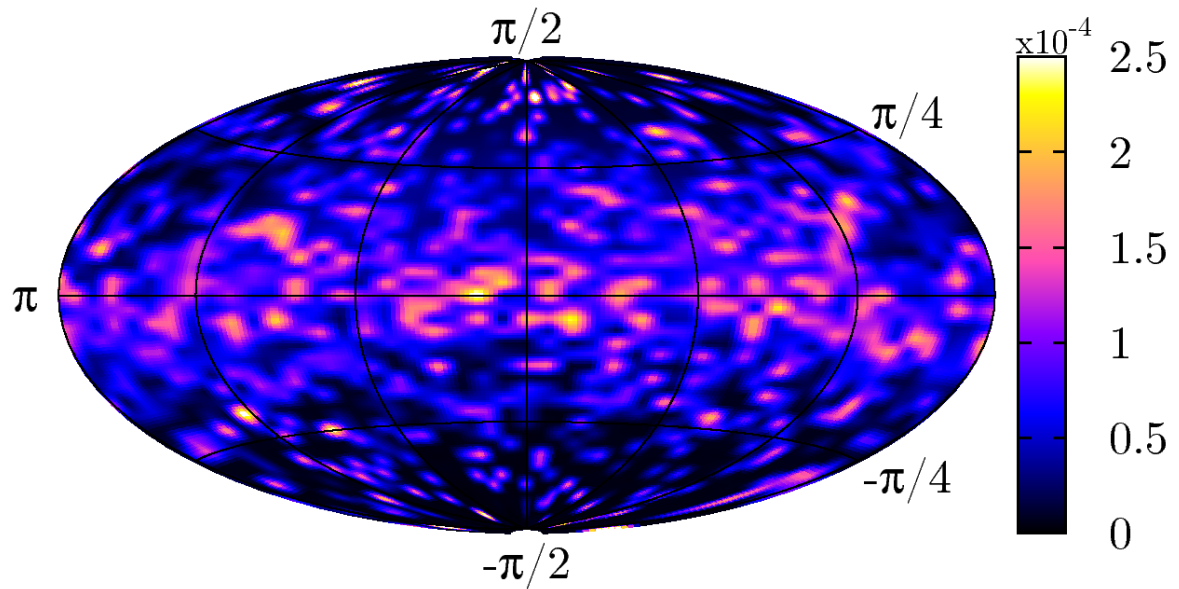
The disk population is less strongly affected by the change in the frequency model than the belt population. For the power-law distribution Figure 7.2 shows that for low ages there are no sources below  $f < 133.3 \bar{\text{Hz}}$ . This is the range of best detector sensitivity with the highest impact on detections. Thus much less younger sources will be detected. For the belt population older sources will have escaped solar neighbourhood by the time they are old (spun down) enough to be detected. For the disk population however, there will be sources at higher ages and closer distances which have spun down to lower frequencies near the optimum sensitivity of the detector. Thus, the power-law distributions dilutes effectively much faster for the sources born in the Gould belt.

### 7.3.3 Age distributions

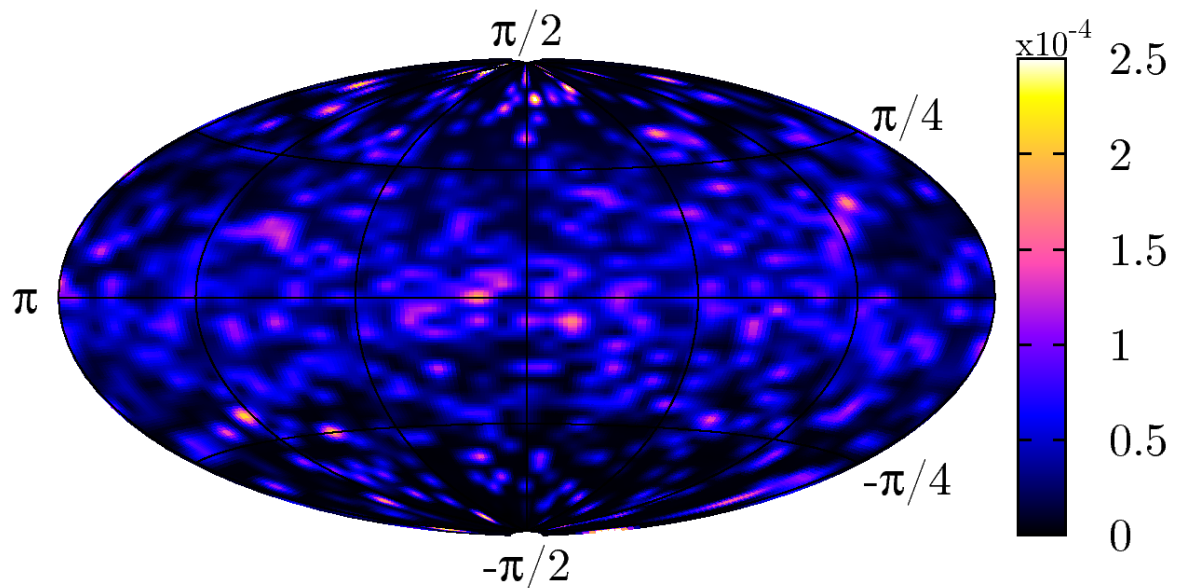
As outlined after Equation (7.42), the detectability for each simulated source can be used as the weight in a histogram of distance or age to obtain the distribution of detectable sources in these quantities. This distribution information is useful in two ways: a) for future search design, where it is conceivable to search only those parts of parameter space with the highest chance of detection for a given amount of computation, or b) in setting population constraints from existing null detection results.

A distribution of detectability as a function of the source age is shown in Figure 7.7. We adopted the most optimistic model (KaG/PnI and KaG/GdB, respectively for  $\bar{\epsilon} = 10^{-6}$ ) and the lognormal initial frequency distribution at different sensitivities. Green lines are for the disk population, orange lines are for the belt distribution. The assumed sensitivities are the projected S5R5 sensitivity (dotted lines), a hypothetical search with ten times the sensitivity of S5R1 50% (dashed lines), and a hypothetical search with twenty times the sensitivity of S5R1 50% (solid lines).

The inset in Figure 7.7 shows the cumulative distribution function (cdf) using the same line code as above, the horizontal axis is age in Myr, and the vertical axis is the value of the cdf. It is apparent that for all assumed sensitivities all detectable sources are younger than

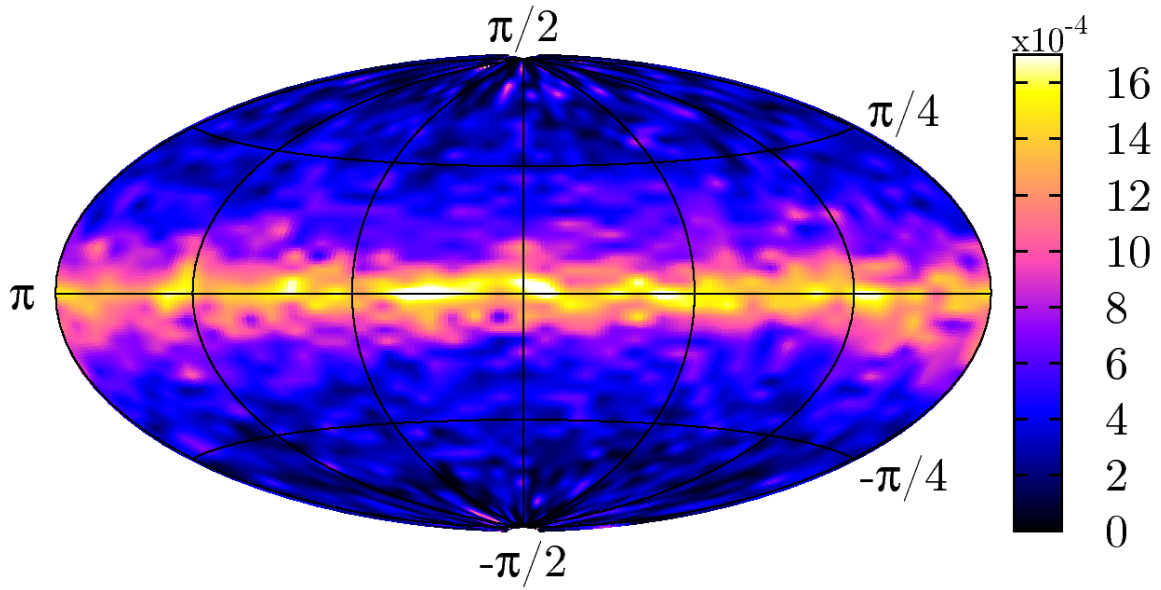


(a)  $\bar{\varepsilon} = 10^{-6}$ , lognormal initial frequency distribution, projected S5R5 sensitivity, KaG/PnI and KaG/GdB,  $\langle N_{\text{tot}} \rangle = 2.5444\gamma$

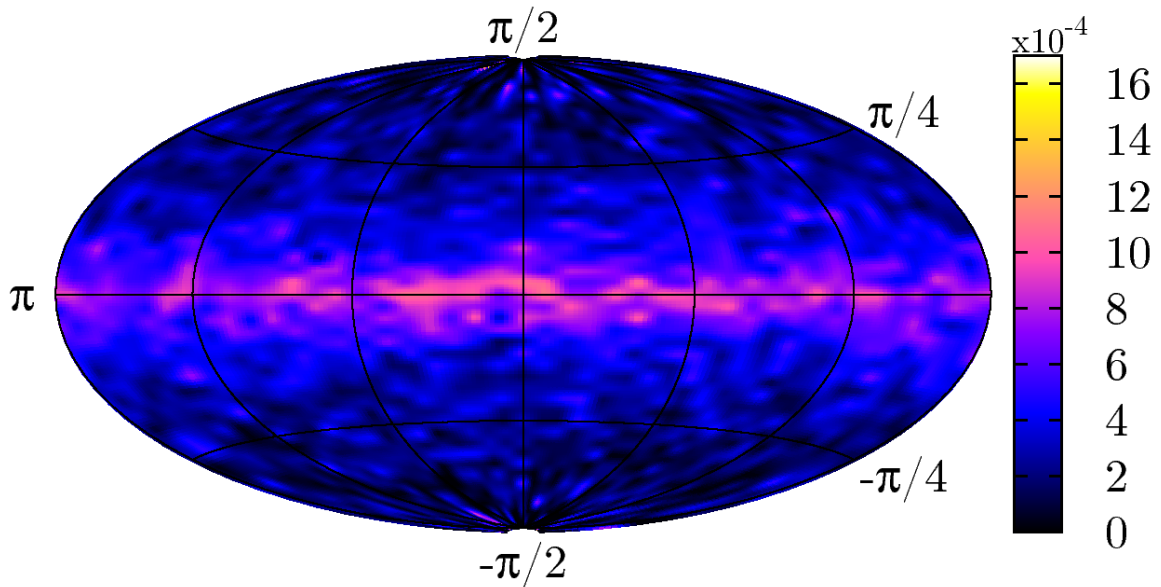


(b)  $\bar{\varepsilon} = 10^{-6}$ , power law initial frequency distribution, projected S5R5 sensitivity, KaG/PnI and KaG/GdB,  $\langle N_{\text{tot}} \rangle = 1.536\gamma$

**Figure 7.4:** Part I of the most optimistic sky density maps for different sensitivities and initial frequency distributions. The area shown is the complete celestial sphere in Galactic coordinates in a Hammer-Aitoff projection, Galactic center in the center, North is up. The colour code shows the detectability density of sources per square degree. Note the changing scale in the different plots.

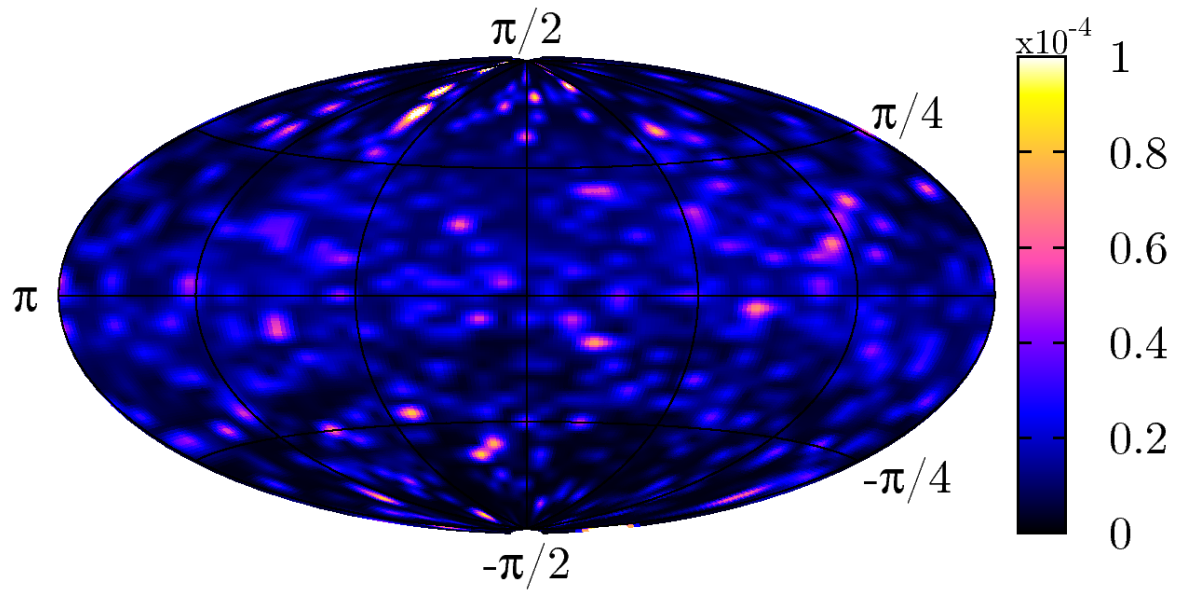


(a)  $\bar{\varepsilon} = 10^{-6}$ , lognormal initial frequency distribution,  $10\times$  S5R1 50% sensitivity, KaG/PnI and KaG/GdB,  $\langle N_{\text{tot}} \rangle = 24.11\gamma$

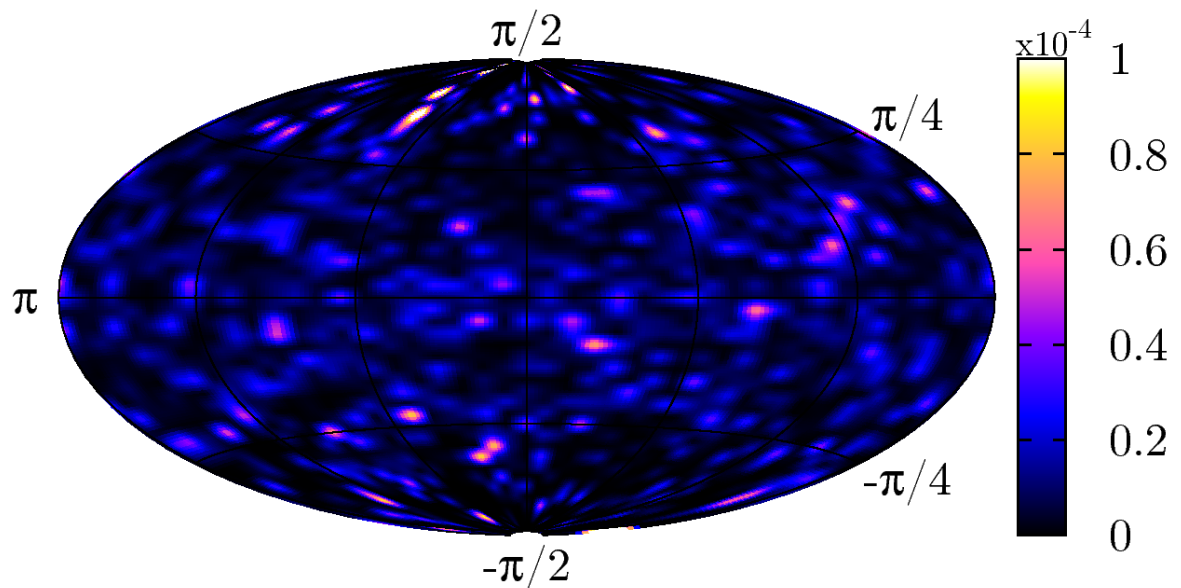


(b)  $\bar{\varepsilon} = 10^{-6}$ , power law initial frequency distribution,  $10\times$  S5R1 50% sensitivity, KaG/PnI and KaG/GdB,  $\langle N_{\text{tot}} \rangle = 15.11\gamma$

**Figure 7.5:** Part II of the most optimistic sky density maps for different sensitivities and initial frequency distributions. The area shown is the complete celestial sphere in Galactic coordinates in a Hammer-Aitoff projection, Galactic center in the center, North is up. The colour code shows the detectability density of sources per square degree. Note the changing scale in the different plots.



(a)  $\bar{\varepsilon} = 10^{-7}$ , lognormal initial frequency distribution,  $10\times$  S5R1 50% sensitivity, KaG/PnI and KaG/GdB,  $\langle N_{\text{tot}} \rangle = 0.9484\gamma$



(b)  $\bar{\varepsilon} = 10^{-7}$ , power law initial frequency distribution,  $10\times$  S5R1 50% sensitivity, KaG/PnI and KaG/GdB,  $\langle N_{\text{tot}} \rangle = 0.3932\gamma$

**Figure 7.6:** Part III of the most optimistic sky density maps for different sensitivities and initial frequency distributions. The area shown is the complete celestial sphere in Galactic coordinates in a Hammer-Aitoff projection, Galactic center in the center, North is up. The colour code shows the detectability density of sources per square degree. Note the changing scale in the different plots.

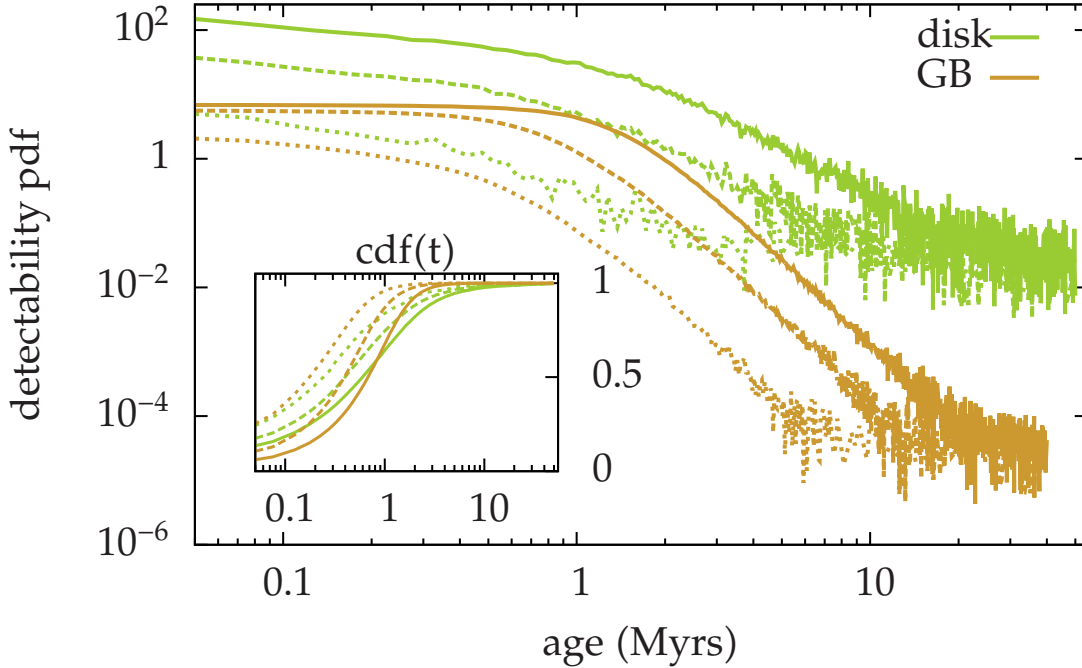


**Figure 7.7:** The probability distribution of the detectability as a function of the source age in a double logarithmic plot. Green curves are for sources from the Galactic disk, orange curves for sources from the Gould belt. All curves assume the most optimistic model (KaG/PnI and KaG/GdB, respectively for  $\bar{\varepsilon} = 10^{-6}$ ) and the lognormal initial frequency distribution from Table 7.4. The assumed sensitivities are the projected S5R5 sensitivity (dotted lines), a hypothetical search with ten times the sensitivity of S5R1 50% (dashed lines), and a hypothetical search with twenty times the sensitivity of S5R1 50% (solid lines). The inset shows the cumulative probability distribution. Almost all detectable sources (>99%) are younger than a few Myrs.

$\lesssim 10$  Myr. Closer inspection of the data shows that more than 99% of the detectable sources are younger than 50 Myr, even at the highest assumed search sensitivity. This justifies our choice to simulate sources only up to an age of 500 Myrs instead of the age of the Galaxy.

For both the disk and the belt population younger sources (i.e.  $t \lesssim 5$  Myr) are the most likely to be detected. The detectability for sources from the Galactic disk is always larger than for sources from the Gould belt. For the disk, the detectability distribution falls off monotonously as a function of the age, while the detectability pdf for Gould belt sources is constant at low ages. The latter is because *all* younger belt sources are at least partially detectable, i.e. the  $P_i^{\text{det}} > 0$  for almost *all* sources; virtually *all* Gould belt sources can be detected at a subset of all possible values of  $\varepsilon$  and initial frequency  $f_0$ . Increasing the sensitivity increases the detectability value for each source of this age but similarly for sources with similar ages. Therefore, the curves are flat in  $t$  and overall detectability increases with sensitivity (the curves for higher sensitivity lie above curves of lower sensitivity). Further, increasing the sensitivity does not render more young sources from the Gould belt detectable for the highest sensitivities: the overall detectability saturates; the detectability pdfs for ten times and twenty times S5R1 50% sensitivity almost agree at ages  $< 0.5$  Myr.

These statements do not hold for the simulated Galactic disk population. There, distribution curves for all sensitivities are falling monotonously as a function of the age. Younger

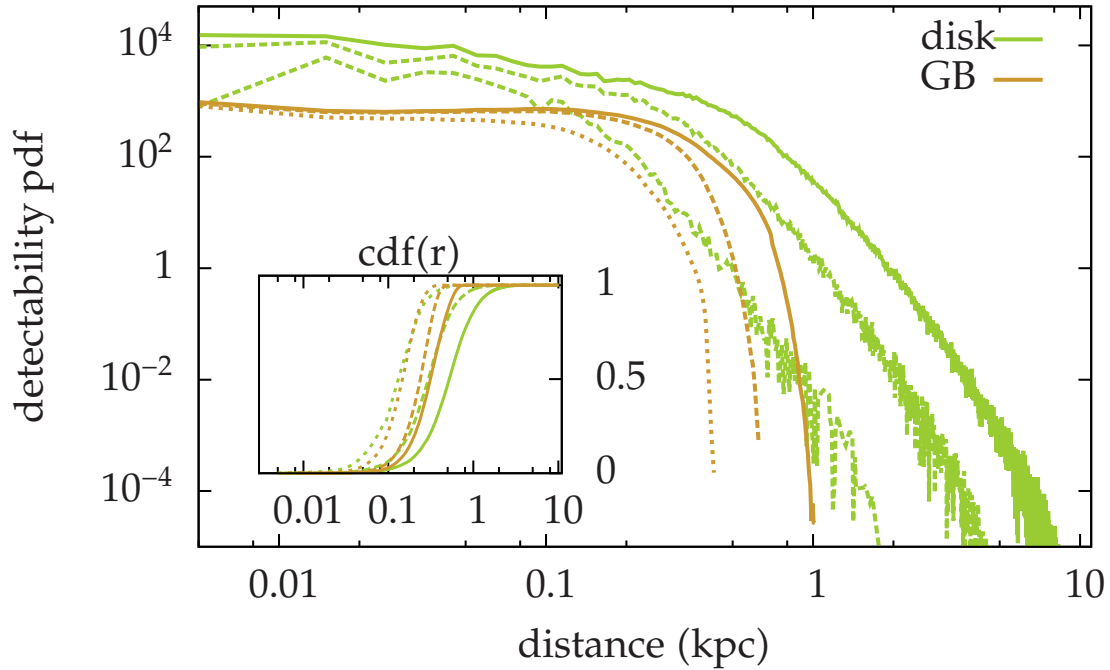


**Figure 7.8:** The probability distribution of the detectability as a function of the source distance to the Sun in a double logarithmic plot. Green curves are for sources from the Galactic disk, orange curves for sources from the Gould belt. All curves assume the most optimistic model KaG/PnI and KaG/GdB, respectively for  $\bar{\epsilon} = 10^{-6}$  and the lognormal initial frequency distribution from Table 7.4. The assumed sensitivities are the projected S5R5 sensitivity (dotted lines), a hypothetical search with ten times the sensitivity of S5R1 50% (dashed lines), and a hypothetical search with twenty times the sensitivity of S5R1 50% (solid lines). The inset shows the cumulative probability distribution. For sources from the Gould belt no sources beyond 1 kpc are detectable, while for the disk, sources up to a distance of up to few kpc are detectable.

sources are always more likely to be detected, independent of search sensitivity. Increasing the sensitivity increases the overall number of detections and for the sensitivities simulated here, no saturation in the overall detectability is visible.

### 7.3.4 Distance distributions

Figure 7.8 shows the corresponding distribution of detectability as a function of the radial distance to the detector for the most optimistic model (KaG/PnI and KaG/GdB, respectively for  $\bar{\epsilon} = 10^{-6}$ ) and the lognormal initial frequency distribution with different sensitivities. The graphs are corrected for the increase in infinitesimal spherical shell volume  $dV = r^2 dr$  with distance  $r$ . Again, green curves show results from disk population simulations, orange curves for the population from the Gould belt; the assumed sensitivities are the projected S5R5 sensitivity (dotted lines), a hypothetical search with ten times the sensitivity of S5R1 50% (dashed lines), and a hypothetical search with twenty times the sensitivity of S5R1 50% (solid lines).

The inset shows the cumulative probability distribution on a logarithmic distance scale. Almost all detectable Galactic disk sources are closer than a few kpc for any sensitivity, all detectable sources from the Gould belt are closer than  $< 0.8$  kpc for any sensitivity.

The increase in distance reach with increasing sensitivity is visible for both the sources from the Gould belt and from the Galactic disk: detectability stays at a higher level for larger distances with increasing simulated search sensitivity.

For sources from the Gould belt, the detectability pdf drops off rapidly at a sensitivity-dependent maximum distance. As we have seen above, mainly young sources are detectable from the belt, thus the limited spatial volume of the belt is a limiting factor to the distance reach. The maximum distance increases with sensitivity since a) older sources can be detected and b) the Gould belt “inflates” from the motion from supernova kicks. Again, similarly as for the age distribution above, the distribution in distance at low exhibits a “saturation effect” at low distances: the pdf curves are almost flat, increasing sensitivity shifts them up to higher probability values. Thus, almost *all* sources at low distances are detectable for the Gould belt. At distances of order 0.1 kpc this behaviour breaks down.

For Galactic disk sources we see a similar saturation at low distances: increasing the sensitivity only marginally increases the overall number of detections and the pdfs are flat for distances up to  $\sim 0.1$  kpc. The drop in detectability at higher distances is not as sharp as for the sources from the Gould belt; the larger Galactic disk population still contains sources at even larger distances, although their respective detectabilities are much lower.

### 7.3.5 Frequency distributions

Figure 7.9 shows the distribution of detectability in frequency for the KaG/PnI and KaG/GdB model, respectively, assuming a mean ellipticity of  $\bar{\epsilon} = 10^{-6}$  and the lognormal initial frequency distribution. Green curves are for sources from the Galactic disk and orange curves for sources from the Gould belt. The sensitivities are indicated by the structure of the curves: the projected S5R5 sensitivity (dotted lines), a hypothetical search with ten times the sensitivity of S5R1 50% (dashed lines), and a hypothetical search with twenty times the sensitivity of S5R1 50% (solid lines). The Figure shows the distributions in the left panel in a double-logarithmic plot and the same distributions with linear axes in the right panel. The logarithmic plot allows an easy overview over the complete set of distributions, while the linear plot emphasises how narrow the distribution in frequency is.

From a comparison of the detectability pdfs for different sensitivities it is clear that increasing the sensitivity mainly shifts the pdfs up but does not alter its shape much. Again, for belt sources an indication of a saturation effect at high sensitivities can be seen.

The shape of the pdfs for sources from the Gould belt and from the Galactic disk are slightly different, which is related to the different age structures and spatial distributions of the two populations. The peaks of the Galactic source pdfs are at slightly lower frequencies than those of the belt sources.

For all sensitivities the distribution in frequency is narrowly peaked around the frequency of highest sensitivity of the detector at around 150 Hz. As we have seen in discussion of Figure 7.7, the detectable sources are mostly younger than  $\sim 1$  Myr; this implies for to the evolved frequency distributions from the upper left panel of Figure 7.2 that the highest number of sources is also expected in the frequency band of highest sensitivity. Thus, the distribution of detectable sources is expected to be show the sharp, observed peak.

From these considerations of detectability alone, it is clear that searching for gravitars at very high frequency bands is much more unlikely to yield detections than searching at frequencies in the range from 200 Hz to 300 Hz. An additional difficulty is the scaling of the computational costs with the frequency, which usually grows with a high power of the frequency; thus, searching the high frequency bands is not only less likely to yield detections

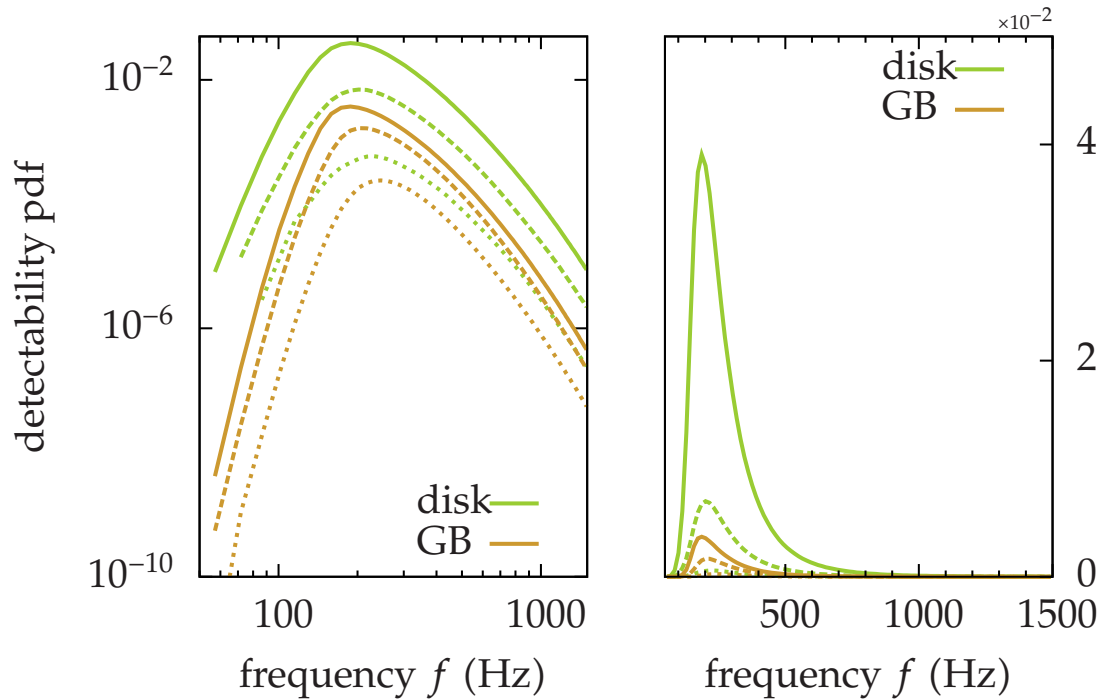


**Figure 7.9:** The distribution of detectable sources in frequency for the most optimistic disk and belt models (KaG/PnI and KaG/GdB, respectively) at  $\bar{\varepsilon} = 10^{-6}$  and the lognormal initial frequency distribution. Orange lines are the Gould belt models, green lines are Galactic disk models. Assumed sensitivities are the projected S5R5 sensitivity (dotted lines), a hypothetical search with ten times the sensitivity of S5R1 50% (dashed lines), and a hypothetical search with twenty times the sensitivity of S5R1 50% (solid lines).

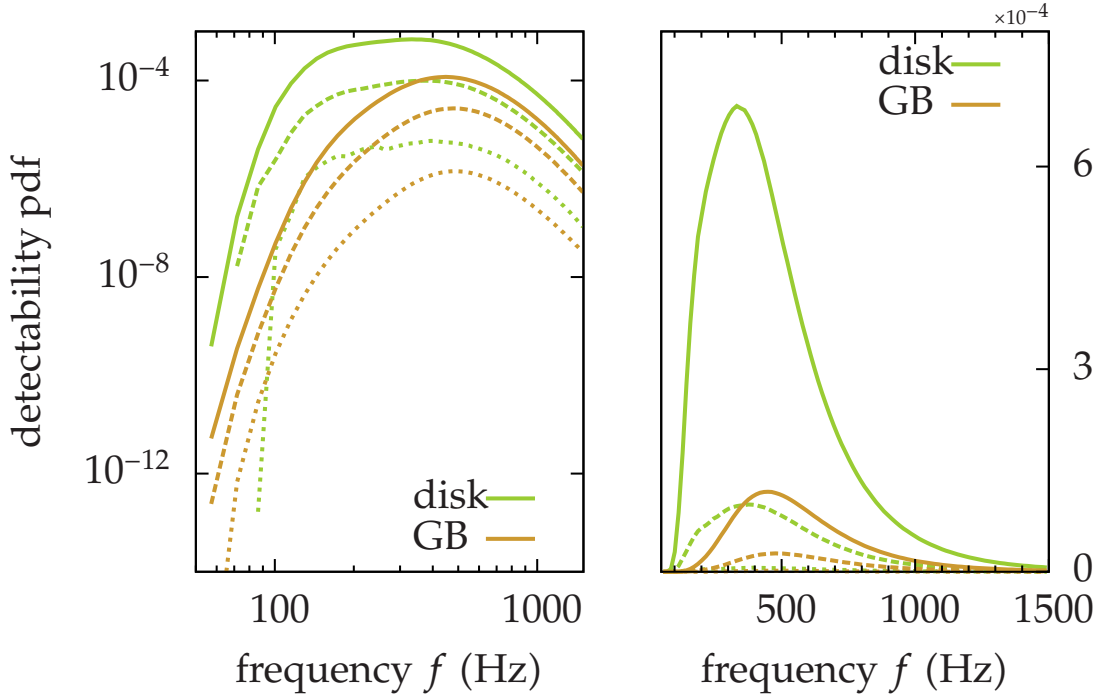
it is also much more expensive to do so. In Section 7.4 we examine in a general way how search strategies can be optimised taking into account prior knowledge from simulations and estimates of the computational costs.

Figure 7.10 is the analog of Figure 7.9 for lower ellipticities. It shows the distribution of detectability in frequency for the KaG/PnI and KaG/GdB model, respectively, assuming a mean ellipticity of  $\bar{\varepsilon} = 10^{-7}$  and the lognormal initial frequency distribution. Green curves are for sources from the Galactic disk and orange curves for sources from the Gould belt. The sensitivities are indicated by the structure of the curves as in Figure 7.9. The Figure shows the distributions in the left panel in a double-logarithmic plot and the same distributions with linear axes in the right panel.

The main difference to the results for  $\bar{\varepsilon} = 10^{-6}$  is the much lower total detectability for  $\bar{\varepsilon} = 10^{-7}$  as we have already seen from Tables 7.4 and 7.5. The peak of the detectability pdfs is about two orders of magnitude lower. Further, the distributions are not quite as narrowly peaked as the ones in Figure 7.9, although the bulk of detectable sources still resides between 100 Hz and 800 Hz or in a smaller range.

The comparison of the pdfs for different sensitivities reveals again only minor changes in shape and the shift to higher values with increasing sensitivities. The saturation effect in the distributions for sources from the Gould belt is less pronounced here.

The difference between the two distributions families for the Galactic disk and the Gould belt sources, respectively, is much more obvious here. The peak for disk sources is broader



**Figure 7.10:** The distribution of detectable sources in frequency for the most optimistic disk and belt models (Kag/PnI and KaG/GdB, respectively) at  $\bar{\epsilon} = 10^{-7}$  and the lognormal initial frequency distribution. Orange lines are the Gould belt models, green lines are Galactic disk models. Assumed sensitivities are the projected S5R5 sensitivity (dotted lines), a hypothetical search with ten times the sensitivity of S5R1 50% (dashed lines), and a hypothetical search with twenty times the sensitivity of S5R1 50% (solid lines).

and at lower frequencies than the peak for belt sources. For  $\bar{\epsilon} = 10^{-7}$  the observed frequency distribution does not change much even over 10 Myr, compare upper right panel in Figure 7.2. For the Gould belt, older sources that have spun down to lower frequencies will not be detectable because they will be too far away from the detector at that time. In the Galactic disk however, older sources will orbit and some of them will be in distances where they can be detected, contributing at lower spin frequencies as observed in Figure 7.10.

Another visible difference in comparison to Figure 7.9 is the alteration of relative contributions between the Gould belt and the Galactic disk population. At the higher ellipticities, the Galactic disk clearly dominates at all sensitivities. At the lower ellipticities, the contributions from the belt reach a similar level as those from the disk, on the other hand, the overall level is much lower.

## 7.4 Optimisation of the search strategy

The search for continuous gravitational-wave signals from unknown gravitars is computationally limited. The whole planet's computational resources do not suffice to perform an optimal search. Various sub-optimal methods have been developed to search a large fraction of parameter space with limited computing resources, see e.g. Abbott et al. (2008a, 2009); Pletsch and Allen (2009). Population synthesis, however, has so far not been considered as input for search optimisation.

In this section we describe how to use limited computational resources in an optimised way guided by models of the source population. We will show that the optimal search strategy is to search the parts of parameters space where the ratio of the density of detectable sources to the search cost density exceeds a certain threshold. In other words: the computational resources should be spent in the most cost-efficient way.

We then provide the reader with a simple toy model to illustrate the general principle before applying a simplified one-dimensional version of the optimisation procedure to broadband searches for continuous gravitational waves. We show that with the restriction of optimisation to the frequency dimension alone, the same expected number of simulated sources is detectable when using only a minor fraction of the computing costs.

### 7.4.1 General description

Let us begin by considering the most general description. Assume the parameter space  $\mathcal{P}$  of a search for gravitars consists of  $n$  parameters:  $\vec{x} = (x_1, x_2, \dots, x_n)$ . Further, assume the distribution of detectable sources in this parameter space is known and can be described by  $\rho_{\text{det}}$ , such that

$$dN_{\text{det}} = \rho_{\text{det}}(\vec{x}) dV \quad (7.44)$$

is the number of detectable sources in the small volume  $dV = dx_1 dx_2 \dots dx_n$ . Assume further that the computational costs of a given search can be described by a *cost function*  $c_{\text{search}}$ , such that

$$dC = c_{\text{search}}(\vec{x}) dV \quad (7.45)$$

is the amount of computational costs (e.g. CPU cycles) that has to be spent to perform the search on the small volume  $dV$ . Let us consider a sub-volume  $\mathcal{U} \subseteq \mathcal{P}$ . The number of detectable sources in  $\mathcal{U}$  and the computational costs to search this volume are given by

$$N_{\text{det}}[\mathcal{U}] = \int_{\mathcal{U}} dV \rho_{\text{det}}(\vec{x}) \quad (7.46)$$

and

$$C_{\text{search}}[\mathcal{U}] = \int_{\mathcal{U}} dV c_{\text{search}}(\vec{x}), \quad (7.47)$$

respectively. A search is called *optimal* if the number of detections  $N_{\text{det}}[\mathcal{U}]$  is maximal at fixed computing costs  $C_0 = C_{\text{search}}[\mathcal{U}]$  for a volume  $\mathcal{U}$ . We will now show how this optimality can be achieved by choosing the parts of the parameter space with the highest cost-efficiency.

### 7.4.2 Optimising cost-efficiency

Let us denote the fixed computing costs by  $C_0$ . The task is now to find  $\mathcal{U}$  such that  $N_{\text{det}}[\mathcal{U}]$  is the maximum achievable value for all  $\mathcal{U} \subseteq \mathcal{P}$  under the constraint  $C_{\text{search}}[\mathcal{U}] = C_0$ .

Applying the method of Lagrange multipliers we define the new function

$$F[\lambda, \mathcal{U}] := N_{\text{det}}[\mathcal{U}] - \lambda C_{\text{search}}[\mathcal{U}], \quad (7.48)$$

where  $\lambda$  is the Lagrange multiplier. Rewriting the previous equation we find that the expression to maximise is

$$F[\lambda, \mathcal{U}] = \int_{\mathcal{U}} dV (\rho_{\text{det}}(\vec{x}) - \lambda c_{\text{search}}(\vec{x})). \quad (7.49)$$

For any  $\lambda$  there is a parameter space volume  $\mathcal{U}_\lambda$  that maximises  $F$  for this value of  $\lambda$ . For  $\lambda < 0$  there is no non-trivial solution to this problem, because the integrand is positive everywhere in  $\mathcal{U}$ . In this case, the only extremum is the trivial one:  $\mathcal{U} = \mathcal{D}$ , or the search over the complete space. For  $\lambda > 0$  there are non-trivial solutions:  $F$  is maximised if  $\mathcal{U}$  is chosen such that the integrand is positive everywhere in  $\mathcal{U}$ . In other words: for a given  $\lambda > 0$ , the parameter space volume  $\mathcal{U}_\lambda$  that maximises  $F[\lambda, \mathcal{U}]$  is:

$$\mathcal{U}_\lambda = \left\{ \vec{x} \in \mathcal{D} \left| \frac{\rho_{\text{det}}(\vec{x})}{c_{\text{search}}(\vec{x})} > \lambda > 0 \right. \right\}. \quad (7.50)$$

This result is readily understood because  $\frac{\rho_{\text{det}}(\vec{x}) dV}{c_{\text{search}}(\vec{x}) dV}$ , the ratio between the possible number of detections in a volume and the cost density for searching that volume, can be read as a *cost-efficiency density*. It determines how much pay-off is granted in relation to the amount that has to be invested. Thresholding on this quantity is therefore readily understood.

The value of  $\lambda$  that belongs to our choice of fixed computing costs  $C_0$  follows from

$$C_0 = C_{\text{search}}[\mathcal{U}_\lambda]. \quad (7.51)$$

So, for any value of  $\lambda$ , use Equation (7.49) to find the  $\mathcal{U}_\lambda$ , that maximises  $F$ . Then, calculate the corresponding computing cost from Equation (7.47). Iterate until they match the fixed costs  $C_0$ .

Let us note that in general,  $\mathcal{U}_\lambda$  does not have to be a single closed domain but can also consist of multiple disjunct domains. Depending on the exact distribution and cost function the cost-efficiency ratio can cross the threshold in separated parts of the parameter space. In practice, the complete parameter space usually is split into smaller partitions anyway, so that the existence of separated domains to search would not complicate the set-up of an optimised search.

Before we illustrate the optimisation procedure in an analytical example, let us remark a different way of understanding these results.

#### A different interpretation – inexpensive semi-blind searches

In general, the value of  $\lambda$  parametrizes a curve in the space of  $N_{\text{det}}$  and  $C_{\text{search}}$  via the (optimal) search volume  $\mathcal{U}_\lambda$  defined by Equation (7.50). Finding the point on the curve (for given  $c_{\text{search}}$  and  $\rho_{\text{det}}$ ) at which the search computational costs agree with the pre-defined value  $C_{\text{search}} = C_0$  is the method described above: it yields the parameter space volume to search which yields the highest chance of detections for the pre-defined costs.

Another way to look at this curve is as savings that can be achieved for an already existing search. Or in other words: assume, we would like to conduct a search with known  $c_{\text{search}}$  and simulated  $\rho_{\text{det}}$ . If the total computational costs are too large to run this search in an acceptable amount of time, where in the parameter space do we have to cut “corners”? Which volume of search parameter space has to be chosen to detect the largest fraction of sources from the simulated population with the assumed search method on a reduced parameter space volume? This way we can design a possibly *inexpensive semi-blind search*, where “inexpensive” stands for low computational costs, and “semi-blind” means that the search is targeted to general regions of the parameter space but not to a single source or sky point as in targeted searches.

Consider a given search over a parameter space  $\mathcal{D}$  with total computational costs  $C_{\text{tot}} = C_{\text{search}}[\mathcal{D}]$  and a total of  $N_{\text{tot}} = N_{\text{det}}[\mathcal{D}]$  simulated detections. For the given search cost

density  $c_{\text{search}}$  and the number density of detectable sources  $\rho_{\text{det}}$ , Equation (7.50) again defines a curve, parametrized by  $\lambda$ . Each  $\mathcal{U}_\lambda$  is a subspace of  $\mathcal{D}$ . We can now interpret the curve of  $C_{\text{search}}[\mathcal{U}_\lambda]$  and  $N_{\text{det}}[\mathcal{U}_\lambda]$  as a smaller version of the full search, each optimised to obtain the maximum number of detections for the reduced computational costs. This interpretation of the results allows one to design a search that achieves almost the design goal at lower computational costs by discarding parts of the parameter space that are unlikely to yield detections.

If the time to the first detection in a search for gravitars is important, the method outlined here provides a guide to minimise the time to a detection. The prioritisation of frequency bands in future blind searches for continuous gravitational waves can be obtained from the results presented here. If one chooses to search a wide frequency range, it is split into many narrow frequency bands in typical searches (Abbott et al., 2009). Using the results from the reduction to an inexpensive semi-targeted search as outlined here, one could search the most cost-efficient frequency bands first, and then proceed to the less cost-efficient ones. Thus, this method can reduce the time to the first detection. In Section 7.4.4 we apply this method to a model of the Einstein@Home S5R5 blind all-sky search for continuous gravitational waves and provide a prioritisation scheme of frequency bands.

### 7.4.3 Analytical toy model

Let us consider a simple one-dimensional example as a toy-model to illustrate the optimisation process. The distribution function chosen here are not meant to be motivated by reality but are rather chosen in such a way that the full problem is analytically solvable. Let the parameter space consist only of the frequency  $f \in \mathbb{R}^+$ , a sub-volume  $\mathcal{U}$  in the parameter space will be an interval  $[f_1, f_2]$ . We assume a distribution of detectable sources

$$\rho_f(f) = \begin{cases} -\alpha(f - \underline{f})(f - \bar{f}) & \text{if } \underline{f} < f < \bar{f} \\ 0 & \text{else} \end{cases}, \quad (7.52)$$

with  $\underline{f} < \bar{f}$  and a cost function

$$c(f) = \beta f^2. \quad (7.53)$$

The total number of detections when searching  $\mathcal{U} = [f_1, f_2]$  is

$$N[\mathcal{U}] = \alpha \left( \frac{f_1^3 - f_2^3}{3} + \frac{\underline{f} + \bar{f}}{2} (f_2^2 - f_1^2) + \underline{f}\bar{f} (f_1 - f_2) \right) \quad (7.54)$$

and the costs for searching the same  $\mathcal{U}$  are

$$C[\mathcal{U}] = \beta (f_2^3 - f_1^3). \quad (7.55)$$

We then find  $f_-(\lambda)$  and  $f_+(\lambda)$  as the solutions of the equation

$$\rho_f(f) - \lambda c(f) = 0 \quad (7.56)$$

and obtain

$$f_\pm(\lambda) = \frac{1}{2} \left( \frac{\underline{f} - \bar{f}}{1 + \frac{\alpha}{\beta}\lambda} \pm \sqrt{\left( \frac{\underline{f} - \bar{f}}{1 + \frac{\alpha}{\beta}\lambda} \right)^2 - \frac{4\underline{f}\bar{f}}{1 + \frac{\alpha}{\beta}\lambda}} \right). \quad (7.57)$$

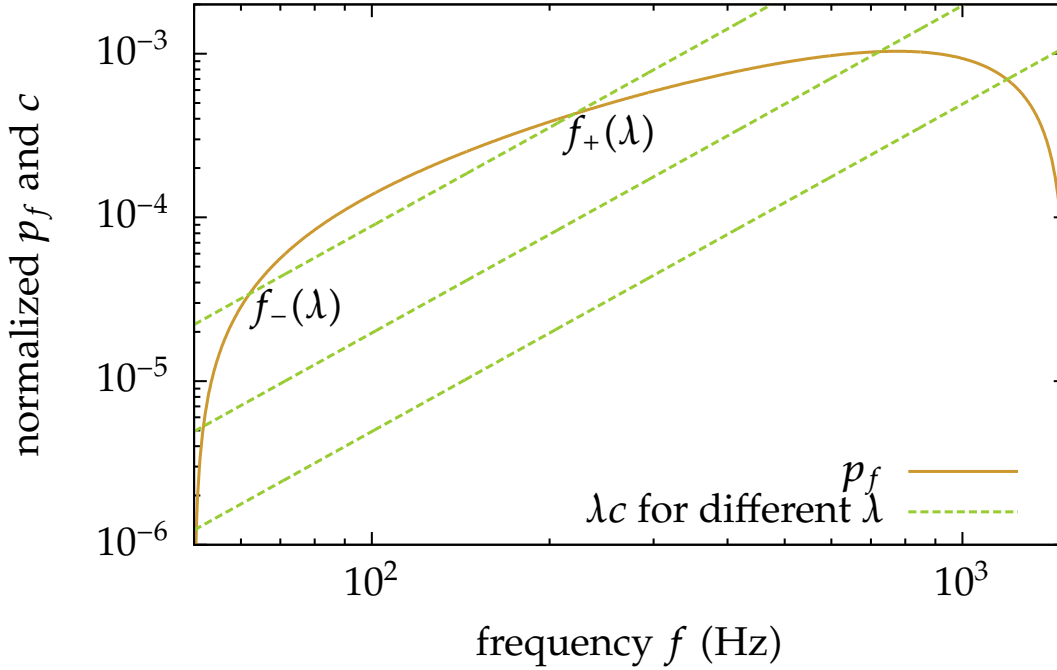


**Figure 7.11:** The distribution function  $p_f(f)$  (curve) and the cost function  $c(f)$  scaled with different values of  $\lambda$  (straight lines) for our toy model. Finding the intersections of the distribution function with the scaled cost function is equivalent to solving Equation (7.56). Here  $f_- = 50$  Hz and  $f_+ = 1.5$  kHz.

Figure 7.11 shows the distribution function and the cost function scaled with different  $\lambda$  and the corresponding values frequency interval  $[f_-(\lambda), f_+(\lambda)]$ .

So, for a given  $\lambda$ , the volume to search would be  $\mathcal{U}_\lambda = [f_-(\lambda), f_+(\lambda)]$ . Plugging the results from Equation (7.57) into Equation (7.54) and Equation (7.55) allows us to obtain  $N[\mathcal{U}_\lambda]$  and  $C[\mathcal{U}_\lambda]$  and to plot them against each other. The result is shown in Figure 7.12, where we plotted the fraction of computing costs versus the fraction of detections.

Interpreted in terms of the principle outlined for the inexpensive semi-targeted searches above, the following applies: if the graph stays at high values of fractional detections for small values of fractional costs, a large potential for saving computation by trimming the search space exists. We can read off that in this simple toy model using only 25 % of the computational resources would be enough to detect 70 % of the sources that would have been detectable with the full search. This is what the concept of a *inexpensive semi-targeted search* conveys: we can lower the search costs to only a quarter of the initially intended search costs by cutting down the parameter space to a subspace of the full space and still recover most (70%) of the detectable sources.

#### 7.4.4 Example application to the simulated gravitar population

In the previous sections we have shown in general and by an analytical toy model how a) a search can be designed that is optimal in the way that it has the highest chance of detection with a fixed amount of computational resources or b) how a constructed search can be conducted in an inexpensive semi-targeted way, which detects a large fraction of all

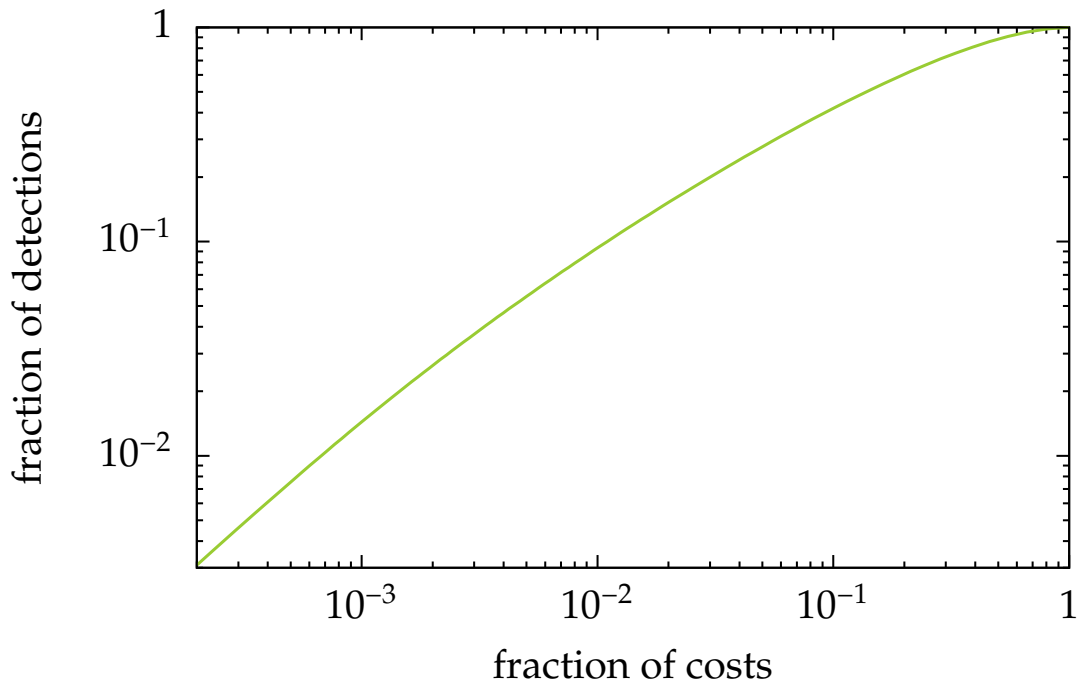


**Figure 7.12:** The fractional number of detections plotted versus the fractional search costs for our toymodel. The point on the graph on the upper right corresponds to conducting the full search. We can read off that using roughly 25 % of the computing costs would have resulted in detecting 70 % of all sources.

sources at drastically reduced computational costs.

Now, we apply the idea of the inexpensive semi-targeted search to the Einstein@Home S5R5 all-sky search. If we wanted to modify this search to be a search for the simulated gravitar populations (see Section 7.3), how much computational costs could be saved if a large fraction (say >99%, or >95%) of all simulated sources still would need to be detectable? As we have shown in Section 7.3, the distribution in frequency is fairly narrowly peaked and almost all sources are concentrated in a rather small frequency band, compared to the full search frequency range; thus, reducing the the frequency range searched is a straightforward way of retaining detectability of most sources while reducing at the same time the computational costs. We now describe the cost function and the density of detectable sources as functions of frequency.

The cost function for this search as a function of frequency then is, see Abbott et al. (2009)

$$c_{\text{E@H}}(f) = \tau_{\text{E@H}} f^3, \quad (7.58)$$

with a normalisation constant  $\tau_{\text{E@H}}$ , which is given from

$$C_{\text{E@H}} \stackrel{!}{=} \int_{\mathcal{V}} dV c_{\text{E@H}}(f) = \int_{50\text{Hz}}^{1.5\text{kHz}} df \tau_{\text{E@H}} f^3, \quad (7.59)$$

where  $\mathcal{V} = [50\text{Hz}, 1.5\text{kHz}]$  is the frequency range of the complete search, which has total computational costs of  $C_{\text{E@H}}$ . The previous equation is our cost model for this search, which simplifies the full search procedure, see e.g. Abbott et al. (2009); Abbott et al. (2009) for

earlier Einstein@Home searches using a similar setup. For the generation of figures of merit, this simplification is justified.

The density of detectable sources is given by the distribution in frequency as shown in the plots in Figures 7.9 and 7.10. For the simulated S5R5 search on gravitar populations these results are constructed as pdfs from tabulated function values and linear interpolation. We thus can construct a source density function  $\rho_{\text{det}}(f)$ , such that  $\rho_{\text{det}}(f) df$  is the number of detectable sources with projected S5R5 sensitivity in the frequency band  $[f, f + df]$ .

Using the two functions  $c_{\text{E@H}}(f)$  and  $\rho_{\text{det}}(f)$  we can now follow the optimisation procedure outlined in Section 7.4 to explore how this simulated S5R5 could be modified into an inexpensive semi-targeted search for gravitars. We solve the equation in the frequency range  $\mathcal{U} = [50 \text{ Hz}, 1.5 \text{ kHz}]$

$$\rho_{\text{det}}(f) - \lambda c_{\text{E@H}}(f) = 0 \quad (7.60)$$

for a given value of  $\lambda$ . The solutions of this equation define the frequency band  $\mathcal{U}_\lambda = [f_{-\lambda}, \bar{f}_\lambda]$  in which the cost-efficiency density exceeds  $\lambda$ . Because of the shape of the cost function and the source density function, here we always have a single frequency band as solution, i.e. the above equation always only has two zeros. For the obtained frequency band  $\mathcal{U}_\lambda$  we compute the number of detectable sources  $N_{\text{det}}[\mathcal{U}_\lambda]$  inside this band by Equation (7.46) and the computational costs  $C_{\text{search}}[\mathcal{U}_\lambda]$  for searching this band by Equation (7.47). We then vary the value of  $\lambda$  over a wide enough range to parametrize a curve in the coordinates  $C_{\text{search}}[\mathcal{U}_\lambda]$  and  $N_{\text{det}}[\mathcal{U}_\lambda]$ . Finally, we normalize the costs by the total costs for the complete search  $C_{\text{E@H}}$  and the number of detections by the number of possible detections in the complete search  $N_{\text{E@H}}$

We repeat this procedure for the complete range of six population models for Galactic disk and Gould belt sources assuming  $\bar{\epsilon} = 10^{-6}$  and both initial frequency distributions. In total this yields twelve curves of  $N_{\text{det}}[\mathcal{U}_\lambda]$  as a function of  $C_{\text{search}}[\mathcal{U}_\lambda]$ .

The results for both initial frequency distributions are shown in Figure 7.13. The top panel shows the results for the lognormal initial frequency distribution, the bottom panel the results for the power-law initial frequency distribution. In both panels, green curves indicate the results for the Galactic disk population and orange curves indicate results for the Gould belt population. Grey dashed lines indicate 90%, 95%, and 99% of the detections in the full search. The horizontal axis shows the search costs as a fraction of the full S5R5 search costs on a logarithmic scale. The vertical axis shows the number of detections as a fraction of the total number of expected detections for the full S5R5 search on a linear scale.

The differences between different spatial models are very small for the Galactic disk and the Gould belt populations: in both panels of Figure 7.13 the green and the orange curves, respectively, lie very close together. Even between the Galactic disk and the Gould belt population results there are only minor differences. In the range of large fractional detection numbers, i.e. where  $N_{\text{det}}[\mathcal{U}_\lambda] / N_{\text{E@H}} > 0.9$ , all model curves in each panel are virtually identical.

From the results in both panels of Figure 7.13 it is clear that only a minor fraction of the computing costs is necessary to conduct an inexpensive semi-targeted search for gravitars with virtually no loss of sensitivity to gravitars compared to the complete Einstein@Home S5R5 run. For the lognormal initial frequency distribution, 99% of the simulated gravitars are detectable using only 10% of the S5R5 computational costs, and for the power-law initial frequency distribution, only 4% of the computational costs are necessary. For 95% of the detections, these numbers are 2% for the lognormal distribution, and 1% for the power-law distribution.

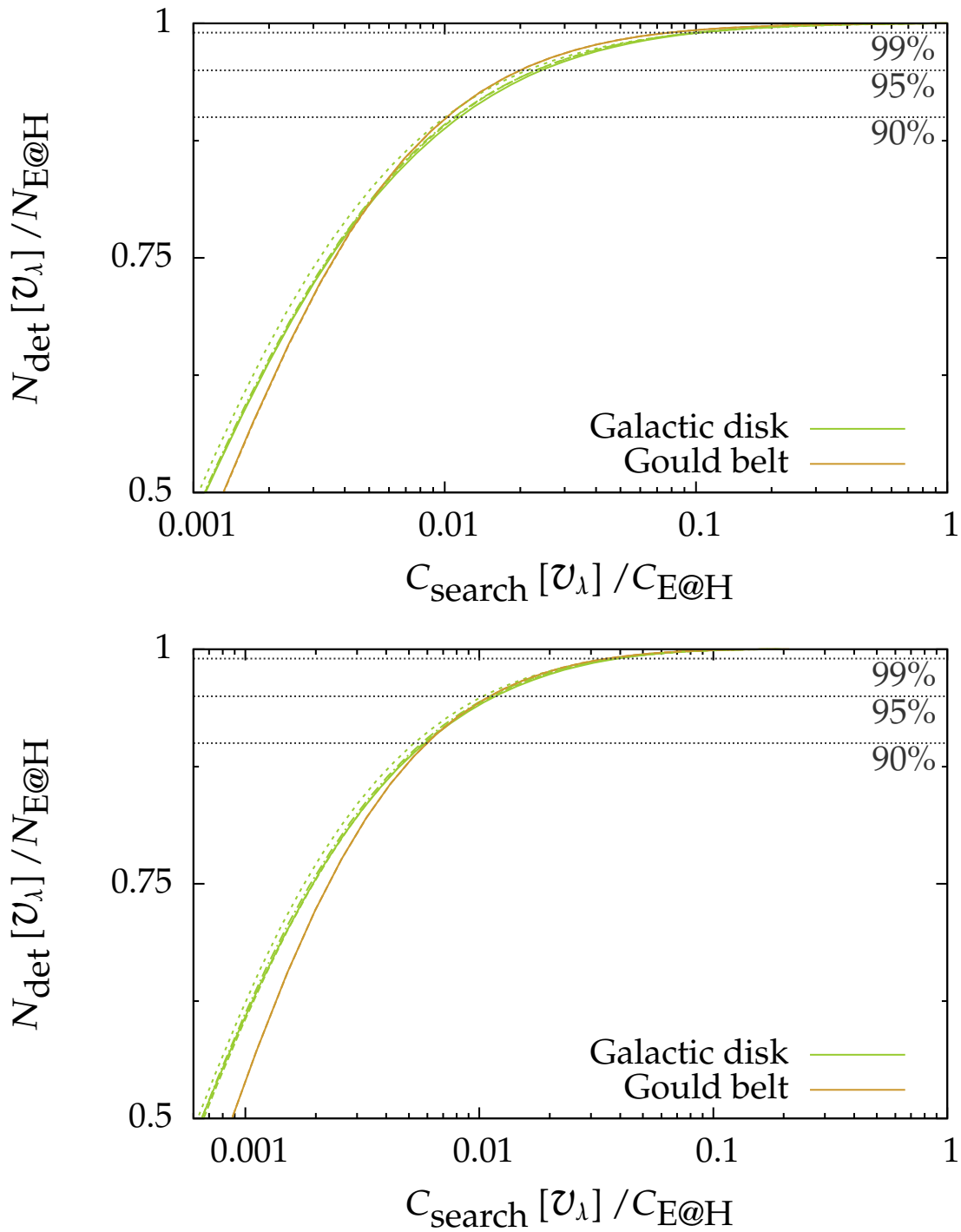


**Figure 7.13:** An inexpensive semi-targeted gravitar search from the Einstein@Home S5R5 search by reducing the frequency range searched. The fractional search costs plotted versus the fractional number of detections for the simulated gravitar population and the projected S5R5 search. Green curves are results for the disk population, orange curves for the Gould belt population. The top panel shows results for the lognormal initial frequency distribution, the bottom panel for the initial power-law frequency distribution.

We would like to stress that these drastic savings in computational costs come from restricting the frequency range alone. Further savings are conceivable by restricting the regions of sky that are searched, compare Figure 7.4 and note the increased density of sources near the Galactic equator.

Figure 7.14 shows the frequency bands that are searched vs. the fractional number of detections. The top panel are the results for the lognormal initial frequency distribution, the bottom panel are the results for the power-law initial frequency distribution. The same models as in Figure 7.13 are plotted. Again, there is virtually no difference between the different models for the Galactic disk in each panel, in only one case in the lower panel the lower limit of the frequency band deviates from the others. The Gould belt population is distributed over a smaller frequency range (as visible from Figure 7.9) and thus favours smaller frequency ranges to search as shown in Figure 7.14.

The results shown in Figure 7.14 can be used to prioritise the order in which frequency bands should be searched. The rate at which the frequency range of the search has to be increased is given by the pairs of curves from this Figure, although we note that the last few percent of possible detections are the computationally most expensive as we have seen in description of Figure 7.13 above. In other searches, this effect might be less pronounced so that the prioritisation proves more useful.

## 7.5 Conclusions

In contrast to previous studies we present a more detailed description of the Galactic gravitar population. For the first time we derive distributions of the detectable sources based on realistic sensitivity curves for blind all-sky searches for continuous gravitational waves. Based on the projected sensitivities for recent (but not fully post-processed) searches and projected future searches we obtain distributions for age, frequency, and distance and detailed sky maps for different models. We also obtain expected numbers of detections for these realistic searches.

We study contributions from two likely sources of gravitars, the Gould belt and the Galactic disk and compare their contributions in a more detailed way than previously available. We find that for most models the dominating contribution comes from the Galactic disk population.

For the first time we show how to split the population synthesis into the spatial distribution and the frequency distribution. This improves the simulation process because results from both parts can be easily combined by the new method described above; changing one of the two aspects of a population synthesis run does not require re-running the complete process. We obtain the analytical description of the evolved frequency distribution. This improvement allows to remove the necessity for Monte-Carlo simulations in the space of frequency. This reduces the number of necessary Monte-Carlo trials and therefore the computational costs for running the simulations.

Future searches will soon reach the sensitivity to constrain the gravitar population models described above. As we have shown above, current searches reach the sensitivity level at which in the most optimistic models of order a few detections are expected. If these searches report a null result, it can be used to constrain some aspects of these most optimistic gravitar population models.

Our work suggests a clear way to design a dedicated search to probe the Galactic population of gravitars. Using the simulation results for the distribution in parameter space as

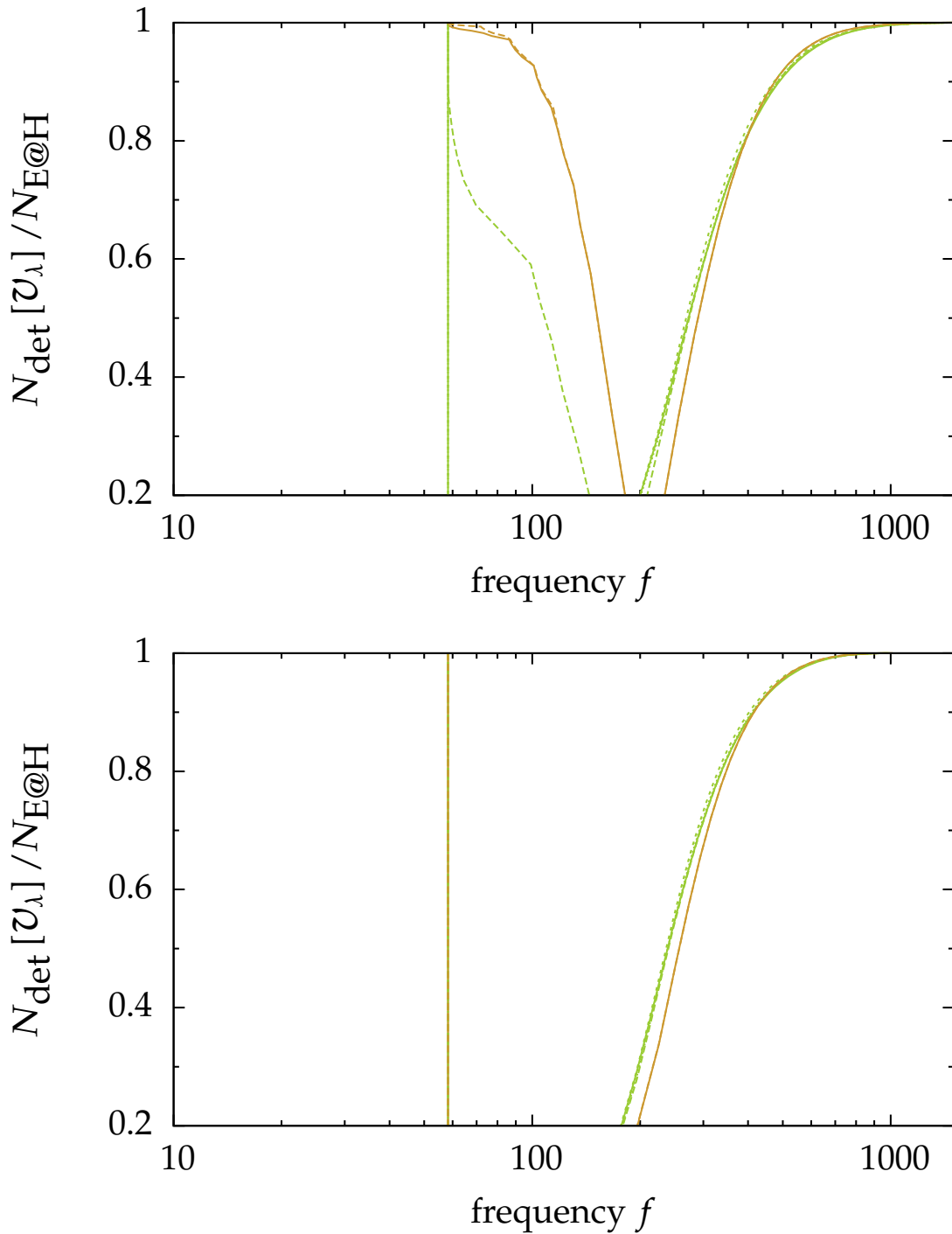


**Figure 7.14:** The frequency bands for an inexpensive semi-targeted gravitar search from the Einstein@Home S5R5 search by reducing the frequency range searched. We plot the fraction of detections compared to the full search as a function of the frequency limits. The left-hand curves are the lower frequency limit, the right-hand curves are the upper frequency limit. Note, how the bandwidth shrinks for lower fractional number of detections. Green curves are results for the disk population, orange curves for the Gould belt population. The top panel shows results for the lognormal initial frequency distribution, the bottom panel for the initial power-law frequency distribution.

input to future blind searches will allow us to constrain the search parameter space to the most cost-efficient parts. We provide the general framework for this optimisation procedure. We show in detail how realistic searches can be constrained in their search parameter space to require only a minor fraction of the computing costs and still obtain almost full sensitivity to the gravitar population. We also provide a way to prioritise future searches by searching the most cost-efficient frequency bands first to minimise the time to a first gravitar detection.



# 8

## Technical details

### 8.1 Zap list for the Einstein@Home radio pulsar search

---

**Table 8.1:** The zap list for the Einstein@Home radio pulsar search. This table lists all frequency bands zapped out in the RFI cleaning stage of the search code. “center” is the central frequency around which a band of width “width” is cleaned.

| center (Hz)   | width (Hz) | center (Hz)   | width (Hz) |
|---------------|------------|---------------|------------|
| 0.0183333335  | 0.0316667  | 355.407456875 | 0.0710815  |
| 0.0408503485  | 0.00166736 | 355.489138389 | 0.0777957  |
| 0.0825084205  | 0.00166684 | 355.574143787 | 0.0711148  |
| 0.834167519   | 0.00166667 | 355.657482979 | 0.0744206  |
| 0.8375008495  | 0.00166667 | 355.741683327 | 0.0727937  |
| 0.84083418    | 0.00166667 | 355.824150995 | 0.0711648  |
| 1.199167275   | 0.00166667 | 355.906657241 | 0.0728282  |
| 1.4141671915  | 0.00166667 | 355.990848899 | 0.0711982  |
| 8.2175002885  | 0.00166667 | 356.074129648 | 0.0712148  |
| 8.3441669265  | 0.00166883 | 356.15580069  | 0.0745295  |
| 8.375833653   | 0.00167517 | 356.239983367 | 0.072898   |
| 8.4708336115  | 0.00169417 | 356.324205851 | 0.0712648  |
| 16.5625005745 | 0.0033125  | 356.405864302 | 0.0712812  |
| 16.8158339305 | 0.00336317 | 356.490864387 | 0.0712982  |
| 20.739167653  | 0.00748121 | 356.572472106 | 0.0713145  |
| 20.9333353055 | 0.0291867  | 356.654117197 | 0.0713308  |

continued on next page

(continued)

| center (Hz)   | width (Hz) | center (Hz)   | width (Hz) |
|---------------|------------|---------------|------------|
| 20.95250097   | 0.00752388 | 356.822485098 | 0.0713645  |
| 21.1216695315 | 0.0492244  | 356.904117353 | 0.0713808  |
| 21.274168536  | 0.0275881  | 357.072466428 | 0.0714145  |
| 21.319168926  | 0.0342643  | 357.322542907 | 0.0714645  |
| 21.4325016075 | 0.0142873  | 357.404148676 | 0.0714808  |
| 21.442500691  | 0.0042885  | 357.570796336 | 0.0715142  |
| 21.510834571  | 0.0143024  | 357.820803343 | 0.0715642  |
| 29.6008342345 | 0.00592017 | 358.319171365 | 0.0716638  |
| 29.60750106   | 0.0059215  | 425.309129558 | 0.0850618  |
| 29.6158346505 | 0.00592317 | 425.474163294 | 0.0850948  |
| 29.622501216  | 0.0059245  | 496.457532279 | 0.0992915  |
| 39.999168417  | 0.00799983 | 564.0466647   | 0.201255   |
| 42.4475014815 | 0.0118228  | 564.347468159 | 0.123061   |
| 43.3675007075 | 0.0086735  | 564.682557342 | 0.122822   |
| 43.4083351525 | 0.0170141  | 565.017565522 | 0.1229     |
| 43.445837252  | 0.0553567  | 567.104325645 | 0.113421   |
| 60            | 0.5        | 567.272576172 | 0.113455   |
| 86.8491714145 | 0.0540353  | 650.855018893 | 0.13822    |
| 120           | 0.5        | 651.19429684  | 0.130239   |
| 124.99917313  | 0.0249998  | 651.529047445 | 0.130306   |
| 130.286675081 | 0.104378   | 673.540831055 | 0.134708   |
| 141.547506316 | 0.0283095  | 707.903967165 | 0.141581   |
| 141.714178943 | 0.0283428  | 708.074391711 | 0.141615   |
| 141.879171159 | 0.0283758  | 708.239380659 | 0.141648   |
| 173.679171194 | 0.071416   | 708.405952027 | 0.141681   |
| 180           | 0.5        | 708.735813767 | 0.141747   |
| 212.52919301  | 0.0425058  | 708.902618757 | 0.141781   |
| 212.612516669 | 0.0425225  | 709.150728571 | 0.308288   |
| 212.778341633 | 0.044231   | 709.570624627 | 0.141914   |
| 212.860841162 | 0.0425722  | 709.904091958 | 0.141981   |
| 260.039206111 | 0.0520078  | 738.041702862 | 0.153056   |
| 260.378324978 | 0.0604147  | 738.29482392  | 0.322629   |
| 260.713333013 | 0.0605032  | 815.340808378 | 0.163068   |

continued on next page

8.1. ZAP LIST FOR THE EINSTEIN@HOME RADIO PULSAR SEARCH

(continued)

| center (Hz)   | width (Hz) | center (Hz)   | width (Hz) |
|---------------|------------|---------------|------------|
| 261.052508884 | 0.0522105  | 824.591646982 | 0.259432   |
| 283.344155191 | 0.0566688  | 825.22839715  | 0.840599   |
| 283.510842305 | 0.0567022  | 850.784397608 | 0.510359   |
| 283.677484235 | 0.0567355  | 921.514610614 | 0.184303   |
| 283.842549701 | 0.0567685  | 998.292436465 | 0.280382   |
| 303.468358974 | 0.0757048  | 998.761098384 | 0.55986    |
| 303.547533027 | 0.0673437  | 999.259558667 | 0.199852   |
| 303.63251054  | 0.0607265  | 1063.27499874 | 0.460246   |
| 303.714215253 | 0.0607428  | 1063.73249292 | 0.382476   |
| 303.803348419 | 0.0757127  | 1085.0988917  | 0.228795   |
| 303.967539307 | 0.0607935  | 1085.44045666 | 0.228871   |
| 304.139216887 | 0.0741479  | 1085.77634093 | 0.217155   |
| 304.22082355  | 0.0608442  | 1098.93613093 | 0.219787   |
| 304.310809059 | 0.0608622  | 1133.20740755 | 0.226641   |
| 304.393343488 | 0.0758888  | 1133.54846904 | 0.395036   |
| 304.47499471  | 0.0759132  | 1133.96556827 | 0.226793   |
| 304.817552979 | 0.0609635  | 1134.75209623 | 1.30859    |
| 346.886721658 | 0.0776801  | 1205.36396033 | 0.749589   |
| 346.96832486  | 0.0777004  | 1259.31897627 | 0.283585   |
| 347.265823954 | 0.152783   | 1346.39386512 | 1.7739     |
| 347.479215531 | 0.0694958  | 1476.25446198 | 0.295251   |
| 347.562547355 | 0.0695125  | 1485.7935995  | 0.297159   |
| 347.814234507 | 0.0695628  | 1488.78491467 | 4.28741    |
| 347.899966704 | 0.0779314  | 1524.32984605 | 0.328104   |
| 350.669132805 | 0.0701338  | 1606.69547193 | 0.659512   |
| 350.832511508 | 0.0701665  | 1630.66965356 | 0.352727   |
| 351.082548986 | 0.0702165  | 1780.42073453 | 0.387786   |
| 351.249150855 | 0.0702498  | 1840.36661943 | 0.368073   |
| 351.330844739 | 0.0702662  | 1843.32044943 | 4.44605    |
| 351.415787424 | 0.0702832  | 1846.34702092 | 0.369269   |
| 351.499165014 | 0.0702998  | 1867.25674211 | 0.408321   |
| 351.580851641 | 0.0703162  | 1914.09541766 | 0.382819   |
| 351.830843251 | 0.0703662  | 2040.94133279 | 0.741424   |

continued on next page

(continued)

| center (Hz)   | width (Hz) | center (Hz)   | width (Hz) |
|---------------|------------|---------------|------------|
| 351.997536721 | 0.0703995  | 2056.04791617 | 0.749396   |
| 352.079207258 | 0.0704158  | 2125.01464643 | 0.560487   |
| 352.165876465 | 0.0704332  | 2127.61432735 | 0.425523   |
| 352.247501068 | 0.0704495  | 2197.87561295 | 3.09644    |
| 352.330901428 | 0.0704662  | 2301.4959954  | 0.460299   |
| 352.414217094 | 0.0704828  | 2339.5918152  | 0.96055    |
| 352.497572173 | 0.0704995  | 2375.01488022 | 0.587828   |
| 352.579226315 | 0.0705158  | 2410.39364138 | 0.482079   |
| 352.663343683 | 0.0721497  | 2552.35523795 | 0.836197   |
| 352.745883279 | 0.0705492  | 2562.03326218 | 0.578053   |
| 352.829146369 | 0.0705658  | 2623.26050513 | 0.868727   |
| 352.913383045 | 0.072202   | 2694.11181076 | 3.73245    |
| 352.997535019 | 0.0705995  | 2875.00902201 | 0.657667   |
| 353.078361492 | 0.0722365  | 2906.80781643 | 0.919377   |
| 353.160035987 | 0.0789887  | 2909.42948998 | 0.581886   |
| 353.242496292 | 0.077262   | 2934.10014084 | 0.58682    |
| 353.329177005 | 0.0706658  | 3048.68854742 | 3.76987    |
| 353.411716872 | 0.0756785  | 3051.0129668  | 0.610203   |
| 353.492483161 | 0.0773214  | 3083.08928626 | 0.616618   |
| 353.578349148 | 0.0723411  | 3169.97403791 | 0.633995   |
| 353.661693154 | 0.0757354  | 3261.31273473 | 0.971347   |
| 353.744137576 | 0.0707488  | 3288.60829387 | 0.657722   |
| 353.827497066 | 0.0707655  | 3332.2781869  | 0.999611   |
| 353.910019264 | 0.0725357  | 3403.1547847  | 1.02807    |
| 353.991703147 | 0.0790693  | 3430.53176672 | 0.686106   |
| 354.077560689 | 0.0708155  | 3544.71663536 | 0.708943   |
| 354.199159823 | 0.160793   | 3572.1940773  | 0.714439   |
| 354.532510657 | 0.494242   | 3615.85194867 | 0.984658   |
| 354.867535332 | 0.15434    | 3625.02722395 | 0.725005   |
| 354.989154559 | 0.0776767  | 3643.12000437 | 0.728624   |
| 355.071651954 | 0.0760574  | 3757.63278328 | 1.17516    |
| 355.156647794 | 0.0793566  | 3855.79336804 | 0.771159   |
| 355.239222984 | 0.0777364  | 3864.73433816 | 0.772947   |

continued on next page

| (continued)   |            |               |            |
|---------------|------------|---------------|------------|
| center (Hz)   | width (Hz) | center (Hz)   | width (Hz) |
| 355.324235138 | 0.0710648  | 3874.99278961 | 0.925169   |
|               |            | 3899.24389039 | 2.60434    |

## 8.2 Commonly used probability distributions

### 8.2.1 Gaussian distribution

The normal distribution, also known as Gaussian distribution, is of importance in the calculation of significances in Fourier analysis and the description of noise in detector data. Detector noise usually is assumed to follow a normal distribution, such that each bin of the time series is drawn from this distribution, independently of the other bins.

It also arises in the Fourier domain description of the data, where the real and imaginary part of each Fourier bin amplitude follow a Gaussian distribution as well.

A variable  $X$  is said to follow a normal / Gaussian distribution, if its probability density function  $p(x)$  is given by

$$p(x; \mu, \sigma) = \frac{1}{\sqrt{2\pi}\sigma} \exp\left(-\frac{(x - \mu)^2}{2\sigma^2}\right). \quad (8.1)$$

Here, the two parameters  $\mu$  and  $\sigma$  describe the mean and the variance of the distribution, respectively. For the description of most data in this thesis, the mean usually can be assumed to be zero, simplifying the distribution to

$$p(x; \mu = 0, \sigma) = \frac{1}{\sqrt{2\pi}\sigma} \exp\left(-\frac{x^2}{2\sigma^2}\right). \quad (8.2)$$

### 8.2.2 Normalised power

Assume, the measured time series  $x(t)$  can be written as a sum of the signal  $s(t)$  and the noise  $n(t)$ :

$$x(t) = s(t) + n(t) \quad (8.3)$$

The continuous Fourier transform is then given by the complex-valued integral

$$\tilde{x}(f) = \int_{-\infty}^{\infty} dt x(t) \exp(-2\pi ift) \quad (8.4)$$

$$= \tilde{s}(f) + \tilde{n}(f), \quad (8.5)$$

because of the linearity of the Fourier transform. In the discrete case, this transforms into

$$\tilde{x}_i = \tilde{s}_i + \tilde{n}_i, \quad (8.6)$$

with complex  $\tilde{x}_i$ ,  $\tilde{s}_i$ , and  $\tilde{n}_i$ , where  $i$  numbers the frequency bins. Often, the *power spectrum* is studied. Its bins  $p_i$  are given by the squared modulus of the discrete Fourier transform

$$p_i = |\tilde{x}_i|^2. \quad (8.7)$$

It is useful to divide the power spectrum by the variance of the noise Fourier transform  $\sigma_n = \text{var}(\tilde{n}_i)$  for normalisation. This defines the *normalised power spectrum* with bins  $\rho_i$  by

$$\rho_i = \frac{p_i}{\sigma_n}. \quad (8.8)$$

Assume, the real and the imaginary part of the noise Fourier transform follow independent normal distributions with zero mean and equal variance; now consider

$$\sigma_n = \text{var}(\tilde{n}_i) = \text{var}(\Re(\tilde{n}_i)) + \text{var}(\Im(\tilde{n}_i)) = 2\text{var}(\Re(\tilde{n}_i)) = 2\text{var}(\Im(\tilde{n}_i)) \quad (8.9)$$

to understand that their variances are given by

$$\text{var}(\Re(\tilde{n}_i)) = \frac{\sigma_n}{2} = \text{var}(\Im(\tilde{n}_i)). \quad (8.10)$$

Now, to consider the probability distribution governing the normalised power, we write for the doubled normalised power

$$2\rho_i = 2\frac{|\tilde{x}_i|^2}{\sigma_n} = \left(\frac{\sqrt{2}\Re(\tilde{x}_i)}{\sqrt{\sigma_n}}\right)^2 + \left(\frac{\sqrt{2}\Im(\tilde{x}_i)}{\sqrt{\sigma_n}}\right)^2 =: \alpha^2 + \beta^2, \quad (8.11)$$

where for  $\alpha$  and  $\beta$  have unit variance in the noise-only case as follows from their definition using Equation (8.10) by

$$\text{var}(\alpha) = \frac{2}{\sigma_n} \text{var}(\Re(\tilde{n}_i)) = \frac{2}{\sigma_n} \frac{\sigma_n}{2} = 1. \quad (8.12)$$

Thus,  $2\rho_i$  follows a probability distribution given by squaring and adding two independent random variables, both following a normal distribution with unit variance; this is the so-called *chi-squared distribution*, which we will derive in the following.

### 8.2.3 Chi-square distribution

The normal distribution ceases to be useful as soon as we want to consider the distribution of the squared modulus of the complex Fourier amplitudes, e.g. for the power spectrum. While the latter follow a normal distribution with zero mean, the squared moduli don't.

#### Chi-square distribution with one degree of freedom

First, assume a random variable  $X$ , following a normal distribution with zero mean and variance  $\sigma^2 = 1$ :

$$p_x(x) = \frac{1}{\sqrt{2\pi}} \exp\left(-\frac{x^2}{2}\right). \quad (8.13)$$

Now, define a random variable  $Y$  by

$$Y = X^2. \quad (8.14)$$

We derive the probability density function of  $Y$  from the defining equation and the coordinate transformation

$$p_x(x) dx = p_y(y) dy \quad (8.15)$$

$$p_x(x) dx = p_x(x(y)) \left| \frac{dx}{dy} \right| dy, \quad (8.16)$$

where

$$x(y) = \pm\sqrt{y} \quad \text{and} \quad p_y(y) = p_x(x(y)) \left| \frac{dx}{dy} \right| \quad (8.17)$$

Then, the definition of  $p_y$  can be rewritten to

$$\begin{aligned} p_y(y) &= p_x(\sqrt{y}) \left| \frac{d}{dy} \sqrt{y} \right| + p_x(-\sqrt{y}) \left| \frac{d}{dy} (-\sqrt{y}) \right| \\ &= \frac{p_x(\sqrt{y})}{2\sqrt{y}} dy + \frac{p_x(-\sqrt{y})}{2\sqrt{y}} \end{aligned} \quad (8.18)$$

$$= \frac{1}{\sqrt{2\pi}} y^{-\frac{1}{2}} \exp\left(-\frac{y}{2}\right). \quad (8.19)$$

This probability distribution function

$$\chi_1^2(x) = \frac{1}{\sqrt{2\pi}} x^{-\frac{1}{2}} \exp\left(-\frac{x}{2}\right) \quad (8.20)$$

is called a *chi-square distribution with one degree of freedom*. It arises when considering the distribution of the square of *one* normally distributed random variable with zero mean and unit variance. In the case of power spectra, the sum of two squared independent normally distributed random variables arises.

### Chi-square distribution with two degrees of freedom

Consider two random variables  $X$  and  $Y$  following a chi-square distribution of one degree of freedom

$$p_x(x) = \frac{1}{\sqrt{2\pi}} x^{-\frac{1}{2}} \exp\left(-\frac{x}{2}\right) \quad \text{and} \quad p_y(y) = \frac{1}{\sqrt{2\pi}} y^{-\frac{1}{2}} \exp\left(-\frac{y}{2}\right). \quad (8.21)$$

The joint probability distribution  $p_{xy}(x, y)$  is given by the product of the individual probability distribution functions, because  $X$  and  $Y$  are independent:

$$p_{xy}(x, y) = \frac{1}{2\pi} (xy)^{-\frac{1}{2}} \exp\left(-\frac{x+y}{2}\right). \quad (8.22)$$

Under a transformation into new coordinates  $u = u(x, y)$  and  $v = v(x, y)$  this function transforms by the defining equation

$$p_{xy}(x, y) dx dy = p_{xy}(x(u, v), y(u, v)) \mathcal{J} du dv, \quad (8.23)$$

as

$$p_{uv}(u, v) = p_{xy}(x(u, v), y(u, v)) \mathcal{J} \quad (8.24)$$

where  $\mathcal{J} = \left| \frac{dx dy}{du dv} \right|$  is the Jacobi determinant of the coordinate transformation.  $p_{xy}$  depends on the product and the sum of  $x$  and  $y$ ; thus, it is useful to define a coordinate transformation to new coordinates

$$u(x, y) = x + y \quad (8.25)$$

$$v(x, y) = xy. \quad (8.26)$$

The inversion of this transformation is

$$x(u, v) = \frac{u}{2} \mp \sqrt{\frac{u^2}{4} - v} \quad \text{and} \quad y(u, v) = \frac{u}{2} \pm \sqrt{\frac{u^2}{4} - v} \quad (8.27)$$

The symmetry in the coordinate inversions means as above to choose one for the computation of the Jacobi determinant and multiply the result of Equation (8.24) by two. We find for the Jacobi determinant (choosing the upper variant of the coordinate transformation):

$$\mathcal{J} = \frac{1}{\sqrt{u^2 - 4v}}. \quad (8.28)$$

Thus, we obtain from Equation (8.24) (mind the factor of two for the above symmetry)

$$p_{uv}(u, v) = \frac{1}{\pi} \frac{v^{-\frac{1}{2}}}{\sqrt{u^2 - 4v}} \exp\left(-\frac{u}{2}\right). \quad (8.29)$$

As we are interested in the distribution of  $x + y = u$ , we now integrate out  $v$  to obtain the probability distribution function of  $u$

$$p_u(u) = \int dv p_{uv}(u, v) = \frac{1}{\pi} \exp\left(-\frac{u}{2}\right) \int_0^{\frac{u^2}{4}} dv \frac{v^{-\frac{1}{2}}}{\sqrt{u^2 - 4v}}. \quad (8.30)$$

Transform via  $v = \frac{u^2}{4} \sin^2(w)$  and  $dv = \frac{u^2}{4} \sin(w) \cos(w) dw$ ; the limits of the integral transform to 0 and  $\frac{\pi}{2}$ , respectively. In the integrand everything cancels out and we are left with

$$p_u(u) = \frac{1}{\pi} \exp\left(-\frac{u}{2}\right) \int_0^{\frac{\pi}{2}} dw = \frac{1}{2} \exp\left(-\frac{u}{2}\right), \quad (8.31)$$

which is a simple exponential distribution and equivalent to a *chi-square distribution with two degrees of freedom*:

$$\chi_2^2(x) = \frac{1}{2} \exp\left(-\frac{x}{2}\right). \quad (8.32)$$

This is the distribution the bins in the power spectrum follow, which is therefore of large importance for the estimation of significances in Fourier analysis.

### Median and mean of $\chi_2^2$

The probability distribution is given by

$$p(x) = \frac{1}{2} e^{-\frac{x}{2}}. \quad (8.33)$$

Then, the median  $m$  follows from:

$$\begin{aligned} \int_0^m dx p(x) &= \frac{1}{2} \\ -e^{-\frac{m}{2}} + 1 &= \frac{1}{2} \\ m &= 2 \ln(2). \end{aligned} \quad (8.34)$$

The mean  $\mu$  is computed from

$$\mu = \int_0^{\infty} dx \, x p(x) = \int_0^{\infty} dx \, \frac{x}{2} e^{-\frac{x}{2}} = 2. \quad (8.35)$$

Note, that the bins of the normalised power spectrum follow a chi-square distribution if multiplied by a factor of two, Equation (8.11); thus the distribution of the  $\rho_i$  is

$$p(\rho_i) = \chi_2^2(2\rho_i) = e^{-\rho_i}, \quad (8.36)$$

and the median and mean of  $p(\rho_i)$  are  $m_p = \ln(2)$  and  $m_p = 1$ , respectively.

In data analysis for radio pulsars, a sum of multiple Fourier bins is used in the process of incoherent harmonic summing to increase the sensitivity of the search to narrow pulses. In this case, multiple chi-square distributions of two degrees of freedom are summed, leading to other chi-square distributions with higher numbers of degrees of freedom.

### Chi-square distribution with $n$ degrees of freedom

Here, we show the derivation<sup>1</sup> of the general chi-square distribution. Consider  $n$  random variables from normal distributions with zero mean and unit variance  $X_1, X_2, \dots, X_n$ . Let their squared sum be denoted by

$$Y = \sum_{i=1}^n X_i^2. \quad (8.37)$$

Their joint probability distribution function is given by

$$P(x_1, x_2, \dots, x_n) = \prod_{i=1}^n \left\{ \frac{1}{\sqrt{2\pi}} \exp\left(-\frac{x_i^2}{2}\right) \right\} = (2\pi)^{-\frac{n}{2}} \exp\left(-\frac{1}{2} \sum_{i=1}^n x_i^2\right). \quad (8.38)$$

We defined in Equation (8.37)  $Y$  to be given by the sum of squares of the  $X_i$ . Thus, any point on the  $(n-1)$ -dimensional surface of a sphere with radius  $r = \sqrt{y}$  in the  $n$ -dimensional space of all  $X_i$ , is a point  $Y$ . Therefore, we need to integrate the joint probability distribution function  $P(x_1, x_2, \dots, x_n)$  over the surface of the  $(n-1)$ -sphere to obtain the probability distribution function in  $Y$ :

$$p_y(y) dy = \int_{S_{n-1}^r} dx^n P(x_1, x_2, \dots, x_n) = \int_{S_{n-1}^r} dx^n (2\pi)^{-\frac{n}{2}} \exp\left(-\frac{1}{2} \sum_{i=1}^n x_i^2\right). \quad (8.39)$$

The term in the argument of the exponential function by definition has the constant value  $y$  on the surface of the  $S_{n-1}^r$ . The integral can thus be re-written as

$$p_y(y) dy = (2\pi)^{-\frac{n}{2}} \exp\left(-\frac{y}{2}\right) \int_{S_{n-1}^r} dx^n, \quad (8.40)$$

and the only integral left to compute is the surface integral over the  $S_{n-1}^r$  times its infinitesimal thickness  $dr = \frac{1}{2\sqrt{y}} dy$ . The surface of the  $S_{n-1}^r$  is given by

$$V_{S_{n-1}^r} = \frac{n\pi^{\frac{n}{2}}}{\Gamma\left(\frac{n}{2} + 1\right)} r^{n-1}, \quad (8.41)$$

<sup>1</sup>[http://en.wikipedia.org/wiki/Proofs\\_related\\_to\\_chi-square\\_distribution](http://en.wikipedia.org/wiki/Proofs_related_to_chi-square_distribution)

where  $\Gamma(x)$  is the Gamma function (Abramowitz and Stegun, 1984). Now, we re-write Equation (8.40) as

$$p_y(y) dy = (2\pi)^{-\frac{n}{2}} \exp\left(-\frac{y}{2}\right) \times \frac{n\pi^{\frac{n}{2}}}{\Gamma\left(\frac{n}{2} + 1\right)} r^{n-1} \times \frac{1}{2\sqrt{y}} dy \quad (8.42)$$

and simplify by using  $\Gamma(x+1) = x\Gamma(x)$  (Abramowitz and Stegun, 1984),  $r = \sqrt{y}$  to obtain

$$p_y(y) dy = \frac{1}{2^{\frac{n}{2}}\Gamma\left(\frac{n}{2}\right)} y^{\frac{n}{2}-1} \exp\left(-\frac{y}{2}\right) dy. \quad (8.43)$$

This propability distribution is called the *chi-square distribution with  $n$  degrees of freedom* (Abramowitz and Stegun, 1984)

$$\chi_n^2(x) = \frac{1}{2^{\frac{n}{2}}\Gamma\left(\frac{n}{2}\right)} x^{\frac{n}{2}-1} \exp\left(-\frac{x}{2}\right). \quad (8.44)$$

A sum of  $n$  squared, independent random variables, each of which following a normal distribution with zero mean and unit variance, is distributed according to a chi-square distribution with  $n$  degrees of freedom.

As we have shown above, two times the normalised power follows a chi-square distribution of two degrees of freedom. Thus, if we sum  $N_h$  bins from the normalised power spectrum in the course of the incoherent harmonic summing, twice the resulting variable will follow a chi-square distribution with  $2N_h$  degrees of freedom  $\chi_{2N_h}^2$ . This can be used to estimate significances of harmonically summed spectra.

### Important properties of $\chi_n^2$

Figure 8.1 shows the probability distribution functions  $\chi_n^2$  for  $n = 2, 4, 8, 16, 32$ . These are the distributions of  $2\mathcal{P}$  arising when summing 1, 2, 4, 8, and 16 harmonics in the power spectrum.

For the estimation of significances, defining the cumulative distribution function is useful; for a probability distribution function  $p(x)$  with  $x \in [0, \infty)$  it is in general given by

$$P(x) = \int_0^x dy p(y). \quad (8.45)$$

Here, we obtain

$$P(x) = \int_0^x dy \frac{1}{2^{\frac{n}{2}}\Gamma\left(\frac{n}{2}\right)} y^{\frac{n}{2}-1} \exp\left(-\frac{y}{2}\right) = \frac{1}{\Gamma\left(\frac{n}{2}\right)} \int_0^{\frac{x}{2}} dy y^{\frac{n}{2}-1} e^{-y} =: \gamma\left(\frac{x}{2}; \frac{n}{2}\right), \quad (8.46)$$

where  $\gamma(x; n) = \frac{1}{\Gamma(n)} \int_0^x dy y^{n-1} e^{-y}$  is the *incomplete lower Gamma function* (Abramowitz and Stegun, 1984). Accordingly we can write the complement of the cumulative distribution function  $Q(x) = 1 - P(x)$  with upper incomplete Gamma function  $\Gamma(x; n)$  (Abramowitz and Stegun, 1984)

$$Q(x) = 1 - \frac{1}{\Gamma\left(\frac{n}{2}\right)} \gamma\left(\frac{x}{2}; \frac{n}{2}\right) = \frac{\Gamma\left(\frac{x}{2}; \frac{n}{2}\right)}{\Gamma\left(\frac{n}{2}\right)} = \frac{1}{\Gamma\left(\frac{n}{2}\right)} \int_{\frac{x}{2}}^{\infty} dy y^{\frac{n}{2}-1} e^{-y}. \quad (8.47)$$

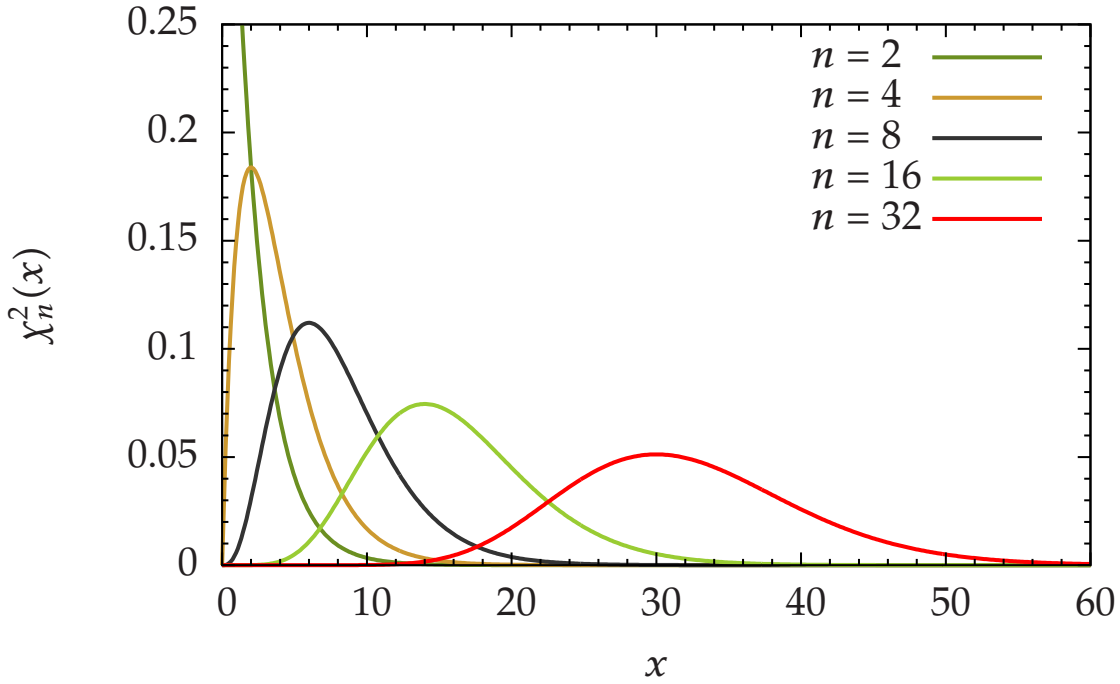


**Figure 8.1:** The probability distribution functions  $\chi_n^2$  for  $n = 2, 4, 8, 16, 32$ . These are the distributions of  $2\mathcal{D}$  arising when summing 1, 2, 4, 8, and 16 harmonics in the power spectrum, respectively. Note that  $\chi_2^2$  is an exponential function and has maximum probability density at  $x = 0$ .

Gamma functions, and upper and lower incomplete Gamma functions are readily available as numerical implementations in computer libraries, e.g. the GSL (Galassi, 2009). This allows for fast and efficient computation of the cumulative distribution functions and its complements necessary for the significance estimates.

The mean  $\mu_n$  of  $\chi_n^2$  is

$$\mu_n = n, \quad (8.48)$$

as can be easily seen from its definition:

$$\mu_n = \int_0^\infty dx \frac{1}{2^{\frac{n}{2}} \Gamma(\frac{n}{2})} x^{\frac{n}{2}-1} \exp\left(-\frac{x}{2}\right) = \frac{2}{\Gamma(\frac{n}{2})} \int_0^\infty dx x^{\frac{n}{2}} e^{-x} = \frac{2}{\Gamma(\frac{n}{2})} \Gamma\left(\frac{n}{2} + 1\right) = n. \quad (8.49)$$

By a similarly simple calculation using the result from Equation (8.49) it can be shown that the variance  $\sigma_n^2$  of  $\chi_n^2$  is

$$\sigma_n^2 = 2n. \quad (8.50)$$

### 8.2.4 Chi-square distribution fact sheet

Here, we present a chi-square distribution fact sheet for the most important properties of the chi-square distribution and related distributions for quick reference.

Table 8.2: Chi-square distribution fact sheet

|   |  |
|---|--|
| probability distribution function (pdf) | $\chi_n^2(x) = \frac{1}{2^{\frac{n}{2}}\Gamma(\frac{n}{2})} x^{\frac{n}{2}-1} \exp\left(-\frac{x}{2}\right)$ |
| (complete) Gamma function               | $\Gamma(x) = \int_0^\infty dy y^{x-1} e^{-y}$  |
| cumulative distribution function (cdf)  | $P_n(x) = \gamma\left(\frac{x}{2}; \frac{n}{2}\right)$   |
| incomplete lower Gamma function         | $\gamma(x; n) = \frac{1}{\Gamma(n)} \int_0^x dy y^{n-1} e^{-y}$  |
| cdf complement                          | $Q_n(x) = \Gamma\left(\frac{x}{2}; \frac{n}{2}\right)$   |
| incomplete upper Gamma function         | $\Gamma(x; n) = \frac{1}{\Gamma(n)} \int_x^\infty dy y^{n-1} e^{-y}$   |
| mean                                    | $\mu_n = n$  |
| variance                                | $\sigma_n^2 = 2n$  |

### 8.3 Beam geometry and Goldreich-Julian model

#### 8.3.1 Beam geometry

We start from (Gil et al., 1984; Lorimer and Kramer, 2005)

$$\cos(\rho) = \cos(\alpha) \cos(\alpha + \beta) + \sin(\alpha) \sin(\alpha + \beta) \cos\left(\frac{W}{2}\right) \quad (8.51)$$

and the additional constraint

$$|\beta| \leq \rho, \quad (8.52)$$

that ensures that the pulsar beam crosses the line of sight. From Equation (8.52) it follows that

$$\cos(\rho) \leq \cos(\beta), \quad (8.53)$$

since both  $-180^\circ \leq \rho \leq 180^\circ$  and  $-180^\circ \leq \beta \leq 180^\circ$ . Let us now consider the border case  $\rho = \beta$ . Inserting into Equation (8.51), expanding the trigonometric functions on the right-hand side and re-arranging the equation yields

$$c_\alpha \left(1 - c_\alpha^2 - c_{W/2} s_\alpha^2\right) = -s_\alpha s_\beta c_\alpha (1 - c_{W/2}), \quad (8.54)$$

where we have defined  $c_x := \cos(x)$  and  $s_x := \sin(x)$  for brevity. Further massaging the equation by replacing  $1 - c_\alpha^2 = s_\alpha^2$  and dividing both sides by  $s_\alpha (1 - A)$  we finally obtain

$$\cos(\beta) \sin(\alpha) = \cos(\alpha) \sin(\beta). \quad (8.55)$$

Any dependence on  $W$  drops out and the only solution for this equation in the relevant ranges is

$$\beta = -\alpha \quad \wedge \quad \beta = 180^\circ - \alpha. \quad (8.56)$$

Since we were initially looking for the range given by Equation (8.53) we find the corresponding solution in  $\alpha, \beta$

$$-\alpha \leq \beta \leq 180^\circ - \alpha. \quad (8.57)$$

### 8.3.2 Goldreich-Julian model

The *Goldreich-Julian model* (Goldreich and Julian, 1969) is the simplest model of the pulsar magnetosphere. It is not a fully realistic model of a neutron star and its magnetosphere, yet some basic principles can be readily understood with its help. In this model, the pulsar is assumed as an aligned rotator, i.e. the magnetic and the rotation axis are pointing in the same direction. The magnetic field is assumed to be a simple dipole field. Further, the pulsar is assumed to be a superconducting sphere inside vacuum. Goldreich and Julian (1969) show that this simple constellation of a highly magnetised, rapidly rotating, superconducting neutron star in vacuum is inconsistent as it leads to a discontinuity in the radial electric field at the surface of the neutron star, much stronger than local gravity. This results in the extraction of charged particles from the neutron star that form a plasma-filled magnetosphere around the neutron star.

Here, we give the full derivation of the model's equations, referred to in Section 2.3.1.

Assume, the magnetic field of the pulsar is that of a magnetic dipole  $\vec{m}$ . It is then given by

$$\vec{B} = \frac{\mu_0}{4\pi r^3} (3\vec{e}_r \cdot (\vec{m} \cdot \vec{e}_r) - \vec{m}). \quad (8.58)$$

We now choose the magnetic moment parallel to the  $z$ -axis in cartesian coordinates of a star-fixed coordinate system as  $\vec{m} = m\vec{e}_z$ , and thus

$$\vec{m} = m (\cos(\theta) \vec{e}_r - \sin(\theta) \vec{e}_\theta) \quad (8.59)$$

in standard spherical coordinates  $(r, \theta, \phi)$ . For the magnetic field  $\vec{B}$  in spherical coordinates we find

$$\vec{B} = \frac{B_R R^3}{2r^3} (2 \cos(\theta) \vec{e}_r + \sin(\theta) \vec{e}_\theta). \quad (8.60)$$

with a magnetic field  $B_R$  at the stellar surface and the above relation  $m = 2\pi B_R R^3 / \mu_0$ . Assuming a rotation of the pulsar around an axis  $\vec{\Omega}$ , points inside the pulsar are moving with a velocity

$$\vec{v} = \vec{\Omega} \times \vec{r}. \quad (8.61)$$

As pointed out above, the Goldreich-Julian model (Goldreich and Julian, 1969) for sake of simplicity assumes that the pulsar rotates around its magnetic field axis; therefore,  $\vec{\Omega} = \Omega \vec{e}_z$  and

$$\vec{v} = \Omega r \sin(\theta) \vec{e}_\phi. \quad (8.62)$$

Note, that in practice small deviations from the alignment must be allowed to observe a pulsing radio signal.

### Induced electric field

The neutron star is assumed to be a super-conducting sphere. Thus, an electric field  $\vec{E}$  is induced by the rotating magnetic field. Inside the super-conduction neutron star, the charge distribution will be re-arranged such that the inside of the sphere is force-free. The force  $\vec{F}$  acting on the charges is the Lorentz force, which in equilibrium vanishes inside the star and is given by

$$\vec{F} = q \left( \vec{E} + \vec{v} \times \vec{B} \right) \stackrel{!}{=} \vec{0}. \quad (8.63)$$

The last equation implies

$$\vec{E}_{<} = -\vec{v} \times \vec{B} = \frac{\Omega B_R R^3}{2r^2} \left( \sin^2(\theta) \vec{e}_r - \sin(2\theta) \vec{e}_\theta \right) \quad (8.64)$$

for the induced electric field  $\vec{E}_{<}$  in the stellar interior. Note, that the electric field is symmetric under rotations in the azimuthal direction. The electrostatic potential  $\Phi_{<}$  inside the neutron star, which must fulfil

$$\vec{E}_{<} (r, \theta) = -\nabla \Phi_{<} (r, \theta) \quad (8.65)$$

can be written as

$$\Phi_{<} (r, \theta) = \frac{\Omega B_R R^3 \sin^2(\theta)}{2} \frac{1}{r} + \chi \quad \text{for } r \leq R \quad (8.66)$$

with some constant  $\chi$ , which we will use below to choose a particular gauge.

### Electrostatic potential in the stellar exterior

The exterior of the neutron star we assume to be charge-free. The exterior charge density  $\rho_{>}$  thus vanishes everywhere  $\rho_{>} \equiv 0$ , and from Maxwell's equations  $\nabla \Phi_{>} \equiv 0$  follows for the exterior electrostatic potential. The electrostatic potential has to be continuously connected to the potential  $\Phi_{<}$  in the interior at the stellar surface  $r = R$ . Also, we impose the boundary condition that the exterior electrostatic potential vanishes at infinity. The exterior potential is then the solution of

$$\nabla \Phi_{>} (r, \theta) \equiv 0 \quad (8.67)$$

with the two boundary conditions

$$\Phi_{>} (r = R, \theta) = \Phi_{<} (r = R, \theta) \quad \text{and} \quad \Phi_{>} \rightarrow 0 \quad \text{for } r \rightarrow \infty \quad (8.68)$$

In charge-free space, and since the system does not depend on angle  $\phi$  in the azimuthal direction, the solution to the Laplace Equation (8.67) of the potential above is given by an expansion in the Legendre polynomials  $P_k$  as a function of  $\cos(\theta)$ . Thus, we can write the solution for the potential in the exterior in the most general way

$$\Phi_{>} (r, \theta) = \sum_{k=0}^{\infty} \left( \alpha_k r^k + \frac{\beta_k}{r^{k+1}} \right) P_k(\cos(\theta)). \quad (8.69)$$

All  $\alpha_k$  vanish because of the boundary condition at  $r \rightarrow \infty$ . The continuity condition contains only terms up to quadratic order in  $\cos(\theta)$ , thus no terms with  $k > 2$  can contribute.

Equation (8.69) then reduces to

$$\begin{aligned}\Phi_{>}(r, \theta) &= \frac{\beta_0}{r} P_0(\cos(\theta)) + \frac{\beta_1}{r^2} P_1(\cos(\theta)) + \frac{\beta_2}{r^3} P_2(\cos(\theta)) \\ &= \frac{\beta_0}{r} + \frac{\beta_1}{r^2} \cos(\theta) + \frac{\beta_2}{2r^3} (3 \cos^2(\theta) - 1)\end{aligned}\quad (8.70)$$

For the boundary condition at  $r = R$  we find

$$\Phi_{<}(R, \theta) = \frac{\Omega B_R R^2}{2} (1 - \cos^2(\theta)) + \chi \stackrel{!}{=} \Phi_{>}(R, \theta), \quad (8.71)$$

which we now compare in each order of  $\cos(\theta)$  to Equation (8.70) to obtain

$$\beta_1 = 0 \quad (8.72)$$

$$\beta_2 = -\frac{\Omega B_R R^5}{3} \quad (8.73)$$

$$\beta_0 = \frac{\Omega B_R R^3}{3} + \chi R, \quad (8.74)$$

where we choose the arbitrary gauge constant  $\chi = -\frac{\Omega B_R R^2}{3}$ , so that  $\beta_0 = 0$  as well.

Thus, we find after a little massage of the closed expression for the electrostatic potential in the interior and in the exterior of the aligned rotating pulsar in vacuo in the Goldreich-Julian model:

$$\Phi(r, \theta) = \begin{cases} \frac{\Omega B_R R^2}{2} \left( \frac{R}{r} \sin^2(\theta) - \frac{2}{3} \right) & \text{for } r \leq R \\ \frac{\Omega B_R R^2}{2} \frac{R^3}{r^3} \left( \sin^2(\theta) - \frac{2}{3} \right) & \text{for } r > R \end{cases}. \quad (8.75)$$

### Exterior charge distribution

Assume, that outside the star a charge distribution is allowed to form. Because charged particles can move freely subject to the Lorentz force, the exterior charge distribution  $\rho_{>}$  in static equilibrium follows from Maxwell's equations and the vanishing Lorentz force, Equation (8.63), as

$$\begin{aligned}\rho_{>}(r, \theta) &= \varepsilon_0 \nabla \cdot \vec{E} \\ &= \varepsilon_0 \nabla \cdot \left( - \left( \vec{\Omega} \times \vec{r} \right) \times \vec{B} \right) \\ &= -2\varepsilon_0 \left( \vec{B} \cdot \vec{\Omega} \right) \\ &= -\frac{\varepsilon_0 \Omega B_R R^3}{r^3} (3 \cos^2(\theta) - 1).\end{aligned}\quad (8.77)$$

This also implies that the surface defined by  $\vec{B} \cdot \vec{\Omega} = 0$  separates space into regions with differing signs of the charge density.

### Co-rotation of the plasma

The plasma in the stellar exterior co-rotates rigidly with the stellar interior. This follows from the condition of vanishing Lorentz force in equilibrium, Equation (8.63), applied to

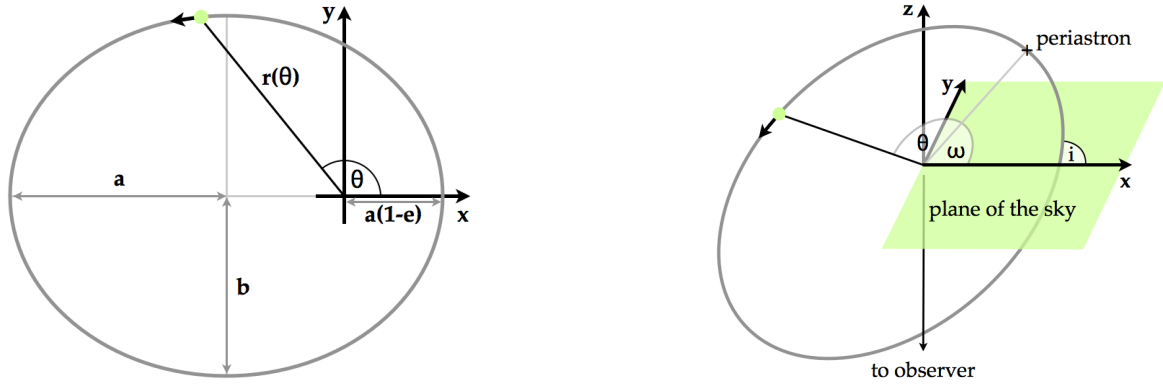


**Figure 8.2:** (Left) Parametrisation of elliptic motion by the true anomaly  $\theta$ , semi-major axis  $a$ , semi-minor axis  $b$ , and eccentricity  $e = \sqrt{1 - b^2/a^2}$  in a specific coordinate system. The coordinate origin coincides with the pulsar system barycentre. (Right) The orientation of the pulsar orbit with respect to the plane of the sky is described by the two angles  $\omega$  (longitude of the periastron) and  $i$  (inclination).

both stellar interior and exterior. Taking the cross product of  $\vec{E} + \vec{v} \times \vec{B} = \vec{0}$  with  $\vec{B}$ , expanding the double cross product, and using  $\vec{v} \cdot \vec{B} = 0$  yields

$$\vec{v} = \frac{\vec{E} \times \vec{B}}{|\vec{B}|^2} \quad (8.78)$$

for the velocity *inside and outside* the star.

## 8.4 Doppler modulation in elliptical orbits

Assume, the semi-major axis  $a$  of the orbital ellipse is oriented along the x-axis, the semi-minor axis  $b$  along the y-axis and the focus of the ellipse is at the coordinate origin (see Figure 8.2). Then, the motion along the orbit as a function of the true anomaly  $\theta$  is described by:

$$\vec{r}(\theta) = r(\theta) \begin{pmatrix} \cos(\theta) \\ \sin(\theta) \\ 0 \end{pmatrix} \quad \text{with} \quad r(\theta) = \frac{b^2}{a(1 + e \cos(\theta))}. \quad (8.79)$$

Note, that  $\theta = \theta(t)$  is a function of the time itself. One can show by taking the derivative of the above equation with respect to  $t$  that the velocity vector along the orbit is given by

$$\vec{v}(\theta) = \dot{\theta} \frac{b^2}{a(1 + e \cos(\theta))^2} \begin{pmatrix} -\sin(\theta) \\ \cos(\theta) + e \\ 0 \end{pmatrix}. \quad (8.80)$$

The time derivative of the true anomaly  $\dot{\theta}$  can be obtained from the defining equations of  $\theta$  and the eccentric anomaly  $E$ :

$$\tan\left(\frac{\theta}{2}\right) = \sqrt{\frac{1+e}{1-e}} \tan\left(\frac{E}{2}\right) \quad (8.81)$$

and

$$E - e \sin(E) = \frac{2\pi}{P_{\text{orb}}} (t - T_0) =: \Omega_{\text{orb}} (t - T_0), \quad (8.82)$$

respectively. From (8.81) we find

$$\dot{\theta} = \sqrt{\frac{1+e}{1-e}} \frac{1 + \frac{1-e}{1+e} \tan^2\left(\frac{\theta}{2}\right)}{1 + \tan^2\left(\frac{\theta}{2}\right)} \dot{E}. \quad (8.83)$$

From (8.82), respectively, we find

$$\dot{E} = \frac{\Omega_{\text{orb}}}{1 - e \cos(E)}, \quad (8.84)$$

where we note that by (8.81) and a trigonometric identity<sup>2</sup>, we can rewrite

$$\cos(E) = \cos\left(2 \arctan\left(\sqrt{\frac{1-e}{1+e}} \tan\left(\frac{\theta}{2}\right)\right)\right) = \frac{1 - \frac{1-e}{1+e} \tan^2\left(\frac{\theta}{2}\right)}{1 + \frac{1-e}{1+e} \tan^2\left(\frac{\theta}{2}\right)}, \quad (8.85)$$

which can now be entered into (8.83) and can be simplified to give

$$\dot{\theta} = \frac{\Omega_{\text{orb}}}{(1 - e^2)^{\frac{3}{2}}} (1 + e \cos(\theta))^2. \quad (8.86)$$

The last expression can now be entered into equation for the velocity (8.80) along with the relation  $b^2 = a^2 (1 - e^2)$  to yield:

$$\vec{v}(\theta) = \frac{a\Omega_{\text{orb}}}{\sqrt{1 - e^2}} \begin{pmatrix} -\sin(\theta) \\ \cos(\theta) + e \\ 0 \end{pmatrix}. \quad (8.87)$$

This solution is valid only for an ellipse in the specific coordinate system illustrated in the left panel of Figure 8.2. For the general case (right panel of the same Figure), two rotations have to be applied. We want the  $x$ - $y$  plane to be the plane of the sky. The longitude of the periastron  $\omega$ , if different from zero is equivalent to a rotation around the  $z$ -axis by  $\omega$ . The orbital inclination by  $i$  is equivalent to a rotation around the  $x$ -axis by  $i$ . Applying both rotations finally yields the most general result for the velocity in an elliptic motion:

$$\vec{v}(\theta) = \frac{a\Omega_{\text{orb}}}{\sqrt{1 - e^2}} \begin{pmatrix} -\sin(\theta + \omega) + e \sin(\omega) \\ \cos(i) (\cos(\theta + \omega) + e \cos(\omega)) \\ \sin(i) (\cos(\theta + \omega) + e \cos(\omega)) \end{pmatrix}. \quad (8.88)$$

With the Doppler effect, only motion along the line of sight is observable, thus only the  $z$ -component contributes

$$v_z = \frac{a \sin(i) \Omega_{\text{orb}}}{\sqrt{1 - e^2}} (\cos(\theta + \omega) + e \cos(\omega)). \quad (8.89)$$

<sup>2</sup> $\cos(2\alpha) = \frac{1 - \tan^2(\alpha)}{1 + \tan^2(\alpha)}$

In the case of  $v_z \ll c$ , the apparent frequency is simply given by

$$f(\theta) = f_0 \left( 1 - \frac{v_z(\theta)}{c} + \mathcal{O}\left(\frac{v_z^2}{c^2}\right) \right), \quad (8.90)$$

where  $f_0$  is the pulsar frequency at the pulsar system barycentre.

The position of the pulsar on an elliptic orbit in the most general case is obtained by applying the same two rotations to (8.79):

$$\vec{r}(\theta) = r(\theta) \begin{pmatrix} \cos(\theta + \omega) \\ \cos(i) \sin(\theta + \omega) \\ \sin(i) \sin(\theta + \omega) \end{pmatrix} \quad \text{with} \quad r(\theta) = \frac{b^2}{a(1 + e \cos(\theta))}. \quad (8.91)$$

## 8.5 Derivation of the metric from the phase model

---

Let the signal be described by phase model  $\Phi(\Lambda; t)$  depending on a tuple of signal parameters  $\Lambda = \{\lambda_i\}$  and the time  $t$ . A signal with parameters  $\Lambda_1$  is then given by

$$S(\Lambda_1; t) = \mathcal{A} \exp(i\Phi(\Lambda_1; t)), \quad (8.92)$$

where  $\mathcal{A}$  is the complex amplitude of the signal. The coherent detection statistic  $\mathcal{P}(\Lambda_1, \Lambda_0)$  (demodulated power) assuming a template at  $\Lambda_0$  is defined as

$$\begin{aligned} \mathcal{P}(\Lambda_1, \Lambda_0) &= \left| \frac{1}{T} \int_0^T dt S(\Lambda_1; t) \exp[-i\Phi(\Lambda_0; t)] \right|^2 \\ &= \left| \frac{\mathcal{A}}{T} \int_0^T dt \exp[i(\Phi(\Lambda_1; t) - \Phi(\Lambda_0; t))] \right|^2. \end{aligned} \quad (8.93)$$

Clearly,  $\mathcal{P}(\Lambda_0, \Lambda_0) = |\mathcal{A}|^2$ . From the detection statistic we define the mismatch  $m$  between a signal at  $\Lambda_1$  and a template at  $\Lambda_0$  as

$$m(\Lambda_1, \Lambda_0) = 1 - \frac{\mathcal{P}(\Lambda_1, \Lambda_0)}{\mathcal{P}(\Lambda_0, \Lambda_0)} = m(\Lambda_0, \Lambda_1). \quad (8.94)$$

This expression is symmetrical in its arguments; the symmetry of  $\mathcal{P}$  with respect to exchange of the arguments is inherited.

Let us consider the mismatch of points  $\Lambda + \Delta\Lambda$  close to a given point  $\Lambda$  in parameter space. We write

$$\mathcal{P}(\Lambda + \Delta\Lambda, \Lambda) = \left| \frac{\mathcal{A}}{T} \int_0^T dt \exp[i(\Phi(\Lambda + \Delta\Lambda; t) - \Phi(\Lambda; t))] \right|^2, \quad (8.95)$$

where we Taylor-expand the argument of the exponential function around  $\Lambda$  by:

$$\Phi(\Lambda + \Delta\Lambda; t) = \Phi(\Lambda; t) + (\partial_i \Phi(\Lambda; t)) \Delta\Lambda^i + \frac{1}{2} (\partial_i \partial_j \Phi(\Lambda; t)) \Delta\Lambda^i \Delta\Lambda^j + \mathcal{O}((\Delta\Lambda)^3), \quad (8.96)$$

where  $\partial_i = \frac{\partial}{\partial \Lambda^i}$  and where we employ Einstein's summing convention for brevity. The term  $i\Phi(\Lambda; t)$  in the argument of the exponential function in Equation (8.95) cancels out and only terms with  $\Delta\Lambda$  are left, thus we obtain

$$\rho(\Lambda + \Delta\Lambda, \Lambda) = \left| \frac{\mathcal{A}}{T} \int_0^T dt \exp[i\Delta\Phi] \right|^2, \quad (8.97)$$

$$\text{with } \Delta\Phi = (\partial_i\Phi) \Delta\Lambda^i + \frac{1}{2} (\partial_i\partial_j\Phi) \Delta\Lambda^i \Delta\Lambda^j \quad (8.98)$$

where we suppressed the argument of  $\Phi$  and higher order terms in the  $\Delta\Lambda$  for clarity. To expand this expression, we can write

$$\begin{aligned} \rho(\Lambda + \Delta\Lambda, \Lambda) &= \left| \frac{\mathcal{A}}{T} \int_0^T dt \exp[i\Delta\Phi] \right|^2 \\ &= \left| \frac{\mathcal{A}}{T} \int_0^T dt \cos(\Delta\Phi) + i \sin(\Delta\Phi) \right|^2 \\ &= |\mathcal{A}|^2 \left( \langle \cos(\Delta\Phi) \rangle_T^2 + \langle \sin(\Delta\Phi) \rangle_T^2 \right), \end{aligned} \quad (8.99)$$

where we have defined the short-hand notation for the time-average of a function  $\mathcal{G}(t)$  as

$$\langle \mathcal{G}(t) \rangle_T \equiv \frac{1}{T} \int_0^T dt \mathcal{G}(t). \quad (8.100)$$

Now, we can write the detection statistic in terms of the small  $\Delta\Lambda$  by expanding the trigonometric functions

$$\cos(\Delta\Phi) = 1 - \frac{1}{2} (\partial_i\Phi) \Delta\Lambda^i (\partial_j\Phi) \Delta\Lambda^j \quad (8.101)$$

$$\sin(\Delta\Phi) = (\partial_i\Phi) \Delta\Lambda^i \quad (8.102)$$

to second order in  $\Delta\Lambda$ . Since Equation (8.99) is quadratic in the trigonometric functions and we wish to obtain at most quadratic terms in  $\Delta\Lambda$  in the final expression, we do not need to consider higher orders here. Now insert Equations (8.101) and (8.102) in Equation (8.99) to obtain

$$\begin{aligned} \rho(\Lambda + \Delta\Lambda, \Lambda) &= |\mathcal{A}|^2 \left( \left\langle 1 - \frac{1}{2} (\partial_i\Phi) \Delta\Lambda^i (\partial_j\Phi) \Delta\Lambda^j \right\rangle_T^2 + \langle (\partial_i\Phi) \Delta\Lambda^i \rangle_T^2 \right) \\ &= |\mathcal{A}|^2 \left( \left( 1 - \frac{1}{2} \langle \partial_i\Phi \partial_j\Phi \rangle_T \Delta\Lambda^i \Delta\Lambda^j \right)^2 + \left( \langle \partial_i\Phi \rangle_T \Delta\Lambda^i \right)^2 \right) \\ &= |\mathcal{A}|^2 \left( 1 - \langle \partial_i\Phi \partial_j\Phi \rangle_T + \langle \partial_i\Phi \rangle_T \langle \partial_j\Phi \rangle_T \right) \Delta\Lambda^i \Delta\Lambda^j. \end{aligned} \quad (8.103)$$

Finally, enter Equation (8.94) into Equation (8.103) to obtain the mismatch in terms of small offsets  $\Delta\Lambda$  from a parameter space point  $\Lambda$  as

$$m(\Lambda + \Delta\Lambda, \Lambda) = \left( \langle \partial_i\Phi \partial_j\Phi \rangle_T - \langle \partial_i\Phi \rangle_T \langle \partial_j\Phi \rangle_T \right) \Delta\Lambda^i \Delta\Lambda^j, \quad (8.104)$$

which inspires the definition of a metric  $g_{ij}$  by

$$m(\Lambda + \Delta\Lambda, \Lambda) = g_{ij} \Delta\Lambda^i \Delta\Lambda^j \quad \text{with} \quad g_{ij} = \langle \partial_i\Phi \partial_j\Phi \rangle_T - \langle \partial_i\Phi \rangle_T \langle \partial_j\Phi \rangle_T. \quad (8.105)$$

## 8.6 The full parameter space metric

Using the method from Section 8.5 and the circular orbital phase model

$$\Phi(t; \Lambda) = 2\pi f (t + \tau \sin(\Omega t + \psi)) + \Phi'_0, \quad (8.106)$$

we can construct a metric on the four-dimensional parameter space of the signal parameter frequency  $f$ , projected orbital radius in light-seconds  $\tau$ , orbital angular velocity  $\Omega$ , and initial orbital phase  $\psi$ . The loss in detection statistic  $\rho$ , see Equation (8.93), from small deviations  $\Delta\Lambda$  in the parameter space coordinates is called mismatch and is defined by

$$m(\Lambda + \Delta\Lambda, \Lambda) = 1 - \frac{\rho(\Lambda + \Delta\Lambda, \Lambda)}{\rho(\Lambda, \Lambda)}. \quad (8.107)$$

It can be described by a metric  $g$  via

$$m(\Lambda + \Delta\Lambda, \Lambda) = g_{ij} \Delta\Lambda^i \Delta\Lambda^j \quad \text{with} \quad g_{\alpha\beta} = \langle \partial_\alpha \Phi \partial_\beta \Phi \rangle_T - \langle \partial_\alpha \Phi \rangle_T \langle \partial_\beta \Phi \rangle_T, \quad (8.108)$$

where we use the definitions from Section 8.5.

Inserting the phase model into the last equation and computing the full metric yields a symmetric four-by-four matrix

$$(g_{\alpha\beta}) = \begin{pmatrix} g_{ff} & g_{f\tau} & g_{f\Omega} & g_{f\psi} \\ g_{f\tau} & g_{\tau\tau} & g_{\tau\Omega} & g_{\tau\psi} \\ g_{f\Omega} & g_{\tau\Omega} & g_{\Omega\Omega} & g_{\psi\Omega} \\ g_{f\psi} & g_{\tau\psi} & g_{\psi\Omega} & g_{\psi\psi} \end{pmatrix} \quad (8.109)$$

with the elements

$$\begin{aligned} g_{ff} &= \frac{\pi^2}{3} (4T^2 + 6\tau^2) \\ &\quad - \frac{\pi^2 \tau}{\Omega^2 T} [8 \sin(\psi) - 8 \sin(\psi + \Omega T) + 8\Omega T \cos(\psi + \Omega T) - \Omega \tau \sin(2\psi) + \Omega \tau \sin(2\psi + 2\Omega T)] \\ &\quad - \frac{\pi^2}{\Omega^2 T^2} [\Omega T^2 + 2\tau \cos(\psi) - 2\tau \cos(\psi + \Omega T)]^2 \end{aligned} \quad (8.110)$$

$$\begin{aligned} g_{f\tau} &= \frac{2\pi^2 f}{\Omega^2 T^2} [\cos(\psi + \Omega T) - \cos(\psi)] \times [\Omega T^2 + 2\tau \cos(\psi) - 2\tau \cos(\psi + \Omega T)] \\ &\quad - \frac{4\pi^2 f}{\Omega^2 T} [\sin(\psi) - \sin(\psi + \Omega T) + \Omega T \cos(\psi + \Omega T)] \\ &\quad + \frac{\pi^2 f \tau}{\Omega T} [\sin(2\psi) - \sin(2\psi + 2\Omega T) + 2\Omega T] \end{aligned} \quad (8.111)$$

$$\begin{aligned} g_{f\Omega} &= \frac{4\pi^2 f \tau}{\Omega^3 T} [2 \sin(\psi) - 2 \sin(\psi + \Omega T) + 2\Omega T \cos(\psi + \Omega T) + \Omega^2 T^2 \sin(\psi + \Omega T)] \\ &\quad - \frac{\pi^2 f \tau^2}{2\Omega^2 T} [\sin(2\psi) - \sin(2\psi + 2\Omega T) + 2\Omega T \cos(2\psi + 2\Omega T)] \\ &\quad - \frac{2\pi^2 f \tau}{\Omega^3 T^2} [\Omega T^2 + 2\tau \cos(\psi) - 2\tau \cos(\psi + \Omega T)] \\ &\quad \times [\cos(\psi + \Omega T) - \cos(\psi) + \Omega T \sin(\psi + \Omega T)] \end{aligned} \quad (8.112)$$

$$g_{f\Psi} = \frac{2\pi^2 f \tau}{\Omega^2 T^2} [T - \tau \sin(\psi) + \tau \sin(\psi + \Omega T)] \times [2 \cos(\psi + \Omega T) - 2 \cos(\psi) + \Omega T \sin(\psi + \Omega T) + \Omega T \sin(\psi)] \quad (8.113)$$

$$g_{\tau\tau} = \frac{\pi^2 f^2}{\Omega T} [2\Omega T + \sin(2\psi) - \sin(2\psi + 2\Omega T)] - \frac{4\pi^2 f^2}{\Omega^2 T^2} [\cos(\psi + \Omega T) - \cos(\psi)]^2 \quad (8.114)$$

$$g_{\tau\Omega} = \frac{4\pi^2 f^2}{\Omega^3 T^2} \tau [\cos(\psi + \Omega T) - \cos(\psi)] \times [\cos(\psi + \Omega T) - \cos(\psi) + \Omega T \sin(\psi + \Omega T)] - \frac{\pi^2 f^2 \tau}{2\Omega^2 T} [\sin(2\psi) - \sin(2\psi + 2\Omega T) + 2\Omega T \cos(2\psi + 2\Omega T)] \quad (8.115)$$

$$g_{\tau\psi} = -\frac{2\pi^2 f^2 \tau}{\Omega^2 T^2} [\cos(\psi + \Omega T) - \cos(\psi)] \times [2 \sin(\psi) - 2 \sin(\psi + \Omega T) + \Omega T \cos(\psi + \Omega T) + \Omega T \cos(\psi)] \quad (8.116)$$

$$g_{\Omega\Omega} = \frac{\pi^2 f^2 \tau^2}{6\Omega^3 T} [3 \sin(2\psi) - 3 \sin(2\psi + 2\Omega T) + 4\Omega^3 T^3 + 6\Omega^2 T^2 \sin(2\psi + 2\Omega T) + 6\Omega T \cos(2\psi + 2\Omega T)] - \frac{4\pi^2 f^2 \tau^2}{\Omega^4 T^2} [\cos(\psi + \Omega T) - \cos(\psi) + \Omega T \sin(\psi + \Omega T)]^2 \quad (8.117)$$

$$g_{\Omega\psi} = \frac{\pi^2 f^2 \tau^2}{\Omega^2 T} [\Omega^2 T^2 + \cos(\psi + \Omega T)^2 - \cos(\psi)^2 + \Omega T \sin(2\psi + 2\Omega T)] - \frac{4\pi^2 \tau^2 f^2}{\Omega^3 T^2} [\sin(\psi + \Omega T) - \sin(\psi)] \times [\cos(\psi + \Omega T) - \cos(\psi) + \Omega T \sin(\psi + \Omega T)] \quad (8.118)$$

$$g_{\psi\psi} = \frac{\pi^2 \tau^2 f^2}{\Omega T} [2\Omega T - \sin(2\psi) + \sin(2\psi + 2\Omega T)] - \frac{4\pi^2 \tau^2 f^2}{\Omega^2 T^2} [\sin(\psi + \Omega T) - \sin(\psi)]^2 \quad (8.119)$$

## 8.7 The frequency-projected parameter space metric

Further, we can construct the frequency-projected metric, Equation (3.31) which is derived from the full metric  $g$ , presented in the previous section by projecting onto the sub-space of constant  $f = f_0$ . We obtain a symmetric three-by-three matrix

$$(\gamma_{ij}) = \begin{pmatrix} \gamma_{\tau\tau} & \gamma_{\tau\Omega} & \gamma_{\tau\psi} \\ \gamma_{\tau\Omega} & \gamma_{\Omega\Omega} & \gamma_{\Omega\psi} \\ \gamma_{\tau\psi} & \gamma_{\Omega\psi} & \gamma_{\psi\psi} \end{pmatrix} \quad (8.120)$$

with the following elements. Note, that for simplicity, all elements have been multiplied by  $g_{ff}$ , Equation (8.110). This is motivated by the definition of the elements of the projected metric from

$$\gamma_{ij} := g_{ij} - \frac{g_{fi}g_{jf}}{g_{ff}}. \quad (8.121)$$

$$\begin{aligned}
 \gamma_{\tau\tau} g_{ff} = & -\frac{\pi^4 f_0^2}{3\Omega^4 T^2} \left[ 48 \cos(2\psi + \Omega T) - 48 \cos(\Omega T) - 24 \cos(2\psi) - 24 \cos(2\psi + 2\Omega T) \right. \\
 & + 16\Omega^2 T^2 - 2\Omega^4 T^4 + 24\Omega T \sin(2\psi) + 8\Omega^2 T^2 \cos(\Omega T) + 8\Omega^2 T^2 \cos(2\psi + \Omega T) \\
 & + 8\Omega^2 T^2 \cos(2\psi + 2\Omega T) + \Omega^3 T^3 \sin(2\psi + 2\Omega T) - 48\Omega T \sin(\Omega T) \\
 & \left. - 24\Omega T \sin(2\psi + 2\Omega T) + 8\Omega^2 T^2 \cos(2\psi) - \Omega^3 T^3 \sin(2\psi) + 48 \right] \quad (8.122)
 \end{aligned}$$

$$\begin{aligned}
 \gamma_{\tau\Omega} g_{ff} = & \left\{ \frac{4\pi^2 f_0}{\Omega^2 T} [\sin(\psi) - \sin(\psi + \Omega T) + \Omega T \cos(\psi + \Omega T)] \right. \\
 & - \frac{\pi^2 f_0 \tau}{\Omega T} [\sin(2\psi) - \sin(2\psi + 2\Omega T) + 2\Omega T] \\
 & \left. - \frac{2\pi^2 f_0}{\Omega^2 T^2} [\cos(\psi + \Omega T) - \cos(\psi)] \times [\Omega T^2 + 2\tau \cos(\psi) - 2\tau \cos(\psi + \Omega T)] \right\} \\
 & \times \left\{ \frac{4\pi^2 f_0 \tau}{\Omega^3 T} [2 \sin(\psi) - 2 \sin(\psi + \Omega T) + 2\Omega T \cos(\psi + \Omega T) + \Omega^2 T^2 \sin(\psi + \Omega T)] \right. \\
 & - \frac{\pi^2 f_0 \tau^2}{2\Omega^2 T} [\sin(2\psi) - \sin(2\psi + 2\Omega T) + 2\Omega T \cos(2\psi + 2\Omega T)] \\
 & - \frac{2\pi^2 f_0 \tau}{\Omega^3 T^2} [\Omega T^2 + 2\tau \cos(\psi) - 2\tau \cos(\psi + \Omega T)] \\
 & \left. \times [\cos(\psi + \Omega T) - \cos(\psi) + \Omega T \sin(\psi + \Omega T)] \right\} \\
 & - \left\{ \frac{\pi^2}{3} (4T^2 + 6\tau^2) - \frac{\pi^2 \tau}{\Omega^2 T} [8 \sin(\psi) - 8 \sin(\psi + \Omega T) + 8\Omega T \cos(\psi + \Omega T) \right. \\
 & - \Omega \tau \sin(2\psi) + \Omega \tau \sin(2\psi + 2\Omega T)] \\
 & \left. - \frac{\pi^2}{\Omega^2 T^2} [\Omega T^2 + 2\tau \cos(\psi) - 2\tau \cos(\psi + \Omega T)]^2 \right\} \\
 & \times \left\{ \frac{\pi^2 f_0^2 \tau}{2\Omega^2 T} [\sin(2\psi) - \sin(2\psi + 2\Omega T) + 2\Omega T \cos(2\psi + 2\Omega T)] \right. \\
 & - \frac{4\pi^2 f_0^2 \tau}{\Omega^3 T^2} [\cos(\psi + \Omega T) - \cos(\psi)] \\
 & \left. \times [\cos(\psi + \Omega T) - \cos(\psi) + \Omega T \sin(\psi + \Omega T)] \right\} \quad (8.123)
 \end{aligned}$$

$$\begin{aligned}
 \gamma_{\tau\psi} g_{ff} = & \frac{2\pi^4 f_0^2 \tau}{3\Omega^4 T^3} [2 \cos(\psi + \Omega T) - 2 \cos(\psi) + \Omega T \sin(\psi + \Omega T) + \Omega T \sin(\psi)] \\
 & \times [24\tau - 24\tau \cos(\Omega T) + 12T \sin(\psi) - 12T \sin(\psi + \Omega T) + 6\Omega T^2 \cos(\psi) \\
 & - 6\Omega^2 T^2 \tau + 6\Omega T^2 \cos(\psi + \Omega T) - \Omega^2 T^3 \sin(\psi) + \Omega^2 T^3 \sin(\psi + \Omega T) \\
 & - 6\Omega T \tau \sin(\Omega T)] \quad (8.124)
 \end{aligned}$$

$$\begin{aligned}
 \gamma_{\Omega\Omega} g_{ff} = & - \left\{ \frac{\pi^2}{3} (4T^2 + 6\tau^2) - \frac{\pi^2\tau}{\Omega^2 T} [8 \sin(\psi) - 8 \sin(\psi + \Omega T) + 8\Omega T \cos(\psi + \Omega T) \right. \\
 & \left. - \Omega\tau \sin(2\psi) + \Omega\tau \sin(2\psi + 2\Omega T)] - \frac{\pi^2}{\Omega^2 T^2} (\Omega T^2 + 2\tau \cos(\psi) - 2\tau \cos(\psi + \Omega T))^2 \right\} \\
 & \times \left\{ \frac{4\pi^2 f_0^2 \tau^2}{\Omega^4 T^2} [\cos(\psi + \Omega T) - \cos(\psi) + \Omega T \sin(\psi + \Omega T)]^2 \right. \\
 & \left. - \frac{\pi^2 f_0^2 \tau^2}{6\Omega^3 T} [3 \sin(2\psi) - 3 \sin(2\psi + 2\Omega T) + 4\Omega^3 T^3 + 6\Omega^2 T^2 \sin(2\psi + 2\Omega T) \right. \\
 & \left. + 6\Omega T \cos(2\psi + 2\Omega T)] \right\} \\
 & - \left\{ \frac{4\pi^2 f_0 \tau}{\Omega^3 T} [2 \sin(\psi) - 2 \sin(\psi + \Omega T) + 2\Omega T \cos(\psi + \Omega T) + \Omega^2 T^2 \sin(\psi + \Omega T)] \right. \\
 & \left. - \frac{\pi^2 f_0 \tau^2}{2\Omega^2 T} [\sin(2\psi) - \sin(2\psi + 2\Omega T) + 2\Omega T \cos(2\psi + 2\Omega T)] \right. \\
 & \left. - \frac{2\pi^2 f_0 \tau}{\Omega^3 T^2} [\Omega T^2 + 2\tau \cos(\psi) - 2\tau \cos(\psi + \Omega T)] \right. \\
 & \left. \times [\cos(\psi + \Omega T) - \cos(\psi) + \Omega T \sin(\psi + \Omega T)] \right\}^2 \quad (8.125)
 \end{aligned}$$

$$\begin{aligned}
 \gamma_{\Omega\psi} g_{ff} = & \left\{ \frac{\pi^2}{3} (4T^2 + 6\tau^2) - \frac{\pi^2\tau}{\Omega^2 T} [8 \sin(\psi) - 8 \sin(\psi + \Omega T) + 8\Omega T \cos(\psi + \Omega T) \right. \\
 & \left. - \Omega\tau \sin(2\psi) + \Omega\tau \sin(2\psi + 2\Omega T)] \right. \\
 & \left. - \frac{\pi^2}{\Omega^2 T^2} [\Omega T^2 + 2\tau \cos(\psi) - 2\tau \cos(\psi + \Omega T)]^2 \right\} \\
 & \times \left\{ \frac{\pi^2 f_0^2 \tau^2}{\Omega^2 T} [\sin(\psi)^2 - \sin(\psi + \Omega T)^2 + \Omega^2 T^2 + \Omega T \sin(2\psi + 2\Omega T)] \right. \\
 & \left. - \frac{4\pi^2 f_0^2 \tau^2}{\Omega^3 T^2} [\sin(\psi + \Omega T) - \sin(\psi)] \right. \\
 & \left. \times [\cos(\psi + \Omega T) - \cos(\psi) + \Omega T \sin(\psi + \Omega T)] \right\} \\
 & - \left\{ \frac{4\pi^2 f_0 \tau}{\Omega^3 T} [2 \sin(\psi) - 2 \sin(\psi + \Omega T) \right. \\
 & \left. + 2\Omega T \cos(\psi + \Omega T) + \Omega^2 T^2 \sin(\psi + \Omega T)] \right. \\
 & \left. - \frac{\pi^2 f_0 \tau^2}{2\Omega^2 T} [\sin(2\psi) - \sin(2\psi + 2\Omega T) + 2\Omega T \cos(2\psi + 2\Omega T)] \right. \\
 & \left. - \frac{2\pi^2 f_0 \tau}{\Omega^3 T^2} [\Omega T^2 + 2\tau \cos(\psi) - 2\tau \cos(\psi + \Omega T)] \right. \\
 & \left. \times [\cos(\psi + \Omega T) - \cos(\psi) + \Omega T \sin(\psi + \Omega T)] \right\}
 \end{aligned}$$

$$\begin{aligned} & \times \left\{ \frac{2\pi^2 f_0 \tau}{\Omega^2 T} \left[ -\Omega \tau \cos(\psi + \Omega T)^2 + 2 \cos(\psi + \Omega T) + \Omega \tau \cos(\psi)^2 - 2 \cos(\psi) \right. \right. \\ & \quad \left. \left. + 2\Omega T \sin(\psi + \Omega T) \right] \right. \\ & \quad \left. - \frac{2\pi^2 f_0 \tau}{\Omega^2 T^2} [\sin(\psi + \Omega T) - \sin(\psi)] \left[ \Omega T^2 + 2\tau \cos(\psi) - 2\tau \cos(\psi + \Omega T) \right] \right\} \end{aligned} \quad (8.126)$$

$$\begin{aligned} \gamma_{\psi\psi} g_{ff} = & - \left\{ \frac{2\pi^2 f_0 \tau}{\Omega^2 T} \left[ -\Omega \tau \cos(\psi + \Omega T)^2 + 2 \cos(\psi + \Omega T) + \Omega \tau \cos(\psi)^2 \right. \right. \\ & \quad \left. \left. - 2 \cos(\psi) + 2\Omega T \sin(\psi + \Omega T) \right] \right. \\ & \quad \left. - \frac{2\pi^2 f_0 \tau}{\Omega^2 T^2} [\sin(\psi + \Omega T) - \sin(\psi)] \times \left[ \Omega T^2 + 2\tau \cos(\psi) - 2\tau \cos(\psi + \Omega T) \right] \right\}^2 \\ & - \left\{ \frac{\pi^2}{3} (4T^2 + 6\tau^2) - \frac{\pi^2 \tau}{\Omega^2 T} [8 \sin(\psi) - 8 \sin(\psi + \Omega T) + 8\Omega T \cos(\psi + \Omega T) \right. \\ & \quad \left. - \Omega \tau \sin(2\psi) + \Omega \tau \sin(2\psi + 2\Omega T)] \right. \\ & \quad \left. - \frac{\pi^2}{\Omega^2 T^2} \left[ \Omega T^2 + 2\tau \cos(\psi) - 2\tau \cos(\psi + \Omega T) \right]^2 \right\} \\ & \times \left\{ \frac{4\pi^2 f_0^2 \tau^2}{\Omega^2 T^2} [\sin(\psi + \Omega T) - \sin(\psi)]^2 \right. \\ & \quad \left. - \frac{\pi^2 f_0^2 \tau^2}{\Omega T} [\sin(2\psi + 2\Omega T) - \sin(2\psi) + 2\Omega T] \right\} \end{aligned} \quad (8.127)$$

The determinant of the frequency-projected metric is used in the Einstein@Home search to place templates in the orbital parameter space with method described in Section 3.4.6. The determinant is given by

$$\gamma = \gamma_{\tau\tau} \gamma_{\Omega\Omega} \gamma_{\psi\psi} + 2\gamma_{\tau\Omega} \gamma_{\Omega\psi} \gamma_{\tau\psi} - \gamma_{\tau\psi}^2 \gamma_{\Omega\Omega} - \gamma_{\tau\tau} \gamma_{\Omega\psi}^2 - \gamma_{\psi\psi} \gamma_{\tau\Omega}^2, \quad (8.128)$$

which, for reasons of brevity, we will not write out explicitly here

## 8.8 Polynomial phase models

For certain applications the search over the four-dimensional space of  $f, \tau, \Omega, \psi$  might be computationally prohibitive. In other cases (e. g. where only a small fraction of the orbit is visible during the observation), other approximative methods have been developed, that allow for computational shortcuts and the dimensional reduction of the search space.

### 8.8.1 Expansion up to cubic order in $t$

We can rewrite the phase model (3.11) using addition relations of the trigonometric functions and by expanding them into a Taylor series in  $\Omega t$  as

$$\Phi(t; \Lambda) = 2\pi f \left( t + \tau \sum_{n=0}^{\infty} (-1)^n \left( \sin(\psi) \frac{(\Omega t)^{2n}}{(2n)!} + \cos(\psi) \frac{(\Omega t)^{2n+1}}{(2n+1)!} \right) \right), \quad (8.129)$$

constant phase terms are dropped because they do not contribute to the parameter space metric that includes derivatives of the phase model only.

Let us now look at the first few terms in this polynomial expansion of the phase model (again dropping one term constant over time in the phase):

$$\Phi(t; \Lambda) = 2\pi f \left( t(1 + \tau\Omega \cos(\psi)) - \frac{\tau\Omega^2}{2} \sin(\psi) t^2 - \frac{\tau\Omega^3}{6} \cos(\psi) t^3 + \mathcal{O}(t^4) \right). \quad (8.130)$$

We now define:

$$\nu := \frac{f}{1 + \tau\Omega \cos(\psi)} \quad (8.131)$$

$$\frac{a}{c} := \frac{\tau\Omega^2 \sin(\psi)}{1 + \tau\Omega \cos(\psi)} \quad (8.132)$$

$$\frac{j}{c} := \frac{\tau\Omega^3 \cos(\psi)}{1 + \tau\Omega \cos(\psi)} \quad (8.133)$$

and obtain the polynomial phase model in the simple form up to cubic order in  $t$

$$\Phi(t; \Lambda) = 2\pi\nu \left( t - \frac{a}{2c} t^2 - \frac{j}{6c} t^3 + \mathcal{O}(t^4) \right). \quad (8.134)$$

Here,  $\nu$  is an instantaneous frequency,  $a$  is the acceleration in the orbit, and  $j$  is the time derivative of the acceleration and is called the ‘‘jerk’’ term.

### 8.8.2 Alternative phase model

We have chosen the above form with an explicit frequency component multiplying each order in  $t$  to reconstruct these physical parameters as well as for consistency with the usual definitions of pulsar astronomy. We note, that there is an alternative possibility to define a phase model by means of defining

$$\nu_1 := f(1 + \tau\Omega \cos(\psi)) \quad (8.135)$$

$$\nu_2 := -\frac{\tau\Omega^2 \sin(\psi)}{2} f \quad (8.136)$$

$$\nu_3 := -\frac{\tau\Omega^3 \cos(\psi)}{6} f \quad (8.137)$$

and rewriting the phase model as

$$\Phi(t; \Lambda_\nu) = 2\pi \left( \nu_1 t + \nu_2 t^2 + \nu_3 t^3 + \mathcal{O}(t^4) \right), \quad (8.138)$$

where  $\Lambda_\nu$  is the collection of the parameters  $\nu_1, \nu_2$ , and  $\nu_3$ . This phase model is useful, because the signal resulting from it is

$$S(t) = \mathcal{A}\Re \left( e^{i\Phi(t)} \right) = \mathcal{A}\Re \left( e^{2\pi i(\nu_2 t^2 + \nu_3 t^3)} e^{2\pi i\nu_1 t} \right) \quad (8.139)$$

$$= \frac{\mathcal{A}}{2} \left( e^{2\pi i(\nu_2 t^2 + \nu_3 t^3)} e^{2\pi i\nu_1 t} + e^{-2\pi i(\nu_2 t^2 + \nu_3 t^3)} e^{-2\pi i\nu_1 t} \right). \quad (8.140)$$

We can write the signal as a product of a single frequency component at  $\nu_1$  with a phase function in the quadratic and cubic terms of  $t$ . Let us now multiply the signal with the inverse of the phase function to obtain

$$S'(t) = e^{-2\pi i(\nu_2 t^2 + \nu_3 t^3)} S(t) \quad (8.141)$$

$$= \frac{\mathcal{A}}{2} \left( e^{2\pi i \nu_1 t} + e^{-4\pi i(\nu_2 t^2 + \nu_3 t^3)} e^{-2\pi i \nu_1 t} \right). \quad (8.142)$$

If we now take the DFT of this expression, the first term dominates the Fourier transform and is a delta function peaking at  $f = \nu_1$ , the second term contributes nothing to the DFT (Ransom, 2001).

In consequence, with this alternative phase model there is no need for time domain re-sampling. The signals time series simply has to multiplied with a time-dependent phase factor at each bin. This phase factor also depends on  $\nu_2, \nu_3$  and has to be recalculated for each new value pair<sup>3</sup>. After the phase factor multiplication,  $\nu_1$  can be obtained from Fourier transforming the complex time series and maximising over frequency.

Whether to use this method of phase factor multiplication or time domain resampling depends on the kind of computing hardware available. The pulsar observation data are always real time series. On a CPU a real-to-complex FFT is faster than a complex-to-complex FFT, since less frequency bins have to be computed and symmetries can be used. So, on a CPU re-defining the time series to complex to allow for phase factor multiplication might in fact slow the computation down.

### 8.8.3 Acceleration phase model

Here, the signal is described by a phase model with terms of up to quadratic order in time  $t$ :

$$\Phi_2(t; a) = 2\pi\nu \left( t - \frac{a}{2c} t^2 \right), \quad (8.143)$$

the phase model has only two parameters: the frequency  $\nu$  and the acceleration  $a$ . From this simplified model we compute the metric  $g$  in the coordinates  $\nu$  and  $a$  and project out the frequency to obtain the projected metric  $\gamma$  in the one-dimensional subspace of acceleration. In a search one would use short-cuts to search the frequency space (with an FFT, for example) and search the acceleration space by resampling the time series for each acceleration trial. With observation time  $T$  we find

$$\gamma_{aa}^{(2)} = \det(\gamma^{(2)}) = \frac{\pi^2 T^4 \nu^2}{180c^2} \mathcal{G}_2(a, T) \quad \text{with} \quad \mathcal{G}_2(a, T) = 1 - \frac{aT}{c} + \frac{4a^2 T^2}{15c^2} \quad (8.144)$$

Using this expression we can compute the distance  $\Delta a$  of templates in  $a$  for a mismatch  $\mu$  by means of

$$\Delta a = 2\sqrt{\frac{\mu}{\gamma_{aa}^{(2)}}} = \frac{c}{\nu T^2} \sqrt{\frac{720\mu}{\pi^2}} \mathcal{G}_2^{-\frac{1}{2}} \approx \frac{cP}{T^2} \sqrt{\frac{\mu}{0.013708}} \quad (8.145)$$

with the pulsar period  $P = 1/\nu$  and  $\mathcal{G}_2^{-\frac{1}{2}} \approx 1$  for normal pulsar orbits. The standard argument is not to allow the signal to drift by more than a single frequency bin over the

<sup>3</sup>If one chooses to use a perpendicular grid of  $(\nu_2, \nu_3)$ -values the computing costs can be reduced by re-using the contribution from  $\nu_2$  and recalculating only for new  $\nu_3$ .

observation time. This leads to  $\Delta a_{\text{standard}} = \frac{cP}{T^2}$  and therefore corresponds to a very strict mismatch of only 1.4% in  $a$ . This is because the standard argument does not take into account correlations between  $\nu$  and  $a$  that reduce the mismatch by compensating an offset in one parameter by an offset in the other.

### 8.8.4 Acceleration + jerk phase model

Here, the signal is described by a phase model with terms of up to cubic order in time  $t$ :

$$\Phi_3(t; a) = 2\pi\nu \left( t - \frac{a}{2c}t^2 - \frac{j}{6c}t^3 \right). \quad (8.146)$$

Parameters are frequency  $\nu$ , acceleration  $a$ , and jerk  $j$  which is the time derivative of the acceleration. Playing the same game of computing the metric in these parameters and projecting out the frequency  $\nu$  we find for the determinant of the projected metric

$$\det(\gamma^{(3)}) = \frac{\pi^4 T^{10} \nu^4}{2016000c^4} G_3(a, T), \quad (8.147)$$

with the multiplying function

$$G_3(a, T) = 1 - \frac{aT}{c} - \frac{3jT^2}{10c} + \frac{ajT^3}{6c^2} + \frac{4a^2T^2}{15c^2} + \frac{3j^2T^4}{112c^2}. \quad (8.148)$$

### 8.8.5 Parameter space of $a$ and $j$

From Equations (8.132) and (8.133) we can describe the parameter space of all possible values of  $a$  and  $j$  for circular orbits. We note that  $a$  and  $j$  can be rewritten in the compact form

$$a = \rho(\tau, \Omega, \psi) \sin(\psi) \quad \text{and} \quad j = \rho(\tau, \Omega, \psi) \Omega \cos(\psi), \quad (8.149)$$

with the pseudo-radius

$$\rho(\tau, \Omega, \psi) = \frac{\tau\Omega^2}{c(1 + \tau\Omega \cos(\psi))}. \quad (8.150)$$

Since  $\Omega\tau \ll 1$  for most orbits, this radius effectively is roughly constant in  $\psi$  for given  $\tau, \Omega$ . Points with varying  $\psi$  and constant  $\tau, \Omega$  lie on an ellipse in the space of  $a$  and  $j$ , we find

$$a^2 + \frac{j^2}{\Omega^2} = \rho_{\text{max}}^2, \quad (8.151)$$

where  $\rho_{\text{max}}$  is the largest value attained by  $\rho(\tau, \Omega, \psi)$ . For the fully coherent search Kepler's third law was used to set an  $\Omega$ -dependent constraint on  $\tau$  in the form

$$\tau \leq \alpha \left( \frac{Gm^3}{(M_{\text{pulsar}} + m)^2} \right)^{\frac{1}{3}} \Omega^{-\frac{2}{3}}, \quad (8.152)$$

where  $0 \leq \alpha \leq 1$  controls the fraction of solid inclination angle covered. For a given search, this expression reduces to  $\tau^3 \Omega^2 \leq R^3$  with some constant  $R$ .

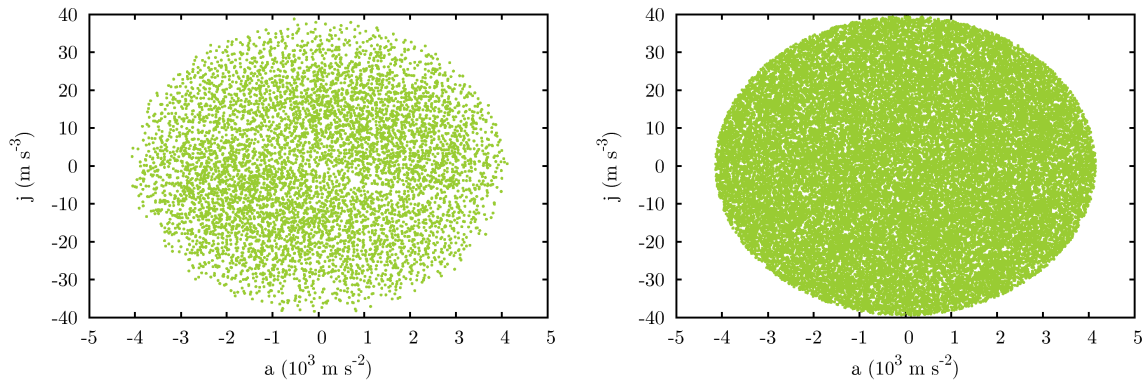


**Figure 8.3:** (Left) The templates from the search with the full orbital model (stochastic template bank) mapped into the space of  $a$  and  $j$  by Equations (8.132) and (8.133). (Right) random template bank, based on the acceleration and jerk term phase model, Equation (8.146)

### Example template banks

As an example, let us now look at a template bank in  $a, j$ -space for the Einstein@Home search on 268-s long Arecibo pointings designed to be similar to the search with the full phase model. The parameters for the search are:

$$f \leq 400 \text{ Hz}, \quad \alpha = 0.5, \quad M_{\text{pulsar}} \geq 1.2 M_{\odot}, \quad m \leq 1.6 M_{\odot}, \quad 660 \text{ s} \leq P_{\text{orb}} \leq 2700 \text{ s} \quad (8.153)$$

This is equivalent to  $\tau \leq 0.15255 \text{ lts} (660 \text{ s}/P_{\text{orb}})^{-\frac{2}{3}}$  and implies the following ranges for  $a$  and  $j$ :

$$|a| \leq 4144 \text{ ms}^{-2} \quad \text{and} \quad |j| \leq 39.46 \text{ ms}^{-3} \quad (8.154)$$

We modified the template bank generation codes for **a**) random template bank generation based on the determinant of the metric and numerical evaluation of the proper volume of the parameter space (`MCTemplates.c`, now `accel_jerk_templates.c`), and for **b**) numerical integration of the phase difference to compute the overlap of templates as well as the generation of stochastic template banks (`get_templatebank.c`, now `get_templatebank_accjerk.c`)

Figure 8.3 contains two diagrams: in the left panel, the templates from the search with the full orbital model were mapped into the space of  $a$  and  $j$  by Equations (8.132) and (8.133); in the right panel, a random template bank is shown, based on the polynomial phase model in  $a, j$ . The number of templates was adjusted based on the determinant of the metric to get the same nominal mismatch and the same covering as for the full orbital search. Integrating the square root of the determinant over the parameter space shown in the Figure yields a total number of  $\mathcal{N}_{\text{templ}} = 32475$  templates for a random template bank with a nominal mismatch of  $\mu^* = 0.3$  at a coverage of  $\eta = 0.9$ . Since the determinant of the metric (8.147) is almost constant in  $a$  and  $j$ , no variation in template density is visible in the right panel.

### 8.8.6 Signal recovery with polynomial phase models

Here, we want to briefly look at how well a search with a polynomial phase model up to cubic terms in  $t$  works in reconstructing signals from binary pulsars in circular orbits. For this purpose, we generate a stochastic template bank in the space of acceleration  $a$  and

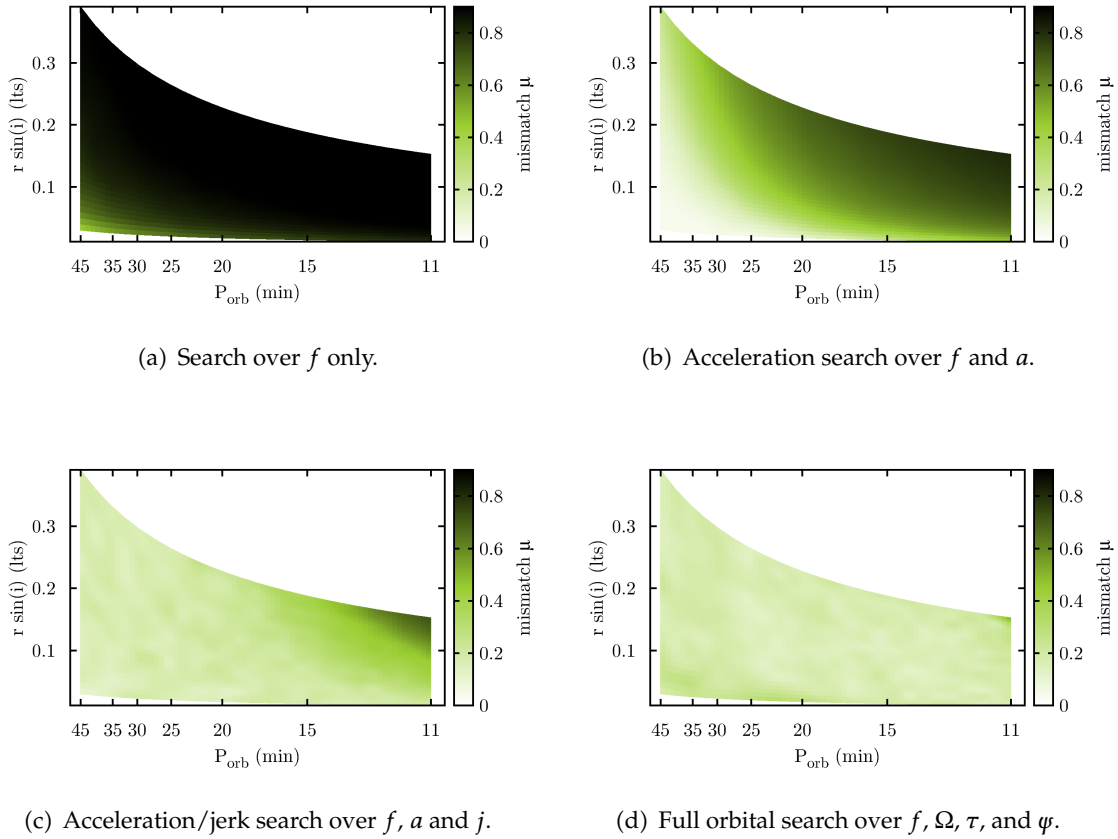


**Figure 8.4:** Recovery of signals from pulsars in circular orbits with different searches. Plots shows the mismatch averaged over 13 values of initial orbital phase. The signal is a single sinusoid at 400 Hz. The cloudy structure in c) and d) comes from using a stochastic template bank with coverage  $\eta = 0.9$ , which can have “holes” with slightly higher mismatch than the nominal one.

jerk  $j$  and also set up a grid of acceleration trial values following the usual prescription of  $\Delta a = cP/T^2$ .

Now, we generate fake sinuoidal signals modulated as if in 268-s circular orbits by choosing 4225 grid points in the three-dimensional orbital parameter space. For each generated signal, we search the resulting time series with the full circular orbit search by the usual Einstein@Home search code and a modified version that either performs: a) a FFT analysis only, b) an acceleration search, or c) a search over the stochastic template bank in acceleration and jerk. For each recovered signal we obtain the mismatch by comparing the recovered signal power with the theoretically expected value. For plotting purposes, we then average the obtained mismatch values over the grid values of initial orbital phase  $\varphi$ .

The resulting mismatch distributions in the two-dimensional parameter space of injected  $\Omega$  and  $\tau$  are shown in Figure 8.4. In the case where only an FFT search is applied it is clear that the loss in detection statistic is small only for the smallest  $\Omega$  and  $\tau$ . The acceleration search expands the recoverable part of the parameter space but still has major problems recovering signals in orbits for with larger  $\tau$ , basically for any  $P_{\text{orb}} \gtrsim 10T_{\text{obs}}$ . Adding the extra jerk term improves the situation even more. Now, in the parameter space considered

here, the mismatch is less than 30% for all orbits longer than  $\sim 4T_{\text{obs}}$ . For the very short orbital periods, the mismatch is still not acceptable for a search. By construction, the full orbital template bank achieves mismatches of less than 30% everywhere in the parameter space. The cloudy structure in the mismatch distribution appears because it is a stochastic template bank, which can have probabilistic holes with larger than average mismatch.

# Bibliography

- B. Abbott, R. Abbott, R. Adhikari, J. Agresti, P. Ajith, B. Allen, R. Amin, S. B. Anderson, W. G. Anderson, M. Arain, and et al. All-sky search for periodic gravitational waves in LIGO S4 data. *PRD*, 77(2):022001–+, Jan. 2008a. doi: 10.1103/PhysRevD.77.022001.
- B. Abbott et al. Limits on Gravitational-Wave Emission from Selected Pulsars Using LIGO Data. *Phys. Rev. Lett.*, 94(18):181103, May 2005. doi: 10.1103/PhysRevLett.94.181103.
- B. Abbott et al. Upper limits on gravitational wave emission from 78 radio pulsars. *Phys. Rev. D*, 76(4):042001, Aug 2007a. doi: 10.1103/PhysRevD.76.042001.
- B. Abbott et al. Beating the Spin-Down Limit on Gravitational Wave Emission from the Crab Pulsar. *ApJ Letters*, 683:L45–L49, Aug. 2008b. doi: 10.1086/591526.
- B. Abbott et al. Einstein@Home search for periodic gravitational waves in LIGO S4 data. *Phys. Rev. D*, 79(2):022001, Jan 2009. doi: 10.1103/PhysRevD.79.022001.
- B. P. Abbott, R. Abbott, R. Adhikari, P. Ajith, B. Allen, G. Allen, R. S. Amin, S. B. Anderson, W. G. Anderson, M. A. Arain, and et al. Einstein@Home search for periodic gravitational waves in early S5 LIGO data. *PRD*, 80(4):042003–+, Aug. 2009. doi: 10.1103/PhysRevD.80.042003.
- B. P. Abbott et al. Searches for periodic gravitational waves from unknown isolated sources and Scorpius X-1: Results from the second LIGO science run. *Phys. Rev. D*, 76(8):082001, Oct 2007b. doi: 10.1103/PhysRevD.76.082001.
- A. A. Abdo, M. Ackermann, M. Ajello, A. Allafort, E. Antolini, W. B. Atwood, M. Axelsson, L. Baldini, J. Ballet, G. Barbiellini, and et al. Fermi Large Area Telescope First Source Catalog. *ApJ Supplement*, 188:405–436, June 2010. doi: 10.1088/0067-0049/188/2/405.
- A. A. Abdo et al. The Fermi Gamma-Ray Space Telescope Discovers the Pulsar in the Young Galactic Supernova Remnant CTA 1. *Science*, 322:1218–, Nov. 2008. doi: 10.1126/science.1165572.
- A. A. Abdo et al. The First Fermi Large Area Telescope Catalog of Gamma-ray Pulsars. *The Astrophysical Journal Supplement Series*, 187(2):460, 2010. URL <http://stacks.iop.org/0067-0049/187/i=2/a=460>.
- A. Abramovici, W. E. Althouse, R. W. P. Drever, Y. Gursel, S. Kawamura, F. J. Raab, D. Shoemaker, L. Sievers, R. E. Spero, and K. S. Thorne. LIGO - The Laser Interferometer Gravitational-Wave Observatory. *Science*, 256:325–333, Apr. 1992. doi: 10.1126/science.256.5055.325.
- M. Abramowitz and I. A. Stegun. *Handbook of mathematical functions : with formulas, graphs, and mathematical tables*. 1984.

- S. L. Adler. Photon splitting and photon dispersion in a strong magnetic field. *Annals of Physics*, 67:599–647, 1971. doi: 10.1016/0003-4916(71)90154-0.
- B. Allen and J. Cordes. Possibilities for processing Arecibo PALFA data with Einstein@Home computing resources (*unpublished*), 2008.
- B. Allen, D. Anderson, C. Aulbert, N. D. R. Bhat, O. Bock, S. Bogdanov, A. Brazier, F. Camilo, D. J. Champion, S. Chatterjee, J. M. Cordes, F. Crawford, P. B. Demorest, J. S. Deneva, H. Fehrmann, P. C. C. Freire, M. E. Gonzalez, D. Hammer, J. W. T. Hessels, F. A. Jenet, L. Kasian, V. M. Kaspi, B. Knispel, M. Kramer, P. Lazarus, J. van Leeuwen, D. R. Lorimer, A. G. Lyne, B. Machenschalk, M. A. McLaughlin, C. Messenger, D. J. Nice, M. A. Papa, H. J. Pletsch, R. Prix, S. M. Ransom, X. Siemens, I. H. Stairs, B. W. Stappers, K. Stovall, and A. Venkataraman. The Einstein@Home search for radio pulsars and PSR J2007+2722 discovery. *in preparation*, 2011.
- D. P. Anderson et al. Designing a runtime system for volunteer computing. In *Proceedings of the 2006 ACM/IEEE Conference on Supercomputing*, page 126, 2006.
- N. Andersson. A New Class of Unstable Modes of Rotating Relativistic Stars. *ApJ*, 502: 708–+, Aug. 1998. doi: 10.1086/305919.
- N. Andersson. TOPICAL REVIEW: Gravitational waves from instabilities in relativistic stars. *Classical and Quantum Gravity*, 20:105–+, Apr. 2003.
- N. Andersson, K. D. Kokkotas, and V. Ferrari. The R-Mode Instability in Rotating Neutron Stars. *International Journal of Modern Physics D*, 10:381–441, 2001. doi: 10.1142/S0218271801001062.
- W. Andrew. *Handbook of semiconductor silicon technology*. Noyes Publication, 1990.
- A. M. Archibald, I. H. Stairs, S. M. Ransom, V. M. Kaspi, V. I. Kondratiev, D. R. Lorimer, M. A. McLaughlin, J. Boyles, J. W. T. Hessels, R. Lynch, J. van Leeuwen, M. S. E. Roberts, F. Jenet, D. J. Champion, R. Rosen, B. N. Barlow, B. H. Dunlap, and R. A. Remillard. A Radio Pulsar/X-ray Binary Link. *Science*, 324:1411–, June 2009. doi: 10.1126/science.1172740.
- M. Armano, M. Benedetti, J. Bogenstahl, D. Bortoluzzi, P. Bosetti, N. Brandt, A. Cavalleri, G. Ciani, I. Cristofolini, A. M. Cruise, K. Danzmann, I. Diepholz, G. Dixon, R. Dolesi, J. Fauste, L. Ferraioli, D. Fertin, W. Fichter, M. Freschi, A. García, C. García, A. Grynagier, F. Guzmán, E. Fitzsimons, G. Heinzl, M. Hewitson, D. Hollington, J. Hough, M. Hueller, D. Hoyland, O. Jennrich, B. Johlander, C. Killow, A. Lobo, D. Mance, I. Mateos, P. W. McNamara, A. Monsky, D. Nicolini, D. Nicolodi, M. Nofrarias, M. Perreux-Lloyd, E. Plagnol, G. D. Racca, J. Ramos-Castro, D. Robertson, J. Sanjuan, M. O. Schulte, D. N. A. Shaul, M. Smit, L. Stagnaro, F. Steier, T. J. Sumner, N. Tateo, D. Tombolato, G. Vischer, S. Vitale, G. Wanner, H. Ward, S. Waschke, V. Wand, P. Wass, W. J. Weber, T. Ziegler, and P. Zweifel. LISA Pathfinder: the experiment and the route to LISA. *Classical and Quantum Gravity*, 26 (9):094001–+, May 2009. doi: 10.1088/0264-9381/26/9/094001.
- Z. Arzoumanian, D. F. Chernoffs, and J. M. Cordes. The Velocity Distribution of Isolated Radio Pulsars. *Astrophys. J.*, 568:289–301, 2002. doi: 10.1086/338805.

- T. D. C. Ash, A. P. Reynolds, P. Roche, A. J. Norton, M. D. Still, and L. Morales-Rueda. The mass of the neutron star in Centaurus X-3. *MNRAS*, 307:357–364, Aug. 1999. doi: 10.1046/j.1365-8711.1999.02605.x.
- W. Baade and F. Zwicky. Cosmic Rays from Super-novae. *Proceedings of the National Academy of Science*, 20:259–263, May 1934. doi: 10.1073/pnas.20.5.259.
- D. C. Backer. Pulsar average wave forms and hollow-cone beam models. *ApJ*, 209:895–907, Nov. 1976. doi: 10.1086/154788.
- D. C. Backer. A pulsar timing tutorial and NRAO Green Bank observations of PSR 1257+12. In J. A. Phillips, S. E. Thorsett, & S. R. Kulkarni, editor, *Planets Around Pulsars*, volume 36 of *Astronomical Society of the Pacific Conference Series*, pages 11–18, Jan. 1993.
- D. C. Backer, J. M. Rankin, and D. B. Campbell. Orthogonal mode emission in geometric models of pulsar polarisation. *Nature*, 263:202–207, Sept. 1976. doi: 10.1038/263202a0.
- R. Balasubramanian, B. S. Sathyaprakash, and S. V. Dhurandhar. Gravitational waves from coalescing binaries: Detection strategies and Monte Carlo estimation of parameters. *Phys. Rev. D*, 53(6):3033–3055, Mar 1996. doi: 10.1103/PhysRevD.53.3033.
- G. Baym and C. Pethick. Physics of neutron stars. *Ann. Rev. Astron. Astrophys.*, 17:415–443, 1979. doi: 10.1146/annurev.aa.17.090179.002215.
- K. Belczynski, D. R. Lorimer, J. P. Ridley, and S. J. Curran. Double and single recycled pulsars: an evolutionary puzzle? *MNRAS*, 407:1245–1254, Sept. 2010. doi: 10.1111/j.1365-2966.2010.16970.x.
- D. L. Bertsch, K. T. S. Brazier, C. E. Fichtel, R. C. Hartman, S. D. Hunter, G. Kanbach, D. A. Kniffen, P. W. Kwok, Y. C. Lin, and J. R. Mattox. Pulsed high-energy gamma-radiation from Geminga (1E0630 + 178). *Nature*, 357:306–+, May 1992. doi: 10.1038/357306a0.
- N. D. R. Bhat, J. M. Cordes, F. Camilo, D. J. Nice, and D. R. Lorimer. Multifrequency Observations of Radio Pulse Broadening and Constraints on Interstellar Electron Density Microstructure. *ApJ*, 605:759–783, Apr. 2004. doi: 10.1086/382680.
- G. F. Bignami, P. A. Caraveo, A. De Luca, and S. Mereghetti. The magnetic field of an isolated neutron star from X-ray cyclotron absorption lines. *Nature*, 423:725–727, June 2003.
- L. Bildsten. Gravitational Radiation and Rotation of Accreting Neutron Stars. *ApJ Letters*, 501:L89+, July 1998. doi: 10.1086/311440.
- C. M. Bishop. *Neural Networks for Pattern Recognition*. Oxford University Press, 1995.
- M. Blaskiewicz, J. M. Cordes, and I. Wasserman. A relativistic model of pulsar polarization. *ApJ*, 370:643–669, Apr. 1991. doi: 10.1086/169850.
- O. Bock. Einsatz von Grafik-Co-Prozessoren und Volunteer Computing in der Datenanalyse: Massive Parallelisierung einer Anwendung zur Suche nach binären Radiopulsarsystemen, 2010.
- P. R. Brady and T. Creighton. Searching for periodic sources with LIGO. II. Hierarchical searches. *PRD*, 61(8):082001–+, Apr. 2000. doi: 10.1103/PhysRevD.61.082001.

- P. R. Brady, T. Creighton, C. Cutler, and B. F. Schutz. Searching for periodic sources with LIGO. *PRD*, 57:2101–2116, Feb. 1998. doi: 10.1103/PhysRevD.57.2101.
- A. Brinklow. *PhD Thesis*. PhD thesis, The University of Manchester, 1989.
- M. Burgay, N. D’Amico, A. Possenti, R. N. Manchester, A. G. Lyne, B. C. Joshi, M. A. McLaughlin, M. Kramer, J. M. Sarkissian, F. Camilo, V. Kalogera, C. Kim, and D. R. Lorimer. An increased estimate of the merger rate of double neutron stars from observations of a highly relativistic system. *Nature*, 426:531–533, Dec. 2003. doi: 10.1038/nature02124.
- F. Camilo, A. G. Lyne, R. N. Manchester, J. F. Bell, I. H. Stairs, N. D’Amico, V. M. Kaspi, A. Possenti, F. Crawford, and N. P. F. McKay. Discovery of Five Binary Radio Pulsars. *ApJ Letters*, 548:L187–L191, Feb. 2001. doi: 10.1086/319120.
- F. Camilo, D. Lorimer, and M. McLaughlin. Deep Multibeam Survey Processing, 2004. URL <http://astro.phys.wvu.edu/dmb/>.
- R. G. Carlberg and K. A. Innanen. Galactic chaos and the circular velocity at the sun. *Astron. J.*, 94:666–670, Sept. 1987. doi: 10.1086/114503.
- B. Caron, A. Dominjon, C. Drezen, R. Flaminio, X. Grave, F. Marion, L. Massonnet, C. Mehmél, R. Morand, B. Mours, V. Sannibale, M. Yvert, D. Babusci, S. Bellucci, S. Candusso, G. Giordano, G. Matone, J. Mackowski, L. Pinard, F. Barone, E. Calloni, L. Di Fiore, M. Flagiello, F. Garufi, A. Grado, M. Longo, M. Lops, S. Marano, L. Milano, S. Solimeno, V. Brisson, F. Cavalier, M. Davier, P. Hello, P. Heusse, P. Mann, Y. Acker, M. Barsuglia, B. Bhawal, F. Bondu, A. Brillet, H. Heitmann, J. Innocent, L. Latrach, C. N. Man, M. Pham-Tu, E. Tournier, M. Taubmann, J. Vinet, C. Boccara, P. Gleyzes, V. Lorientte, J. Roger, G. Cagnoli, L. Gammaitoni, J. Kovalik, F. Marchesoni, M. Punturo, M. Beccaria, M. Bernardini, E. Bougleux, S. Braccini, C. Bradaschia, G. Cella, A. Ciampa, E. Cuoco, G. Curci, R. DeFabbro, R. DeSalvo, A. Di Virgilio, D. Enard, I. Ferrante, F. Fidecaro, A. Giassi, A. Giazotto, L. Holloway, P. La Penna, G. Losurdo, S. Mancini, M. Mazzoni, F. Palla, H. Pan, D. Passuello, P. Pelfer, R. Poggiani, R. Stanga, A. Viceré, Z. Zhang, V. Ferrari, E. Majorana, P. Puppó, P. Rapagnani, and F. Ricci. The Virgo interferometer. *Classical and Quantum Gravity*, 14:1461–1469, June 1997. doi: 10.1088/0264-9381/14/6/011.
- D. Chakrabarty and E. H. Morgan. The two-hour orbit of a binary millisecond X-ray pulsar. *Nature*, 394:346–348, July 1998. doi: 10.1038/28561.
- D. J. Champion, S. M. Ransom, P. Lazarus, F. Camilo, C. Bassa, V. M. Kaspi, D. J. Nice, P. C. C. Freire, I. H. Stairs, J. van Leeuwen, B. W. Stappers, J. M. Cordes, J. W. T. Hessels, D. R. Lorimer, Z. Arzoumanian, D. C. Backer, N. D. R. Bhat, S. Chatterjee, I. Cognard, J. S. Deneva, C. Faucher-Giguère, B. M. Gaensler, J. Han, F. A. Jenet, L. Kasian, V. I. Kondratiev, M. Kramer, J. Lazio, M. A. McLaughlin, A. Venkataraman, and W. Vlemmings. An Eccentric Binary Millisecond Pulsar in the Galactic Plane. *Science*, 320:1309–, June 2008. doi: 10.1126/science.1157580.
- A. M. Chandler. *Pulsar Searches: from Radio to Gamma-Rays*. PhD thesis, California Institute of Technology, 2003. URL <http://www.srl.caltech.edu/personnel/amc/work/>.
- S. Chandrasekhar. The highly collapsed configurations of a stellar mass. *MNRAS*, 91:456–466, Mar. 1931.

- S. Chandrasekhar. The highly collapsed configurations of a stellar mass (Second paper). *MNRAS*, 95:207–225, Jan. 1935.
- G. Chodil, H. Mark, R. Rodrigues, F. Seward, C. D. Swift, W. A. Hiltner, G. Wallerstein, and E. J. Mannery. Spectral and Location Measurements of Several Cosmic X-Ray Sources Including a Variable Source in Centaurus. *Physical Review Letters*, 19:681–683, Sept. 1967. doi: 10.1103/PhysRevLett.19.681.
- T. R. Clifton, A. G. Lyne, A. W. Jones, J. McKenna, and M. Ashworth. A high-frequency survey of the galactic plane for young and distant pulsars. *MNRAS*, 254:177–184, Jan. 1992.
- J. J. Condon, W. D. Cotton, E. W. Greisen, Q. F. Yin, R. A. Perley, G. B. Taylor, and J. J. Broderick. The NRAO VLA Sky Survey. *AJ*, 115:1693–1716, May 1998. doi: 10.1086/300337.
- J. M. Cordes. private communication, 2009.
- J. M. Cordes and T. J. W. Lazio. NE2001.I. A New Model for the Galactic Distribution of Free Electrons and its Fluctuations. *ArXiv Astrophysics e-prints*, July 2002.
- J. M. Cordes and M. A. McLaughlin. Searches for Fast Radio Transients. *ApJ*, 596:1142–1154, Oct. 2003. doi: 10.1086/378231.
- J. M. Cordes, P. C. C. Freire, D. R. Lorimer, F. Camilo, D. J. Champion, D. J. Nice, R. Ramachandran, J. W. T. Hessels, W. Vlemmings, J. van Leeuwen, S. M. Ransom, N. D. R. Bhat, Z. Arzoumanian, M. A. McLaughlin, V. M. Kaspi, L. Kasian, J. S. Deneva, B. Reid, S. Chatterjee, J. L. Han, D. C. Backer, I. H. Stairs, A. A. Deshpande, and C. Faucher-Giguère. Arecibo Pulsar Survey Using ALFA. I. Survey Strategy and First Discoveries. *ApJ*, 637:446–455, Jan. 2006. doi: 10.1086/498335.
- J. M. Cordes et al. Arecibo Pulsar Survey Using ALFA. I. Survey Strategy and First Discoveries. *The Astrophysical Journal*, 637(1):446, 2006. URL <http://stacks.iop.org/0004-637X/637/i=1/a=446>.
- C. Cutler. An improved, “phase-relaxed” F-statistic for gravitational-wave data analysis. *ArXiv e-prints*, Apr. 2011.
- C. Cutler and D. I. Jones. Gravitational wave damping of neutron star wobble. *PRD*, 63(2):024002–+, Jan. 2001. doi: 10.1103/PhysRevD.63.024002.
- K. Danzmann. LISA - An ESA cornerstone mission for the detection and observation of gravitational waves. *Advances in Space Research*, 32:1233–1242, Oct. 2003. doi: 10.1016/S0273-1177(03)90323-1.
- K. Danzmann and A. Rüdiger. LISA technology - concept, status, prospects. *Classical and Quantum Gravity*, 20:1–+, May 2003. doi: 10.1088/0264-9381/20/10/301.
- K. Danzmann, H. Lück, A. Rüdiger, R. Schilling, M. Schrempel, W. Winkler, J. Hough, G. P. Newton, N. A. Robertson, H. Ward, A. M. Campbell, J. E. Logan, D. I. Robertson, K. A. Strain, J. R. J. Bennett, V. Kose, M. Kühne, B. F. Schutz, D. Nicholson, J. Shuttleworth, H. Welling, P. Aufmuth, R. Rinkleff, A. Tünnermann, and B. Willke. GEO 600 - a 600 m

- laser interferometric gravitational wave antenna. In E. Coccia, G. Pizzella, & F. Ronga, editor, *First Edoardo Amaldi Conference on Gravitational Wave Experiments*, pages 100–111, 1995.
- J. K. Daugherty and A. K. Harding. Pair production in superstrong magnetic fields. *ApJ*, 273:761–773, Oct. 1983. doi: 10.1086/161411.
- J. K. Daugherty and A. K. Harding. Compton scattering in strong magnetic fields. *ApJ*, 309: 362–371, Oct. 1986. doi: 10.1086/164608.
- O. C. de Jager. Lower Limits on Pulsar Pair Production Multiplicities from H.E.S.S. Observations of Pulsar Wind Nebulae. *ApJ*, 658:1177–1182, Apr. 2007. doi: 10.1086/511950.
- P. B. Demorest, T. Pennucci, S. M. Ransom, M. S. E. Roberts, and J. W. T. Hessels. A two-solar-mass neutron star measured using Shapiro delay. *Nature*, 467:1081–1083, Oct. 2010. doi: 10.1038/nature09466.
- J. S. Deneva, J. M. Cordes, M. A. McLaughlin, D. J. Nice, D. R. Lorimer, F. Crawford, N. D. R. Bhat, F. Camilo, D. J. Champion, P. C. C. Freire, S. Edel, V. I. Kondratiev, J. W. T. Hessels, F. A. Jenet, L. Kasian, V. M. Kaspi, M. Kramer, P. Lazarus, S. M. Ransom, I. H. Stairs, B. W. Stappers, J. van Leeuwen, A. Brazier, A. Venkataraman, J. A. Zollweg, and S. Bogdanov. Arecibo Pulsar Survey Using ALFA: Probing Radio Pulsar Intermittency And Transients. *ApJ*, 703:2259–2274, Oct. 2009. doi: 10.1088/0004-637X/703/2/2259.
- A. Dowd, W. Sisk, and J. Hagen. WAPP — Wideband Arecibo Pulsar Processor. In M. Kramer, N. Wex, & R. Wielebinski, editor, *IAU Colloq. 177: Pulsar Astronomy - 2000 and Beyond*, volume 202 of *Astronomical Society of the Pacific Conference Series*, pages 275–+, 2000.
- R. P. Eatough. *A search for relativistic binary pulsars in the Galactic plane*. PhD thesis, University of Manchester, 2009.
- R. P. Eatough, N. Molkenhain, M. Kramer, A. Noutsos, M. J. Keith, B. W. Stappers, and A. G. Lyne. Selection of radio pulsar candidates using artificial neural networks. *MNRAS*, 407: 2443–2450, Oct. 2010. doi: 10.1111/j.1365-2966.2010.17082.x.
- T. Erber. High-Energy Electromagnetic Conversion Processes in Intense Magnetic Fields. *Reviews of Modern Physics*, 38:626–659, Oct. 1966. doi: 10.1103/RevModPhys.38.626.
- R. D. Ferdman, I. H. Stairs, M. Kramer, M. A. McLaughlin, D. R. Lorimer, D. J. Nice, R. N. Manchester, G. Hobbs, A. G. Lyne, F. Camilo, A. Possenti, P. B. Demorest, I. Cognard, G. Desvignes, G. Theureau, A. Faulkner, and D. C. Backer. A Precise Mass Measurement of the Intermediate-Mass Binary Pulsar PSR J1802 - 2124. *ApJ*, 711:764–771, Mar. 2010. doi: 10.1088/0004-637X/711/2/764.
- I. Foster. Globus Toolkit Version 4: Software for Service-Oriented Systems. In *IFIP International Conference on Network and Parallel Computing*, pages 2–13. Springer Verlag, 2006. URL <http://www.globus.org/toolkit/>.
- P. C. Freire, M. Kramer, and A. G. Lyne. Determination of the orbital parameters of binary pulsars. *MNRAS*, 322:885–890, Apr. 2001a. doi: 10.1046/j.1365-8711.2001.04200.x.

- P. C. Freire, M. Kramer, A. G. Lyne, F. Camilo, R. N. Manchester, and N. D'Amico. Detection of Ionized Gas in the Globular Cluster 47 Tucanae. *ApJ Letters*, 557:L105–L108, Aug. 2001b. doi: 10.1086/323248.
- P. C. C. Freire. Possible tilings for non-drifting ALFA surveys. *ALFA Tech. Memo 2003-07; Arecibo: NAIC*, 2003. URL <http://www.naic.edu/~pfreire/tiling/>.
- P. C. C. Freire and N. Wex. The orthometric parametrization of the Shapiro delay and an improved test of general relativity with binary pulsars. *MNRAS*, 409:199–212, Nov. 2010. doi: 10.1111/j.1365-2966.2010.17319.x.
- P. C. C. Freire, S. M. Ransom, and Y. Gupta. Timing the Eccentric Binary Millisecond Pulsar in NGC 1851. *ApJ*, 662:1177–1182, June 2007. doi: 10.1086/517904.
- P. C. C. Freire, C. G. Bassa, N. Wex, I. H. Stairs, D. J. Champion, S. M. Ransom, P. Lazarus, V. M. Kaspi, J. W. T. Hessels, M. Kramer, J. M. Cordes, J. P. W. Verbiest, P. Podsiadlowski, D. J. Nice, J. S. Deneva, D. R. Lorimer, B. W. Stappers, M. A. McLaughlin, and F. Camilo. On the nature and evolution of the unique binary pulsar J1903+0327. *MNRAS*, pages 275–+, Mar. 2011. doi: 10.1111/j.1365-2966.2010.18109.x.
- J. L. Friedman and S. M. Morsink. Axial Instability of Rotating Relativistic Stars. *ApJ*, 502: 714–+, Aug. 1998. doi: 10.1086/305920.
- M. Frigo and S. G. Johnson. The Design and Implementation of FFTW3. *Proceedings of the IEEE*, 93(2):216–231, 2005. Special issue on “Program Generation, Optimization, and Platform Adaptation”.
- M. Frigo and S. G. Johnson., 2010. URL <http://www.fftw.org/>.
- B. M. Gaensler, M. McLaughlin, S. Reynolds, K. Borkowski, N. Rea, A. Possenti, G. Israel, M. Burgay, F. Camilo, S. Chatterjee, M. Kramer, A. Lyne, and I. Stairs. Chandra smells a RRAT: X-ray Detection of a Rotating Radio Transient. *Astrophysics and Space Science*, 308: 95–99, Apr. 2007. doi: 10.1007/s10509-007-9352-8.
- M. e. a. Galassi. GNU Scientific Library Reference Manual - Third Edition, 2009. URL <http://www.gnu.org/software/gsl/>.
- R. T. Gangadhara and Y. Gupta. Understanding the Radio Emission Geometry of PSR B0329+54. *ApJ*, 555:31–39, July 2001. doi: 10.1086/321439.
- R. Giacconi, H. Gursky, E. Kellogg, E. Schreier, and H. Tananbaum. Discovery of Periodic X-Ray Pulsations in Centaurus X-3 from UHURU. *ApJ Letters*, 167:L67+, July 1971. doi: 10.1086/180762.
- J. Gil, P. Gronkowski, and W. Rudnicki. Geometry of the emission region of PSR 0950+08. *A&A*, 132:312–316, Mar. 1984.
- J. A. Gil, J. Kijak, and J. H. Seiradakis. On the Two-Dimensional Structure of Pulsar Beams. *A&A*, 272:268–+, May 1993.
- N. K. Glendenning. Limiting rotational period of neutron stars. *PRD*, 46:4161–4168, Nov. 1992. doi: 10.1103/PhysRevD.46.4161.

## BIBLIOGRAPHY

---

- T. Gold. Rotating Neutron Stars as the Origin of the Pulsating Radio Sources. *Nature*, 218: 731–732, May 1968. doi: 10.1038/218731a0.
- P. Goldreich and W. H. Julian. Pulsar Electrodynamics. *ApJ*, 157:869–+, Aug. 1969. doi: 10.1086/150119.
- P. C. Gregory. *Bayesian Logical Data Analysis for the Physical Sciences: A Comparative Approach with 'Mathematica' Support*. Cambridge University Press, 2005.
- H. M. Guenther, S. J. Wolk, R. A. Gutermuth, B. Spitzbart, T. L. Bourke, I. Pillitteri, and K. DeRose. IRAS 20050+2720: Anatomy of a young stellar cluster. *ArXiv e-prints*, Dec. 2010.
- J. P. Halpern and E. V. Gotthelf. Spin-Down Measurement of PSR J1852+0040 in Kesteven 79: Central Compact Objects as Anti-Magnetars. *The Astrophysical Journal*, 709(1):436, 2010. URL <http://stacks.iop.org/0004-637X/709/i=1/a=436>.
- J. P. Halpern and S. S. Holt. Discovery of soft X-ray pulsations from the gamma-ray source Geminga. *Nature*, 357:222–224, May 1992. doi: 10.1038/357222a0.
- J. L. Han and R. N. Manchester. The shape of pulsar radio beams. *MNRAS*, 320:L35–L39, Jan. 2001. doi: 10.1046/j.1365-8711.2001.04146.x.
- I. W. Harry, B. Allen, and B. S. Sathyaprakash. Stochastic template placement algorithm for gravitational wave data analysis. *Phys. Rev. D*, 80(10):104014, Nov 2009. doi: 10.1103/PhysRevD.80.104014.
- W. K. Hastings. Monte Carlo sampling methods using Markov chains and their applications. *Biometrika*, 57(1):97–109, 1970. doi: 10.1093/biomet/57.1.97. URL <http://biomet.oxfordjournals.org/content/57/1/97.abstract>.
- J. W. T. Hessels, S. M. Ransom, I. H. Stairs, P. C. C. Freire, V. M. Kaspi, and F. Camilo. A Radio Pulsar Spinning at 716 Hz. *Science*, 311:1901–1904, Mar. 2006. doi: 10.1126/science.1123430.
- A. Hewish, S. J. Bell, J. D. H. Pilkington, P. F. Scott, and R. A. Collins. Observation of a Rapidly Pulsating Radio Source. *Nature*, 217:709–713, Feb. 1968. doi: 10.1038/217709a0.
- J. A. Hibschan and J. Arons. Polarization Sweeps in Rotation-powered Pulsars. *ApJ*, 546: 382–393, Jan. 2001a. doi: 10.1086/318224.
- J. A. Hibschan and J. Arons. Pair Multiplicities and Pulsar Death. *ApJ*, 554:624–635, June 2001b. doi: 10.1086/321378.
- J. A. Hibschan and J. Arons. Pair Production Multiplicities in Rotation-powered Pulsars. *ApJ*, 560:871–884, Oct. 2001c. doi: 10.1086/323069.
- G. Hobbs, D. R. Lorimer, A. G. Lyne, and M. Kramer. A statistical study of 233 pulsar proper motions. *Mon. Not. Roy. Astron. Soc.*, 360:974–992, 2005. doi: 10.1111/j.1365-2966.2005.09087.x.
- C. J. Horowitz and K. Kadau. Breaking Strain of Neutron Star Crust and Gravitational Waves. *Physical Review Letters*, 102(19):191102–+, May 2009. doi: 10.1103/PhysRevLett.102.191102.

- F. Hoyle, J. V. Narlikar, and J. A. Wheeler. Electromagnetic Waves from Very Dense Stars. *Nature*, 203:914–916, Aug. 1964. doi: 10.1038/203914a0.
- S. A. Hughes. LISA sources and science. *ArXiv e-prints*, Nov. 2007.
- R. A. Hulse and J. H. Taylor. Discovery of a pulsar in a binary system. *ApJ Letters*, 195: L51–L53, Jan. 1975a. doi: 10.1086/181708.
- R. A. Hulse and J. H. Taylor. A deep sample of new pulsars and their spatial extent in the galaxy. *ApJ Letters*, 201:L55–L59, Oct. 1975b. doi: 10.1086/181941.
- H. M. Johnston and S. R. Kulkarni. On the detectability of pulsars in close binary systems. *ApJ*, 368:504–514, Feb. 1991. doi: 10.1086/169715.
- S. Johnston, D. R. Lorimer, P. A. Harrison, M. Bailes, A. G. Lyne, J. F. Bell, V. M. Kaspi, R. N. Manchester, N. D’Amico, and L. Nicastro. Discovery of a very bright, nearby binary millisecond pulsar. *Nature*, 361:613–615, Feb. 1993. doi: 10.1038/361613a0.
- D. I. Jones. Gravitational wave emission from rotating superfluid neutron stars. *MNRAS*, 402:2503–2519, Mar. 2010. doi: 10.1111/j.1365-2966.2009.16059.x.
- D. I. Jones and N. Andersson. Gravitational waves from freely precessing neutron stars. *MNRAS*, 331:203–220, Mar. 2002. doi: 10.1046/j.1365-8711.2002.05180.x.
- V. Kalogera, C. Kim, D. R. Lorimer, M. Burgay, N. D’Amico, A. Possenti, R. N. Manchester, A. G. Lyne, B. C. Joshi, M. A. McLaughlin, M. Kramer, J. M. Sarkissian, and F. Camilo. The Cosmic Coalescence Rates for Double Neutron Star Binaries. *ApJ Letters*, 601:L179–L182, Feb. 2004a. doi: 10.1086/382155.
- V. Kalogera, C. Kim, D. R. Lorimer, M. Burgay, N. D’Amico, A. Possenti, R. N. Manchester, A. G. Lyne, B. C. Joshi, M. A. McLaughlin, M. Kramer, J. M. Sarkissian, and F. Camilo. Erratum: “The Cosmic Coalescence Rates for Double Neutron Star Binaries” (</abs/2004ApJ...601L.179K>)>ApJ, 601, L179 [2004]</A>. *ApJ Letters*, 614:L137–L138, Oct. 2004b. doi: 10.1086/425868.
- A. Karastergiou and S. Johnston. An empirical model for the beams of radio pulsars. *MNRAS*, 380:1678–1684, Oct. 2007. doi: 10.1111/j.1365-2966.2007.12237.x.
- R. Karuppusamy, B. Stappers, and W. van Straten. PuMa-II: A Wide Band Pulsar Machine for the Westerbork Synthesis Radio Telescope. *Publications of the Astronomical Society of the Pacific*, 120:191–202, Feb. 2008. doi: 10.1086/528699.
- E. F. Keane and M. Kramer. On the birthrates of Galactic neutron stars. *MNRAS*, 391: 2009–2016, Dec. 2008. doi: 10.1111/j.1365-2966.2008.14045.x.
- J. Kijak and J. Gil. Structure of pulsar beams: Conal versus patchy. *A&A*, 392:189–196, Sept. 2002. doi: 10.1051/0004-6361:20020946.
- B. Knispel and B. Allen. Blandford’s argument: The strongest continuous gravitational wave signal. *Phys. Rev. D*, 78(4):044031, Aug 2008. doi: 10.1103/PhysRevD.78.044031.

- B. Knispel, B. Allen, J. M. Cordes, J. S. Deneva, D. Anderson, C. Aulbert, N. D. R. Bhat, O. Bock, S. Bogdanov, A. Brazier, F. Camilo, D. J. Champion, S. Chatterjee, F. Crawford, P. B. Demorest, H. Fehrmann, P. C. C. Freire, M. E. Gonzalez, D. Hammer, J. W. T. Hessels, F. A. Jenet, L. Kasian, V. M. Kaspi, M. Kramer, P. Lazarus, J. van Leeuwen, D. R. Lorimer, A. G. Lyne, B. Machenschalk, M. A. McLaughlin, C. Messenger, D. J. Nice, M. A. Papa, H. J. Pletsch, R. Prix, S. M. Ransom, X. Siemens, I. H. Stairs, B. W. Stappers, K. Stovall, and A. Venkataraman. Pulsar Discovery by Global Volunteer Computing. *Science*, 329: 1305–, Sept. 2010. doi: 10.1126/science.1195253.
- M. M. Komesaroff. Possible Mechanism for the Pulsar Radio Emission. *Nature*, 225:612–614, Feb. 1970. doi: 10.1038/225612a0.
- M. Konacki and A. Wolszczan. Masses and Orbital Inclinations of Planets in the PSR B1257+12 System. *ApJ Letters*, 591:L147–L150, July 2003. doi: 10.1086/377093.
- M. Kramer and N. Wex. TOPICAL REVIEW: The double pulsar system: a unique laboratory for gravity. *Classical and Quantum Gravity*, 26(7):073001–+, Apr. 2009. doi: 10.1088/0264-9381/26/7/073001.
- M. Kramer, R. Wielebinski, A. Jessner, J. A. Gil, and J. H. Seiradakis. Geometrical analysis of average pulsar profiles using multi-component Gaussian FITS at several frequencies. I. Method and analysis. *Astron. Astrophys. Suppl.*, 107:515–526, Nov. 1994.
- M. Kramer, A. G. Lyne, G. Hobbs, O. Löhmer, P. Carr, C. Jordan, and A. Wolszczan. The Proper Motion, Age, and Initial Spin Period of PSR J0538+2817 in S147. *ApJ L*, 593:L31–L34, Aug. 2003. doi: 10.1086/378082.
- M. Kramer, A. G. Lyne, J. T. O’Brien, C. A. Jordan, and D. R. Lorimer. A Periodically Active Pulsar Giving Insight into Magnetospheric Physics. *Science*, 312:549–551, Apr. 2006a. doi: 10.1126/science.1124060.
- M. Kramer, I. H. Stairs, R. N. Manchester, M. A. McLaughlin, A. G. Lyne, R. D. Ferdman, M. Burgay, D. R. Lorimer, A. Possenti, N. D’Amico, J. M. Sarkissian, G. B. Hobbs, J. E. Reynolds, P. C. C. Freire, and F. Camilo. Tests of General Relativity from Timing the Double Pulsar. *Science*, 314:97–102, Oct. 2006b. doi: 10.1126/science.1132305.
- K. Kuijken and G. Gilmore. The Mass Distribution in the Galactic Disc - Part III - the Local Volume Mass Density. *Mon. Not. Roy. Astron. Soc.*, 239:651–664, Aug. 1989.
- L. D. Landau and E. M. Lifshitz. *Lehrbuch der Theoretischen Physik*. Verlag Harri Deutsch, 1997.
- C. Lange, F. Camilo, N. Wex, M. Kramer, D. C. Backer, A. G. Lyne, and O. Doroshenko. Precision timing measurements of PSR J1012+5307. *MNRAS*, 326:274–282, Sept. 2001. doi: 10.1046/j.1365-8711.2001.04606.x.
- J. M. Lattimer and M. Prakash. Neutron Star Structure and the Equation of State. *ApJ*, 550: 426–442, Mar. 2001. doi: 10.1086/319702.
- J. M. Lattimer and M. Prakash. The Physics of Neutron Stars. *Science*, 304:536–542, Apr. 2004. doi: 10.1126/science.1090720.

- J. M. Lattimer, M. Prakash, D. Masak, and A. Yahil. Rapidly rotating pulsars and the equation of state. *ApJ*, 355:241–254, May 1990. doi: 10.1086/168758.
- D. A. Lloyd. Model atmospheres and thermal spectra of magnetized neutron stars. *ArXiv Astrophysics e-prints*, Mar. 2003.
- D. Lorimer, 2002. URL <http://sigproc.sourceforge.net/>.
- D. Lorimer and M. Kramer. *Handbook of Pulsar Astronomy*. Cambridge University Press, 2005.
- D. R. Lorimer. Binary and Millisecond Pulsars. *Living Reviews in Relativity*, 11:8–+, Nov. 2008.
- D. R. Lorimer, A. J. Faulkner, A. G. Lyne, R. N. Manchester, M. Kramer, M. A. McLaughlin, G. Hobbs, A. Possenti, I. H. Stairs, F. Camilo, M. Burgay, N. D’Amico, A. Corongiu, and F. Crawford. The Parkes Multibeam Pulsar Survey - VI. Discovery and timing of 142 pulsars and a Galactic population analysis. *MNRAS*, 372:777–800, Oct. 2006. doi: 10.1111/j.1365-2966.2006.10887.x.
- A. G. Lyne and F. Graham-Smith. *Pulsar Astronomy*. Cambridge University Press, July 2005.
- A. G. Lyne and R. N. Manchester. The shape of pulsar radio beams. *MNRAS*, 234:477–508, Oct. 1988.
- A. G. Lyne, A. Brinklow, J. Middleditch, S. R. Kulkarni, and D. C. Backer. The discovery of a millisecond pulsar in the globular cluster M28. *Nature*, 328:399–401, July 1987. doi: 10.1038/328399a0.
- A. G. Lyne, F. Camilo, R. N. Manchester, J. F. Bell, V. M. Kaspi, N. D’Amico, N. P. F. McKay, F. Crawford, D. J. Morris, D. C. Sheppard, and I. H. Stairs. The Parkes Multibeam Pulsar Survey: PSR J1811-1736, a pulsar in a highly eccentric binary system. *MNRAS*, 312:698–702, Mar. 2000. doi: 10.1046/j.1365-8711.2000.03231.x.
- A. G. Lyne, M. Burgay, M. Kramer, A. Possenti, R. N. Manchester, F. Camilo, M. A. McLaughlin, D. R. Lorimer, N. D’Amico, B. C. Joshi, J. Reynolds, and P. C. C. Freire. A Double-Pulsar System: A Rare Laboratory for Relativistic Gravity and Plasma Physics. *Science*, 303:1153–1157, Feb. 2004. doi: 10.1126/science.1094645.
- G. M. Manca and M. Vallisneri. Cover art: Issues in the metric-guided and metric-less placement of random and stochastic template banks. *PRD*, 81(2):024004–+, Jan. 2010. doi: 10.1103/PhysRevD.81.024004.
- R. N. Manchester, A. G. Lyne, F. Camilo, J. F. Bell, V. M. Kaspi, N. D’Amico, N. P. F. McKay, F. Crawford, I. H. Stairs, A. Possenti, M. Kramer, and D. C. Sheppard. The Parkes multi-beam pulsar survey - I. Observing and data analysis systems, discovery and timing of 100 pulsars. *MNRAS*, 328:17–35, Nov. 2001. doi: 10.1046/j.1365-8711.2001.04751.x.
- R. N. Manchester, G. B. Hobbs, A. Teoh, and M. Hobbs. The Australia Telescope National Facility Pulsar Catalogue. *AJ*, 129:1993–2006, Apr. 2005. doi: 10.1086/428488.
- M. Mayor and D. Queloz. A Jupiter-mass companion to a solar-type star. *Nature*, 378: 355–359, Nov. 1995. doi: 10.1038/378355a0.

## BIBLIOGRAPHY

---

- M. A. McLaughlin, A. G. Lyne, D. R. Lorimer, M. Kramer, A. J. Faulkner, R. N. Manchester, J. M. Cordes, F. Camilo, A. Possenti, I. H. Stairs, G. Hobbs, N. D'Amico, M. Burgay, and J. T. O'Brien. Transient radio bursts from rotating neutron stars. *Nature*, 439:817–820, Feb. 2006. doi: 10.1038/nature04440.
- J. Meeus. *Astronomical algorithms*. 1991.
- A. Melatos and D. J. B. Payne. Gravitational Radiation from an Accreting Millisecond Pulsar with a Magnetically Confined Mountain. *ApJ*, 623:1044–1050, Apr. 2005. doi: 10.1086/428600.
- C. Messenger. Estimating the number of templates for a search for short period binary systems (*unpublished*), 2008.
- C. Messenger, R. Prix, and M. A. Papa. Random template banks and relaxed lattice coverings. *Phys. Rev. D*, 79(10):104017, May 2009. doi: 10.1103/PhysRevD.79.104017.
- N. Metropolis, A. W. Rosenbluth, M. N. Rosenbluth, A. H. Teller, and E. Teller. Equation of State Calculations by Fast Computing Machines. *JCP*, 21:1087–1092, June 1953. doi: 10.1063/1.1699114.
- M. C. Miller. Model atmospheres for neutron stars. *MNRAS*, 255:129–145, Mar. 1992.
- D. Mitra and J. M. Rankin. Toward an Empirical Theory of Pulsar Emission. VII. On the Spectral Behavior of Conal Beam Radii and Emission Heights. *ApJ*, 577:322–336, Sept. 2002. doi: 10.1086/342136.
- G. E. Moore. Cramming more components onto integrated circuits. *Electronics*, 38(8), Apr. 1965. URL [ftp://download.intel.com/museum/Moores\\_Law/Articles-Press\\_Releases/Gordon\\_Moore\\_1965\\_Article.pdf](ftp://download.intel.com/museum/Moores_Law/Articles-Press_Releases/Gordon_Moore_1965_Article.pdf).
- D. J. Nice, A. S. Fruchter, and J. H. Taylor. A Search for Fast Pulsars along the Galactic Plane. *ApJ*, 449:156–+, Aug. 1995. doi: 10.1086/176041.
- J. R. Oppenheimer and G. M. Volkoff. On Massive Neutron Cores. *Physical Review*, 55:374–381, Feb. 1939. doi: 10.1103/PhysRev.55.374.
- B. J. Owen. Search templates for gravitational waves from inspiraling binaries: Choice of template spacing. *Phys. Rev. D*, 53(12):6749–6761, Jun 1996. doi: 10.1103/PhysRevD.53.6749.
- B. J. Owen. Maximum Elastic Deformations of Compact Stars with Exotic Equations of State. *Physical Review Letters*, 95(21):211101–+, Nov. 2005. doi: 10.1103/PhysRevLett.95.211101.
- B. J. Owen and B. S. Sathyaprakash. Matched filtering of gravitational waves from inspiraling compact binaries: Computational cost and template placement. *Phys. Rev. D*, 60(2):022002, Jun 1999. doi: 10.1103/PhysRevD.60.022002.
- B. J. Owen, L. Lindblom, C. Cutler, B. F. Schutz, A. Vecchio, and N. Andersson. Gravitational waves from hot young rapidly rotating neutron stars. *PRD*, 58(8):084020–+, Oct. 1998. doi: 10.1103/PhysRevD.58.084020.

- F. Pacini. Energy Emission from a Neutron Star. *Nature*, 216:567–568, Nov. 1967. doi: 10.1038/216567a0.
- F. Pacini. Rotating Neutron Stars, Pulsars and Supernova Remnants. *Nature*, 219:145–146, July 1968. doi: 10.1038/219145a0.
- F. Pacini and E. E. Salpeter. Some Models for Pulsed Radio Sources. *Nature*, 218:733–734, May 1968. doi: 10.1038/218733a0.
- B. Paczynski. A test of the galactic origin of gamma-ray bursts. *Astrophys. J.*, 348:485–494, Jan. 1990. doi: 10.1086/168257.
- C. Palomba. Simulation of a population of isolated neutron stars evolving through the emission of gravitational waves. *Mon. Not. Roy. Astron. Soc.*, 359:1150–1164, 2005. doi: 10.1111/j.1365-2966.2005.08975.x/abs/.
- P. C. Peters. Gravitational Radiation and the Motion of Two Point Masses. *Physical Review*, 136:1224–1232, Nov. 1964. doi: 10.1103/PhysRev.136.B1224.
- E. S. Phinney. Pulsars as Probes of Newtonian Dynamical Systems. *Royal Society of London Philosophical Transactions Series A*, 341:39–75, Oct. 1992. doi: 10.1098/rsta.1992.0084.
- D. Pines and M. A. Alpar. Superfluidity in neutron stars. *Nature*, 316:27–32, July 1985. doi: 10.1038/316027a0.
- H. J. Pletsch. Parameter-space correlations of the optimal statistic for continuous gravitational-wave detection. *PRD*, 78(10):102005–+, Nov. 2008. doi: 10.1103/PhysRevD.78.102005.
- H. J. Pletsch. *Data Analysis for Continuous Gravitational Waves – Deepest All-Sky Surveys*. PhD thesis, Leibniz Universität Hannover, 2009.
- H. J. Pletsch. private communication, 2010.
- H. J. Pletsch and B. Allen. Exploiting Large-Scale Correlations to Detect Continuous Gravitational Waves. *Physical Review Letters*, 103(18):181102–+, Oct. 2009. doi: 10.1103/PhysRevLett.103.181102.
- S. B. Popov, M. Colpi, A. Treves, R. Turolla, V. M. Lipunov, and M. E. Prokhorov. The Neutron Star Census. *The Astrophysical Journal*, 530(2):896, 2000. URL <http://stacks.iop.org/0004-637X/530/i=2/a=896>.
- W. H. Press, S. A. Teukolsky, W. T. Vetterling, and B. P. Flannery. *Numerical recipes in C. The art of scientific computing*. Cambridge University Press, 1992.
- R. Prix. Template-based searches for gravitational waves: efficient lattice covering of flat parameter spaces. *Classical and Quantum Gravity*, 24:481–+, Oct. 2007. doi: 10.1088/0264-9381/24/19/S11.
- V. Radhakrishnan and D. J. Cooke. Magnetic Poles and the Polarization Structure of Pulsar Radiation. *ApJ Letters*, 3:225–+, 1969.

## BIBLIOGRAPHY

---

- V. Radhakrishnan and J. M. Rankin. Toward an empirical theory of pulsar emission. V - On the circular polarization in pulsar radiation. *ApJ*, 352:258–266, Mar. 1990. doi: 10.1086/168531.
- J. M. Rankin. Toward an empirical theory of pulsar emission. I Morphological taxonomy. *ApJ*, 274:333–368, Nov. 1983a. doi: 10.1086/161450.
- J. M. Rankin. Toward an Empirical Theory of Pulsar Emission - Part Two - on the Spectral Behavior of Component Width. *ApJ*, 274:359–+, Nov. 1983b. doi: 10.1086/161451.
- J. M. Rankin. Toward an empirical theory of pulsar emission. III - Mode changing, drifting subpulses, and pulse nulling. *ApJ*, 301:901–922, Feb. 1986. doi: 10.1086/163955.
- J. M. Rankin. Toward an empirical theory of pulsar emission. IV - Geometry of the core emission region. *ApJ*, 352:247–257, Mar. 1990. doi: 10.1086/168530.
- J. M. Rankin. Toward an empirical theory of pulsar emission. VI - The geometry of the conal emission region. *ApJ*, 405:285–297, Mar. 1993a. doi: 10.1086/172361.
- J. M. Rankin. Toward an empirical theory of pulsar emission. VI - The geometry of the conal emission region: Appendix and tables. *ApJ Supplement*, 85:145–161, Mar. 1993b. doi: 10.1086/191758.
- J. M. Rankin and R. Ramachandran. Toward an Empirical Theory of Pulsar Emission. VIII. Subbeam Circulation and the Polarization-Modal Structure of Conal Beams. *ApJ*, 590:411–423, June 2003. doi: 10.1086/374884.
- S. M. Ransom. *New Search Techniques for Binary Pulsars*. PhD thesis, Harvard University, 2001. URL [http://www.cv.nrao.edu/%7Esransom/ransom\\_thesis\\_2001.pdf](http://www.cv.nrao.edu/%7Esransom/ransom_thesis_2001.pdf).
- S. M. Ransom, S. S. Eikenberry, and J. Middleditch. Fourier Techniques for Very Long Astrophysical Time-Series Analysis. *The Astronomical Journal*, 124(3):1788, 2002. URL <http://stacks.iop.org/1538-3881/124/i=3/a=1788>.
- S. M. Ransom, J. M. Cordes, and S. S. Eikenberry. A New Search Technique for Short Orbital Period Binary Pulsars. *ApJ*, 589:911–920, June 2003. doi: 10.1086/374806.
- R. W. Romani. Model atmospheres for cooling neutron stars. *ApJ*, 313:718–726, Feb. 1987. doi: 10.1086/165010.
- R. W. Romani. Gamma-Ray Pulsars: Radiation Processes in the Outer Magnetosphere. *ApJ*, 470:469–+, Oct. 1996. doi: 10.1086/177878.
- M. A. Ruderman and P. G. Sutherland. Theory of pulsars - Polar caps, sparks, and coherent microwave radiation. *ApJ*, 196:51–72, Feb. 1975. doi: 10.1086/153393.
- E. Schreier, R. Levinson, H. Gursky, E. Kellogg, H. Tananbaum, and R. Giacconi. Evidence for the Binary Nature of Centaurus X-3 from UHURU X-Ray Observations. *ApJ Letters*, 172:L79+, Mar. 1972. doi: 10.1086/180896.
- D. A. Shaddock. Space-based gravitational wave detection with LISA. *Classical and Quantum Gravity*, 25(11):114012–+, June 2008. doi: 10.1088/0264-9381/25/11/114012.

- S. L. Shapiro and S. A. Teukolsky. *Black holes, white dwarfs, and neutron stars: The physics of compact objects*. 1983.
- A. P. Smale, K. O. Mason, and K. Mukai. The period of the globular cluster X-ray source X1820-303 Confirmation from Ariel V data. *MNRAS*, 225:7P–9P, Mar. 1987.
- I. H. Stairs. Pulsars in Binary Systems: Probing Binary Stellar Evolution and General Relativity. *Science*, 304:547–552, Apr. 2004. doi: 10.1126/science.1096986.
- N. Stergioulas. Rotating Stars in Relativity. *Living Reviews in Relativity*, 6:3–+, June 2003.
- G. H. Stokes, J. H. Taylor, J. M. Welsberg, and R. J. Dewey. A survey for short-period pulsars. *Nature*, 317:787–+, Oct. 1985. doi: 10.1038/317787a0.
- G. H. Stokes, D. J. Segelstein, J. H. Taylor, and R. J. Dewey. Results of two surveys for fast pulsars. *ApJ*, 311:694–700, Dec. 1986. doi: 10.1086/164808.
- P. A. Sturrock. A Model of Pulsars. *ApJ*, 164:529–+, Mar. 1971. doi: 10.1086/150865.
- J. H. Taylor and J. M. Weisberg. Further experimental tests of relativistic gravity using the binary pulsar PSR 1913 + 16. *ApJ*, 345:434–450, Oct. 1989. doi: 10.1086/167917.
- J. H. Taylor, R. N. Manchester, D. J. Nice, J. M. Weisberg, A. Irwin, N. Wex, et al. Obtained using the tempo software package and the JPL DE405 ephemeris, 2010. URL <http://tempo.sourceforge.net/>.
- K. S. Thorne. *Three Hundred Years of Gravitation*. Cambridge University Press, 1987.
- S. E. Thorsett, Z. Arzoumanian, and J. H. Taylor. PSR B1620-26 - A binary radio pulsar with a planetary companion? *ApJ Letters*, 412:L33–L36, July 1993. doi: 10.1086/186933.
- R. C. Tolman. Static Solutions of Einstein's Field Equations for Spheres of Fluid. *Physical Review*, 55:364–373, Feb. 1939. doi: 10.1103/PhysRev.55.364.
- J. Truemper, W. Pietsch, C. Reppin, W. Voges, R. Staubert, and E. Kendziorra. Evidence for strong cyclotron line emission in the hard X-ray spectrum of Hercules X-1. *ApJ Letters*, 219:L105–L110, Feb. 1978. doi: 10.1086/182617.
- C. Van Den Broeck. The gravitational wave spectrum of non-axisymmetric, freely precessing neutron stars. *Classical and Quantum Gravity*, 22:1825–1839, May 2005. doi: 10.1088/0264-9381/22/9/022.
- J. P. W. Verbiest, M. Bailes, W. van Straten, G. B. Hobbs, R. T. Edwards, R. N. Manchester, N. D. R. Bhat, J. M. Sarkissian, B. A. Jacoby, and S. R. Kulkarni. Precision Timing of PSR J0437-4715: An Accurate Pulsar Distance, a High Pulsar Mass, and a Limit on the Variation of Newton's Gravitational Constant. *ApJ*, 679:675–680, May 2008. doi: 10.1086/529576.
- R. V. Wagoner. Conditions for Steady Gravitational Radiation from Accreting Neutron Stars. *ApJ Letters*, 578:L63–L66, Oct. 2002. doi: 10.1086/344502.
- J. M. Weisberg and J. H. Taylor. The Relativistic Binary Pulsar B1913+16: Thirty Years of Observations and Analysis. In F. A. Rasio & I. H. Stairs, editor, *Binary Radio Pulsars*, volume 328 of *Astronomical Society of the Pacific Conference Series*, pages 25–+, July 2005.

## BIBLIOGRAPHY

---

- J. M. Weisberg, J. M. Cordes, S. C. Lundgren, B. R. Dawson, J. T. Despotes, J. J. Morgan, K. A. Weitz, E. C. Zink, and D. C. Backer. Arecibo 1418 MHz Polarimetry of 98 Pulsars: Full Stokes Profiles and Morphological Classifications. *ApJ Supplement*, 121:171–217, Mar. 1999. doi: 10.1086/313189.
- W. A. Wheaton, J. P. Doty, F. A. Primini, B. A. Cooke, C. A. Dobson, A. Goldman, M. Hecht, S. K. Howe, J. A. Hoffman, and A. Scheepmaker. An absorption feature in the spectrum of the pulsed hard X-ray flux from 4U0115 + 63. *Nature*, 282:240–243, Nov. 1979. doi: 10.1038/282240a0.
- R. Wijnands and M. van der Klis. A millisecond pulsar in an X-ray binary system. *Nature*, 394:344–346, July 1998. doi: 10.1038/28557.
- A. Wolszczan. Confirmation of Earth-Mass Planets Orbiting the Millisecond Pulsar PSR B1257+12. *Science*, 264:538–542, Apr. 1994. doi: 10.1126/science.264.5158.538.
- A. Wolszczan and D. A. Frail. A planetary system around the millisecond pulsar PSR1257 + 12. *Nature*, 355:145–147, Jan. 1992. doi: 10.1038/355145a0.
- A. Wolszczan, O. Doroshenko, M. Konacki, M. Kramer, A. Jessner, R. Wielebinski, F. Camilo, D. J. Nice, and J. H. Taylor. Timing Observations of Four Millisecond Pulsars with the Arecibo and Effelsberg Radio Telescopes. *ApJ*, 528:907–912, Jan. 2000. doi: 10.1086/308206.
- M. D. Young, R. N. Manchester, and S. Johnston. A radio pulsar with an 8.5-second period that challenges emission models. *Nature*, 400:848–849, Aug. 1999. doi: 10.1038/23650.
- I. Yusifov and I. Kucuk. Revisiting the radial distribution of pulsars in the Galaxy. *Astron. Astrophys.*, 422:545–553, 2004. doi: 10.1051/0004-6361:20040152.
- V. E. Zavlin and G. G. Pavlov. Modeling Neutron Star Atmospheres. In W. Becker, H. Lesch, & J. Trümper, editor, *Neutron Stars, Pulsars, and Supernova Remnants*, pages 263–+, 2002.
- M. Zimmermann and E. Szedenits, Jr. Gravitational waves from rotating and precessing rigid bodies - Simple models and applications to pulsars. *PRD*, 20:351–355, July 1979. doi: 10.1103/PhysRevD.20.351.

# Acknowledgements

A summer night, more than sixteen years ago, a bright “star”<sup>4</sup> in the constellation of Scorpius sparked my interest in astronomy. I followed astronomy as an ever-exciting and fascinating hobby and passion during my school years and my diploma studies. When I started my doctoral studies, I did not expect that I would end up writing a PhD thesis, which, among other things, reports the discovery of two new radio pulsars. The moment of discovery is a truly great experience; the split second in which one realises to see and know something as first human being is a feeling I will not forget.

I would like to thank my supervisor, Bruce Allen, for making this possible by offering me the chance to work on these very interesting projects and letting me contribute to a fascinating scientific field. I am deeply grateful for his sustained valuable advice and help throughout my PhD studies and most of all for his honest and true interest in my scientific progress. I appreciate the possibilities of travelling to broaden my horizon by meeting other scientists and sharing their knowledge: my observing trip to the Arecibo telescope clearly was one of the highlights of the past years. I am also very grateful for the freedom of research I experienced while working at the AEI.

I am grateful to all PALFA survey collaboration members for their work, advice and help that enabled this thesis and the Einstein@Home search. I would like to thank Jim Cordes, who helped us to kick-start the Einstein@Home search, Julia Deneva, who taught me how to observe pulsars with the Arecibo telescope, and Scott Ransom for quick help with various PRESTO issues. I would like to thank Michael Kramer for co-refereeing this thesis.

I am thankful to all AEI colleagues involved in the radio pulsar search. Their work, coding, and help made it possible: I would like to thank Oliver Bock, Bernd Machenschalk, Chris Messenger, Holger Pletsch, and Reinhard Prix. My thanks go to Carsten Aulbert and Henning Fehrmann for their support and help with making effective use of the ATLAS cluster and other computer things.

I also would like to thank the tens of thousands of Einstein@Home volunteers whose interest in science and donation of computing cycles enabled this work.

I want to thank my office mates, with whom I shared the various offices I stayed in during my PhD studies. I stopped counting at some point, but I think I moved office five or more times as our division of the AEI grew. For enjoyable working days, inspiration, and enlightening scientific discussions, I would like to thank my fellow PhD students and office mates Pablo Rosado, Holger Pletsch, Dipongkar Talukder, David Keitel, Berit Behnke, Karl Wette, Ajith Parameswaran, Letizia Sammut, and Shaon Gosh<sup>5</sup>.

I am grateful to my family for their constant support and encouragement. I thank my parents for arousing my curiosity to anything in nature when I was a child and answering my countless questions with patience. Most of all, I thank Silke for her love and support.

---

<sup>4</sup>As it turned out, that “star” actually was the giant gas planet Jupiter and also that I was one year late to watch the impact of comet Shoemaker-Levy 9 on that same planet...

<sup>5</sup>Names are in order of the corresponding MD5 hashes.



# Curriculum Vitae

**Benjamin Knispel**

Name

2007 – 2011

Doctoral Studies, International Max Planck Research School on Gravitational Wave Astronomy, Max Planck Institute for Gravitational Physics (Albert-Einstein-Institut Hannover) and Leibniz Universität Hannover, Germany

2006 – 2007

Diploma in Physics, Institute for Theoretical Physics, Leibniz Universität Hannover, Germany

2002 – 2006

Diploma studies in Physics, Leibniz Universität Hannover, Germany

2001 – 2002

Civilian Service

2001

Abitur, Gymnasium Grossburgwedel, Germany

Großburgwedel

Place of birth

February 23, 1983

Date of birth



# List of publications

The work in this thesis is based on and has been published in the publications listed here.

## Refereed publications

---

1. **B. Knispel** and B. Allen, *Blandford's argument: The strongest continuous gravitational wave signal*, **Phys. Rev. D** 78, 044031 (2008)
2. **B. Knispel**, B. Allen, J. M. Cordes, J. S. Deneva, D. Anderson, C. Aulbert, N. D. R. Bhat, O. Bock, S. Bogdanov, A. Brazier, F. Camilo, D. J. Champion, S. Chatterjee, F. Crawford, P. B. Demorest, H. Fehrmann, P. C. C. Freire, M. E. Gonzalez, D. Hammer, J. W. T. Hessels, F. A. Jenet, L. Kasian, V. M. Kaspi, M. Kramer, P. Lazarus, J. van Leeuwen, D. R. Lorimer, A. G. Lyne, B. Machenschalk, M. A. McLaughlin, C. Messenger, D. J. Nice, M. A. Papa, H. J. Pletsch, R. Prix, S. M. Ransom, X. Siemens, I. H. Stairs, B. W. Stappers, K. Stovall, and A. Venkataraman, *Pulsar Discovery by Global Volunteer Computing*, **Science**, 329, 5997 (2010)
3. **B. Knispel**, P. Lazarus, B. Allen, C. Aulbert, N. D. R. Bhat, O. Bock, S. Bogdanov, A. Brazier, F. Camilo, S. Chatterjee, J. M. Cordes, F. Crawford, J. S. Deneva, G. Desvignes, H. Fehrmann, P. C. C. Freire, D. Hammer, J. W. T. Hessels, F. A. Jenet, V. M. Kaspi, M. Kramer, J. van Leeuwen, D. R. Lorimer, A. G. Lyne, B. Machenschalk, M. A. McLaughlin, C. Messenger, D. J. Nice, H. J. Pletsch, R. Prix, S. M. Ransom, X. Siemens, I. H. Stairs, B. W. Stappers, K. Stovall, and A. Venkataraman, *Arecibo PALFA Survey and Einstein@Home: Binary Pulsar Discovery by Volunteer Computing*, **The Astrophysical Journal Letters**, 732, 1, L1 (2011)

## Publications in preparation and popular science publications

---

1. **B. Knispel**, *Gravitar Population Modelling and Detection Predictions for LIGO Searches*, to be submitted to **Phys. Rev. D**
2. **B. Knispel**, *Pulsare mit dem Heimcomputer entdeckt!*, **Sterne und Weltraum**, 12/2010 (2010)